S J CRIMP
S C VAN DEN HEEVER
P C D'ABRETON
P D TYSON
S J MASON

MESOSCALE MODELLING OF TROPICAL-TEMPERATE TROUGHS AND ASSOCIATED SYSTEMS OVER SOUTHERN AFRICA

Report to the
WATER RESEARCH COMMISSION
by the
CLIMATOLOGY RESEARCH GROUP
UNIVERSITY OF THE WITWATERSRAND

Report No : 595/1/97
ISBN No : 1 86845 315 4

Executive Summary

Tropical-temperate troughs and their associated cloud bands are important contributors to late summer rainfall over southern Africa. These structures have been observed in both the northern and southern hemispheres, and are thought to facilitate the poleward flow of energy and momentum from the tropics to the mid-latitudes along the leading edge of the upper westerly waves. Variability in southern African rainfall during January to March is caused primarily by changes in the position, frequency and intensity of tropical-temperate troughs. The troughs tend to be situated over the interior during wet summers and displaced east and are weaker during dry summers. Such variability exerts a significant influence on whether the late summer season over the subcontinent is to be wet or dry, an important consideration for semi-arid to arid southern Africa.

Research into southern African tropical-temperate troughs has been hindered by the scarcity of data over the subcontinent and adjacent oceans. Such a problem can be alleviated to a degree by the application of a suitable mesoscale numerical model, which allows for an investigation into tropical-temperate trough systems on a finer grid resolution than is provided by the current data network. The importance of the factors controlling tropical-temperate trough development and dissipation can be determined through sensitivity experiments that identify important variables by allowing the modification and addition of specific variables. Despite the importance of tropical-temperate troughs to southern African rainfall, these systems have not been previously simulated. Numerous observations and hypotheses regarding the kinematic, thermodynamic and moisture characteristics of tropical-temperate troughs during wet and dry periods have been made with the use of station data and global data sets, but require further substantiation. The same can be said for the identification of major vapour sources and sinks surrounding southern Africa. Through the use of the Regional Atmospheric Modelling System (RAMS) and a Lagrangian Trajectory Model such hypotheses can be tested. Two case studies were selected for modelling and analysis. The first involved a tropical-temperate trough that formed across the subcontinent over the period 21-24 January 1981 and immediately preceded the development of a cut-off low that was responsible for widespread rains across the subcontinent. The second case

study involved a tropical-temperate trough that formed during the period 6-8 January 1980 and was found predominantly to the east of the subcontinent. Southern Africa experienced generally dry conditions except in the northeast where the tropical anchor-point for the trough was situated over central Mozambique. The use of RAMS provided accurate simulations of circulation conditions for the wet and dry case studies investigated and provided new insights into the structure and evolution of tropical-temperate troughs as well as new characteristics of the Walker circulation. Sensitivity experiments were conducted to determine the effects of a finer grid resolution, change in soil moisture, the inclusion of resolvable microphysics and the addition of sea-surface temperature anomalies on tropical-temperate trough development. The analysis of these experiments has contributed significantly to an improvement in the understanding of the structure and dynamics of tropical-temperate troughs in the Southern African region. Backward and forward Lagrangian trajectory modelling of rain and no-rain days over the central interior of South Africa in mid-summer highlight the major sources of moisture for the development of large scale synoptic features. No-rain days (rain days) are shown to be characterised by dry (moist) southwesterly (northerly to northeasterly) flow originating over the South Atlantic (tropical Indian) Ocean. Air parcels for tropical-temperate troughs originate over the tropical Indian Ocean and trace south and southeastwards across southern Africa, corresponding closely to the position of the trough-associated cloud band. Trajectory modelling of a cut-off low pressure system reveals the presence and interaction of a cold, dry, descending conveyor from the south and a warm, moist, ascending conveyor from the north.

The project has enabled the development of skills and resources in two significant areas, namely mesoscale and lagrangian trajectory modelling. These tools and skills have provided an enhancement of understanding of the structure and dynamics of important rainfall-producing systems over southern Africa that could be used effectively in future modelling work. The synthesis of knowledge provided by this project should facilitate improvements in the forecasting of the development and dissipation of tropical-temperate troughs and hence of rainfall over southern Africa. The development of the mesoscale modelling capability has enabled the definition of important differences between wet and dry tropical temperate trough cases. During dry cases a northward displacement of the tropical low and of the westerlies, and an eastward displacement of the sub-tropical trough are indicated. The mesoscale model used did not show a high sensitivity to soil moisture or sea-surface temperature anomalies, but did indicate changes in the boundary layer that are consistent with expected climatic responses to surface anomalies. The lagrangian trajectory model has been developed at the Climatology Research Group and has been successfully used in the identification of major moisture streams feeding rain-producing systems over southern Africa. It has been confirmed that the main source of moisture is from the north-easterly flow originating over the tropical western Indian Ocean, while the south-west Indian Ocean acts as a secondary source. A number of additional applications for the trajectory model have been identified and successfully implemented, including transport modelling of atmospheric pollutants and validation of rainfall forecasts by numerical models. Given the contributions to the enhancement of understanding by the modelling facilities that have been developed in this project, additional applications should be encouraged and alternative mesoscale models should be implemented. This should provide progress in the understanding of the dynamics of the atmosphere and ultimately should enable improvements in the accuracy of rainfall forecasts in the region.

Parts of Chapters 4,5,7,8 and 9 were presented at the Tenth, Eleventh, Twelfth and Thirteenth South African Society of Atmospheric Science annual conferences. The presentation at the Tenth annual meeting received the award for the best paper presented by a junior scientist. Chapter 7 has been published in the South African Journal of Science, January 1997, and Chapter 10 appears in WaterSA in volume 22 dated October 1996. ECMWF and NMC data sets were obtained from the National Centre for Atmospheric Research (NCAR). Sea-surface temperatures were acquired from the Meteorological Office Historical sea-surface temperature data set supplied by the United Kingdom Meteorological Office. Upper air data, rainfall figures, and synoptic and upper air charts were all supplied by the South African Weather Bureau, and Mrs Glenda Swart is thanked for all her help in this regard. All the RAMS simulations were performed on the Cray YMP and EL at the South African Weather Bureau, without which this project would not have been possible. Thanks are also extended to Professor W.R. Cotton for allowing the use of facilities at Colorado State University, and to Dr Bob Walko for patiently answering many questions. Further gratitude is extended to Dr Noel De Villiers for his invaluable help. Finally, a special thanks must go the Water Research Commission for their generous funding of the project.

CONTENTS

CHAPTER 1

BACKGROUND

Introduction

The growing population of arid to semi-arid southern Africa is placing increasing pressure on already limited water resources. A large majority of the population rely on agriculture at a subsistence level for food, or at a more advanced level to generate income, and are therefore particularly susceptible to changes in rainfall and climate. This problem is exacerbated by the high degree of inter- and intra-annual rainfall variability over the southern African subcontinent which results in wet or dry periods ranging from weeks to years in duration. Improving the understanding and methods of prediction of the rainfall systems affecting southern Africa will be of great assistance to engineers, hydrologists and agriculturalists in the planning and development of effective water management policies.

Rainfall over southern Africa is strongly seasonal, reaching a maximum during summer (October to March) over most of the subcontinental interior (Jackson, 1961; Tyson, 1986; Nicholson *et al.*, 1988; Lindesay, 1993) (Fig. 1.1). During the last two decades, rainfall variability over southern Africa has been extensively studied. Temporal variations in rainfall on an intra- and inter-annual scale (Taljaard, 1958, 1986; Triegaardt and Kits, 1963; Hofmeyr and Gouws, 1964; Tyson *et al.*, 1975; Tyson and Dyer, 1978, 1980; Tyson, 1981, 1984, 1986; Miron and Lindesay, 1983; Miron and Tyson, 1984), as well as spatial variations ranging from the regional scale (Estié, 1981;Tyson, 1981, 1984, 1986; Miron and Tyson, 1984; Taljaard, 1985; Lindesay and Jury, 1991; D'Abreton and Lindesay, 1993) to the hemispheric scale (Dyer and Tyson, 1978; Dyer, 1979; Harrison, 1986a; Lindesay *et al.*, 1986; Nicholson, 1986, Lindesay, 1988a) have been investigated. The effects of circulation changes on rainfall have likewise been examined (Harangozo and Harrison, 1983; Harrison, 1983a, 1986a; Lindesay *et al.*, 1986; Lindesay, 1988a; Lindesay and Jury, 1991; Matarira and Jury, 1992; D'Abreton and Lindesay, 1993; D'Abreton and Tyson, 1994).

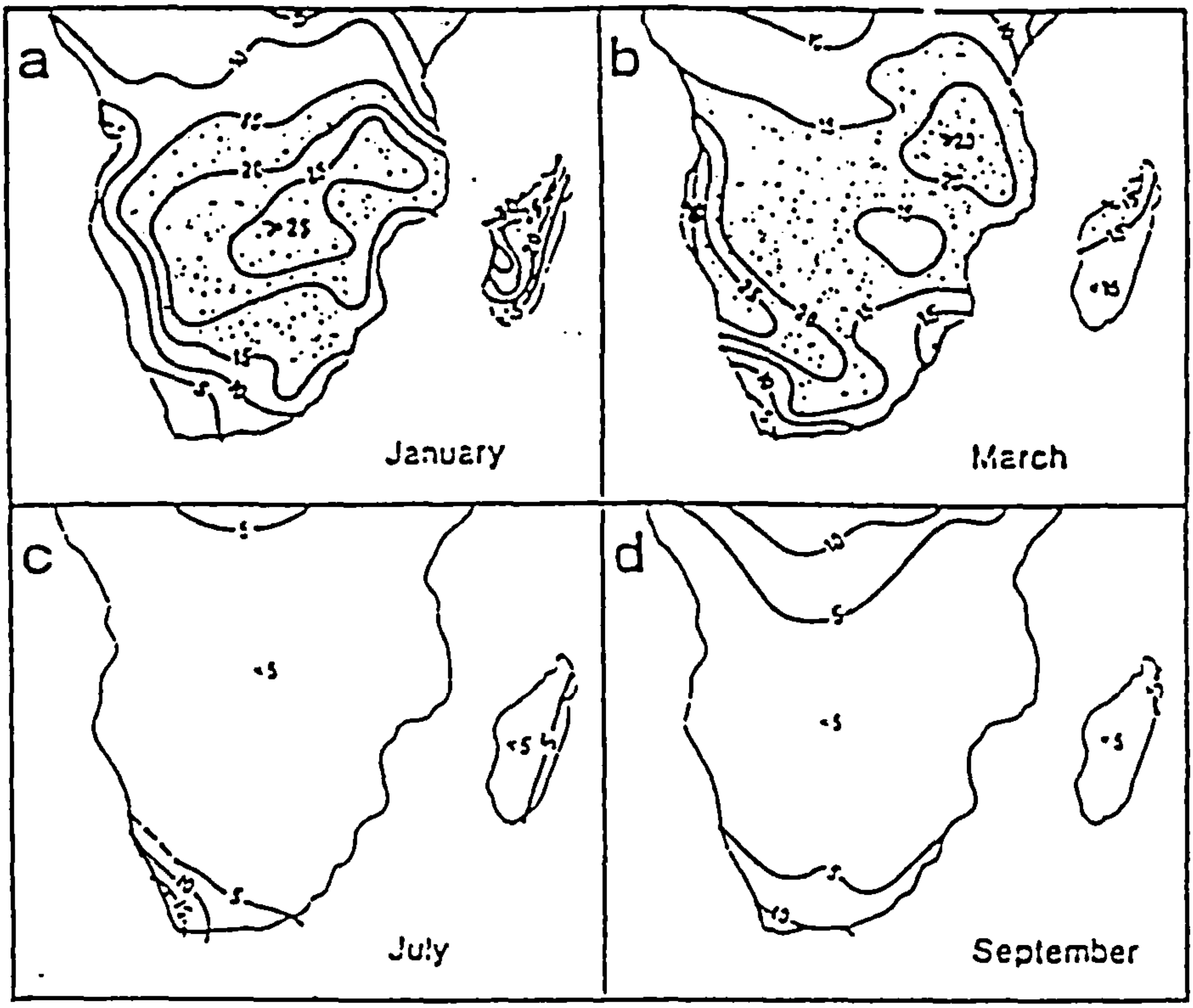

Figure 1.1: Monthly rainfall as a percentage of the annual total, in (a) January, (b) March, (c) July and (d) September (after Jackson, 1961). Areas where more than 15 per cent of annual rainfall is received in any month are shaded.

The Climate of Southern Africa

The climate of South Africa (20 -35^{0}S, 18 -30^{0}E) is influenced by three main physical factors, the most important of which is the orography (Tyson, 1986; Harrison and Theron, 1991; Lindesay, 1993). The escarpment, which exceeds 3000 metres in places, separates most of the interior plateau with an average elevation of 1600 metres, from the relatively narrow, low-lying coastal regions (Fig. 1.2). The mechanical influences of this topography include the frictional effects on airflow, the forcing of coastal disturbances by the trapping of Kelvin waves (de Wet, 1979; Bannon, 1981), topographically-forced vertical motions (Tyson, 1964; Vianello, 1985), barrier formation of coastal jets (Kelbe, 1988) and the enhancement of convection near the escarpment (Garstang *et al.*, 1987). Monthly mean temperature and pressure fields over southern Africa are substantially modified through spatial differences in surface heat fluxes (Theron and Harrison, 1990) and local aridity occurs in most of the major deep river valleys of southern Africa (Tyson, 1986). Rainfall is highest along the eastern side of the escarpment and decreases on the leeward slope and toward the western interior (Tyson, 1986; Lindesay, 1993). The atmospheric circulation, and hence the rainfall over the southern African region, are substantially affected by the land mass.

The oceans and currents surrounding southern Africa are likewise important factors affecting the climate of the region (Fig. 1.2). Sea surface temperatures in the warm Mozambique and Agulhas currents to the east of the subcontinent vary between 22 and 28^{0}C in summer, while those in the cold Benguela current to the west of South Africa are seldom greater than 16^{0}C (Shannon, 1985; Walker, 1989; Lindesay, 1993). Air temperature and moisture availability are influenced by these currents (Walker and Lindesay, 1989). The eastern coast of South Africa receives the highest rainfall where sea surface temperatures and evaporation are high. Lowest precipitation over the subcontinent falls over the west coast as a result of lower sea surface temperatures and lower evaporation (Walker, 1989).

Southern Africa's position in relation to the tropical, subtropical and mid-latitude pressure regimes is an important factor influencing the climate of the subcontinent (Fig. 1.3) (Tyson, 1986; Lindesay, 1993). The thermally-direct Hadley cell and the thermally-indirect Ferrel cell both descend in the subtropics, resulting in the quasi-stationary subtropical high pressure belt. The positions of the South Atlantic and South Indian Anticyclones within this zone of high

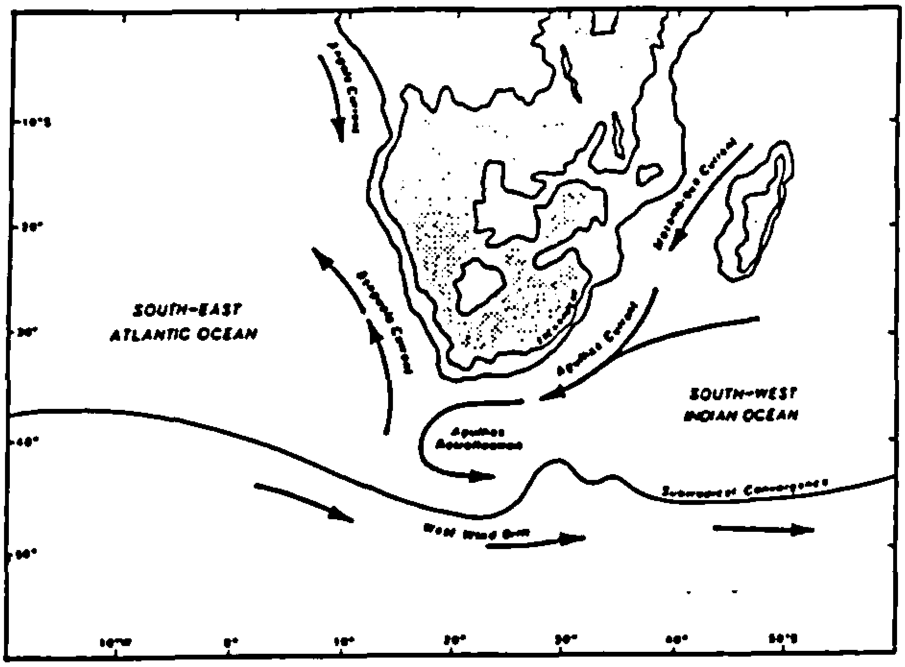

Figure 1.2: Physical features of the southern African region. Shading indicates relief greater than 1000 metres and major oceanographic currents are indicated (after Lindesay, 1993)

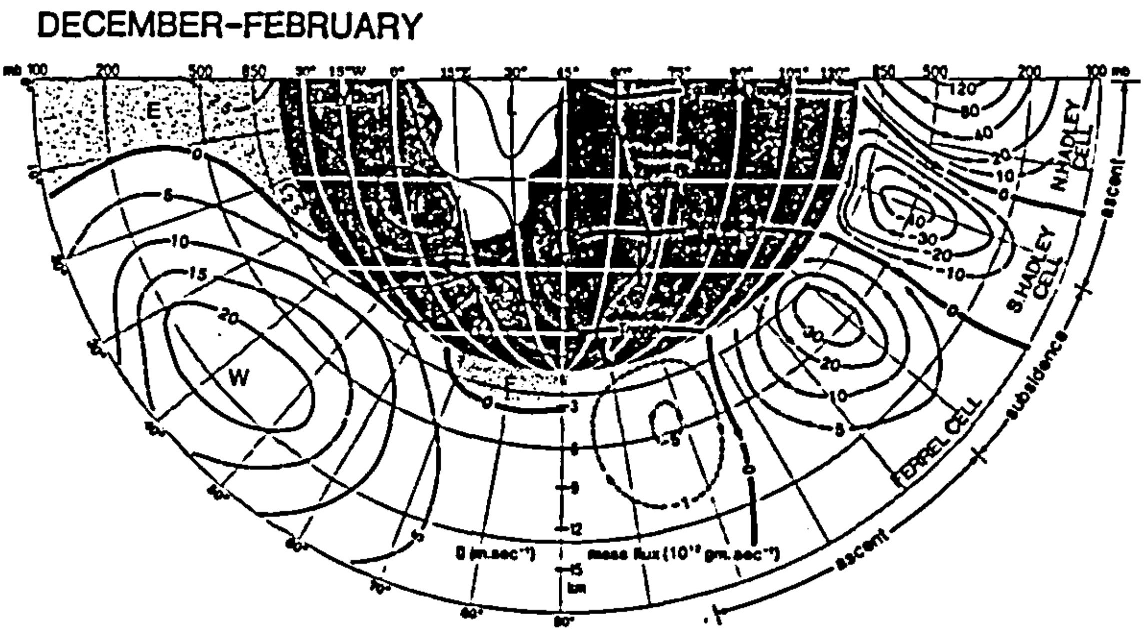

Figure 1.3: Mean December to February zonal wind and mass flux in the Southern Hemisphere (after Tyson, 1986 - data taken from Newell *et al.*, 1972).

pressure vary throughout the year (Tyson, 1981, 1984). Ridging of the South Atlantic Anticyclone to the south of South Africa in summer accounts for 16 to 25 per cent of the rainfall variance over the region (Tyson, 1984). The proximity of the South Indian Anticyclone to the southern African coast influences the amount of maritime moisture transported over the escarpment to the interior. The anticyclone affecting the winter climate of southern Africa has been attributed to an independent cell of high pressure (Streten, 1980), caused by subsiding air originating in the monsoon system of Asia (Harrison, 1986a; 1993; Tyson, 1986; Lindesay, 1993). To the south of the subtropical high pressure belt, mid-latitude depressions are driven eastward by the circumpolar westerlies. The position of the mid-latitude depressions is controlled by the seasonal displacement of the high pressure belt and mainly affect the southwestern regions of South Africa in winter when they track five to ten degrees further north than in summer (Tyson, 1986). To the north of the subtropical belt a zone of easterly waves and tropical lows supply the northern regions of southern Africa with tropical moisture and heat. At the 850 and 500 hPa levels, tropical easterly waves account for between 16 and 49 per cent of the rainfall variance over the northeastern interior of South Africa (Tyson, 1984).

In summer, the low-level, recurved southwesterly South Atlantic air at 12°S, the northeasterly monsoon that moves south across the equator from the northeast and the deep tropical easterlies from the South Indian Ocean all converge north of about 20°S in the Inter-Tropical Convergence (Fig. 1.4) (Taljaard, 1972; Torrance, 1972, 1979; Tyson, 1986; Lindesay, 1993). The Inter-Tropical Convergence is a zone of pronounced convective activity and high latent heat release, and undergoes a seasonal migration, being situated north of the equator in the austral winter and south in the austral summer (Von der Haar, 1968; Webster, 1972; 1983; Tyson, 1986). The Zaïre Air Boundary, another zone of convergence, forms where tropical easterlies from the South Indian Ocean and recurved southwesterlies from the South Atlantic Ocean converge over southern Angola and northern Namibia and Botswana (Fig. 1.4). This region was found to be a preferential zone for the development of low pressure systems (Taljaard, 1972). Easterly waves and troughs occasionally extend southward from these semi-stationary lows, often resulting in heavy rainfall over the summer rainfall region (Tyson, 1984, 1986; Lindesay, 1993).

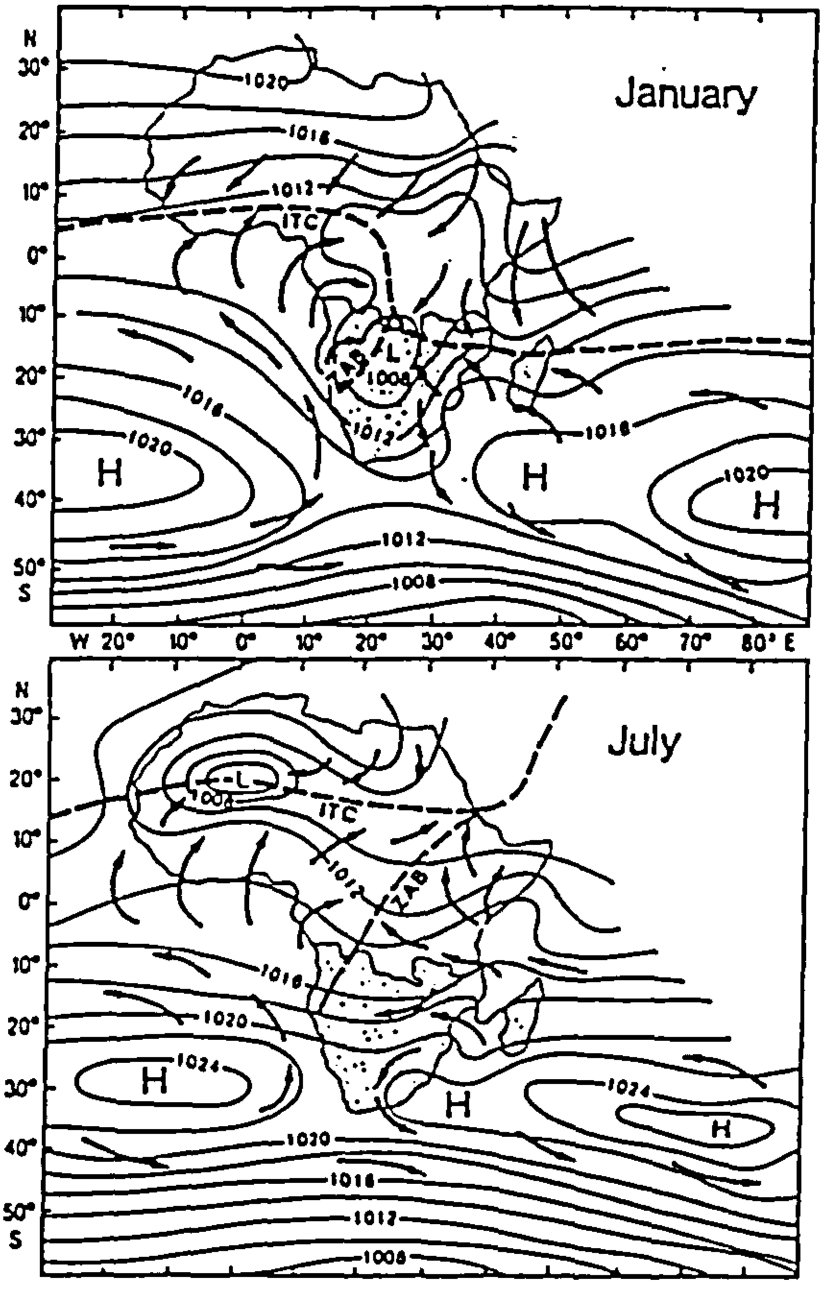

Figure 1.4: Schematic representation of the mean surface pressures, the Inter Tropical Convergence (ITC) and the mean wind directions in January (summer) and July (winter) (after Lindesay, 1993).

Much of the rainfall that occurs in summer, particularly during late summer, results from the interaction of tropical and mid-latitude dynamic systems (Webster, 1983; Harrison, 1986a; Harangozo, 1989; Lyons, 1991). The influence of the equatorward penetration of mid-latitude disturbances on diabatic heating in the tropics and the importance of the effects that tropical disturbances have on mid-latitude systems have been stressed (for example, Horel and Wallace, 1981; James and Anderson, 1984; Hastenrath, 1985; Harrison, 1986a; D'Abreton and Lindesay, 1993). During the last decade, tropical-temperate interactions over southern Africa have received an increasing amount of investigation (Harangozo and Harrison, 1983; Harrison, 1984b, 1986a, 1986b; Harangozo, 1989; Lindesay and Jury, 1991; Matarira and Jury, 1992; D'Abreton, 1992; Jury *et al.*, 1993; D'Abreton and Tyson, 1994; Jury and Lyons, 1994). The system that forms when tropical and temperate synoptic systems interact and become linked by a zone of effectively organised convection, has been classified by Harrison (1986a) as a tropical-temperate trough.

Tropical-Temperate Troughs

Numerous attempts have been made to develop a synoptic classification of the summer rainfall-producing systems over southern Africa. Early classifications (for example, Bergeron, 1930; Dubief and Queney, 1935; Vowinckel, 1955, 1956; Taljaard, 1959; Longley, 1976) were based on surface data alone and failed to include any synoptic forcing in the upper air. These classifications also tended to be locally focused. The need to include upper air forcing led to the development of more generalised classification schemes based on satellite-observed cloud patterns (Harangozo and Harrison, 1983; Harrison, 1984a, 1984b; Tyson, 1986). A synoptic classification of diurnal rainfall events in Natal has also been developed (Preston-Whyte *et al.*, 1991). In all the recent classifications of summer rainfall-producing systems which include upper level forcing, tropical-temperate troughs have been identified as the systems contributing substantially more to the rainfall over southern Africa than any other (Erasmus, 1980; Harrison, 1984a, 1984b; Tyson, 1986; Preston-Whyte *et al.*, 1991). Tropical-temperate troughs are zones of enhanced convergence that link tropical and temperate circulation systems and are represented by long cloud bands on satellite imagery. Much of the rainfall variability over southern Africa, particularly during late summer (January to March), has been attributed to differences in the frequency of tropical-temperate trough formation (Harrison, 1986a; Tyson, 1986). These systems have also been associated with major flood events over the subcontinental interior (Lindesay and Jury, 1991). The first stage of any research attempting to model and predict important rainfall systems over southern Africa should concentrate on the structure, development and controls of tropical-temperate troughs.

Tropical-temperate troughs and their associated cloud bands form frequently in numerous parts of the world (Streten, 1968, 1973; Yasunari, 1977; Vincent, 1982; Kuhnel, 1989) and have been referred to in the past as 'cloud surges' (Anderson and Oliver, 1970), 'jetstream associated cloudbands' (De Felice and Viltard, 1976), 'shear bands' (Zwatz-Meise and Hailzl, 1980), 'moisture bursts' (McGuirk *et al.*, 1987), 'tropical-extratropical cloudbands' (Kuhnel, 1989, 1990) or simply 'cloud bands' (Bell, 1986; Wright, 1988). The use of satellite data to investigate phenomena such as the water vapour mass distribution above 500 hPa (Raschke and Bandeen, 1967), or the mean cloudiness distribution (Sadler, 1968), gave rise to an initial description of the average climatological positions of major cloud bands over the South Pacific and the western South Atlantic. Specific investigations into the occurrence and development of these phenomena then followed. It was observed that cloud bands normally occur when an upper tropospheric trough approaches the equator (Anderson and Oliver, 1970), that they extend from tropical storms poleward into the Northern Hemisphere westerlies (Erickson and Winston, 1972), that cloud band locations in the Southern Hemisphere are associated with the tracks of depressions and regions of persistent convection (Streten, 1968, 1973) and that cloud bands are generally closely related to the long-wave hemispheric pattern (Streten, 1968, 1973). From these observations it was suggested that cloud bands are situated eastward of the upper long-wave troughs (Streten, 1973) and are a visible representation of channels between the tropics and mid-latitudes, along which energy in the form of heat and moisture is transported poleward (Erickson and Winston, 1972). The importance of cloud bands in rainfall production and the forecasting difficulties they present, has resulted in intensive investigations into their structure and formation on a global scale (Kuhnel, 1989), in regions of Australia (Downey *et al.*, 1981; Bell, 1982, 1986; Tapp and Barrell, 1984; Wright, 1988; Kuhnel, 1990), over South America (Gray and Clapp, 1978; Kousky, 1979; Paegle *et al.*, 1983; Kalnay and Paegle, 1983; Kousky *et al.*, 1983; Virji and Kousky, 1983), in the North Pacific Ocean (McGuirk *et al.*, 1987) and over southern Africa (Harangozo and Harrison, 1983; Harrison, 1984a, 1984b, 1986a; Smith 1985; Harangozo, 1989; Lindesay and Jury, 1991; D'Abreton, 1992).

The definitions of what constitutes a cloud band are all similar. According to Streten (1973), a cloud band has to cross at least 20 consecutive lines of latitude and be at least five degrees wide on average. Harrison (1986a) states that a tropical-temperate trough must have its origin between the Equator and 20°N or 20°S, a length of at least 25 degrees, a maximal width of five degrees and a more or less homogeneous texture. Kuhnel (1989) adds that cloud bands should be diagonally aligned, crossing at least 10 degrees of longitude. These definitions are similar to those of Bell (1982) and Tapp and Barrell (1984). As the definition of what constitutes a tropical-temperate trough over southern Africa was first outlined by Harrison (1986a), this definition is used.

In a global study of cloud bands (Kuhnel 1989), 14 different zones of cloud band formation were identfied, seven in each hemisphere. Seven regions of regular cloud band formation in the Northern Hemisphere have also been identified by Thepenier (1981). Kuhnel (1989) found that cloud band formation is strongly influenced by intertropical disturbances and the intrusion of extratropical air masses into low latitudes, which are associated with the climatological positions of longwave troughs or with regions where the Inter-Tropical Convergence is displaced into the tropics. The influence of the longwave trough position is predominant in the Northern Hemisphere, whereas the effects of the Inter-Tropical Convergence displacements are more significant in the Southern Hemisphere. This explains why the majority of cloud bands are winter phenomena in the Northern Hemisphere but form more frequently in summer in the Southern Hemisphere. Kuhnel (1989) also found that cloud band development is influenced by anomalous changes in mean sea level pressure and sea surface temperatures, and that band frequency in most regions of the world correlates significantly with the Southern Oscillation Index.

The cloud bands over Australia, unlike most of their Southern Hemisphere counterparts, occur most frequently from mid-Autumn to early-Spring (Tapp and Barrell, 1984), when they account for approximately 68 per cent of the annual cloud band frequency (Kuhnel, 1990). These bands are referred to in the literature as the Northwest Australian Cloud Band and generally have a duration of one to four days (Tapp and Barrell, 1984; Bell, 1986; Wright, 1988). Extensive rain over inland and eastern Australia and about half of the total winter rainfall in northern Victoria result from the Northwest Australian Cloud Bands which may be thousands of kilometres long and only a few hundred kilometres wide. Northwest Australian Cloud Bands extend in a northwest-southeast direction from a tropical cloud cluster over the eastern South Indian Ocean to the mid-latitudes (Tapp and Barrell, 1984; Bell, 1986; Wright, 1988; Kuhnel, 1990). The cloud bands that occur over Australia during summer most often originate from tropical cyclones over western and northern Australia and are normally associated with the western North Pacific cloud bands described by McGuirk *et al.* (1987). Occasionally, summer cloud bands over Australia originate from a large-scale region of low pressure related to the monsoon over northern Australia (Kuhnel, 1990).

Northwest Australian Cloud Bands normally originate to the east of a large amplitude trough off the western coast of Australia in low latitudes and develop progressively southeastward. The main features associated with the Northwest Australian Cloud Band are schematically illustrated in Figure 1.5a. They are formed by the gradual ascent of moist tropical air along sloping isentropic surfaces in regions of strong baroclinicity. These regions develop when tropical air is advected southwestward in the easterly wave and subpolar air northward in the westerly wave (Bell, 1986; Wright, 1988). The isentropic surfaces slope upwards along the cloud band. They are lowest in the northwest and highest in the southeast. They also slope across the band where they are lower on the warm, northeast side and higher on the cold, southwest side (Bell, 1986). The cloud edge is sharpest and highest on the southern, cold side of the band in the region of maximum baroclinicity and the cloud and cloud heights increase along the band in a poleward direction (Bell, 1986). The jetstream that often occurs simultaneously with the Northwest Australian Cloud Band appears to be enhanced by the zones of marked baroclinicity. Cut-off lows have also been associated with cloud bands over Australia (Kuhnel, 1990). The low frequency of significant cloud bands over Australia during summer is probably due to reduced baroclinicity as a result of the reduced meridional thermal gradients between the sub-polar and tropical air (Tapp and Barrell, 1984).

There is some disagreement on the importance of convective activity in the development of Australian cloud bands. Convective activity on the equatorward side of the band has been suggested as a means of injecting moisture into the mid-troposphere from where it is then

a

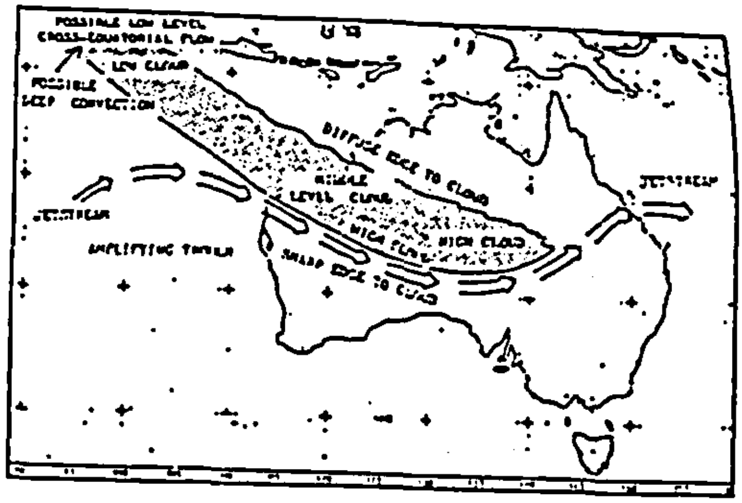

b

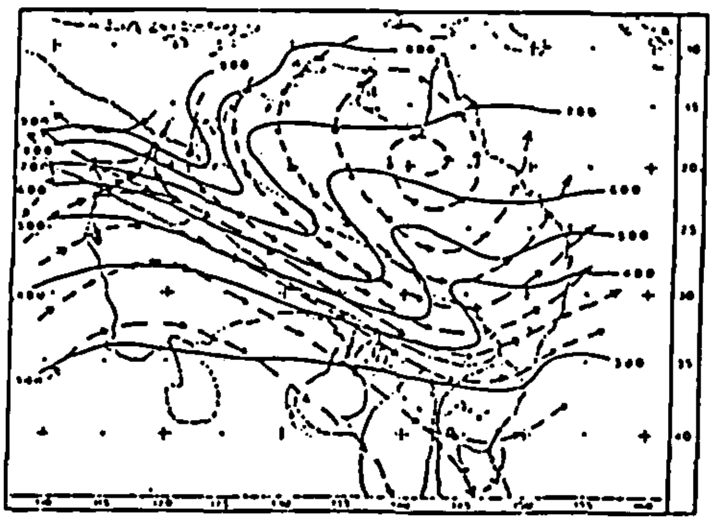

Figure 1.5: (a) Schematic representation of the main features associated with a typical Northwest Australian Cloud Band (after Bell, 1986); and (b) pressure surfaces associated with the 16°C wet bulb potential temperature surface on 27 July 1980 (after Bell, 1986). Pressures are in hPa.

advected southeastward along the band (Whitaker, 1981). Tapp and Barrell (1984) observed that although convective activity is often present, it is not always so, and cannot be considered as a prerequisite for band formation. Kuhnel (1990) observed that 85 per cent of all the cloud bands, and 73 per cent of winter occurrences, had convective activity occurring at the cloud band origin, and stresses the importance of convective activity in cloud band development. Others have suggested that the convection in the equatorward region of the cloud band is most likely due to the same mechanism as that causing the cloud band (Bell, 1986; Wright, 1988).

An analysis of wet bulb potential temperatures associated with Northwest Australian Cloud Bands has revealed a tongue of warm, moist air aligned in a northwest-southeast direction. This indicates that even though ascent is taking place in the cloudy air, the advection of moist air from the tropics is of great importance (Bell, 1986) (Fig. 1.5b). The importance of the poleward moisture advection along the isentropic surfaces is supported by the height of the cloud tops which varied from 480 hPa at the northwest coast to 300 hPa at the southern end of the band, despite the wet bulb potential temperature being almost constant (Bell, 1986). Northwest Australian Cloud Bands over Victoria also normally consist of middle to upper level clouds (Wright, 1988). Exceptionally high surface dew point temperatures (15 to 20^{0}C) suggest that very moist air is entering the system from the north and northwest. The moisture source for the Northwest Australian Cloud Bands therefore seems to be in the boundary layer equatorward of the band, where moist trade wind air ascends in the cloud band (Bell, 1986; Wright, 1988).

The amount of rainfall produced by Australian cloud bands has been found to be linked to the Southern Oscillation. During the 1979 to 1983 period, 50 per cent of the cloud bands during wet years could be expected to produce substantial rainfall, whereas during dry years this figure dropped to between 14 and 25 per cent (Kuhnel, 1990). The frequency and intensity of cloud band activity is also related to tropical sea surface temperature and mean sea level pressure anomalies (Wright, 1988; Kuhnel, 1990), the latter appearing to be the more predominant influence (Kuhnel, 1990). Anomalously low convection in the eastern South Indian Ocean is associated with lower cloud band activity and lower rainfall production (Kuhnel, 1990).

Bands of middle and high clouds over the North Pacific Ocean have been found to be extremely common (McGuirk *et al.*, 1987). They last on average 2,5 days, but maximum durations of about 10 days have been observed. The North Pacific cloud bands, like their Australian counterparts, have also been found to be related to sea-surface temperature anomalies and the Southern Oscillation El Niño phenomenon (McGuirk *et al.*, 1987). The frequency of North Pacific cloud bands has been found to increase when the Inter-Tropical Convergence is weakest. The Hadley circulation has been found to be significantly stronger during cloud band days than during the five day periods preceding these events. However, the Hadley circulation also strengthened during days when cloud bands were not present and the relationship between the North Pacific cloud bands and the Hadley circulation is not clear (McGuirk *et al.*, 1987). A connection between the Hadley circulation and the Northwest Australian Cloud Band appears to exist during winter (Kuhnel, 1990).

The South American cloud band occurs predominantly in summer months (Kousky *et al.*, 1983). They form when mid-latitude frontal systems penetrate into the Inter-Tropical Convergence in lower latitudes and result in the organisation and enhancement of convection over tropical South America (Virji and Kousky, 1979; McGuirk *et al.*, 1987). The mid-latitude trough is thought to accelerate the upper level flow, thus strengthening upper air divergence, which enhances convergence and convection in lower levels and strengthens the meridional flow (Virji and Kousky, 1979; McGuirk *et al.*, 1987). Cold fronts associated with the cloud bands also enhance convection by increasing low-level convergence. The Andes may be important in the initial organisation of a region of enhanced convection (Virji and Kousky, 1983). The cloud bands over South America appear to represent local amplifications of the Hadley circulation and have been found to be important in the redistribution of energy, mass and momentum poleward (Virji and Kousky, 1983; McGuirk *et al.*, 1987).

Cloud bands that form in the preferred locations of the Southern Hemisphere have numerous characteristics in common. They all contribute significantly to the regional rainfall and variations in their position and frequency affect the rainfall distribution over the region. All cloud bands are found to link temperate and tropical circulation regimes and appear to facilitate the transport of energy and momentum from the tropics to the mid-latitudes. All form eastward of upper air, semi-stationary long waves in the atmosphere. These long waves may be orographically forced (Palmén and Newton, 1969; Mechoso, 1981) or thermally forced

(Webster and Holton, 1982; Webster, 1983), and enhance the formation of cloud bands. The need for a region of strong baroclinicity in the formation of the Australian cloud bands and the low frequency of these bands during summer, suggest that they are generally orographically forced (Harrison, 1986b). On the other hand, the long waves associated with the South American cloud bands, being driven by regions of strong convection and the resultant intensification of the Hadley circulation, are thought to be mainly thermally forced (Paegle *et al.*, 1983; Paegle and Kalnay, 1983).

Tropical-temperate troughs over southern Africa have been investigated (Harangozo and Harrison, 1983; Harrison, 1984a, 1984b, 1986a; Smith, 1985; Harangozo, 1989; Lindesay and Jury, 1991; D'Abreton, 1992). These systems form when a tropical disturbance such as an easterly low, is linked to a westerly wave or low in the upper atmosphere. Under such conditions an elongated trough extends in a northwest-southeast direction across the subcontinent and the southwest Indian Ocean (Harangozo and Harrison, 1983; Harrison, 1986a). Surface convection and upper air divergence result in ideal conditions for strong vertical uplift and the formation of the cloud bands. Tropical-temperate trough systems contribute about 30 per cent of the October and December rainfall totals, 60 per cent of the January total and about 39 per cent of the mean annual total, making them the single most important contributors to summer rainfall over the central interior (Harrison, 1984a, 1984b, 1986a) (Fig. 1.6). Truncated tropical-temperate troughs and west coast troughs are variants that contribute another 13 per cent to the annual rainfall (Harrison, 1984a, 1984b). Other systems affecting the southern subcontinent do not individually contribute more than 14 per cent to the annual total rainfall over the central interior (Harrison, 1986a). Westerly waves may contribute as much as 24 per cent over Natal (Preston-Whyte *et al.*, 1991). Cloud band contributions to the annual rainfall over Zimbabwe are also substantial (Smith, 1985). These band systems affect African regions as far north as Zambia (Bhalotra, 1973; Kumar, 1978; Acharya and Bhaskara Rao, 1981; Lyons, 1991). Although tropical-temperate troughs are important contributors to rainfall totals in early summer (October to December), frontal bands associated with baroclinic westerly waves of the southern mid-latitudes and cut-off lows are more important during these months (Torrance, 1979; Harrison, 1984a; Smith, 1985; Taljaard, 1985; Kelbe, 1988). Cut-off lows have been the cause of many of the flood events over southern Africa. They are most frequent during March to May and September to November

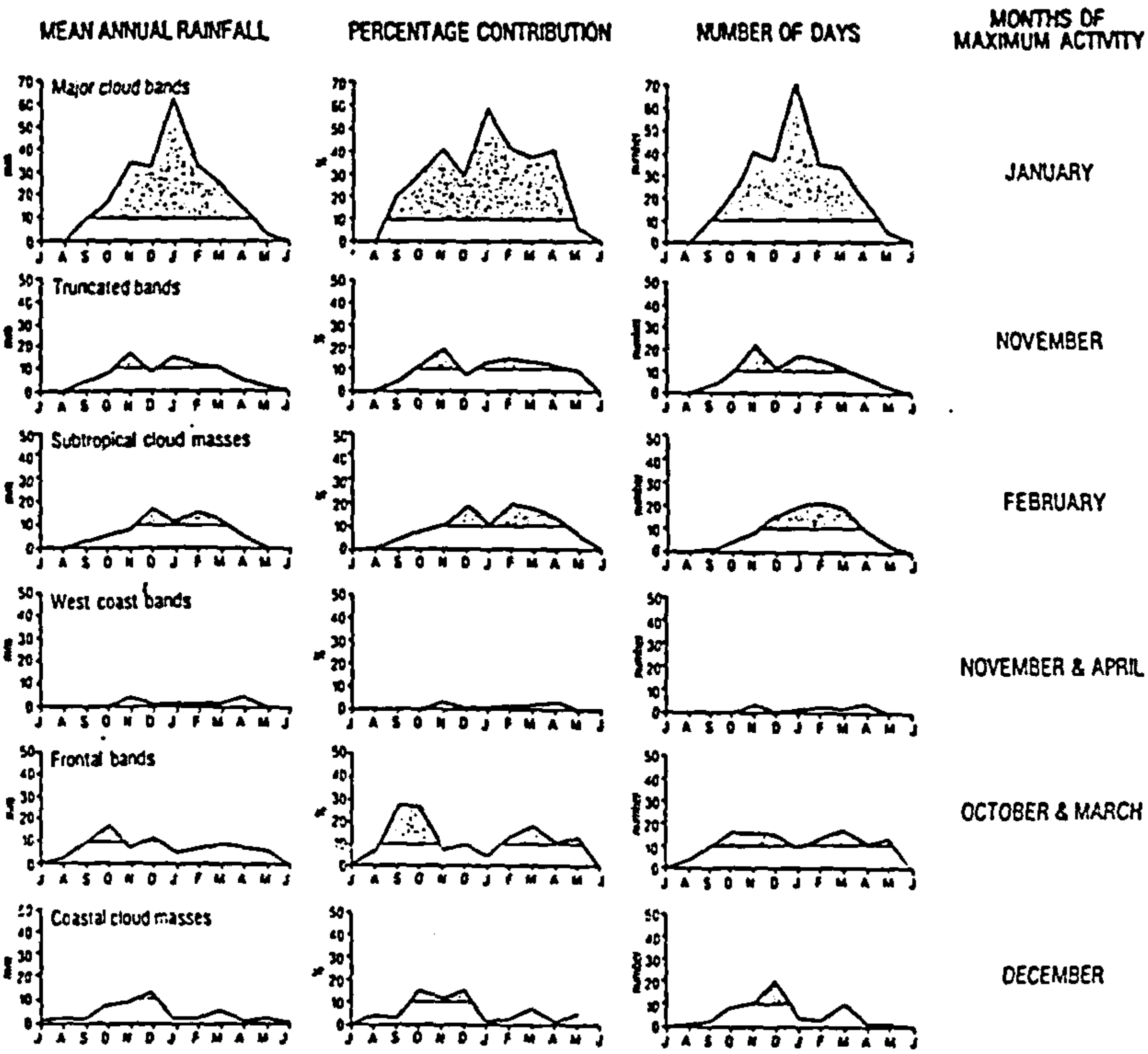

Figure 1.6: Annual cycles of significant rainfall, of percentage contribution and of the frequency of significant raindays for different cloud-producing circulation types over the central interior of South Africa (after Tyson, 1986, modified after Harrison, 1984a).

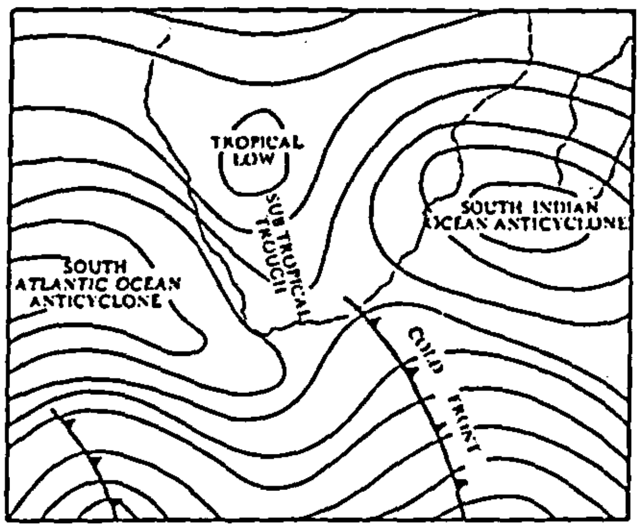

Figure 1.7: Schematic representation of the synoptic circulations associated with tropical-temperate troughs (after Harangozo and Harrison, 1983).

and at their lowest frequency during December to February (Estié, 1981; Taljaard, 1981, 1985). Systems like cut-off lows, may occur simultaneously with tropical-temperate troughs, often enhancing convection and rainfall production. The disastrous Lainsburg flood that occurred during February 1981 is evidence of the effects that a combination of these two systems can have on southern African rainfall (Estié, 1981; Taljaard, 1985; Tyson, 1986).

The synoptic circulations associated with the cloud bands over southern Africa were first examined by Harangozo and Harrison (1983). They found that all the cloud bands they studied were associated with tropical lows, subtropical troughs and temperate westerly wave disturbances (Fig. 1.7). Tropical lows were common to all cloud bands and were situated over the central-western interior during wet summers and over the eastern subcontinent during dry months. They occurred about five degrees further north (15°S) during dry months, in comparison to wet months (20°S) (Harangozo and Harrison, 1983). No other synoptic system was common to all the bands. Numerous cases occurred when both tropical lows and cold fronts were present, but did not develop into cloud bands. On band-free days, a cloud free region was present between the tropical and temperate cloud masses. A necessary condition for cloud band formation is the coupling of tropical depressions with westerly waves. Westerly waves and tropical lows have also been found to be significant features of wet-period mean circulation fields (Triegaardt and Kits, 1963; Hofmeyr and Gouws, 1964). During the particularly wet period of January to March 1974, the main features of the mean circulation were an upper westerly wave, a tropical low and enhanced tropical easterly flow (Taljaard, 1981). A westerly trough over the western subcontinent at the 500 and 700 hPa levels and a tropical low over northern Namibia/Botswana have been observed to occur during wet, but not dry periods (Dyer, 1982; Tyson, 1986). The trough at 700 hPa may be representative of the long wave trough at the 500 hPa level (Taljaard, 1989; Triegaardt, 1989; Triegaardt *et al.*, 1991). The regular association of tropical lows, subtropical troughs and westerly waves with wetter conditions suggests a link between tropical-temperate trough frequency and higher rainfall.

Tropical-temperate troughs form most frequently over southern Africa during January when the Inter-Tropical Convergence is situated furthest south. This allows for a more regular interaction between temperate westerly waves and the region of tropical convergence. This interaction is inhibited in winter due to the northward displacement of the Inter-Tropical Convergence Zone. Tropical-temperate troughs therefore seldom occur over southern Africa during winter (Harrison, 1986a). The dissipation of cloud bands occurs with the eastward or westward movement of the tropical-temperate trough and/or the eastward or westward extension of a ridge of high pressure at 700 hPa. In such a manner the link between the tropic and temperate circulations is broken (D'Abreton, 1992). Rainfall from tropical-temperate troughs decreases during December relative to January and November. This hiatus is indicative of the progression from an early summer, baroclinic westerly circulation to a late summer circulation dominated by barotropic controls over southern Africa (Harrison, 1986a; D'Abreton, 1992).

The poleward distribution of mass, momentum and energy from the tropics to the mid-latitudes is facilitated by cloud bands (Kousky *et al.*, 1983; Virji and Kousky, 1983; Smith, 1985; Bell, 1986; Harrison, 1986a; Wright, 1988; Kuhnel, 1989, 1990). Transport over southern Africa of latent heat, water vapour and kinetic energy occurs primarily within tropical-temperate troughs along the leading edge of the upper trough. This is important for the maintenance of the Hadley circulation over the subcontinent (Riehl, 1979; Webster, 1983; Harrison, 1986a; Lindesay, 1988a). Poleward momentum transport and rainfall have been positively correlated during mid-to late-summer months over the subcontinent (Harrison, 1986a; Tyson, 1986). D'Abreton (1992) points out that the verification of the Eliassen-Palm relationship and the generally lower latent heat values over southern Africa during early summer, imply an orographic forcing of the upper level westerly wave associated with tropical-temperate trough formation. However, during late summer, greater latent heat values and the non-verification of the Eliassen-Palm relationship suggest that the quasi-stationary wave associated with cloud bands is thermally forced by the release of latent heat over the tropics (Eliassen and Palm, 1960; Vonder Haar, 1968; Harrison, 1986b; D'Abreton, 1992). The long waves associated with tropical-temperate trough formation over southern Africa during early summer therefore appear to be baroclinically or orographically forced like those of most of the Australian cloud bands, and thermally forced during late summer, like those associated with the South American cloud bands. This implies that an intensification of the Hadley cell over southern Africa, due to an increase in latent heat release over the tropics, is associated with higher late summer rainfall (Rind and Rossow, 1984; Harrison, 1986a).

As tropical-temperate troughs facilitate the poleward transport of moisture, momentum and energy, variations in their formation, strength and position, will have a marked effect on southern African rainfall variation. The thermally-forced Walker Circulation (Harrison, 1983b; Johnson *et al.*, 1985; Zillman and Johnson, 1985) is one of the factors causing such tropical-temperate trough variations. Cloud-band rainfall, particularly during late summer, is strongly correlated with the Southern Oscillation (Harrison, 1986a). The effects of the Walker Circulation and the Southern Oscillation on southern African rainfall have been well documented (for example, Harrison, 1986a; Lindesay, 1988a). Rainfall over the central subcontinent is above normal during the high phase and below normal during the low phase of the Southern Oscillation (Stoeckenius, 1981; Lindesay *et al.*, 1986; Nicholson and Entekhabi, 1986; Lindesay, 1988a). Wet years are characterised by anomalously westerly winds at low levels and easterly winds at higher levels over the tropics, while the opposite is true for dry years (Fig. 1.8). Poleward flow over southern Africa increases during the high phase and equatorward flow during the low phase. During the high phase of the Southern Oscillation, the ascending limb of the Indian Ocean Walker cell is situated over tropical Africa, resulting in strong convection in these regions and a resultant enhancement of the Hadley circulation. This causes a strengthening of the Inter-Tropical Convergence at 20^0S and the subtropical anticyclone at 30^0S, which in turn strengthens the north-south pressure gradient thereby strengthening the easterly flow (Harrison, 1986a). The Walker Circulation therefore modulates the easterly flow transporting moisture into the African Inter-Tropical Convergence (Tyson, 1986). The strengthened Hadley circulation is associated with more frequent tropical-temperate trough formation and a wet summer over southern Africa. With the shift of the Walker Circulation during the low phase of the Southern Oscillation and the associated eastward shift of the regions of convection, tropical-temperate troughs form more frequently to the east of the subcontinent. Water vapour, momentum and latent heat are transported poleward over Madagascar and the South Indian Ocean resulting in dry southern African summers (Lindesay, 1988a; D'Abreton, 1992). Wet southern African summers are characterised by a high frequency of tropical-temperate trough formation over the subcontinent, while during dry summers the cloud bands occur more frequently over Madagascar (Fig. 1.9). The strength, position and frequency of tropical-temperate troughs during late summer are therefore substantially influenced by the Walker Circulation and the Southern Oscillation. During early summer, when the upper level waves over the subcontinent

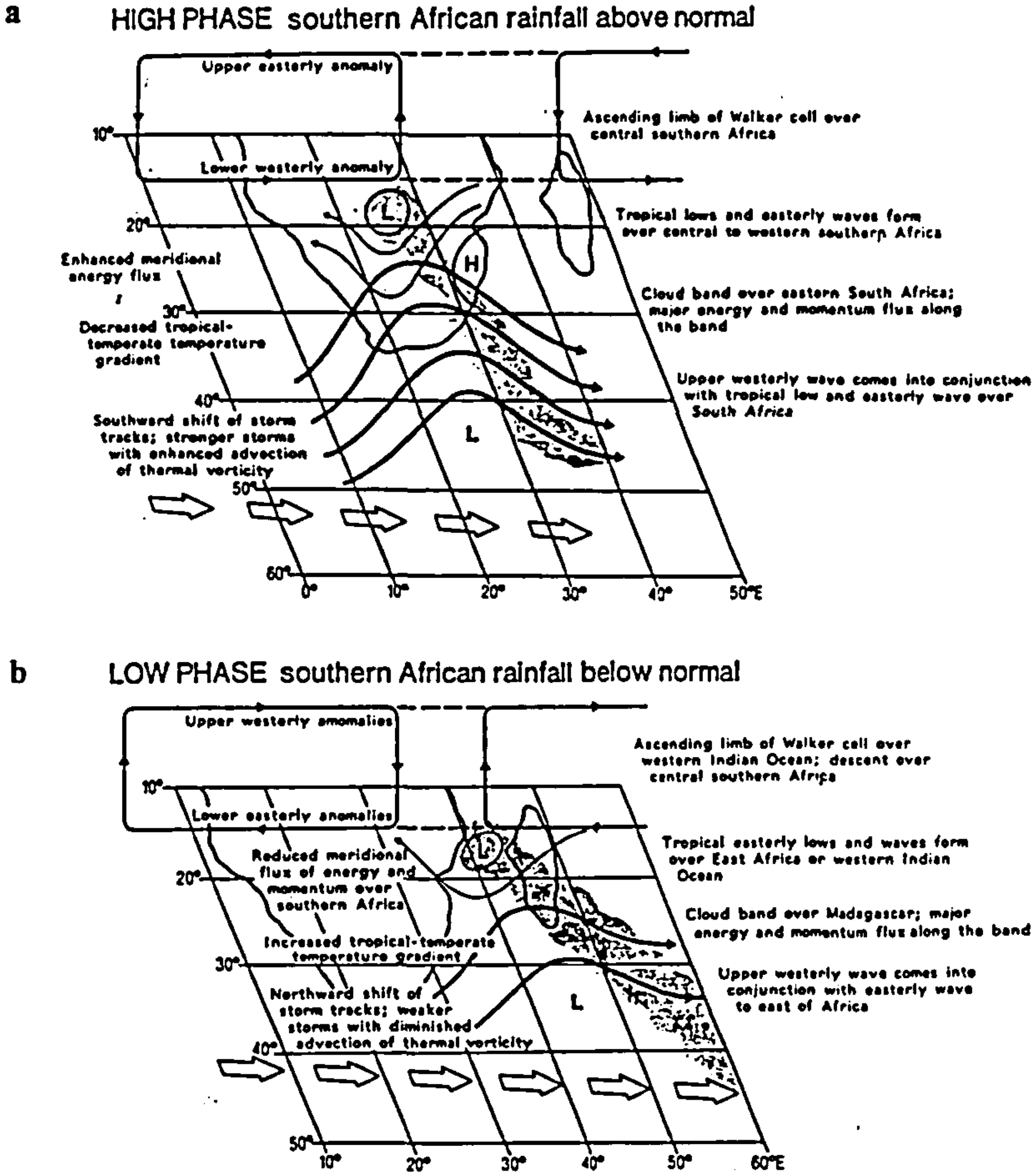

Figure 1.8: Schematic representation of the anomalous Walker circulation over Africa during the high phase (a) of the Southern Oscillation showing the derived flow resulting in above-normal rainfall over southern Africa, and during the low phase (b) showing the flow resulting in below-normal rainfall (after Harrison, 1986a; Tyson, 1986). Light and heavy lines denote surface and upper tropospheric flow respectively.

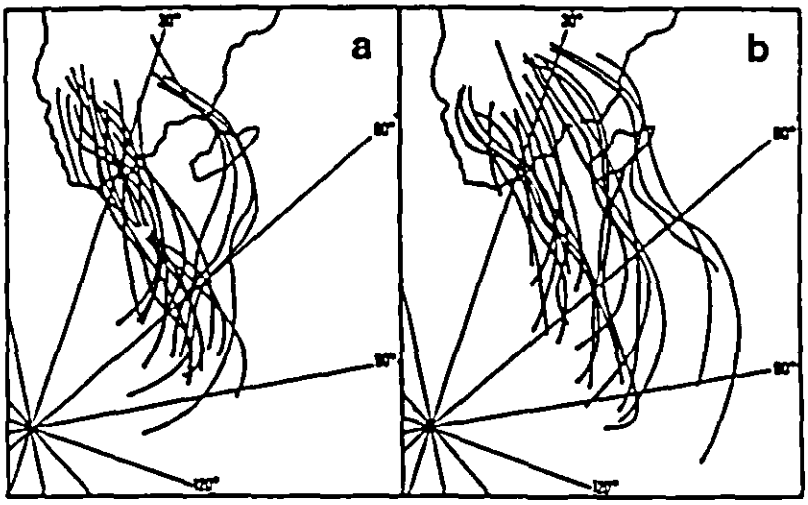

Figure 1.9: Positions of the major cloud bands during (a) the wet January of 1974 and during (b) the dry January of 1973 (after Harrison, 1984c).

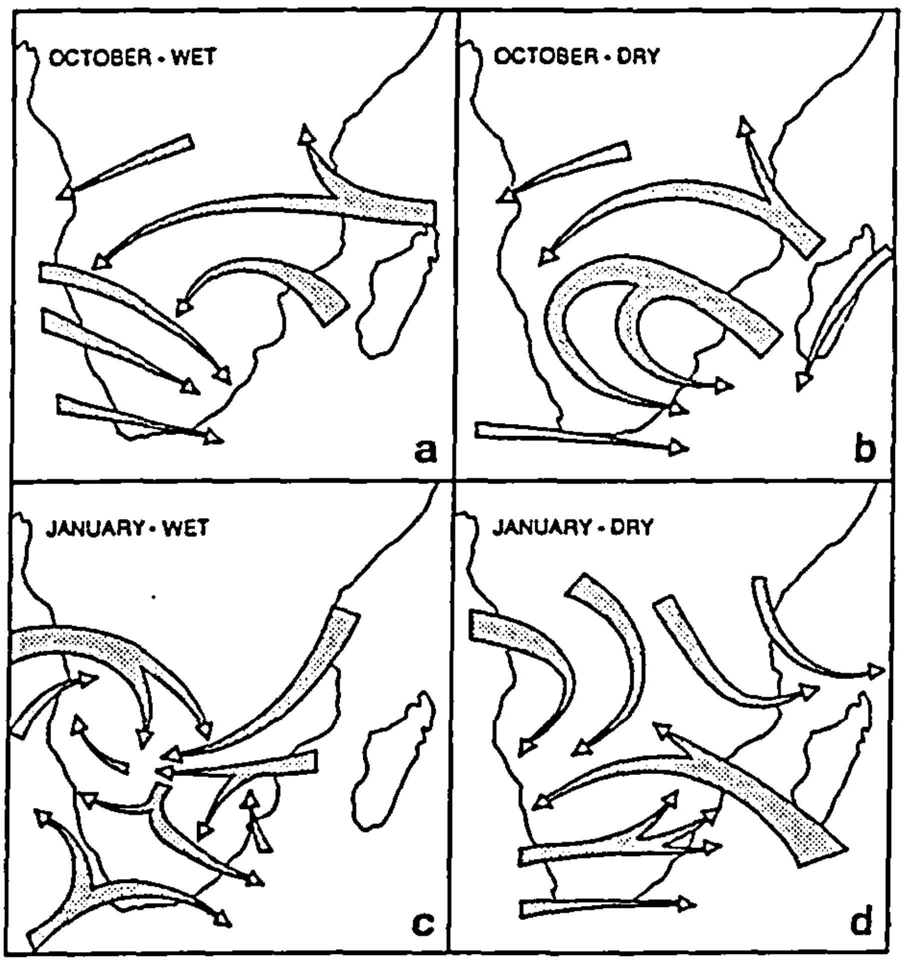

Figure 1.10: Schematic representation of the main vertically integrated circulation vapour transport over southern Africa during wet and dry months of (a,b) October and (c,d) January (after D'Abreton and Lindesay, 1993).

appear to be baroclinically forced, association between southern African rainfall and the Southern Oscillation is weaker than in late summer (Harrison, 1986a; Lindesay, 1988a, 1988b).

Very little (6 to 14 per cent) of the water vapour available for rainfall over South Africa is of local origin thus necessitating moisture transport from regions elsewhere (Kriel, 1983; D'Abreton and Tyson, 1994). The source of water vapour supply over southern Africa and for the formation of cloud bands has been debated in the past. The tropics have been considered an important source from which water vapour is transported along the Inter-Tropical Convergence and the Zaïre Air Boundary, and then southward over South Africa (Harrison, 1986a). Others have suggested that the South Indian Ocean is the most important water vapour source from which moisture is advected around the South Indian Anticyclone westward and southward over the interior (Taljaard, 1986, 1987, 1990; Tyson, 1986). Recurved flow from the South Atlantic Ocean has also been found to supply moisture to the interior (Tyson, 1986). More recent in-depth investigations have, however, revealed that the source of water vapour supply to South Africa varies from being both the tropical Indian and Atlantic Oceans during wet early summers to just the Indian Ocean during dry early summers, and from the western tropical Indian Ocean north of Madagascar during wet late summers, to a reduced supply from the same source during dry late summers (Fig. 1.10) (D'Abreton, 1992; D'Abreton and Tyson, 1994). Westerly zonal moisture transport is important in promoting early summer rainfall, while northerly meridional moisture transport appears to be of greater importance to late summer rainfall production (D'Abreton, 1992; D'Abreton and Lindesay, 1993; D'Abreton and Tyson, 1994). This meridional transport of water vapour during late summers occurs primarily within tropical-temperate troughs. The importance of tropical-temperate troughs to southern African rainfall is once again evident.

During wet periods, the high frequency of tropical-temperate troughs situated over the interior results in an increase in poleward momentum transport along the leading edge of the westerly wave. This causes the observed strengthening in the westerlies over Marion Island (Fig. 1.11a) (Harrison, 1986a; Tyson, 1986). During dry periods, the eastward shift of the Walker Circulation results in the poleward transport of momentum across Madagascar and the western Indian Ocean. The South Atlantic standing wave also affects momentum transport

a

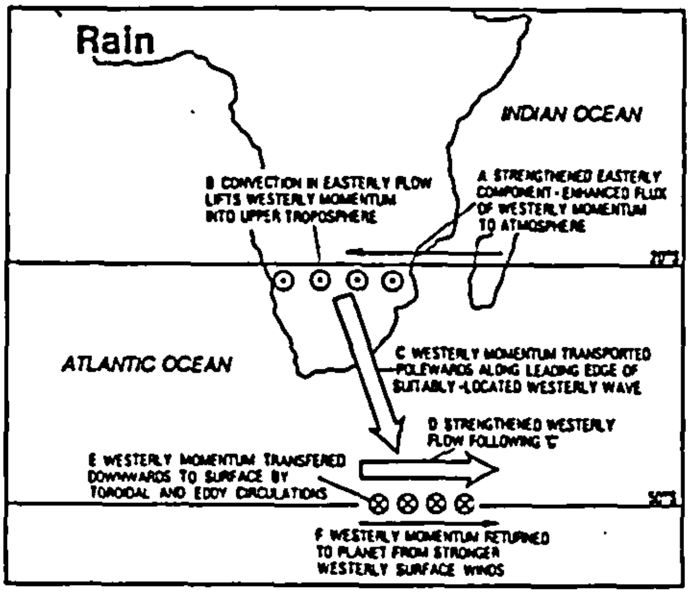

b

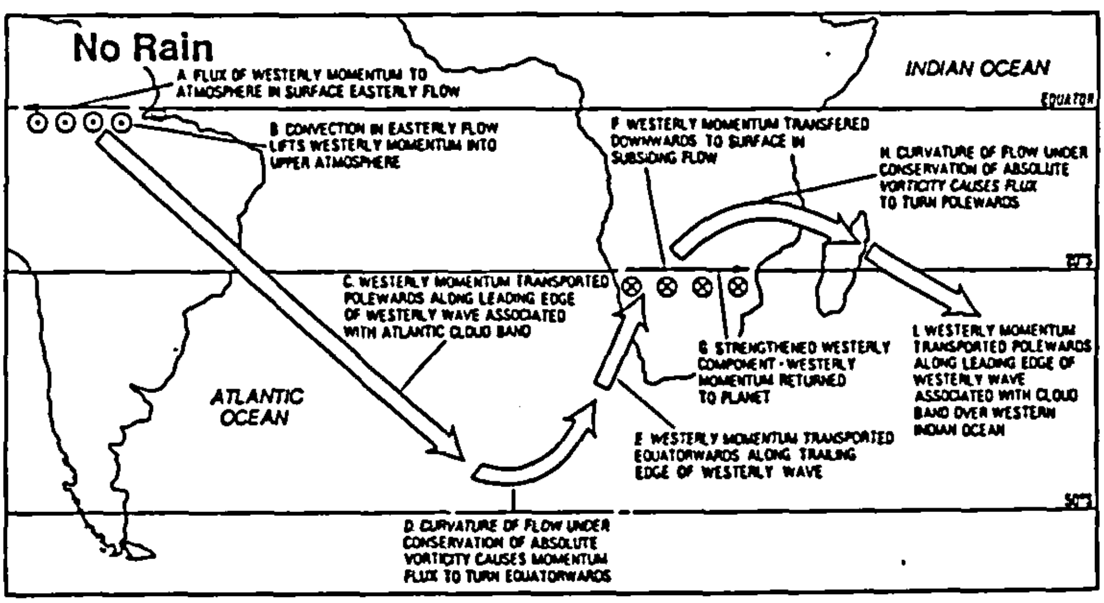

Figure 1.11: Schematic model of mean summer circulation associated with (a) wet and (b) dry summers over southern Africa (after Tyson, 1986; modified after Harrison, 1986a). Double arrows represent upper tropospheric flows and single arrows surface flow; dots within circles represent ascent and crosses in circles descent.

over the southern African region during dry periods (Harrison, 1986a; Tyson, 1986). Westerly angular momentum generated over the South American tropical regions is lifted by convection over the Amazon Basin and is transported across the Atlantic along the leading edge of the South Atlantic wave. The flow recurves to the west of the southern Africa subcontinent and is transported equatorward over southern Africa, after which it recurves again thereby enhancing the poleward transport of momentum over Madagascar (Fig. 1.11b). During wet periods the Atlantic wave either moves westward and weakens (Harrison, 1986a; Tyson, 1986). The magnitude of latent heat transport over southern Africa increases throughout summer, reaching a maximum during late summer. The southeastward transport from a tropical source occurs over the southern subcontinent during wet years, and is shifted eastward to occur over Madagascar during dry years (Fig. 1.12). The investigation of particular case studies reveals that maximum latent heat occurs on the cloud band days and that the regions of maximum latent heat closely correspond to the position of the cloud band (D'Abreton, 1990).

Sea-surface temperatures and ocean-atmosphere interactions

The thermal and dynamical properties of oceans make them extremely important energy sources and sinks (Johnson, *et al.*, 1985). The fact that water is a fluid complicates the energy exchange at the ocean/atmosphere interface (Fig 1.13). The atmosphere interacts with the sea surface through a complex balance of heat fluxes, transfer of momentum, and turbulent mixing, which plays a significant role in the determination of climate on daily, seasonal and longer time scales. In recent years increased attention has been given to the association between sea-surface temperature and local southern African atmospheric circulation and rainfall variability (Nicholls, 1984; Folland *et al.*, 1986, Walker, 1989,1990; Jury *et al.*, 1991, 1992; Jury, 1993,1996; Mason, 1990, 1992,1995). South African rainfall distribution is strongly correlated to sea-surface temperature fields and surface heat flux characteristics of the adjacent oceans (Kershaw, 1988; Jury and Reason, 1989; Mason, 1990, 1992, 1995; Jury and Lindesay, 1991; Jury and Pathack, 1991; Jury *et al.*, 1992; Mason and Tyson, 1992; Mason *et al.*, 1994; Mason and Jury, 1996). Maximum annual rainfall figures are found along the eastern and southeastern coasts of South Africa where sea-surface temperatures and hence heat fluxes are high (Tyson, 1986; Walker, 1989,1990). On the west coast by comparison the low annual rainfall occurs in the oceanic region with the lowest sea-surface temperatures (Tyson, 1986;

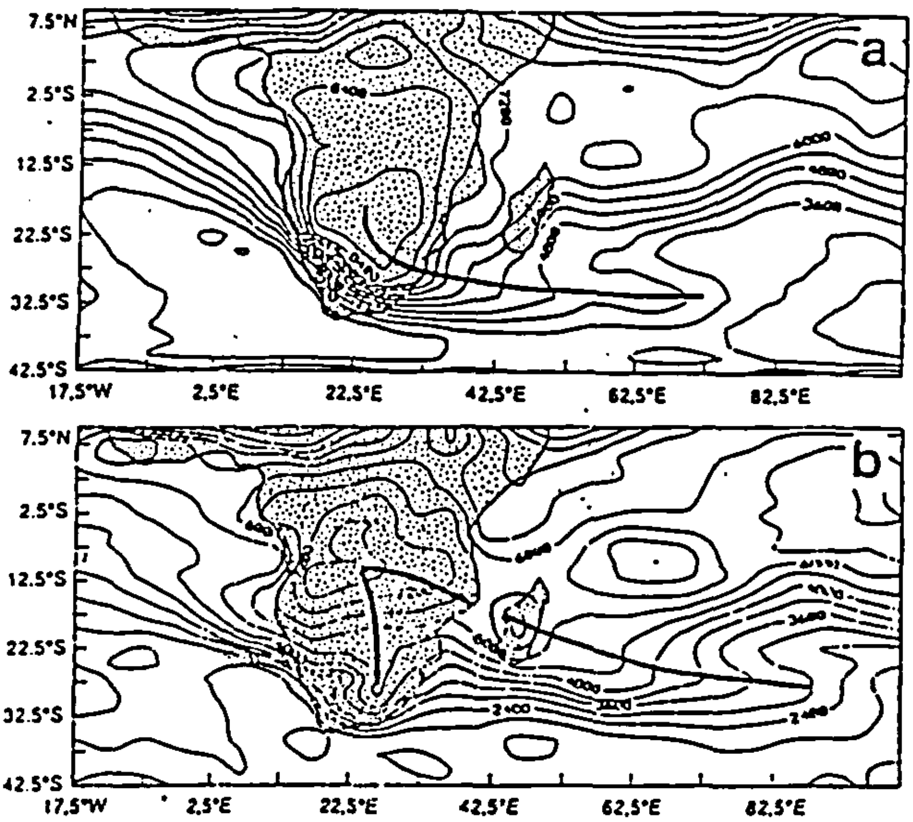

Figure 1.12: Latent heat for (a) mean wet Januaries and (b) mean dry Januaries. Units are $J.cm^{-2}$. Heavy black lines indicate axes of relative maximum latent heat (after D'Abreton, 1992).

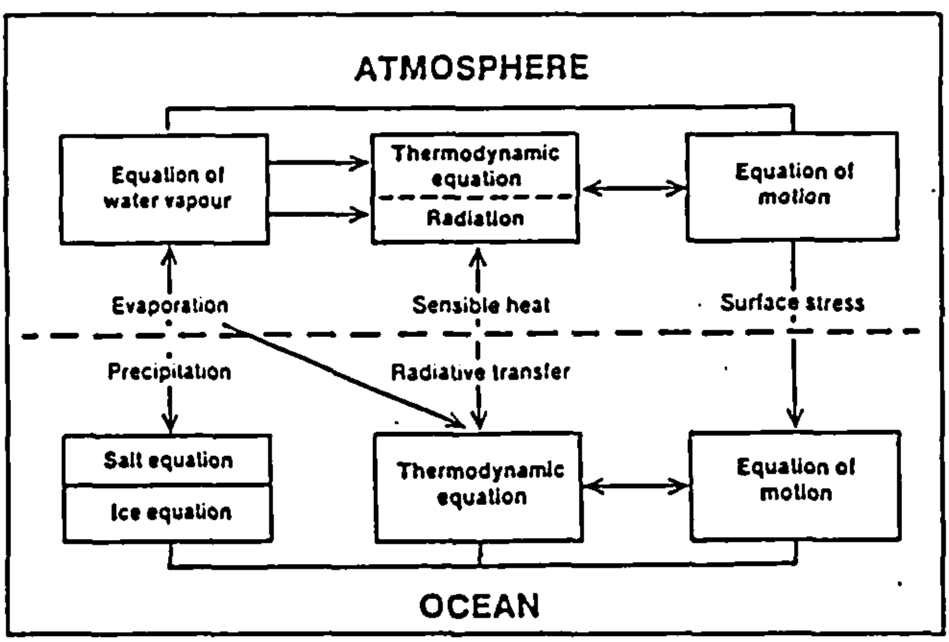

Figure 1.13: A schematic representation of the interaction of the atmosphere and Ocean (after Gates, 1979)

Walker, 1989,1990). The tropical atmospheric response to sea-surface temperature anomalies are thought to be of a order of magnitude greater than in mid-latitude regions, as a result of a significantly greater incidence of convective activity and the absence of a strong coriolis force (Shukla, 1986). Over areas of high sea-surface temperatures, atmospheric heat anomalies occur because of large latent energy supply and pre-existing convective motion (Webster, 1981). The low-level convergence that develops serves to maintain the supply of latent energy and thus promotes continued convection (Trenberth, 1991).

In the mid-latitudes the atmospheric response to warm oceanic anomalies differs from that in the tropics (Bjerknes, 1969; Newell, 1979; Harrison 1984a, Love, 1985b). Usually the response is restricted to shallow sensible heating, with significant latent heating impacting only on pre-existing cyclogenesis and vertical instability (Lindesay, 1988a; Walker and Lindesay, 1988; Walker, 1990; Jury and Pathack, 1991; Mason 1995).

Significant statistical correlations exist between sea surface temperatures in the Indian and Atlantic Oceans and rainfall variability over southern Africa (Hirst and Hastenrath, 1983; Nicholson and Entekhabi, 1987; Lindesay, 1988a; Walker, 1989; Walker and Lindesay, 1989; Jury and Pathack, 1991; Mason, 1992; D'Abreton, 1992). During early summer, significant correlations exist between southern African rainfall and sea surface temperatures in the tropical South Atlantic Ocean. In the late summer, these correlations shift to the tropical Indian Ocean, the region northeast of Madagascar yielding the highest and most significant correlations (Walker, 1989; Mason, 1992). Sea surface temperatures have also been found to affect the Walker Circulation. During wet (dry) late summers when the Southern Oscillation is in the high (low) phase, sea surface temperatures in the tropical Indian Ocean are relatively low (high). This causes cooling (warming) in the atmosphere above the surface which results in an increase (decrease) in surface pressure and strong subsidence (convection) over these oceanic regions (Bjerknes, 1969) (Fig 1.8). The influence of sea surface temperatures on water vapour supply and the Walker Circulation, and hence on the formation, intensity and positioning of tropical-temperate troughs over southern Africa is substantial. Summer rainfall regions of the subcontinent are positively correlated with sea-surface temperatures in the Agulhas Current retroflection region and tropical western Atlantic Ocean. The tropical Indian

Ocean north and east of Madagascar is, however negatively correlated with precipitation in the summer rainfall region (Fig 1.14) (Walker, 1989, 1990).

In the tropical Indian Ocean the development of positive sea-surface temperatures promotes the development of cyclogenesis north of Madagascar (Walker, 1989, 1990; Mason 1992, 1995). The presence of enhanced cyclogenesis causes moisture redirection to the region of instability, thus reducing moisture availability over the subcontinent (Walker, 1989, 1990; Mason, 1992, 1995). On the east coast of South Africa warmer sea-surface temperatures have been found to precede and accompany higher rainfall conditions (Walker, 1989, 1990). The warmer atmospheric boundary layer and heightened instability are translated inland by the tropical easterly flow producing higher moisture convergence over the immediate interior (Walker 1990; Mason, 1992, 1995). Warm anomalies developing at the Agulhas retroflection are found to influence the atmospheric boundary layer by generating strong surface heat fluxes, and thus again enhancing instability and moisture levels (Walker 1989, 1990). The presence of positive anomalies both to the east and south of South Africa increase the likelihood of tropical-temperate trough development by increasing moisture availability and by increasing the amplitude of the westerly wave (Walker, 1989,1990).

Objectives

Tropical-temperate troughs clearly have a considerable influence on summer rainfall over southern Africa. Despite past research, the actual structure, antecedent conditions and dissipation of tropical-temperate troughs, and the factors controlling the variations in these systems are still not well understood. Gaining an understanding of tropical-temperate troughs has been impeded by the tremendous lack of data over southern African and the adjacent oceans. The increasing availability of satellites during the 1970s and 1980s, such as the NOAA series and the geostationary METEOSAT, has allowed for a far more uniform and regular coverage of the climate and weather over southern Africa (Barclay *et al.*, 1993; Lindesay, 1993). However, these are also generally only taken at 12 hour intervals. The lack of upper air data and the long intervals between measurements makes it extremely difficult to obtain and examine the structure of synoptic systems over oceanic regions.

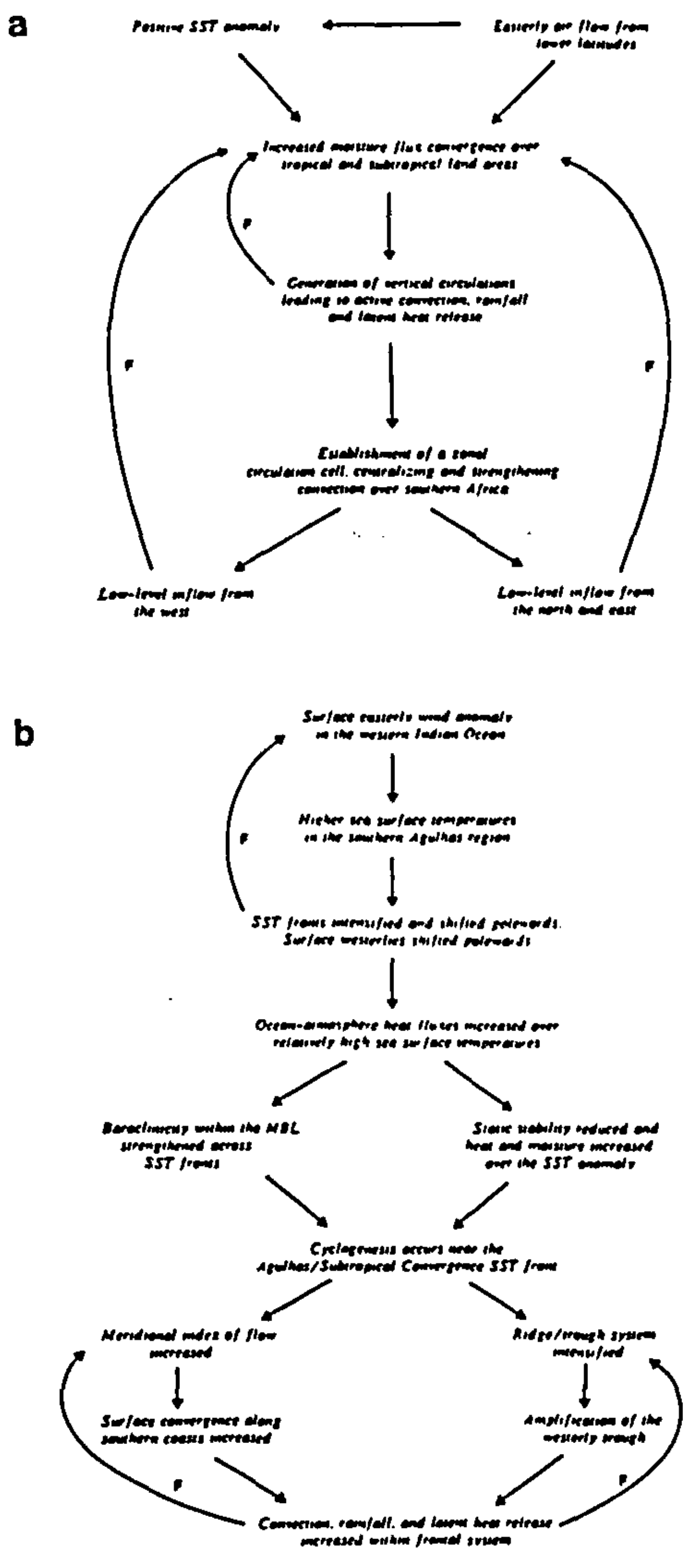

Figure 1.14: Possible ocean/atmosphere interactions along (a) the east coast and (b) the south coast of southern Africa (after Walker, 1989).

Tropical-temperate troughs which extend over southern Africa from the tropics to about 50^{0}S, are particularly difficult to research as they overlie regions that are especially data sparse (the ocean and the African tropics). Although a relatively good understanding of the dynamics and certain characteristics of these systems has been obtained from the available data, further details cannot be resolved from the sparse network of upper air stations. The simulation of mesoscale systems using numerical models, such as the Regional Atmospheric Modelling System developed by Colorado State University, have been used in the past to alleviate some of the problems associated with scarcity of data. Providing that the model simulations show a close approximation to reality, more detailed investigations into the structure, development and movement of such systems are made possible by a much higher space and time resolution than could be supplied by the station network. The degree of influence that certain factors have on a circulation system can also be determined through sensitivity tests.

No attempt has been made previously to numerically model and/or predict the formation, behaviour, structure and resultant rainfall of tropical-temperate troughs over southern Africa and adjacent oceans. The main objectives are:

(a) to determine the suitability of RAMS as a tool for researching tropical-temperate troughs over southern Africa;

(b) to investigate the thermodynamic and kinematic characteristics of tropical-temperate troughs and their rainfall production over southern Africa during wet and dry years;

(c) to investigate the structure, formation and dissipation of tropical-temperate troughs during wet and dry years;

(d) to further investigate the large-scale circulation controls associated with tropical-temperate troughs;

(e) to examine in further detail the moisture sources and water vapour transport associated with tropical-temperate troughs during wet and dry years, and for specific synoptic conditions;

(f) to determine what the effects of a change in soil moisture will have on tropical-temperate trough formation, structure and development using RAMS; and

(g) to investigate what the effects of a change in the grid resolution and the moisture related parameterisation schemes of RAMS will have on the development, structure and rainfall production of tropical-temperate troughs;

(h) to investigate the sensitivity of RAMS, to the development of warm oceanic anomlies;

(i) to ascertain if the model sensitivity will closely parallel what is expected at the climatological time scale.

Achieving these objectives will create a basis from which for the occurrence and distribution of rainfall from tropical-temperate troughs may be better forecast.

Synopsis

Tropical-temperate troughs and their associated cloud bands are the single most important systems contributing to the rainfall over the southern African interior during late summer. The cloud bands are situated along the leading edge of upper westerly waves which facilitate the poleward transport of energy and momentum. As the systems extend from the tropics to the mid-latitudes and often occur over the ocean, research into these systems has been hampered by the scarcity of data over the African subcontinent and adjacent oceans. Numerous observations and hypotheses regarding the large scale circulation controls and the kinematic, thermodynamic and moisture characteristics of tropical-temperate troughs over southern Africa have been made in the past, but require further substantiation using more spatially comprehensive data. In order to substantiate some of these hypotheses and to achieve the objectives outlined, the Regional Atmospheric Modelling System developed at Colorado State University will be used to model tropical-temperate troughs over southern Africa.

CHAPTER 2

CASE STUDY SIMULATION COMPARISONS

Introduction

Two cases have been chosen for detailed study, one during a wet year (22 to 24 January 1981) and one during a dry year (6 to 8 January 1980). Both cases represent late-summer occurrences of tropical-temperate troughs and were specifically chosen as the related moisture sources, water vapour transport and related latent heat release have been previously examined (D'Abreton, 1992). As most of the lower tropospheric water vapour transport over South Africa occurs below the 700 hPa level (McGee, 1970), the surface and 700 hPa levels will be the lower levels investigated. The 300 hPa level will be used to represent the upper atmosphere and the air flow contributing to the upper-level zonal and meridional flow throughout the region. Results and data from 500 hPa analyses will be used when appropriate.

In order to determine whether the RAMS model output is representative of reality, the output from the wet and dry case studies needs to be compared with actual data. Charts and data supplied by the South African Weather Bureau will be utilised for this purpose. Data from Gough and Marion Islands have been excluded since no other upper air data are available between these two islands and the subcontinent, which can lead to a biased interpolation and possible misrepresentation of the data fields over the oceanic regions. A similar problem occurs over Namibia. Unfortunately upper air data at 12:00 UT during 1980 and 1981 are not available for Windhoek which is situated close to the origin of the tropical-temperate trough. This resulted in a poor interpolation and misrepresentation of the tropical-temperate trough system over northern Namibia, particularly in the moisture fields. The contours over northern Namibia, plotted using the Surfer package (see Chapter 3), have therefore been blanked out.

The Wet Case Study: 22-24 January 1981

Sequence of Events

On 22 January (Day 1), the pre-cloud band day, much of western and central Africa south of the equator was covered by tropical cloud (Plate 2.1a). The cloud cover to the south of the subcontinent was associated with the approaching westerly wave. By 23 January (Day 2), the tropical-temperate trough had formed by linking with a tropical system to the north and with the temperate westerly wave to the south (Plate 2.1b,c). The tropical link occurred at approximately 20°S and the temperate link over the southern coastal regions of the subcontinent. The cloud band had begun to dissipate by the morning of 24 January (Day 3), leaving remnants over the interior (Plate 2.1d). This dissipation was accompanied by a significant reduction in tropical cloud cover and the eastward displacement of the westerly wave. Some cloud cover was still present over the southern regions of South Africa and to the south of the subcontinent. The cloud band had started to re-form by the night of 24 January (Plate 2.1e). Full dissipation of the band finally occurred by 27 January. Kuhnel (1989) observed that cloud bands over Australia often re-form when strengthened by new flows of energy, thus making the decision of whether to classify them as one or two systems, difficult. It was decided that the period from 12:00 UTC on 22 January 1981 to 12:00 UTC on 24 January 1981 would be considered as the time period of the development and dissipation of the tropical-temperate trough for the purposes of the mesoscale model.

Associated with the formation of the tropical-temperate trough during the 22 to 24 January period was the development of a particularly intense cut-off low over the south western regions of southern Africa. This resulted in the devastating floods that wrecked the southern Karoo town of Lainsburg late on the afternoon of 25 January, an event described in detail by Estié (1981) and Taljaard (1985).

a

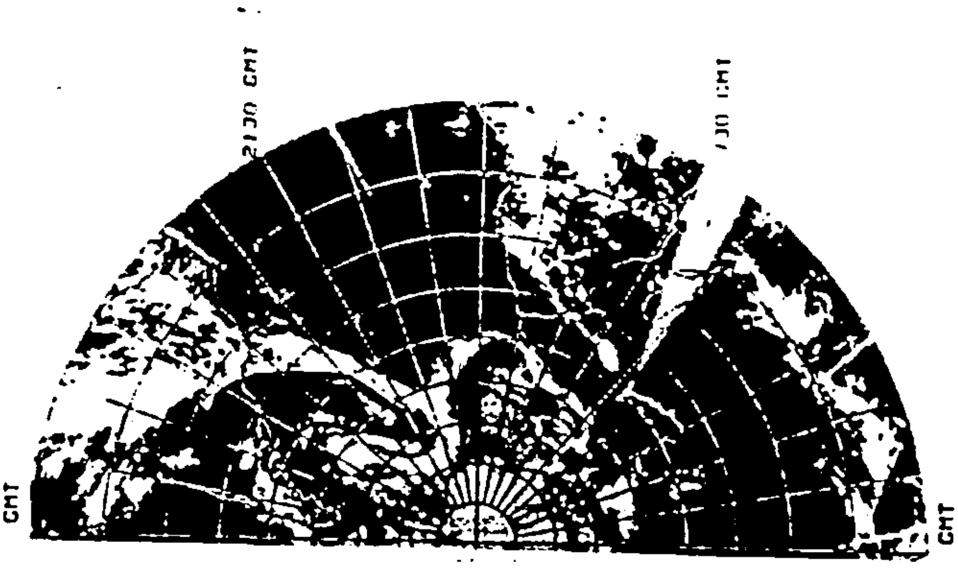

b

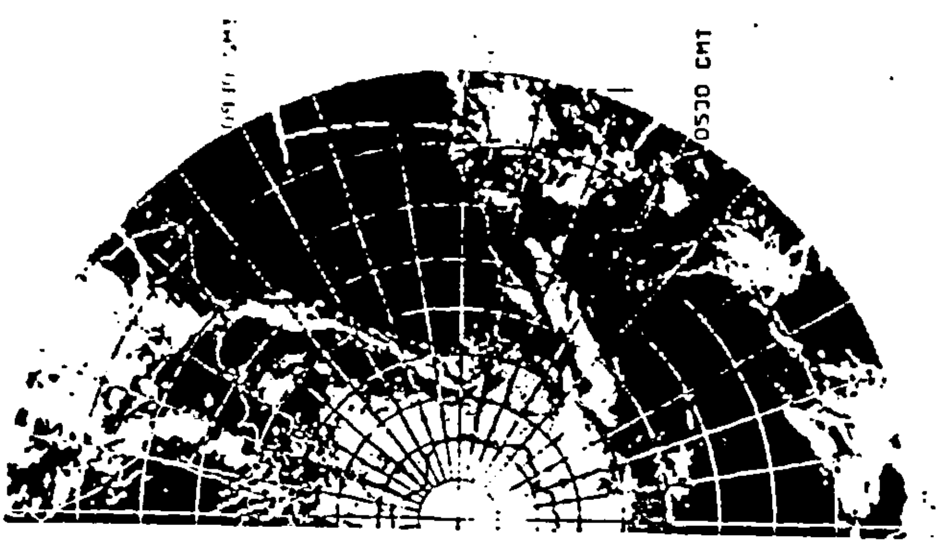

c

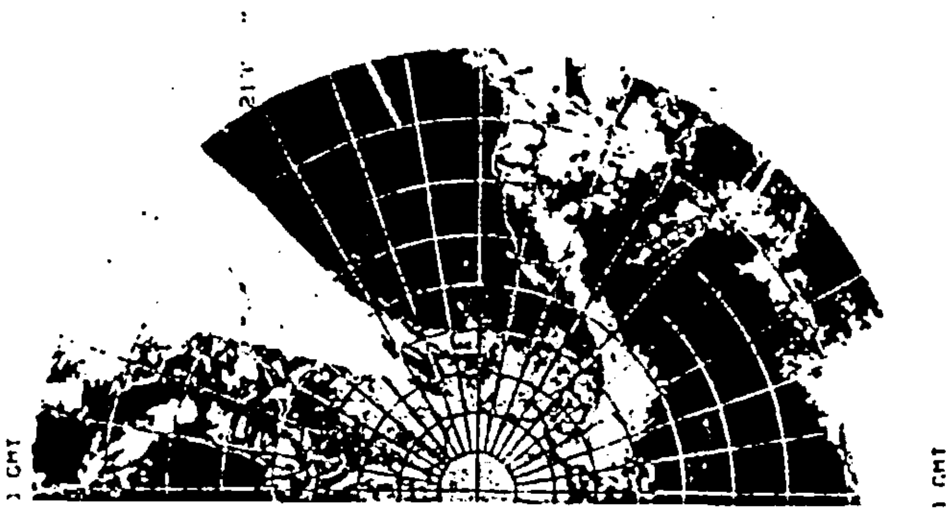

Plate 2.1: NOAA infra-red satellite imagery for (a) 22 January, (b and c) 23 January, and (d and e) 24 January. The universal time that the image was taken is indicated on the plate.

d

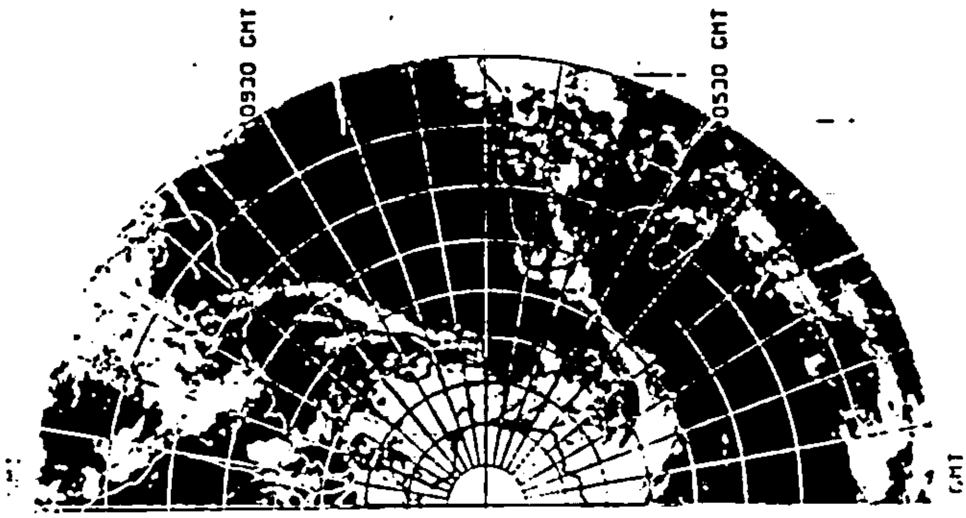

e

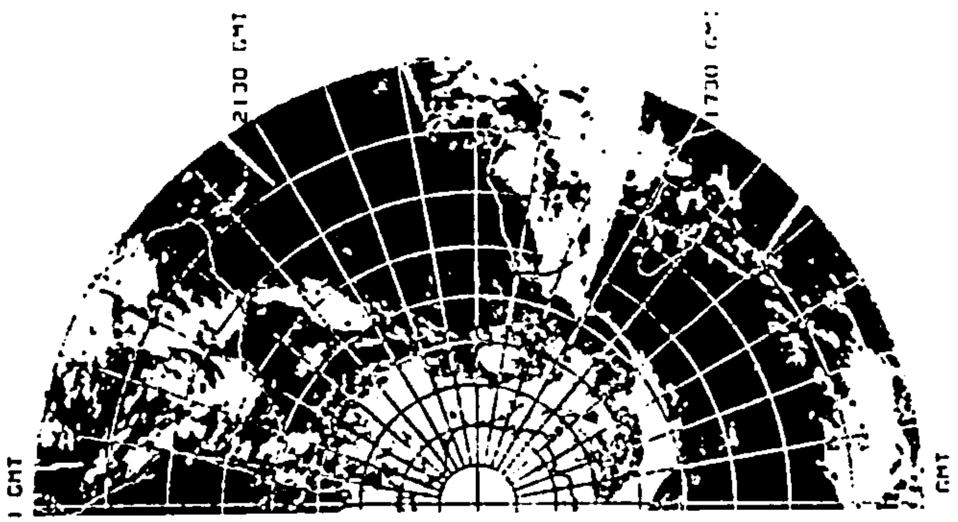

Plate 2.1: NOAA infra-red satellite imagery for (d and e) 24 January. The universal time that the image was taken is indicated on the plate.

Hemispheric Circulation Controls

Wave numbers 1 to 3 in the Southern Hemisphere are large-scale, quasi-stationary features that are equivalent barotropic in structure (Trenberth, 1980; Tyson, 1986). The higher number waves (4 to 8) are shorter and more transient than the lower number waves, are tilted westward with height, have a baroclinic structure and tend to be steered by the semi-stationary waves (Tyson, 1986). Wave numbers 4 to 6 have been found to contribute over 25 per cent to the variance of the 500 hPa level heights in summer (van Loon, 1972) and changes in the variance of these travelling short-waves have an immediate effect on the weather. It is along the leading edge of these transient waves over southern Africa that cloud bands form and are steered eastward (Tyson, 1986). During 22 to 24 January 1981, the circumpolar westerly circulation in the Southern Hemisphere was dominated by a 6-wave structure (Fig. 2.1). Of particular relevance is the wave to the south of the subcontinent on 22 January (Day 1) (Fig. 2.1a) which resulted in the formation of the tropical-temperate trough. By 23 January (Day 2), the trough amplitude had increased significantly and the wave was situated over the western interior, extending as far north as the northern borders of Namibia and to Port Elizabeth on the southern coast (Fig. 2.1b). On 24 January the eastward progression of the wave had caused further westerly tilting of the trough axis (Fig. 2.1c).

Synoptic and Regional Circulation Controls

A tropical low over Windhoek, a trough orientated in a northwest-southeast direction across the Karoo and western Orange Free State, a cold front approaching the subcontinent from the southwest and the South Atlantic and South Indian Anticyclones were the prominent surface level features at 12:00 UTC on 22 January (Day 1) (Fig. 2.2a). High dewpoint temperatures (289-293K) occurred along the leading edge of the surface trough (Fig. 2.2a) and are reflected by the high relative humidities at the surface and 700 hPa levels (Fig. 2.3h). Neither the tropical nor temperate links with the interior trough had yet formed (Plate 2.1a). The tropical low was embedded in the easterly wave which was present throughout most of the troposphere (Figs 2.2a and 2.3a,b), and which was transporting moist tropical air southward. The South Indian Anticyclone over the Mozambique Channel was supplying moist air to the interior from over the South Indian Ocean and the easterly flow on its northerly periphery was steering easterly perturbations westward. The cold

a

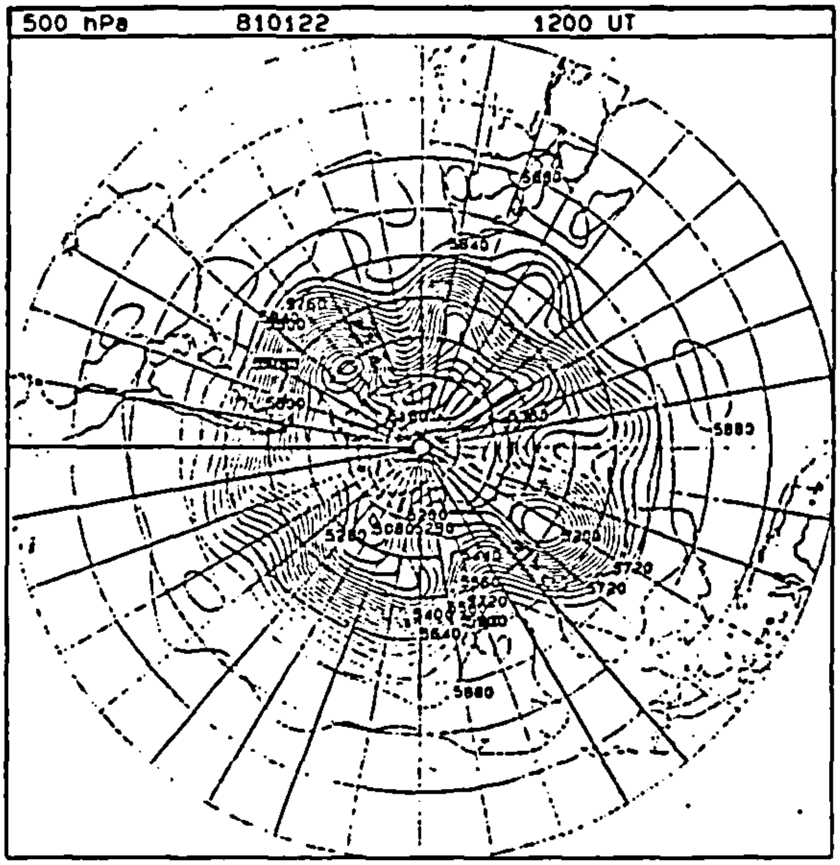

b

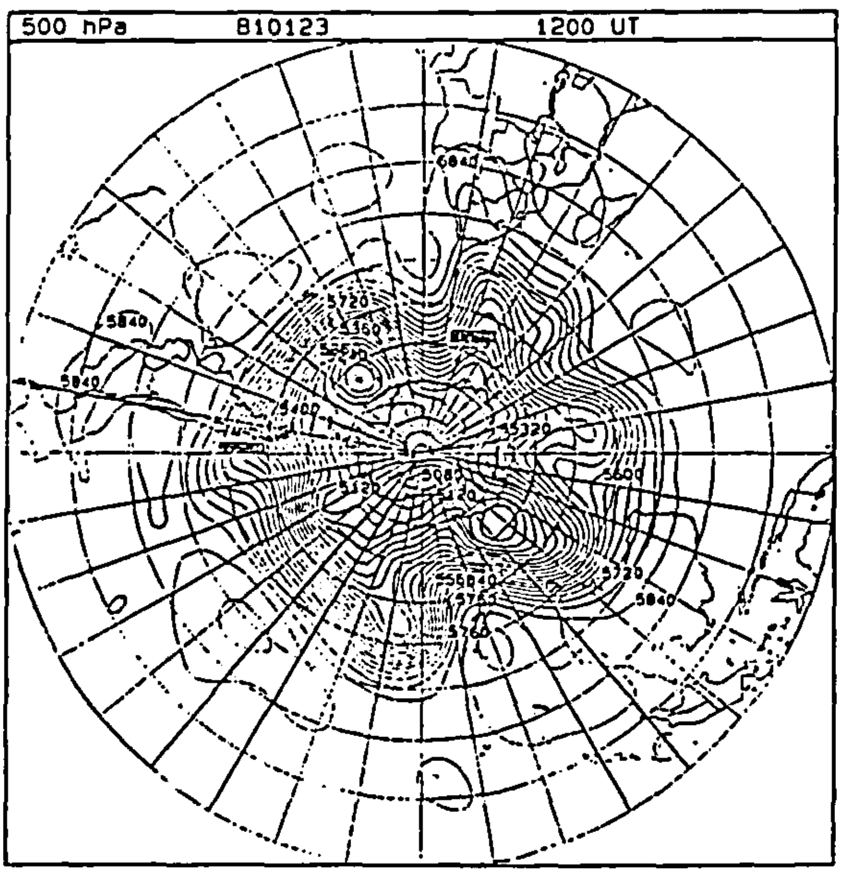

Figure 2.1: The circumpolar wave structure at 500 hPa on (a) 22 January, (b) 23 January, (c) 24 January.

c

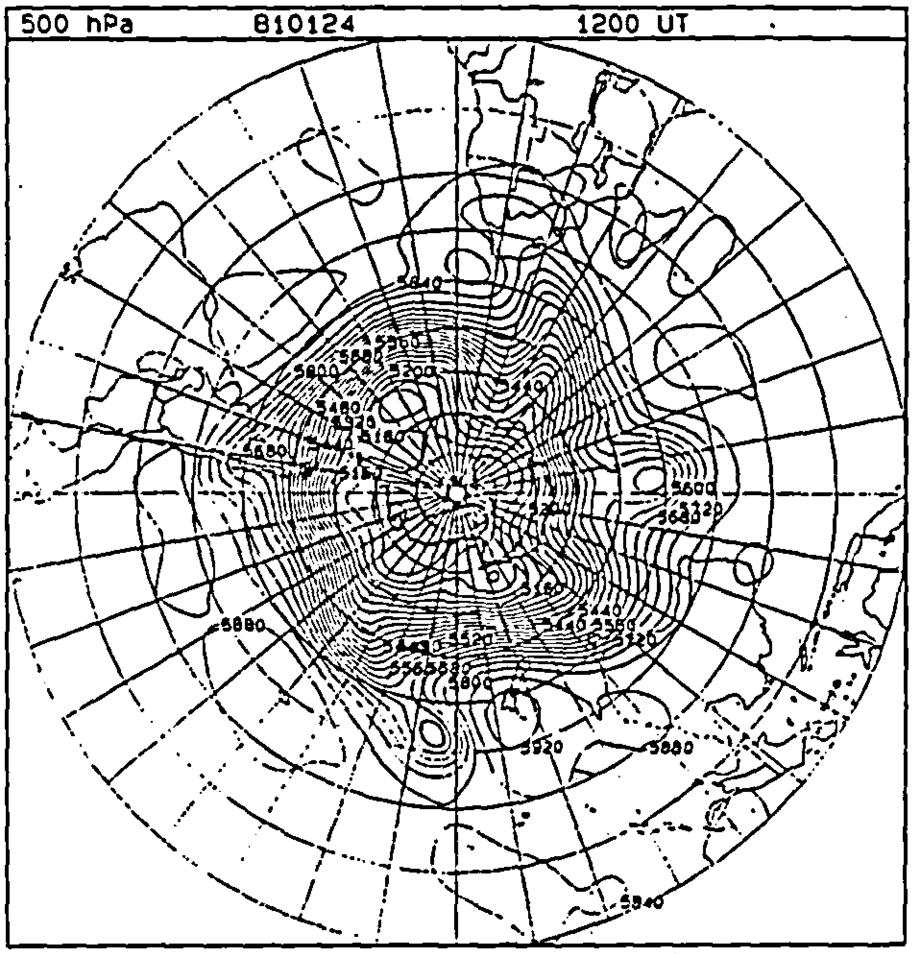

Figure 2.1: The circumpolar wave structure at 500 hPa on (c) 24 January.

a

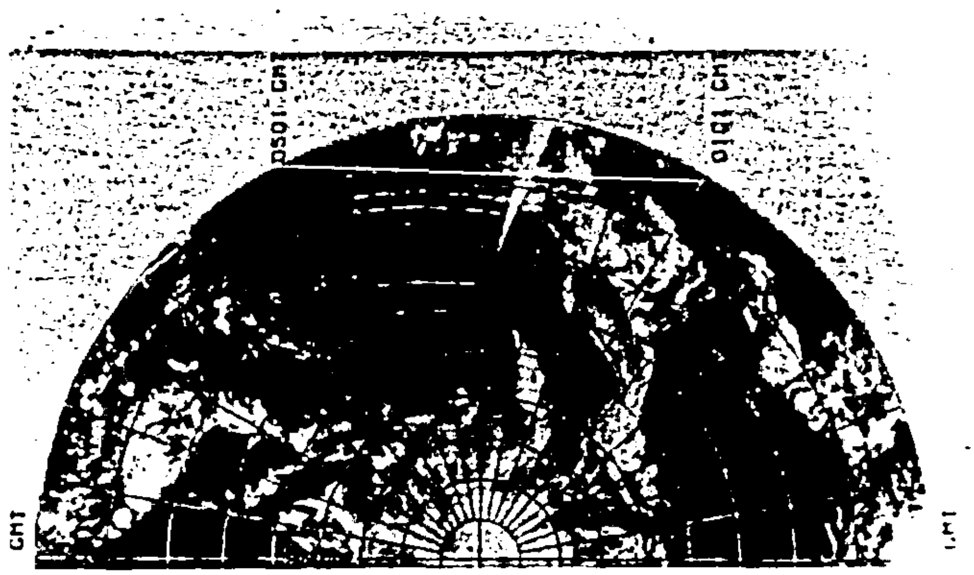

b

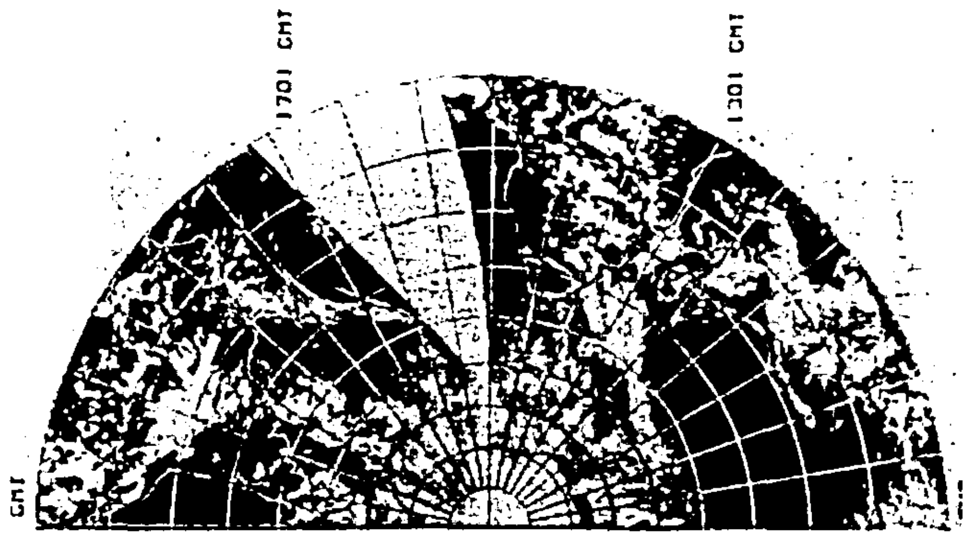

c

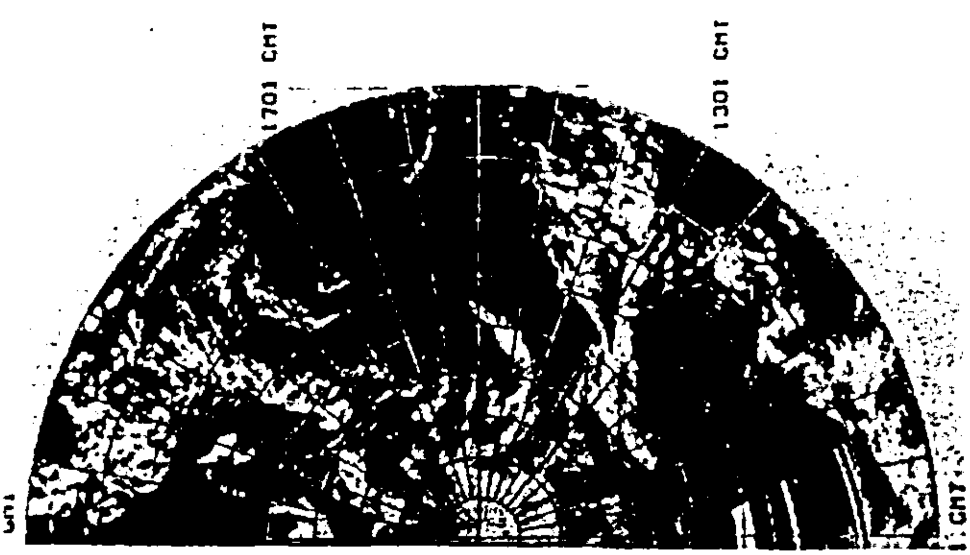

Plate 2.2: NOAA infra-red satellite imagery for (a) 6 January, (b and c) 7 January, and (d and e) 8 January. The universal time that the image was taken is indicated on the plate.

d

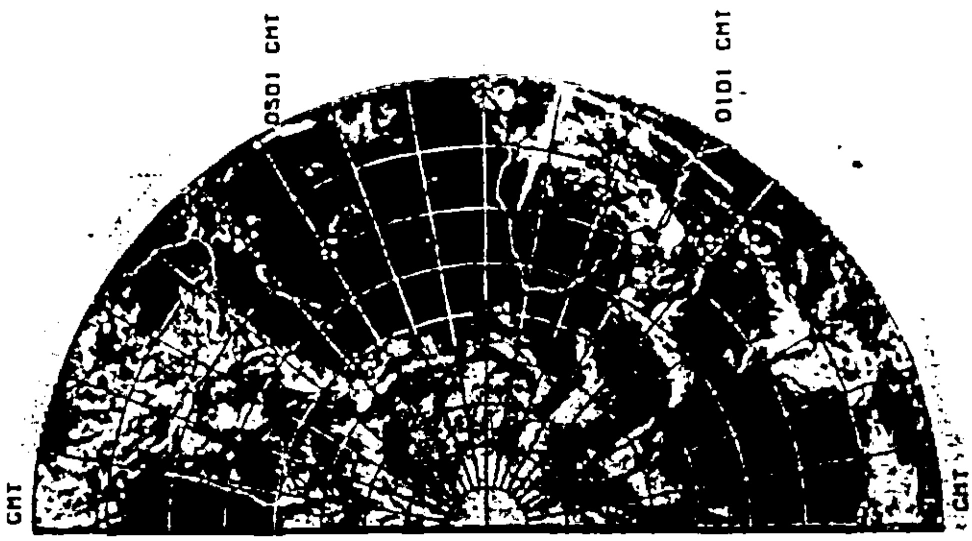

e

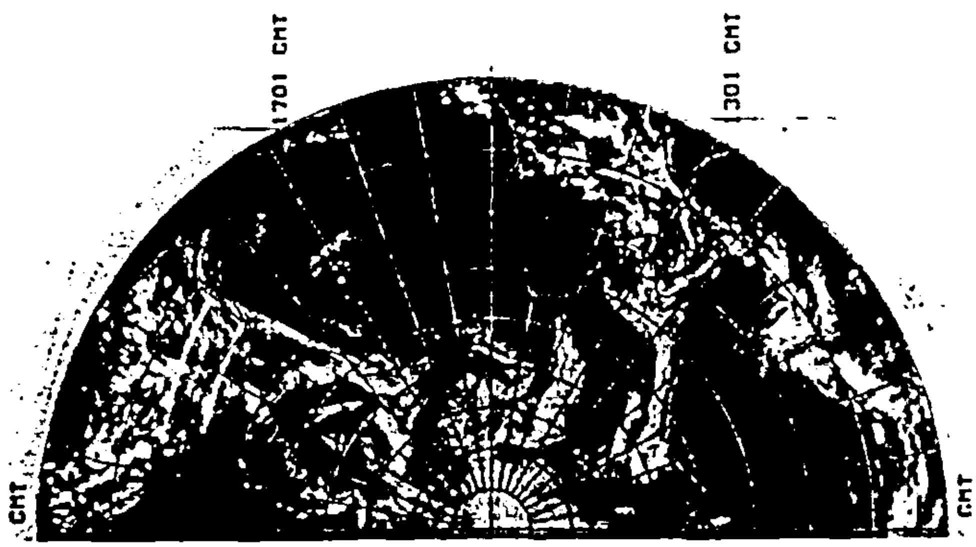

Plate 2.2: NOAA infra-red satellite imagery for (a) 6 January, (b and c) 7 January, and (d and e) 8 January. The universal time that the image was taken is indicated on the plate.

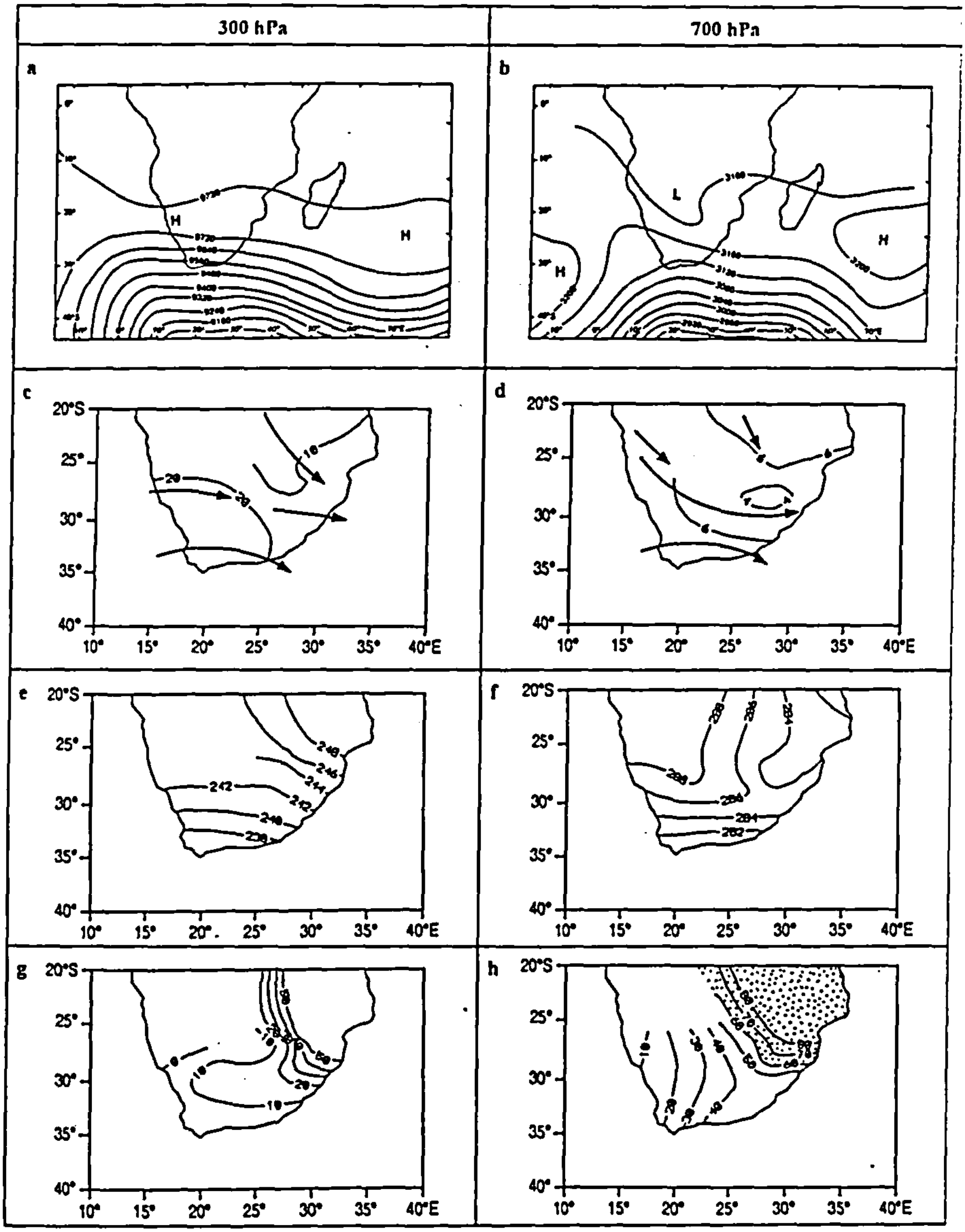

Figure 2.3: Geopotential height (gpm) at (a) 300 hPa and (b) 700 hPa; wind speed ($m.s^{-1}$, thin isotachs) and streamlines (bold lines) at (c) 300 hPa and (d) 700 hPa; temperature (K) at (e) 300 hPa and (f) 700 hPa; and relative humidity at (g) 300 hPa and (h) 700 hPa on 22 January at 12:00 UT. Areas where relative humidity exceeds 60 per cent are shaded in (g) and (h).

front to the south of the subcontinent was steered by the relatively warm, strong South Atlantic Anticyclone. The interior surface trough was tilted westward with height (Fig. 2.3a,b), such that its axis was situated to the west of the continent in the mid to upper troposphere (Fig. 2.1a). Upper tropospheric winds ahead of the approaching westerly wave were westerly (Fig. 2.3c). Northwesterly winds occurred in the lower levels along the eastern edge of the interior trough (Fig. 2.3d) and were transporting warmer air from the north along the trough (Fig. 2.3f). To the west of the interior trough, dew point temperatures were low (279-285K) and the air was dry (Fig. 2.3g,h) as a result of the subsidence associated with the anticyclonic flow in the lower troposphere. The strong discontinuity between clear and cloudy sky is evident throughout the study period.

By the evening of 22 January (Day 1), the tropical link between the interior trough and the tropical low had formed. The temperate link with the approaching cold front had yet to materialise (Plate 2.1b). Tropical air was still being transported to the south and southwest by the easterly wave and flow around the South Indian Anticyclone (Fig. 2.4a,b). It would seem that this tropical air is then circulated along the interior trough (Fig. 2.4d), thereby increasing the relative humidity throughout the troposphere over the northern regions of South Africa (Fig. 2.4g,h). At the 700 hPa level, westerly winds from the approaching westerly wave and flow from the north and northwest converged along the interior trough (Fig. 2.4c,d). The recurved air flow and decreasing temperatures (Fig. 2.4e,f) over the southern regions of South Africa are indicative of the increased influence of the westerly wave. A closed low is evident at the 700 hPa level.

The tropical link had temporarily broken by 05:30 UTC on 23 January (Day 2), but the temperate link between the interior trough and the cold front to the south of the continent had formed. By 12:00 UTC the tropical link had been re-established (Fig. 2.2b) and the tropical-temperate trough was reaching the mature stage of its development. The westerly wave had increased in amplitude, narrowed and strengthened (Figs 2.1b and 2.5a,b). Its trough axis was situated over the western regions of the subcontinent in the lower levels. Divergence in the upper westerly wave overlay convergence in the tropical low and interior trough, thus promoting ideal conditions for convection along the cloud band. Surface dew point temperatures had increased east of the trough (291-299K) (Fig. 2.2b) and are indicative of the warm, moist tropical air in circulation. Moist maritime air was also being fed onshore over the Natal coast by the weak coastal low that had developed (Fig. 2.2b).

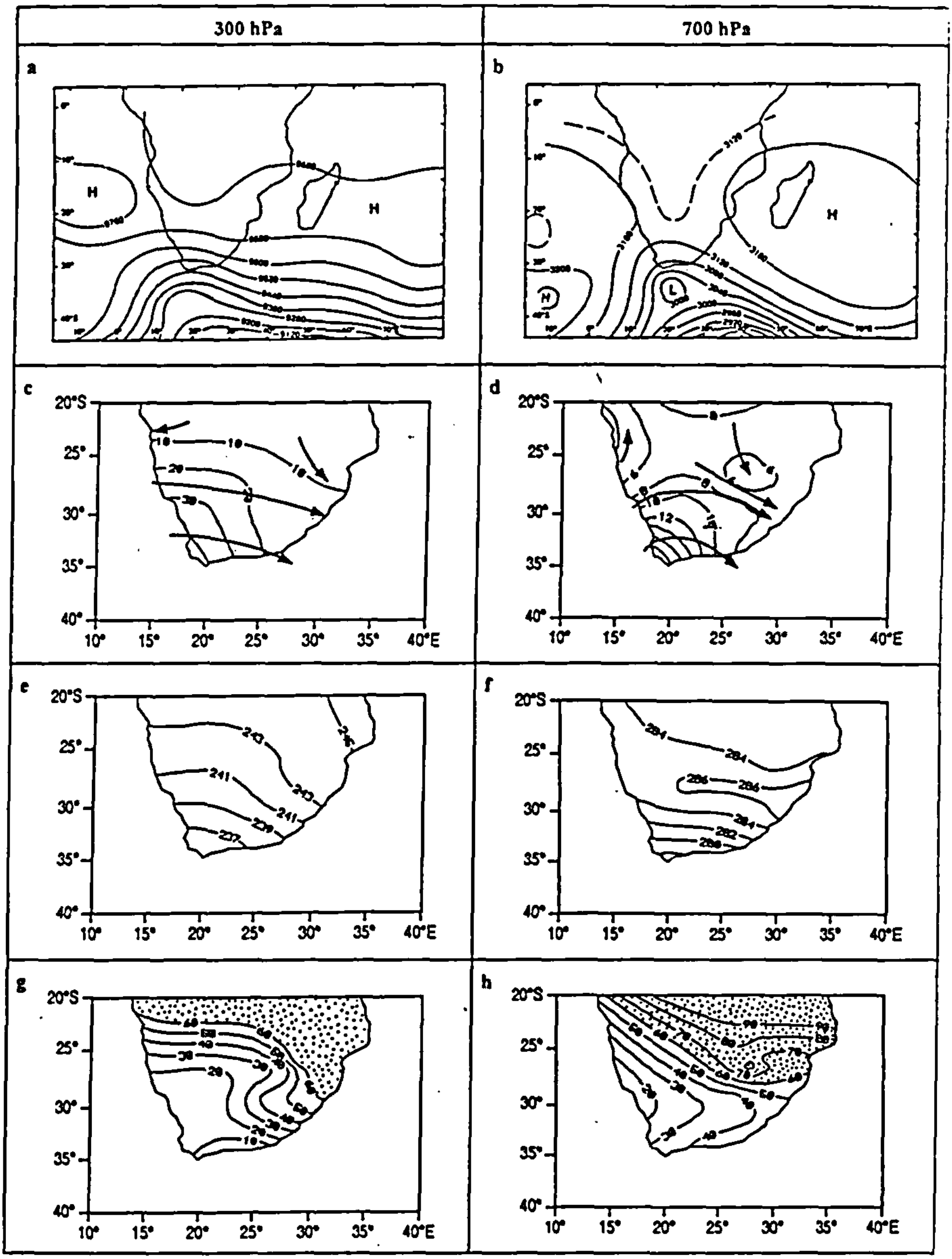

Figure 2.4: Geopotential height (gpm) at (a) 300 hPa and (b) 700 hPa; wind speed (m.s^{-1}, thin isotachs) and streamlines (bold lines) at (c) 300 hPa and (d) 700 hPa; temperature (K) at (e) 300 hPa and (f) 700 hPa; and relative humidity at (g) 300 hPa and (h) 700 hPa on 23 January at 00:00 UT. Areas where relative humidity exceeds 60 per cent are shaded in (g) and (h)

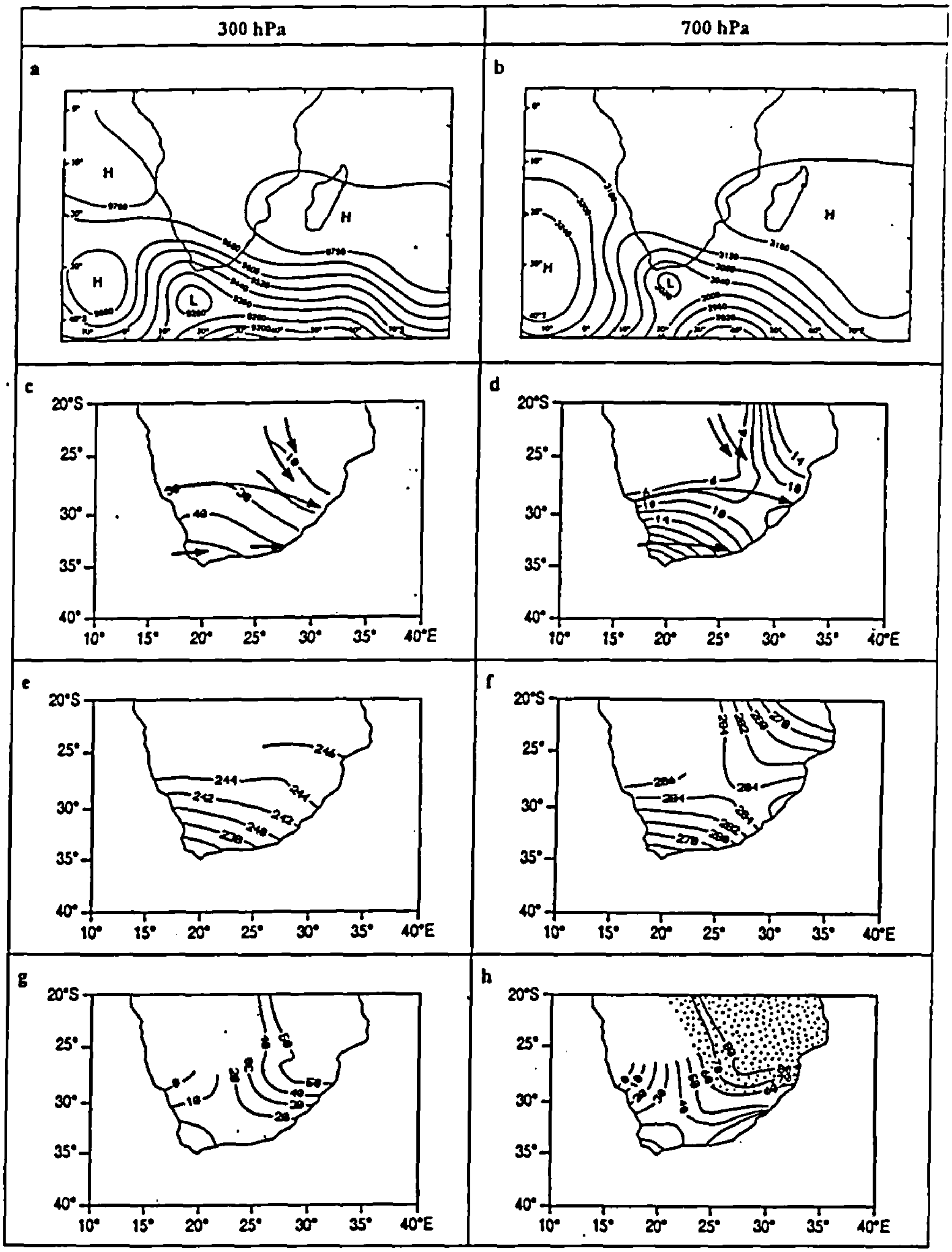

Figure 2.5: Geopotential height (gpm) at (a) 300 hPa and (b) 700 hPa; wind speed ($m.s^{-1}$, thin isotachs) and streamlines (bold lines) at (c) 300 hPa and (d) 700 hPa; temperature (K) at (e) 300 hPa and (f) 700 hPa; and relative humidity at (g) 300 hPa and (h) 700 hPa on 23 January at 12:00 UT. Areas where relative humidity exceeds 60 per cent are shaded in (g) and (h)

Convergence of the southwesterlies and the predominantly northwesterly flow in the region of the tropical-temperate trough (Fig. 2.5e,f) continued to enhance convection. The closed low had deepened and is obvious at the 300 hPa level (Fig. 2.5a). By 17:30 UTC, the fully developed tropical-temperate trough system and considerable tropical cloud are evident (Plate 2.1c). The tropical moisture that was being transported poleward could now be most efficiently utilised in the region of organised convection along the cloud band, and heavy rainfall occurred in the region of the tropical-temperate trough. The dry regions to the west of the cloud band (Fig. 2.5g,h) were enhanced by subsidence to the rear of the upper westerly wave.

By 00:00 UTC on 24 January (Day 3), the westerly trough had become narrower. Its trough axis was situated further eastward (Fig. 2.6a,b). The tropical link of the tropical-temperate trough appears to have broken, the temperate link was weak and the cloud band was beginning to disintegrate. Remnants of the cloud band are evident over the interior (Plate 2.1d). The break of the tropical link and the associated decline in tropical moisture supply resulted in the decrease in relative humidity. There was a large decline in tropical cloud cover (Plate 2.1d). Areas of highest relative humidity were confined to the southern regions of the subcontinent (Fig. 2.6g,h) and are indicative of the coastal cloud cover (Plate 2.1d) caused by the orographic uplift of maritime air. Cloud cover also occurred over the southwestern Cape coastal regions and was associated with the closed low that had further intensified (Fig. 2.6b). The cold-cored low is evidenced by the significant drop in temperature at the 700 hPa level (Fig. 2.6d).

The tropical-temperate trough had dissipated by 12:00 UTC on 24 January (Day 3) despite the presence of the interior trough. The zone of high relative humidity had shrunk and moved eastward (Fig. 2.7g,h) and surface dew point temperatures to the east of the interior trough had dropped (285 - 295K) (Fig. 2.2c). The ridging of the South Atlantic Anticyclone behind the cold front was at its strongest (Fig. 2.2c) and is obvious at all levels (Fig. 2.7a,b). Relative humidities were still high along the southern coastal regions in the lower levels due to the onshore flow around the ridging anticyclone. The cold front had moved approximately 15 degrees of longitude between 35 and 45°S in 12 hours. The closed low had shifted northeast at 700 hPa and was centred over the extreme south western Cape at the 300 hPa level (Fig. 2.7a,b).This closed low developed into the

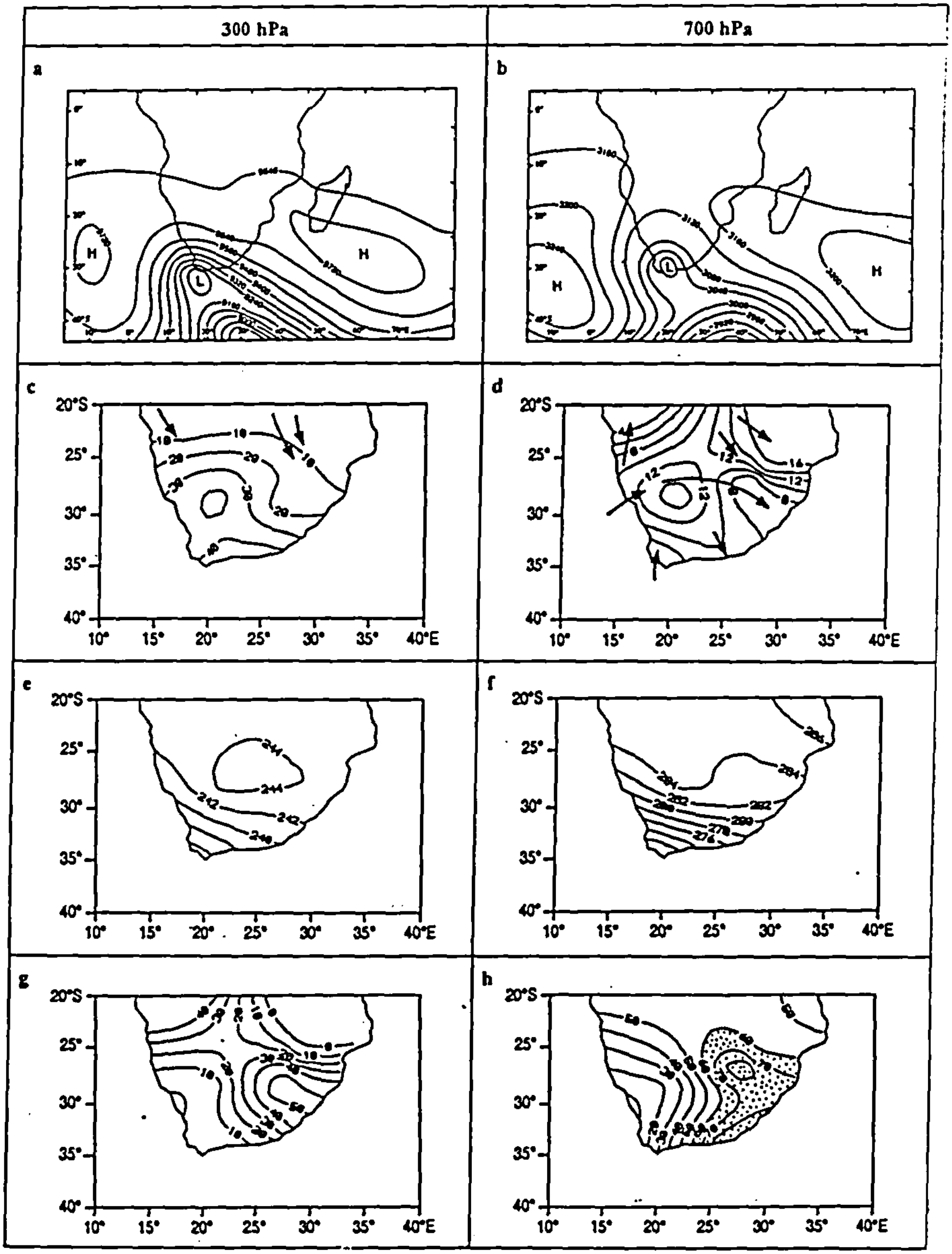

Figure 2.6: Geopotential height (gpm) at (a) 300 hPa and (b) 700 hPa; wind speed ($m.s^{-1}$, thin isotachs) and streamlines (bold lines) at (c) 300 hPa and (d) 700 hPa; temperature (K) at (e) 300 hPa and (f) 700 hPa; and relative humidity at (g) 300 hPa and (h) 700 hPa on 24 January at 00:00 UT. Areas where relative humidity exceeds 60 per cent are shaded in (g) and (h).

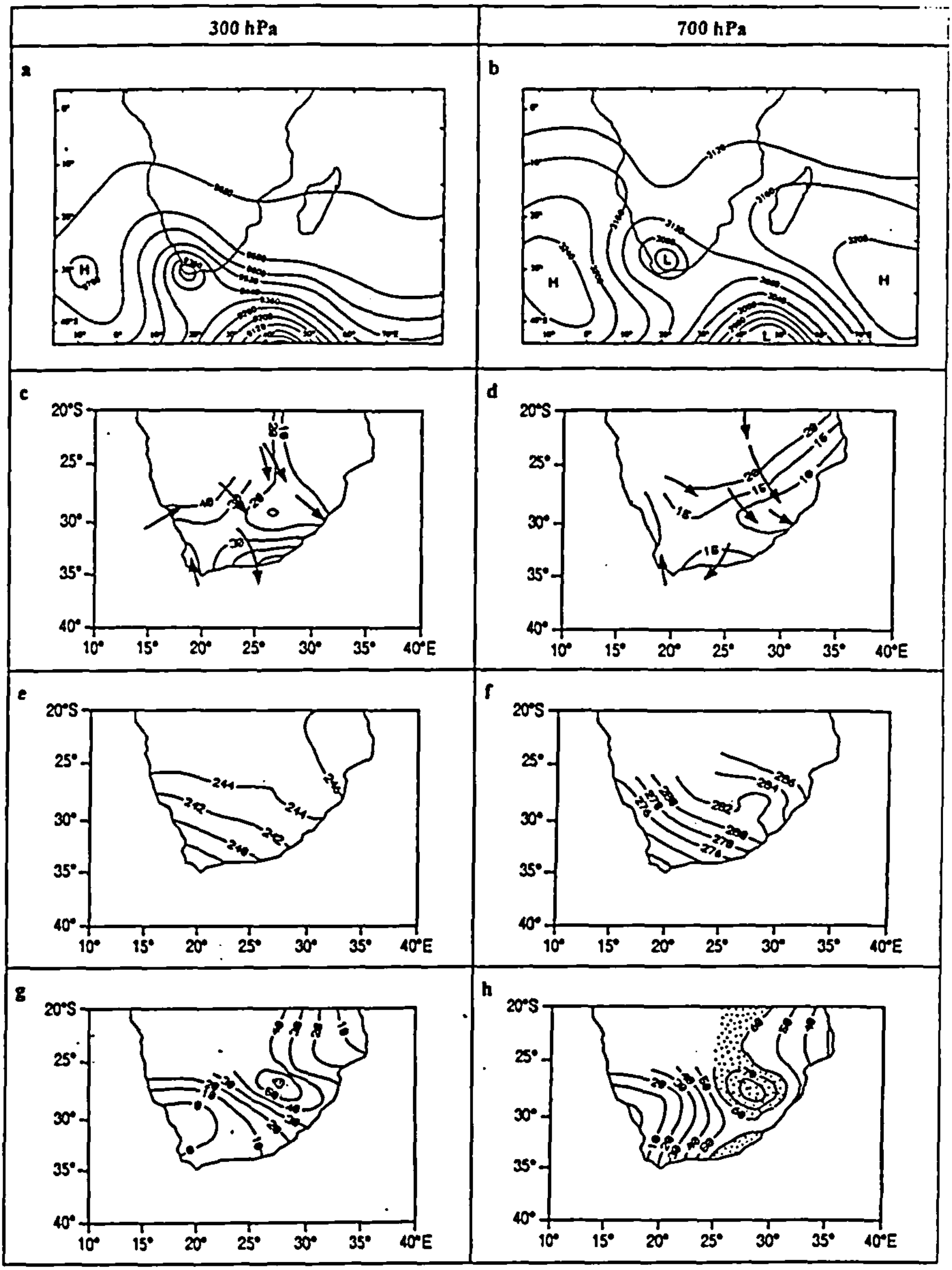

Figure 2.7: Geopotential height (gpm) at (a) 300 hPa and (b) 700 hPa; wind speed ($m.s^{-1}$, thin isotachs) and streamlines (bold lines) at (c) 300 hPa and (d) 700 hPa; temperature (K) at (e) 300 hPa and (f) 700 hPa; and relative humidity at (g) 300 hPa and (h) 700 hPa on 24 January at 12 00 UT. Areas where relative humidity exceeds 60 per cent are shaded in (g) and (h).

intense cut-off low that was responsible for the Lainsburg floods on the afternoon of 25 January 1981.

Rainfall

The heaviest rainfall recorded over the 24 hour period until 06:00 UTC on 23 January (Fig. 2.8a), was over the central interior in a zone orientated in a northwest-southeast direction, which corresponded to the position of the interior trough. Light falls occurred along the southern coast. Subsiding air over the northern and northwestern Cape inhibited rainfall over this region. By 06:00 UTC on 24 January (Fig. 2.8b), the rainfall over the central interior had increased significantly as a result of the development and intensification of the tropical-temperate trough. The increase in rainfall over the southern Cape coastal belt is due to the onshore flow of maritime air behind the cold front. Humid tropical air flowing southeastward within the tropical-temperate trough over the Natal coastal region, is likely to have been undercut and forced to rise by the cooler maritime air circulating onshore around the coastal low, causing the rainfall along this coast. Some rainfall was recorded over the extreme southwestern Cape due to the influence of the closed low situated over the region. The northwest-southeast alignment of the rainfall over the interior, corresponding to the position of the tropical-temperate trough, is evident in the accumulated rainfall totals for 22 to 23 January (Fig. 2.8c).

Thermodynamic Characteristics

Over Pretoria (Fig. 2.9f) and Bloemfontein (Fig. 2.9a), which are situated in the region of the tropical-temperate trough, the temperature decreased by approximately 3K in the lower levels due to heavy cloud cover. The southeastward transport of warm tropical air along the tropical-temperate trough is evidenced in the temperature increase in the lower and middle tropospheric levels over Durban (Fig. 2.9c) and Marion Island (Fig. 2.9d). The temperatures decreased following the tropical-temperate trough dissipation on 24 January. The eastward movement of the cold front associated with the cloud band dissipation resulted in the temperature drop in the lower to middle tropospheric levels over Port Elizabeth on 24 January (Fig. 2.9e). The decline in temperature throughout most of the troposphere over Cape Town on 23 and 24 January (Fig. 2.9b)

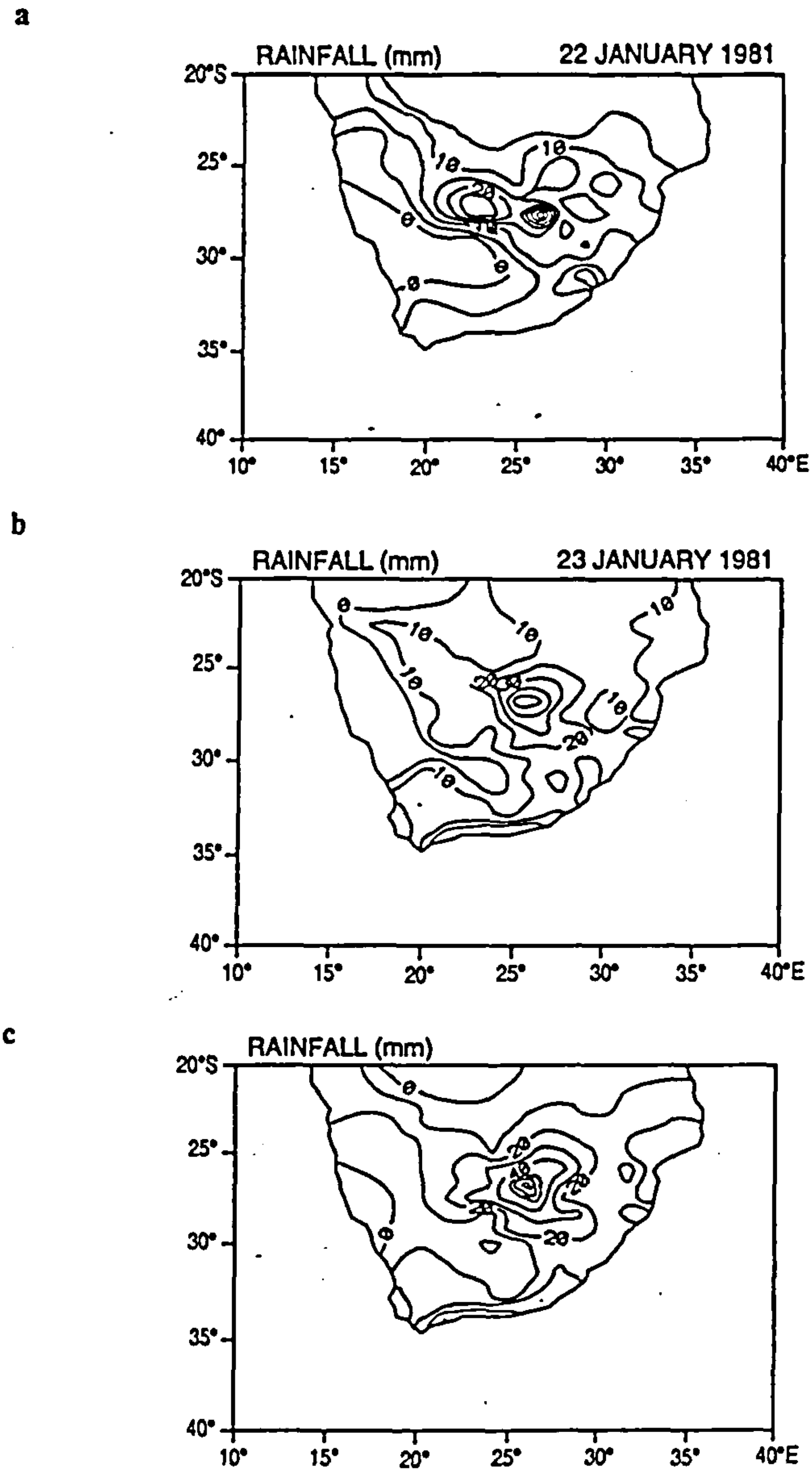

Figure 2.8: Rainfall recorded for the 24 hour period ending at 6:00 UT on the day following the indicated date for (a) 22 January and (b) 23 January. Accumulated rainfall for the period (c) 22 Jan 6:00 UT to 24 Jan 6:00 UT.

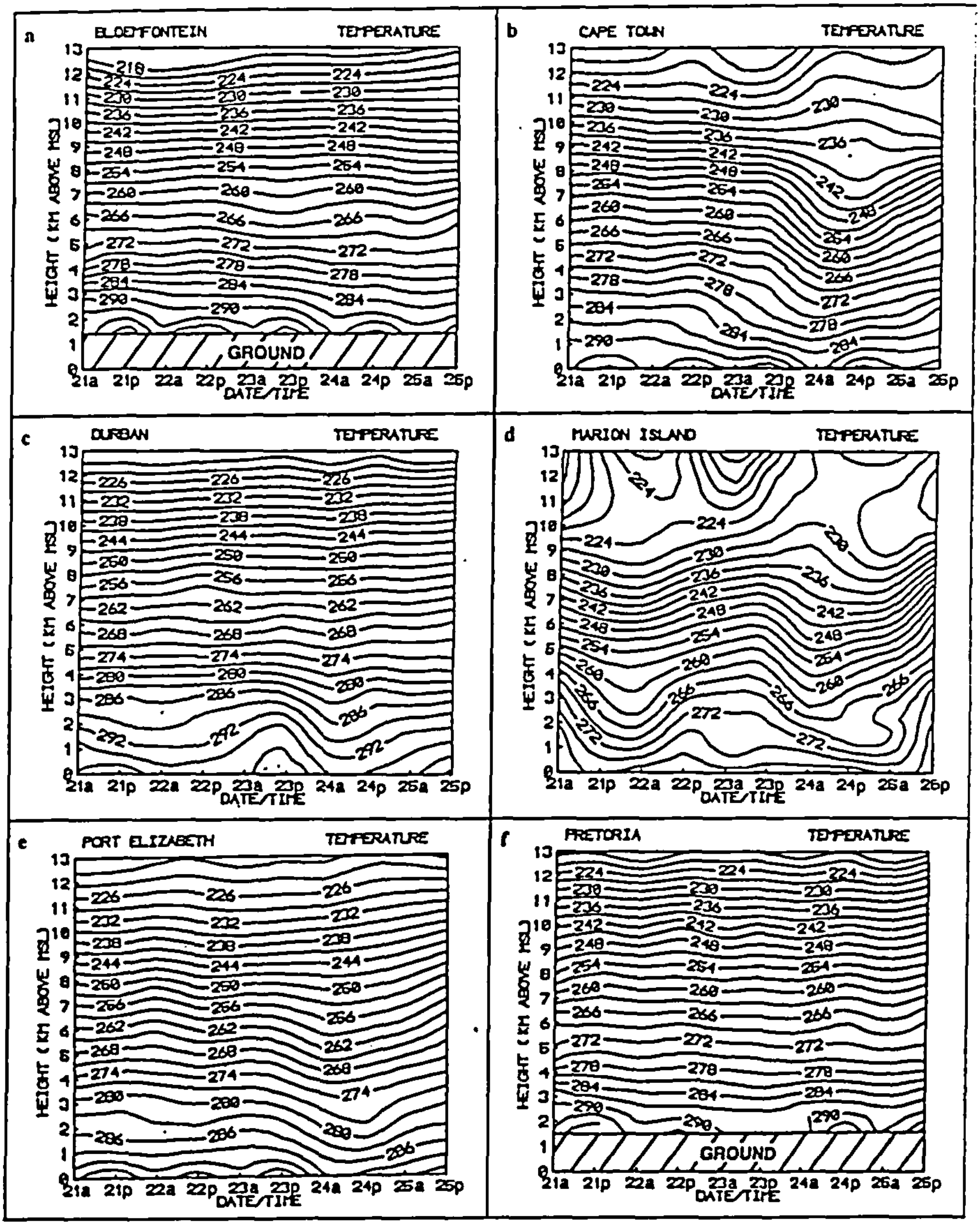

Figure 2.9: Temperature (K) structure of the troposphere for the period 00:00 UT on 21 January to 12:00 UT on 25 January for (a) Bloemfontein, (b) Cape Town, (c) Durban, (d) Marion Island, (e) Port Elizabeth, (f) Pretoria.

is indicative of the depth and strength of the cut-off low that was present over the region. The presence of the tropical-temperate trough over Windhoek (Fig. 2.10f) is evident in the high relative humidity values over the region, particularly on 23 January. The fairly high relative humidity throughout much of the troposphere on 23 January at Bloemfontein (Fig. 2.10a), Pretoria (Fig. 2.10e) and Marion Island (Fig. 2.10c), followed by a drop in these values on 24 January, are indicative of the development and dissipation of the tropical-temperate trough over these regions. Re-formation of the tropical-temperate trough over the interior on 25 January is also evident in the relative humidity fields over Pretoria and Bloemfontein. The relative humidity over Cape Town (not shown) and Port Elizabeth (Fig. 2.10d) increased on 24 and 25 January due to the presence of the cut-off low and the onshore flow around the ridging South Atlantic High, respectively. Over Durban (Fig. 2.10b) a layer of drier air separated the humid air associated with the coastal low in the lower levels and the tropical-temperate trough in the middle levels. An increase in humidity on 24 and 25 January is indicative of the cloud band remnants.

Kinematic Characteristics

Transport of the tropical and maritime air into the tropical low during the initial stages of development of the tropical-temperate trough, was facilitated by the easterlies evident in the lower and middle levels over Pretoria (Fig. 2.11e) and Windhoek (Fig. 2.11f) and by the northerlies over Pretoria (Fig. 2.12e). The easterly flow over Pretoria and Windhoek then became westerly due to the circulation along the tropical-temperate trough and westerly wave. Circulation around the tropical low at Windhoek was the cause of the southerly flow in the lower layers over region. The surface poleward flow along the tropical-temperate trough occurred just south of this station (Fig. 2.2a,b,c) and northerly flow was dominant in the upper atmosphere. The airflow along the tropical-temperate trough and the westerly wave resulted in the predominantly westerly and southward flow over Port Elizabeth (Figs 2.11d and 2.12d), Bloemfontein (Fig. 2.11a) and (not shown) and Durban (not shown and Fig. 2.12b). The poleward flow over Durban was undercut by the onshore flow around the coastal low in the lower levels on 23 and 24 January (Fig. 2.2c). The importance of tropical-temperate troughs in transporting momentum from the tropics to the mid-latitudes is apparent in the strong poleward flow (Fig. 2.12c), the high relative angular momentum values (Fig. 2.13) and the increased westerly flow between about 400 and 200 hPa that occurred over Marion

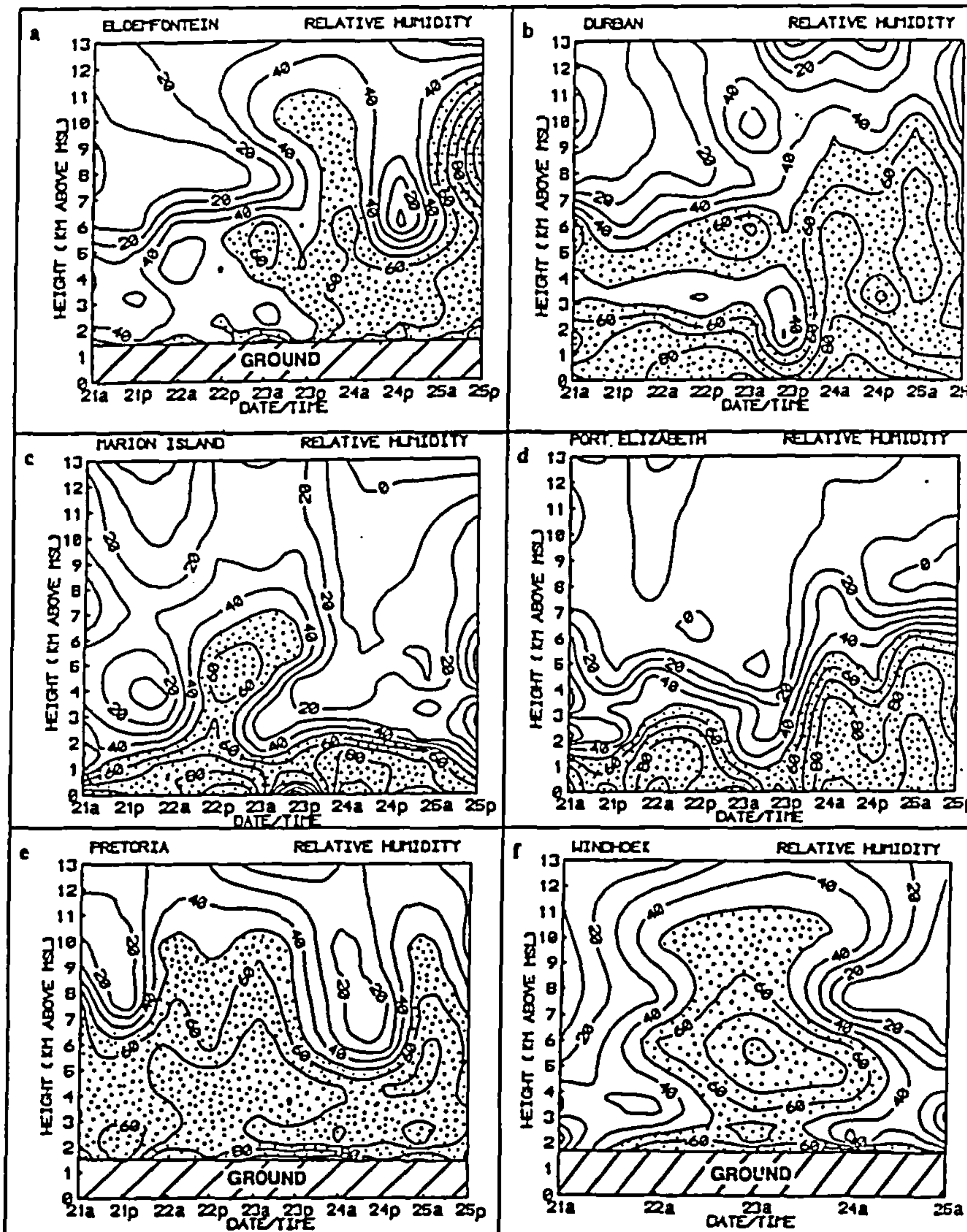

Figure 2.10: Relative humidity (%) from 00:00 UT on 21 January to 12:00 UT on 25 January for (a) Bloemfontein, (b) Durban, (c) Marion Island, (d) Port Elizabeth, (e) Pretoria, (f) Windhoek. Regions where relative humidity exceeds 50 per cent are shaded.

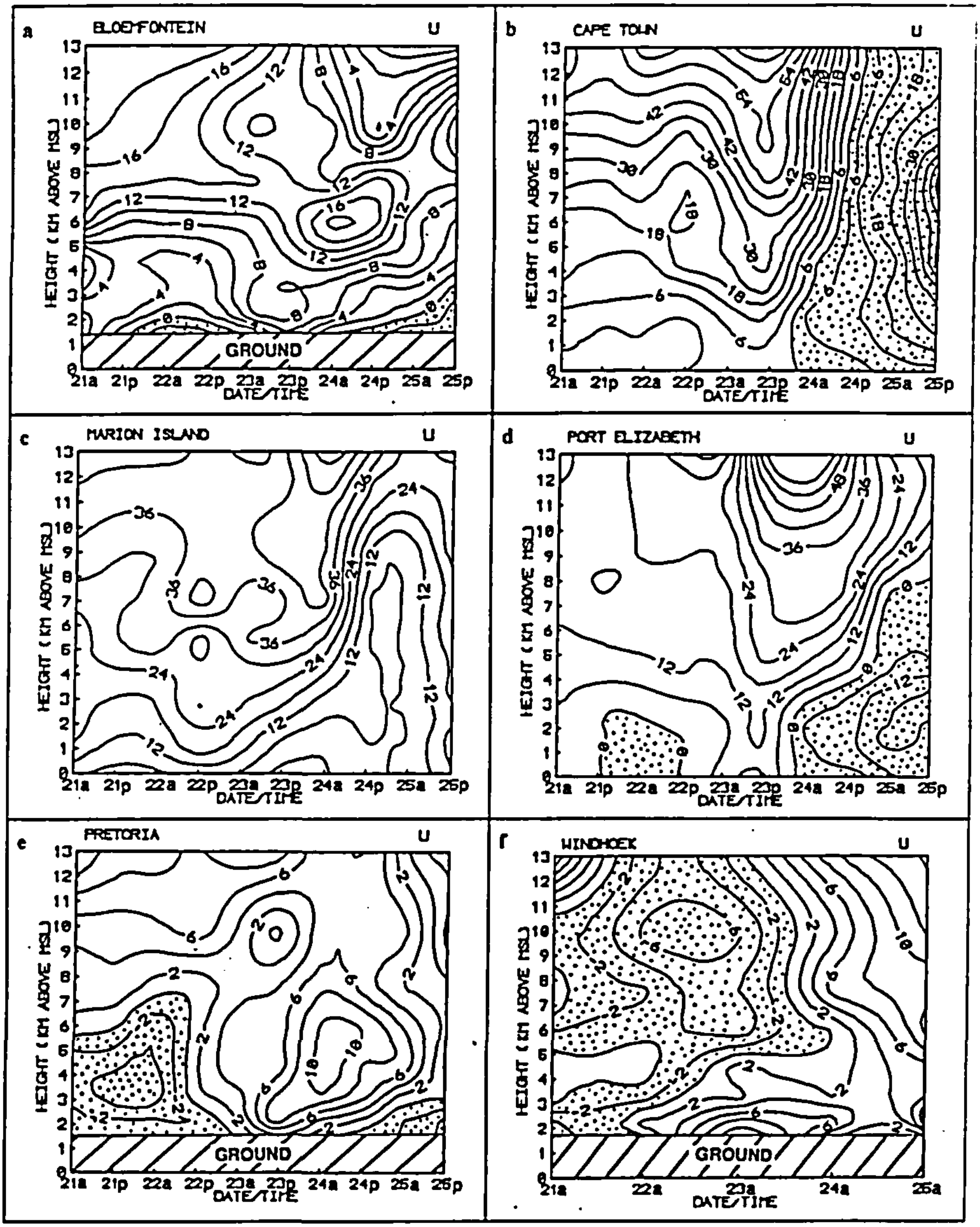

Figure 2.11: Zonal component of the wind flow ($m.s^{-1}$) from 00:00 UT on 21 January to 12:00 UT on 25 January for (a) Bloemfontein, (b) Cape Town, (c) Marion Island, (d) Port Elizabeth, (e) Pretoria and (f) Windhoek. Easterly components are shaded.

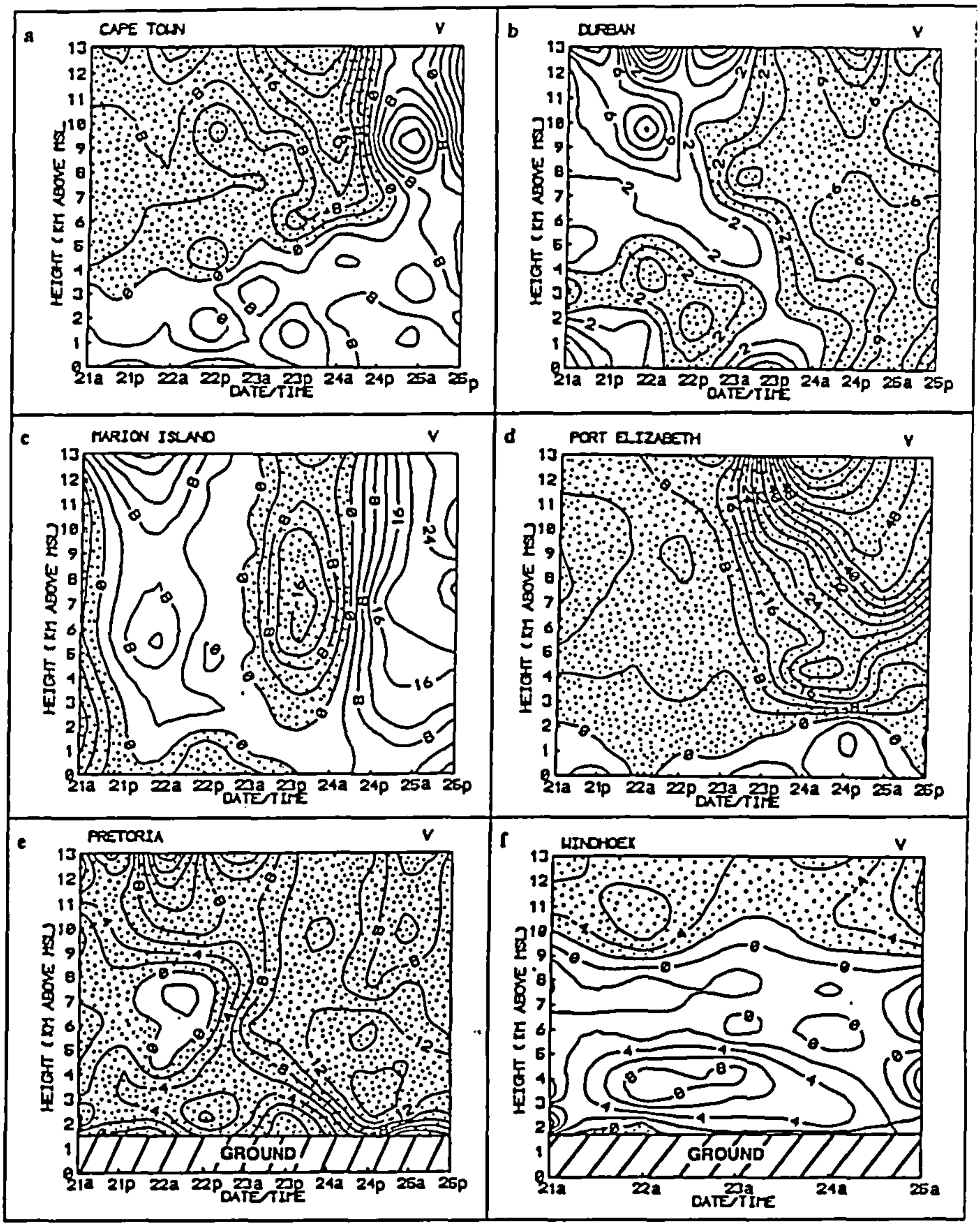

Figure 2.12: Meridional component of the wind flow (m.s⁻¹) from 00:00 UT on 21 January to 12:00 UT on 25 January for (a) Cape Town, (b) Durban, (c) Marion Island, (d) Port Elizabeth, (e) Pretoria and (f) Windhoek. Northerly components are shaded.

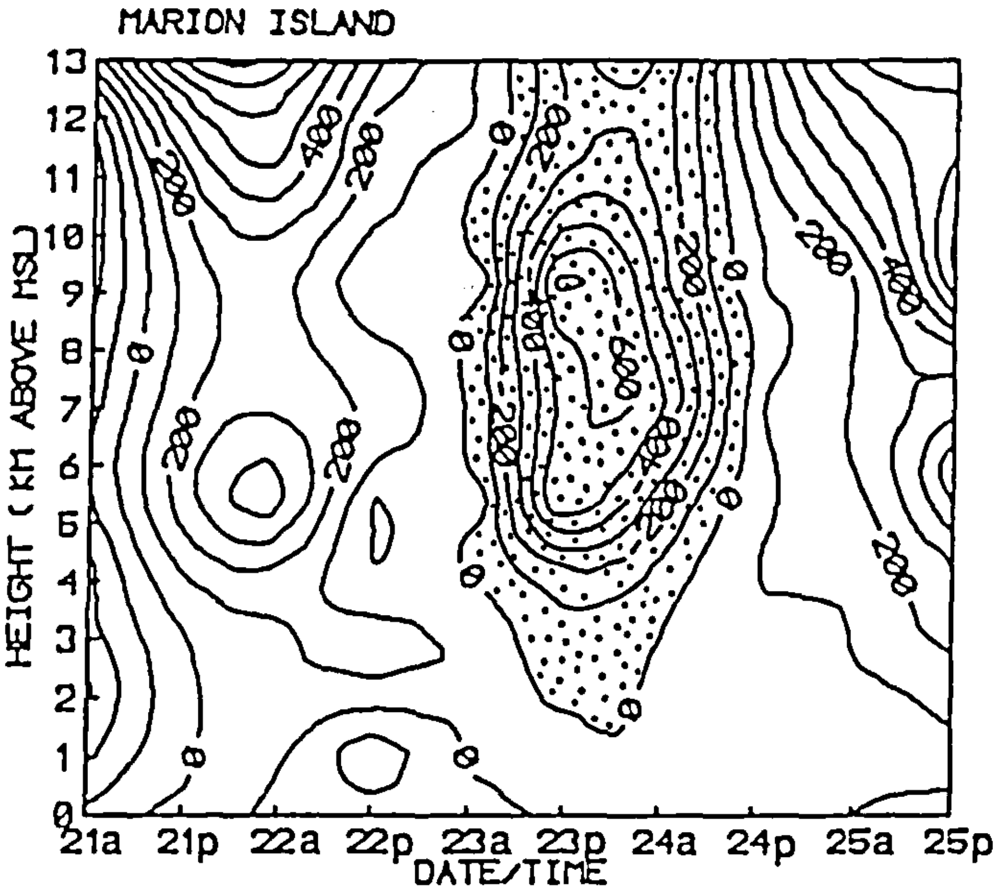

Figure 2.13: Relative angular momentum over Marion Island from 00:00 UTC on 21 January to 12:00 UTC on 25 January.

Island on the 23 January. Once the cloud band dissipated and the supply of westerly angular momentum decreased, the westerlies and relative angular momentum decreased, and the poleward flow was replaced by southerly flow. Ridging of the South Atlantic Anticyclone which enhanced the dissipation of the tropical-temperate trough is evident in the easterly (Fig. 2.11d) and southerly (Fig. 2.12d) flow in the lower levels over Port Elizabeth on 24 January (Fig. 2.11d). The influence that the cut-off low had on the zonal and meridional flow over Cape Town is apparent from 24 January (Figs 2.11b and 2.12a).

The Dry Case Study: 6-8 January 1980

To investigate the structure of dry-year tropical-temperate troughs is particularly difficult, as they develop preferentially over the ocean between Madagascar and the southern African subcontinent or to the east of Madagascar, where data is sparse of non-existent. Part of the northern section of the tropical-temperate trough in the 6 to 8 January 1980 case study occurs over the northeastern regions of southern Africa and can be examined with the use of station data. However, satellite imagery and synoptic and upper air charts will have to be relied upon for examining the rest of the system.

Sequence of events

Most of central Africa and the eastern regions of southern Africa were covered by tropical cloud on 6 January (Day 1), the pre-cloud band day (Plate 2.2a). Well-developed cloud clusters occurred over the Mozambique Channel and to the southeast of southern Africa a cold front is also evident. By early morning on 7 January (Day 2), the extensive tropical cloud had shifted eastward and linked with the cold front that had progressed eastward (Plate 2.2b). The tropical-temperate trough was fully developed by 12:00 UTC on 7 January and was situated over the eastern regions of tropical and southern Africa, the Mozambique Channel and Madagascar (Plate 2.2c). The tropical-temperate trough started to dissipate early on 8 January (Day 3) (Plate 2.2d) and the tropical cloud cover had reduced significantly. By midday on 8 January the tropical-temperate trough had dissipated. Remnants were situated over Madagascar and the Mozambique Channel (Plate 2.2e).

a

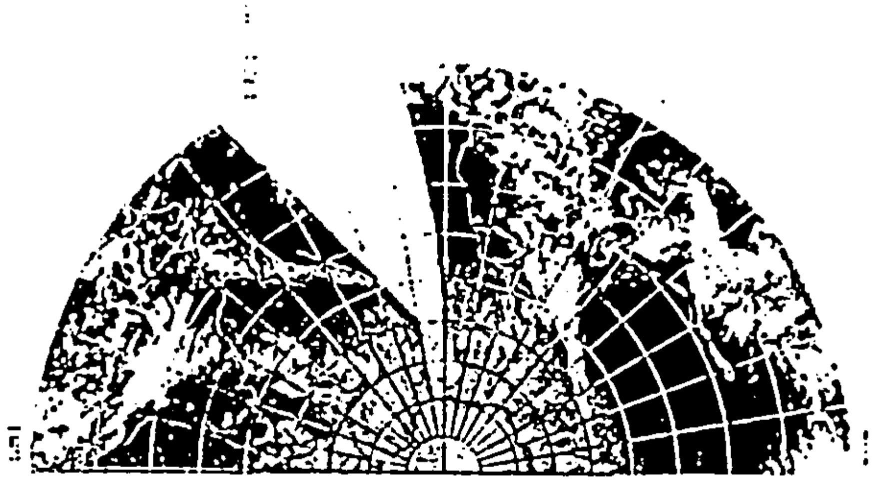

b

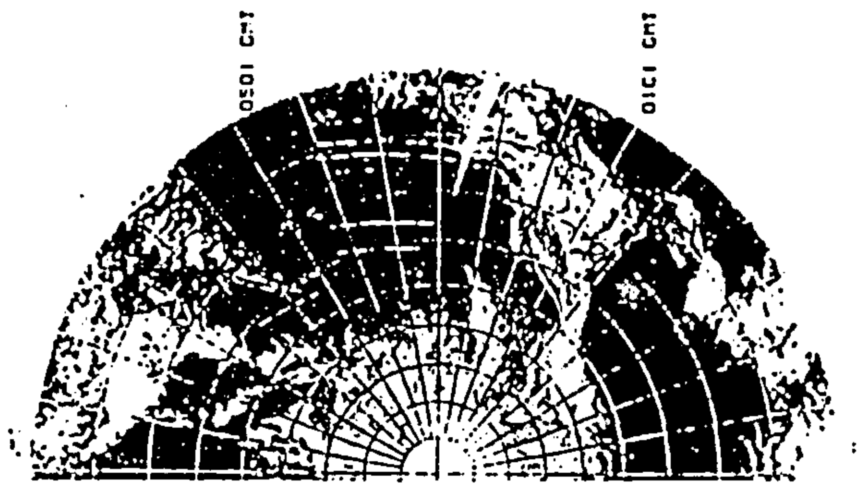

c

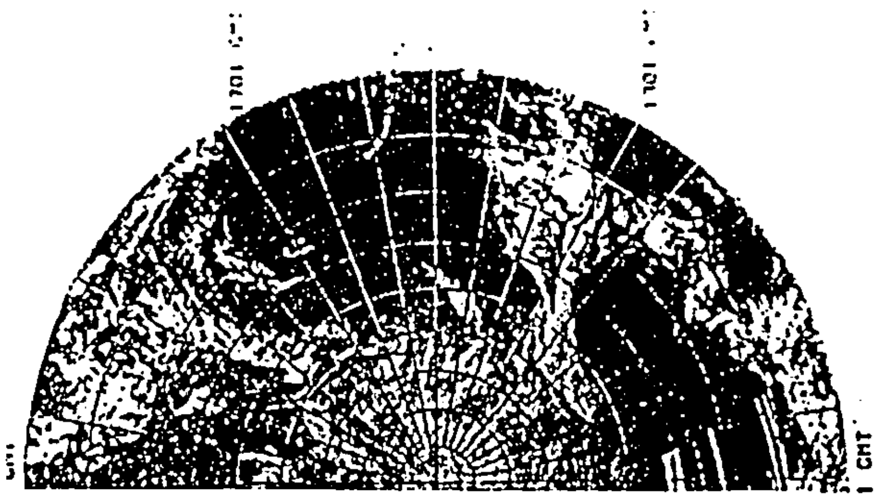

Plate 2.2: NOAA infra-red satellite imagery for (a) 6 January, (b and c) 7 January, and (d and e) 8 January. The universal time that the image was taken is indicated on the plate.

d

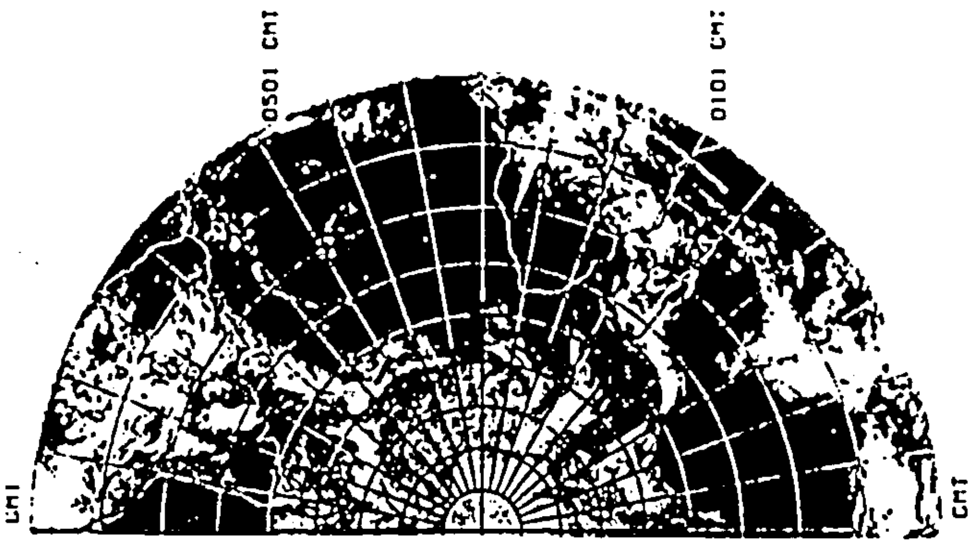

c

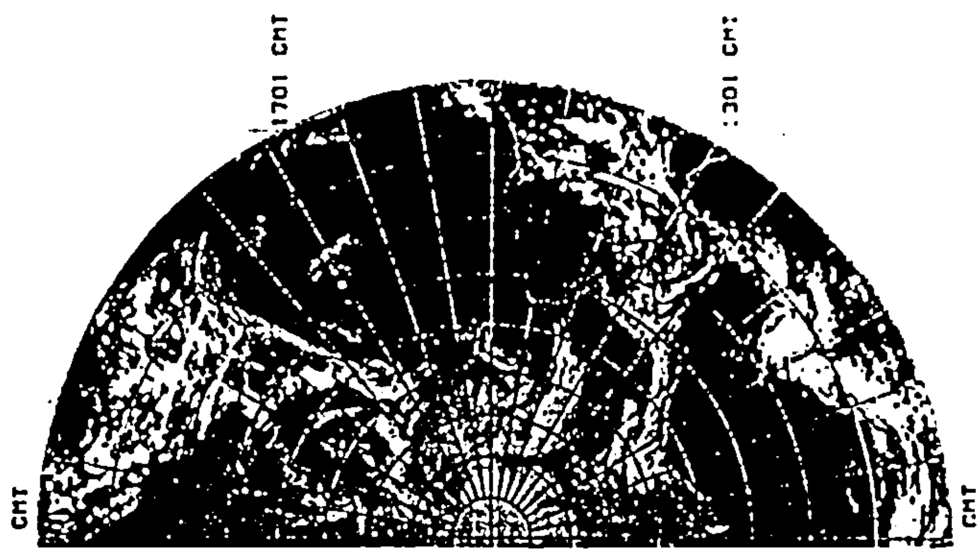

Plate 2.2: NOAA infra-red satellite imagery for (d and e) 8 January. The universal time that the image was taken is indicated on the plate.

Hemispheric Circulation Controls

During the period of 6 to 8 January, the circulation in the Southern Hemisphere was dominated by a 6-wave structure. Development of the tropical-temperate trough occurred along the westerly wave to the southeast of the subcontinent. The axis of the wave was situated over the eastern regions of southern Africa on 6 January (Day 1) (Fig. 2.14a), overlay Madagascar on the cloud band day (Day 2) (Fig. 2.14b), and then moved eastward of Madagascar on 8 January (Day 3) (Fig. 2.14c).

Synoptic and Regional Circulation Controls

An extensive cold front system to the southeast of the subcontinent, a ridge of the South Atlantic Anticyclone extending behind this cold front, a secondary cold front approaching the country from the southwest, the South Indian Anticyclone centred to the southeast of Madagascar and two regions of low pressure over the interior were all significant features at the surface level on 6 January 1980 (Day 1) (Fig. 2.15a). The frontal system to the southeast constituted the temperate section of the tropical-temperate trough and heavy cloud cover occurred in association with this system (Plate 2.2a). Cyclonic circulation around the low pressure cell within the frontal system caused the onshore flow of moist air along the Natal coast (Fig. 2.16d) and the high relative humidities at the 700 hPa level (Fig. 2.16h). The region of low pressure over central Mozambique (Fig. 2.15a) became part of the tropical-temperate trough, but the satellite imagery (Plate 2.2a,b) reveals that the tropical low that formed the tropical link was situated over northern Mozambique. Easterly flow from around the South Indian High occurred over the southern African coast between 15° and 25°S. Moisture was also transported westward across the northern Mozambique Channel to the east coast of subtropical Africa. The ridge of the South Atlantic High extended particularly far eastward (Fig. 2.15a and Plate 2.2a) and was responsible for the dry conditions and low relative humidities throughout the troposphere over the western and southwestern Cape (Fig. 2.16g,h). The southwesterly (Fig. 2.16d) and westerly (Fig. 2.16c) winds and the temperature distribution (Fig. 2.16e,f) are indicative of the tilted westerly wave over the central and western regions of southern Africa. By 00:00 UTC on 7 January (Day 2), the westerly wave had progressed eastward and the trough axis associated with the leading cold front was situated between 35° and

a

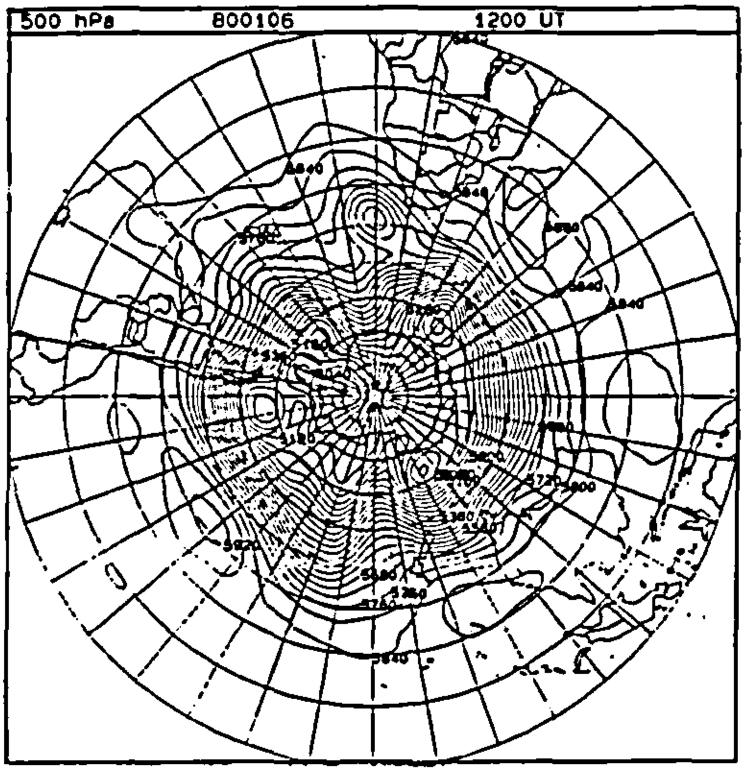

b

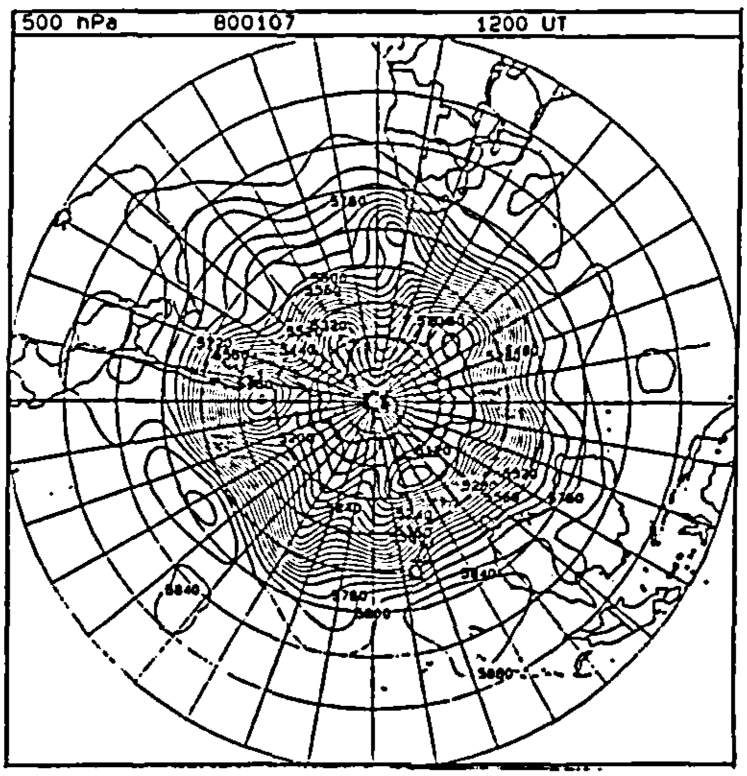

Figure 2.14: The circumpolar wave structure at 500 hPa on (a) 6 January, (b) 7 January, and (c) 8 January.

c

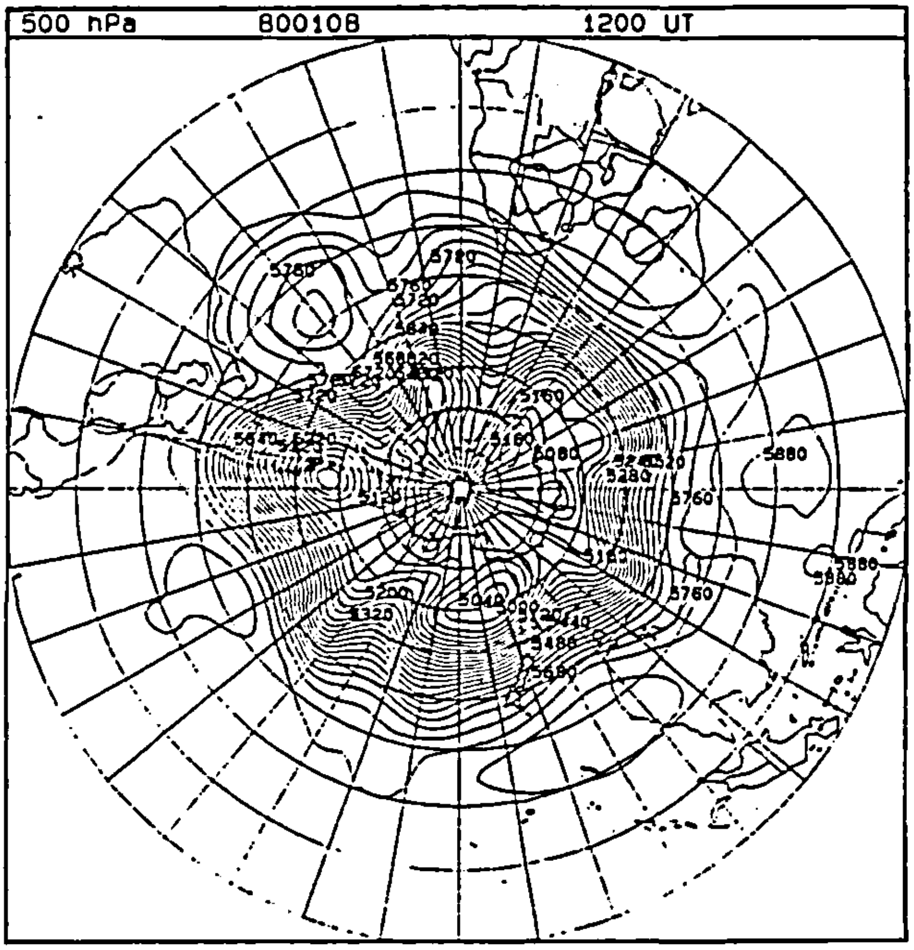

Figure 2.14: The circumpolar wave structure at 500 hPa on (c) 8 January.

a

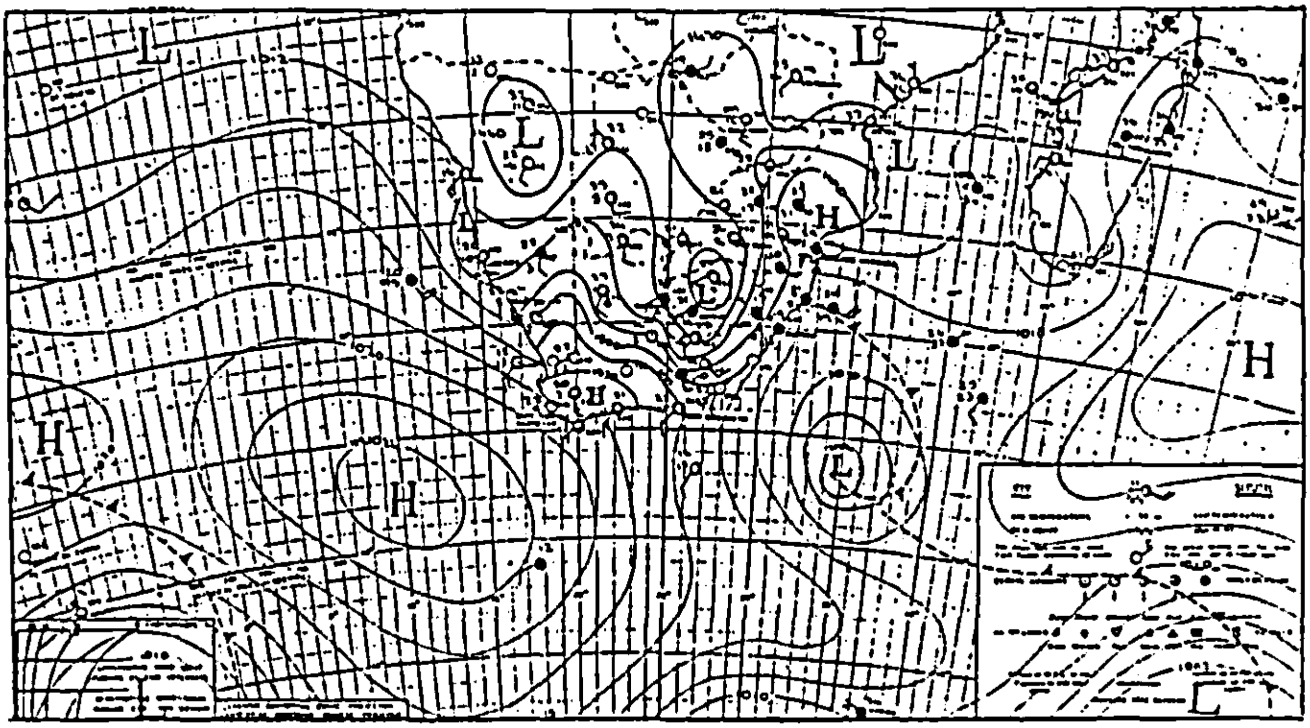

b

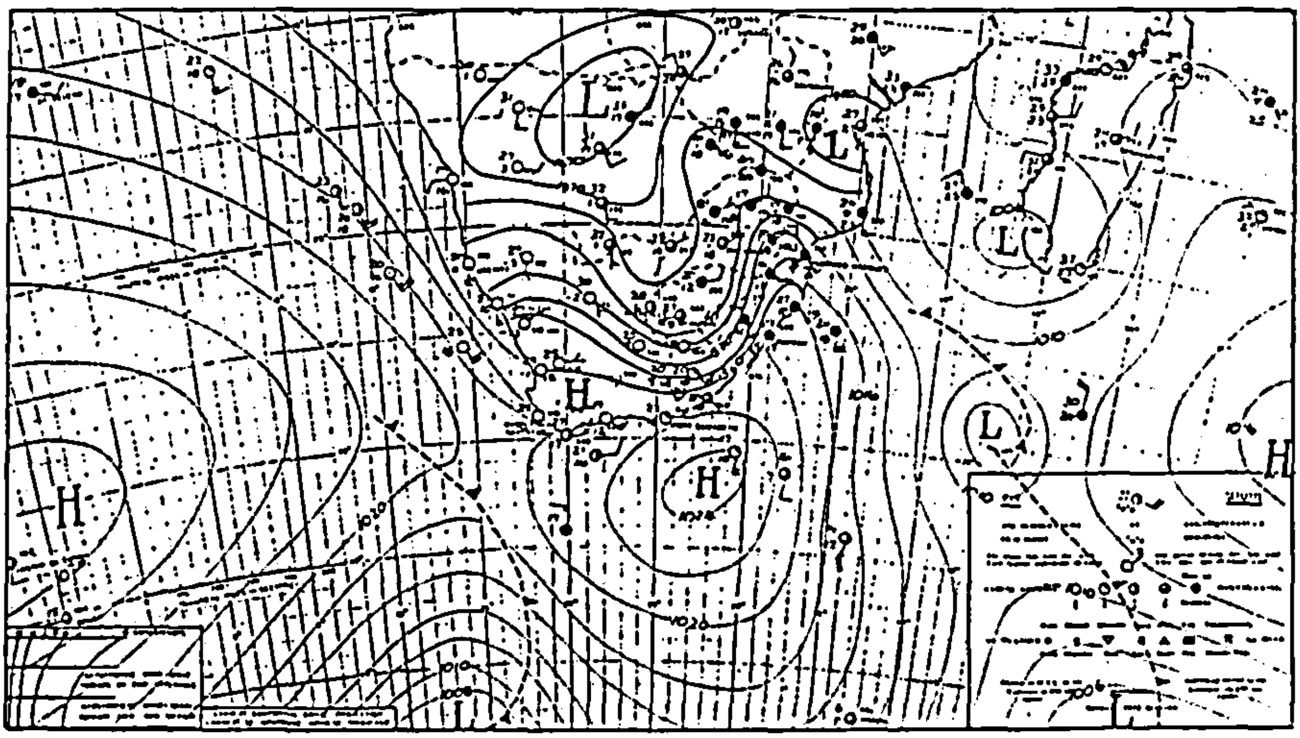

Figure 2.15: Synoptic charts at 12:00 UTC for (a) 6 January, (b) 7 January, and (c) 8 January. Isobars at mean sea level are in hPa and contours over the land of the 850 hPa surface are in geopotential metres.

c

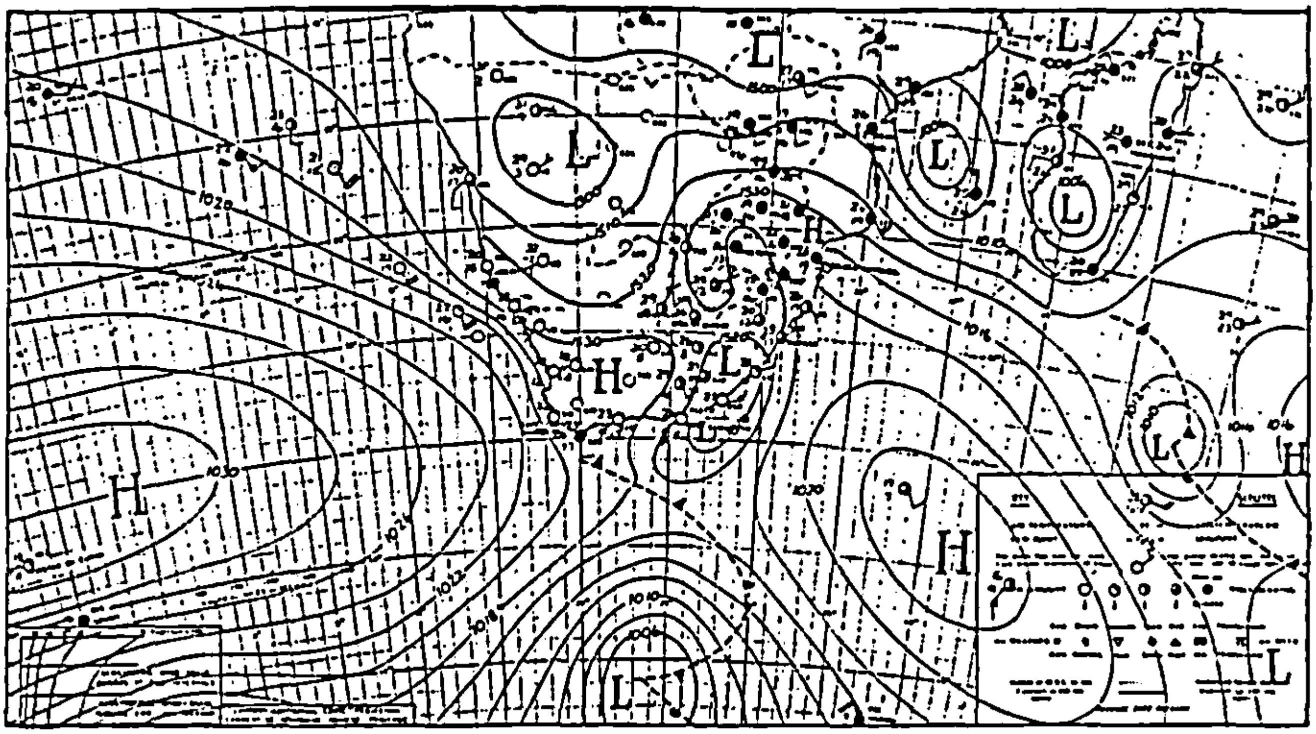

Figure 2.15: Synoptic charts at 12:00 UTC for (c) 8 January. Isobars at mean sea level are in hPa and contours over the land of the 850 hPa surface are in geopotential metres.

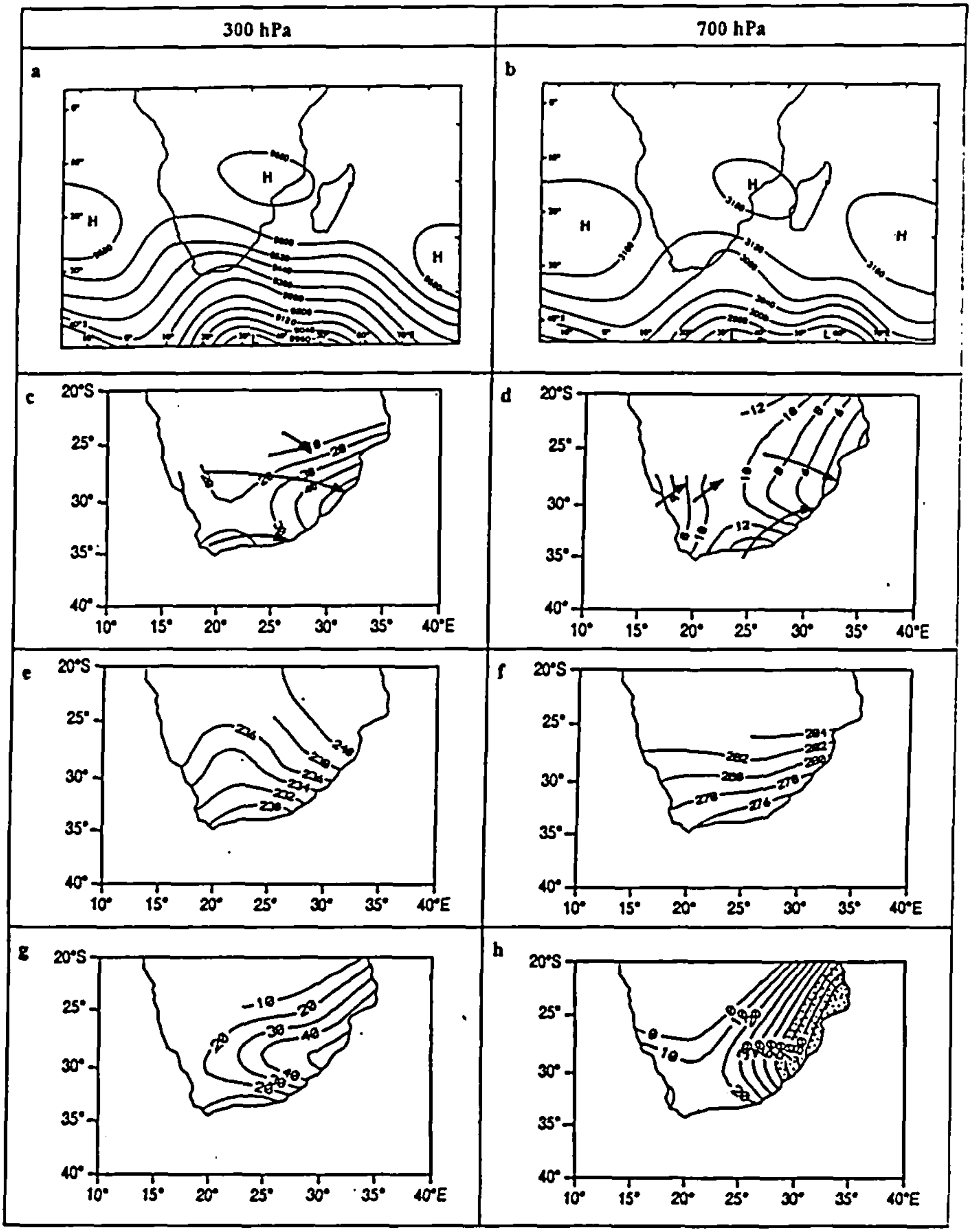

Figure 2.16: Geopotential height (gpm) at (a) 300 hPa and (b) 700 hPa; wind speed (m.s⁻¹, thin isotachs) and streamlines (bold lines) at (c) 300 hPa and (d) 700 hPa; temperature (K) at (e) 300 hPa and (f) 700 hPa; and relative humidity at (g) 300 hPa and (h) 700 hPa on 6 January at 12:00 UT. Areas where relative humidity exceeds 60 per cent are shaded in (g) and (h).

40°E at 700 hPa (Fig. 2.17b), and over the central interior at 300 hPa (Fig. 2.17a and Plate 2.2b). By midday, the eastward movement of the westerly wave had aligned the cold front system with the trough extending from over central Mozambique and the southern regions of Madagascar which resulted in the establishment of the temperate link. The tropical link had formed over northern Mozambique (Plate 2.2b,c). The tropical-temperate trough was now well-developed (Plate 2.2c) and extensive tropical cloud existed over Madagascar, the Mozambique Channel and the eastern regions of Africa. A cell of the South Atlantic High had broken off and was positioned between the tropical-temperate trough and the secondary cold front (Fig. 2.15b). Circulation around this high pressure cell fed maritime air over the Natal coast thereby increasing the relative humidity in the lower atmospheric levels (Fig. 2.18g). Easterly flow at the surface continued to supply central Mozambique with tropical air and dew point temperatures in this region were exceptionally high (292-295K) (Fig. 2.15b). It appears from the few surface observations over the sea that airflow along the tropical temperate trough was poleward at the surface. This flow is likely to have been enhanced by southward flow along the leading arm of the upper westerly wave (Fig. 2.18a,b), but there are no upper air wind observations over this region to confirm this.

By early morning on 8 January (Day 3), the tropical-temperate trough had started to dissipate. The tropical link had broken and the temperate link had weakened (Plate 2.2d). The westerly wave was still situated over the interior at 300 hPa, although the axis had been tilted southwestward (Fig. 2.19a). The tropical cloud over the eastern regions of Africa had decreased (Plate 2.2d) and almost all of southern Africa, with the exception of the northeastern sector, was cloud free. By 12:00 UT, the tropical-temperate trough had dissipated, the remnants of which were situated over Madagascar and the oceanic regions to the southeast of the island (Plate 2.2e). The leading cold front was located to the east of Madagascar making any link with the tropical low over northern Mozambique impossible (Fig. 2.15c). The high pressure cell, which enhanced the eastward movement of the cold front, continued to feed maritime air onshore (Figs 2.15c and 2.20h). The upper atmosphere was particularly dry at this stage (Fig. 2.20g) due to subsidence to the rear of the westerly wave. Temperatures were lowest throughout the atmosphere over the southern Cape (Fig. 2.20e,f) due to the approach of the second cold front.

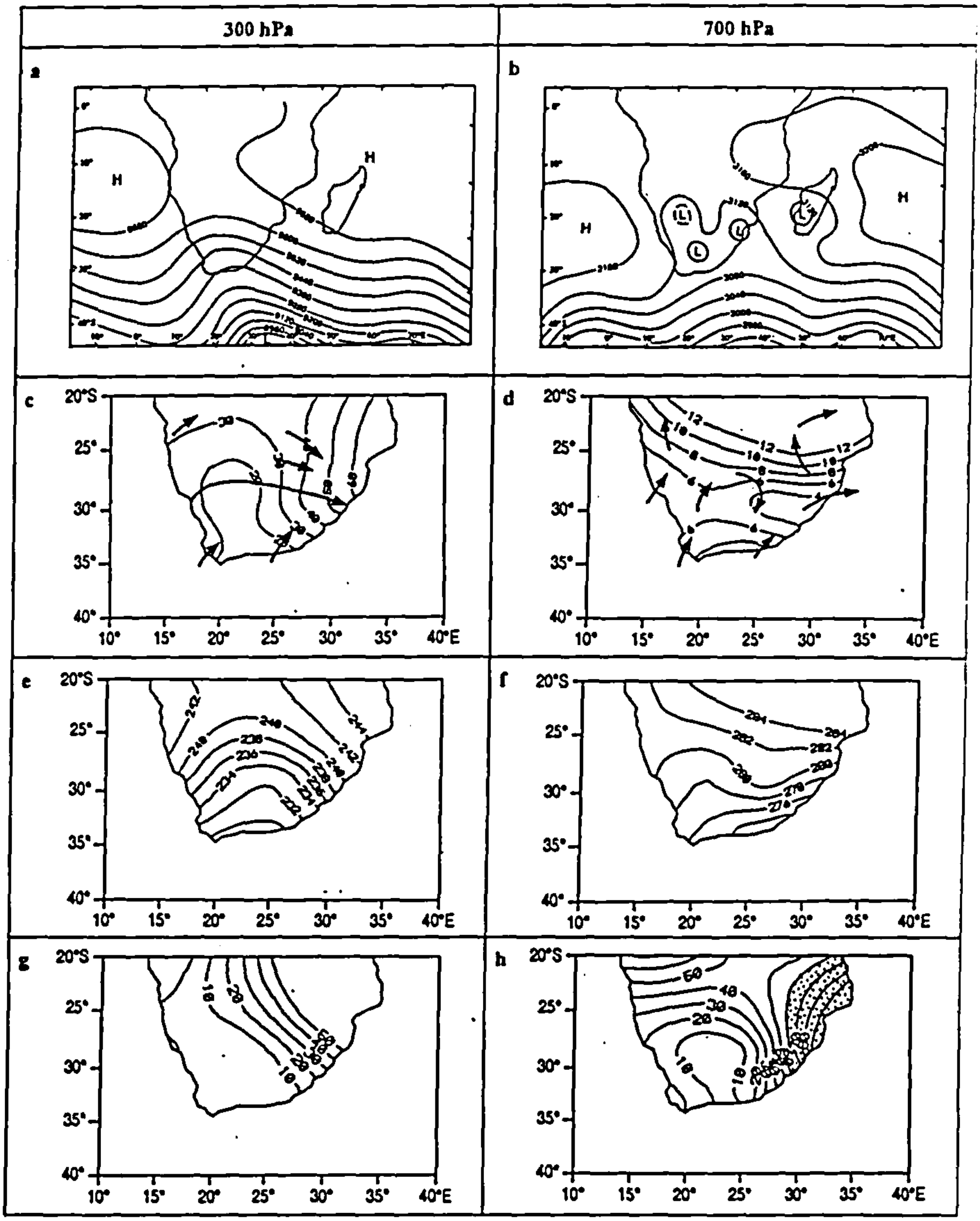

Figure 2.17: Geopotential height (gpm) at (a) 300 hPa and (b) 700 hPa; wind speed (m.s^{-1}, thin isotachs) and streamlines (bold lines) at (c) 300 hPa and (d) 700 hPa; temperature (K) at (e) 300 hPa and (f) 700 hPa; and relative humidity at (g) 300 hPa and (h) 700 hPa on 7 January at 00:00 UT. Areas where relative humidity exceeds 60 per cent are shaded in (g) and (h).

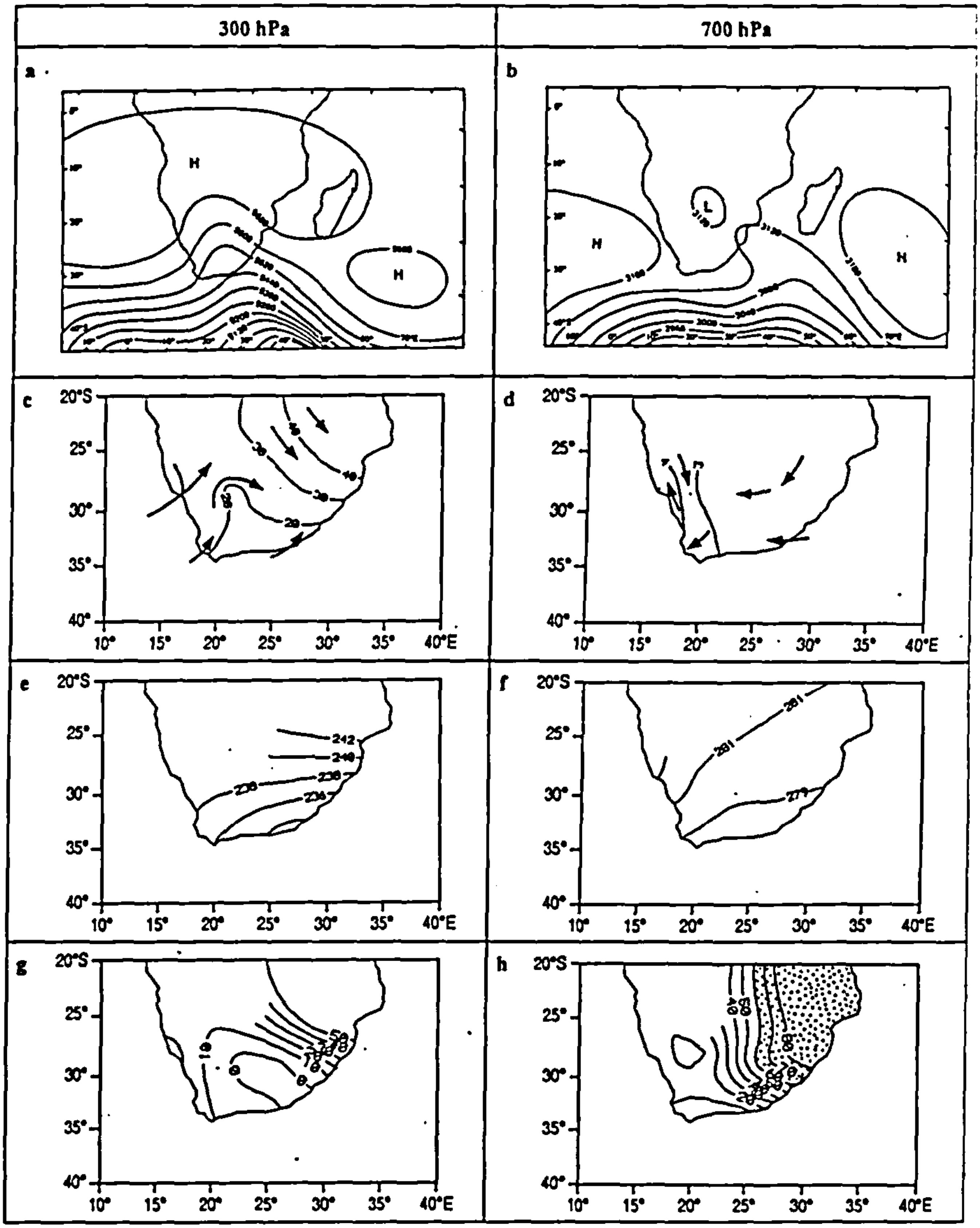

Figure 2.18: Geopotential height (gpm) at (a) 300 hPa and (b) 700 hPa; wind speed ($m.s^{-1}$, thin isotachs) and streamlines (bold lines) at (c) 300 hPa and (d) 700 hPa; temperature (K) at (e) 300 hPa and (f) 700 hPa; and relative humidity at (g) 300 hPa and (h) 700 hPa on 7 January at 12:00 UT. Areas where relative humidity exceeds 60 per cent are shaded in (g) and (h).

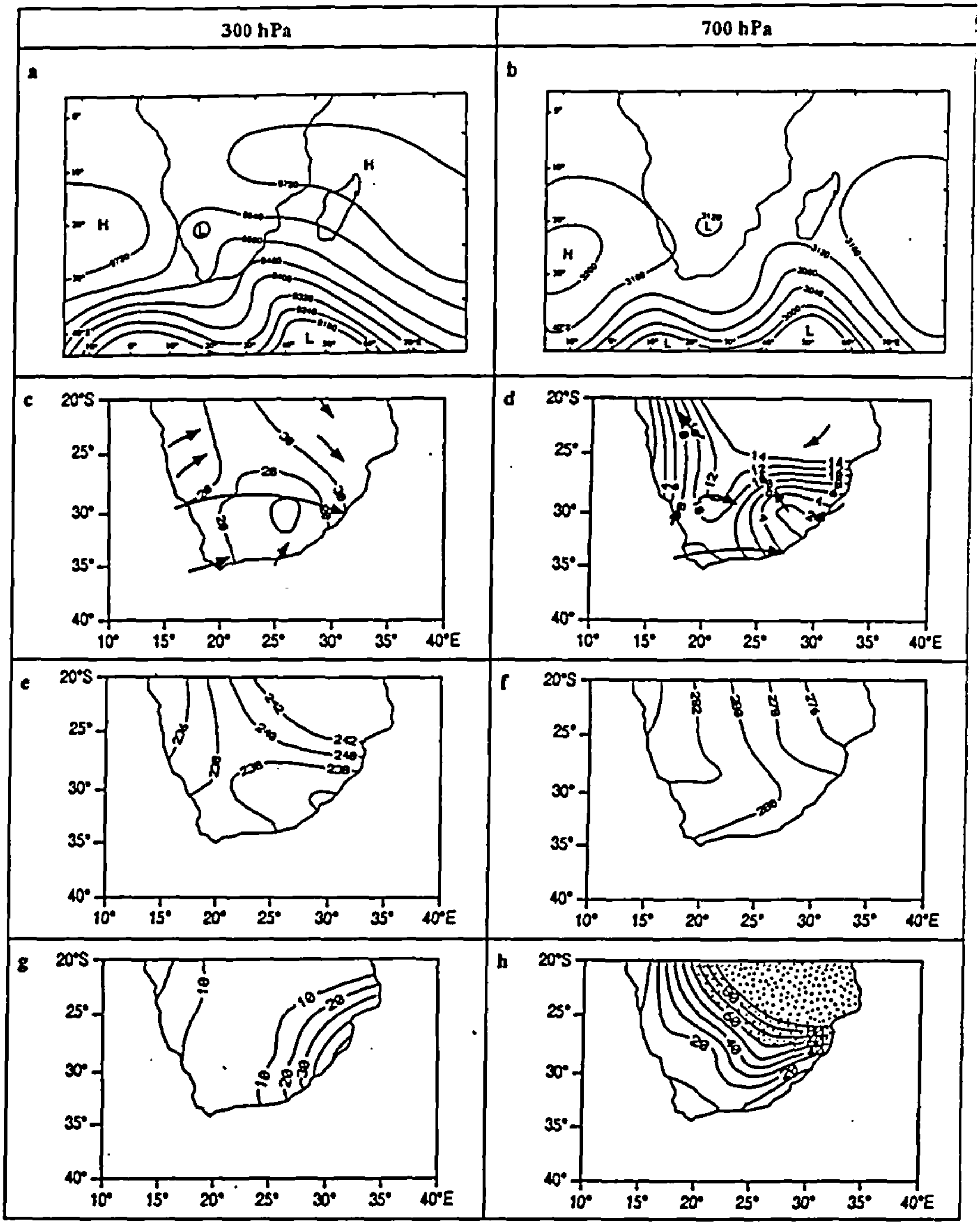

Figure 2.19: Geopotential height (gpm) at (a) 300 hPa and (b) 700 hPa; wind speed ($m.s^{-1}$, thin isotachs) and streamlines (bold lines) at (c) 300 hPa and (d) 700 hPa; temperature (K) at (e) 300 hPa and (f) 700 hPa; and relative humidity at (g) 300 hPa and (h) 700 hPa on *8 January at 00:00 UT. Areas where relative humidity exceeds 60 per cent are shaded in (g) and (h).*

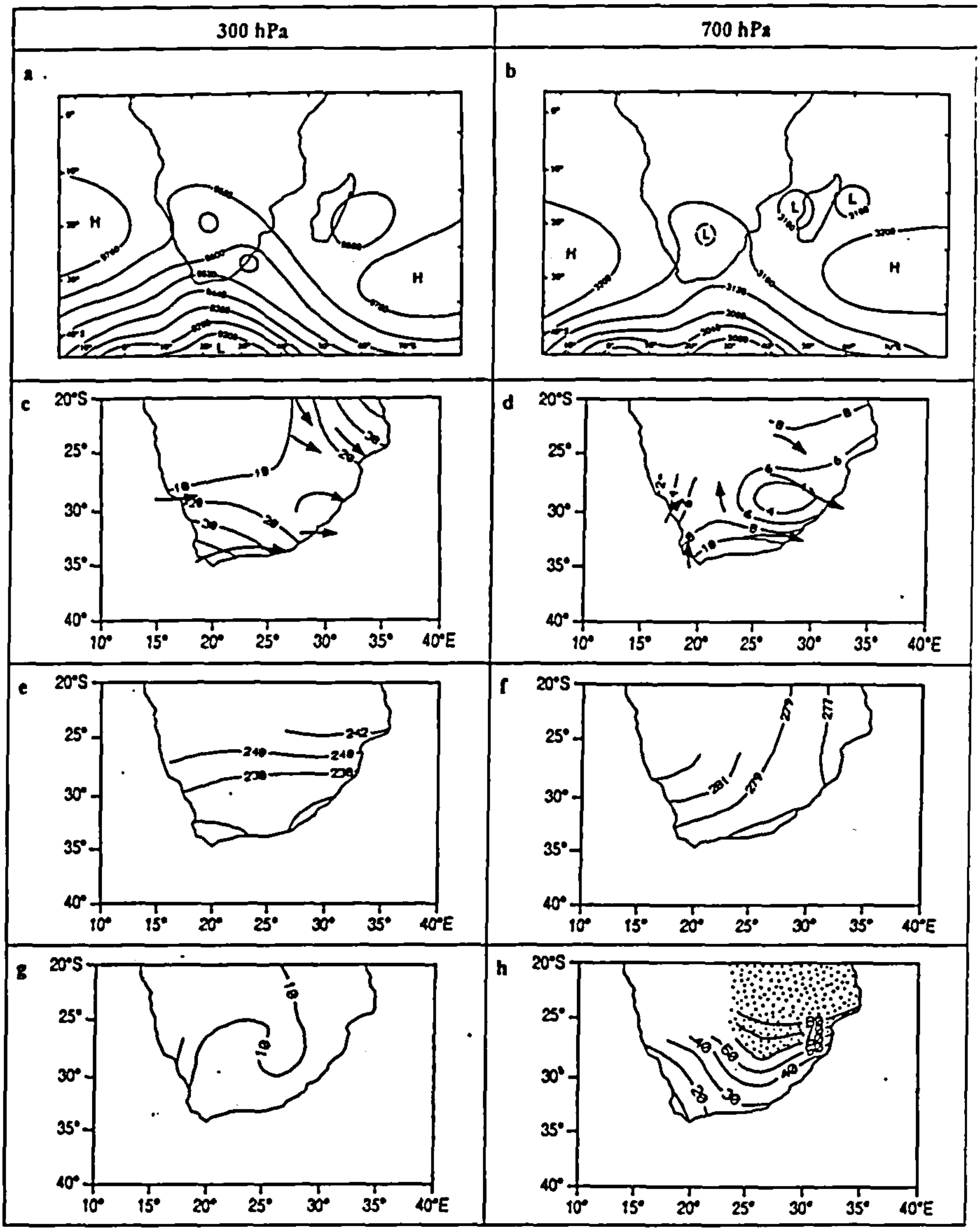

Figure 2.20: Geopotential height (gpm) at (a) 300 hPa and (b) 700 hPa; wind speed (m.s⁻¹, thin isotachs) and streamlines (bold lines) at (c) 300 hPa and (d) 700 hPa; temperature (K) at (e) 300 hPa and (f) 700 hPa; and relative humidity at (g) 300 hPa and (h) 700 hPa on 8 January at 12:00 UT. Areas where relative humidity exceeds 60 per cent are shaded in (g) and (h).

Rainfall

Regions of high rainfall were limited to the eastern regions of southern Africa on 6 and 7 January (Fig. 2.21a,b). Moisture was fed onshore by the easterly flow between 15 and 25°S and by the circulations around the cold front system on 6 January (Fig. 2.15a) and around the high pressure cell on 7 January (Fig. 2.15b). The central and western regions remained particularly dry throughout the study period. The sharp boundary between the relatively high rainfall over the eastern regions and the low rainfall over the central and western interior is evident in the accumulated rainfall for the 6 to 7 January (Fig. 2.21c). Measurements of the rainfall produced by the tropical-temperate trough over the oceanic regions are not available.

Thermodynamic Characteristics

The decrease in temperature over Pretoria (Fig. 2.22f) in the lower atmospheric levels was due to the presence of heavy cloud cover. With the cloud dissipation on the afternoon of 8 January, it increased. Except for a normal diurnal oscillation, the temperature structure over Bloemfontein (Fig. 2.22a) and Windhoek (not shown) changed very little. The temperature changes over Cape Town (Fig. 2.22b), Durban (Fig. 2.22c), Marion Island (Fig. 2.22d) and Port Elizabeth (Fig. 2.22e) are due to the position and movements of the westerly wave and the high pressure cell (Fig. 2.15a-c). These systems determined whether cold polar air from the south or warmer continental air from the north was transported over the station.

Kinematic Characteristics

Westerly zonal flow occurred throughout most of the middle and upper troposphere for all of the stations and was caused by the eastward progression of both westerly waves across southern Africa (Figs 2.16a,b-2.20a,b). The circulation around the surface low over Windhoek (Fig. 2.15a-c) caused the low level easterly flow in this region (Fig. 2.23f). The low level easterly flow over Bloemfontein (Fig. 2.23a), Cape Town (Fig. 2.23b), Port Elizabeth (Fig. 2.23d) and Durban (not shown) was due to circulation around the high pressure cell between the two cold fronts (Fig. 2.15a-c). Weak easterly flow over Bloemfontein (Fig. 2.23a) was also due to the circulation around

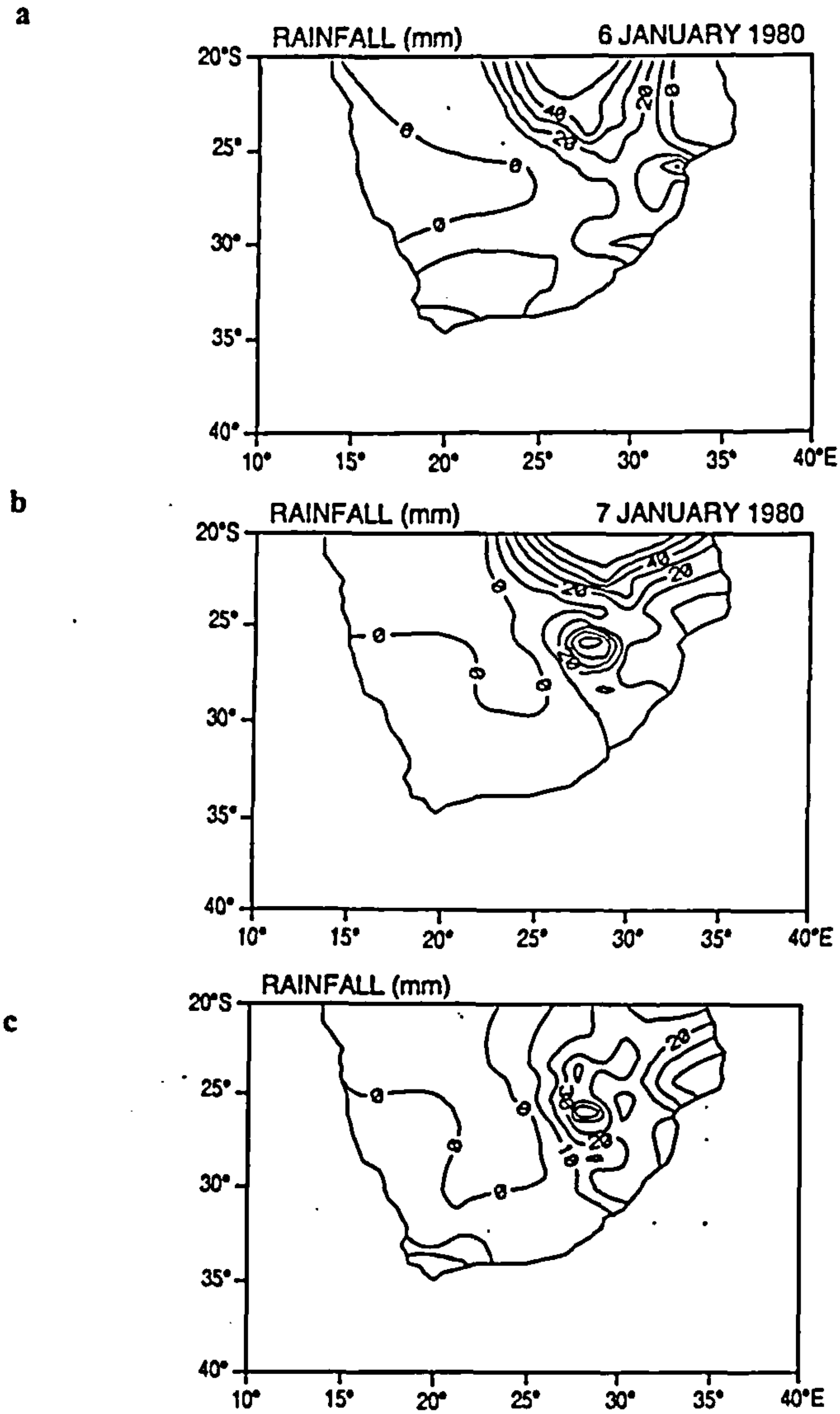

Figure 2.21: Rainfall recorded during the 24 hour period ending at 6:00 UT on the day following the indicated date for (a) 6 January and (b) 7 January. Accumulated rainfall for the period (c) 6 Jan 6:00 UT to 8 Jan 6:00 UT.

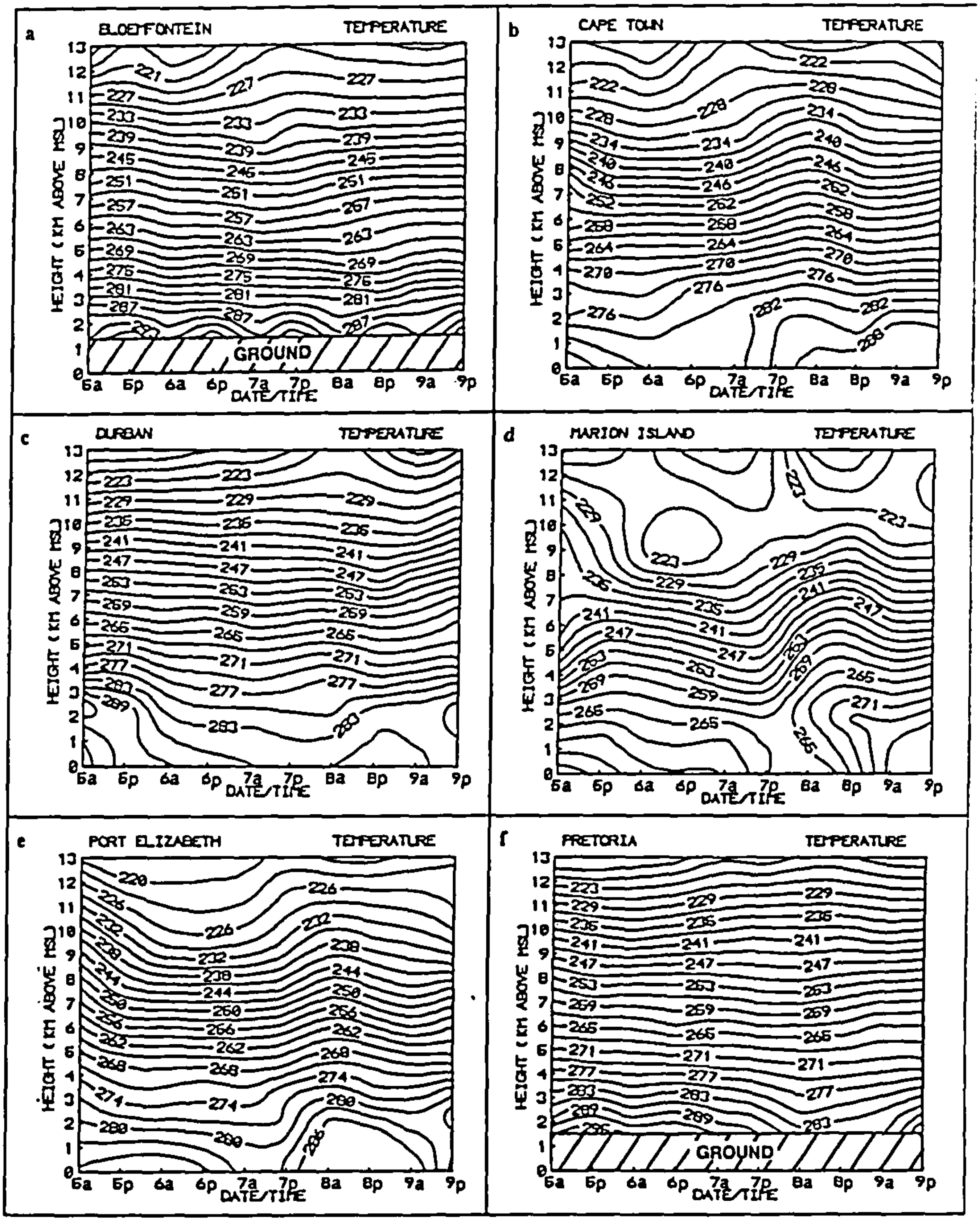

Figure 2.22: Temperature (K) structure of the troposphere for the period 00:00 UT on 5 January to 12:00 UT on 9 January for (a) Bloemfontein, (b) Cape Town, (c) Durban, (d) Marion Island, (e) Port Elizabeth, (f) Pretoria.

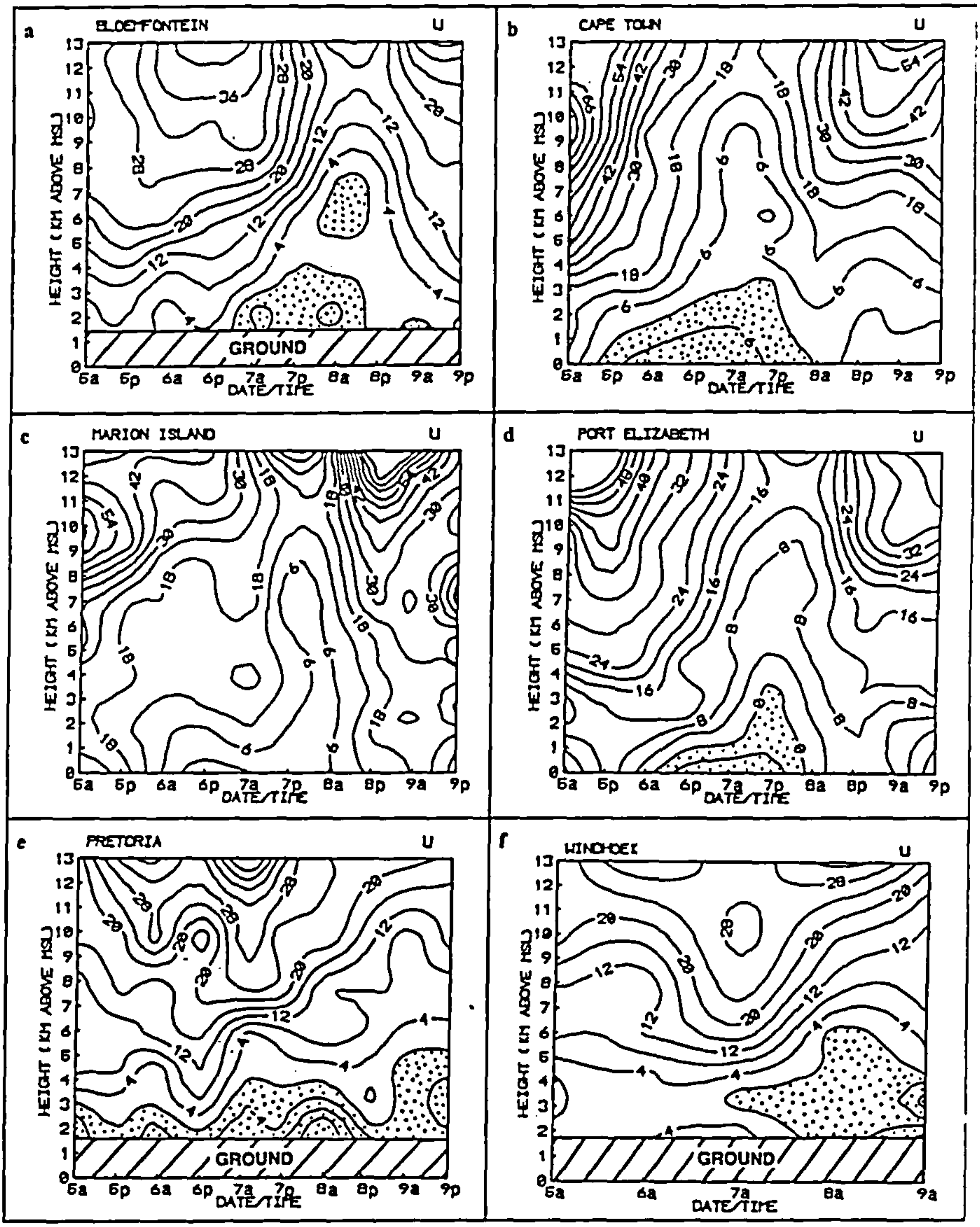

Figure 2.23: Zonal component of the wind flow ($m.s^{-1}$) from 00:00 UT on 5 January to 12:00 UT on 9 January for (a) Bloemfontein, (b) Cape Town, (c) Marion Island, (d) Port Elizabeth, (e) Pretoria and (f) Windhoek. Easterly components are shaded.

the interior trough. The predominant westerly flow over Marion Island (Fig. 2.23c) was strongest when the leading arm of the westerly waves was situated over the station (Fig. 2.15a-c).

Northerly meridional flow was dominant over Pretoria (Fig 2.24e) due to the poleward flow along the eastern edge of the interior trough (Fig. 2.15a-c). Changes in the meridional flow over Cape Town (Fig. 2.24b), Port Elizabeth (Fig. 2.24e), Durban (Fig. 2.24c) and Marion Island (Fig. 2.24f) were caused by the eastward movement of the westerly waves. Flow was southward when the leading arm of the westerly wave occurred over the region and northward when the trailing arm was situated over the station. The northerly flow over Bloemfontein (Fig. 2.24a) was enhanced by the circulation around the interior trough in the lower levels (Figure 2.15a-c).

The situation and northwest-southeast alignment of the tropical-temperate trough over the interior of southern African (over the eastern regions of the subcontinent and the Mozambique Channel), the large (relatively small) amplitude of the westerly wave, linkage with a tropical low along the Zaïre Air Boundary (over the eastern regions of the tropical subcontinent), poleward transport of moisture and momentum over southern Africa and Marion Island (Madagascar and the Mozambique Channel) and the dissipation of the tropical-temperate trough in association with the eastward movement of the South Atlantic High are all characteristics of wet-year (dry-year) tropical-temperate troughs. The 1980 and 1981 case studies are therefore representative of typical tropical-temperate trough systems that develop during dry and wet years.

Synopsis

The events and large-scale circulation associated with the development of a tropical-temperate trough during a wet and dry late summer have been described. Synoptic and upper air charts for these particular case studies have been presented. Observations of wind direction and magnitude, zonal and meridional wind components, relative humidity, temperature and angular momentum fields have been considered. These provide the means of comparison between the recorded data and the simulated fields to be modelled using RAMS. The model setup used to perform the simulations will be considered in the following chapter.

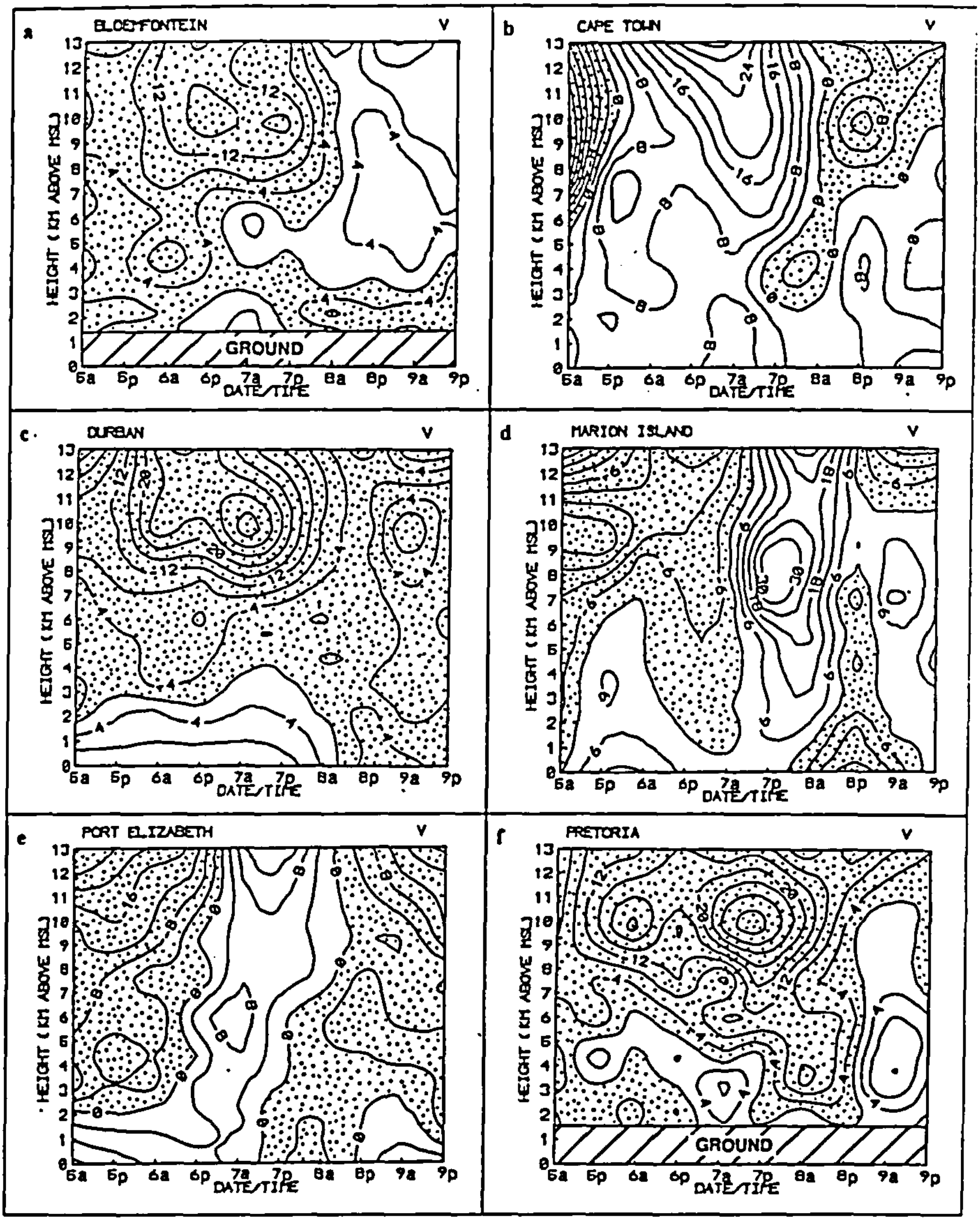

Figure 2.24: Meridional component of the wind flow ($m.s^{-1}$) from 00:00 UT on 5 January to 12:00 UT on 9 January for (a) Bloemfontein, (b) Cape Town, (c) Durban, (d) Marion Island, (e) Port Elizabeth and (f) Pretoria. Northerly components are shaded.

CHAPTER 3

DATA, METHODOLOGY AND MODEL DESCRIPTION

Introduction

The Regional Atmospheric Modelling System (RAMS) (Tremback *et al.*, 1986; Cotton *et al.*, 1988; Walko and Tremback, 1991; Pielke *et al.*, 1992) was developed at Colorado State University by combining a non-hydrostatic cloud model (Cotton *et al.*, 1982; Tripoli and Cotton, 1982) and two hydrostatic mesoscale models (Pielke, 1974; Mahrer and Pielke, 1977; Tremback *et al.*, 1985). RAMS is a modular, flexible and general modelling system. It has been used successfully to simulate a variety of atmospheric systems ranging from one hundred metres in size to thousands of kilometres in extent (Walko and Tremback, 1991). These simulations include the interaction between sea-breezes and deep convection over South Florida (Nicholls *et al.*, 1991), orographic cloud systems (Meyers and Cotton, 1992), intense thunderstorms (Grasso, 1992) and squall line structures (Cram *et al.*, 1992a, 1992b).

The three main components that constitute RAMS are the Atmospheric Model, an Isentropic and Analysis package (ISAN) and a Visualisation and Analysis package (VAN). The Atmospheric Model, which performs the actual simulations, is constructed around the full set of primitive dynamical equations governing atmospheric motion. These equations may be supplemented by optional parameterisation schemes selected by the user. ISAN combines observed surface, radiosonde and global meteorological data to construct an initial data set for the atmospheric model, and VAN provides graphical and visual output of the results (Walko and Tremback, 1991).

In this chapter, the data sets used with RAMS and the calculations utilised to represent the case studies will be described. The model initialisation, the main model features, the parameterisation schemes and the various parameter settings will be outlined.

Data and Methodology

Most of the data sets used with RAMS were obtained from the National Center for Atmospheric Research (NCAR), in Boulder, Colorado. These include the European Centre for Medium Range Weather Forecasts (ECMWF) III-b Global Analysis Data Set, the National Meteorological Center (NMC) observational upper air and surface data sets, and the topographical and land percentage data sets. The ECMWF data set is the NCAR-archived analyses from the ECMWF numerical weather model (NCAR data set 110.0). These analyses are available for the 1000, 850, 700, 500, 300, 200 and 100 hPa standard pressure levels, on a 2,5 degree resolution at 00:00 UTC and 12:00 UTC daily. The variables included in the ECMWF data set are temperature, relative humidity, zonal and meridional wind components, vertical wind velocity and height. The global NMC operational surface data set (NCAR data set 464.0) includes temperature, relative humidity, pressure, and wind speed and direction. The global NMC operational upper air data set (NCAR data set 353.4) includes the same variables as the surface data set, as well as height at both mandatory and significant levels. The stations supplying these variables are shown in Figure 3.1. Data at 00:00 UTC and 12:00 UTC were obtained from both the NMC data sets. The topographical and land percentage data sets are both at 10 minute resolutions. To obtain more realistic sea surface temperatures for the case studies in question, the Meteorological Office Historical Sea Surface Temperature data set as 1° intervals was combined with sea-surface temperature from the British Meteorological Office (Parker, 1987; Parker and Folland, 1988). For the three oceanic sensitivity simulations RAMS utilised individually modified sea-surface temperature data sets that included a +2°C sea-surface temperature anomaly core bounded by a +1°C anomaly for each of the oceanic regions identified. The +1°C anomaly imposed on the boundary of the +2°C core was included to minimise any unwanted effects of strong sea-surface temperature gradients (Cione and Raman, 1995). The anomalies were added to an area north of Madagascar centred between the 10°N latitude and 20°S latitude and east of 50°E, for the first oceanic sensitivity experiment (Chapter 7). The second sensitivity test (Chapter 8) utilised the same anomaly fields but placed them between the 33°S and 40°S latitudes and 14°E and 24°E longitudes in the Agulhas retroflection region. In the third sensitivity test (Chapter 9) the anomalies were placed between 4°N and 20°S, and east of 6°W in the tropical eastern Atlantic Ocean region.

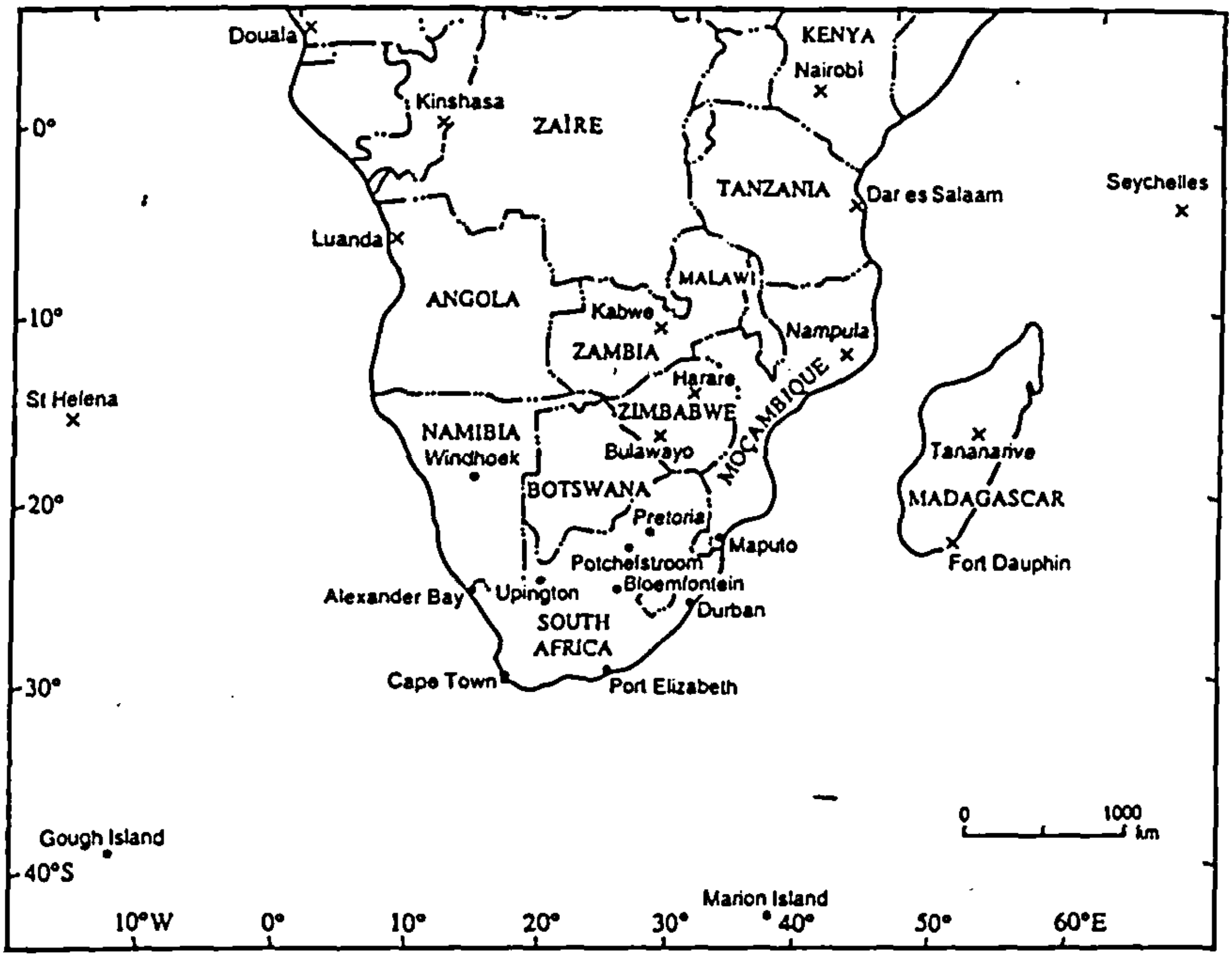

Figure 3.1: Upper air stations included in the SAWB and NMC observational data sets. Stations exclusive to the NMC data set are indicated by an 'X'.

Visual images of the tropical-temperate trough case studies were obtained from the National *Oceanic and Atmospheric Administration Environmental* Data and *Information* Service's TIROS-N and NOAA6 polar orbiting satellite imagery (NOAA, 1980, 1981). Daily rainfall totals were obtained from the South African Weather Bureau (SAWB). These totals are recorded at approximately 2300 stations for a 24-hour period starting at 6:00 UTC. Cumulative rainfall totals for the duration of the tropical-temperate trough systems were calculated from the daily totals. Tephigrams and meteorological variables at the surface and the 1000, 950, 900, 850, 800, 700, 600, 500, 400, 300, 250, 200, 150, 100, 70, 50, 30, and 20 hPa levels for 12 upper air stations were also obtained from the SAWB. These stations are indicated in Figure 3.1. The variables include temperature, height, dew point temperature, wind speed and direction. Relative humidity values were also available for the 1981 case study, but not for the 1980 case study, which necessitated the calculation of these values. The meridional and zonal wind components and relative angular momentum fluxes were also calculated using these data. Geopotential fields for the 700 and 300 hPa levels were redrawn using SAWB upper air charts, and wind speed and direction, relative humidity and temperature fields at the 700 and 300 hPa levels were mapped using the standard pressure level data. The polar orbiting wave patterns for the 500 hPa level were drawn using ECMWF data and a plotting routine supplied by the SAWB. All the SAWB data manipulation and calculations were performed on an IBM 486 DX PC and the SURFER plotting package was used for contouring. As the data sources for RAMS and the case study investigations differ, the comparison between the simulated output and observed data fields is strengthened. All of the RAMS simulations were performed on the Cray YMP supercomputer at the SAWB.

Model Initialisation

RAMS may either be variably initialised or horizontally homogeneously initialised. The horizontal initialisation is performed using a single sounding. This is not suitable for the large domain being utilised as the large-scale synoptic forcing important to tropical-temperate trough development cannot be included. For variable initialisation, initialisation files produced by ISAN provide the model with 3-D atmospheric fields at the initial time-step. These time-dependent initialisation files are also used in the nudging of lateral boundaries. The ISAN package is described in detail by Cram

(1990), Tremback (1990) and Pielke *et al.* (1992). The data analysis is objective and is performed hydrostatically on user specified isentropic surfaces (Tremback, 1990; Cram, 1992a). ISAN combines relative humidity, pressure and the horizontal wind components from the ECMWF data set, with any available data from the NMC surface and radiosonde data sets. These variables are then interpolated vertically to the isentropic levels. Isentropic levels of 2 K intervals from the surface to 300 K, 5 K intervals to 400 K, and 10 K intervals to 500 K were used. Interpolation is achieved by the Barnes (1973) objective analysis scheme and the Montgomery streamfunction is obtained hydrostatically. The surface variables are analysed in a similar manner. Sea surface temperatures are also interpolated to the isentropic grid at this stage. The isentropic initialisation files are produced at 12-hour intervals. After the isentropic data set has been constructed, it is interpolated to the model grid, the horizontal grid resolution, number of vertical levels and domain size of which have been specified by the user.

Model Features and Parameter Options

Version 2C of the model was used. Only the basic features and parameters of the model applicable to this study will be considered. They are summarised in Table 3.1. Details are available from Tremback *et al.* (1986), Cotton *et al.* (1988), Cram (1990), Tremback (1990), Walko and Tremback (1991) and Pielke *et al.* (1992; Snook *et al.*, 1995). Numerous parameters were tested in order that the most representative control simulations for the wet and dry case studies could be obtained (Manton *et al.*, 1977).

Model Variables

Zonal and meridional wind components, vertical motion, the Exner function (π), ice-liquid water potential temperature and the mixing ratios of rain, pristine ice crystals, snow, aggregates, graupel and total water are all predicted in RAMS. Diagnostically-calculated variables include potential temperature, temperature, water vapour mixing ratios, cloud droplet mixing ratios, pressure, vertical velocity and vapour and cloud mixing ratios (Tripoli and Cotton, 1982; Cotton *et al.*, 1986; Meyers, 1989).

Grid Structure and Two-way Interactive Nesting

All simulations were performed in three dimensions. The grid used in RAMS is the horizontally and vertically staggered Arakawa C grid (Mesinger and Arakawa, 1976; Fox-Rabinovitz, 1991). A polar stereographic coordinate system was used for the horizontal coordinates. In this system, the curvature of the earth is taken into account by activating map factors which allow for variable resolution (Walko and Tremback, 1991). The vertical coordinate system used is the terrain-following σ_z system described by Gal-Chen and Somerville (1975a,b) and by Clark (1977; Maher and Pielke, 1977; Zanjic and Zanjic, 1993). The width and number of vertical levels are specified by the user. Any number of finer grids may be nested within a larger scale grid. The grids communicate on a two-way interactive scheme based on that of Clark and Farley (1984) in which the larger scale grid provides the initial conditions and lateral boundary conditions at each timestep for the fine grid. An average of the fine grid variables is passed back to the larger scale grid (Cram, 1990). This results in improved boundary conditions for the fine grid and more accurate coarse grid simulations.

Tropical-temperate troughs over the southern African region are generally thousands of kilometres long, but comprise of numerous cloud clusters that rely on smaller scale processes. A large model domain stretching from the equator to at least 45°S, and from the Greenwich Meridian to about 60°E, is necessary to incorporate the entire tropical-temperate trough system, the associated moisture sources and other related synoptic circulations, while a relatively fine resolution is necessary to simulate the smaller scale cloud processes. The nesting option available in RAMS seemed suitable for such a situation. Initially a coarse grid with a 120 kilometre grid resolution and a nested grid with 30 kilometre grid resolution were used. For the coarse grid to cover a sufficiently large area with these grid resolutions, the areal coverage of the fine grid had to be smaller than necessary as a result of memory constraints. This resulted in the interference of the lateral boundaries with the cloud band system. The only grid resolutions with which the nested and coarse grids covered a sufficiently large area were 55 and 120 kilometres respectively. The coarse to fine grid ratio at these resolutions was not worth the computational time and expense. It was therefore decided not to use the nesting option, but rather to obtain the necessary domain size with as fine a grid resolution as possible. Sensitivity experiments with an even finer resolution grid that sufficiently covered the cloud band system, although not necessarily the regions of moisture supply, were also performed. The grid resolutions of the coarse and finer grids are 80 and 50 kilometres respectively. The finer grid covers a much larger area than was obtainable with the nested grid. The grid resolutions were the same in both the wet and dry case studies and the domains covered by the coarse and fine grids for both case studies are illustrated in Figure 3.2. There were 85x83 and 90x75 points in the horizontal for the coarse wet and dry case studies, and 78x75 and 75x75 points were used for the fine grids in the wet and dry cases. Thirty vertical levels were used in all the simulations, ranging from 300 metres at ground level, to a maximum depth of 750 metres. The vertical grid was stretched by a 1.1 grid stretch ratio resulting in a vertical model depth of 18,3 kilometres.

Non-hydrostatic Option

Both non-hydrostatic (Tripoli and Cotton, 1980) and hydrostatic (Tremback *et al.*, 1985) options are included in RAMS. The non-hydrostatic option was used. The numerics associated with the non-hydrostatic, compressible option have been described in detail by Tripoli and Cotton (1982). A leapfrog-time differencing scheme is utilised with the non-hydrostatic option. The prognostic equations are split to allow for the computation of the terms involving the movement of sound waves on the short timestep, while the leapfrog scheme is applied to the terms controlling other processes, such as the advective processes, on the long timestep (Tripoli and Cotton, 1982). A large timestep of 90 seconds and a small timestep of 30 seconds were used for both the 80 and 50 kilometre grids and all the simulations were run for 48 hours with the exception of some of the initial tests and the oceanic sensitivity experiments. The user may select between a second or fourth order of accuracy for the horizontal advection scheme. The second order was chosen as differences between the two orders seem to be small and the second order scheme requires less computer time (Cram, 1990; Walko and Tremback, 1991).

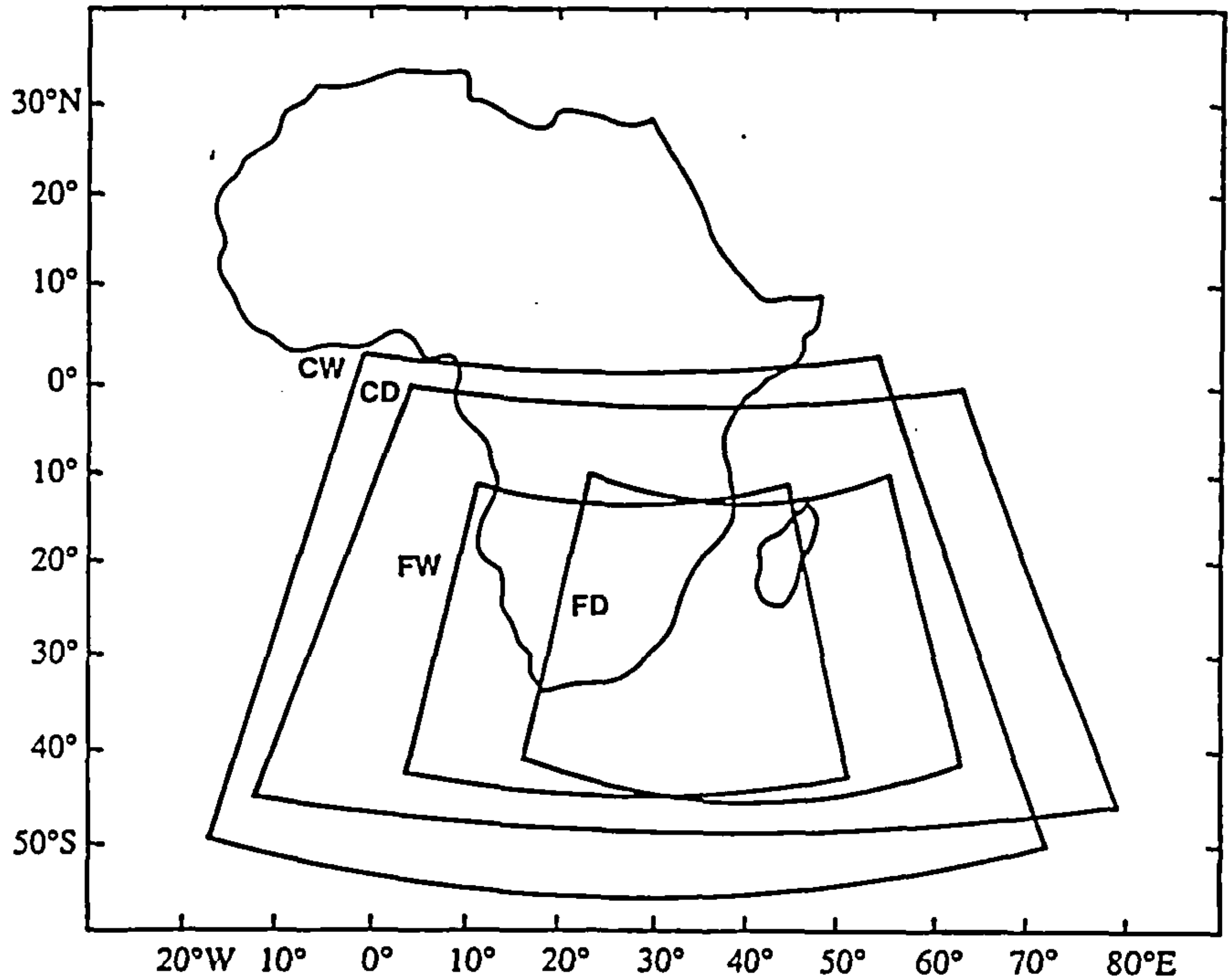

Figure 3.2: Model domains covered by the coarse grid for the wet (CW) and dry (CD) case studies, and by the fine grid for the wet (FW) and dry (FD) case studies.

Boundary Conditions

The Klemp and Wilhelmson (1978a,b) radiative type boundary condition was used for the lateral boundaries. Synoptic-scale boundary forcing was performed using the Davies (1983) nudging condition. The Davies condition causes the computed values of the prognostic variables in a region both at and to the inside of the lateral boundary, to be forced to the observed variables contained in the objectively analysed initialisation files produced by ISAN. The observed variables are time-interpolated between two successive initialisation files. This forcing supplies external information to the grid boundaries and immediate interior (Walko and Tremback, 1991; Perkey and Kreitzberg, 1976; Klemp and Wilhelmson, 1978a), and the width and weighting of the region to which the Davies nudging is applied, are specified by the user. The region used here was five grid points wide, and the weighting values, determined by testing, were .15, .09, .05, .02, .01 from the lateral boundary inward. The influence of the model's predicted value is then 1 minus the weighting values specified. A rigid lid at the top of the model domain was used for the upper boundary with the vertical velocity of propagated gravity waves towards this boundary reduced to zero (Cram, 1990).

Microphysics Module and the Cumulus Parameterisation Scheme

The degree of moisture complexity in the model must be specified by the user. Two different levels of moisture complexity were employed. The first incorporates the condensation of supersaturation to cloud water and the related latent heat release, but precipitation of the condensate does not occur (Tremback, 1990). The only forms of water considered are water vapour and cloud water (Walko and Tremback, 1991). In the second level of moisture complexity, the microphysics are resolved on the grid scale and precipitation is allowed to occur (Walko and Tremback, 1991). The microphysics module is described in detail by Flateau *et al.* (1993). The concentrations and mixing ratios of five condensate species are diagnosed and prognosed, respectively. The five species included in the microphysics module are rain, pristine ice, snow, aggregates, and graupel. Only rain, pristine ice and aggregates were allowed to occur. Graupel, which is mainly formed in active convective updrafts, was not used as the updrafts are parameterised with the grid resolutions that were used (Tremback, 1990). The model default options specifying the mean diameter of the water species were applied (Flateau *et al.*, 1993).

The convective parameterisation scheme used in RAMS is based on the scheme developed by Kuo (1965, 1974) and modified by Tremback (1990). When the horizontal grid resolution is too coarse for the model to generate its own convective motion once a region becomes superadiabatic or convectively unstable, the convective parameterisation is utilised to vertically redistribute heat and moisture (Walko and Tremback, 1991). Cloud aspects, including the lifting condensation level and the cloud top, are determined using vertical motion and moisture convergence within the grid column. The minimum updraft required at the cloud base to initiate convection must be specified and was arbitrarily set to a value of 0,5 $cm.s^{-1}$. The frequency with which the convective parameterisation is updated must also be specified by the user and testing revealed that an update every 1800 seconds was suitable.

Radiation Parameterisation

Two radiation parameterisation schemes are available in RAMS. The Mahrer and Pielke scheme (1977) does not include the radiative effects of liquid water or ice, whereas the scheme developed by Chen and Cotton (1983, 1987) does. The Chen and Cotton scheme is computationally expensive (Walko and Tremback, 1991). The Mahrer and Pielke scheme was used instead. Both schemes include long-wave and short-wave radiation fluxes and the shortwave radiation is longitudinally and time variable.

Turbulence Parameterisation

The turbulence parameterisation scheme used in this study is the deformation-K closure scheme based on that of Smagorinsky (1963). The diffusion coefficients are calculated by multiplying the local fluid deformation rate and the square of a length scale that is related to the grid dimensions (Tripoli and Cotton, 1982; Tremback, 1990; Walko and Tremback, 1991). The vertical length scale used to compute the vertical diffusion coefficients was set to the vertical grid spacing. The horizontal length scale was set to the square root of the product of the x and y horizontal grid resolutions. Both vertical and horizontal velocity components were used in calculating the vertical diffusion coefficients, whereas only the horizontal velocity components were used for the horizontal coefficients. A multiplying factor incorporating the Richardson number, which modifies the diffusion coefficient by including the effects of static stability or instability (Walko and Tremback, 1991), was employed in both stable and unstable conditions. A value needs to be assigned to the namelist variable AKMIN which places a lower limit on the horizontal diffusion coefficients throughout the model domain. A low value of AKMIN has very little effect on the horizontal diffusion, whereas large AKMIN values result in an increase of the horizontal diffusion over and above that computed by the deformation scheme. Testing revealed that low values of AKMIN (0,1 to 0,6) resulted in noise in the outputs of different variable fields, while high values of AKMIN (1,0 to 2,0) caused a substantial reduction in vertical motion, thereby impeding the development of the cloud band system. Changes in the horizontal diffusion coefficient have been suggested as an alternative means of dealing with noise in the variable fields (Tremback, 1990; Walko and Tremback, 1991), but did not help. Cram (1990) made use of a fourth-order filter when dealing with a similar problem. After experimenting with numerous low AKMIN values, AKMIN was set to 0,2, and the fourth-order filter was used every 360 seconds to remove the 2 Δx noise.

Topographical Layout

The silhouette-averaging technique (Bossert, 1990) was used to smooth the topography in order to ensure numerical stability in the model. The topography of the grids used is shown in Figure 3.3. The major topographical features such as the Escarpment and the Lesotho and Angola Highlands are all evident.

Surface Parameterisation

The soil model used in this study was that which is based on the schemes of Mahrer and Pielke (1977) and McCumber and Pielke (1981), and modified by Tremback and Kessler (1985). A loam soil and tall grass were specified for the soil and vegetation types over the entire domain and the surface roughness was set to 10 centimetres. Ten soil levels, constituting a soil depth of 50 centimetres, were employed. The soil temperature was set to 4 K lower than the soil surface

a

b

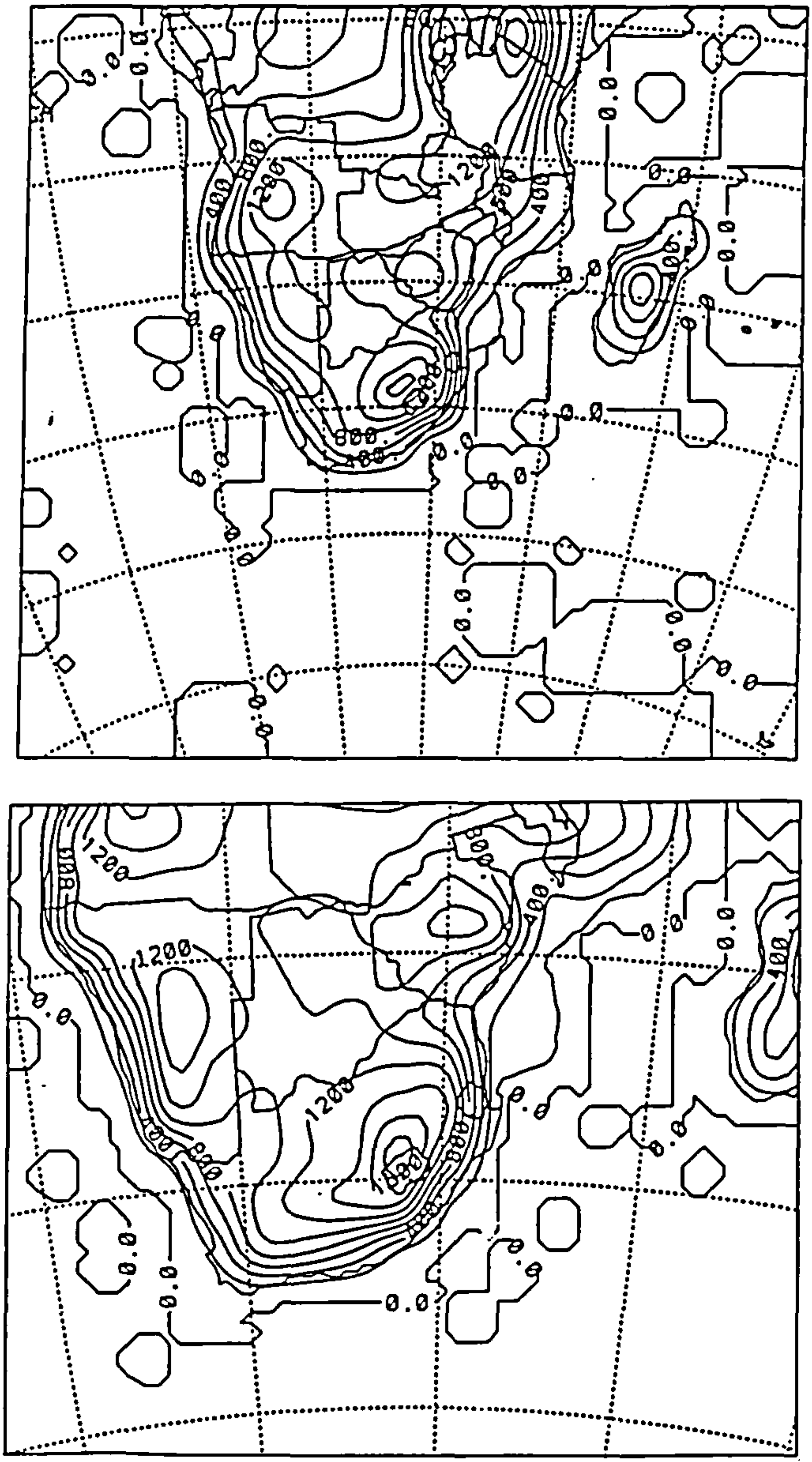

Figure 3.3: Model topography of the (a) 80 km and (b) 50 km grids.

temperature at a depth of 10 centimetres, 10 K lower than the surface temperature at a depth of 30 centimetres, and increased to 8 K lower than the surface temperature at 50 centimetres. This temperature profile is based on a mean afternoon soil temperature profile given by Sellers (1965).

Table 3.1: Selected RAMS formulation options

CATEGORY	OPTION UTILISED
• Basic Equations	• Non-hydrostatic
• Time-differencing	• Leapfrog time-differencing • Second-order advection • Timesteps: long - 90 secs; short - 30 secs
• Dimensions	• 3 Dimensional
• Number of Grids	• Nesting option not suitable • Two separate grids of different resolutions
• Grid Structure	• Staggered Arakawa C grid structure
• Horizontal Coordinates	• Polar stereographic transformation • Coarse grid: $\Delta x = \Delta y = 80$ km • Fine gird: $\Delta x = \Delta y = 50$ km
• Vertical Coordinates	• Terrain-following σ_z system • 30 Vertical levels • Total height: 18,3 km • Vertical level width: 300 m at base, 750 m at grid top
• Topography	• Silhouette-averaging technique
• Lateral Boundaries	• Klemp and Wilhelmson Radiative boundary condition • Davies nudging condition

• Upper Boundary	• Rigid lid
• Lower Boundary	• Tremback and Kessler soil model • 10 soil levels: total depth of 50 cm • Loam soil and tall grass
• Cumulus Parameterisation	• Modified Kuo scheme
• Microphysics	• Rain, pristine ice and aggregates
• Turbulence	• Smagorinsky deformation-K closure parameterisation
• Radiation	• Mahrer and Pielke radiation scheme
• Initialisation	• Horizontally variable
• Total Simulation Time	• 48 Hours and 72 Hours for the oceanic sensitivity tests

As accurate soil moisture measurements are difficult to obtain, the relative humidity of the upper soil surface layer is made equal to the relative humidity of the lowest atmospheric level. The soil surface moisture is then increased linearly to double its value at 50 centimetres (Tremback, 1990). The soil moisture was limited to between 40 per cent and 80 per cent of saturation at the surface. Sensitivity tests were performed in which the soil moisture values were changed and the results are analysed in Chapter 6.

Approach Followed

A control run which best approximated the overall development and movement of the tropical-temperate trough system under investigation, needed to be established for each case study. Once these control runs had been established, the results of the control runs were then re-examined to further investigate the characteristics and controls of tropical-temperate troughs during wet and dry years. The model output was also compared with previous hypotheses regarding the characteristics of these cloud band systems. Sensitivity experiments, discussed in detail in the following chapters and summarised in Table 3.2, were also performed and compared with the control run. These experiments included testing the model sensitivity to a finer grid resolution and

Table 3.2: Sensitivity tests performed with RAMS

SIMULATION	GRID	DESCRIPTION
CONTROL	COARSE	CONTROL SIMULATION
SENSITIVITY 1	FINE	FINE GRID RESOLUTION
SENSITIVITY 2	FINE	MICROPHYSICS MODULE INCLUDED
SENSITIVITY 3	COARSE	HIGH SOIL MOISTURE: 75-90% SATURATION
SENSITIVITY 4	COARSE	LOW SOIL MOISTURE: 10-20% SATURATION
SENSITIVITY 5	COARSE	TROPICAL INDIAN OCEAN ANOMALY
SENSITIVITY 6	COARSE	AGULHAS CURRENT RETROFLECTION ANOMALY
SENSITIVITY 7	COARSE	TROPICAL EASTERN ATLANTIC ANOMALY

the inclusion of resolvable microphysics, as well as determining the influence of soil moisture on the formation and development of tropical-temperate troughs. All the sensitivity tests , except for the three oceanic sensitivity experiments, were performed for both the wet and dry case studies. The model output from the control simulations and the results of the sensitivity tests will be presented and analysed in the chapters that follow.

In Chapter 10 a kinematic trajectory analysis with the European Centre for Medium Range Weather Forecasts (ECMWF) GRIB IIIb dataset, on a 2.5° grid, has been used for three January case studies, namely those of 1980, 1981 and 1991. The selection was done on the basis of one anomalously wet month (1981), one anomalously dry month (1980) and one month with average precipitation (1991). Daily rainfall statistics have been obtained from the South African Weather Bureau for the summer rainfall regions on the plateau of South Africa. Satellite imagery is from NOAA2 and NOAA5 polar-orbiting satellite (published by the Environmental Data Service of the

United States Oceanic and Atmospheric Administration) and the geostationary Meteosat imagery (published by the European Space Agency/EUMETSAT).

The trajectory model is Lagrangian, with atmospheric motion being described in terms of individual air parcels moving with air streams resulting from changing synoptic circulation patterns (D'Abreton, 1996). The model uses the explicit method of integration defined by

$$x(t+dt) = x(t) + V[x(t)]dt \tag{1}$$

where $x(t+dt)$ is the new three-dimensional parcel position at $t + dt$, $x(t)$ is the old position and $V(t)$ is the parcel velocity vector. The time step (dt) used in the analysis is 15 minutes. A more complete description of the trajectory methodology is to be found in D'Abreton (1996). Forward and backward trajectories have been performed from designated points of interest as origin to give 20-day trajectories for each air parcel analysed.

Lagrangian methods have been applied extensively in the evaluation of synoptic-scale transport of anthropogenically-produced air pollutants and biogenic aerosols and trace gases (Eliassen, 1978; 1980; Eliassen and Saltbones, 1975; Krishnamurti *et al.*, 1993; Tyson *et al.*, 1996a; Garstang *et al.*, 1996). An attempt is made to apply the principles used in studies of the Lagrangian transport of aerosols and trace gases to water vapour transport. The water vapour tendency equation has been used to calculate the approximate water content of the air parcel at each point along the trajectory. The tendency equation is given by

$$\frac{\partial q}{\partial t} + V \bullet \nabla q + \omega\frac{\partial q}{\partial p} + (p - e) \tag{2}$$

where q is specific humidity, V is the horizontal wind vector and ω the vertical velocity. Sub-grid scale processes have been ignored. The major assumption made is that water vapour is a passive tracer. This assumption is flawed in that evaporation and precipitation processes in the parcel are not represented in the model. Notwithstanding, the model represents processes occurring on a larger spatial scale than the grid scale and gives a useful indication of the moisture convergence or divergence within air parcels and, in general, an highly informative representation of large-scale moisture transport.

A statistical analysis of back trajectory pathways for 18 rain and 19 no-rain days has been performed using a modified version of a programme developed at the University of Virginia(Tyson *et al.*, 1996a: Garstang *et al.*, 1996). A total of 83 back and forward trajectories have been modelled. Frequencies and percentages of trajectories passing through imaginary walls of longitude at various latitudes and altitudes are calculated, transport fields are delineated and maximum frequency pathways determined. The approach has considerable potential for assessing the contrasting pathways of mid-summer water vapour transport to the central summer rainfall region of South Africa during wet and dry conditions.

Vertical transport of water vapour has been calculated from the relationship

$$\omega q = \omega^{*} q^{*} + \omega' q' \tag{3}$$

where the total vertical water vapour transport is equal to the sum of the mean circulation, standing eddy and transient eddy vertical water vapour transport.

Synopsis

The data sets used with RAMS, the model initialisation, the model features and parameter options have been examined. The model setup utilised to obtain the control runs for the wet and dry case studies and the changes made to conduct the sensitivity tests have been described. The model output from the control runs and the sensitivity tests will be presented and analysed in the following chapters. In chapter 10 a lagragian kinematic trajectory analysis of the periods 1980 and 81, (analysed for the numerical model simulations), and 1991 are initiated.

CHAPTER 4

CONTROL RUNS FOR THE WET AND DRY CASE STUDIES

Introduction

The characteristics of tropical-temperate troughs that develop during wet and dry periods have been found to differ significantly (Harangozo and Harrison, 1983; Harrison, 1986a; D'Abreton, 1992). As tropical-temperate troughs are the single most important contributors to rainfall over the interior of southern Africa (Harrison, 1986a; Tyson, 1986), the eastward shift from their position over the subcontinent during wet summers, to over the Mozambique Channel and Madagascar during dry summers, has a significant effect on southern African rainfall. Changes in temperature, wind flow, atmospheric moisture and rainfall over southern Africa are associated with the variation in wet- and dry-year positions of tropical-temperate troughs. RAMS has been used to investigate the characteristics of mesoscale systems at higher resolutions than those of present observational data sets. The first objective in attempting to investigate wet- and dry-year tropical-temperate trough characteristics using this mesoscale model is to establish a suitable control run.

If a model is to be used to investigate an atmospheric system, it needs to be determined how closely the model simulates reality. Model outputs have in the past been compared with NMC or ECMWF data analyses. These analyses have, however, been smoothed. This results in the elimination of detail in the data sets and defeats the purpose of using a numerical model to investigate systems on a higher space and time resolution than is possible with observational data sets (Tremback, 1990; D'Abreton, 1992). As model outputs need to be considered as areal or grid volume averages, to compare them with actual radiosonde or surface data which are point measurements, is not meaningful (Tremback, 1990). The model results will therefore be compared with the satellite imagery and with the movement and development of the systems as illustrated by the charts and data presented in Chapter 2. For variables which lend themselves to quantitative comparisons, such as rainfall, an assessment of the suitability of RAMS as a research and forecasting tool will be made.

The model setup was the same for both control runs with the exception of the grid position. This ensures that differences in the output for the wet and dry case studies are due primarily to actual atmospheric differences, rather than to the use of different model schemes. In the case of the oceanic sensitivity experiments an extended control simulation (72 hours) was utilised in order to allow a greater residence time for the sea-surface temperature anomalies. In these three cases a period from 21 to 24 January 1981 is simulated and compared to the oceanic sensitivity simulations of the same time period. Numerous variables have been selected to compare the simulated output with observational data. These are streamlines, pressure, vertical velocity, horizontal wind components, vapour and cloud mixing ratios, convective precipitation rate, and accumulated convective precipitation. The magnitude of the wind flow, which is not represented by the streamlines, will be investigated using the simulated zonal and meridional wind components.

Control Run for the Wet Case Study

Streamlines

At 15:00 UTC on 22 January 1981 (Day 1), three hours into the simulation period, the interior trough extending in a northwest-southeast direction from the region of convergence over Windhoek is clearly visible in the surface streamlines (Fig. 4.1a). Convection-enhancing convergence of the South Atlantic maritime air and the northeasterly tropical air occurs along this interior trough. The trough is evident at the 700 hPa level with the extension of the westerly wave over the interior (Fig. 4.2a). The simulated streamlines closely correspond with the ECMWF pressure field at 700 hPa (Fig. 4.3a). Northeasterly flow from eastern tropical African and the adjacent oceanic regions and the easterly flow over the Mozambique Channel, both of which have been found to be particularly important in transporting moisture over southern Africa during late summer (Taljaard, 1981, 1990; Miron and Lindesay, 1983; Lindesay and Jury, 1991; D'Abreton, 1992; D'Abreton and Lindesay, 1993), are clearly

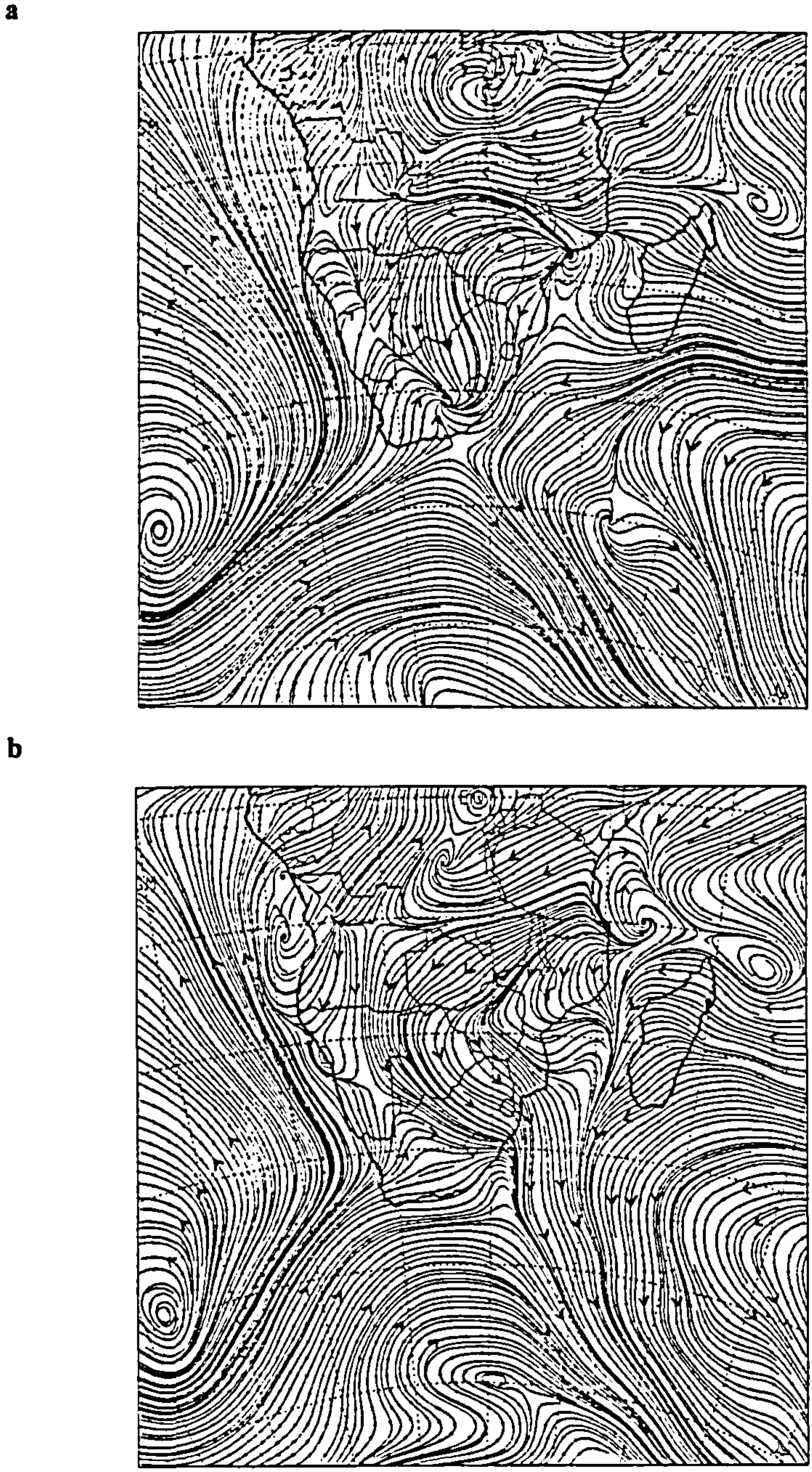

Figure 4.1: Surface streamlines (on the terrain-following coordinate surface 146,4 m above the ground) from the wet case control run at (a) 22 Jan 15:00 UT and (b) 23 Jan 9:00 UT.

c

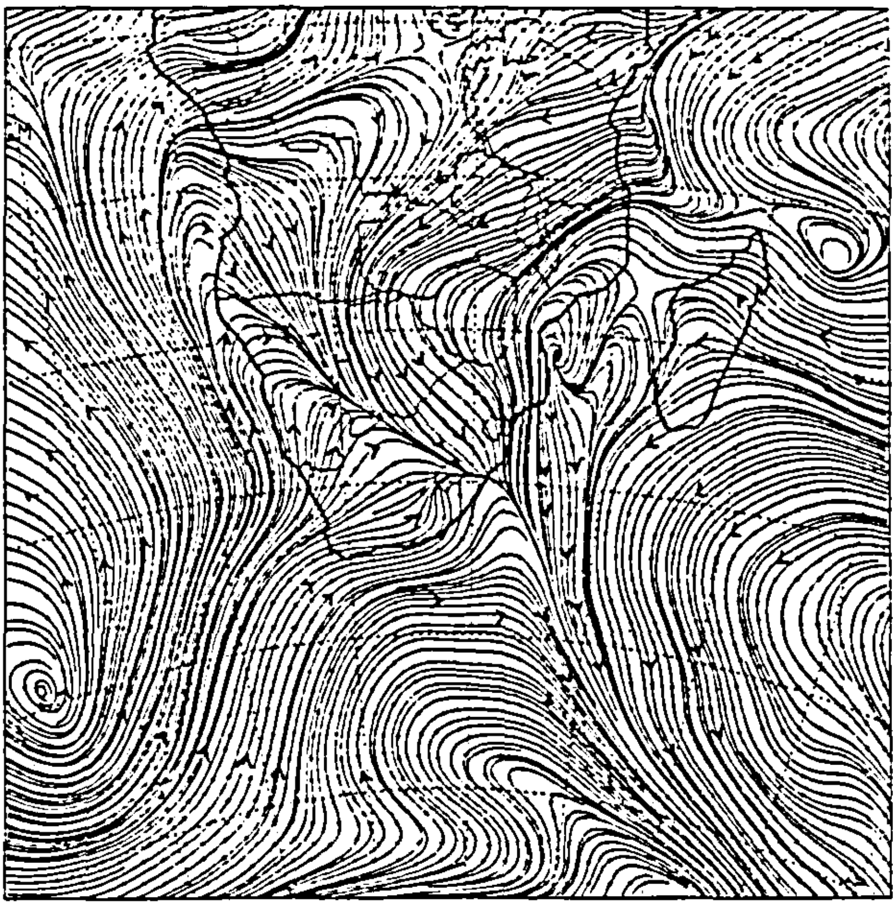

d

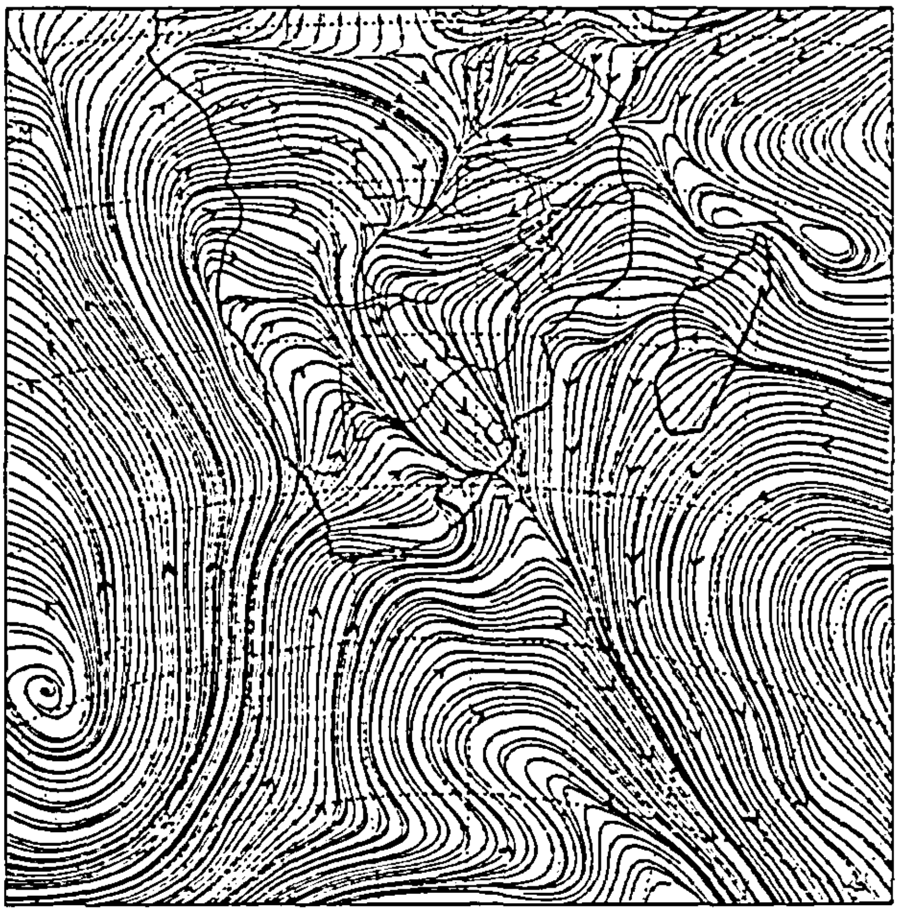

Figure 4.1 cont: Surface streamlines (on the terrain-following coordinate surface 146,4 m above the ground) from the wet case control run at (c) 23 Jan 15:00 UT and (d) 23 Jan 21:00 UT.

e

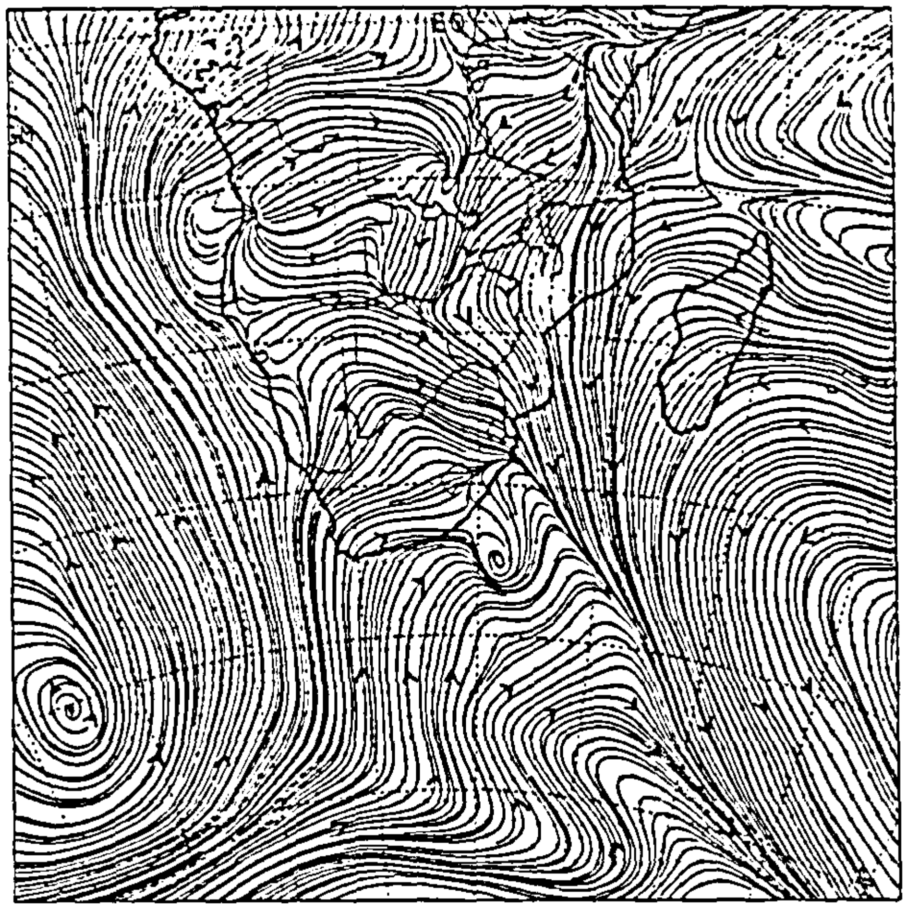

f

Figure 4.1 cont: Surface streamlines (on the terrain-following coordinate surface 146,4 m above the ground) from the wet case control run at (e) 24 Jan 6:00 UT and (f) 24 Jan 12:00 UT.

a

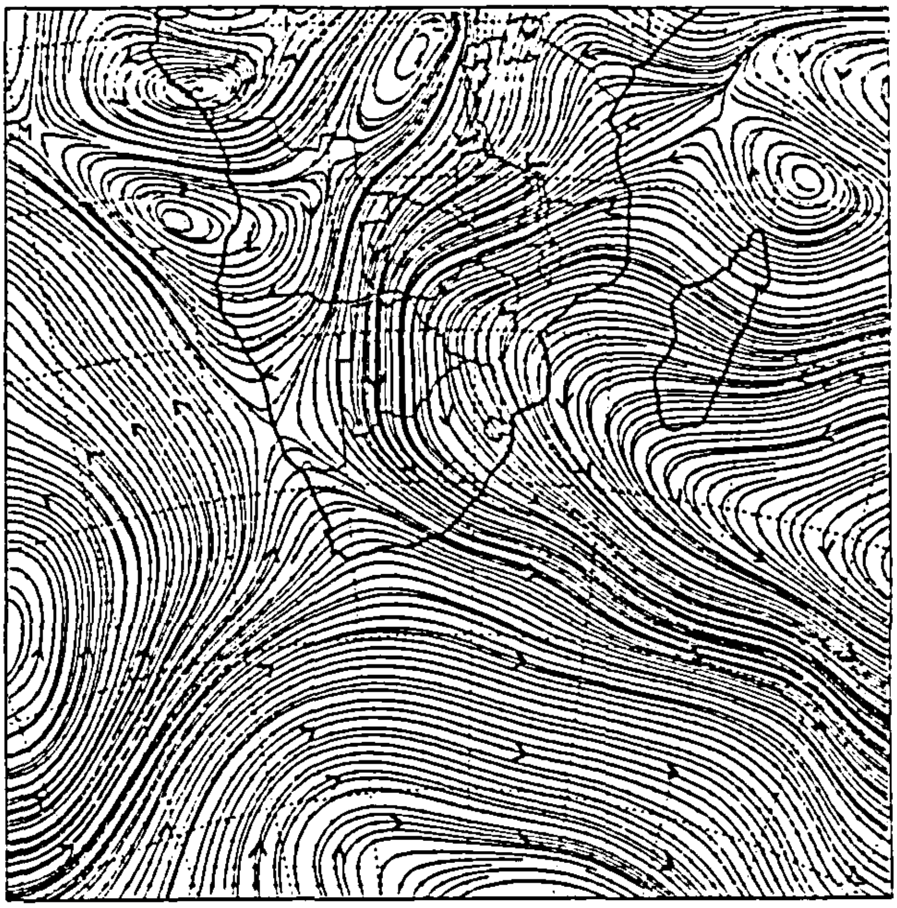

b

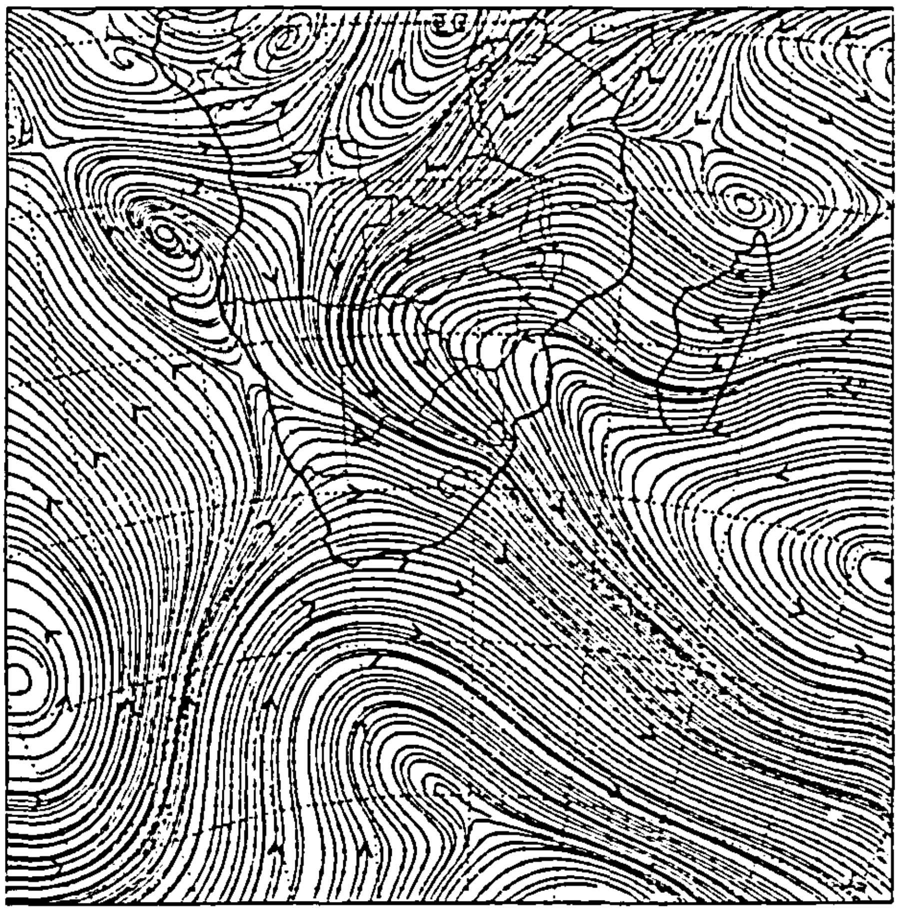

Figure 4.2: Streamlines at 3,13 km (~ 700 hPa) above sea level from the wet case control run at (a) 22 Jan 15:00 UT and (b) 23 Jan 9:00 UT.

c

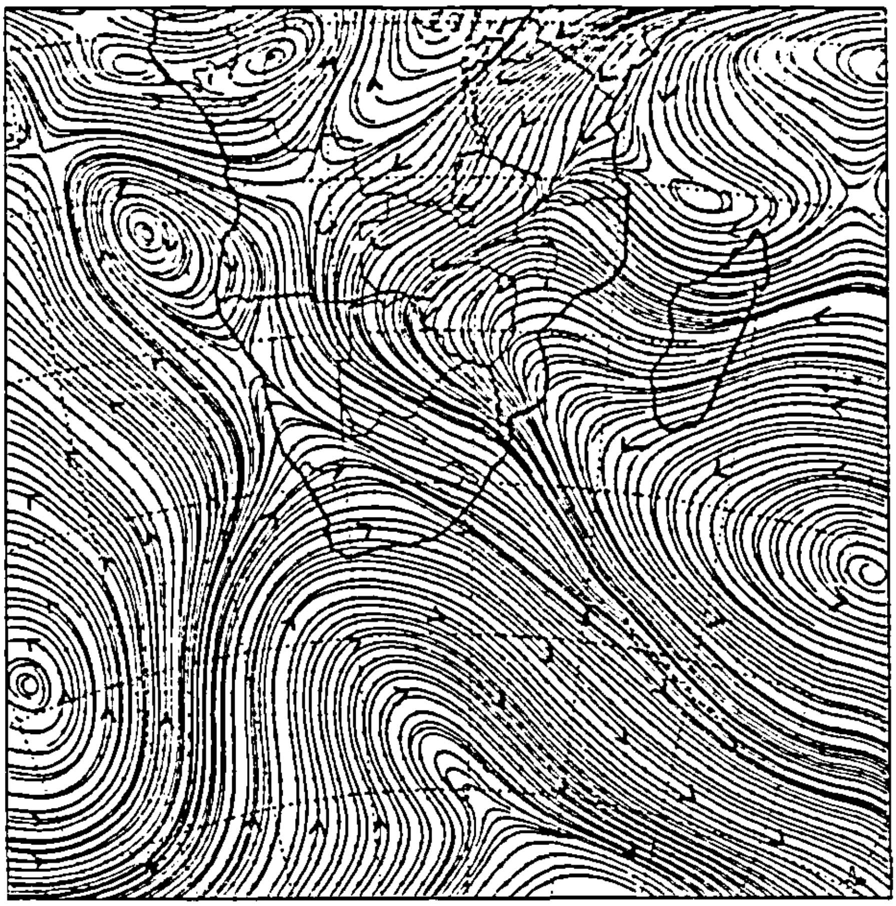

d

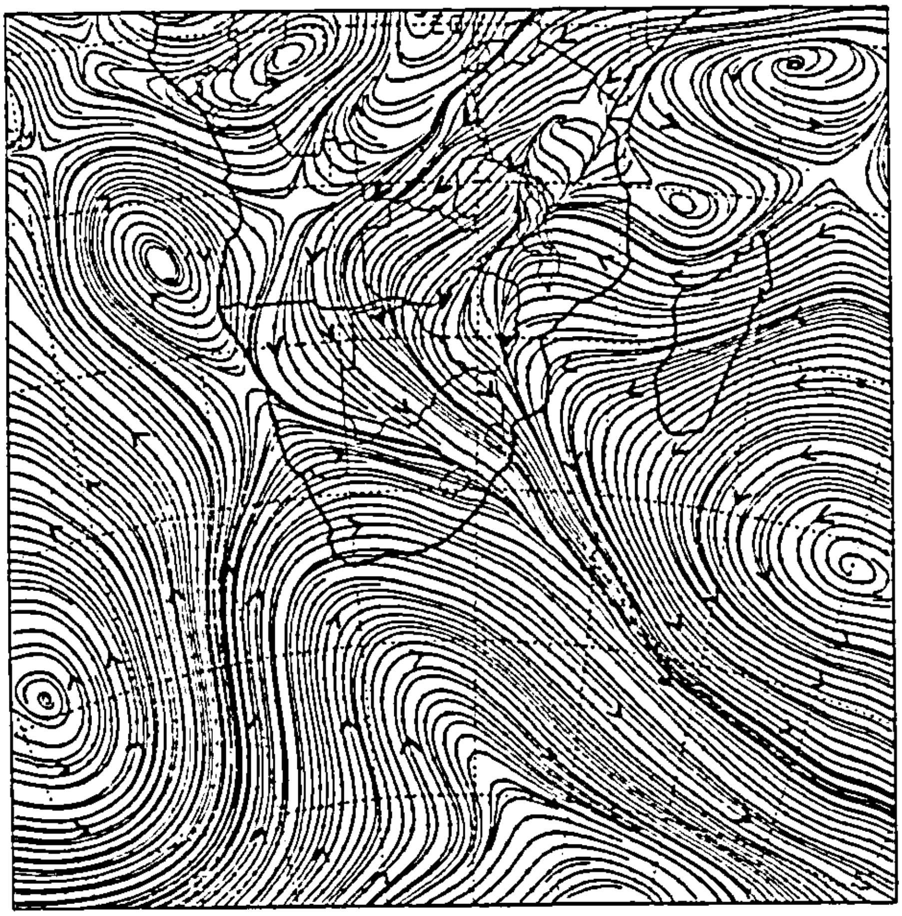

Figure 4.2 cont: Streamlines at 3,13 km (~ 700 hPa) above sea level from the wet case control run at (c) 23 Jan 15:00 UT and (d) 23 Jan 21:00 UT.

e

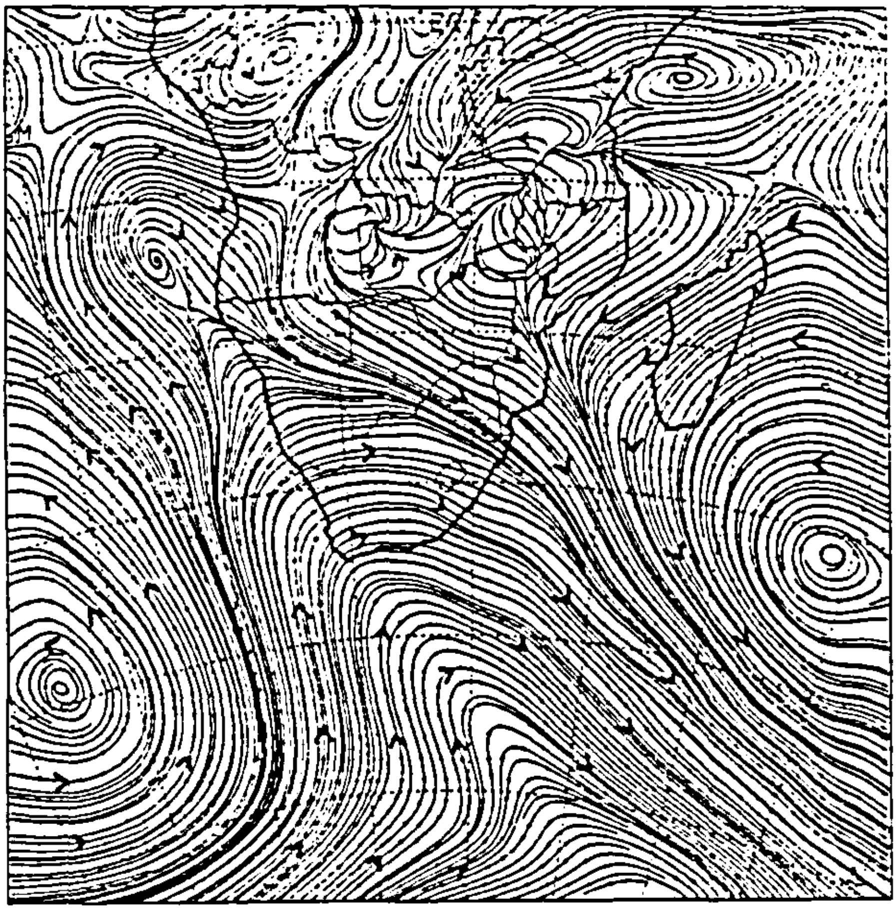

f

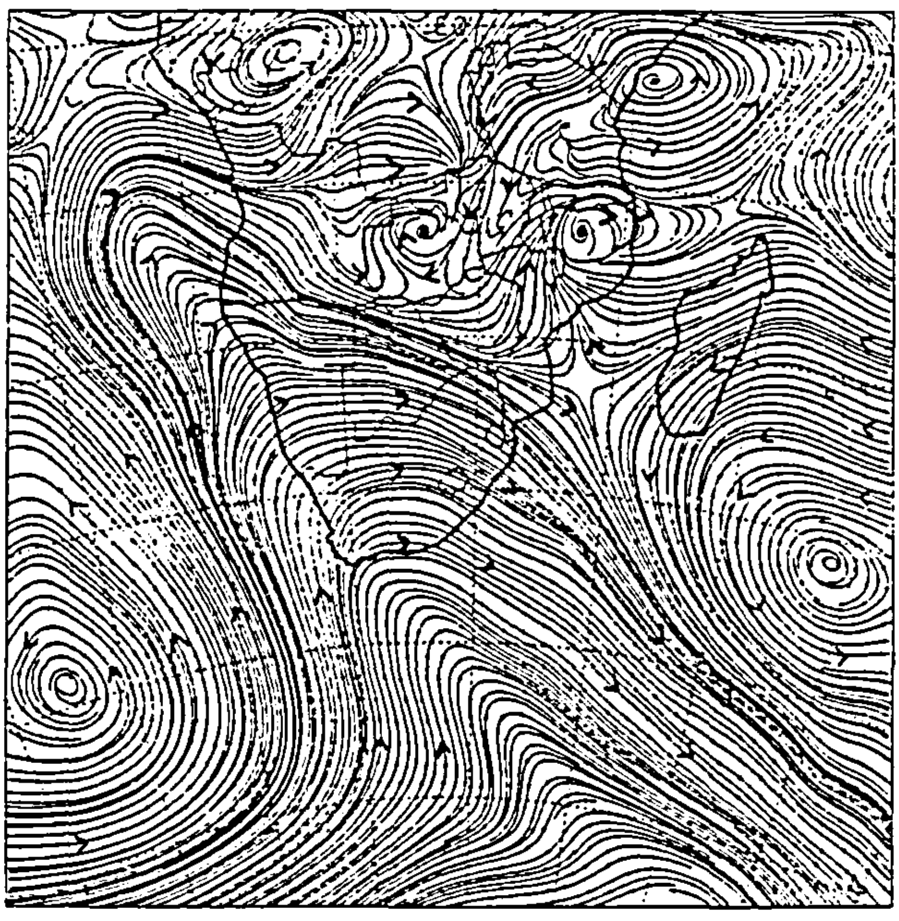

Figure 4.2 cont: Streamlines at 3,13 km (~ 700 hPa) above sea level from the wet case control run at (e) 24 Jan 6:00 UT and (f) 24 Jan 12:00 UT.

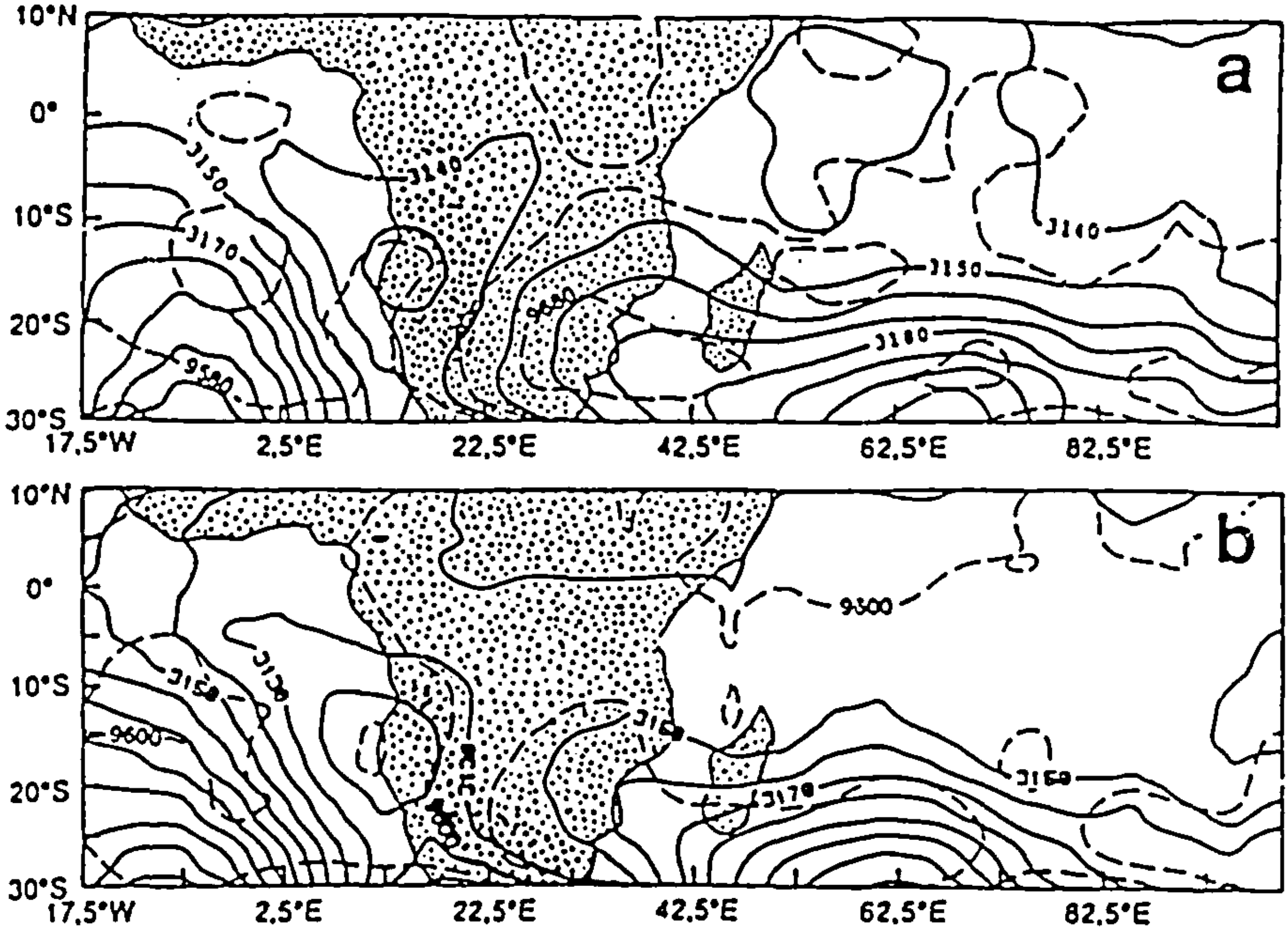

Figure 4.3: Pressure fields at 700 hPa and 300 hPa for (a) 22 January 1981 and (b) 23 January 1981 (after D'Abreton, 1992). Dark solid lines represent the 700 hPa level and light dashed lines the 300 hPa level.

obvious in the modelled surface and 700 hPa streamlines (Figs 4.1a, 4.2a). The modelled South Atlantic and South Indian Anticyclones and the width and amplitude of the approaching westerly wave throughout the troposphere (Figs 4.2a, 4.4a) correspond closely with the observed circulation fields (Figs 2.2a, 2.3a).

The increase in the amplitude of the westerly wave trough and the westward tilt of the trough with height, which enhances the baroclinicity of the atmosphere (Webster and Curtin, 1975), are obvious at all levels in the simulation by 09:00 UTC on 23 January (Day 2) (Figs 4.1b, 4.2b, 4.4b). The tropical low is evident over western Namibia at the surface (Fig. 4.1b). Formation of a closed cell of cyclonic circulation in the simulated westerly flow at the lower levels closely matches that of the synoptic chart and 700 hPa pressure fields (Figs 2.2b, 2.5b). The South Indian Anticyclone at 300 hPa has moved further eastward (Fig. 4.4b) and the upper tropospheric westerly wave now overlies the extreme western regions of southern Africa (Fig. 4.4b).

By 15:00 UTC on 23 January (Day 2), the model shows that owing to the eastward movement of the westerly wave, the leading arm of the westerly wave has aligned with the interior trough at the surface and 700 hPa (Figs 4.1c, 4.2c). Poleward flow along the tropical-temperate trough is clearly visible at all tropospheric levels and extends along the leading edge of the westerly wave to the most southern regions of the model domain (Figs 4.1c, 4.2c, 4.4c). The substantial contribution to this poleward flow by the northeasterly flow from over the tropics and by the easterlies enhanced by the South Indian Anticyclone is obvious (Figs 4.1c, 4.2c, 4.4c). Upper-level flow around the South Indian High has moved further east. Divergence in the westerly wave at the 300 hPa level, which now overlies the regions of convergence in the lower levels (Fig 4.4c), will enhance vertical uplift thus promoting ideal conditions for tropical-temperate trough development. Ridging of the South Atlantic High pressure cell behind the westerly wave is evident in the surface level streamlines (Fig. 4.1c).

The simulated region of convergence at the surface has shifted further eastward by 21:00 UTC on 23 January (Day 2). Poleward flow within the convergence zone crosses the coast in the region of Durban (30°S, 31°E) (Fig. 4.1d) and corresponds exactly with the satellite position

a

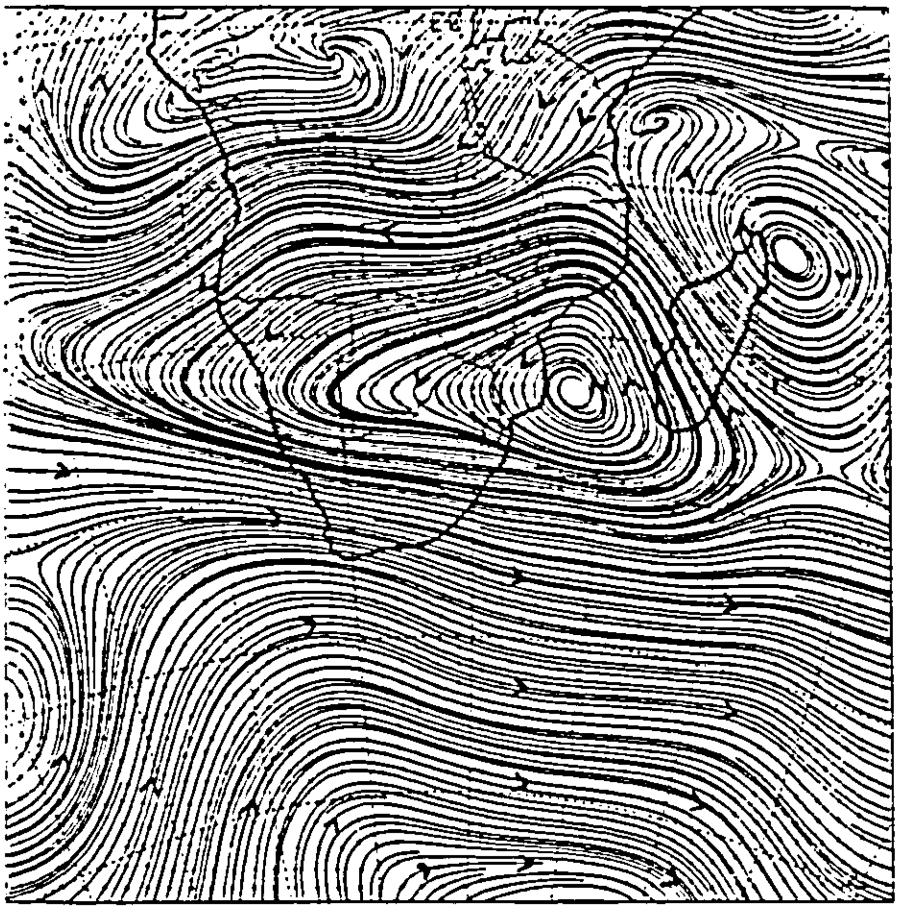

b

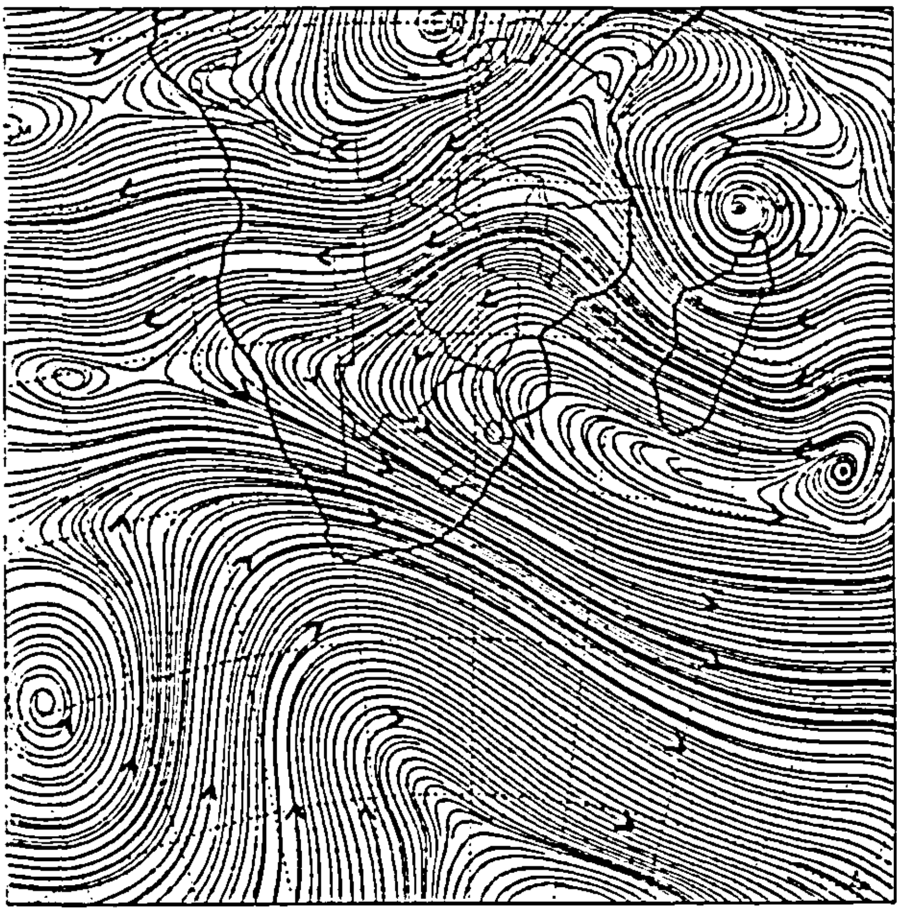

Figure 4.4: Streamlines at 9,66 km (~ 300 hPa) above sea level from the wet case control run at (a) 22 Jan 15:00 UT and (b) 23 Jan 9:00 UT.

c

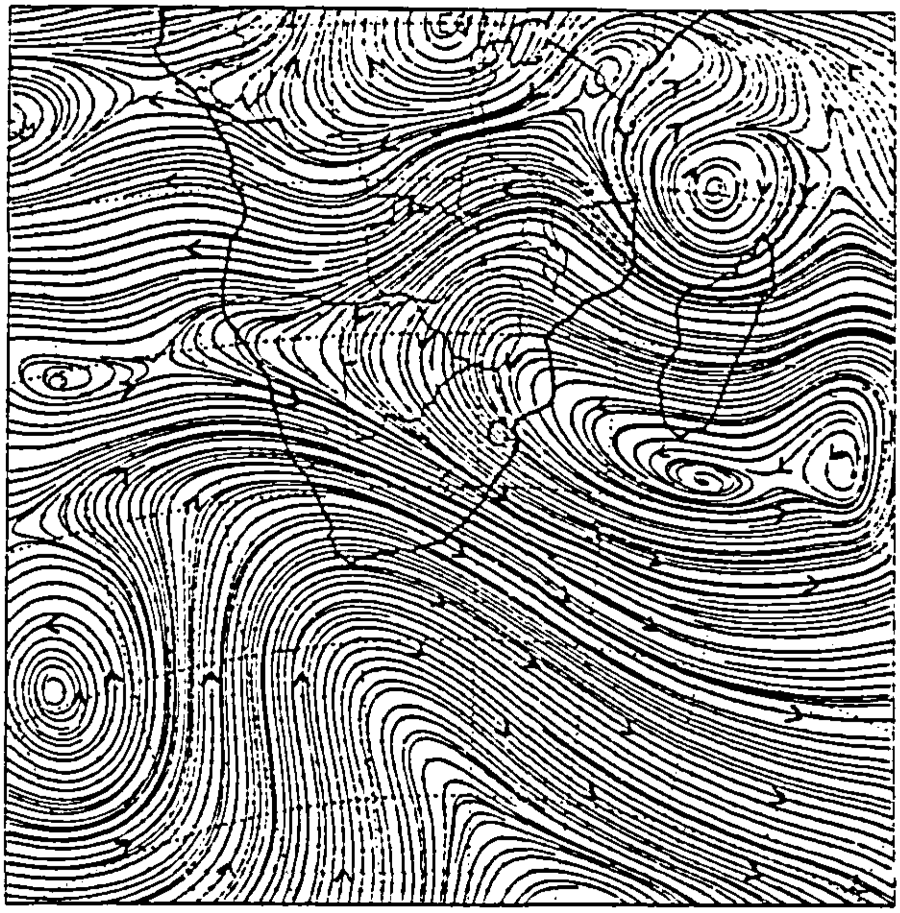

d

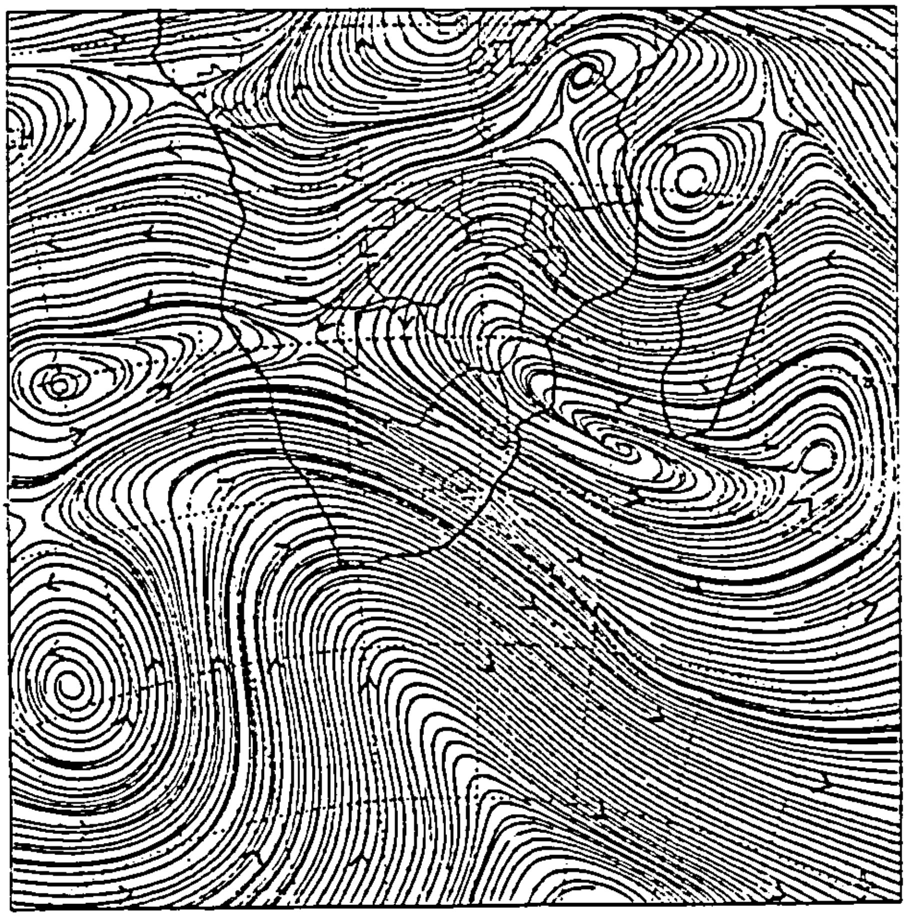

Figure 4.4 cont: Streamlines at 9,66 km (~ 300 hPa) above sea level from the wet case control run at (c) 23 Jan 15:00 UT and (d) 23 Jan 21:00 UT.

e

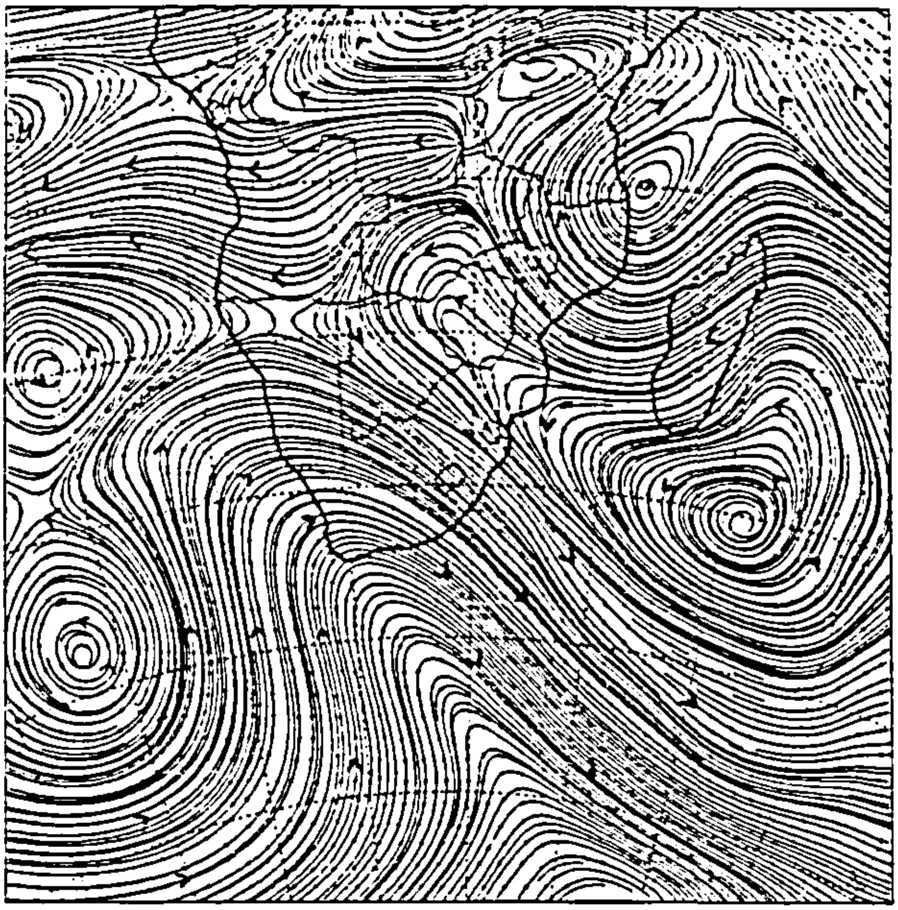

f

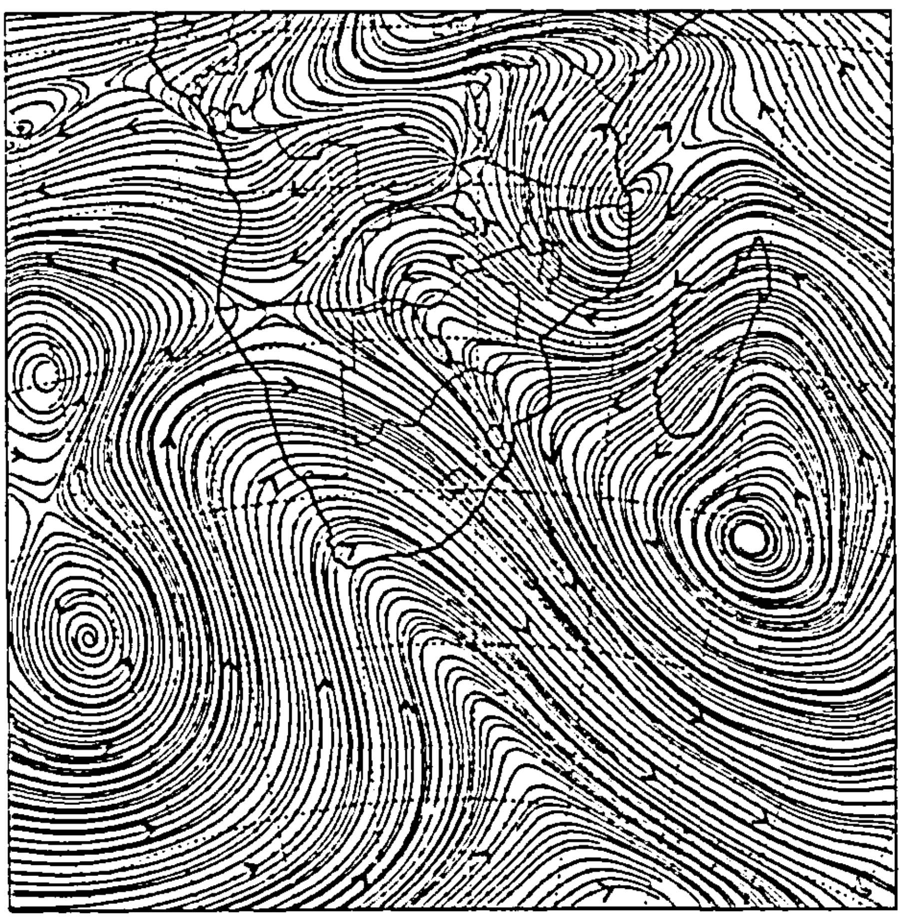

Figure 4.4 cont: Streamlines at 9,66 km (~ 300 hPa) above sea level from the wet case control run at (e) 24 Jan 6:00 UT and (f) 24 Jan 12:00 UT.

of the fully developed tropical-temperate trough (Plate 2.1c). The poleward flow is evident at all tropospheric levels (Figs 4.1d, 4.2d, 4.4d). Onshore flow around the coastal low in the Durban region appears to meet the poleward flow along the tropical-temperate trough (Fig. 4.1d) and produces local undercutting and uplift of the tropical air flowing along the cloud band. Ridging of the South Atlantic High behind the westerly wave occurs at all levels (Figs 4.1d, 4.2d, 4.4d).

By the morning of 24 January (Day 3), the model shows that at the surface and 700 hPa levels the northeasterly flow from the tropics has decreased and a significant eastward shift of the westerly wave has occurred (Figs 4.1e,f and 4.2e,f). Flow at the surface has become more easterly across the tropical regions (Fig. 4.1e,f). At 700 hPa numerous cyclonic cells have formed (Fig. 4.2e,f). These are associated with the tropical cloud cover evident in the satellite imagery over these regions (Plate 2.1f). The breakdown in the northeasterly flow accompanies the dissipation of the tropical-temperate trough and highlights the importance of tropical air in cloud band development. The main source of airflow along the remnants of the tropical-temperate trough at this stage is from the South Indian Anticyclone. Ridging of the South Atlantic High and the resultant onshore flow over the southern Cape coastal belt at surface levels is clear (Fig. 4.1e,f). At upper levels, the modelled westerly wave has narrowed considerably and is tilted even further to the west (Figs 4.2e,f and 4.4e,f). Dissipation of the tropical-temperate trough occurs with the eastward movement of the westerly wave, which is followed by the development of a ridging anticyclone.

The observed circulation systems associated with the tropical-temperate trough development are clearly obvious in the streamlines generated by RAMS. One exception exists. The separation of the westerly trough from the mainstream westerly flow is evident in the model output, but the closed cell of cyclonic flow in the 700 and 300 hPa levels over the southwestern Cape is not generated.

Pressure

The simulated pressure field on the terrain-following surface is largely a function of the topography. Regions of greater elevation such as the Lesotho and Angola Highlands, are associated with lower pressure and the pressure gradient along the Escarpment is obvious (Fig. 4.5a). A trough is, however, evident over the interior throughout the simulation period (Figs 4.5a,b). In the reduced mean sea level pressure field, the interior trough and the westerly wave to the south of the country are clearly obvious during the initial stages of the simulation (Fig. 4.5c). During the mature stages of the tropical-temperate trough development on 23 January (Day 2), the temperate link between the westerly wave and the interior trough is evident. The trough extends from the central interior to the extreme southern regions of the model domain (Fig. 4.5d,e). Dissipation of the system the following day is associated with the southeastward movement of the westerly wave (Fig. 4.5f). The model shows that the break in the temperate link occurs at approximately 30°S and 30°E in the region shown by D'Abreton (1992) to be that of the highest frequency of tropical-temperate trough dissipation. The narrowing, increase in amplitude and westward tilting of the westerly wave are all evident in the simulated pressure fields in the upper levels (Figs 4.6a-c and 4.6d-f). An increase in pressure over the interior and along the tropical-temperate trough is associated with the simulated dissipative stages at 700 hPa (Fig. 4.6b,c) as the westerly wave moves eastward.

The simulated pressure fields appear to be accurate in their representation of the tropical-temperate trough development, despite two exceptions. While the development of the cut-off low at 700 hPa between 40° and 50°S by 15:00 UTC on 23 January is predicted (Fig. 4.6b), the simulated cut-off low is situated further south than the observed system (Fig. 2.5b) and is not simulated the next day either at the surface (Fig. 4.6c) or at 300 hPa (Fig. 4.6f). The second difference regards the presence of a low pressure cell at 700 hPa over northwestern Namibia in the simulated output (Fig. 4.6a) which is not evident in the SAWB charts (Figs 2.3b, 2.4b). The low is, however, obvious in the pressure fields presented by D'Abreton (1992) (Fig. 4.3a).

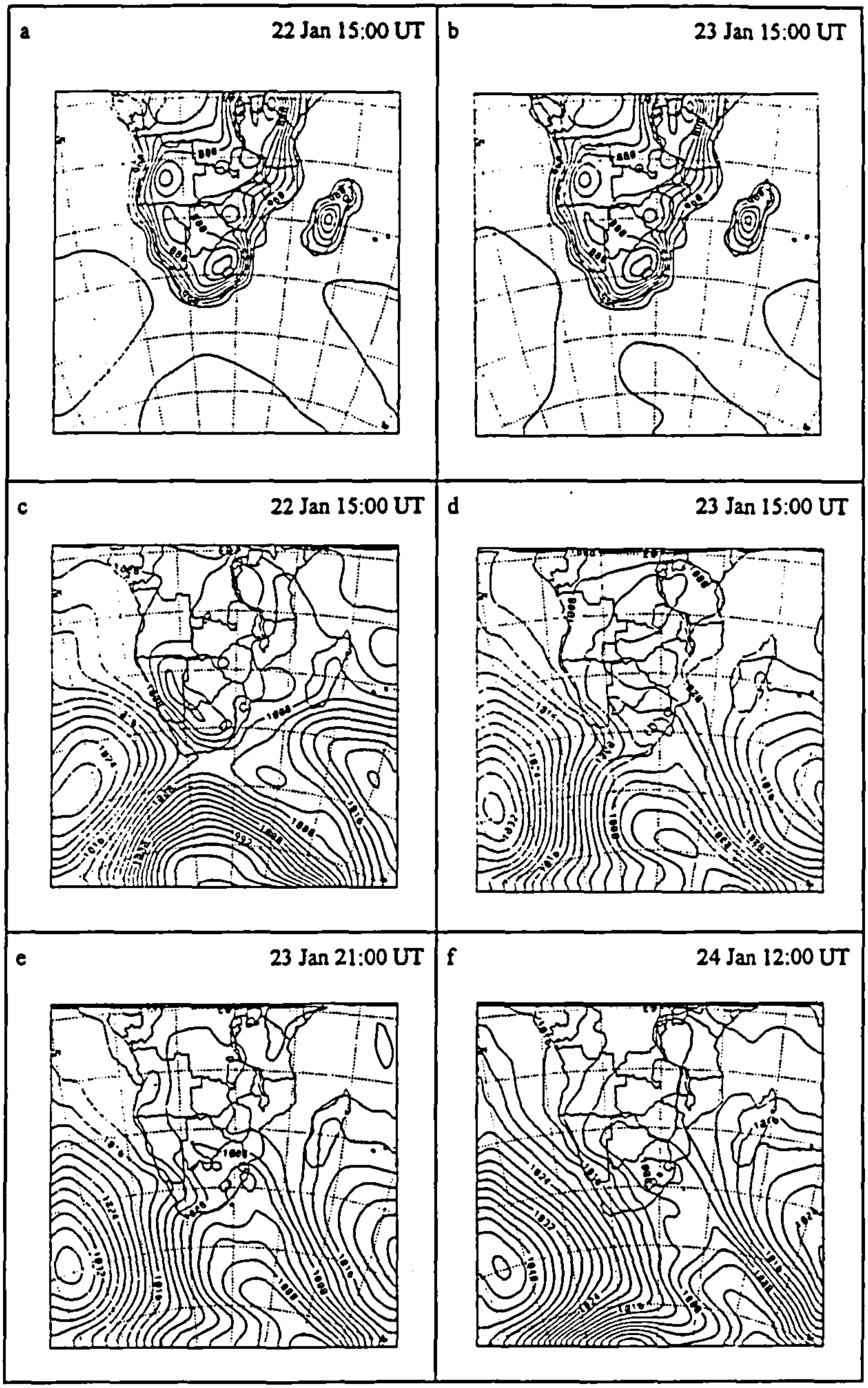

Figure 4.5: Surface pressure (on the terrain-following coordinate surface 146,4 m above the ground) from the wet case control run at (a) 22 Jan 15:00 UT and (b) 23 Jan 15:00 UT (hPa, contour interval of 20 hPa), and the reduced mean sea level pressure field from the wet case control run at (c) 22 Jan 15:00 UT, (d) 23 Jan 15:00 UT, (e) 23 Jan 21:00 UT and (f) 24 Jan 12:00 UT (hPa, contour interval of 2 hPa).

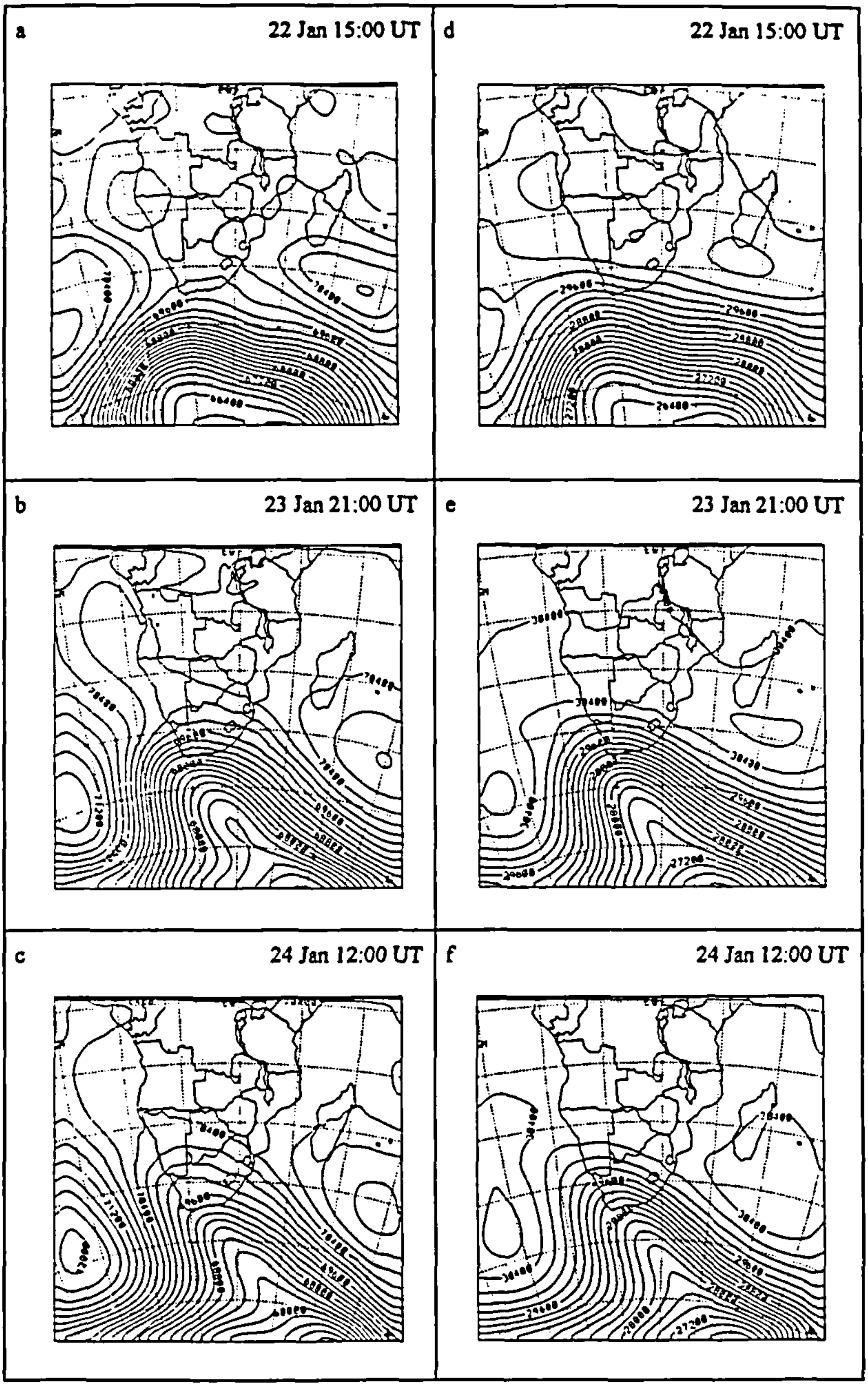

Figure 4.6: Pressure at 3,13 km (~ 700 hPa) above sea level from the wet case control run at (a) 22 Jan 15:00 UT, (b) 23 Jan 21:00 UT and (c) 24 Jan 12:00 UT, and at 9,66 km above sea level from the wet case control run at (d) 22 Jan 15:00 UT, (e) 23 Jan 21:00 UT and (f) 24 Jan 12:00 UT (Pa, contour interval of 200 Pa).

Vertical Velocity

The vertical velocity field at 15:00 UTC on 22 January (Day 1) reveals the presence of the tropical low over Windhoek and the interior trough over the western regions over southern Africa at the 700 hPa level (Fig. 4.7a). An area of weaker uplift occurs over the Natal coast and is due to orographic uplift in the onshore flow around the South Indian Anticyclone at surface levels (Fig. 2.2a). Weak vertical velocities are found in the region of the approaching westerly wave and are surrounded by regions of subsidence associated with the South Atlantic and South Indian Anticyclones. The vertical winds between 50° and 60°E and 40° to 50°S are caused by the presence of a cold frontal system (Fig. 2.2a). Vertical uplift is also evident over Madagascar where the easterly flow is forced to rise over the steep topography of the island.

By 09:00 UTC on 23 January (Day 2), vertical uplift still occurs in the region of the tropical low and the interior trough, but is weaker than the previous afternoon (Fig. 4.7b). The break of the tropical link between the tropical low and the interior trough, and the transient formation of the temperate link between the interior trough and westerly wave, both of which occurred in the early morning of 23 January (see chapter 2), are evident. Uplift along the westerly wave is now more organised. The pattern of the vertical velocity at 15:00 UTC (not shown) and 18:00 UTC (Fig. 4.7c) on 23 January (Day 2) are similar. The vertical velocity has increased significantly from earlier in the day and the northwest-southeast alignment of the interior trough is visible. The simulated northern extremity of the convection along the band is still the tropical low over Namibia and corresponds well with observations. Uplift over the Natal coast is caused by the onshore flow associated with the presence of the coastal low at the surface layer (clearly evident in the simulated streamlines) and orographic uplift in the region of the Escarpment. This enhances convection in the tropical air flowing southward and produces the cloud cluster that forms part of the tropical-temperate trough in this area (Plate 2.2c). A region of positive vertical flow occurs over the southwestern Cape at 18:00 UTC in association with the development of the closed low over this region. By 21:00 UTC, strong vertical uplift is obvious along the entire tropical-temperate trough system to approximately 40°S (Fig. 4.7d).

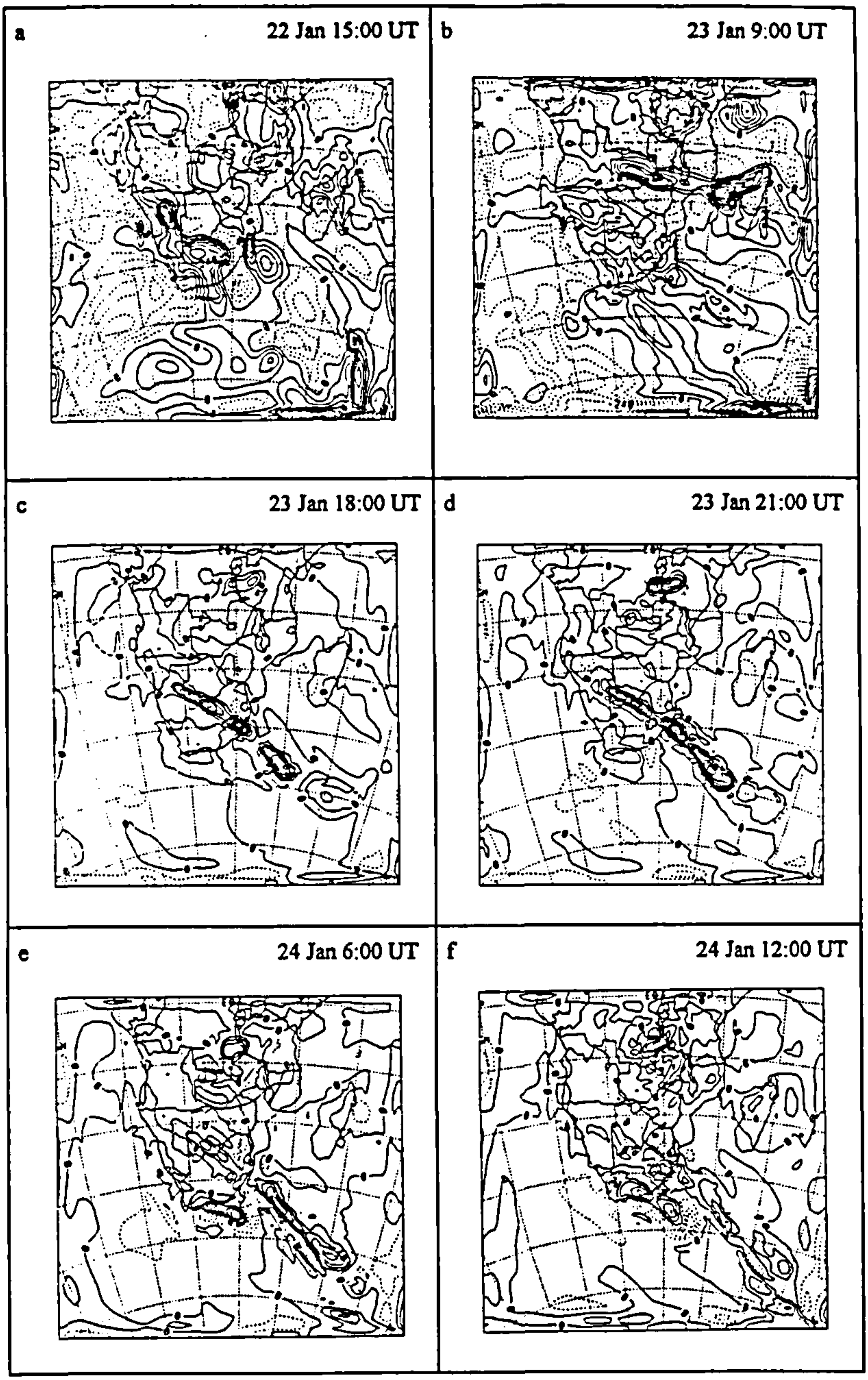

Figure 4.7: Vertical velocity at 3,13 km (~ 700 hPa) above sea level from the wet case control run at (a) 22 Jan 15:00 UT, (b) 23 Jan 9:00 UT, (c) 23 Jan 18:00 UT, (d) 23 Jan 21:00 UT, (e) 24 Jan 6:00 UT and (f) 24 Jan 12:00 UT (cm.s^{-1}; contour interval of 0,6 cm.s^{-1} for a and b, and 2 cm.s^{-1} for c-f; labels multiplied by 10^2 in a and b, and by 10 in c-f; solid lines indicate uplift and dashed lines indicate subsidence).

The area of uplift over the ocean did not extend as far poleward as the cloud band evident in the satellite imagery (Plate 2.1c). The synoptic chart for 23 January reveals that the centre of the low pressure cell associated with the cold front is situated between 43° and 45°S. Strong vertical uplift is not likely to be found further south of this position. The region of strongest vertical uplift associated with the westerly wave will probably occur between 37° and 42°S. Also, the tephigram for Marion Island (47°S, 38°E) indicates an inversion layer between the surface and approximately 725 hPa (Fig. 4.8) which will impede vertical uplift. The simulated poleward extent of the vertical uplift at 18:00 UTC therefore seems reasonable.

Partial dissipation of the tropical-temperate trough is obvious in the vertical velocity fields at 06:00 UTC on 24 January (Day 3) (Fig. 4.7e). Vertical uplift over the interior has weakened substantially. Orographic uplift of the onshore winds is the cause of the increased vertical velocity along the southern Cape coastal belt. The vertical wind associated with the closed low is no longer evident at this stage. By 12:00 UTC, dissipation of vertical uplift along the cold front is obvious. Simulated vertical velocities over the interior are insignificant, with the exception of those over the Natal region which coincide with the presence of the cloud band remnants (Plate 2.1e). The zone of strong vertical winds evident over tropical Africa develops throughout the study period and is associated with a thick tropical cloud cluster evident in the satellite imagery (Plate 2.1).

Vertical uplift associated with the *tropical-temperate trough development is evident throughout the troposphere to at least the 300 hPa level (Fig. 4.9). This is indicative of the strength of the convection within cloud band systems.* The simulated vertical velocity clearly illustrates the development of the tropical-temperate trough. The closed low is, however, inadequately simulated.

Convective Precipitation Rate

The control runs for both the wet and dry case studies included the modified Kuo parameterisation scheme, but did not include any resolvable microphysics. Condensation occurs in the regions of supersaturation and the resultant latent heat is released, but the

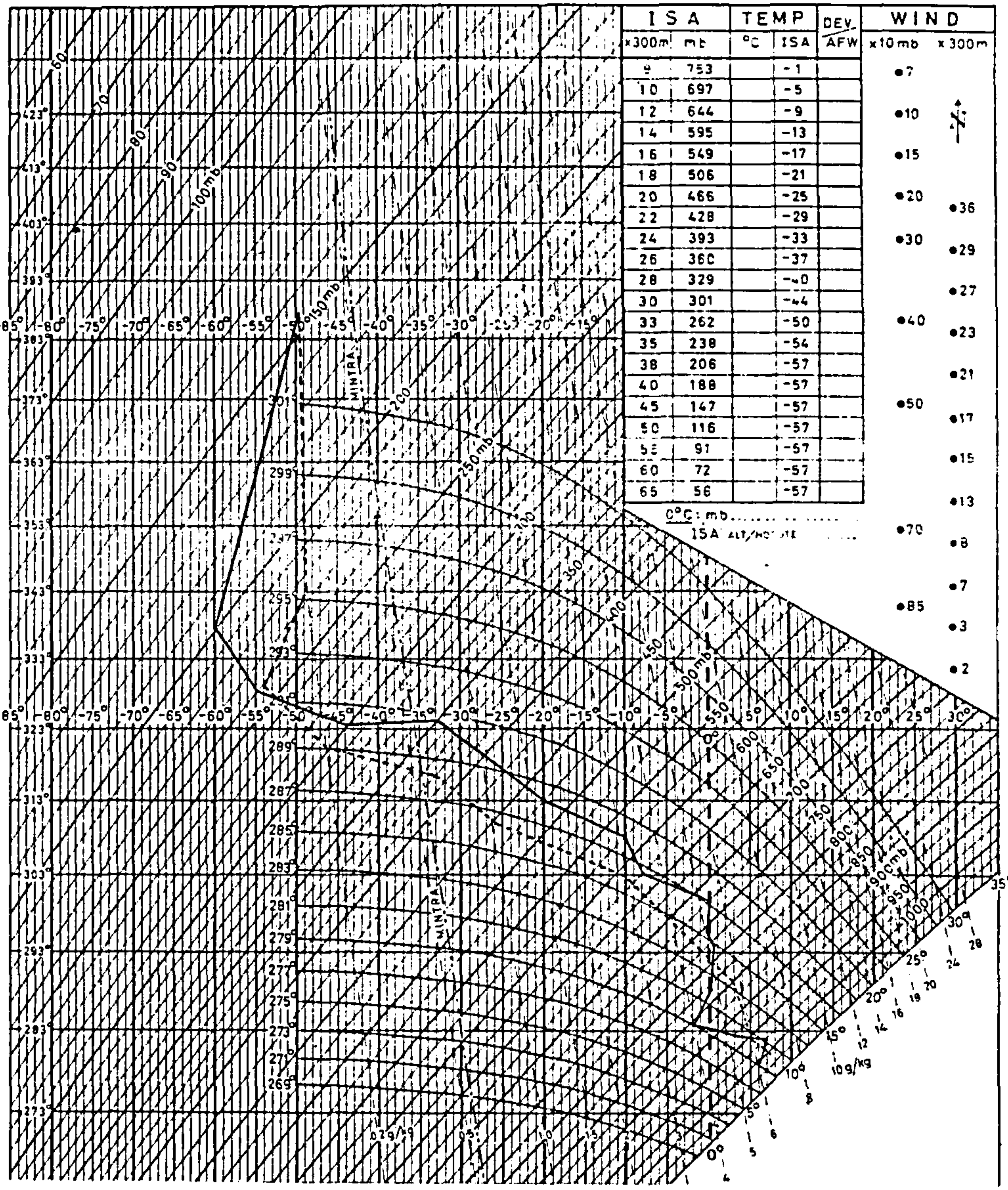

Figure 4.8: Marion Island (47°S, 38°E) tephigram for 23 January 1981. The solid line represents temperature at 00:00 UT and the dashed line the temperature at 12:00 UT.

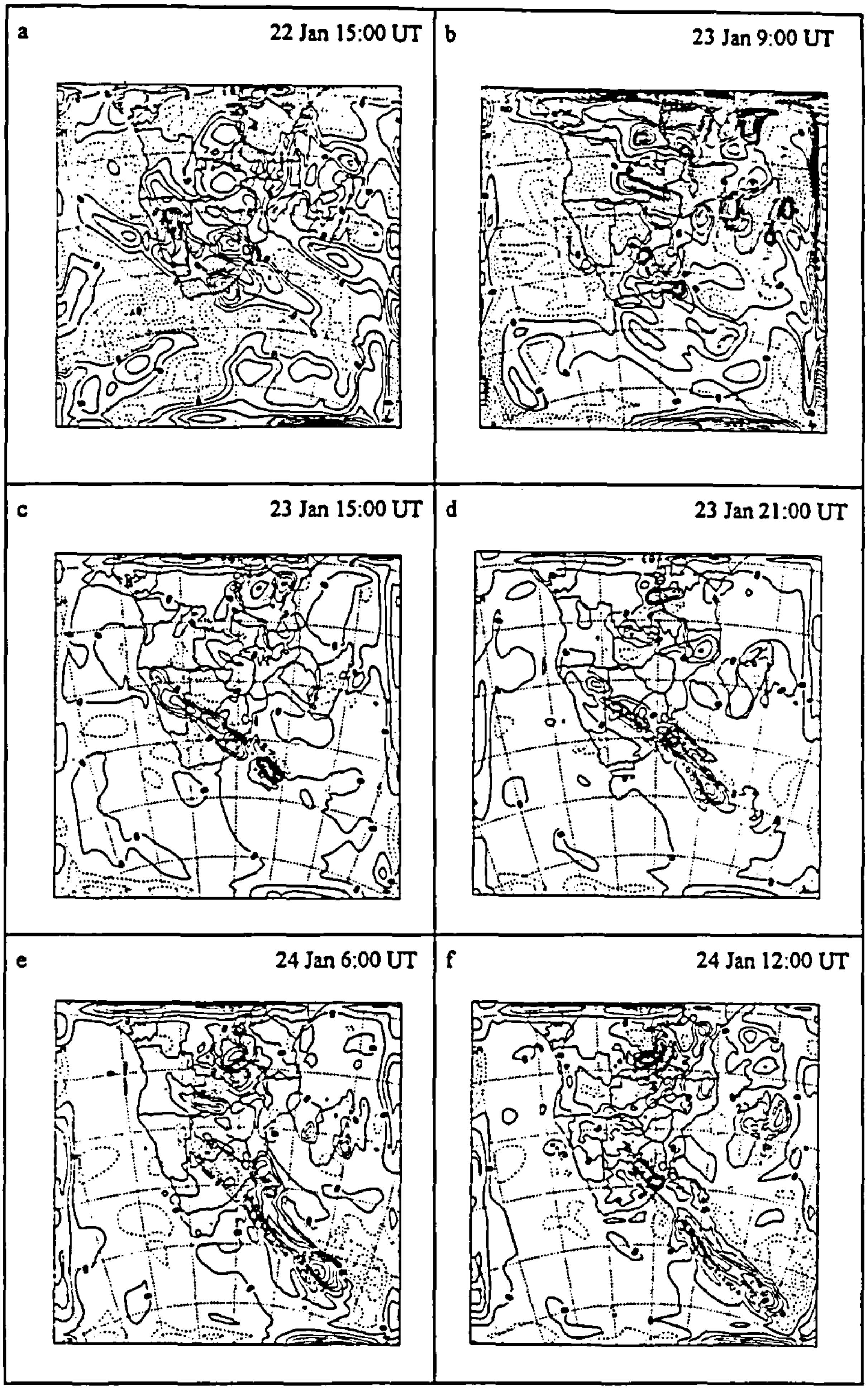

Figure 4.9: Vertical velocity at 9,66 km (~ 300 hPa) above sea level from the wet case control run at (a) 22 Jan 15:00 UT, (b) 23 Jan 9:00 UT, (c) 23 Jan 15:00 UT, (d) 23 Jan 21:00 UT, (e) 24 Jan 6:00 UT and (f) 24 Jan 12:00 UT (cm.s^{-1}; contour interval of 1 cm.s^{-1} for a and b, and 2 cm.s^{-1} for c-f; labels multiplied by 10; solid lines indicate uplift and dashed lines indicate subsidence).

precipitation process does not occur (Walko and Tremback, 1991). The convective precipitation rate is the rate of precipitation computed by the convective parameterisation scheme and only indicates the precipitation obtained from deep convection. Precipitation resulting from other processes, such as those involved with stratiform type clouds, is not simulated (Tremback, 1990). As the convective precipitation is simply a picture of what is occurring at a specific moment, comparing the regions of convective precipitation with satellite imagery or synoptic charts, does not always yield a close correspondence. Nevertheless, the convective precipitation rate is indicative of regions of deep convection and is an important variable to examine even though it does not give a complete picture of total rainfall.

The simulated convective precipitation rate over South Africa at 15:00 UTC on 22 January (Day 1) is high over the region of the interior trough (Fig. 4.10a). Other regions of convective precipitation are obvious over Zimbabwe, Madagascar and the eastern regions of tropical Africa and are related to the presence of tropical cloud clusters (Plate 2.1a). A significant reduction in the modelled convective precipitation rate is evident over southern Africa at 09:00 UTC on 23 January (Day 2) (Fig. 4.10b) and may be associated with the temporary weakening of the interior trough (Fig. 4.8b). By 15:00 UTC, however, the convective precipitation rate has increased substantially and extends over the ocean as a result of the strengthening of the interior trough and the formation of both the tropical and temperate links (Fig. 4.10c). The band structure of the tropical-temperate trough is now clearly obvious. Strong convective precipitation is evident along the fully developed trough by 21:00 UTC (Fig. 4.10d). Some convective activity is also still observed over the tropics. The confinement of the convective precipitation to north of approximately 35°S is in keeping with the southerly extent of the region of vertical uplift.

Partial dissipation of the tropical-temperate trough by the morning of 24 January (Day 3) results in the absence of convective precipitation over most of southern Africa at 06:00 UTC (Fig. 4.10e). By 12:00 UTC, the remnants of the interior trough over the eastern regions of South Africa are evident in the simulated convective precipitation field. The break in the temperate link as a result of the eastward movement of the westerly wave away from the

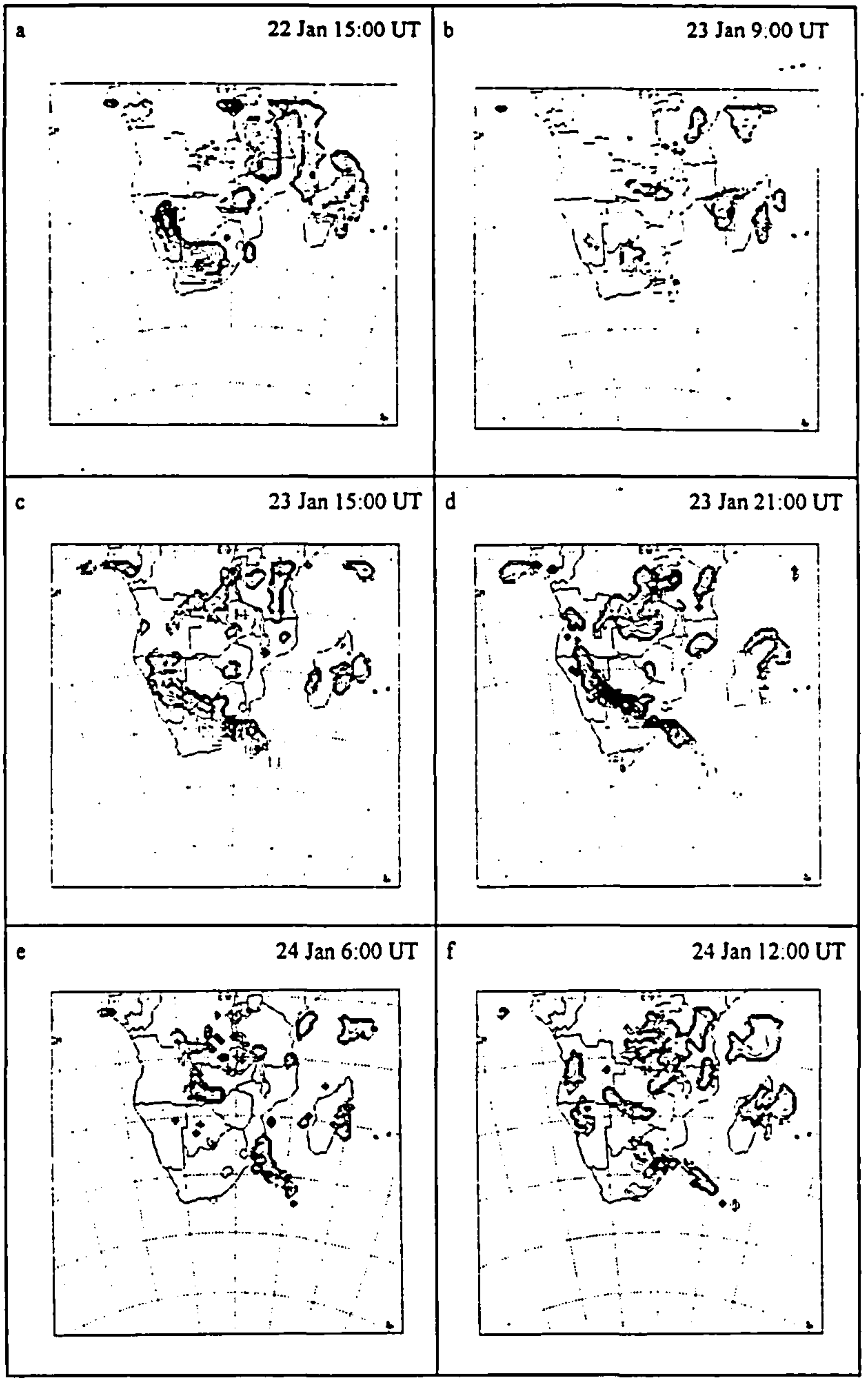

Figure 4.10: Convective parameterisation precipitation rate from the wet case control run at (a) 22 Jan 15:00 UT, (b) 23 Jan 9:00 UT, (c) 23 Jan 15:00 UT, (d) 23 Jan 21:00 UT, (e) 24 Jan 6:00 UT and (f) 24 Jan 12:00 UT (mm s^{-1}; contour interval of 0,000035 mm s^{-1}; labels multiplied by 10^{*}).

interior is particularly obvious at this time (Fig. 4.10f). The convective activity along the southeastern Cape coast from the onshore flow of the ridging South Atlantic High is also evident at 12:00 UTC. A clear line of demarcation exists between the region of no convective precipitation to the west of the cloud band and the convective precipitation within the cloud band in the modelled convective precipitation fields throughout the simulation. This is in accord with the cloudless sky over this region in the satellite imagery (Plate 2.1).

The accumulated convective precipitation for the 48-hour simulation period, from 12:00 UTC on 22 January (Day 1) to 12:00 UTC on 24 January (Day 3) (Fig. 4.11), reveals as to be expected, that the strongest convective precipitation rates are situated in the region of the tropical-temperate trough. Regions of high convective precipitation also occur over Madagascar. The rainfall that occurred over the southern Cape coastal regions (Fig. 2.8b,c) is not, however, evident in the modelled accumulated convective precipitation. The simulated convective precipitation total is only about 30 per cent of the observed precipitation that occurred during the 48 hour study period (Fig. 2.8c). Underestimation of the actual rainfall by the RAMS convective precipitation scheme has been previously noted. In the simulation of a squall line event, the modelled convective precipitation constituted only about 50 per cent of the total observed rainfall (Cram, 1990). It has also been found that resolved precipitation can contribute as much as 30 to 40 per cent of the total rainfall when simulating mesoscale convective systems (Zhang, 1985). These findings point to the importance of the inclusion of resolvable microphysics in the model. This point will be investigated further in the analysis of the sensitivity test including the microphysics module (see Chapter 6). Despite the underestimation of the rainfall, the modelling of the tropical-temperate trough development and associated regions of convective activity correspond closely with the actual conditions.

Control Run for the Dry Case Study

Streamlines

The troughs associated with the primary and secondary cold fronts to the east and west of the subcontinent, and the ridging of the high pressure cell from the South Atlantic Anticyclone

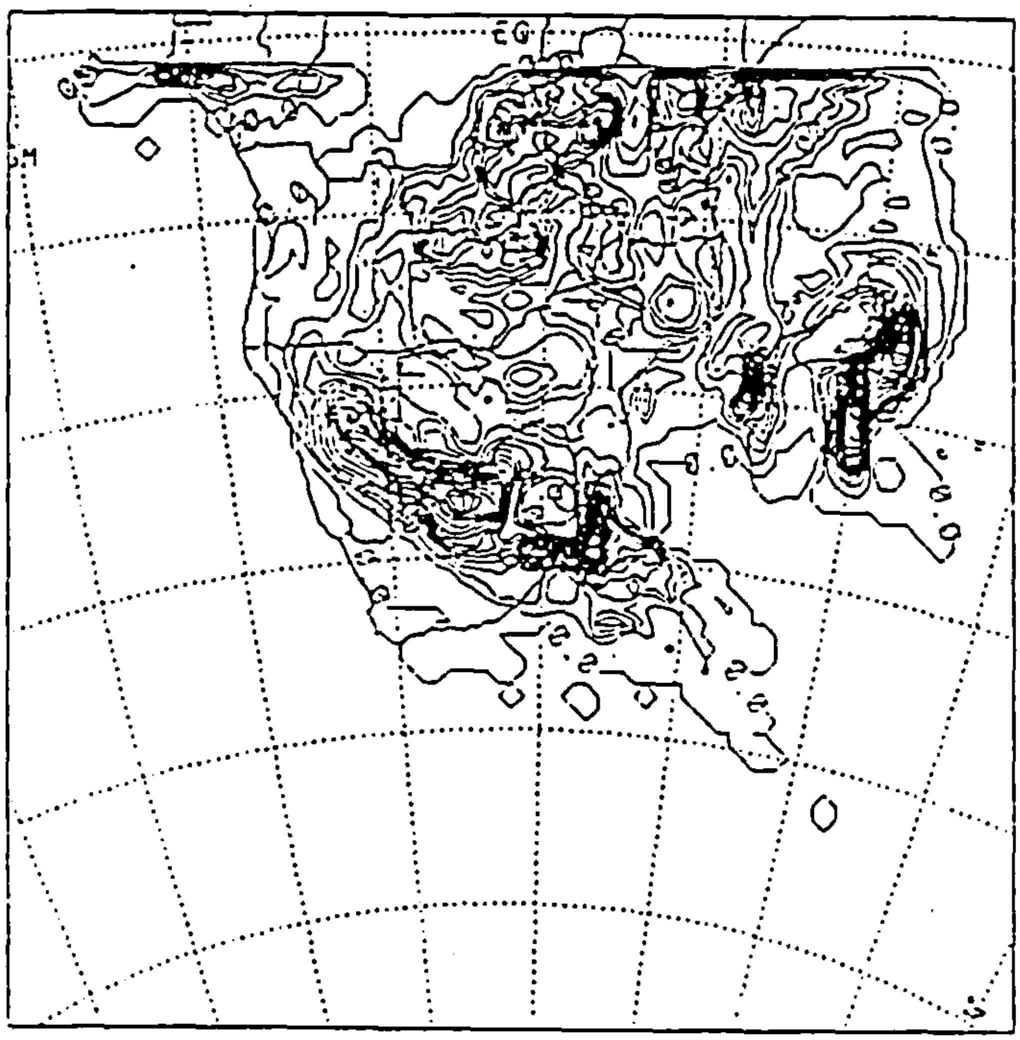

Figure 4.11: Precipitation produced by the cumulus parameterisation scheme between 22 Jan 12:00 UTC and 24 Jan 12:00 UTC from the wet case control run (mm; contour interval of 1 mm, maximum value of 18 mm).

that occurred between these two troughs, are clearly simulated by the model at 15:00 UTC on 6 January (Day 1) (Fig. 4.12a). The cell of low pressure associated with the northern section of the primary frontal system and the ridging of the high pressure cell both occur further south in the simulated field than on the synoptic chart (Fig. 2.15a). As both of these systems are situated over data sparse oceanic regions it is not possible to say whether the modelled output or the observations are better representations of actual conditions. A trough extending in a northwest-southeast direction is evident over northern Mozambique. This forms the link between the tropical low and the westerly wave and is only partially evident on the synoptic chart (Fig. 2.15a). The modelled centres of both the South Atlantic and South Indian Anticyclones concur closely with those indicated on the synoptic chart (Fig. 2.15a). All the circulation systems evident in the 700 (Fig. 2.16b) and 300 hPa (Fig. 2.16a) upper air charts are accurately simulated (Figs 4.13a, 4.14a).

The model reveals that by 09:00 UTC on 7 January (Day 2), the tropical low has developed and is evident to the west of Malawi (Fig. 4.12b). Some convergence along the trough over Mozambique is also apparent. The tropical low is situated on the border of northern Mozambique and Malawi by 12:00 UTC and has joined with the trough extending across northern Mozambique, thus forming the tropical link (Fig. 4.12c). The simulated eastward movement of the westerly wave has diagonally aligned the primary cold front with the trough over northern Mozambique, thereby establishing the temperate link. Northeasterlies blow into the region of the tropical low from over tropical Africa and the oceanic region to the northwest of Madagascar. Northerly flow into the tropical low originates over the northeastern regions of the South Atlantic Ocean.

Intensification of the simulated tropical low over northern Mozambique and Malawi is evident at the 700 hPa level (Fig. 4.13b). Divergence associated with the anticyclonic circulation at 300 hPa over this region serves to strengthen the tropical low (Fig. 4.14b). Convergence in the lower levels stretches along the modelled tropical-temperate trough which is now fully developed (Fig.4.12c). Divergence in the leading edge of the upper westerly wave is associated with low level convergence and promotes strong uplift in the region of the tropical-temperate trough (Fig.4.14b). The model shows that poleward flow does not occur along the

a

b

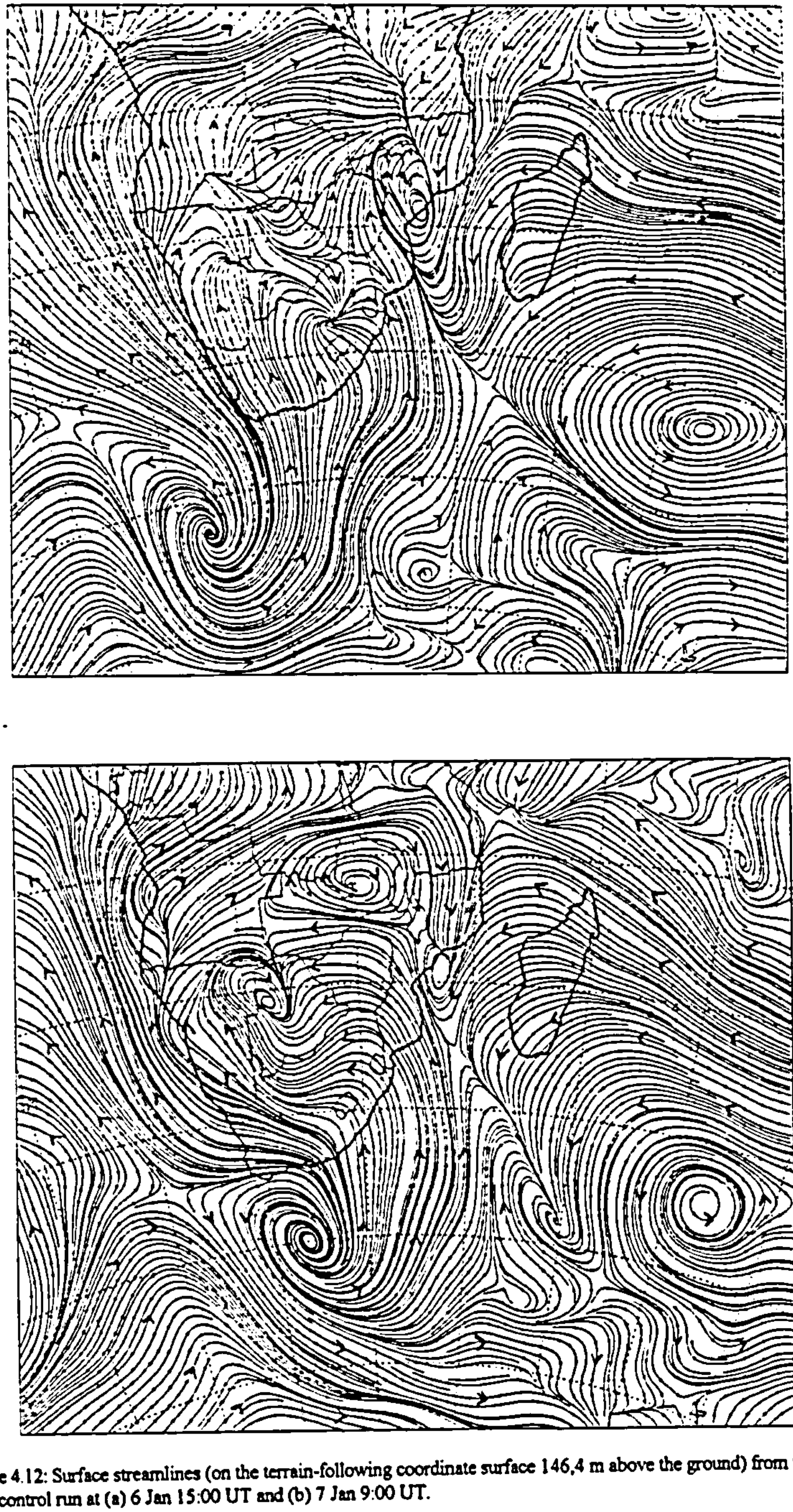

Figure 4.12: Surface streamlines (on the terrain-following coordinate surface 146,4 m above the ground) from the dry case control run at (a) 6 Jan 15:00 UT and (b) 7 Jan 9:00 UT.

c

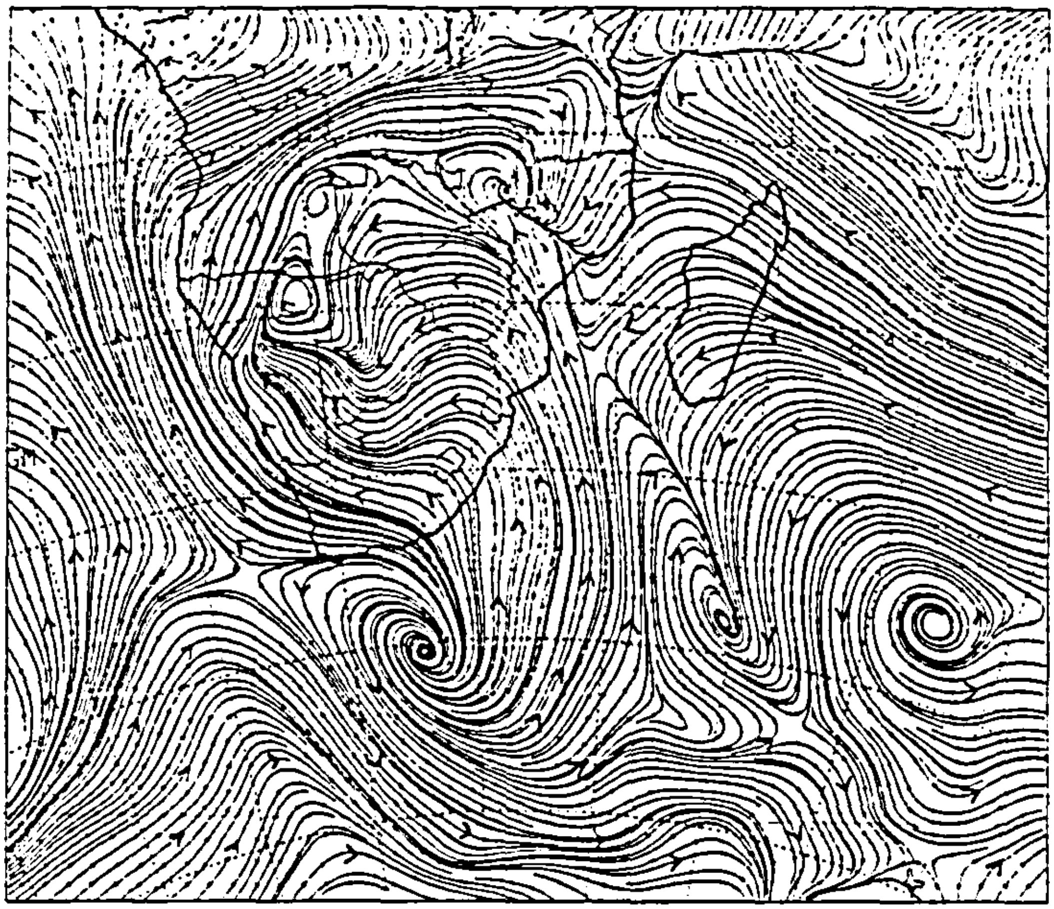

d

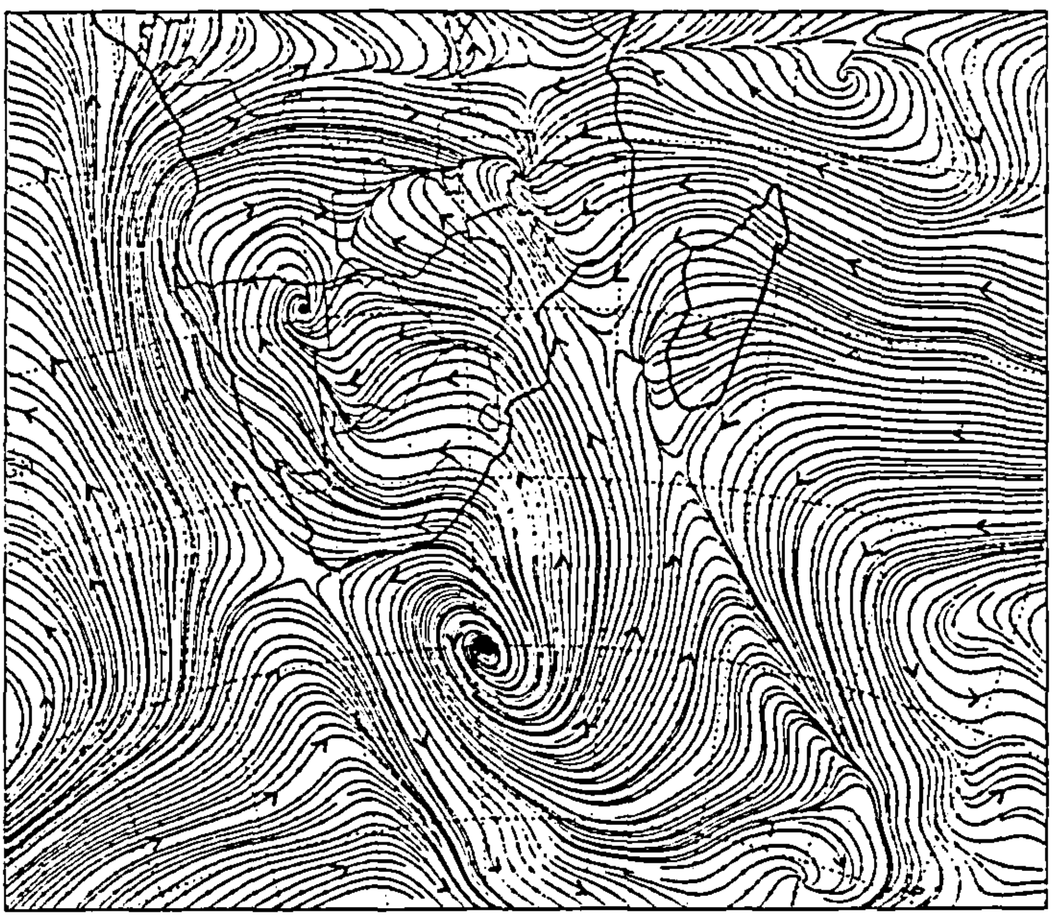

Figure 4.12 cont: Surface streamlines (on the terrain-following coordinate surface 146,4 m above the ground) from the dry case control run at (c) 7 Jan 12:00 UT and (d) 7 Jan 21:00 UT.

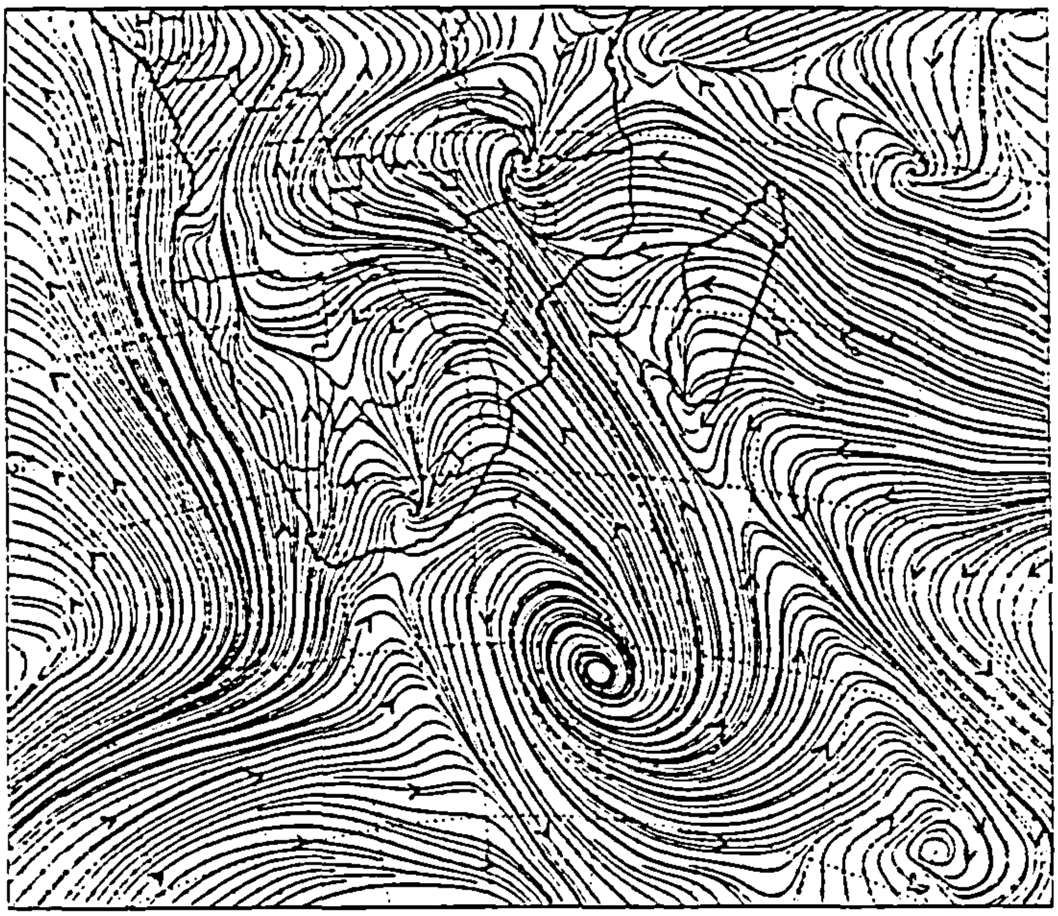

Figure 4.12 cont: Surface streamlines (on the terrain-following coordinate surface 146.4 m above the ground) from the dry case control run at (c) 8 Jan 12:00 UTC.

a

b

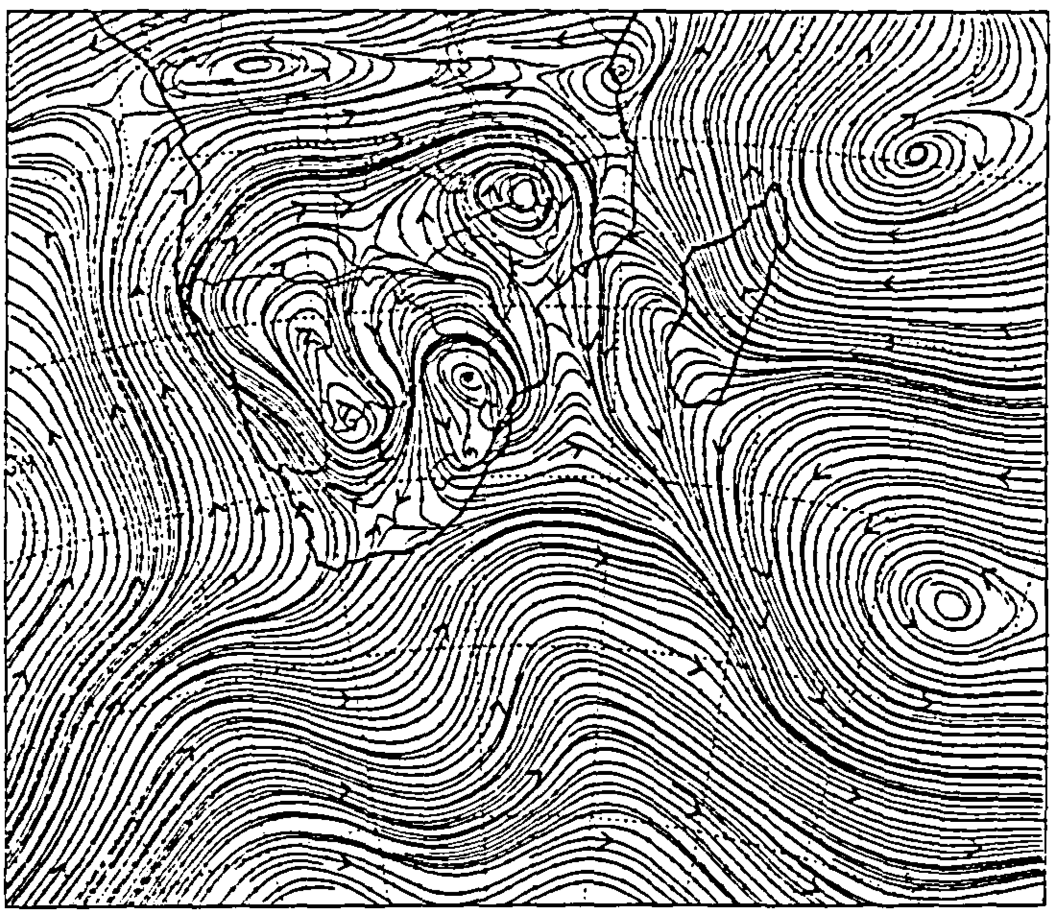

Figure 4.13: Streamlines at 3,13 km (~ 700 hPa) above sea level from the dry case control run at (a) 6 Jan 15:00 UT and (b) 7 Jan 12:00 UT.

c

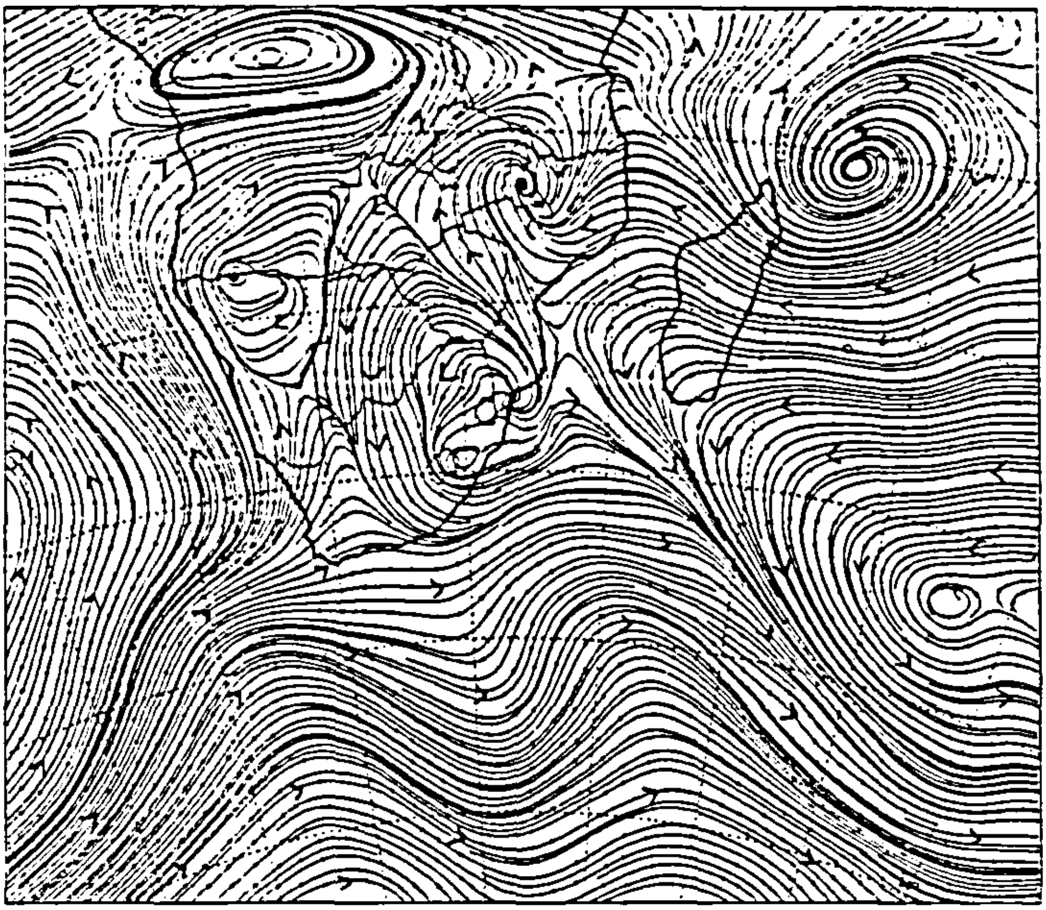

d

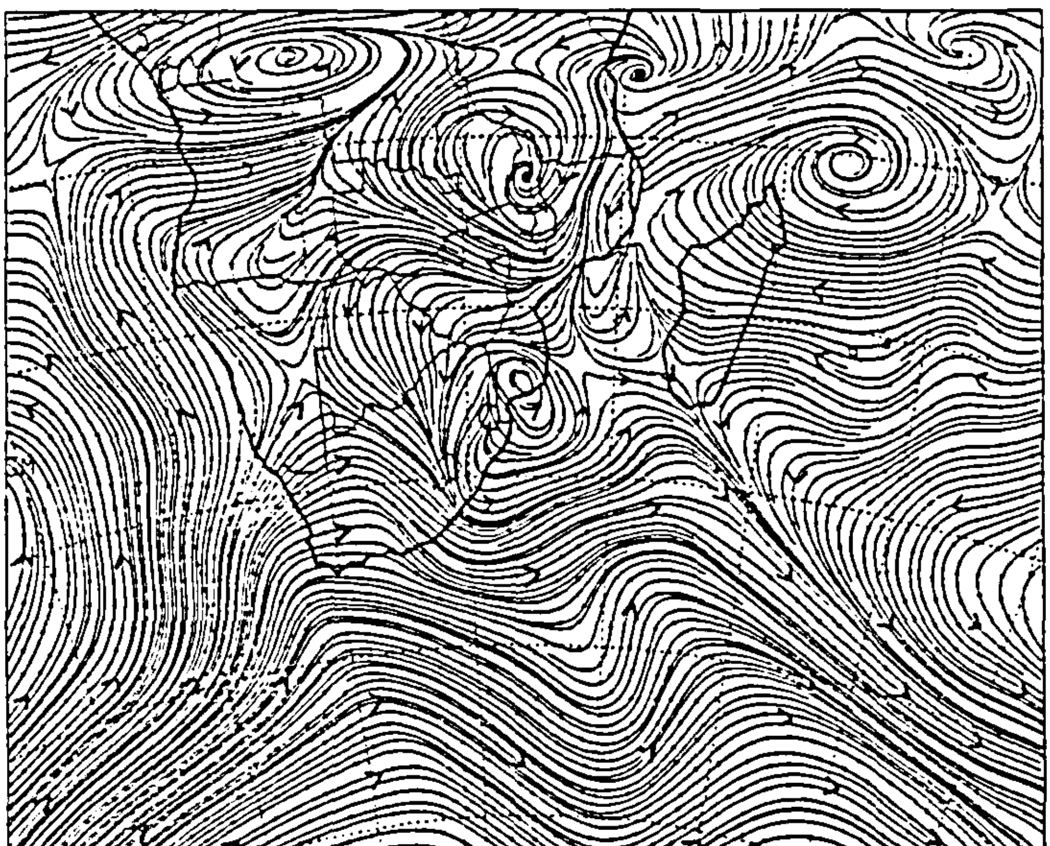

Figure 4.13 cont: Streamlines at 3,13 km (~ 700 hPa) above sea level from the dry case control run at (c) 7 Jan 21:00 UT and (d) 8 Jan 12:00 UT.

a

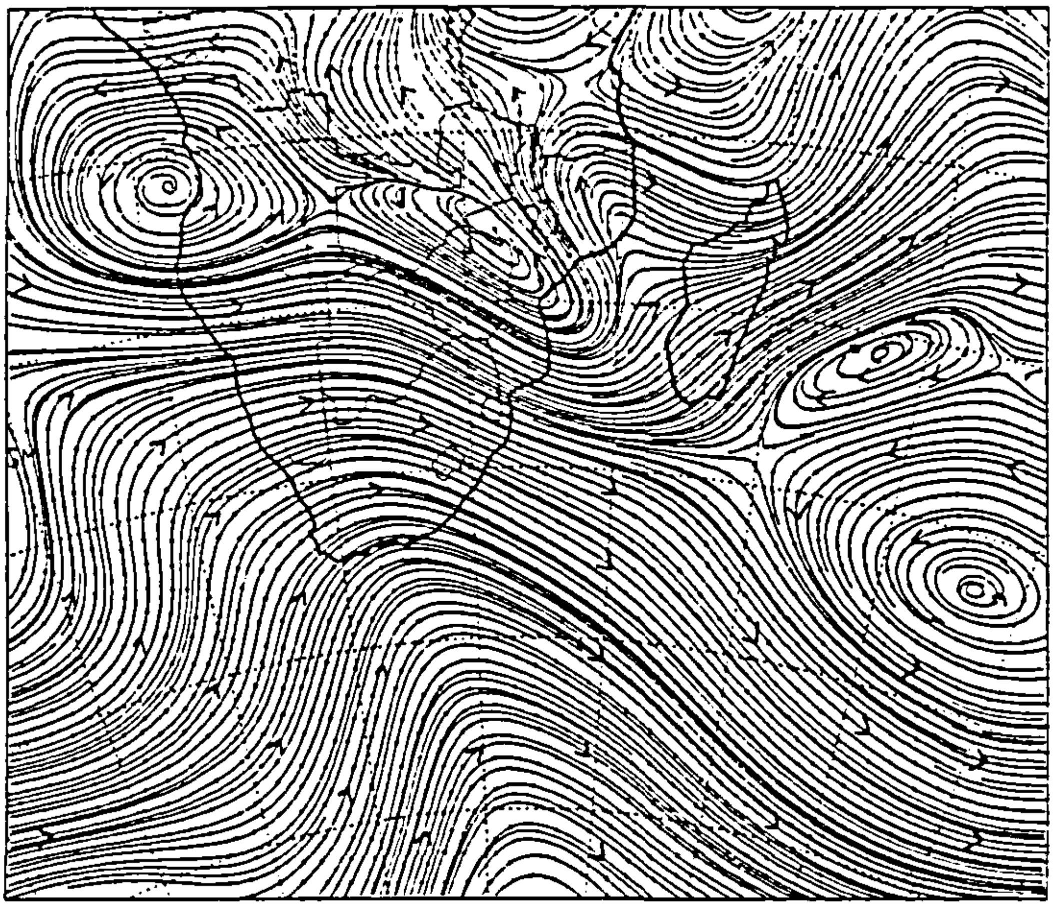

b

Figure 4.14: Streamlines at 9,66 km (~ 300 hPa) above sea level from the dry case control run at (a) 6 Jan 15:00 UT and (b) 7 Jan 12:00 UT.

c

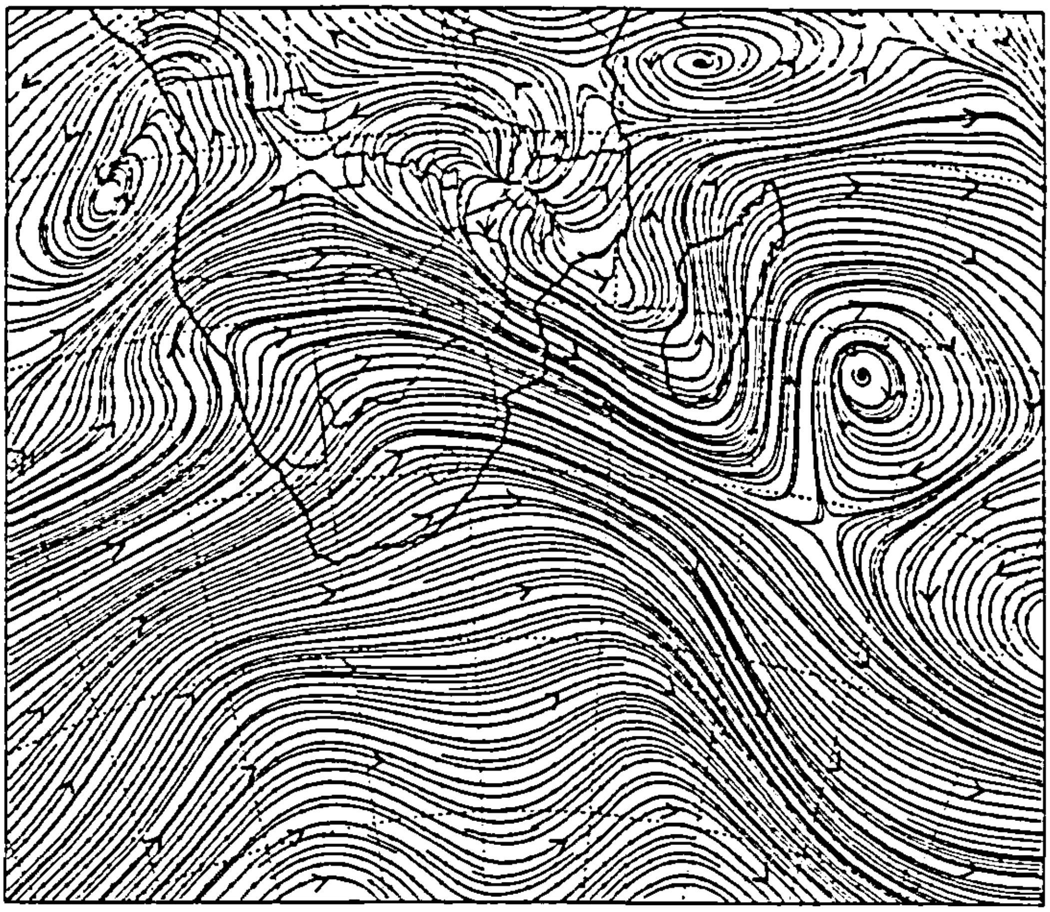

d

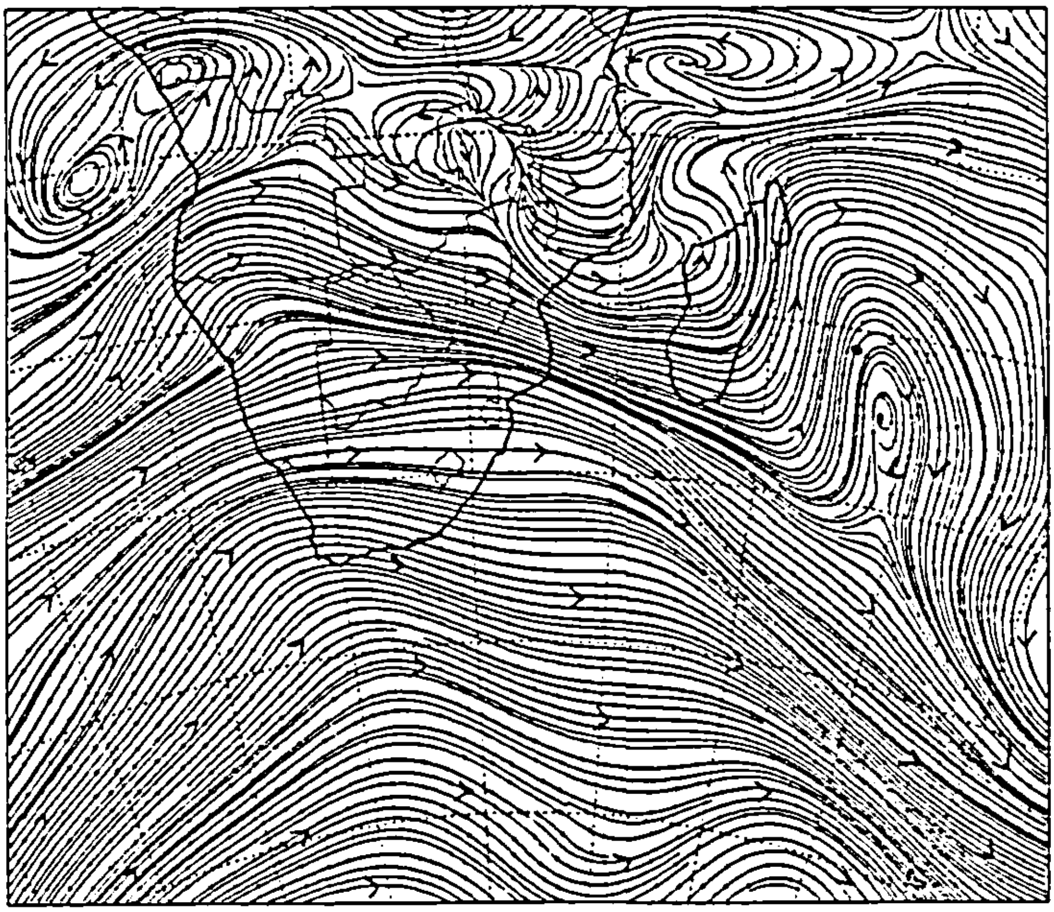

Figure 4.14 cont: Streamlines at 9,66 km (~ 300 hPa) above sea level from the dry case control run at (c) 7 Jan 21:00 UT and (d) 8 Jan 12:00 UT.

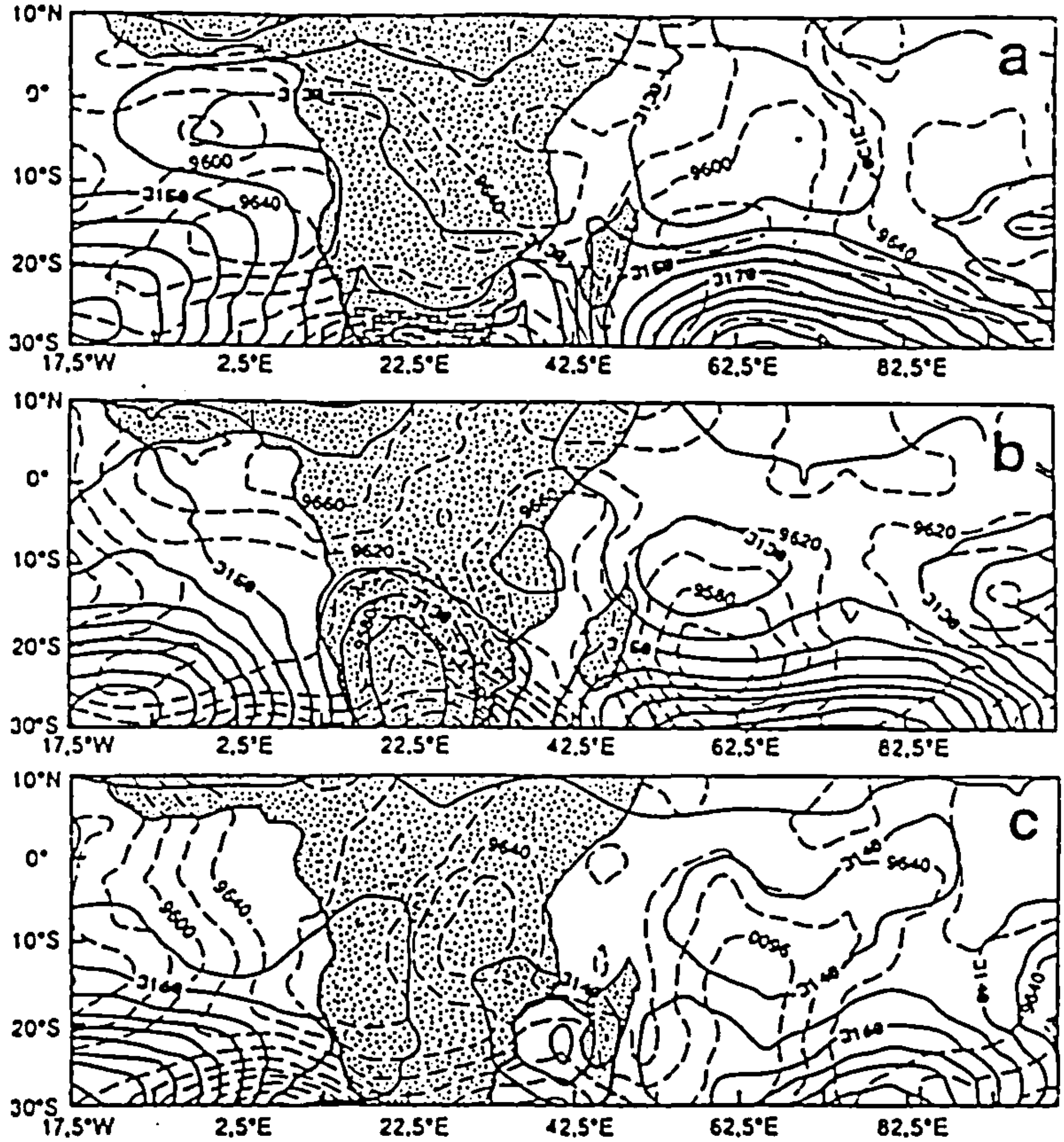

Figure 4.15: Pressure fields at 700 hPa and 300 hPa for (a) 6 January 1980, (b) 7 January 1980 and (c) 8 January 1980 (after D'Abreton, 1992). Dark lines represent the 700 hPa level and light lines the 300 hPa level.

entire tropical-temperate trough at the surface level, but that it is clearly obvious at the 700 and 300 hPa levels. The simulated easterly winds over Madagascar from around the South Indian High appear to enhance convergence in the lower levels and also contributes to the poleward flow along the southern sections of the tropical-temperate trough. At 700 hPa, the anticyclonic flow over the eastern regions of southern Africa which becomes cyclonic around the trough that has developed over the central regions (Fig. 4.13b) corresponds closely with the upper air chart at 12:00 UTC (Fig. 2.15b). The trough is also evident in the pressure fields presented by D'Abreton (Fig. 4.15b). At the 300 hPa level the modelled westward tilt and positioning of the westerly wave over southern Africa and the predominant anticyclonic circulation north of approximately 20°S over the continent (Fig. 4.14b) concur closely with upper air observations (Fig. 2.18a).

By 21:00 UTC on 7 January (Day 2), both westerly troughs and the high pressure cell have moved eastward resulting in the eastward shift of the tropical-temperate trough (Figs 4.12d, 4.13c, 4.14c). The simulated lower level streamlines show that the temperate link has broken and that the poleward flow along the cloud band is confined to the regions south of 20°S (Figs 4.12d, 4.13c). This is indicative of the start of the dissipation of the system. Associated with the dissipation, as with the wet case study, is the replacement of the lower level northerly and northeasterly winds in the region of the tropical low with easterly winds. The simulated eastward movement and southwestward tilt of the tropical-temperate trough, as well as the weakening of the temperate link, are clearly substantiated by the satellite imagery at 01:00 UTC on 8 January (Plate 2.2d).

The modelled westerly waves and the cell of high pressure have moved even further eastward by 12:00 UTC on 8 January (Day 3) (Figs 4.12e, 4.13d, 4.14d). The tropical low has intensified, but the trough which linked the westerly wave with the tropical low is no longer evident (Fig. 4.12e). The model reveals that poleward flow along the tropical-temperate trough in the lower levels is now limited to regions south of 25°S which is a further indication of the dissipation of the tropical-temperate trough system. The high pressure cell between the two cold fronts is centred at approximately 40°S and 40°E (Fig. 4.12e) and corresponds exactly with the centre on the synoptic chart (Fig. 2.15c).

It is clear that the streamlines provide an accurate representation of the synoptic circulation systems associated with the development of the dry case tropical-temperate trough. Certain minor inconsistencies exist between the SAWB data fields and the simulated airflow over the oceanic regions around Madagascar and the areas north of the southern Africa. The cause of these discrepancies is most likely due to the lack of data over these regions. A close correspondence does, however, exist between the simulated streamlines and the pressure fields interpolated by D'Abreton (1992) using the global ECMWF data set (Fig. 4.15a-c).

Pressure

All the main features of the surface pressure field are evident in the simulated mean sea level pressure fields at 15:00 UTC on 6 January (Day 1) (Fig. 4.16a). The cell of low pressure incorporated in the primary frontal system and the ridging of the high pressure cell behind this frontal system are further south in the simulated output than those on the synoptic chart (Fig. 2.15a). It is obvious from the mean sea level pressure fields at 15:00 UTC that the westerly wave and the tropical low have not yet linked. The pressure fields at the 700 (Fig. 4.17a) and 300 (Fig. 4.18a) hPa levels closely correspond with those of the upper air charts, with the exception of the high pressure cell evident in the charts at approximately 20°S. This cell is not apparent in the pressure fields presented by D'Abreton either (Fig. 4.15a).

The mean sea level pressure fields at 12:00 UTC on 7 January (Day 2) clearly reveal that the tropical-temperate trough is now fully developed (Fig. 4.16b) and extends from northern Mozambique to beyond 40°S. The simulated eastward shift of the primary westerly wave over the Mozambique Channel which enabled the formation of the tropical-temperate trough, is evident at 700 hPa (Fig. 4.17b). The presence of the weak trough over the western regions of southern Africa is substantiated by the pressure fields presented by D'Abreton (1992) (Fig. 4.15b). The position of the westerly wave over southern Africa at 300 hPa (Fig. 4.18b) closely matches that of the upper air chart (Fig. 2.15a), however, the simulated secondary wave axis appears to be further east than that in the upper air chart. By 21:00 UTC, the modelled mean sea level pressure field reveals that the tropical-temperate trough has intensified and extended southward (Fig. 4.16c). The tropical-temperate trough has reached its mature stage of

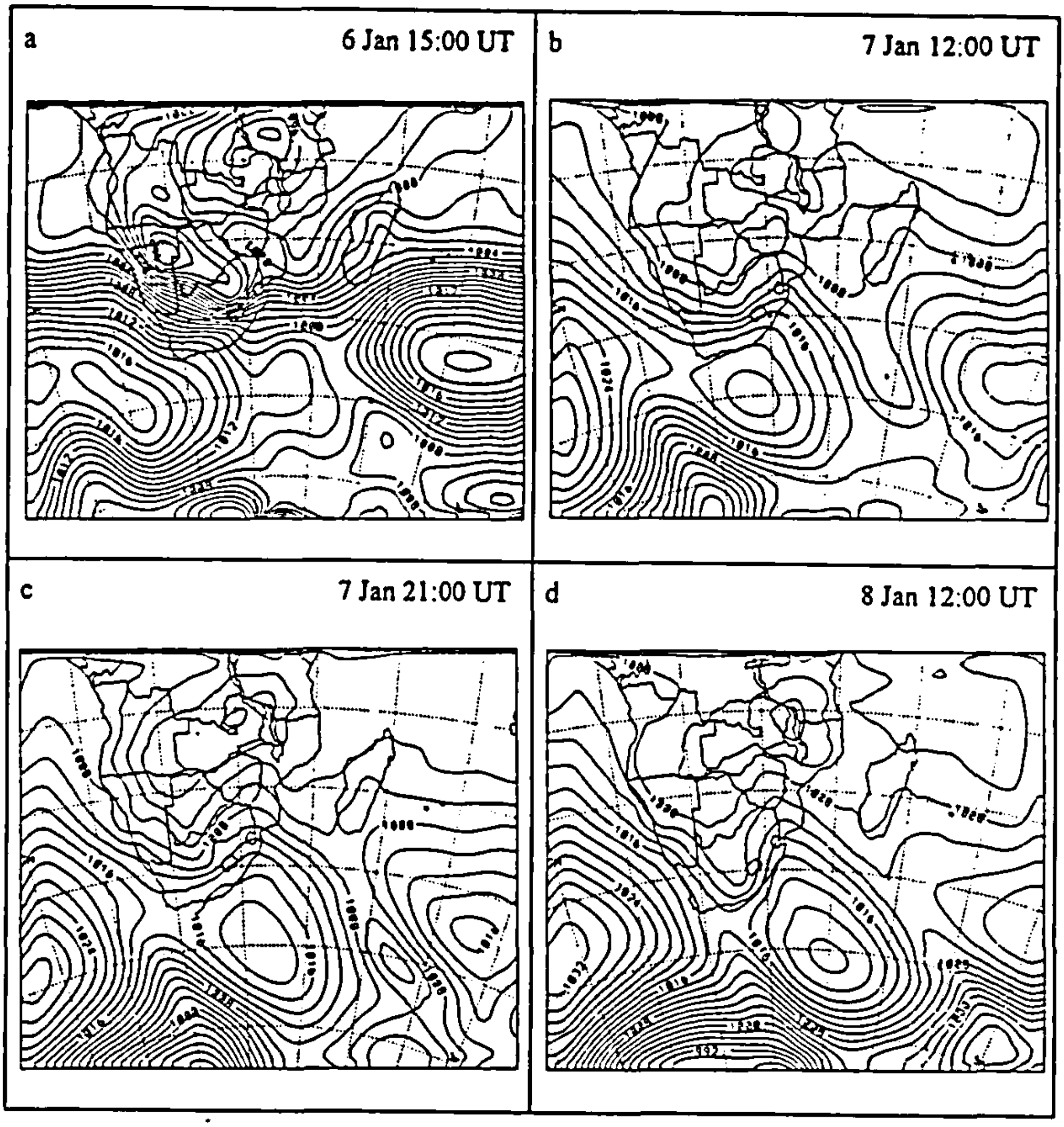

Figure 4.16: Reduced mean sea level pressure from the dry case control run at (a) 6 Jan 15:00 UT, (b) 7 Jan 12:00 UT, (c) 7 Jan 21:00 UT and (d) 8 Jan 12:00 UT (hPa; contour interval of 1 hPa for a, and 2 hPa for b-d).

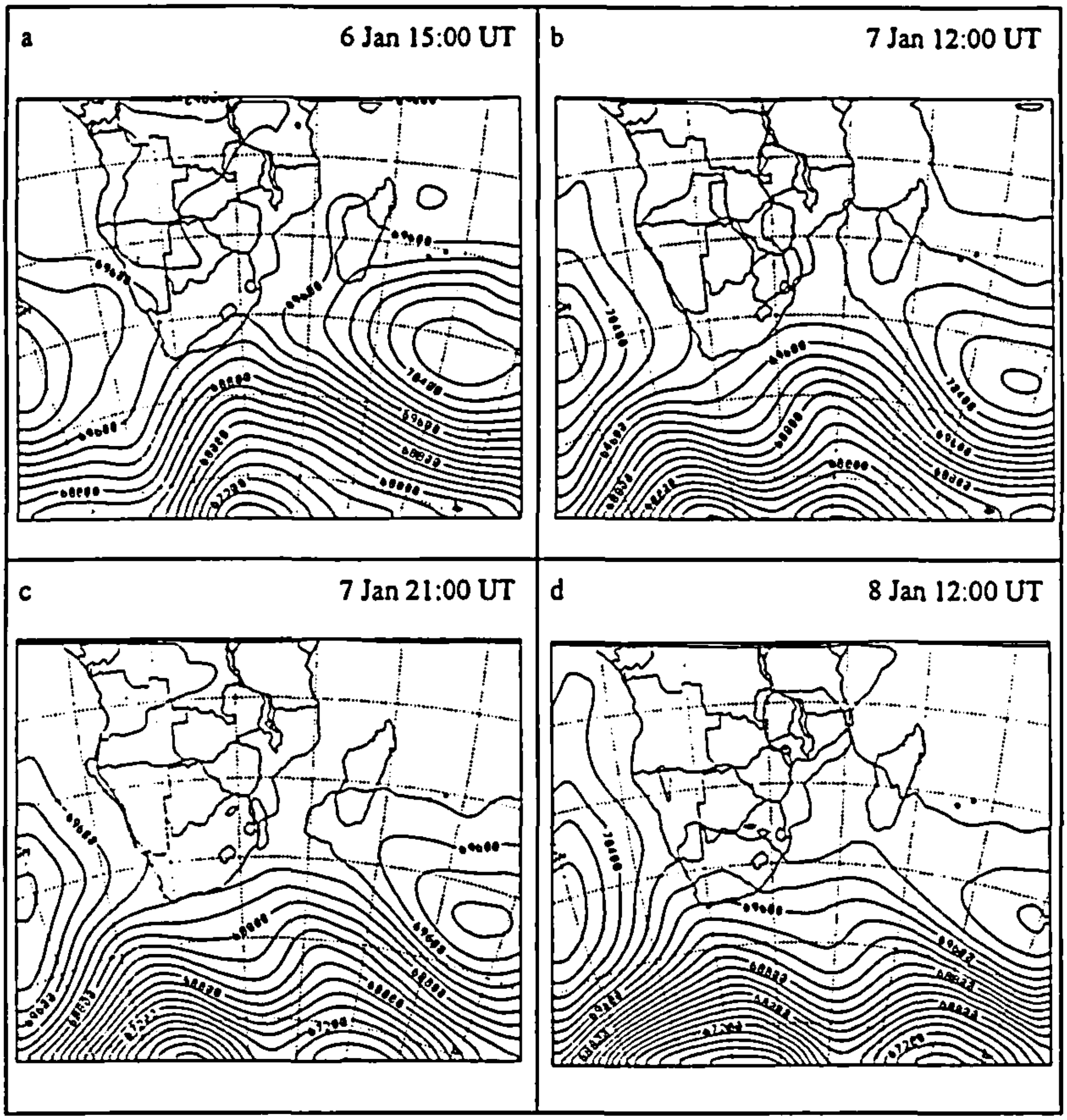

Figure 4.17: Pressure field at 3,13 km (~ 700 hPa) above sea level from the dry case control run at (a) 6 Jan 15:00 UT, (b) 7 Jan 12:00 UT, (c) 7 Jan 21:00 UT and (d) 8 Jan 12:00 UT (Pa; contour interval of 200 Pa).

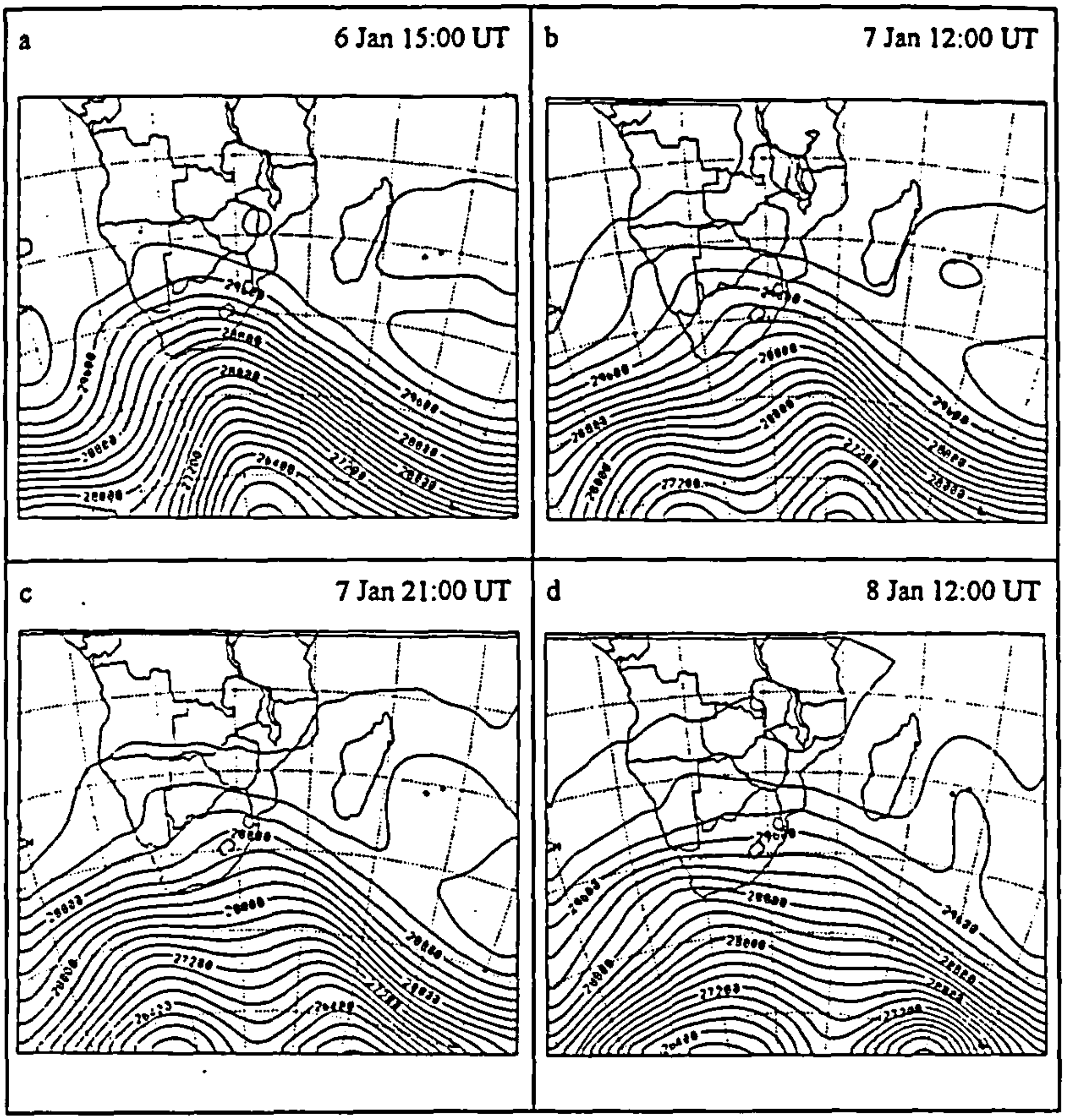

Figure 4.18: Pressure field at 9,66 km (~ 300 hPa) above sea level from the dry case control run at (a) 6 Jan 15:00 UTC, (b) 7 Jan 12:00 UTC, (c) 7 Jan 21:00 UTC and (d) 8 Jan 12:00 UTC (Pa; contour interval of 200 Pa).

development. The drop in pressure throughout the troposphere to the southeast of Madagascar as a result of the eastward movement of the westerly wave is evident at the 700 (Fig. 4.17c) and 300 hPa level (Fig. 4.18c). Dissipation of the tropical-temperate trough by 12:00 UTC the following day (8 January) is associated with an increase in pressure in the region of the trough throughout the troposphere (Figs 4.16d, 4.17d, 4.18d). The model shows that the links between the temperate and tropical regions have broken. Strengthening and eastward ridging of the high pressure cell behind the westerly wave is associated with the dissipative stage (Figs 4.16d, 4.17d).

Vertical Velocity

The vertical motion associated with the tropical low over northern Mozambique, the trough over the interior and both westerly waves are evident at the 700 hPa level at 15:00 UTC on 6 January (Day 1) (Fig. 4.19a). Subsidence over the southwestern Cape and to the south of the subcontinent are as a result of the high pressure cell to the south of the country and the ridging of this high pressure cell behind the frontal system are simulated by the model.

By 12:00 UTC the following day (7 January), the simulated vertical uplift occurs along the near fully developed tropical-temperate trough, extending from the tropical low to beyond 40°S (Fig. 4.19b). This corresponds with the satellite imagery of the cloud band (Plate 2.2c). The orographically-enhanced vertical motion over the eastern regions of South Africa has strengthened due to the advancing high pressure cell. Weakening of the temperate link in the lower tropospheric levels by 21:00 UTC indicates the onset of the tropical-temperate trough dissipation (Fig. 4.19c). The model reveals that this occurs despite the increase in vertical uplift in the region of the tropical low.

The vertical velocity along the southern sectors of the cloud band has decreased substantially by 12:00 UTC on 8 January (Day 3) in association with the tropical-temperate trough dissipation and is limited to the regions south of 30°S (Fig. 4.19d). Convection in the region of the tropical low has, however, increased. The simulated southeastward extension and

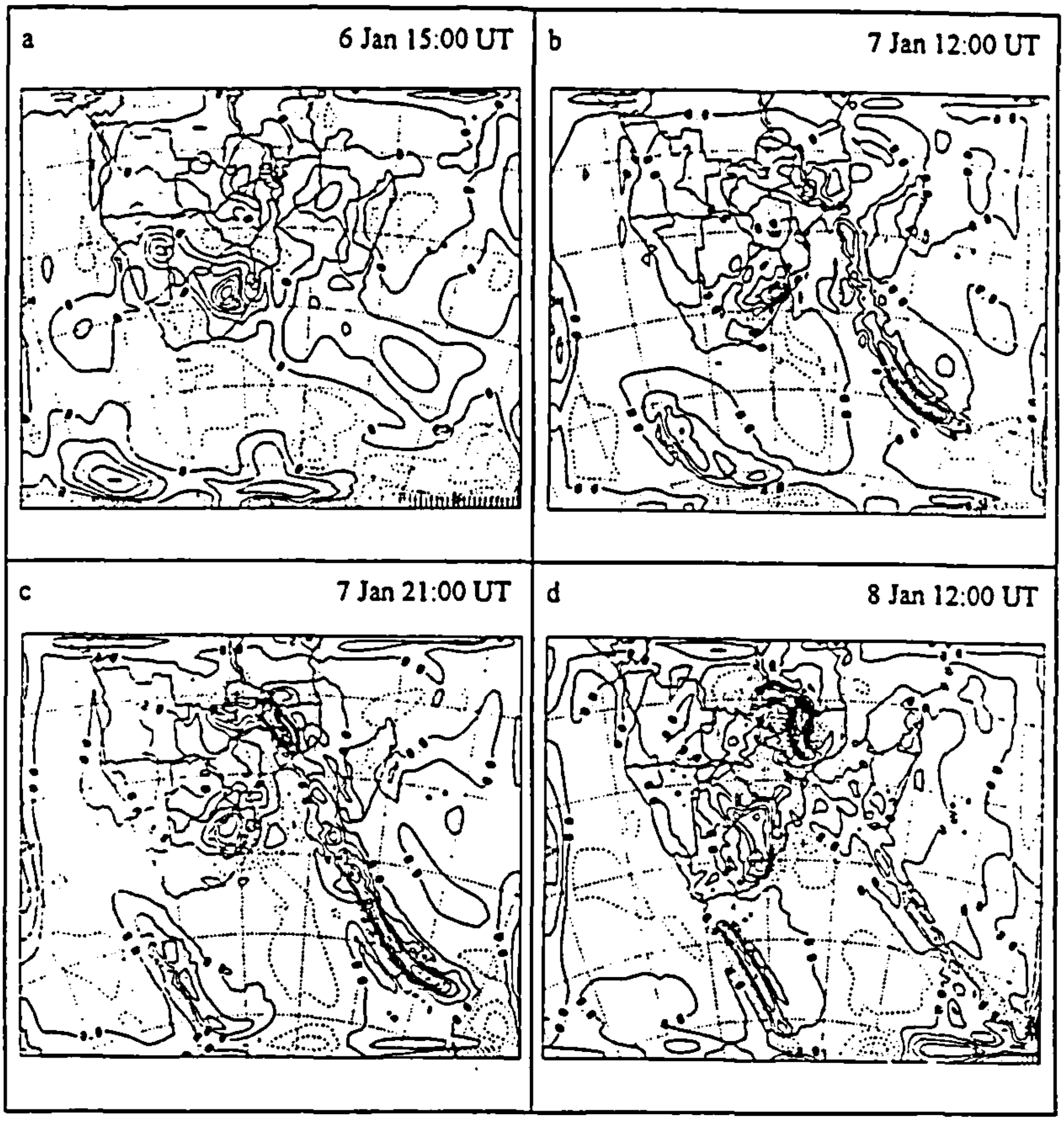

Figure 4.19: Vertical velocity field at 3,13 km (~ 700 hPa) above sea level from the dry case control run at (a) 6 Jan 15:00 UTC, (b) 7 Jan 12:00 UTC, (c) 7 Jan 21:00 UTC and (d) 8 Jan 12:00 UTC ($cm.s^{-1}$; contour interval of 0,01 $cm.s^{-1}$ for a and 0,02 $cm.s^{-1}$ for b-d; labels multiplied by 10^{-2} for b-d; solid lines indicate uplift and dashed lines indicate subsidence).

narrowing of the cloud band along the temperate sections of the tropical-temperate trough is also evident in the satellite imagery at 13:00 UTC (Plate 2.2e).

The simulated vertical velocity fields reveal that the uplift associated with tropical-temperate troughs extends into the upper tropospheric levels (Fig. 4.20a-d). Vertical velocities at the 300 hPa level closely mirror those at the 700 hPa level, although the structure of the cloud band is not as clearly obvious at the 300 hPa level as at the 700 hPa level. The importance of tropical-temperate troughs in the organisation and enhancement of convection is clearly illustrated by RAMS.

Convective Precipitation Rate

At 15:00 UTC on 6 January (Day 1), the modelled convective precipitation rate over the tropical regions of Africa (Fig. 4.21a) closely coincides with the well developed tropical cloud clusters evident in the satellite imagery (Plate 2.2a). Convective activity is also present over the eastern regions of South Africa as a result of the orographic effect on the easterly onshore flow. By 12:00 UTC the next day (7 January), convective precipitation occurs along most of the mature tropical-temperate trough from the tropical low over northern Mozambique to about 35°S (Fig. 4.21b). The temperate link with the trough and tropical low over northern Mozambique is no longer obvious in the simulated convective precipitation field at 21:00 UTC (Fig. 4.21c). The convective activity associated with the temperate section of the tropical-temperate trough has progressed further eastward and is situated over southern Madagascar. This is indicative of the eastward movement of the westerly wave which is instrumental in the dissipative process. Tropical convection is still evident over the coastal regions of central Mozambique being associated with the low pressure over the Beira region (Fig. 2.15b,c). By 12:00 UTC on 8 January (Day 3), the dissipation of the tropical-temperate trough is clearly simulated with the total absence of convective precipitation over the oceanic regions to the south of Madagascar (Fig. 4.21d). Convective activity associated with the intensified tropical low is still evident and concurs with the extensive tropical cloud cover evident in the satellite imagery over this region (Plate 2.2e).

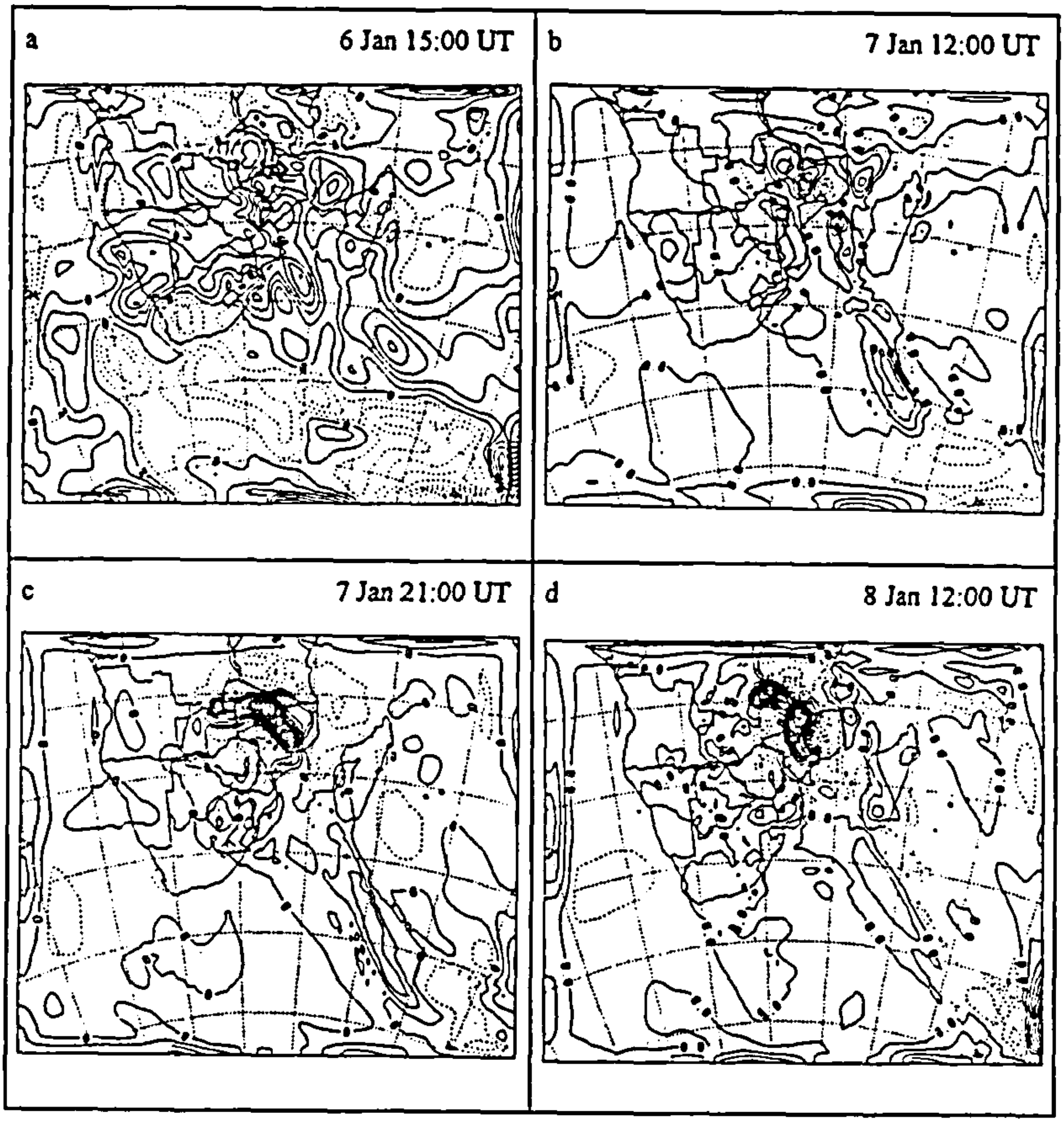

Figure 4.20: Vertical velocity field at 9,66 km (~ 300 hPa) above sea level from the dry case control run at (a) 6 Jan 15:00 UTC, (b) 7 Jan 12:00 UTC, (c) 7 Jan 21:00 UTC and (d) 8 Jan 12:00 UTC ($cm.s^{-1}$; contour interval of 0,01 $cm.s^{-1}$ for a and 0,03 $cm.s^{-1}$ for b-d; labels multiplied by 10 for a and by 10^{-2} for b-d; solid lines indicate uplift and dashed lines indicate subsidence).

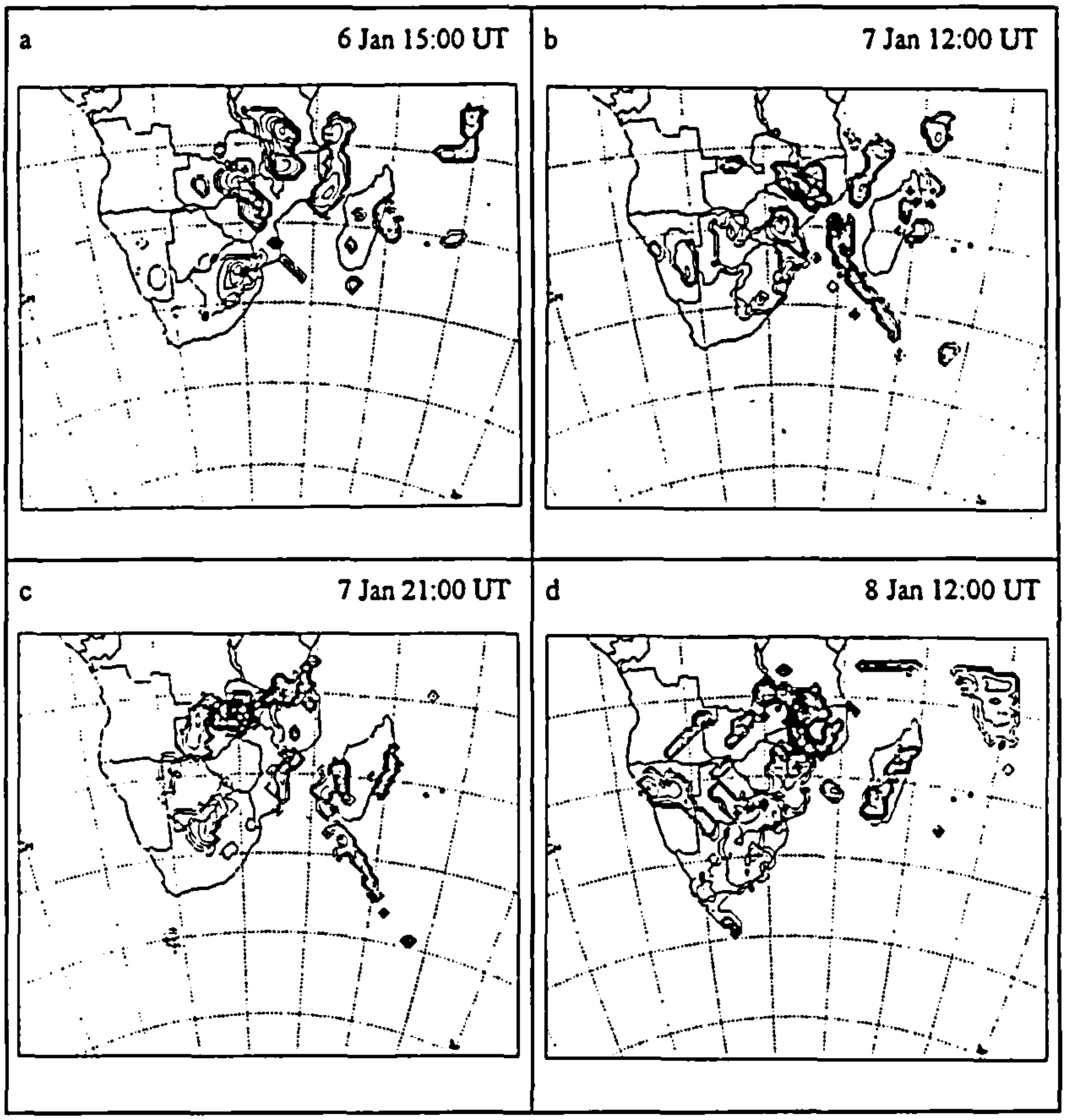

Figure 4.21: Convective parameterisation precipitation rate from the dry case control run at (a) 6 Jan 15:00 UTC, (b) 7 Jan 12:00 UTC, (c) 7 Jan 21:00 UTC and (d) 8 Jan 12:00 UTC (mm.s^{-1}; contour interval of 0,000035 mm.s^{-1}; labels multiplied by 10^7).

To determine the degree of correspondence between the observed rainfall produced by the tropical-temperate trough during the 48 hour study period and the modelled accumulated convective precipitation is particularly difficult in this case study, as most of the rainfall occurs over the ocean where no rainfall data are available. Over the southern Africa region the zone of maximum rainfall between 25° and 30°S and 25° and 30°E and the exceptionally dry western and southwestern areas do correspond closely with those in the model output. However, as with the wet case study, the simulated precipitation constitutes only about 30 per cent of the recorded rainfall total (Fig. 4.22). The importance of including the microphysics module is again emphasised. Despite the underestimation of the rainfall totals the simulated areas of convective precipitation correspond very closely with the cloud cover evident in the satellite imagery (Plate 2.1), and appear to provide an accurate representation of the convective activity associated with the tropical-temperate trough.

Discussion

It is clear that RAMS is a powerful tool with which to investigate the stages of development and the mechanisms associated with the development of tropical-temperate troughs. As the modelled streamlines, pressure, vertical velocity and convective precipitation fields provide an accurate representation of the stages of development of both the wet- and dry-case tropical-temperate troughs, the simulations described will serve as suitable control runs. These control runs may now be used with a high degree of confidence to further investigate the characteristics of the wet- and dry-year tropical-temperate troughs. A tropical low, a westerly wave and a trough connecting the tropical low and westerly wave constituted the three main components of the wet- and dry-year tropical-temperate troughs. The necessity of these three components has been previously considered (Harangozo and Harrison, 1983). It is apparent from the model output that the tropical low during the wet case is situated further south (20°S) than that of the dry case (12°S) and is positioned over the western regions of southern Africa. The dry case tropical low is situated over eastern Africa. This is supported by previous observations regarding the position of the tropical low and the resultant cloud band (Harrison,

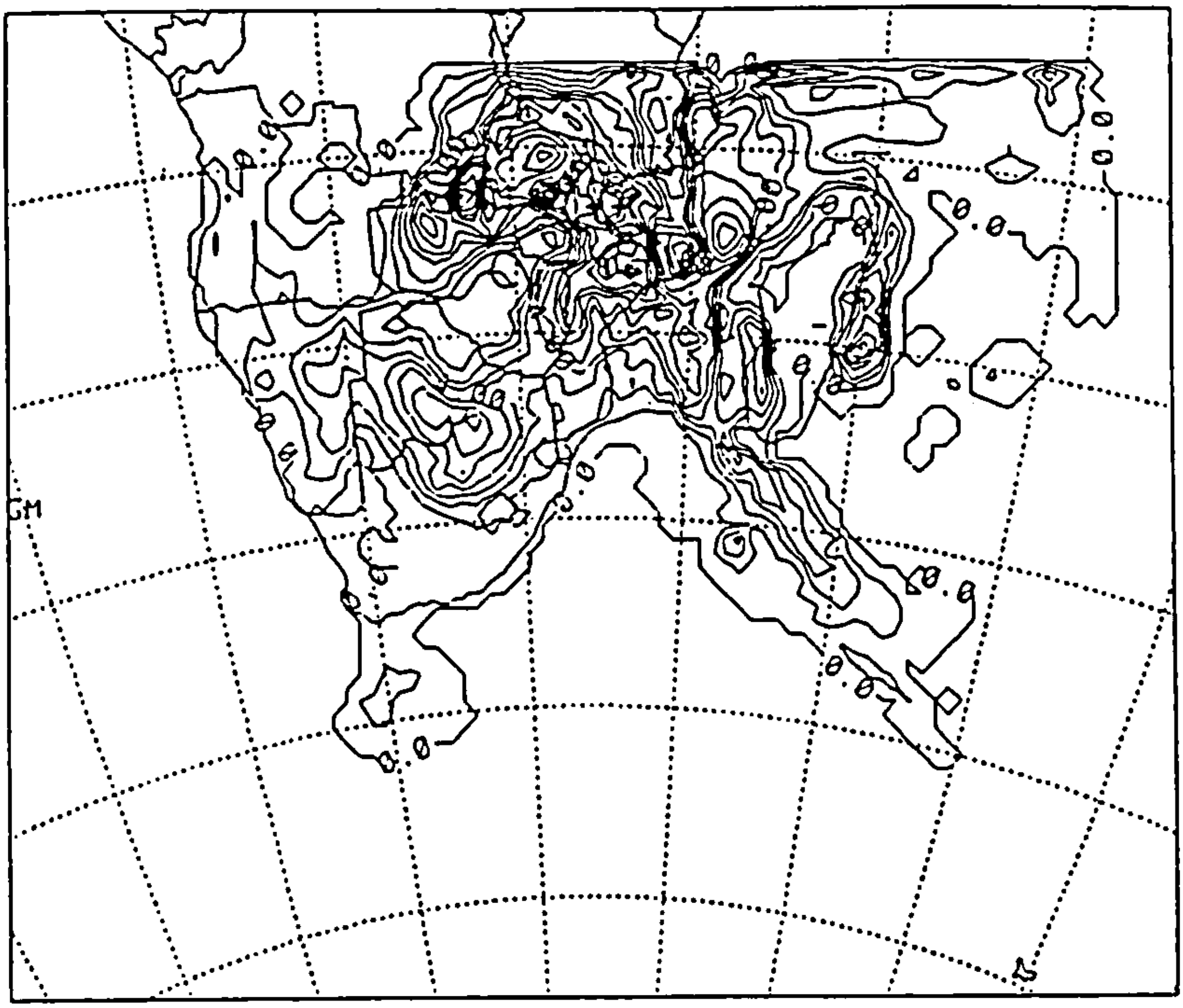

Figure 4.22: Precipitation produced by the cumulus parameterisation scheme between 6 Jan 12:00 UTC and 8 Jan 12:00 UTC from the dry case control run (mm; contour interval of 1 mm; maximum value of 13 mm).

1986a). Both tropical lows are embedded within the easterly flow which appears to enhance their development.

The model output revealed that both tropical-temperate trough systems only formed after the establishment of the tropical link between the tropical low and the connecting trough and the temperate link between the westerly wave trough and the linking trough. The trough over the western interior of southern Africa forms the connection during the wet case study, while the trough over northern Mozambique provides the link between the tropics and mid-latitudes during the dry case study. The model indicates weakening of interior troughs during the night corroborating the notion that these troughs are thermally forced (Taljaard, 1953, 1981; Harangozo, 1989). The linking trough over northern Mozambique also appears to be thermally forced.

Simulations show that the influence of the westerly wave on the development of the tropical-temperate trough is evident at all tropospheric levels in both the wet and dry case studies. In the lower levels, the alignment of the leading arm of the westerly wave with the interior trough which results in the establishment of the temperate link and the subsequent development of the tropical-temperate trough, is evident in both the mean sea level pressure fields and the streamlines. Positioning of the divergence within the leading arm of the upper level westerly wave over the regions of convergence associated with the lower level trough as a result of the westward tilt in height of the westerly wave, enhances the vertical uplift at all tropospheric levels along the tropical-temperate trough, thereby strengthening the system. This strong vertical uplift is evident throughout the troposphere in the simulated vertical velocity fields. The model shows how dissipation of the tropical-temperate trough occurs with the eastward movement of the westerly wave and eastward ridging of the South Atlantic Anticyclone according with the suggestion by D'Abreton (1992).

The development of the tropical-temperate trough results in the organisation and enhancement of poleward flow along the cloud band over southern Africa during wet seasons and over the Mozambique Channel in dry seasons over South Africa. RAMS shows that poleward flow along mature tropical-temperate troughs is a major means of transferring moisture and energy from the tropics into temperate and high latitudes and accords with the findings of Kousky *et al.* (1983), Virji and Kousky (1983), Smith (1985), Bell (1986), Harrison (1986a), Wright (1988) and Kuhnel (1989, 1990).

Recurved southwesterlies around the South Atlantic High (A in Fig. 4.23a), westerlies associated with the westerly wave (B in Fig. 4.23a), easterlies enhanced by the South Indian High (C in Fig. 4.23a), northwesterlies along the tropical-temperate trough (D in Fig. 4.23a) and northeasterlies from the eastern regions of tropical Africa (E in Fig. 4.23a) are all modelled successfully over the subcontinent for the wet case study. During the dry case study, the predominant wind flows over the subcontinent include southeasterlies around the high pressure cell to the south of the country (A in Fig. 4.23c), northwesterlies over the east coast of tropical Africa due to the presence of the tropical-temperate trough (B in Fig. 4.23c), westerlies over the southern regions of the subcontinent (C in Fig. 4.23c) and recurved South Atlantic air over the southern (D in Fig. 4.23c) and central (E in Fig. 4.23c) regions of western Africa. A comparison between the main wind flows simulated by the model and the recently hypothesised vapour fluxes over southern Africa during wet (Fig. 4.23b) and dry (Fig. 4.23d) late summers (D'Abreton and Lindesay, 1993), reveals a good correspondence between them.

The importance of the northeasterly flow into the region of the tropical low is evident in both the wet and dry case simulations. During wet conditions, northeasterlies extend across the subcontinent from the eastern regions of tropical Africa and the oceanic region to the northwest of Madagascar to the tropical low over northern Botswana, both at the surface and 700 hPa level. Enhanced northeasterly flow has been previously observed over southern Africa during wet summers (Taljaard, 1981; Miron and Lindesay, 1983; Tyson, 1986; Lindesay and Jury, 1991; D'Abreton, 1992) and in association with the development of wet-year tropical-temperate troughs (Harrison, 1986a; Lindesay and Jury, 1991; D'Abreton, 1992; D'Abreton and Lindesay, 1993). During dry conditions, the tropical low and linking trough at the surface level over northern Mozambique are fed by northeasterly winds which originate over the oceanic regions to the northwest of Madagascar. At the 700 hPa level, recurved southeasterlies from over the oceanic region to the northwest of Madagascar and westerlies from the South Atlantic Ocean blow into the tropical low. The southward extent of the

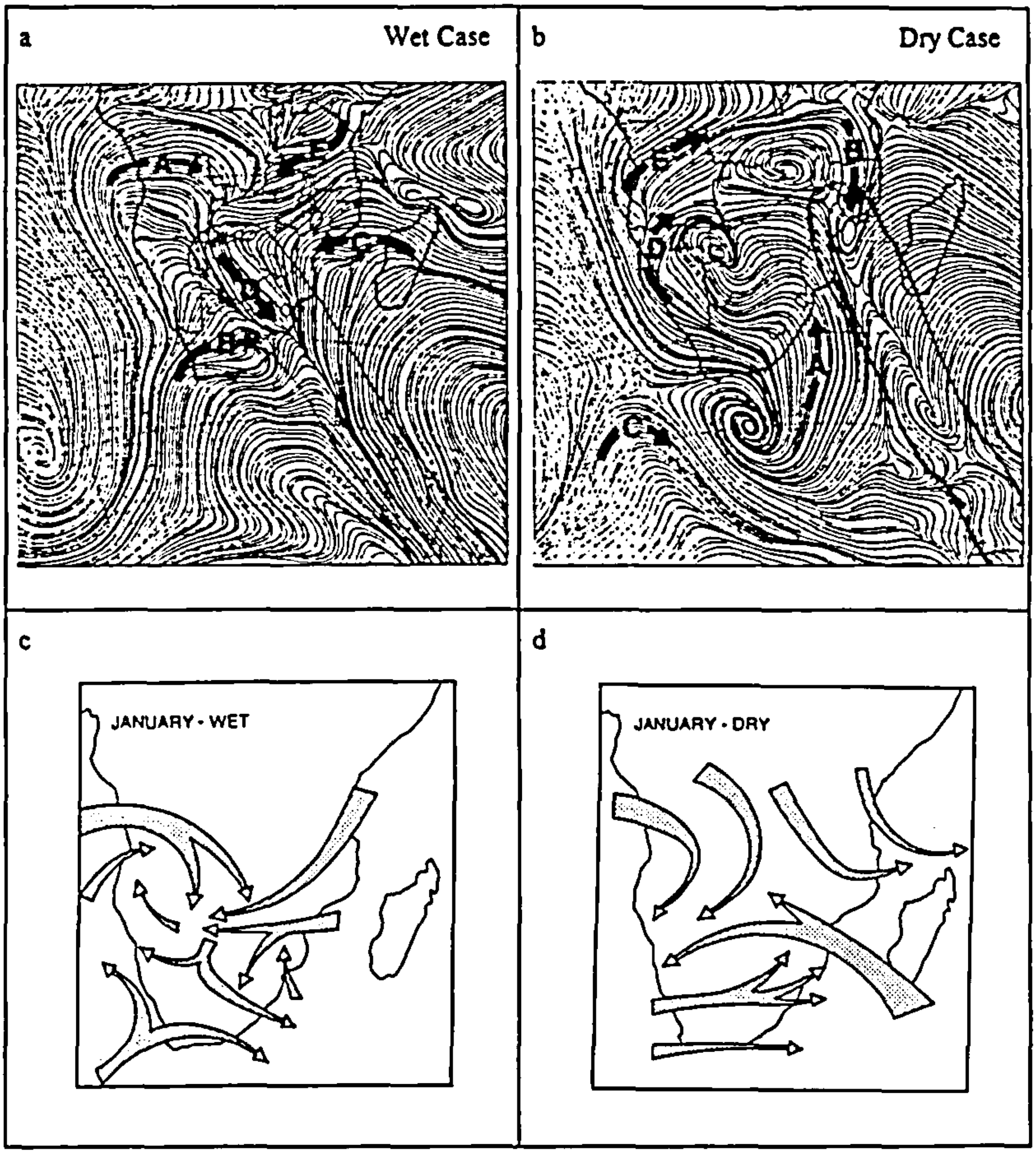

Figure 4.23: Surface streamlines (on the terrain-following coordinate surface 146,4 m above the ground) from the (a) wet case control run at 23 Jan 21:00 UTC and (b) dry case control run at 7 Jan 09:00 UTC, and a schematic representation of the main vertically integrated vapour fluxes over southern Africa during (c) wet and (d) dry Januaries (after D'Abreton and Lindesay, 1993). Shading indicates the cloud band.

northeasterlies during the dry case is far less than that of the wet case. The passage of the northeasterly air flow over the oceanic regions to the northwest of Madagascar supports the suggestion that this oceanic region is an important source of the water vapour flux over South Africa during wet and dry late summers (D'Abreton and Tyson, 1994). It is evident from the model output that dissipation of the tropical-temperate trough is associated with a breakdown in the northeasterly flow in both wet and dry conditions. During the dissipation of the wet-year tropical-temperate trough, the lower level northeasterlies were replaced by westerlies. At the 700 hPa level the northeasterly flow broke down into cells of cyclonic circulation. Easterly to southeasterly flow over Madagascar replaced the lower level northeasterlies into northern Mozambique during the dry case simulation. Whether the breakdown in the northeasterly flow is a causative or resultant factor of the dissipation process remains to be determined.

It appears from the simulated output that easterly to northeasterly winds around the South Indian High contribute to the poleward flow along the southern regions of the tropical-temperate trough in both cases, although their influence appears to be greater during the dry case study when the South Indian High is situated further eastward. During the wet case study, the South Indian High is situated closer to the subcontinent and enhances the easterly flow at 700 hPa over the Mozambique Channel and the southern Africa interior during the initial and mature phases of the tropical-temperate trough development. During the dry case study, the eastward shift of the South Indian High reduces its influence on the subcontinent. A similar shift of the South Indian High between wet and dry periods has been previously observed (D'Abreton, 1992).

The position of the trailing arm of the upper level westerly wave over the subcontinent during the dry case is evident in both the simulated streamlines and pressure fields. The associated subsidence results in the dry conditions occurring over most of southern Africa. During the wet case, the trailing arm of the westerly wave is over the western interior and South Atlantic Ocean resulting in the dry conditions over the southwestern Cape. This shift in the position of the westerly waves between wet and dry periods is attributed to phase changes of the Southern Oscillation (Lindesay, 1988a) and to the movement of the upper tropospheric Atlantic wave (Harrison, 1986a).

The model control runs for the wet and dry case studies have proved to be accurate representations of the tropical-temperate troughs that formed during 22 and 24 January 1981, and 6 to 8 January 1980. RAMS is therefore an eminently suitable model for the investigation of mesoscale systems over southern Africa. In establishing suitable control runs for the wet and dry case study, the control run for the wet case study was determined first. The same model setup was then used for the dry case study. The successful model output adds credibility to the forecasting potential of RAMS, in that the development of the tropical-temperate trough was well simulated without any further adjustment to the parameter settings being necessary. Also, in determining how accurately the model simulates observed conditions, the output from the control runs has supported numerous hypotheses regarding tropical-temperate troughs which previously have been difficult to substantiate due to the scarcity and coarse resolution of the data over the African subcontinent and adjacent oceanic regions. As both control runs appear to be suitable, the structure, stages of development and the kinematic, thermodynamic and moisture characteristics of tropical-temperate troughs can be further investigated using the control run output.

Synopsis

The control runs established using the model setup described in Chapter 3 appear to be accurate representations of the tropical-temperate trough development during the wet and dry case studies. RAMS has been established as a most suitable research tool for the investigation of cloud band systems over southern Africa. As the model setup that was used for the wet case study was also utilised for the dry case study without any further parameter modifications being necessary, the strength of RAMS as a potential forecasting tool is enhanced. Investigation into the control runs also resulted in the substantiation of numerous previous hypotheses and revealed some new characteristics regarding the structure, development and dissipation of tropical-temperate troughs over the southern African region.

CHAPTER 5

SIMULATED KINEMATIC, MOISTURE AND THERMODYNAMIC CHARACTERISTICS OF TROPICAL-TEMPERATE TROUGHS

Introduction

The eastward shift of tropical-temperate troughs from over the southern African subcontinent during wet summers, to over the Mozambique Channel and Madagascar during dry summers, has been attributed to the Southern Oscillation and the associated Walker Circulation (Harrison, 1986a; Lindesay, 1988a; D'Abreton, 1992). Convection caused by the ascending arm of the Walker cell situated over the central regions of southern Africa during wet late summers, results in an enhanced Hadley circulation over the entire subcontinent west of about 30°E. Associated with the strengthened Hadley circulation is an increase in the frequency of tropical-temperate trough formation which appear to facilitate the transferral of momentum and energy poleward. This is important in the maintenance of the Hadley circulation (Riehl, 1979; Webster, 1983; Harrison, 1986a; Lindesay, 1993). The Hadley circulation has also been found to be significantly stronger during cloud-band days over the North Pacific Ocean than during the five day periods preceding these events. However, strengthening of the Hadley circulation has also been observed on non-cloud band days (McGuirk *et al.*, 1987; Kuhnel, 1990). A relationship between the winter cloud bands over Australia and the Hadley circulation has also been found (Kuhnel, 1990). With the westward shift of the convection associated with the Walker cell during dry late summers and the resultant Ferrel circulation over the central regions of southern Africa, tropical-temperate troughs form more frequently to the east of the subcontinent (Harrison, 1986a; Lindesay, 1988a). Associated with the Walker and Hadley circulation shifts and the concomitant cloud band movements, are changes in the direction and magnitude of the water vapour fluxes over southern Africa (D'Abreton and Lindesay, 1993, D'Abreton and Tyson, 1994). The apparent facilitation of the poleward transport of tropical air by tropical-temperate troughs has also been found to cause a change in the temperature structure of the atmosphere (Lindesay and Jury, 1991).

The investigation into the effects of the Walker and Hadley circulations on tropical-temperate troughs and the resultant wind, temperature and moisture changes over southern Africa, has been hampered by the lack of data over the subcontinent. Recent research using the ECMWF global data set (D'Abreton, 1992; D'Abreton and Lindesay, 1993; D'Abreton, 1994) has revealed that the Walker circulation appears to be more complex than previously thought and that the sources and fluxes of water vapour over southern Africa differ from those previously regarded as important. These hypotheses require further investigation and substantiation using more spatially comprehensive data sets (D'Abreton and Lindesay, 1993). This is possible given the resolution of the control runs simulated using RAMS. Modelled kinematic, moisture and thermodynamic characteristics of the tropical-temperate troughs will be used to asses the formation and dissipation of these systems during the wet and dry conditions.

Kinematic Characteristics

The influence of the Walker circulation on the synoptic circulation associated with cloud bands has been investigated by Harrison (1986a). Zonal and meridional circulation changes over southern Africa during the high and low phases of the Southern Oscillation have been extensively studied by Lindesay (1988a). In general, the high phase has been found to be associated with an increase in the poleward flow and a strengthening of the easterly zonal flow over southern Africa, whereas enhanced equatorward flow and a stronger westerly wind component are predominant during the low phase. In recent work by D'Abreton (1992), a more complex Walker circulation has been suggested, in which the region of convection during the high phase extends from 10°E to 30°E and covers a larger area than previously thought. During the low phase the convection is centred over 10°E. The Hadley and Ferrel circulations suggested by Harrison (1986a), Lindesay (1988a) and D'Abreton (1992) generally concur. However, differences do exist in the zonal flow associated with the more complex system of Walker cells.

Simulated Zonal Flow Patterns

The Wet Case

It is evident from the simulated zonal flow at 700 hPa that the tropical low associated with the initial stages of the development of the tropical-temperate trough was embedded in easterly winds (Fig. 5.1a). The easterly flow, which enhances the formation of the tropical lows (Harrison, 1986a), transported heat and moisture to northern Namibia. Predominant westerly flow occurred to the south of the subcontinent due to the westerly wind belt and the approaching westerly wave. Before the development of the mature tropical-temperate trough on 23 January (Day 2), the weakening easterly flow over northern Namibia reversed to westerly (Fig. 5.1b). Thereafter, a westerly zonal component is evident over northern Namibia and the western regions of tropical Africa throughout the period. By contrast, the modelled easterly flow predominated at the 700 hPa level over the eastern and central regions of tropical Africa until approximately 21:00 UTC on 23 January (Day 2), and continued to supply the extreme northern section of the tropical-temperate trough with tropical heat and moisture (Fig. 5.1c). A weakening in the easterly zonal flow accompanied the dissipation of the tropical-temperate trough and regions of westerly flow are evident over eastern tropical Africa by 24 January (Day 3) (Fig. 5.1d). The flow along the tropical-temperate trough was predominantly westerly throughout the troposphere as the westerly wave trough, which constituted the temperate section of the tropical-temperate trough, crossed the subcontinent (Figs 5.1a-d, 5.2a-d). This flow was strongest toward the end of the period when the wave amplitude was greatest and the trough narrowest. The easterly zonal wind component associated with the ridging of the South Atlantic High behind the cold front is clearly simulated at all tropospheric levels. In the upper troposphere, a distinct band of easterlies prevailed north of about 20°S throughout the period (Fig. 5.2a-d). To the south of 20°S, westerlies dominated.

The Dry Case

The tropical low that formed the northern extension of the tropical-temperate trough was embedded in the easterly flow that extended from Madagascar over Mozambique and Zimbabwe by the morning of 7 January (Day 2) (Fig. 5.3a-d). This low transported tropical

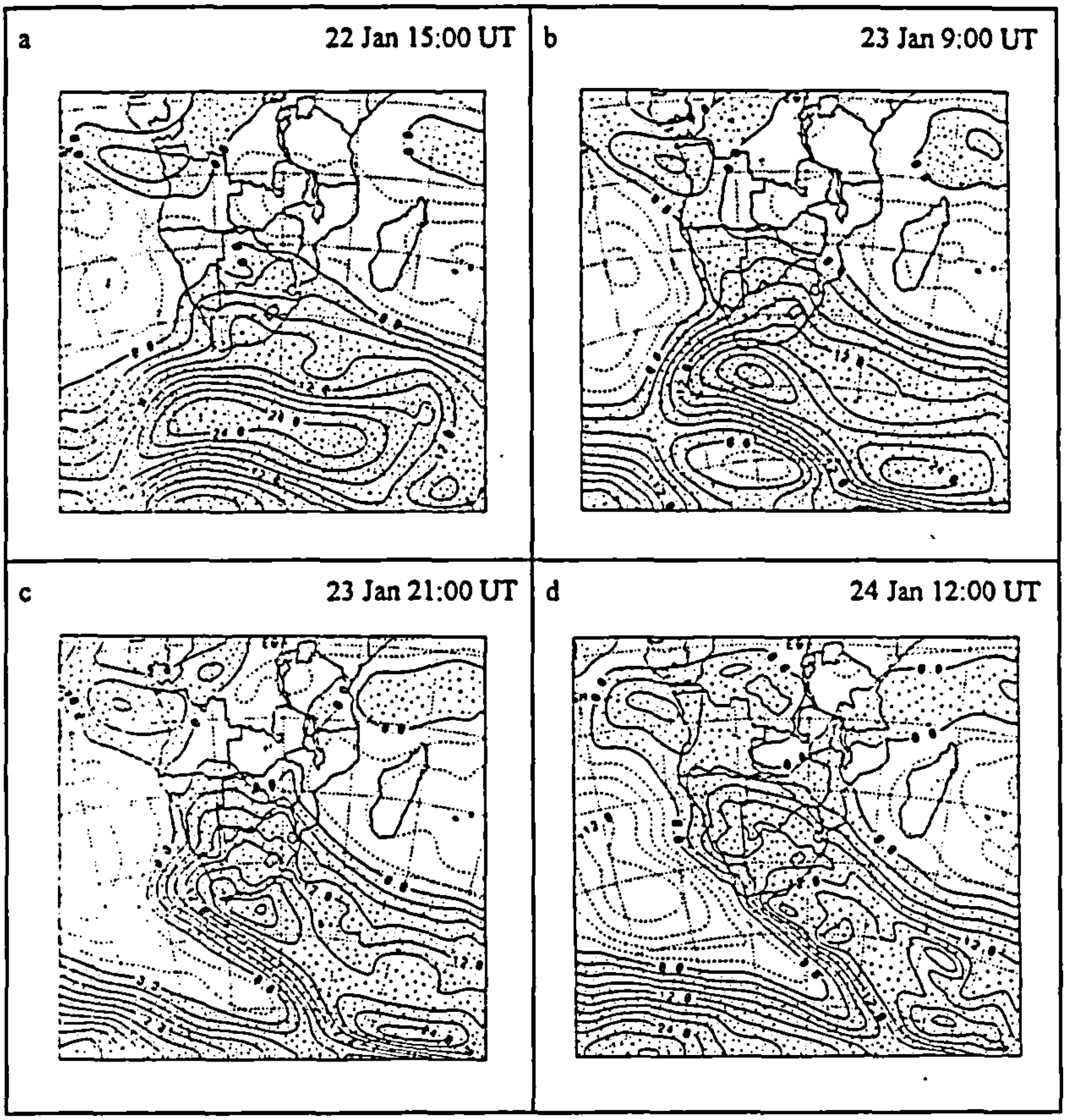

Figure 5.1: Zonal wind component field at 3,13 km (~ 700 hPa) above sea level from the wet case control run at (a) 22 Jan 15:00 UTC, (b) 23 Jan 9:00 UTC, (c) 23 Jan 21:00 UTC and (d) 24 Jan 12:00 UTC ($m.s^{-1}$; contour interval of 3 $m.s^{-1}$; solid lines indicate westerly components and dashed lines easterly components; westerly components are shaded).

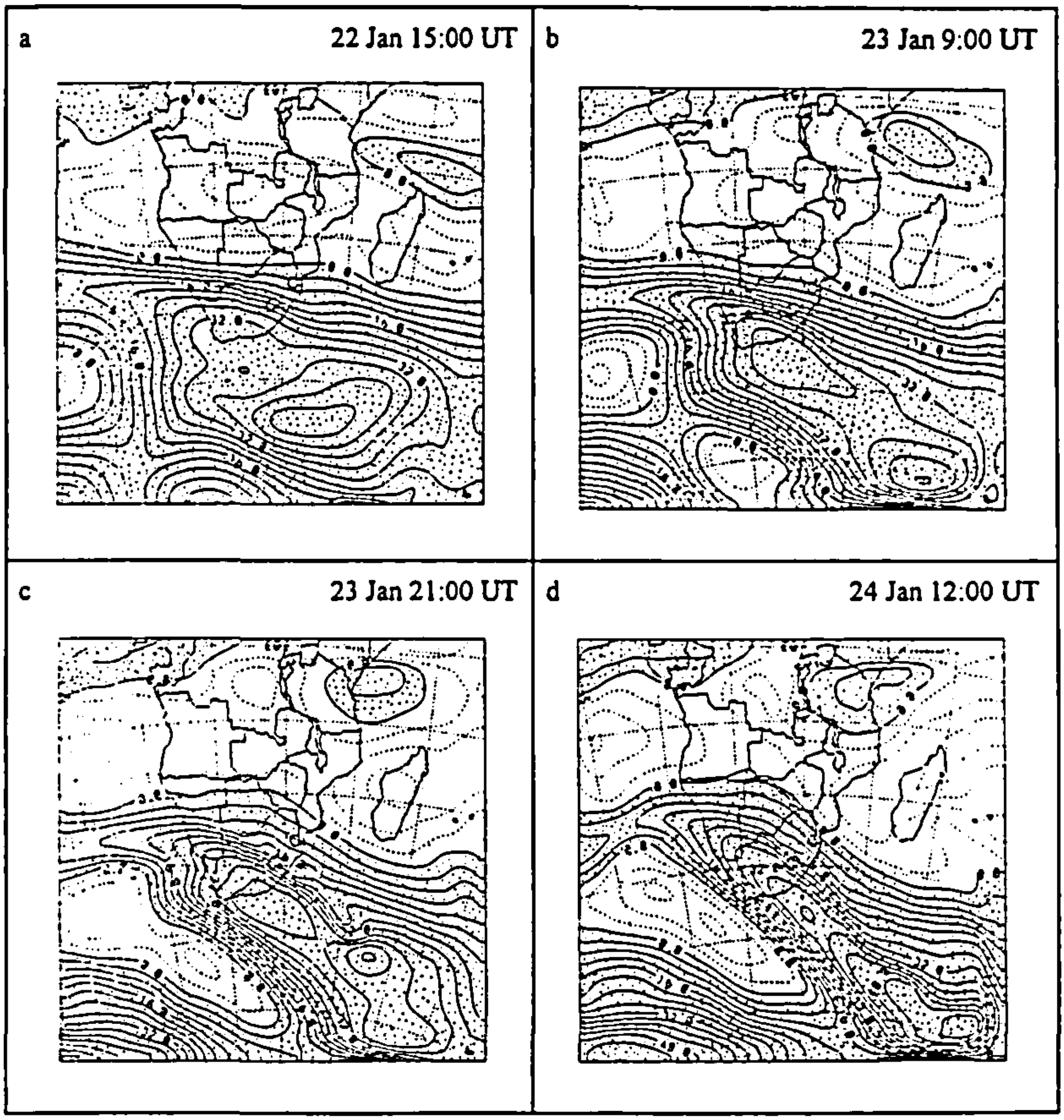

Figure 5.2: Zonal wind component field at 9,66 km (~ 300 hPa) above sea level from the wet case control run at (a) 22 Jan 15:00 UTC, (b) 23 Jan 9:00 UTC, (c) 23 Jan 21:00 UTC and (d) 24 Jan 12:00 UTC ($m.s^{-1}$; contour interval of 4 $m.s^{-1}$; solid lines indicate westerly components and dashed lines easterly components; westerly components are shaded).

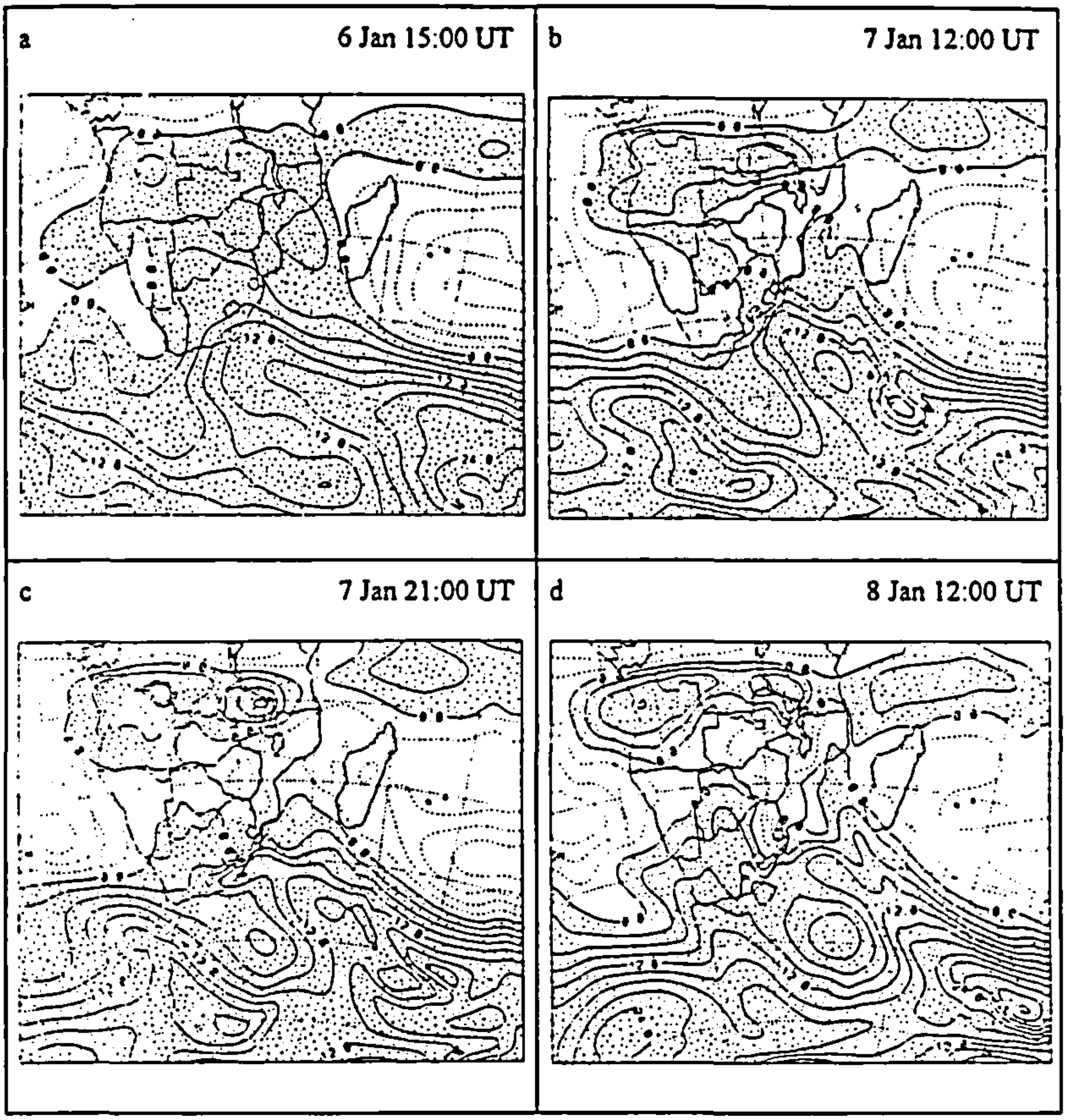

Figure 5.3: Zonal wind component field at 3,13 km (~ 700 hPa) above sea level from the dry case control run at (a) 6 Jan 15:00 UTC, (b) 7 Jan 12:00 UTC, (c) 7 Jan 21:00 UTC and (d) 8 Jan 12:00 UTC (m.s^{-1}; contour interval of 3 m.s^{-1}; solid lines indicate westerly components and dashed lines easterly components; westerly components are shaded).

moisture to the northern regions of the tropical-temperate trough. The eastward movement and alignment of the westerly wave with the tropical low which resulted in the establishment of the temperate link and the mature tropical-temperate trough on 7 January (Day 2), are evident in the modelled zonal flow in the lower levels (Fig. 5.3b,c). The westerly wave in the upper levels was positioned to the west of the lower level wave which encouraged the development of the cloud band by enhancing the baroclinicity (Fig. 5.4b,c). Dissipation of the tropical-temperate trough followed the breaking of the temperate link with the eastward movement of the westerly wave on 8 January (Day 3). This movement of the westerly wave and the weakening of the westerlies in the region of the cloud band are obvious throughout the troposphere (Figs 5.3d, 5.4d).

The model shows that, in general, the zonal circulation associated with the development of the tropical-temperate troughs was westerly throughout the troposphere in the mid-latitudes during wet and dry conditions. Over the tropical regions, the upper level flow was easterly during wet conditions. Both westerlies and easterlies occurred during dry conditions, but the westerly flow appears to have been dominant. Low-level easterly flow was predominant over the eastern and central regions of tropical Africa during the initial and mature stages of the wet case tropical-temperate trough formation, but became predominantly westerly over these regions during and after the dissipation of the tropical-temperate trough. During the dry case, the low-level tropical zonal flow was predominantly westerly. The constant zone of westerly flow over the western regions of tropical Africa during both the wet and dry conditions needs to be examined further.

Simulated Meridional Flow Patterns

The Wet Case

Poleward flow transporting energy and moisture from the tropics southwestward to northern Namibia and then southeastward into the mid-latitudes along the cloud band is evident throughout the period in the region of the tropical-temperate trough (Figs 5.5a-d, 5.6a-d). The poleward flow from the north of about 20°S was weak throughout the period. During the initial stages of development, the lower-level poleward flow over southern Africa in the region

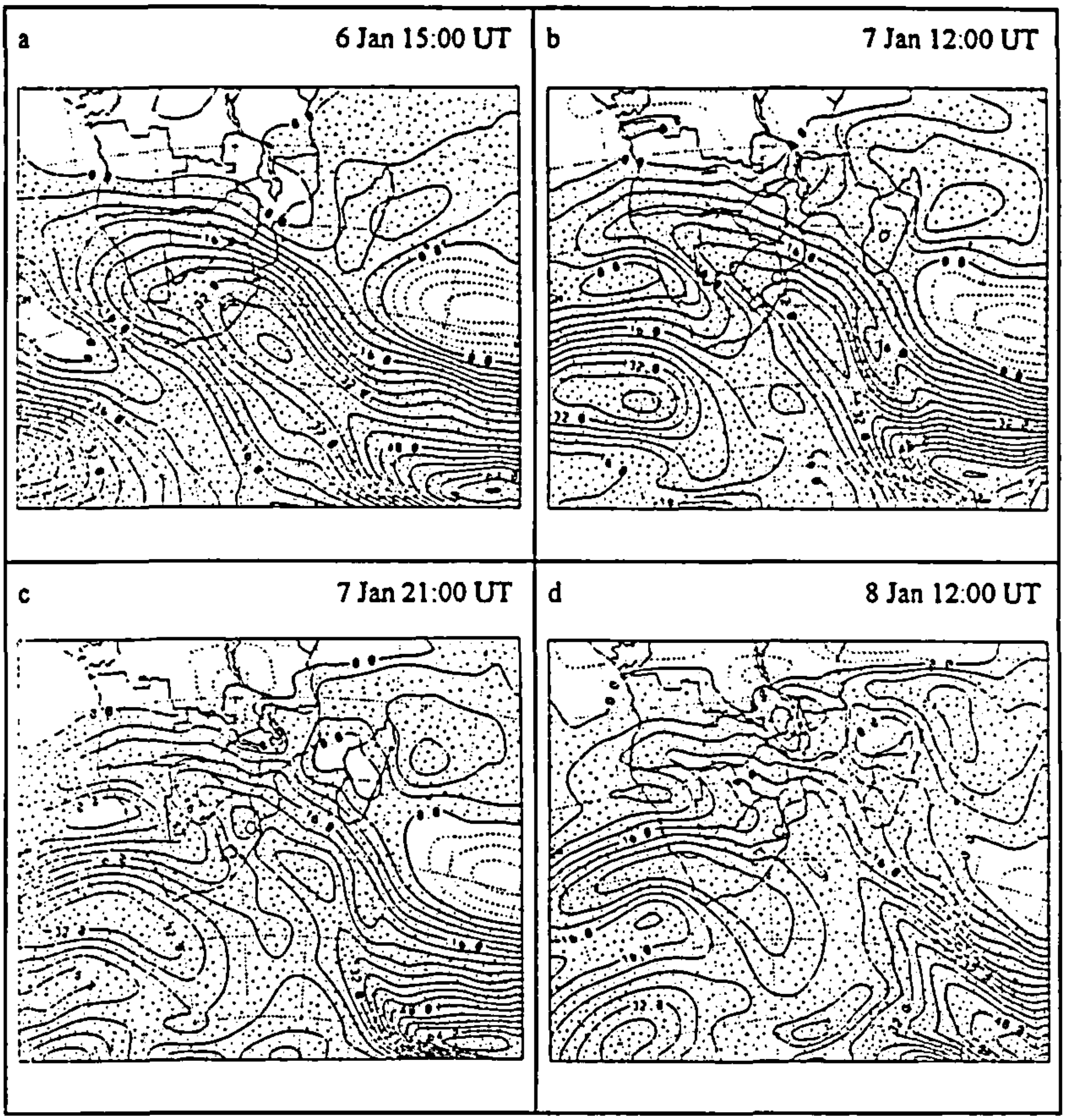

Figure 5.4: Zonal wind component field at 9,66 km (~ 300 hPa) above sea level from the dry case control run at (a) 6 Jan 15:00 UTC, (b) 7 Jan 12:00 UTC, (c) 7 Jan 21:00 UTC and (d) 8 Jan 12:00 UTC ($m.s^{-1}$; contour interval of 4 $m.s^{-1}$; solid lines indicate westerly components and dashed lines easterly components; westerly components are shaded).

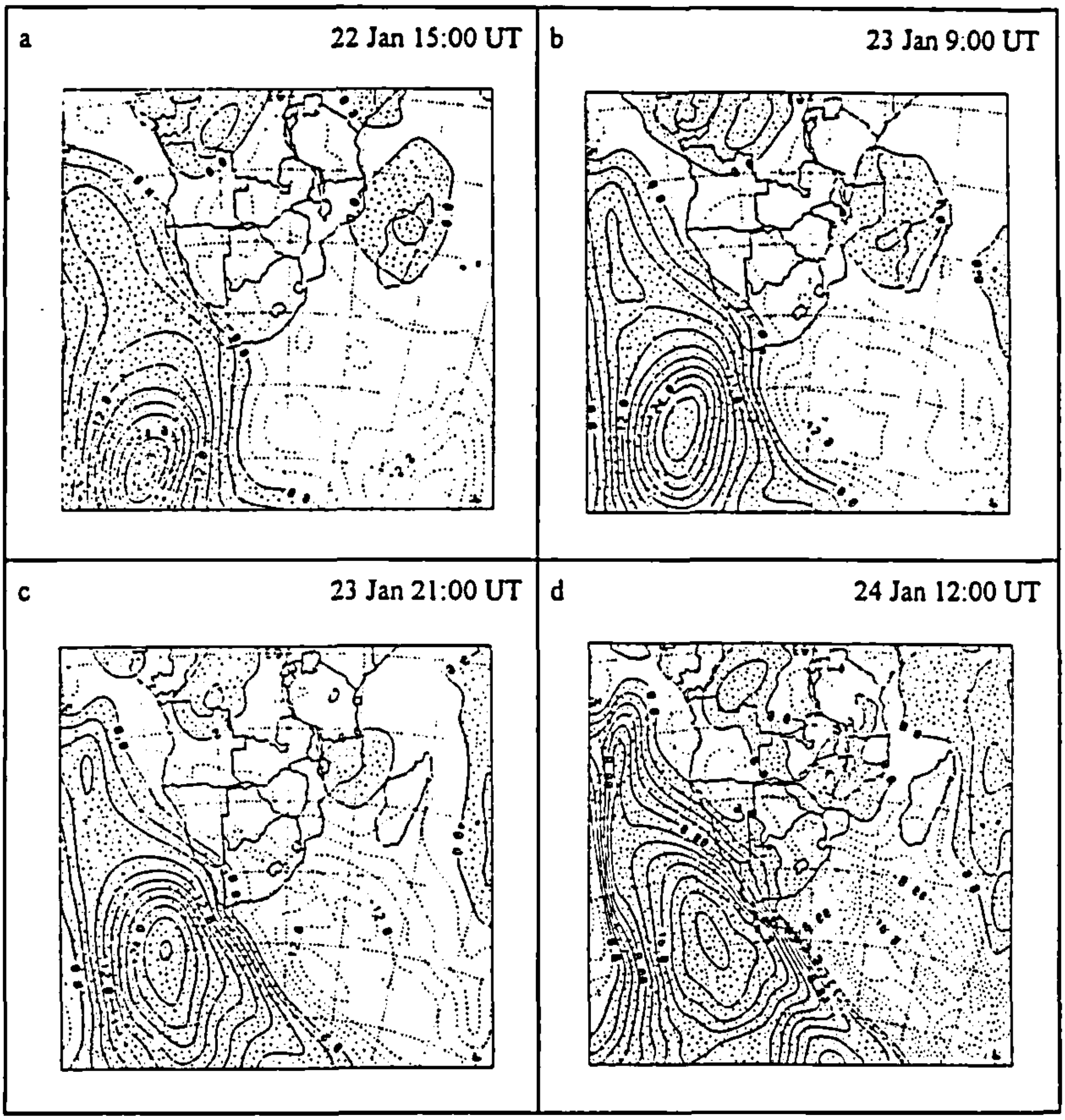

Figure 5.5: Meridional wind component field at 3,13 km (~ 700 hPa) above sea level from the wet case control run at (a) 22 Jan 15:00 UTC, (b) 23 Jan 9:00 UTC, (c) 23 Jan 21:00 UTC and (d) 24 Jan 12:00 UT ($m.s^{-1}$; contour interval of 3 $m.s^{-1}$ for a-c, 2 $m.s^{-1}$ for d; solid lines indicate southerly components and dashed lines northerly components; southerly components are shaded).

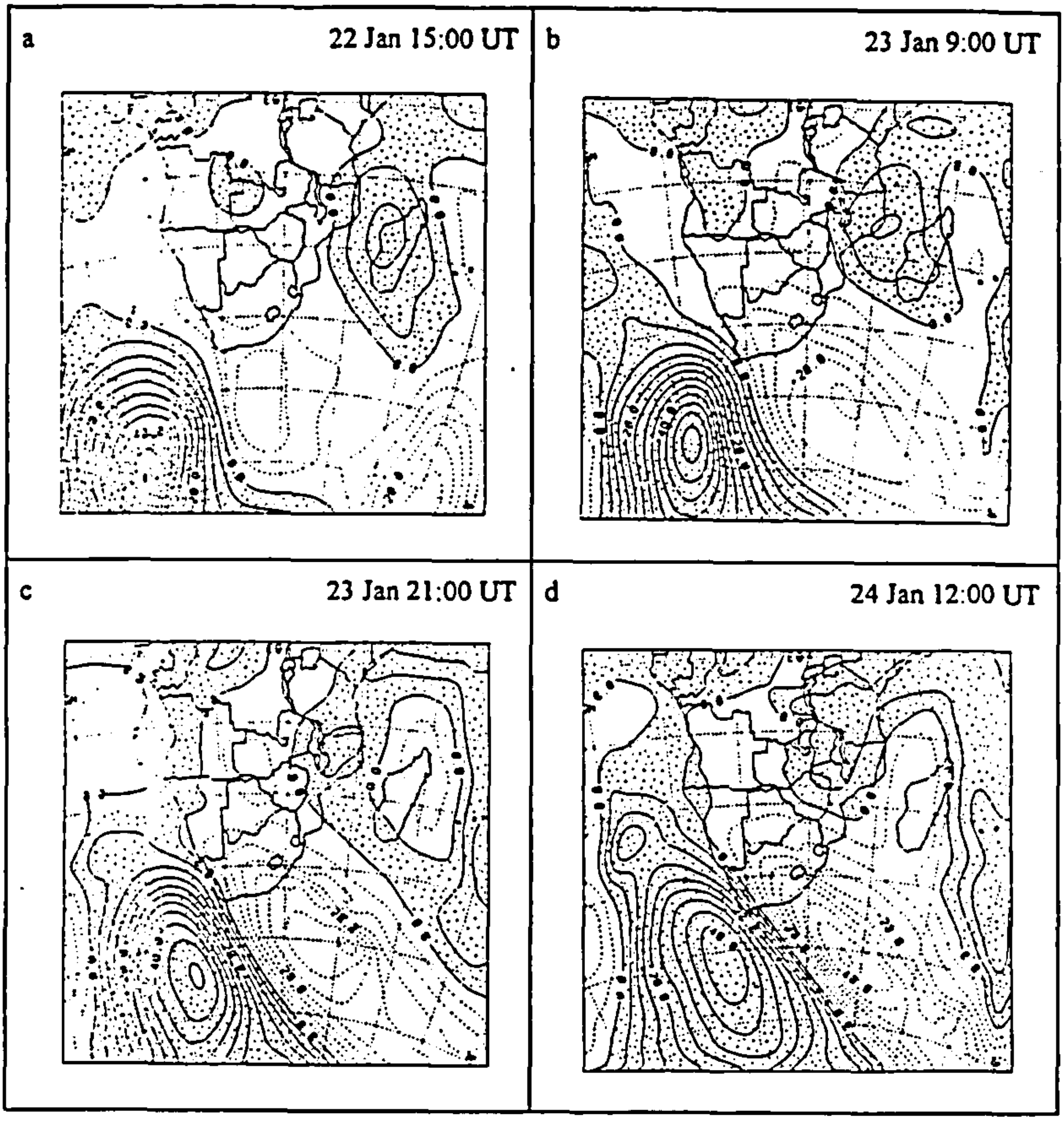

Figure 5.6: Meridional wind component field at 9,66 km (~ 300 hPa) above sea level from the wet case control run at (a) 22 Jan 15:00 UTC, (b) 23 Jan 09:00 UTC, (c) 23 Jan 21:00 UTC and (d) 24 Jan 12:00 UTC ($m.s^{-1}$; contour interval of 5 $m.s^{-1}$; solid lines indicate southerly components and dashed lines northerly components; southerly components are shaded).

of the tropical-temperate trough was weak (3 $m.s^{-1}$) (Figs 5.5a, 5.6a). Following the link with the westerly wave and the development of the mature cloud band by 21:00 UTC on 23 January (Day 2), the poleward flow over the interior strengthened (6 $m.s^{-1}$) (Fig. 5.5c). The southward flow was restricted to the eastern regions of the interior and had decreased by 12:00 UTC the following day (24 January) as a result of the tropical-temperate trough dissipation caused by the eastward movement of the westerly wave (Fig. 5.5d). The supply of air from the tropics ceased following the dissipative process (Fig. 5.5d). The strengthened poleward flow during the mature stages of the cloud band, followed by a weakening of the flow during dissipation is indicative of the need of the temperate connection with the westerly wave to enhance the poleward transport of tropical air over southern Africa by kinematic divergence. To the west and southwest of the subcontinent, the northward flow is enhanced by the circulation around the South Atlantic Anticyclone and the northerly flow in the trailing arm of the westerly wave (Figs 5.5a-d, 5.6a-d). This becomes diagonally aligned with the westerly tilt of the westerly wave toward the end of the simulation.

The Dry Case

The simulated meridional flow component during the initial stages of the cloud band development (6 January) was poleward over most of tropical Africa and over the South Indian Ocean (Fig. 5.7a). By 12:00 UTC on 7 January (Day 2), the low-level southward flow along the westerly wave had increased substantially and transported tropical air from northern Mozambique to the mid-latitudes along the cloud band (Fig. 5.7b). Poleward flow in the region of the tropical low had increased significantly by 21:00 UTC (Fig. 5.7d), possibly due to the kinematic divergence in the temperate section of the tropical-temperate trough which would enhance such flow. The zone of maximum poleward flow had also shifted further southeast, resulting in the start of the dissipative process. By the morning of 8 January (Day 3), the breakdown in the poleward flow associated with the dissipation of the tropical-temperate trough, caused by the southeastward shift of the westerly wave and the subsequent break in the temperate link, is clearly obvious in the meridional flow fields (Fig. 5.7d). The positioning of the upper-tropospheric westerly wave to the west of the wave in the lower levels and the eastward movement of this upper westerly wave are evident in the simulated flow at 300 hPa (Fig. 5.8a-d).

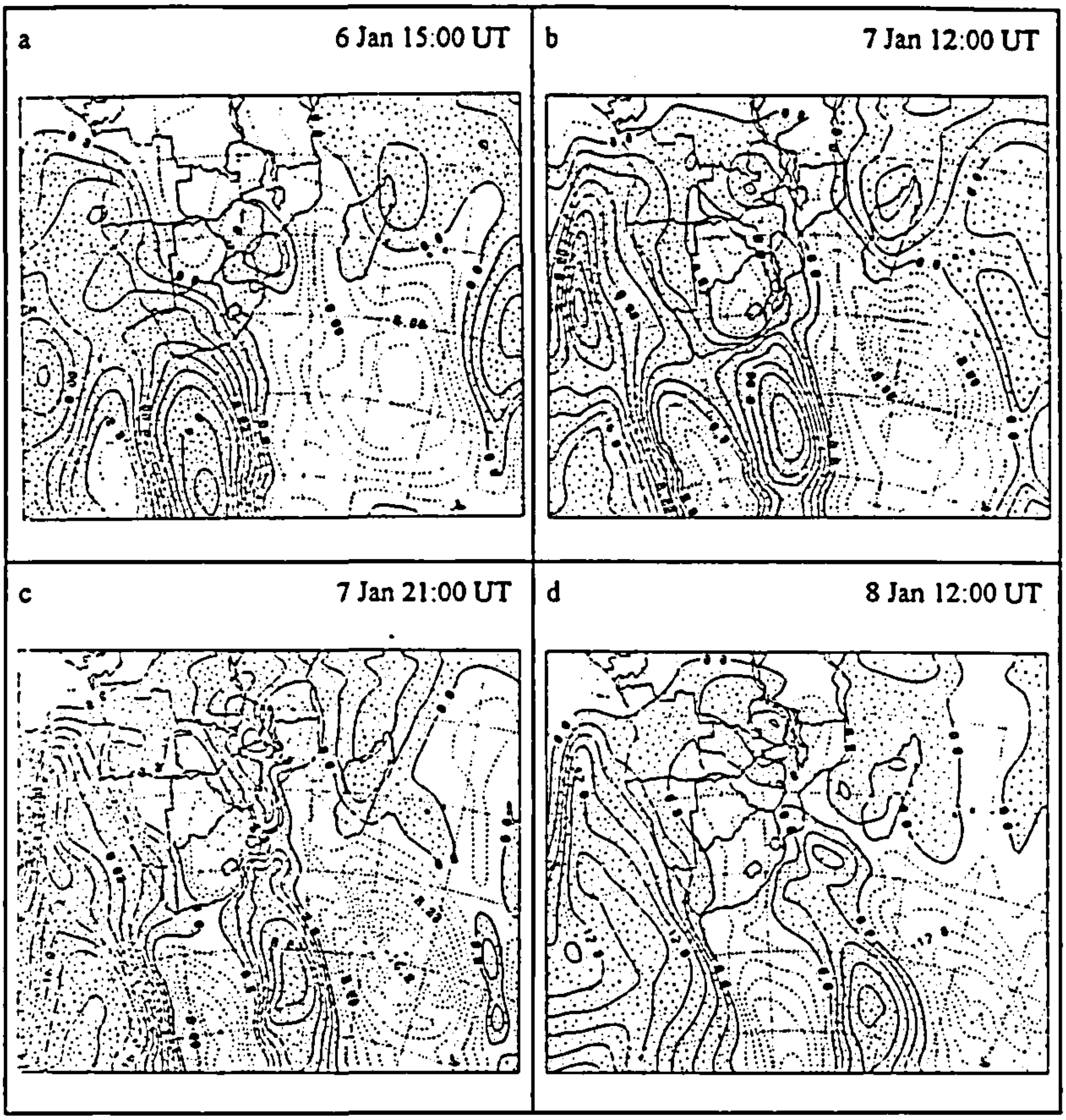

Figure 5.7: Meridional wind component field at 3,13 km (~ 700 hPa) above sea level from the dry case control run at (a) 6 Jan 15:00 UTC, (b) 7 Jan 12:00 UTC, (c) 7 Jan 21:00 UTC and (d) 8 Jan 12:00 UTC (m.s^{-1}; contour interval of 2 m.s^{-1} for a-c, 3 m.s^{-1} for d; solid lines indicate southerly components and dashed lines northerly components; southerly components are shaded).

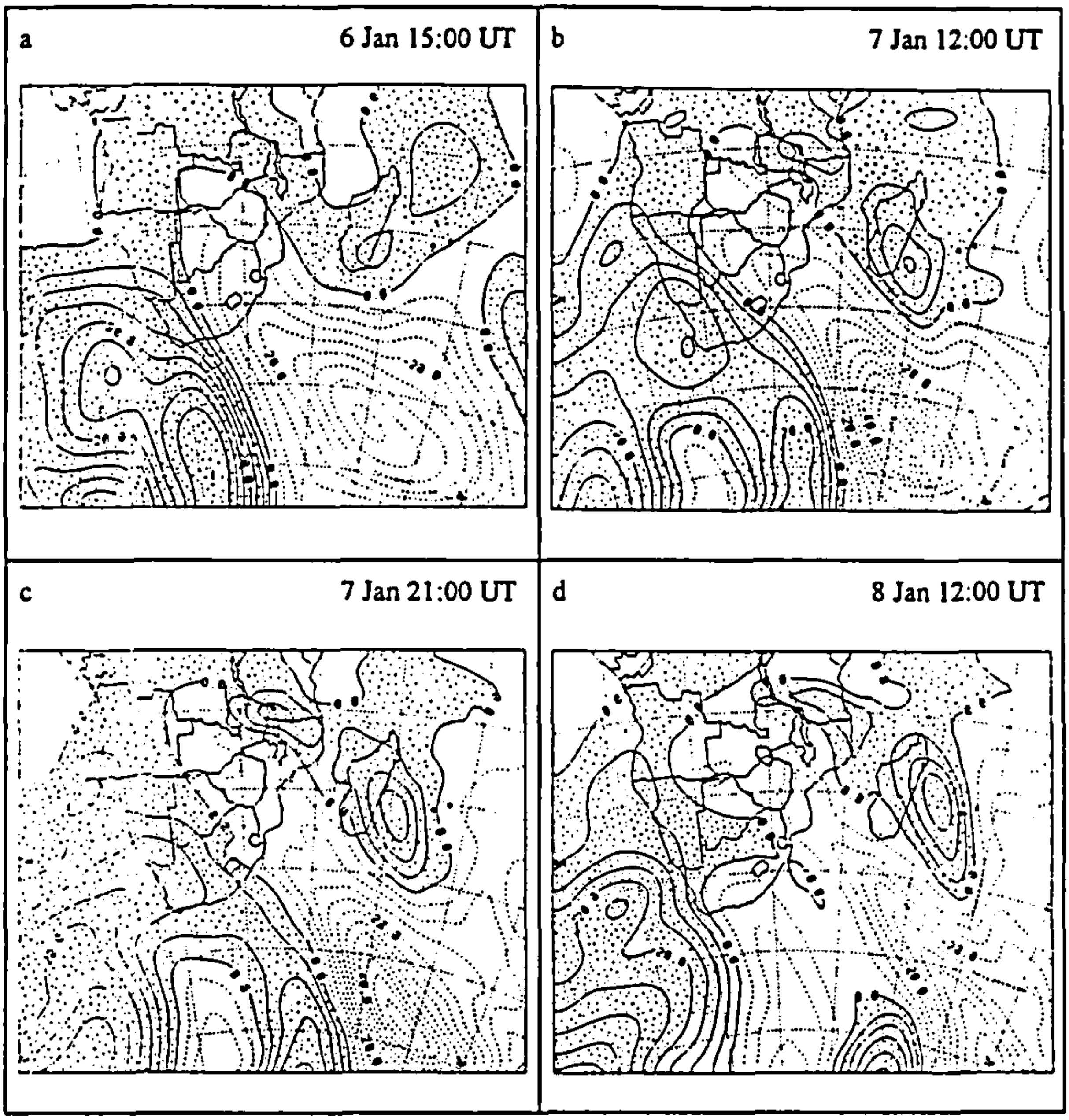

Figure 5.8: Meridional wind component field at 9,66 km (~ 300 hPa) above sea level from the dry case control run at (a) 6 Jan 15:00 UTC, (b) 7 Jan 12:00 UTC, (c) 7 Jan 21:00 UTC and (d) 8 Jan 12:00 UTC (m.s^{-1}; contour interval of 5 m.s^{-1}; solid lines indicate southerly components and dashed lines northerly components; southerly components are shaded).

In general, the simulated output reveals that the meridional circulation during the wet case was predominantly equatorward to the west of the subcontinent and poleward over the subcontinent and the southern regions of the South Indian Ocean. The poleward flow over the subcontinent was, however, weak north of about 20°S. During the dry case, predominantly poleward flow occurred throughout the troposphere over the eastern regions of tropical and southern Africa and the adjacent South Indian Ocean. Equatorward flow tended to be dominant over the western and central regions of southern Africa and over the South Atlantic Ocean.

Discussion

From the model it is evident that the mid-latitude zonal flow associated with the tropical-temperate trough development is westerly throughout the troposphere for both wet and dry conditions. This result is not surprising considering the positioning of the westerly wind belt. The band of westerlies extends much further north during the dry case study than the wet. The upper air westerlies extend further equatorward than those at the lower levels in both case studies. This is particularly obvious in the cross sections of the zonal wind components along 17 E (Figs 5.9a-c, 5.10a-c) and 30°E (Figs 5.9d-f, 5.10d-f). These findings are in accord with previous observations of the positioning of the westerlies (Fig. 5.11) (Harrison, 1986a; Tyson, 1986; Lindesay, 1988a; D'Abreton, 1992).

The importance of the easterly waves in the formation of tropical-temperate troughs during both wet and dry years is self-evident. During the initial stages of the cloud band development, the tropical low, which is the equatorward component system of the system, is embedded in easterly flow along the northern regions of the trough. The dissipative stage of the system is associated with the weakening of the easterly flow (Figs 5.1d; 5.3d). The easterlies in the upper troposphere are better developed and extend further southward during the wet case than the dry case in association with the southward displacement of the ITC during wet summers. The positioning of stronger easterly flow further southward has been linked with wetter

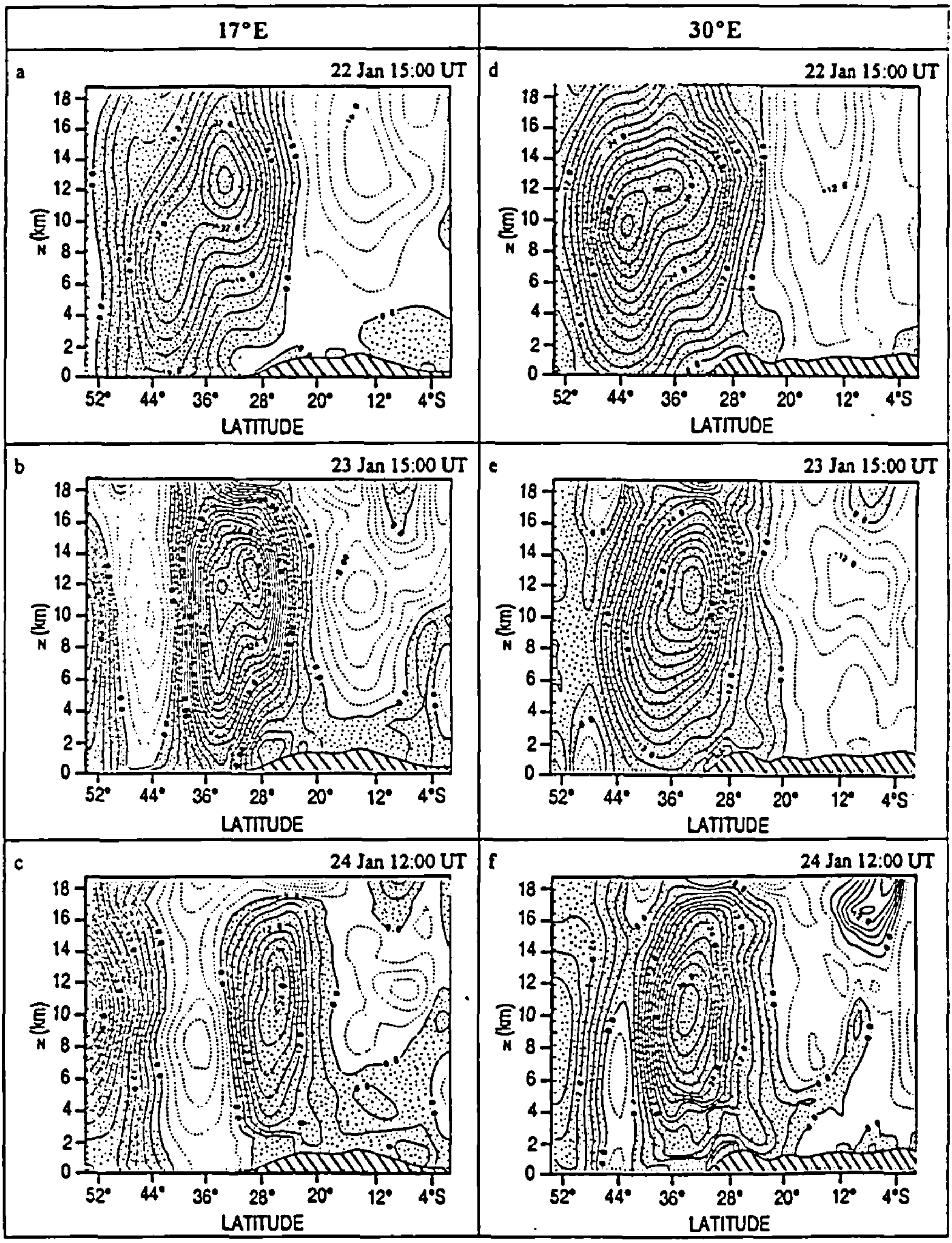

Figure 5.9: Zonal wind component cross sections from the wet case control run along 17°E at (a) 22 Jan 15:00 UT, (b) 23 Jan 15:00 UT and (c) 24 Jan 12:00 UT, and along 30°E at (d) 22 Jan 15.00 UT, (e) 23 Jan 15.00 UT and (f) 24 Jan 12:00 UT ($m.s^{-1}$; contour interval of 4 $m.s^{-1}$ for a, 2 $m.s^{-1}$ for b, and 3 $m.s^{-1}$ for c-f, solid lines indicate westerly components and dashed lines easterly components; westerly components are shaded).

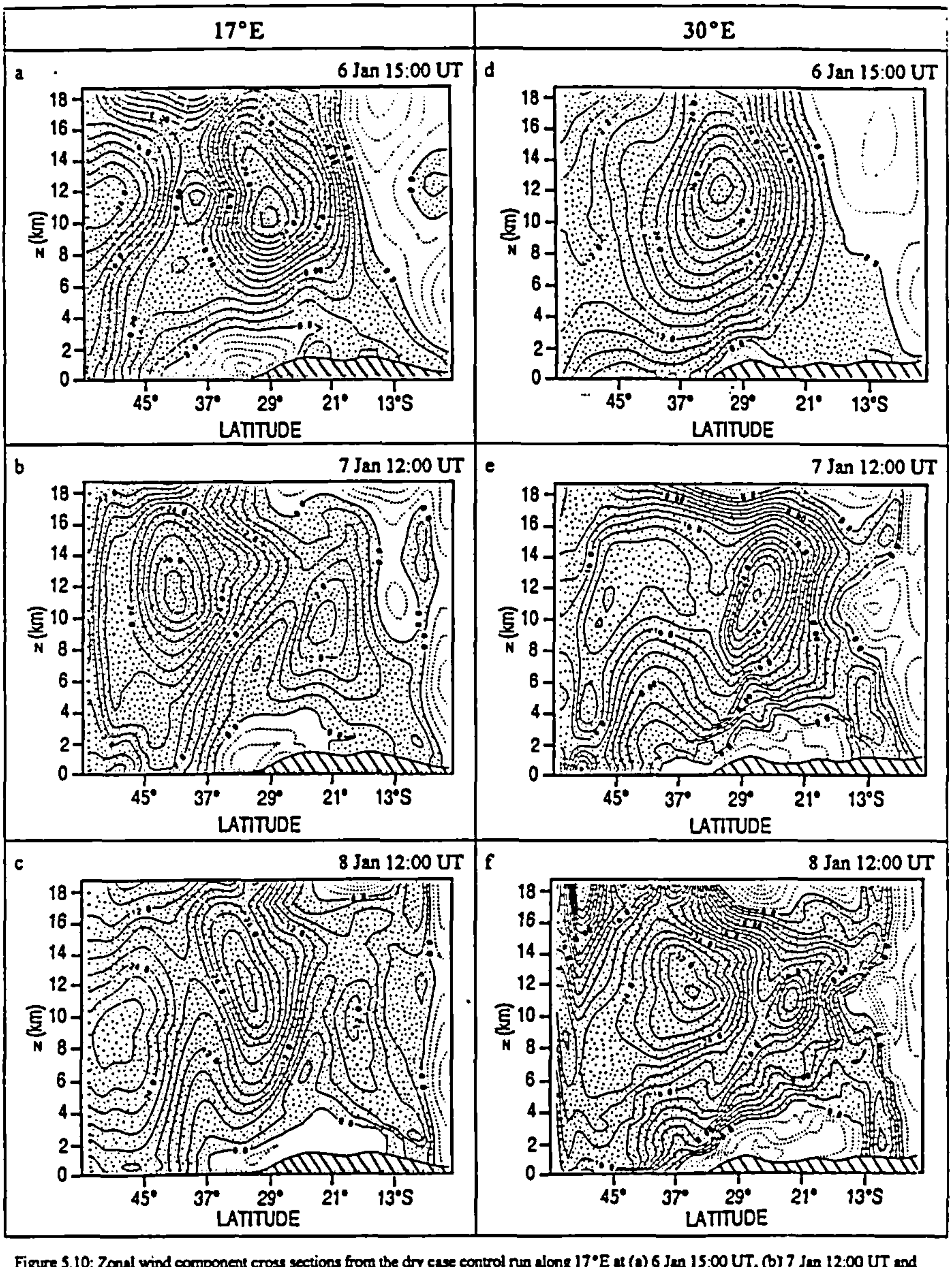

Figure 5.10: Zonal wind component cross sections from the dry case control run along 17°E at (a) 6 Jan 15:00 UT, (b) 7 Jan 12:00 UT and (c) 8 Jan 12:00 UT, and along 30°E at (d) 6 Jan 15:00 UT, (e) 7 Jan 12:00 UT and (f) 8 Jan 12:00 UT ($m.s^{-1}$; contour interval of 2 $m.s^{-1}$ for a,e-f, and 3 $m.s^{-1}$ for b-d; solid lines indicate westerly components and dashed lines easterly components; westerly components are shaded).

periods over southern Africa (Fig. 5.11) (Taljaard, 1981; Tyson, 1986; Lindesay, 1988a). The importance of the easterlies in supplying tropical heat and moisture for the formation of tropical-temperate troughs has also been stressed (Lindesay and Jury, 1991; D'Abreton, 1992; D'Abreton and Lindesay, 1993).

Significant zonal flow differences over the tropics exist between the wet and dry case studies. During the wet case, two zones of low-level westerly flow, one over western Africa and the other over the western South Indian Ocean, are separated by easterly flow throughout the simulation period (Fig. 5.1). Convergence between the low-level westerly flow over western Africa and the easterly flow over the central regions occurs at approximately 20°E throughout the initial and mature stages of the cloud band development (Fig. 5.1a-c). During the dissipative stage, the easterlies decrease and the region of convergence undergoes a concomitant shift eastward to be situated over 30°E at 700 hPa (Fig. 5.1c,d). The eastward movement of the tropical-temperate trough therefore appears to follow the migration of the region of convergence, which corroborates the suggestion of D'Abreton (1992) that cloud bands coincide with the convergence of easterly and westerly vapour transport along 10°S. The upper atmosphere is dominated by easterly flow throughout the entire study period (Fig. 5.2). The westerly and easterly flow in the lower level, the region of lower level convergence between 5 and 15°S and the predominant easterly flow in the upper troposphere are all characteristics of the more complex system of wet late summer Walker circulation cells recently described by D'Abreton (1992) and D'Abreton and Lindesay (1993) (Fig. 5.12a). The Walker Circulation cells, the deep easterly flow to the east of 30°E and the eastward movement of the region of convergence are all obvious in the zonal flow along 17°E (Fig. 5.9a-c), 30°E (Fig. 5.9d-f) and 15°S (Fig. 5.13a,b).

During the dry case, the zone of convergence between the low-level easterlies and westerlies between 10°and 20°S occurs at about 20°E after the initial stages of the simulation (Fig. 5.3). This zone remains at 20°E throughout the development of the cloud band, unlike that during the wet case study which progresses eastward. The low-level flow and region of convergence over the continent corroborate those presented by D'Abreton (1992) for dry late summers (Fig. 5.12b). The divergence between the modelled westerlies and the easterlies to the north of

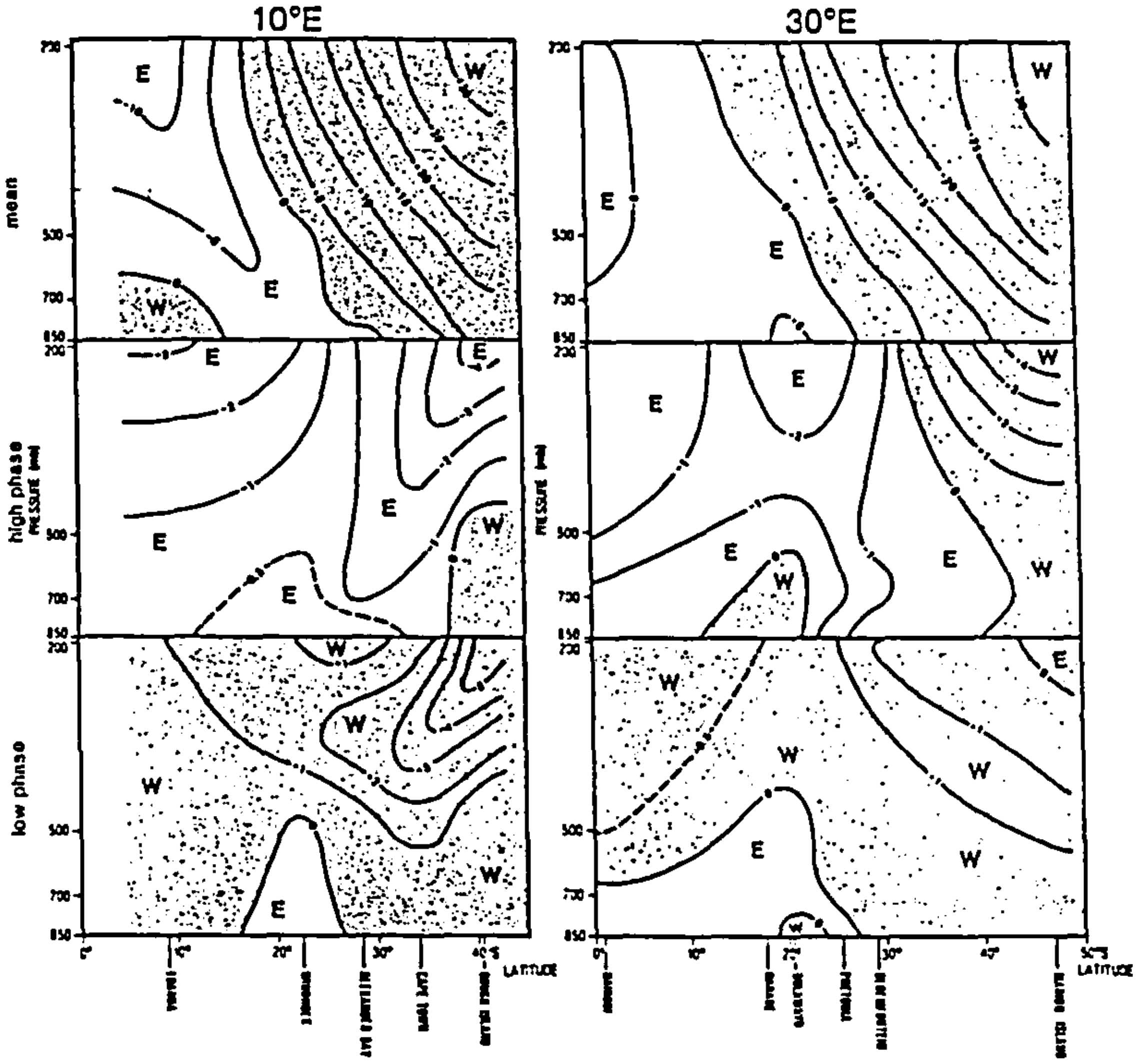

Figure 5.11: Sections taken along 10°E and 30°E to show the late summer mean zonal wind component ($m.s^{-1}$) and high- and low-phase deviations from the mean. Positive wind speeds and departures are westerly (W) and shaded; negative speeds and departures are easterly (E) (after Lindesay, 1988).

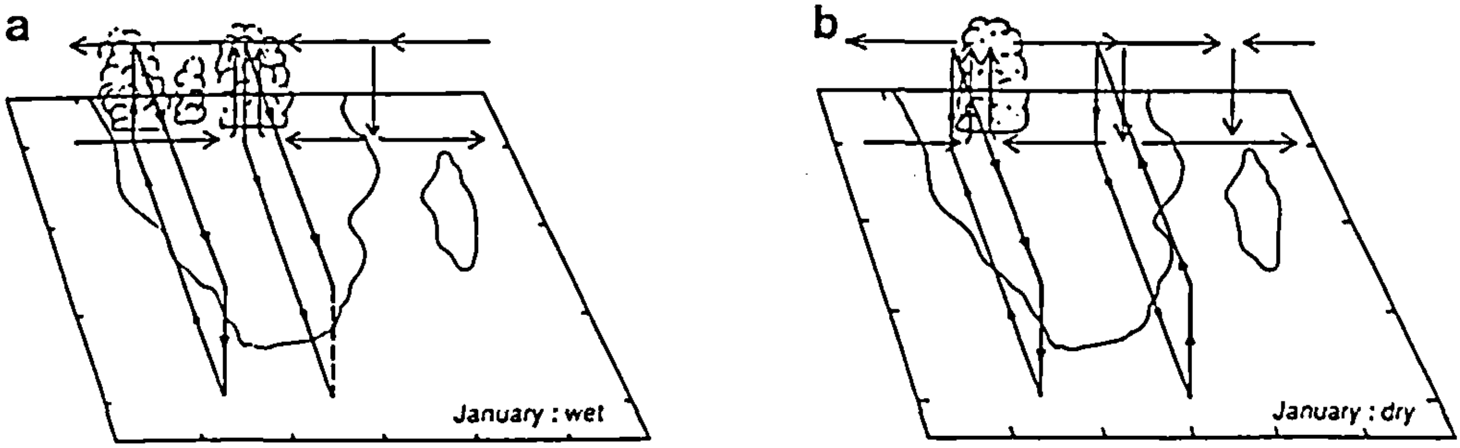

Figure 5.12: Schematic illustration of the zonal and meridional circulations associated with changes in vapour fluxes over southern Africa between (a) wet and (b) dry months of January (after D'Abreton and Lindesay, 1993).

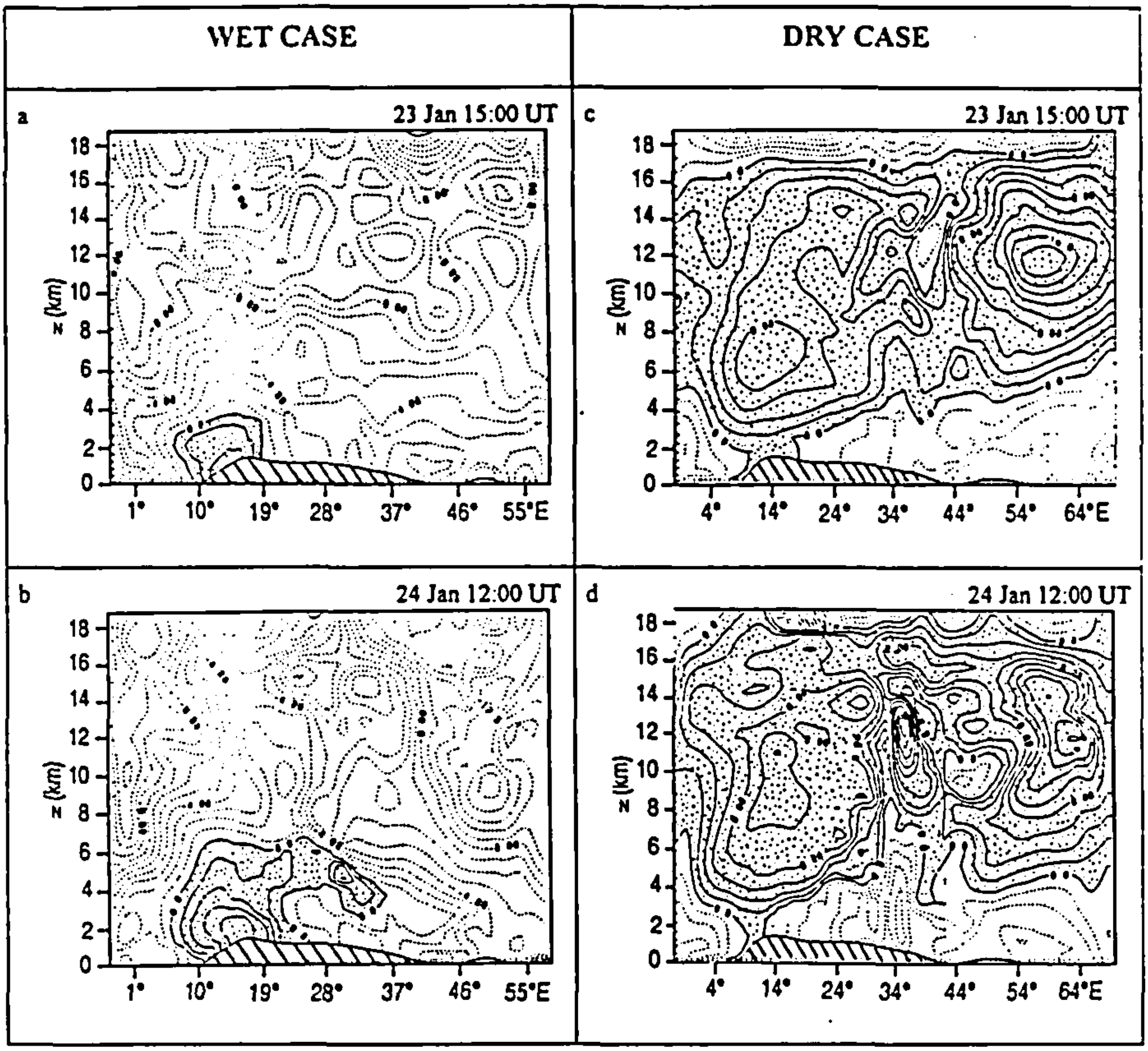

Figure 5.13: Zonal wind component cross sections along 30°S from the wet case control run at (a) 23 Jan 15:00 UTC and (b) 24 Jan 12:00 UTC, and from the dry case control run at (c) 7 Jan 12:00 UTC and (d) 8 Jan 12:00 UTC ($m.s^{-1}$; contour interval of 1 $m.s^{-1}$ for a-b and 2 $m.s^{-1}$ for c-d; solid lines indicate westerly components and dashed lines easterly components; westerly components are shaded).

Madagascar at about 40°E (Fig. 5.3) has been identified as being important in the distribution of water vapour toward the central regions of tropical Africa and over Madagascar during wet (Fig. 5.14a) and dry late summers (Fig. 5.14b) (D'Abreton, 1992; D'Abreton and Tyson, 1994). This region of divergence is also apparent in the simulated zonal flow for the wet case study (Fig. 5.1).

The simulated low-level westerly flow associated with the Walker circulation cell over eastern Africa is situated further north and east than that suggested by D'Abreton (1992) (Fig. 5.12b). This allows for the easterly flow over northern Mozambique in which the tropical low develops. An easterly wave over the eastern region of tropical Africa has been previously observed to occur with the formation of dry-summer cloud bands (Fig. 1.11) (Harrison, 1986a). The low-level westerly flow suggested by D'Abreton (1992) and D'Abreton and Lindesay (1993) (Fig. 5.12b) and the distribution of the divergent water vapour transport in this region (D'Abreton, 1992; D'Abreton and Tyson, 1994) (Fig. 5.14b) operate in opposite directions. The model reveals that the positioning of the low-level westerlies further eastward supports the easterly divergent flow over tropical Africa and contradicts the positioning of the westerlies.

The upper-level easterly flow associated with the more complex Walker circulation (Fig. 5.12b) over the western regions of tropical Africa is not clearly obvious in the model output, although easterlies are evident further north between the Equator and about 12°S. Upper-level easterlies and low-level westerlies are evident during the mature stages of the cloud band development over the northern regions of western tropical Africa along 17°E (Fig. 5.10a,b), but become predominantly westerly toward the end of the simulation (Fig. 5.10c). The low-level easterlies and the upper westerlies over the central regions of tropical Africa are evident throughout the simulation along 30°E (Fig. 5.10d-f) and the zone of convergence between the easterlies and westerlies in the lower levels is obvious along 15°S (Fig. 5.13c,d).

During the wet case, poleward flow occurred throughout the troposphere over most of tropical and southern Africa. Equatorward flow occurred to the west and southwest of the subcontinent and to the east of Madagascar (Figs 5.5, 5.6). During the dry case, poleward

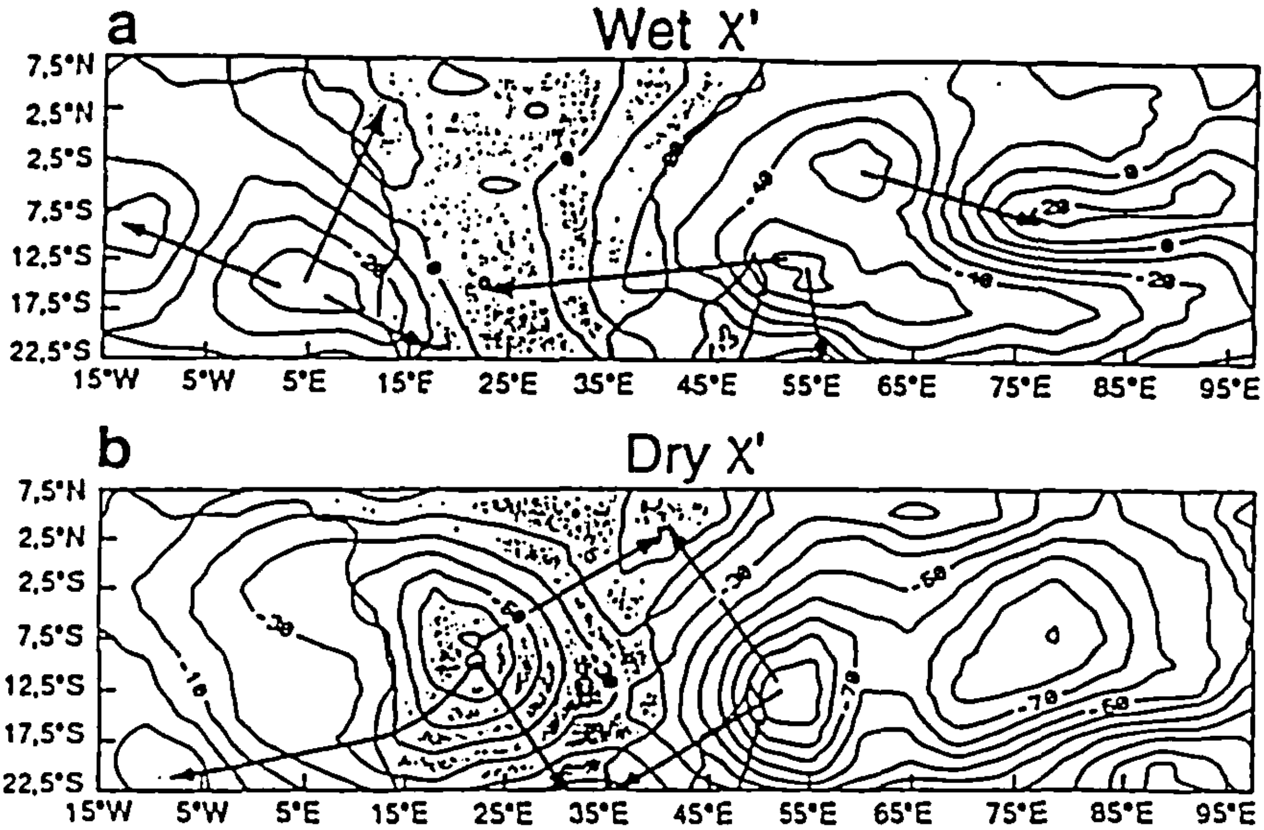

Figure 5.14: Distribution of divergent (x) vertically-integrated circulation water vapour transport for (a) mean wet Januaries and (b) mean dry Januaries (after D'Abreton, 1992). Integration is between 850 and 700 hPa; arrows represent direction of divergent transport; units are 10^6 kg.s^{-1}.

flow occurred predominantly over the eastern regions of tropical and subtropical Africa and the western regions of the South Indian Ocean. Equatorward flow was evident over the central and western regions of tropical and southern Africa in the upper levels and over the western regions in the lower levels. These differences in the placement of the poleward and equatorward flow are influenced by the position of the westerly wave and by shifts in the Walker Circulation cells (Harrison, 1986a; Lindesay, 1988a; D'Abreton, 1992).

During the wet case, the leading arm of the westerly wave associated with the development of the tropical-temperate trough was situated over the eastern regions of the southern African subcontinent and the trailing arm was positioned over the western regions and adjacent oceans of southern Africa. This resulted in the respective poleward and equatorward flow over these regions. During the dry case study, however, the modelled westerly wave was situated further east. The leading arm was positioned over Madagascar and the extreme eastern regions of the African continent and the adjacent ocean, while the trailing arm was situated over the central and western regions of the continent. This caused the predominant poleward flow over the eastern regions of southern Africa and the equatorward flow over the western and central regions of southern Africa in the upper tropospheric levels. The shift in the position of the westerly waves and the concomitant shift in the position of the cloud bands between wet and dry periods are therefore obvious in the simulated meridional flow. Such a shift has been suggested previously (Fig. 1.8) (Harrison, 1986a). Subsidence in the trailing arm of the westerly wave caused the stable and exceptionally dry conditions over the western subcontinent during the wet case and over most of the interior during the dry case. The influence of a shift in the position of tropical-temperate troughs on the conditions over the southern African interior are clearly obvious.

A simulated Hadley-type circulation occurs over the western regions of Africa between 10° and 35°S during the wet case (Fig. 5.15a-c), although the weak poleward flow in the lower levels does not occur along the entire meridian initially. South of about 35°S, the predominant equatorward flow is associated with the westerly wave transporting cold polar air northward in this region. Over the eastern and central regions of southern Africa deep poleward flow is obvious from the equator to beyond 50°S during the initial and mature stages of tropical-

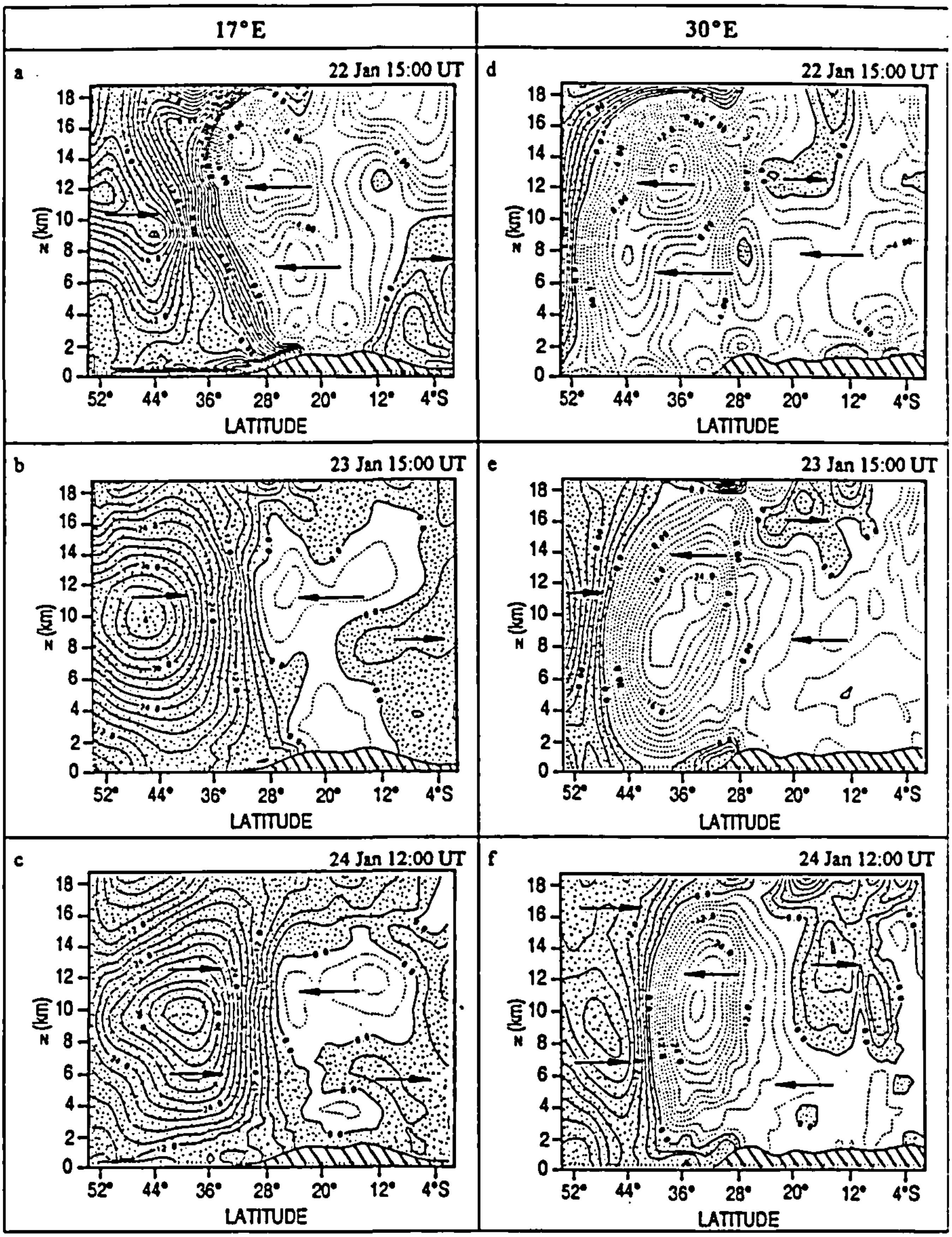

Figure 5.15: Meridional wind component cross sections from the wet case control run along 17°E at (a) 22 Jan 15:00 UT, (b) 23 Jan 15:00 UT and (c) 24 Jan 12:00 UT, and along 30°E at (d) 22 Jan 15:00 UT, (e) 23 Jan 15:00 UT and (f) 24 Jan 12:00 UT (m.s^{-1}; contour interval of 1 m.s^{-1} for a,d, 2 m.s^{-1} for e, and 3 m.s^{-1} for b-c,f, solid lines indicate southerly components, dashed lines northerly components; southerly components are shaded).

temperate trough development (Fig. 5.15d-f). This corroborates previous descriptions of tropical-temperate troughs as being representative of Hadley cell intensifications (Lindesay, 1988a, 1993). Both the Hadley circulation and the poleward flow have been observed by Lindesay (Fig. 5.16) (1988a) and D'Abreton (Fig. 5.12a) (1992).

Evidence of a weak Hadley cell is apparent over the western regions of Africa during the initial and dissipative stages of the tropical-temperate trough during the dry case (Fig. 5.15a,c), however, equatorward flow in the trailing arm of the westerly wave is predominant during the mature stage (Fig. 5.15b). Over the eastern regions of southern Africa, the Ferrel-type circulation described by Lindesay (1988a) (Fig. 5.16) and D'Abreton (1992) (Fig. 5.12b) only occurs during the initial stages between the Equator and approximately 20°S (Fig. 5.17d). Throughout the mature and dissipative stages of the cloud band, circulation of the Hadley-type is apparent in this region (Fig. 5.17e,f). Along 40°E, however, a Ferrel-type circulation occurs between the Equator and 30°S initially (Fig. 5.18a), and is then restricted to 20°S for the rest of the simulation (Fig. 5.18b,c). To the south of the Ferrel cell, the tropical-temperate trough enhances the Hadley-type circulation (Fig. 5.18b,c). A weakening in this circulation is evident during the dissipative stages of the cloud band when the deep poleward flow is replaced by the equatorward flow along the trailing arm of the westerly wave. The better developed Ferrel circulation along 40°E coincides with the positioning of the East Africa Walker cell further to the east. The simulated meridional flow along 40°E clearly shows how low-level poleward flow from the Equator to approximately 15°S associated with the Ferrel-type circulation, is vertically lifted and incorporated into the middle to upper level flow by the Hadley-type circulation beyond 15°S (Fig. 5.18a,b). The low-level poleward flow therefore transports energy into the tropical low from where it is then uplifted and transported along the temperate sections of the tropical-temperate trough. During the dissipation of the tropical-temperate trough this link between the lower and upper level poleward flow weakens (Fig. 5.18c).

At 15:00 UTC on 22 January (Day 1), the zone westerly winds greater than 36 $m.s^{-1}$ along 37°S is centred at about 200 hPa and at approximately 18°E (Fig. 5.19a). By the following day (23 January), this zone has shifted eastward, increased in size and stretches to the lower tropospheric levels. The maximum westerly zonal flow has also increased. This increase

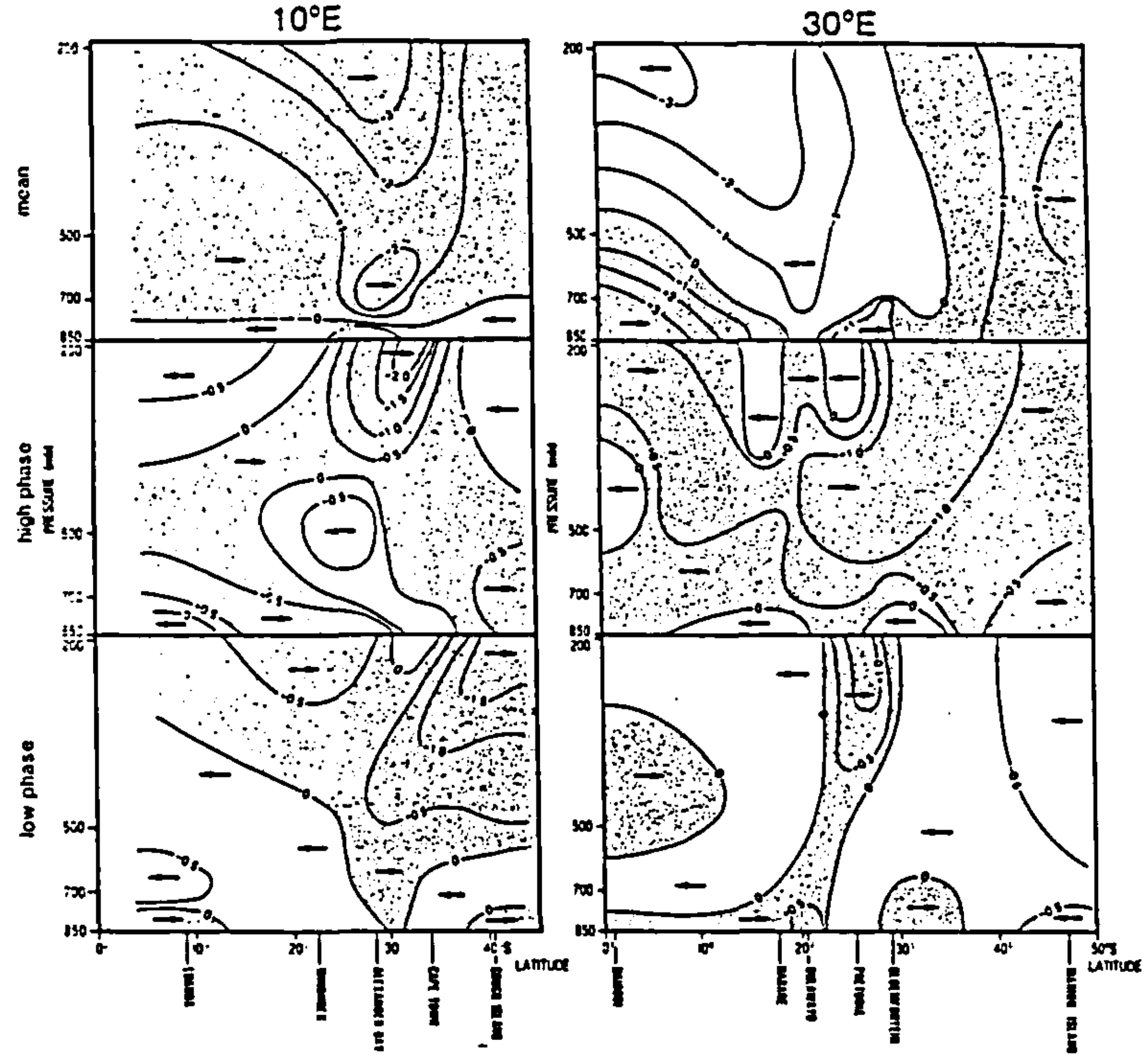

Figure 5.16: Sections taken along 10°E and 30°E to show the late summer mean meridional wind components ($m.s^{-1}$) and high- and low-phase deviations from the mean. Positive wind speeds or departures are poleward and shaded; negative are equatorward (after Lindesay, 1988a).

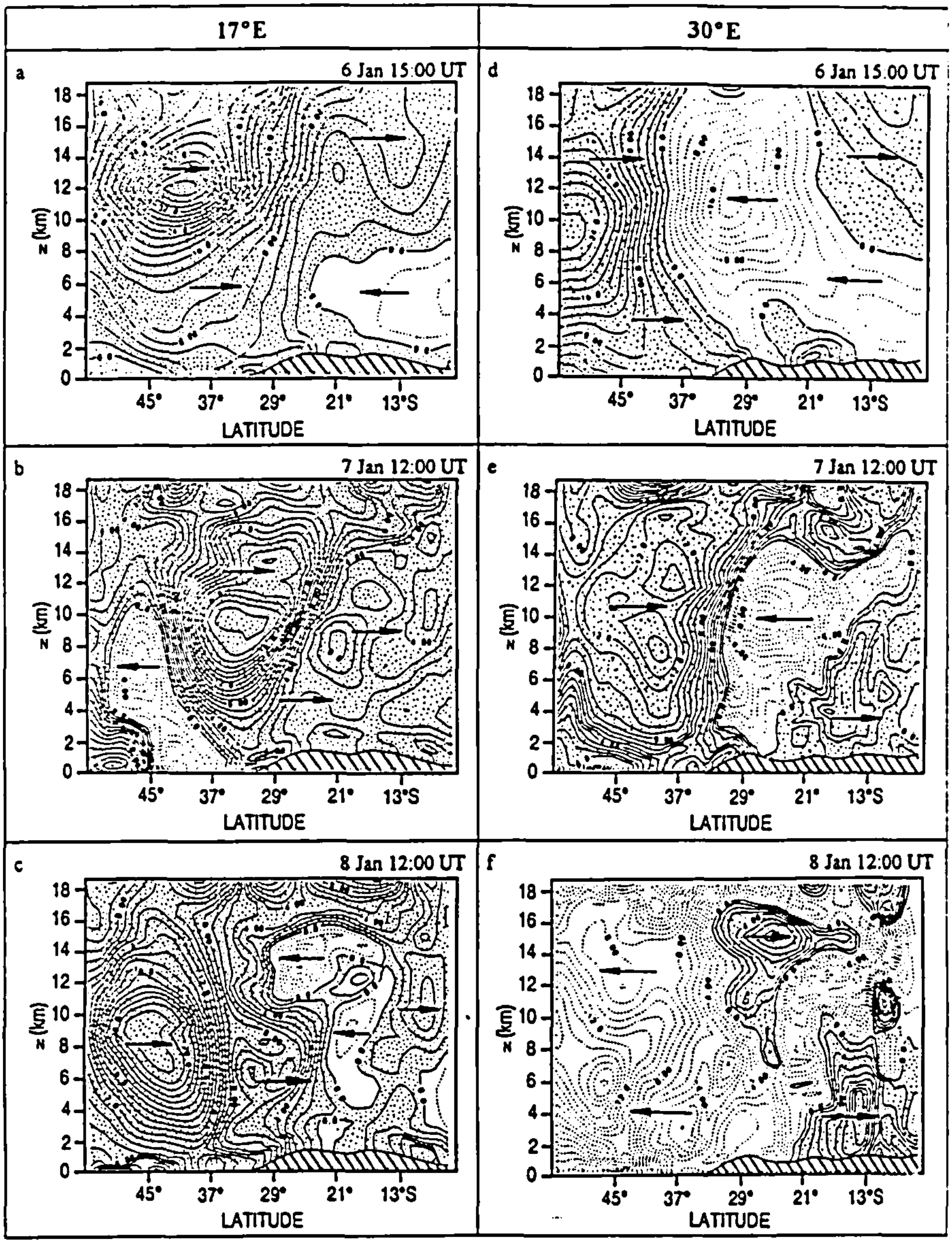

Figure 5.17: Meridional wind component cross sections from the dry case control run along 17°E at (a) 6 Jan 15.00 UT, (b) 7 Jan 12:00 UT and (c) 8 Jan 12:00 UT, and along 30°E at (d) 6 Jan 15:00 UT, (e) 7 Jan 12.00 UT and (f) 8 Jan 12:00 UT ($m.s^{-1}$; contour interval of 2 $m.s^{-1}$ for a,d, and 1 $m.s^{-1}$ for b-c, e-f, solid lines indicate southerly components and dashed lines northerly components; southerly components are shaded).

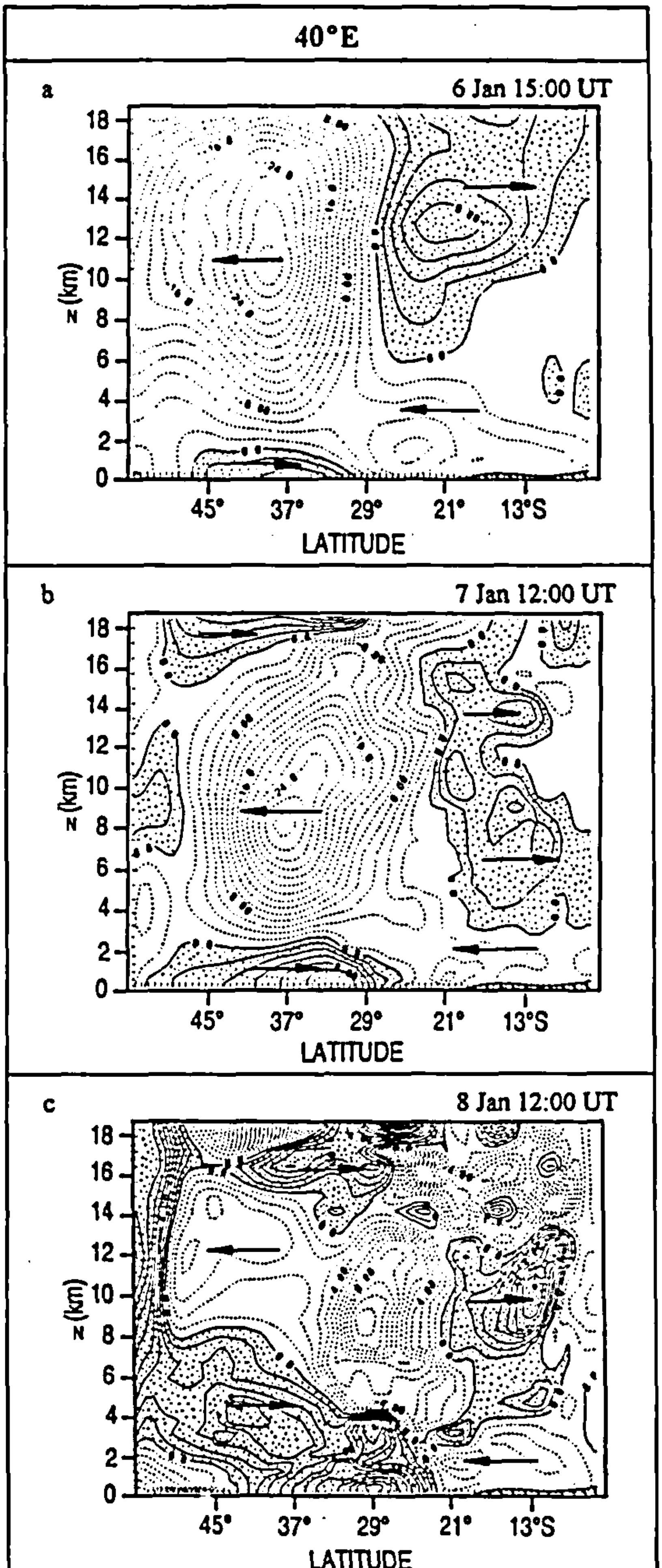

Figure 5.18: Meridional wind component cross sections from the dry case control run along 40°E at (a) 6 Jan 15:00 UT, (b) 7 Jan 12:00 UT and (c) 8 Jan 12:00 UT (m.s^{-1}; contour interval of 2 m.s^{-1} for a-b and 1 m.s^{-1} for c; solid lines indicate southerly components and dashed lines northerly components; southerly components are shaded).

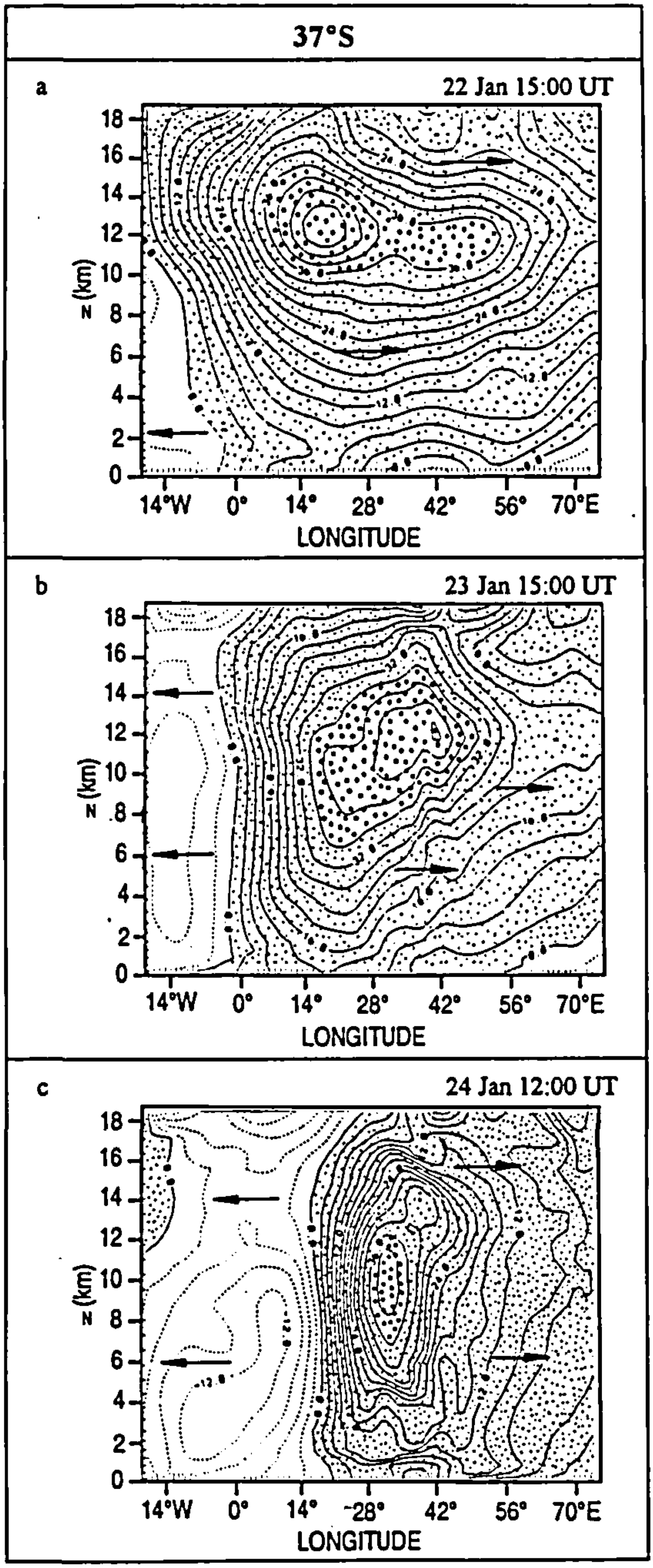

Figure 5.19: Zonal wind component cross sections from the wet case control run along 37°S at (a) 22 Jan 15:00 UT, (b) 23 Jan 15:00 UT and (c) 24 Jan 12:00 UT (m.s^{-1}; contour interval of 3 m.s^{-1} for a,c and 4 m.s^{-1} for b; solid lines indicate westerly components and dashed lines easterly components; westerly components are shaded; speeds greater than 36 m.s^{-1} are shaded in bold dots).

occurs as a result of the increase in the transferral of angular momentum to the region, facilitated by the mature tropical-temperate trough. The angular momentum increase is also evident in the SAWB interpolations (Fig. 2.13) and has been previously observed over the interior (Harrison, 1986a) and Marion Island (Lindesay and Jury, 1990) during the presence of a tropical-temperate trough. Following the cloud band dissipation on 24 January (Day 3), the zone of maximum wind flow is still situated in the region of the tropical-temperate trough remnants, but has reduced significantly in size and strength (Fig. 5.19c). Further evidence of the enhanced poleward transport of angular momentum along the tropical-temperate trough is apparent along 17° and 30°E (Fig. 5.9a-f). During the initial stages of the tropical-temperate trough development, the magnitudes of the westerly flow along 17° and 30°E were similar (Fig. 5.9a,d). During the mature stage of development (23 January), the westerly flow is substantially stronger along 30°E which is to the east of the tropical-temperate trough, than along 17°E to the west of the tropical-temperate trough (Fig. 5.9b,e). A similar increase in the westerlies to the east of the mature dry case tropical-temperate trough is also obvious (Fig. 5.20a-c). The model output therefore confirms the importance of tropical-temperate troughs in transporting westerly angular momentum poleward (Webster and Curtin, 1975; Harrison, 1986a; Tyson, 1986; Preston-Whyte and Tyson, 1988; Lindesay and Jury, 1991).

Moisture Characteristics

Previous research into the water vapour fluxes over southern Africa and the adjacent oceans has revealed significant differences in these fluxes between wet and dry periods (D'Abreton, 1992; D'Abreton and Lindesay, 1993). The modelled streamlines substantiated and strengthened these findings. The simulated moisture fields now require further investigation.

The Wet Case

During the initial stages of development, the regions of the highest total water mixing ratios (greater than 8 $g.kg^{-1}$) at 700 hPa are situated over the western and central interior and over

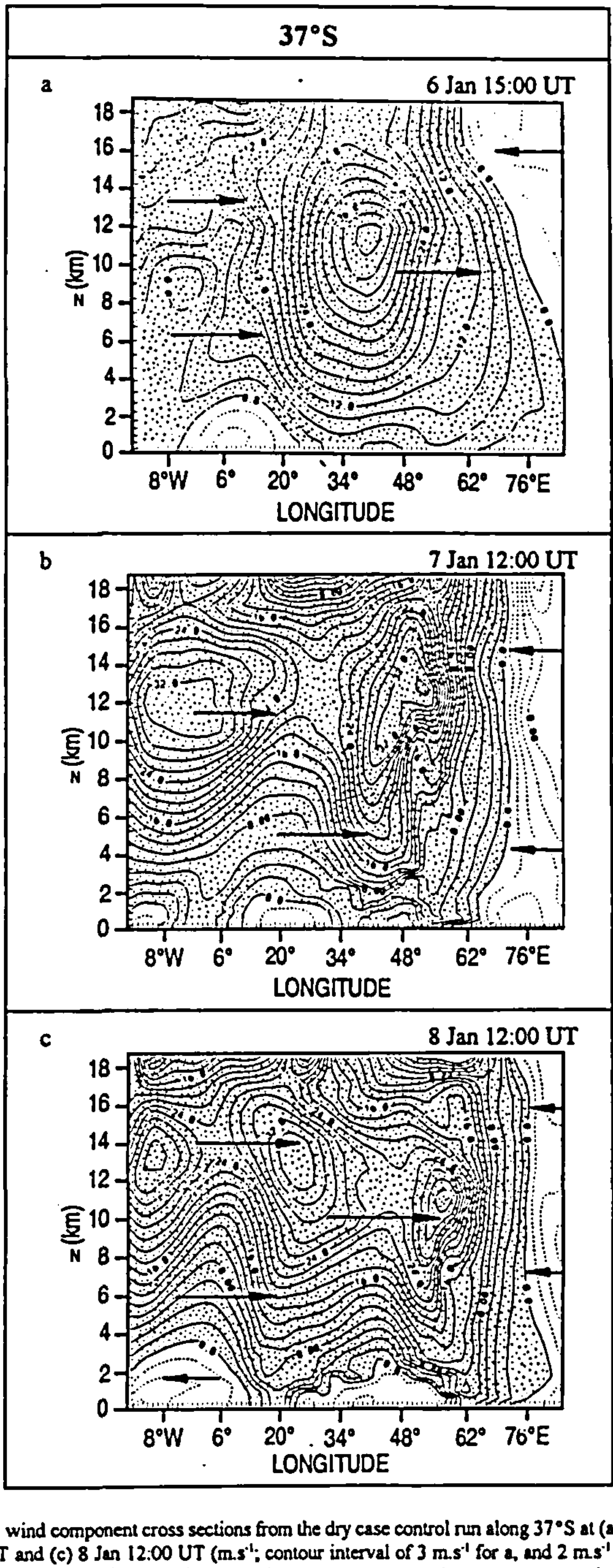

Figure 5.20: Zonal wind component cross sections from the dry case control run along 37°S at (a) 6 Jan 15:00 UT, (b) 7 Jan 12:00 UT and (c) 8 Jan 12:00 UT (m.s^{-1}; contour interval of 3 m.s^{-1} for a, and 2 m.s^{-1} for b-c; solid lines indicate westerly components and dashed lines easterly components; westerly components are shaded).

the eastern regions of southern Africa (Fig. 5.21a,b). By the afternoon of 23 January (Day 2) (Fig. 5.21c), the northeast-southwest alignment of the highest mixing ratios over tropical Africa to about 20°S and the switch to a northwest-southeast alignment along the tropical-temperate trough, together with the lower level streamlines (Figs 4.1c,d; 4.2c,d), are indicative of the poleward transport of moisture from the tropics to the mid-latitudes by the easterlies and then along the cloud band. Mixing ratios greater than 9,8 $g.kg^{-1}$ are evident along the mature tropical-temperate trough by 21:00 UTC (Fig. 5.21d) in association with the strengthened vertical uplift (Fig. 4.7d). The southward extension of the medium to high mixing ratios (between 7,0 and 8,4 $g.kg^{-1}$) beyond the regions of the convective activity associated with the tropical-temperate trough (Fig. 4.7d) implies that even though ascent is taking place in the cloudy air, poleward advection of moisture along the cloud band is also important. The poleward meridional component in the regions of the tropical-temperate trough are in support of this (Fig. 5.5). By 24 January (Day 3), the highest mixing ratios are associated with the convection along the cloud band remnants situated over the eastern regions of southern Africa and the adjacent ocean (Fig. 5.21e,f). A narrow band of high mixing ratios is still evident along the temperate remnants of the tropical-temperate tough, being advected southward by the strong poleward flow still present over these regions (Fig. 5.5c,d). The continued presence of the high mixing ratios is also apparent in time/longitude interpolations of observed meridional water vapour transport along 25°S (Fig. 5.22a) (D'Abreton, 1992). The strong moisture discontinuity between the tropical-temperate trough and the regions to the west of the cloud band is apparent in the total mixing ratio fields throughout the simulation.

The simulated total water mixing ratio field for the 300 hPa level reveals significant differences between upper and lower level moisture transport. During the initial stages of the simulation (Day 1), the total mixing ratios are very low (Fig. 5.23a,b). By the afternoon of 23 January (Day 2), a significant increase in the mixing ratios in association with the mature stage of the tropical-temperate trough development, is evident (Fig. 5.23c,d). The highest levels of moisture correspond with the regions of strongest uplift along the tropical-temperate trough. This, together with the exceptionally low levels of moisture over the tropics, suggests that the vertical uplift of low-level moisture is the most important mode of moisture transport into these levels. By the end of the simulation (Day 3), the highest mixing ratios occur in the region

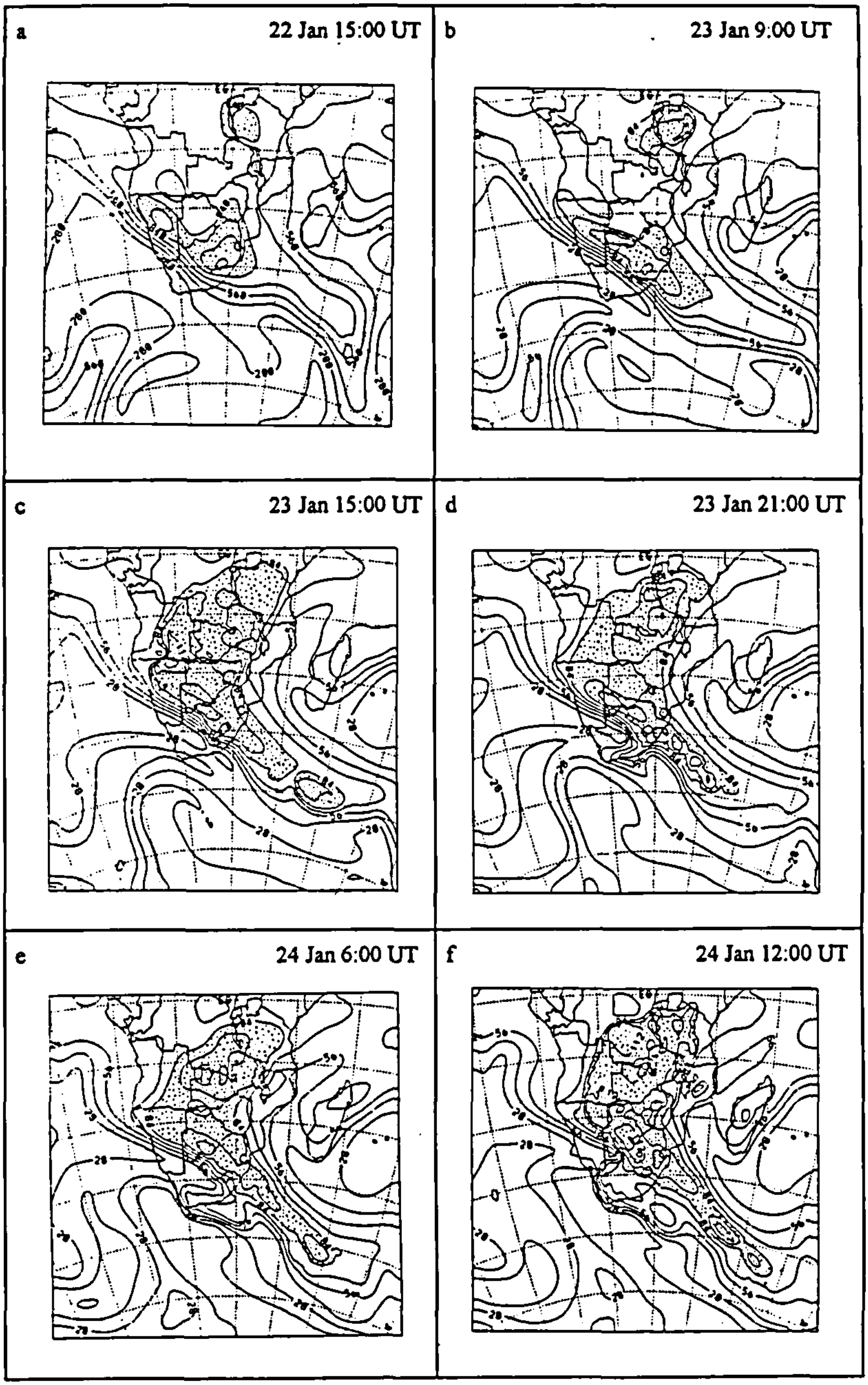

Figure 5.21: Total water mixing ratio at 3,13 km (~ 700 hPa) above sea level from the wet case control run at (a) 22 Jan 15:00 UT, (b) 23 Jan 9:00 UT, (c) 23 Jan 15:00 UT, (d) 23 Jan 21:00 UT, (e) 24 Jan 6:00 UT and (f) 24 Jan 12:00 UT ($g.kg^{-1}$; contour interval of 1,4 $g.kg^{-1}$; labels multiplied by 100 in a, by 10 in b-f). Regions where the total mixing ratio is greater than 8,4 $g.kg^{-1}$ are shaded.

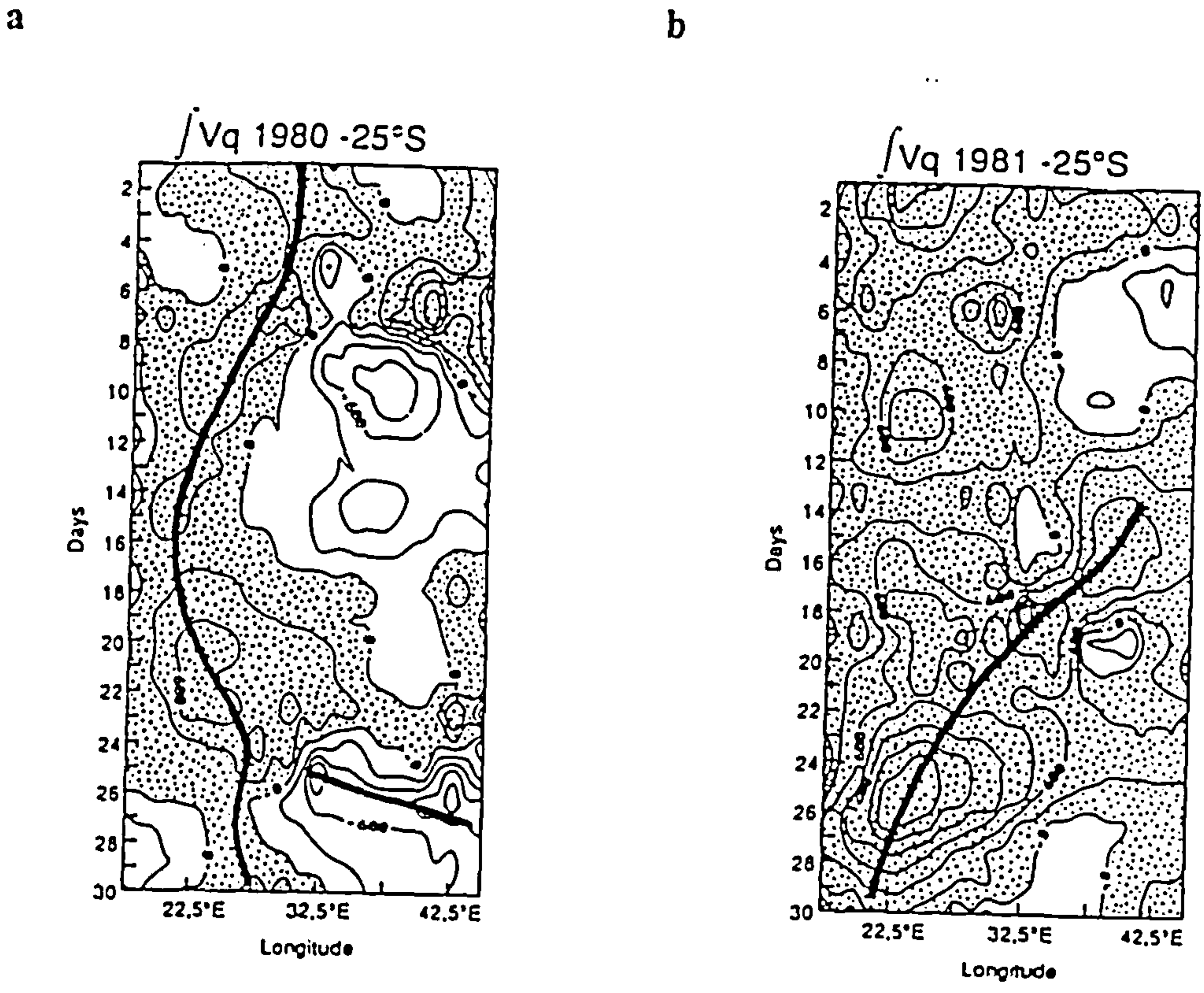

Figure 5.22: Time-longitude plot of meridional water vapour transport for (a) January 1980 and (b) January 1981 (after D'Abreton, 1992). *Shading indicates regions of northerly vapour transport and heavy lines indicate* trains of meridional transport. Units are g.cm^{-1}.s^{-1}.

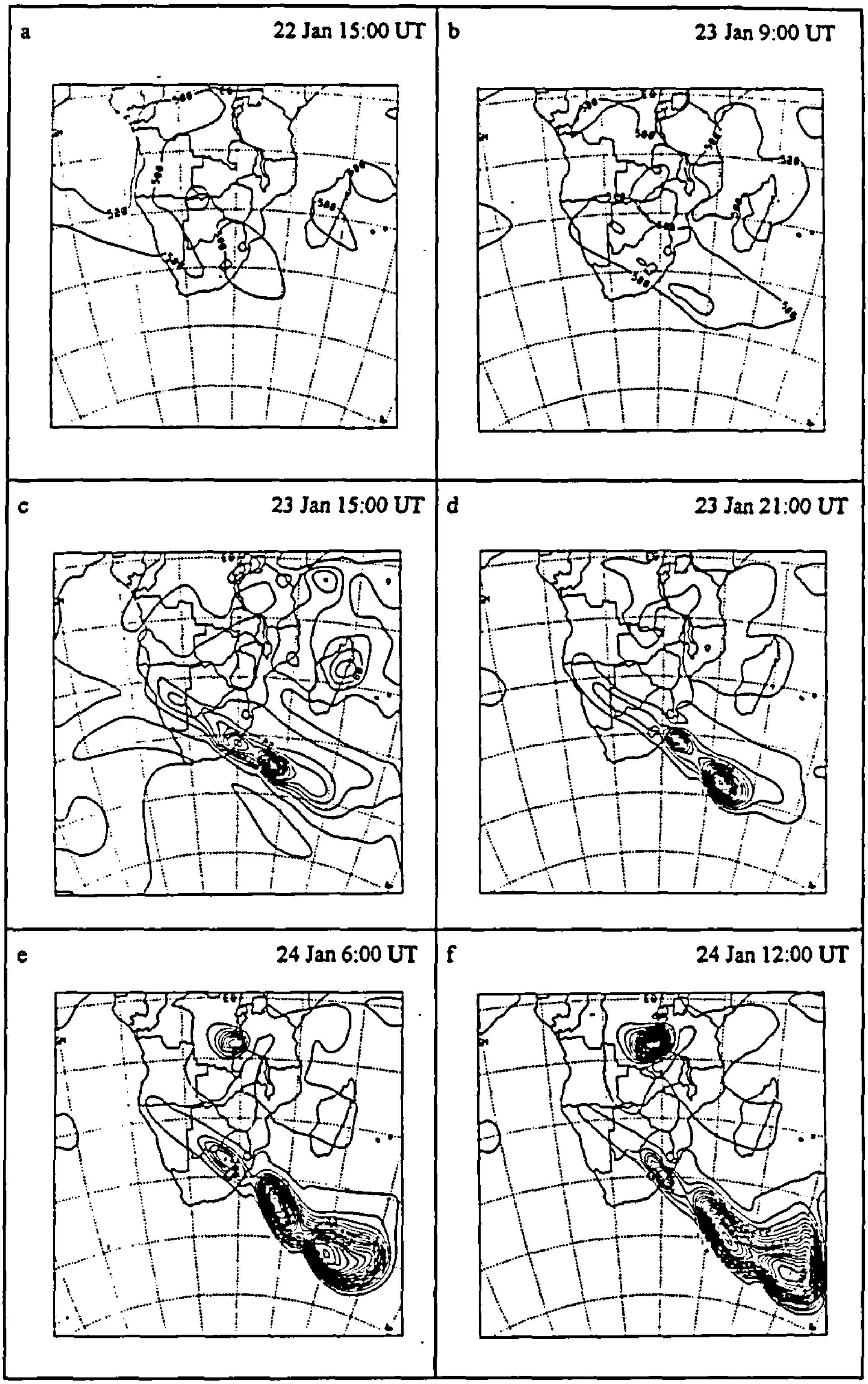

Figure 5.23: Total water mixing ratio at 9,66 km (~ 700 hPa) above sea level from the wet case control run at (a) 22 Jan 15:00 UT, (b) 23 Jan 9:00 UT, (c) 23 Jan 15:00 UT, (d) 23 Jan 21:00 UT, (e) 24 Jan 6:00 UT and (f) 24 Jan 12:00 UT ($g.kg^{-1}$; contour interval of 0,5 $g.kg^{-1}$; labels multiplied by 10^3 in a-b, and by 10^2 in b-f).

of the temperate remnants of the tropical-temperate trough (Fig. 5.23e,f) in association with the vertical uplift along the westerly wave (Fig. 4.9e,f). The occurrence of the highest mixing ratios along the southern regions of the tropical-temperate trough suggest an increase in cloud height along the band in a poleward direction.

The Dry Case

The highest mixing ratios (greater than 7 $g.kg^{-1}$) on 6 January (Day 1) at the 700 hPa level occur over the central and eastern regions of tropical Africa and over the northern Mozambique Channel (Fig. 5.24a). The southward extension of the high mixing ratios by the afternoon of 7 January (Day 2) (Fig. 5.24b,c) occurs with the development of the tropical-temperate trough. This, together with the poleward flow indicated by the streamlines at the surface and 700 hPa (Figs 4.12b,c; 4.12b,c) are evidence of the facilitation of poleward transport of moisture by tropical-temperate troughs. The high mixing ratios over the eastern regions of South Africa correspond closely with the cloud cover indicated in the satellite imagery (Plate 2.2c) and are due to the onshore flow around the cell of high pressure to the south of the country (Figs 2.15b; 4.12b). The region of highest mixing ratios reaches its furthest southward extent during the mature stage of the tropical-temperate trough (Day 2) when the poleward meridional flow along the cloud band is strongest (Fig. 5.7c). The decrease in the moisture flux from the tropics on 8 January (Day 3) as a result of the cloud band dissipation, causes the decrease in the magnitude and extent of the mixing ratios in the region of the trough (Fig. 5.24d). This decrease is also evident in the time-longitude plot of the water vapour transport at 25°S (Fig. 5.22b) (D'Abreton, 1992).

The highest mixing ratios at the 300 hPa level reflect the regions of greatest vertical uplift. Divergence along the leading edge of the westerly wave enhances vertical uplift in the temperate sections of the tropical-temperate trough, resulting in the high mixing ratios along the southern sections of the cloud band (Fig. 5.25). The positioning of the highest total mixing ratios along the southern regions of the tropical-temperate trough at 21:00 UT (Fig. 5.25c) are indicative, like those of the wet case, of an increase in cloud top height along the cloud band. The decrease in the low-level poleward transport of water vapour and the weaker uplift

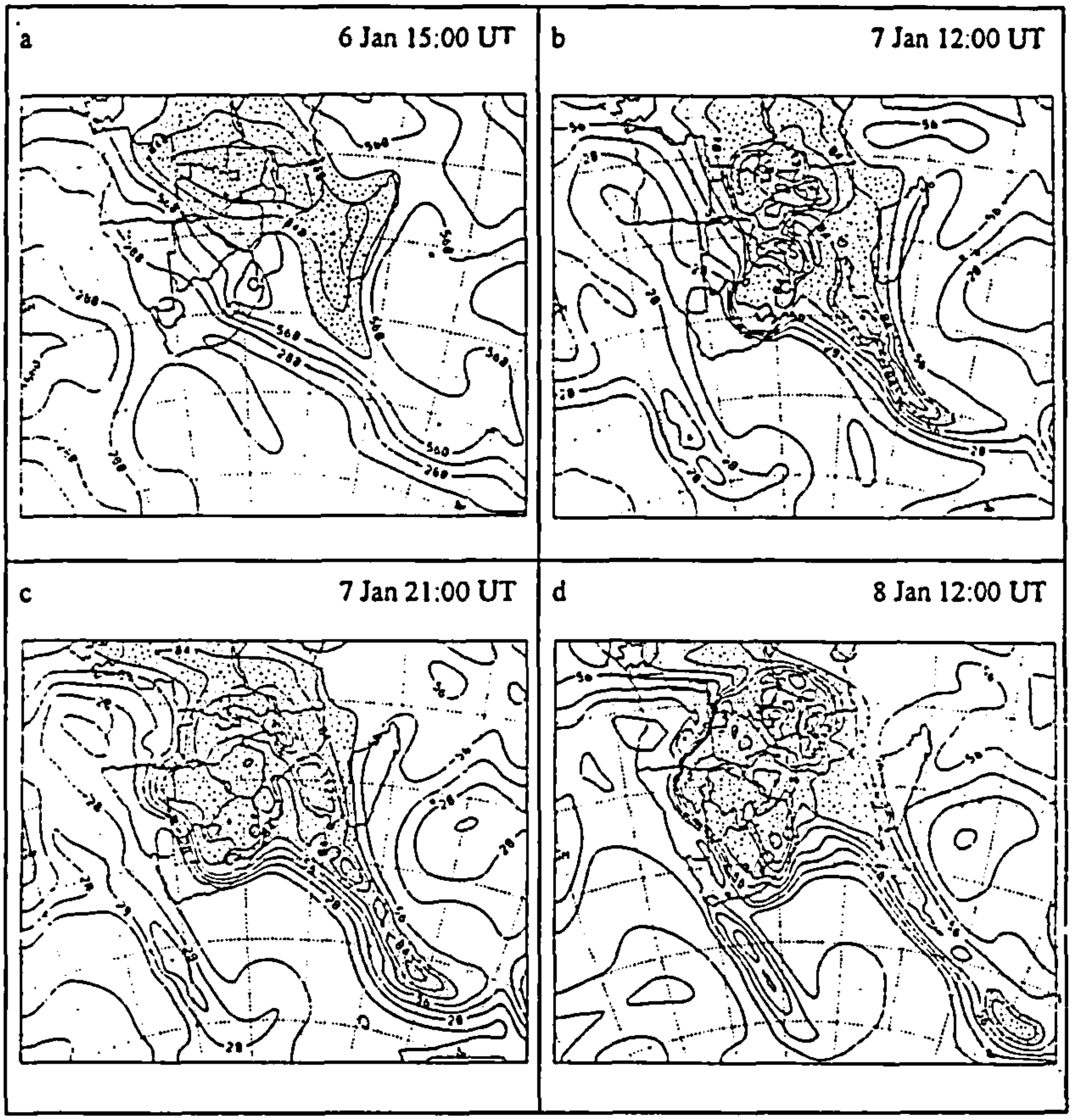

Figure 5.24: Total water mixing ratio at 3,13 km (~ 700 hPa) above sea level from the dry case control run at (a) 6 Jan 15:00 UTC, (b) 7 Jan 12:00 UTC, (c) 7 Jan 21:00 UTC and (d) 8 Jan 12:00 UTC ($g.kg^{-1}$; contour interval of 1,4 $g.kg^{-1}$; labels multiplied by 100 in a, by 10 in b-d). Regions where the total mixing ratio is greater than 7 $g.kg^{-1}$ are shaded.

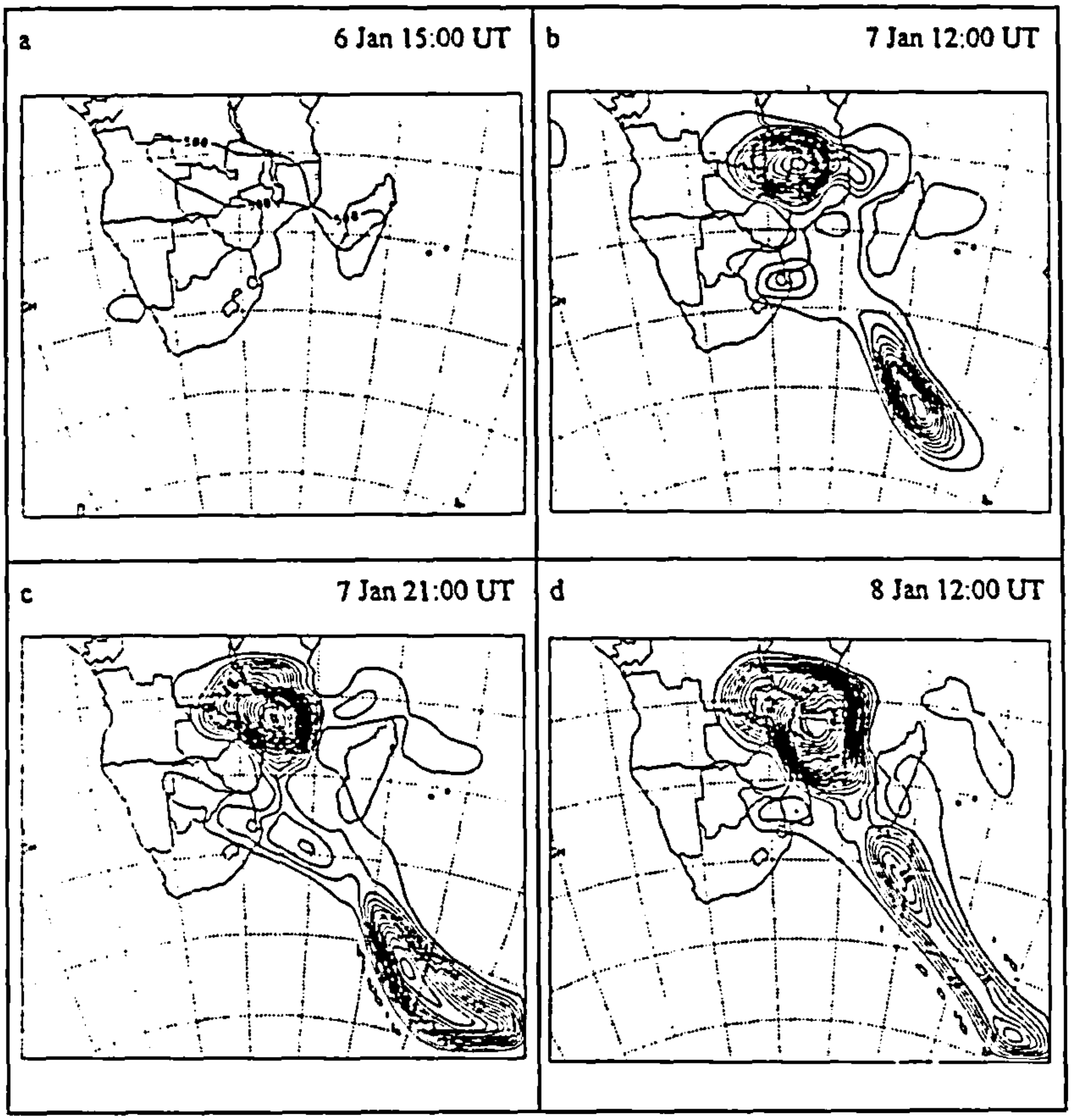

Figure 5.25: Total water mixing ratio at 9,66 km (~ 300 hPa) above sea level from the dry case control run at (a) 6 Jan 15:00 UTC, (b) 7 Jan 12:00 UTC, (c) 7 Jan 21:00 UTC and (d) 8 Jan 12:00 UTC ($g.kg^{-1}$; contour interval of 0,5 $g.kg^{-1}$; labels multiplied by 10^3 in a, 10^2 in b, by 10 in c,d).

associated with the tropical-temperate trough dissipation, result in less water vapour being vertically lifted to the 300 hPa level (Fig. 5.25d).

Discussion

During both the wet and dry conditions, the development of the tropical-temperate troughs was accompanied by an increase in the total water mixing ratios along the cloud band at 700 hPa. This is partially due to the increase in vertical velocity which transports surface moisture upward. However, the southward progression of higher mixing ratios with the development of the tropical-temperate trough, the extension of the high mixing ratios beyond the regions of strong convective activity and the southward air flow along the tropical-temperate trough are all evidence of the importance of tropical-temperate troughs in the facilitation of the advection of tropical moisture poleward.

A decrease in the mixing ratios along the cloud band with the break in the temperate link and the resultant dissipation of the tropical-temperate trough, is clearly evident during the dry case. During the wet case, mixing ratios greater than 8,4 $g.kg^{-1}$ still occur in the region of the cloud band following the dissipation of the cloud band, however, the zone of mixing ratios greater than 9,8 $g.kg^{-1}$ is no longer evident. The continued presence of high mixing ratios in the region of the cloud band remnants is indicative of the partial dissipative process, rather than a complete dissipation of the tropical-temperate trough on 24 January (Day 3). A significant decrease in the water vapour transport only becomes apparent in the time-longitude interpolation after the final dissipation of the tropical-temperate trough on 27 January (Fig. 5.22a) (D'Abreton, 1992). The increase in water vapour transport along the cloud band with the development of the tropical-temperate trough and the decline associated with the dissipative process is obvious in both case studies, despite the partial dissipation of the wet case cloud band. This corroborates previous hypotheses that cloud bands facilitate the poleward flow of water vapour from the tropics to the mid-latitudes (Erickson and Winston, 1972; Streten, 1973; Harrison, 1986a). The high upper tropospheric mixing ratios associated with the tropical-temperate trough occurred predominantly along the southern regions of the cloud band and were due to the vertical uplift associated with the westerly wave. This is indicative of an increase in the height of the cloud tops along the tropical-temperate trough in a poleward direction and suggests that the structure of tropical-temperate troughs over southern Africa is similar to those over Australia (Bell, 1986; Wright, 1988).

Thermodynamic Characteristics

A three-layered temperature anomaly structure was observed over the interior in association with the tropical-temperate trough that caused the floods over southern Africa during 1988 (Lindesay and Jury, 1991). Below average temperatures were found in the lower and upper troposphere and above average temperatures in the middle troposphere, which is characteristic of tropical air. No such temperature structure was found over Marion Island situated at the southern extremity of the cloud band. These findings substantiated the suggestion that tropical-temperate troughs assist in the poleward transport of warm tropical air over southern Africa. It has also been observed that an increase in latent heat occurs along the cloud band with the maturity of the tropical-temperate trough (D'Abreton, 1992). Tropical-temperate trough development is therefore likely to be accompanied by an increase in temperature in the region of the cloud band. This can be further investigated using the model output.

The Wet Case

Narrowing of the westerly wave, its northward penetration to form the tropical-temperate trough by the afternoon of 23 January (Day 2) (Fig. 5.26b), the separation of the main body of westerly flow from the trough and the lower temperatures associated with the closed low over the extreme southern regions of the southwestern Cape on 24 January (Day 3) (Fig. 5.26c) are evident in the modelled temperature fields at 700 hPa. The simulated temperatures over the southern regions of the subcontinent correspond quite closely with the observational data (Figs 2.3f; 2.4f; 2.5f; 2,6f; 2.7f), but less closely with those over the northern regions of southern Africa where there are fewer stations.

Along 17°E, south of approximately 25°S, the modelled temperature drops throughout the period with the passage of the cold front over the region (Fig. 5.27a-c). Particularly evident is

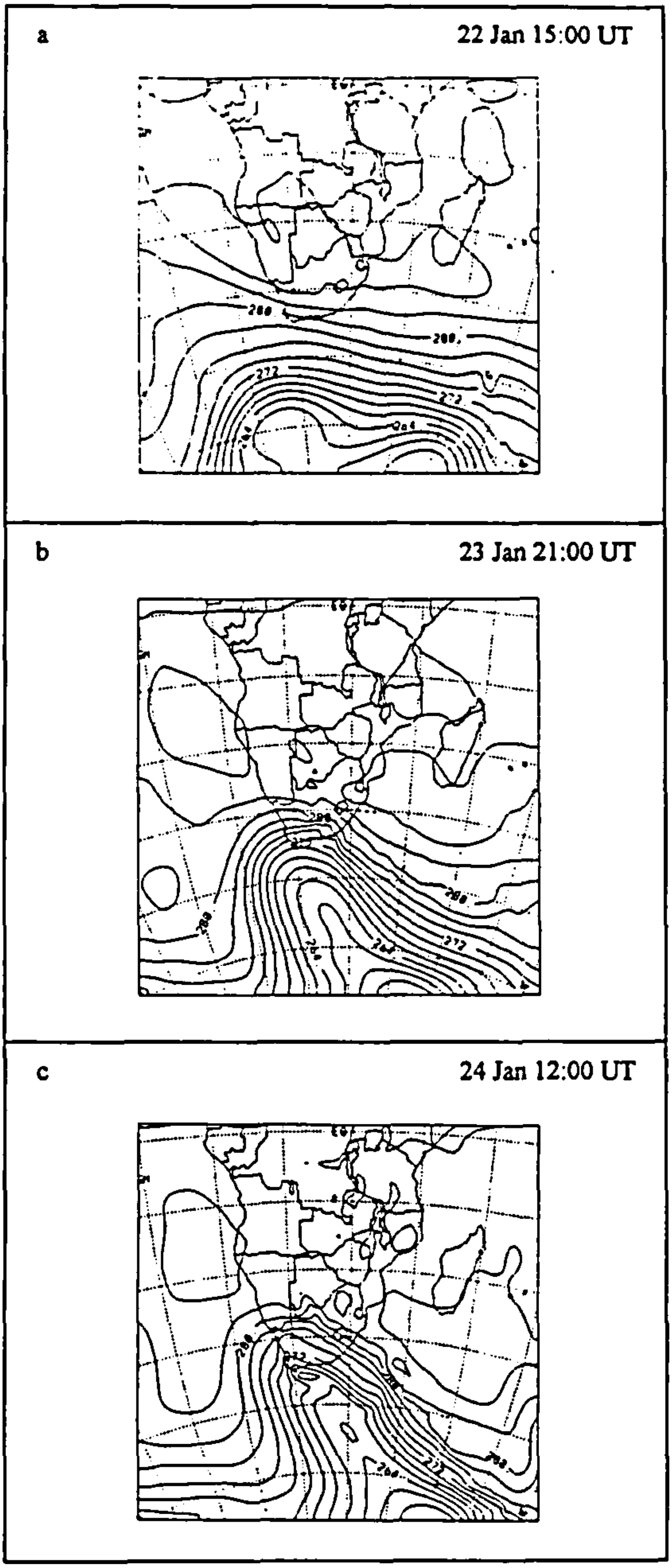

Figure 5.26: Temperature at 3,13 km (~ 700 hPa) above sea level from the wet case control run at (a) 22 Jan 15:00 UT, (b) 23 Jan 21:00 UT and (c) 24 Jan 12:00 UT (K, contour interval of 2 K).

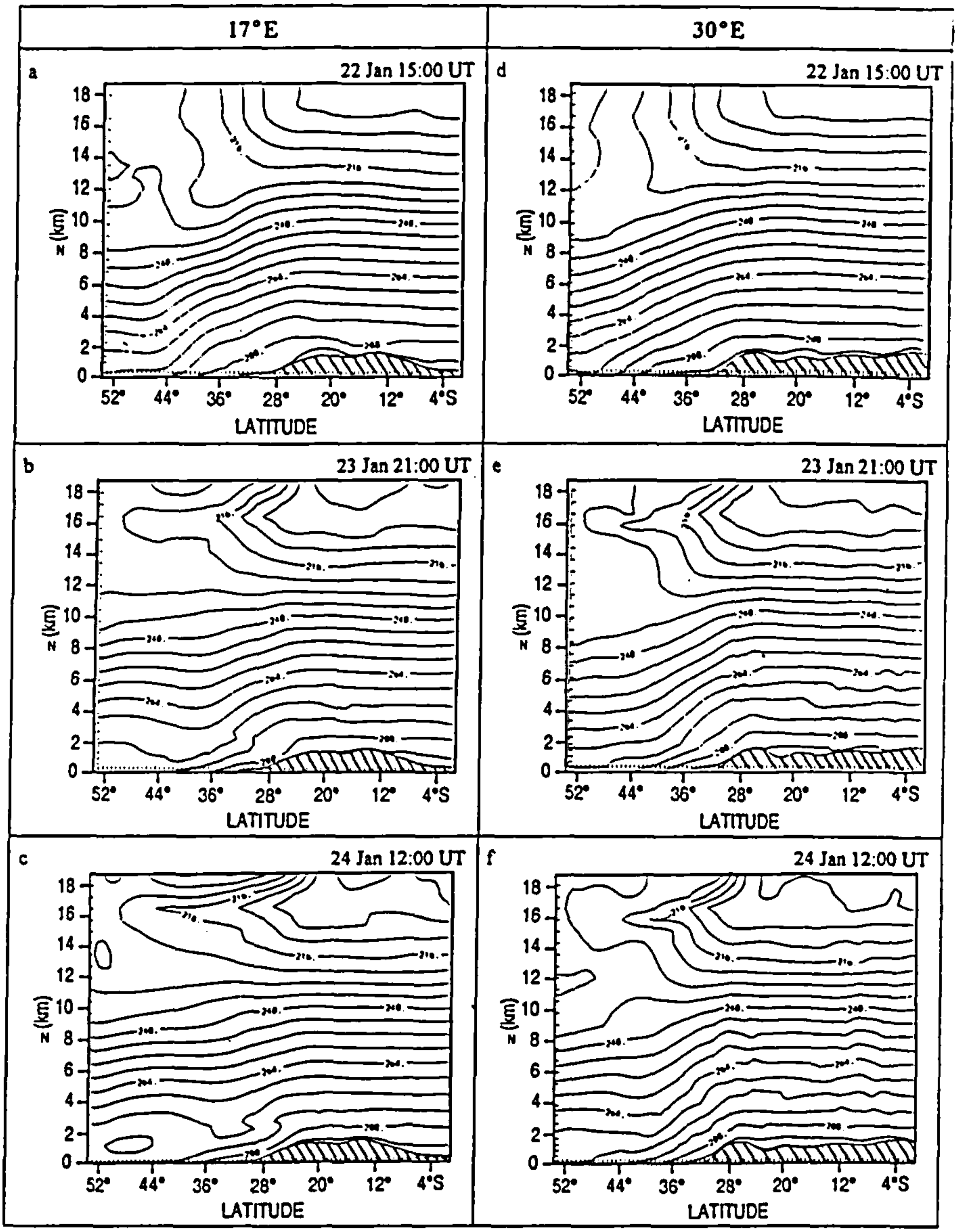

Figure 5.27: Cross sections of the temperature fields from the wet case control run along 17°E at (a) 22 Jan 15:00 UT, (b) 23 Jan 21:00 UT and (c) 24 Jan 12:00 UT, and along 30°E at (d) 22 Jan 15:00 UT, (e) 23 Jan 21:00 UT and (f) 24 Jan 12:00 UT (K, contour interval 6 K).

the sharp drop in temperature in the region of 35°S due to the presence of the cold-cored closed low. The cold front also causes the decrease in temperature over the coastal regions along 30°E (Fig. 5.27e). An increase in temperature is apparent over the Escarpment along 30°E on 24 January (Day 3) (Fig. 5.27e,f) when compared with those during the initial stages (Day 1) (Fig. 5.27d) and with those of the surrounding atmosphere. As the 30° meridian intersects the tropical-temperate trough in this region, it appears that higher temperatures are associated with the presence of the tropical-temperate trough.

The Dry Case

The eastward movement of the westerly waves and the northward transport of cold polar air within these westerly waves are evident in the simulated temperature field at 700 hPa (Fig. 5.28a-c). The 40° meridian intersects the cloud band between the centre and about 600 kilometres to the south of it. An increase in temperature in a poleward direction along the developing tropical-temperate trough is clearly obvious at the 700 hPa level (Fig. 5.28d-f).

Discussion

An increase in temperature is apparent in the region of the tropical-temperate trough during both the wet and dry case studies. This, together with the simulated meridional wind components and streamlines confirm the poleward transport of warm tropical air along tropical-temperate troughs (Lindesay and Jury, 1991). The increase in temperature in the region of the tropical-temperate trough may also be attributable to the release of latent heat within the cloud band (D'Abreton, 1992), but this is not immediately apparent from the modelled output.

Formation, Dissipation and Structure of Tropical-Temperate Troughs

The model reveals that the development of the tropical-temperate troughs is similar during wet and dry conditions. A tropical low, the westerly wave and a trough linking the low and the westerly wave are features common to both cases. The linking trough over northern Mozambique in the dry case is much smaller and weaker than that over the western interior

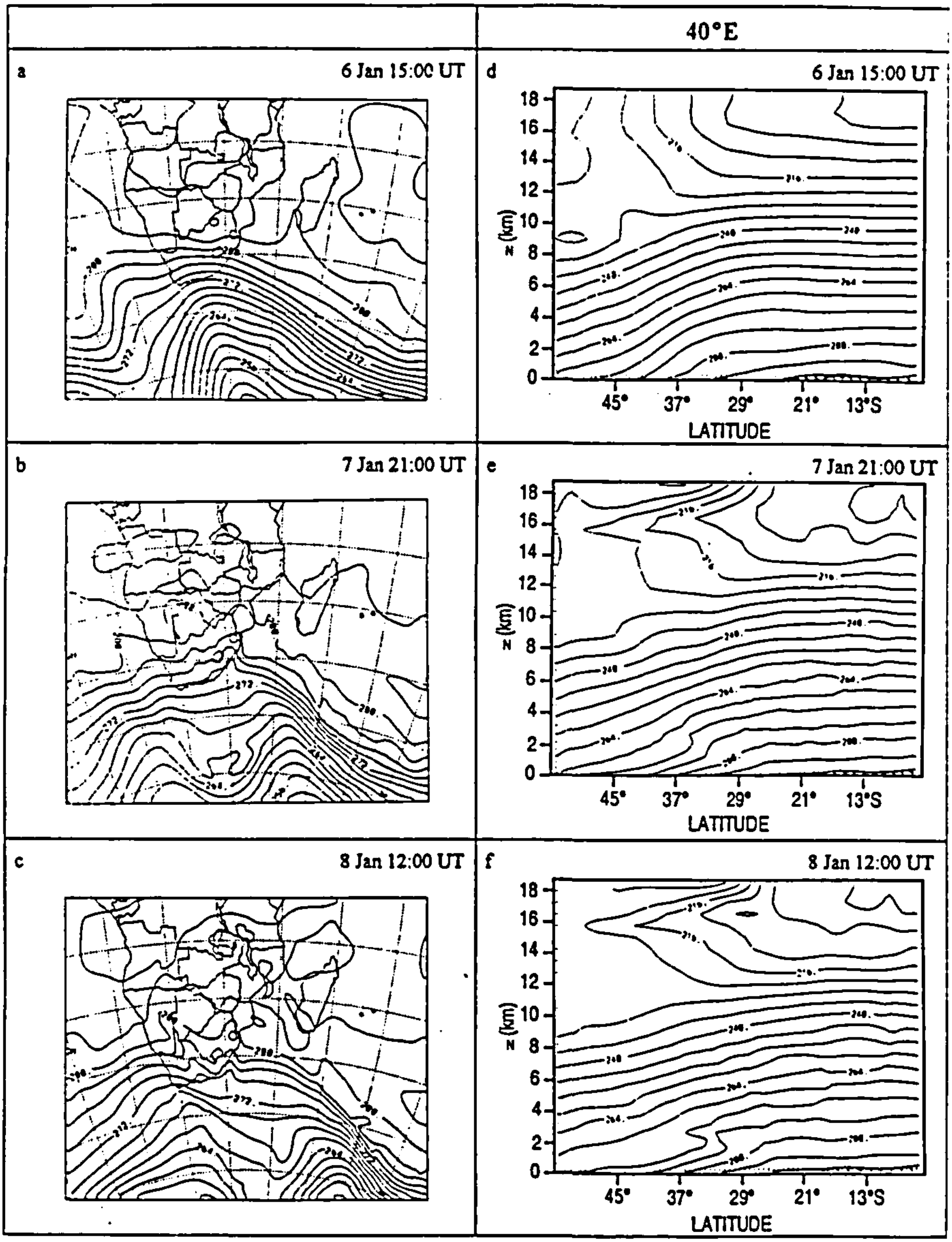

Figure 5.28: Temperature at 3,13 km (~ 700 hPa) above sea level from the dry case control run at (a) 6 Jan 15:00 UT, (b) 7 Jan 21:00 UT and (c) 8 Jan 12:00 UT (K, contour interval 2 K), and cross sections of the temperature field from the dry case control run along 40°E at (d) 6 Jan 15:00 UT, (e) 7 Jan 21:00 UT and (f) 8 Jan 12:00 UT (K, contour interval 6 K).

during the wet case, but performs the same function. In both cases, the tropical low developed in the tropical easterlies which appears to enhance their formation (Harrison, 1986a). Clearly evident in the streamlines and meridional wind components during the initial stages of both the wet and dry case studies is the northerly and northeasterly flow into the region of the tropical low. This wind flow transports moisture from the eastern regions of tropical Africa and from the adjacent oceanic regions to the northwest of Madagascar, to the northern regions of the tropical-temperate trough. Flow around the South Indian Anticyclone contributes to the southern sections of the wet case tropical-temperate trough, particularly toward the end of the period. The model reveals, however, that the northeasterly contribution is far more significant and corroborates previous suggestions to this effect (Miron and Lindesay, 1983; Harrison, 1986a; Lindesay and Jury, 1991; D'Abreton and Lindesay, 1993). The contribution of the South Indian Anticyclone circulation to the poleward flow along the dry case tropical-temperate trough is far greater than that of the wet case, but the southeastward progression of moisture along the cloud band is indicative of the predominant northeasterlies. During both case studies, the tropical connection between the tropical low and connecting trough formed first. Eastward movement of the westerly wave, which aligned the westerly wave trough with the linking trough, then resulted in the temperate link. The tropical low in the dry case is situated much further north than that of the wet case thus forcing a greater northward extension of the westerly wave to establish the temperate connection.

The poleward flow within the temperate sections of the tropical-temperate trough is substantially stronger than that associated with the tropical low and the linking trough. The establishment of the temperate link appears to enhance the poleward flow in the region of the tropical low and linking trough by kinematic divergence. The divergence along the linking trough is then likely to enhance the northeasterly and easterly flow into the region of the tropical-temperate trough, resulting in further tropical heat and moisture supply to the northern regions of the tropical-temperate trough. Convection in the tropical low and the linking trough then vertically lifts the tropical moisture into the lower and middle tropospheric levels. Divergence in the leading arm of the upper westerly wave, which is situated over the low-level convergence in the central and southern sections of the cloud band, serves to enhance the vertical uplift. This transports the tropical moisture into the upper tropospheric levels resulting in the increase of the cloud top heights along the central and southern section of the cloud band in a poleward direction. The increase in cloud top height with latitude is evident in the simulated cloud water fields along 28°and 37°S for both the wet (Fig. 5.29a,b) and dry (Fig. 5.29c,d) cases. The cloud development over the eastern regions of southern Africa along 28°S during the dry case (Fig. 5.29c) should not be confused with that of the tropical-temperate trough to the east of it. Poleward flow along the cloud band throughout the troposphere also advects the tropical moisture southward. This is evident in the poleward progression of the high mixing ratios with the development of the tropical-temperate trough. The structure of the tropical-temperate troughs during both wet and dry conditions therefore appears to be one of an increase in cloud top heights and depth with latitude, and an increase in the poleward flow and mixing ratios in a southward direction along the cloud band.

It is evident from the model output that the dissipation of the wet and dry case tropical-temperate troughs occurs with the eastward movement of the westerly wave trough which breaks the temperate link. Following this break, the poleward flow in the region of the tropical low and linking trough decreases and the northeasterlies and easterlies weaken and become less focused. It therefore appears that the temperate link is vital in enhancing the poleward flow of tropical air along the linking trough. The tropical low is important in lifting the tropical heat and moisture into the air in the northern regions of the tropical-temperate trough from where it is then more effectively transported southward.

The model has revealed new aspects of the development, structure and dissipation of southern African tropical-temperate troughs. One of the greatest strengths of mesoscale numerical models is the ability to change a variable, thereby determining the degree of its influence on the system being modelled. The effects of a change in soil moisture, the degree of moisture complexity activated and a finer grid resolution on the characteristics, development and structure of tropical-temperate troughs will be investigated in the following chapter.

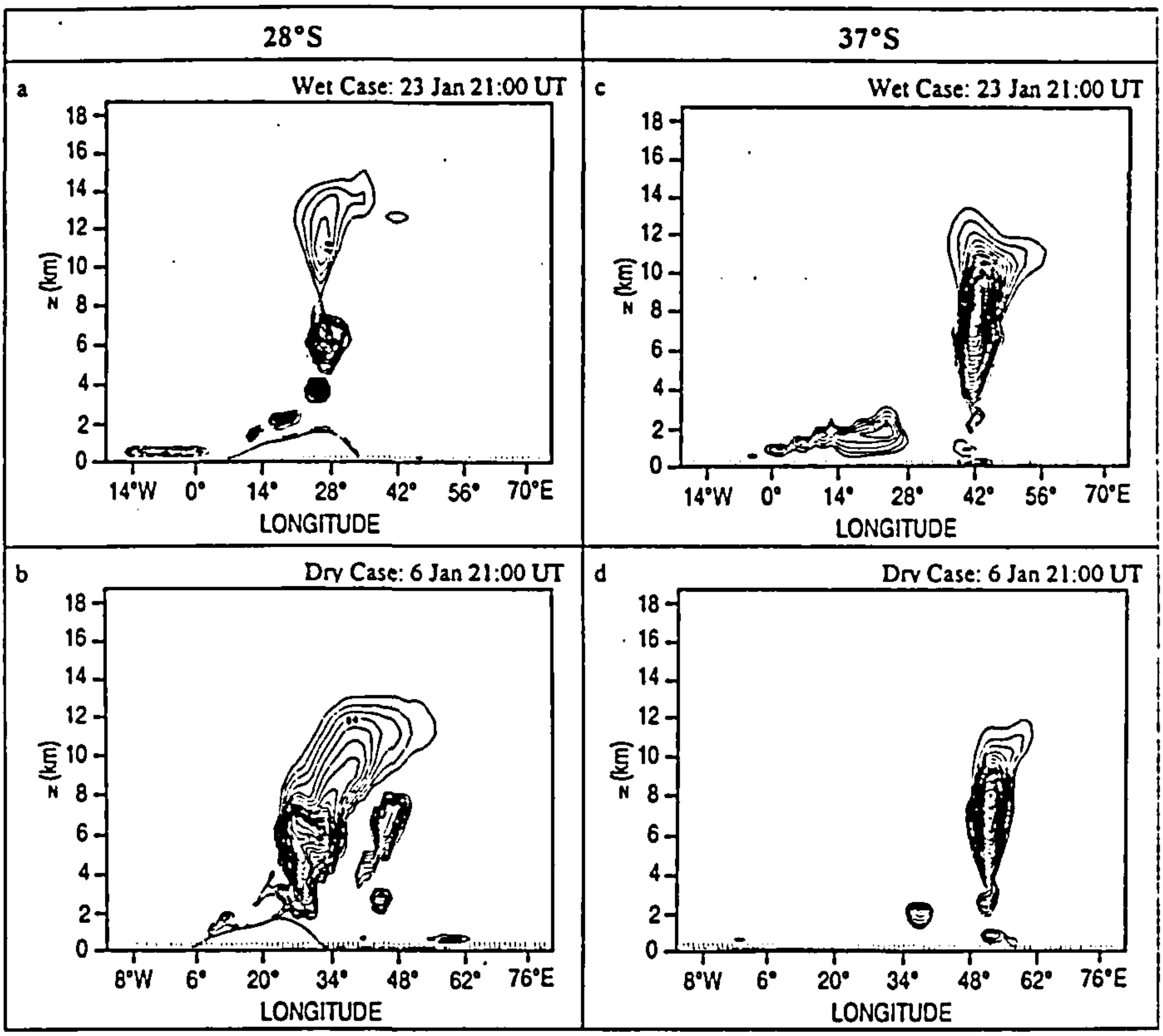

Figure 5.29: Cloud water mixing ratio along 28°S for the (a) wet and (b) dry case control runs, and along 37°S for the (c) wet and (d) dry case control runs ($g.kg^{-1}$; contour interval 0,1 $g.kg^{-1}$ for a, 0,3 $g.kg^{-1}$ for b-d; labels multiplied by 10^{2}).

Synopsis

The simulated thermodynamic, kinematic and moisture characteristics of tropical-temperate troughs have been investigated. Previous observations of a more complex Walker circulation, the Hadley- and Ferrel-type circulation patterns and the transport of warm, moist tropical air along the cloud band have been corroborated by the model. New aspects of the development, dissipation and actual structure of tropical-temperate troughs have been revealed by the model. These include the importance of the temperate link with the westerly wave, the function of the tropical low, dissipation of the tropical-temperate trough with the eastward movement of the westerly wave and an increase in cloud top heights with latitude along the cloud band.

CHAPTER 6

EFFECTS OF GRID RESOLUTION, RESOLVABLE MICROPHYSICS AND SOIL MOISTURE

Introduction

Important factors influencing the performance of mesoscale models include the boundary conditions which determine the interaction of the model domain with the external factors, the grid resolution which determines how effectively the mesoscale circulation is resolved and the moisture schemes and degree of moisture complexity activated. The output of sensitivity tests performed to determine the influence of these factors when utilising RAMS will be the focus of this chapter. Although the sensitivity tests were performed for both the wet and dry case studies, the concentration will be on the wet case study and supplemented with output from the dry case study when necessary.

Higher Resolution Sensitivity

All of the simulations discussed so far were performed using a coarse grid resolution of 80 Km. At such a resolution, the mesoscale circulations associated with tropical-temperate troughs are somewhat crudely resolved. A grid resolution of 50 Km was used to determine the effects of a finer resolution on the circulation. The spatial extent of the finer grid (Fig.3.2) is necessarily smaller than the coarse grid due to computer limitations. The oceanic region to the northwest of Madagascar, which is an important water vapour source for tropical-temperate troughs during late summers, cannot be included in the model domain. Apart from changing the grid resolution, no other changes were made to the model setup. Differences between the coarse control run and the finer resolution sensitivity test can therefore be attributed either to the change in the grid resolution or to the change in position of the lateral boundaries in relation to the tropical-temperate trough system.

Streamlines

The most significant differences between the coarse control run and the finer resolution sensitivity tests occur at the surface during the initial stages and at 700 hPa during the dissipative stages of the cloud band development. On the morning of 23 January (Day 2), onshore flow occurs at the surface along the Natal coast in the finer resolution run (Fig. 6.1b), compared with the poleward flow in this region in the control run (Fig. 4.1b). By 24 January (Day 3), the development (Fig. 6.2d) and movement (Fig. 6.2e) of the cut-off low resulting in the Laingsburg flood is obvious in the streamlines of the finer resolution output at 700 hPa. This low was not adequately resolved by the coarse resolution of the control run (Fig. 4.2f). The closed low is a smaller-scale system and this result is not therefore surprising. The simulated cut-off low is situated slightly further northwest than the actual event (Fig. 6.3), but follows the observed course of development quite closely. Very little difference is apparent between the upper air streamlines of the finer resolution output (Fig. 6.4a-d) and those of the coarse control run (Fig. 4.4a-f).

Pressure

The cut-off low is obvious on 24 January (Day 3) in the pressure fields at the 700 hPa level in the finer resolution run (Fig. 6.5c) but not in the control run (Fig. 4.6c), which again is attributable to the improved resolution of the circulation when using the finer grid. The modelled separation of the westerly trough from the mainstream westerly flow during the mature stages (Day 2), evident in the finer resolution pressure fields at both the 700 hPa (Fig. 6.5b) and 300 hPa (Fig. 6.5e) levels, shows a higher degree of correspondence with the SAWB upper air charts (Figs 2.5b; 2.6b) than those of the control run. The reduced mean sea level pressure (Fig. 6.6) and the pressure at 700 hPa (Fig. 6.5a-c) and 300 hPa (Fig. 6.5d-f) are initially higher in the finer resolution sensitivity test than those of the control run, but become significantly lower during the mature stages (Day 2) of the cloud band development.

a

b

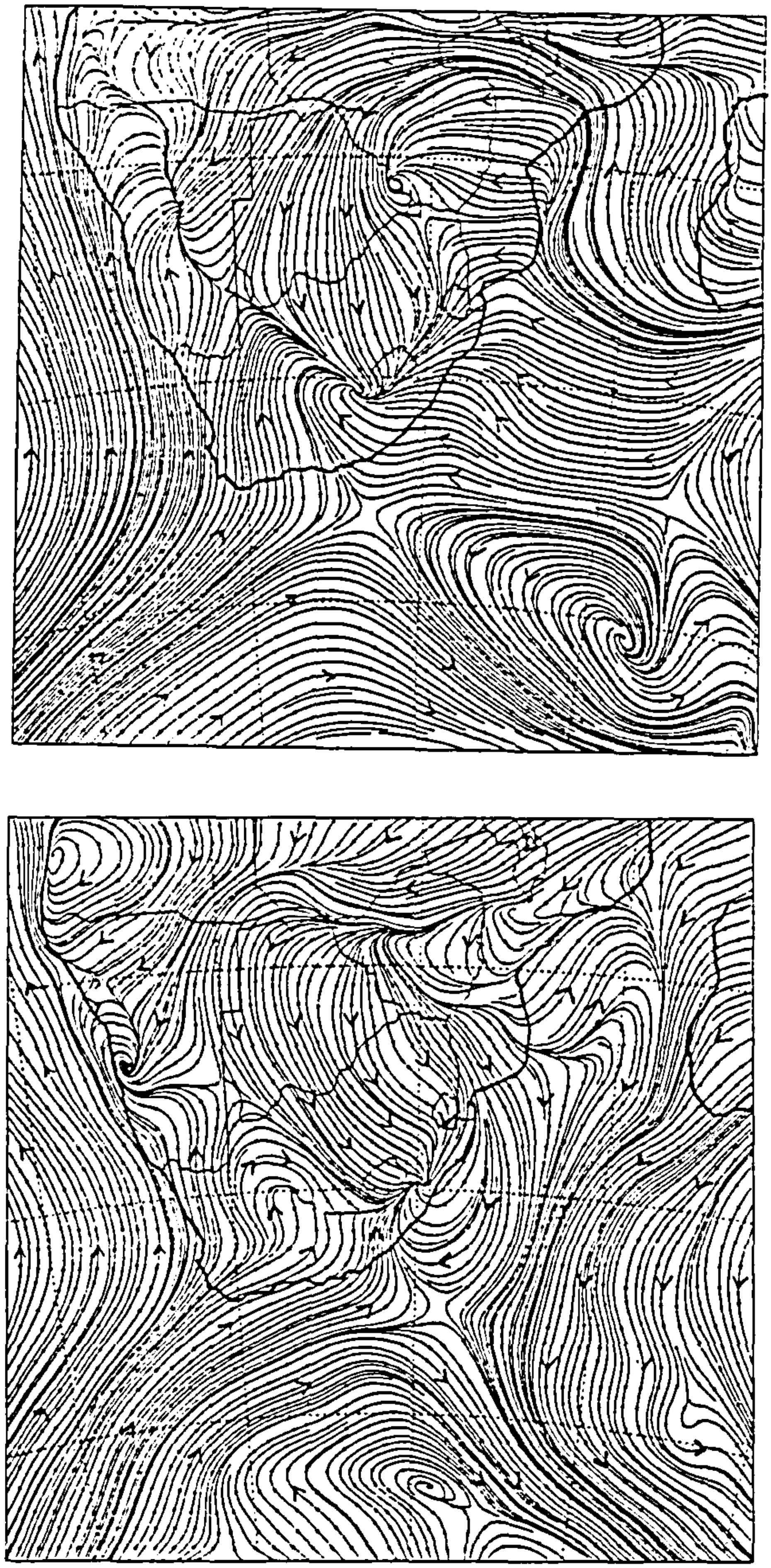

Figure 6.1: Surface streamlines (on the terrain-following coordinate surface 146,4 m above the ground) from the finer resolution sensitivity test at (a) 22 Jan 15:00 UT and (b) 23 Jan 9:00 UT.

c

d

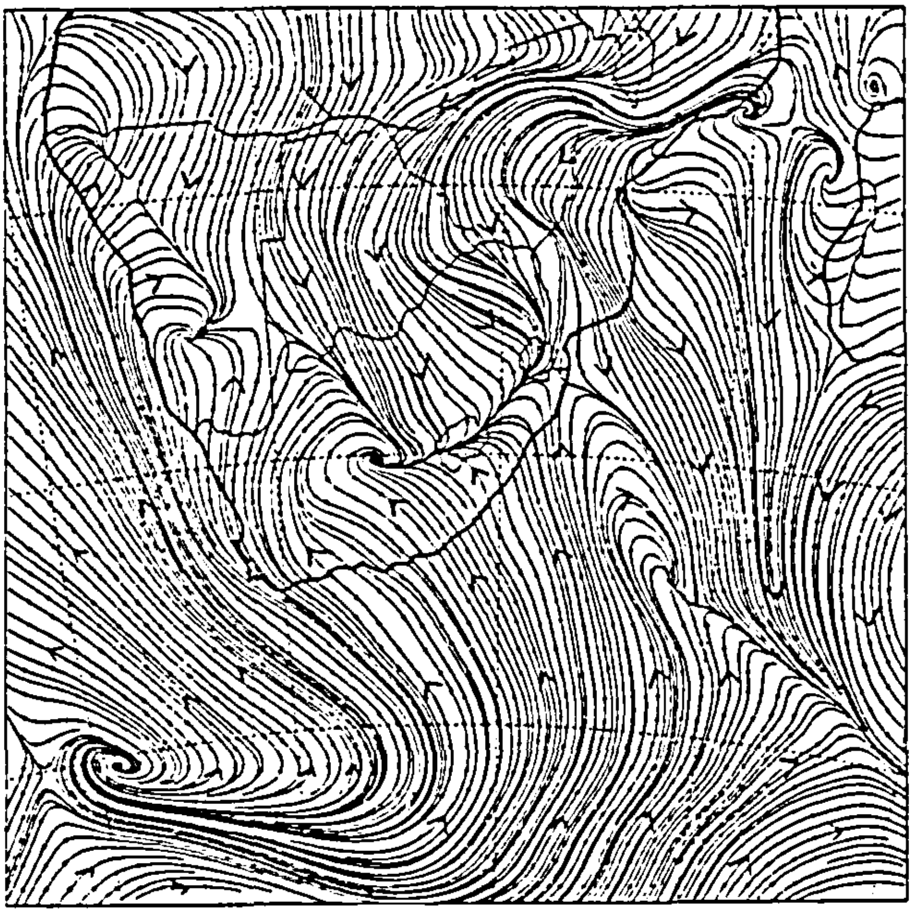

Figure 6.1 cont: Surface streamlines (on the terrain-following coordinate surface 146,4 m above the ground) from the finer resolution sensitivity test at (c) 23 Jan 21:00 UT and (d) 24 Jan 12:00 UT.

a

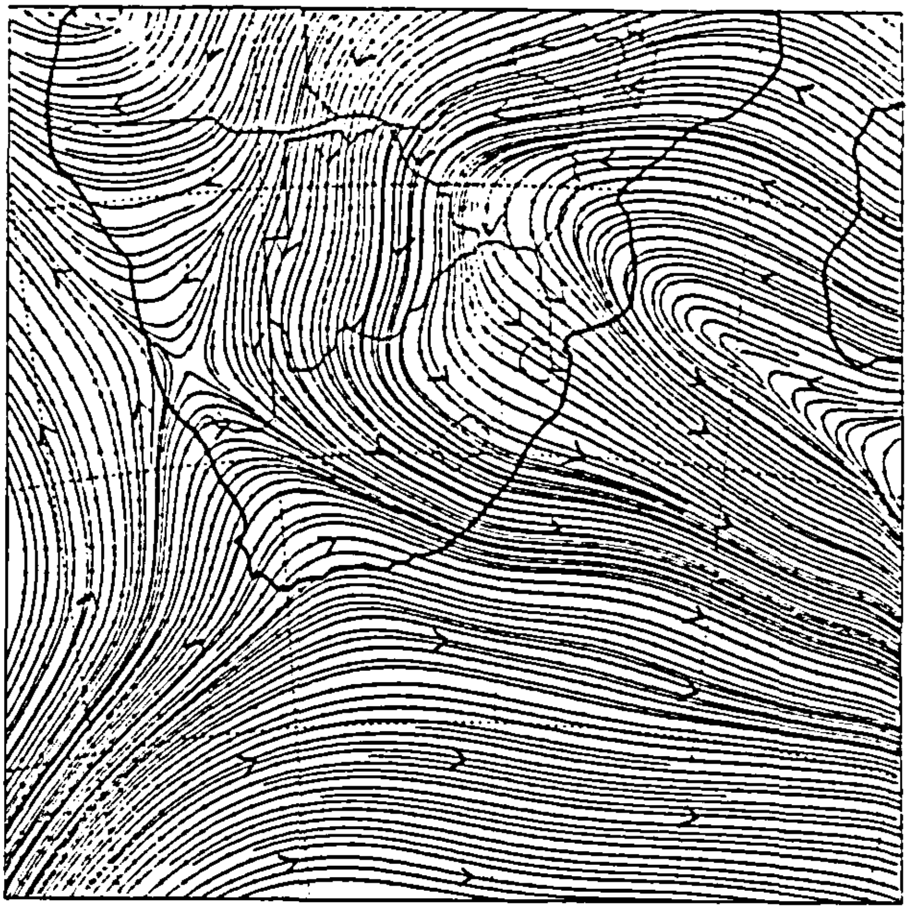

b

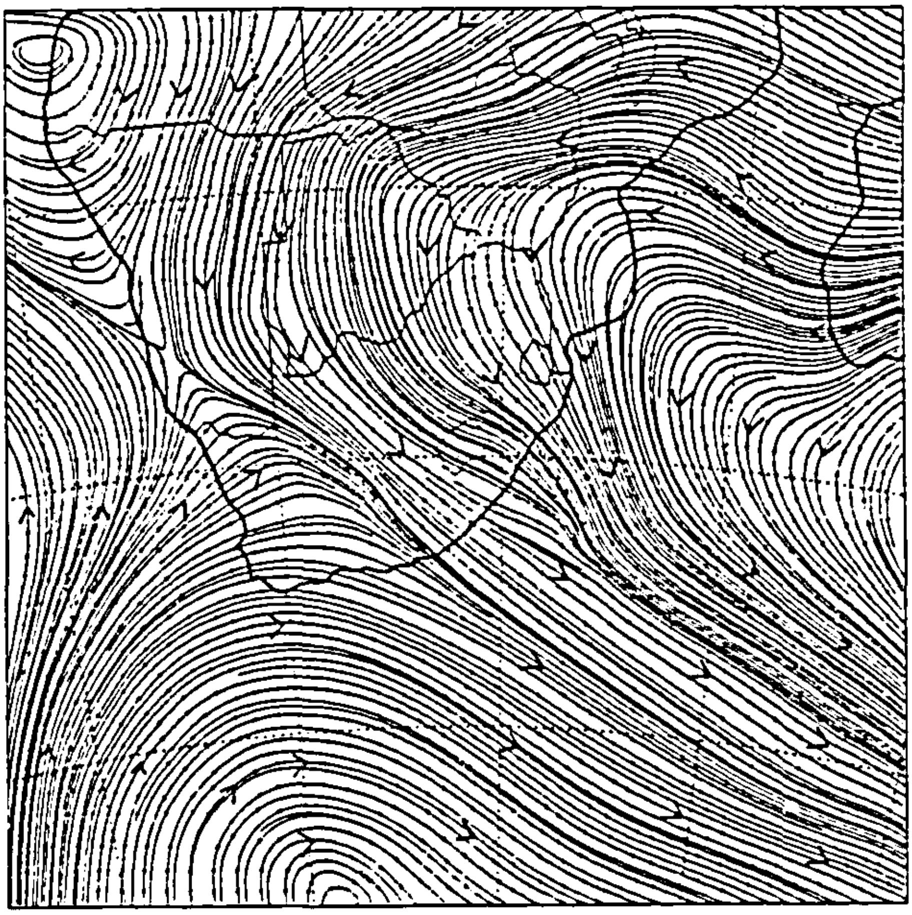

Figure 6.2: Streamlines at 3,13 km (~ 700 hPa) above sea level from the finer resolution sensitivity test at (a) 22 Jan 15:00 UT and (b) 23 Jan 9:00 UT.

c

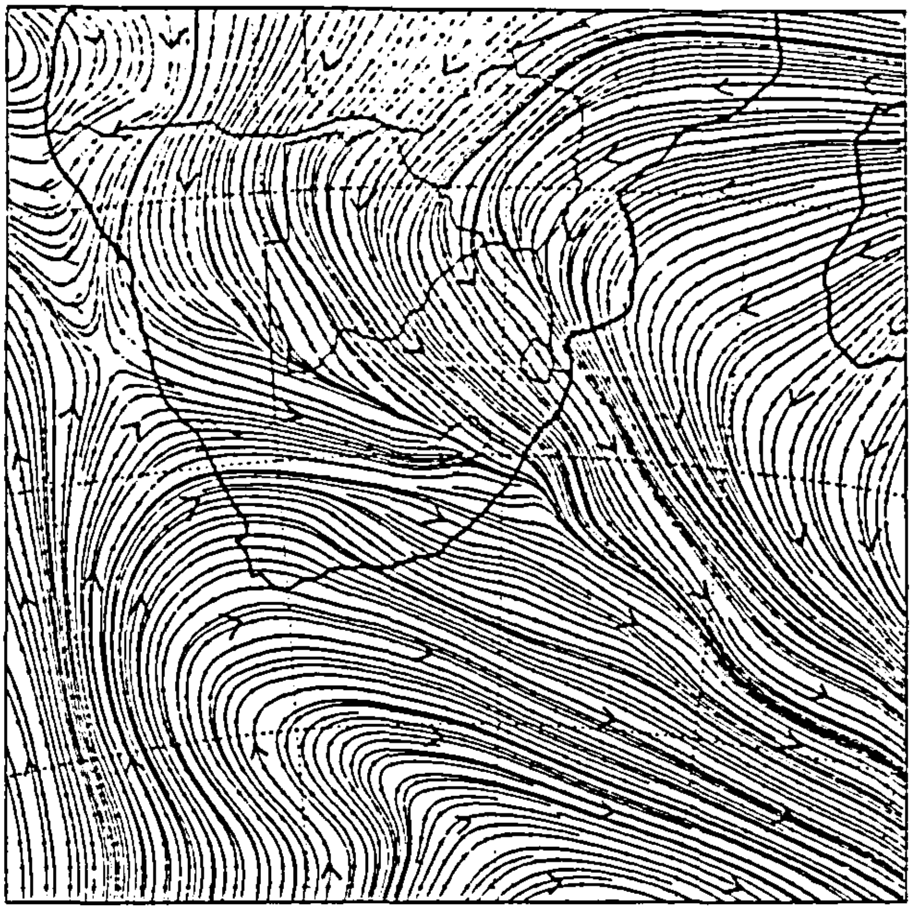

d

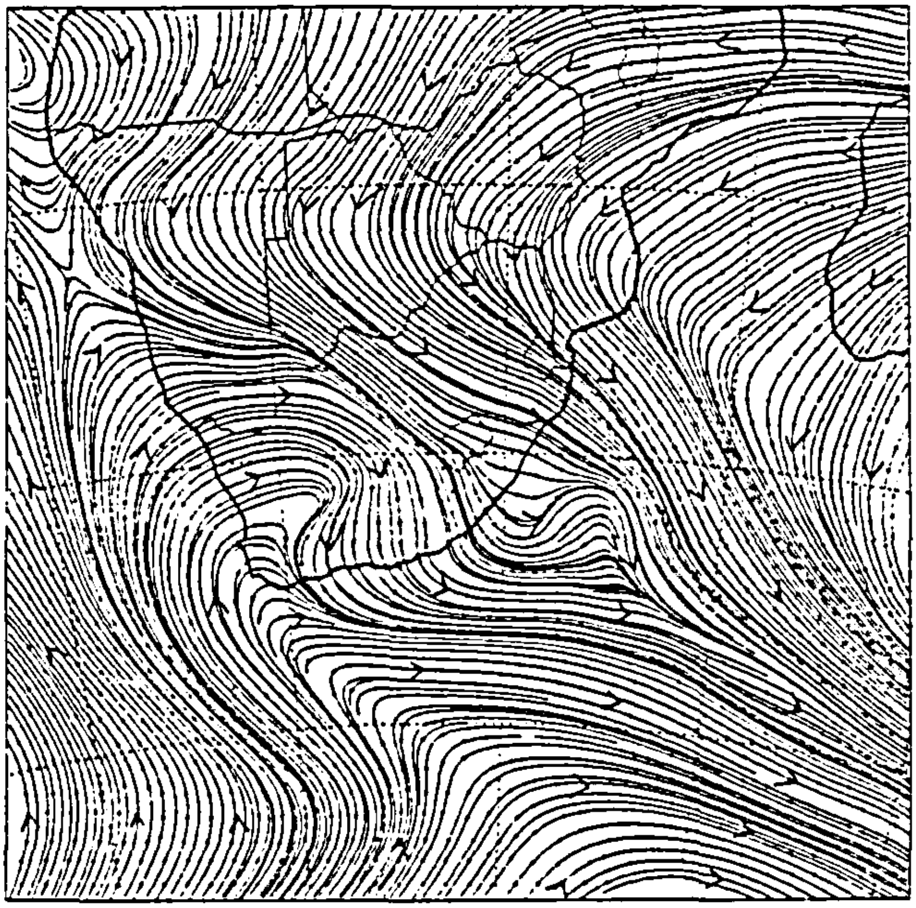

Figure 6.2 cont: Streamlines at 3,13 km (~ 700 hPa) above sea level from the finer resolution sensitivity test at (c) 23 Jan 21:00 UT and (d) 24 Jan 6:00 UT.

e

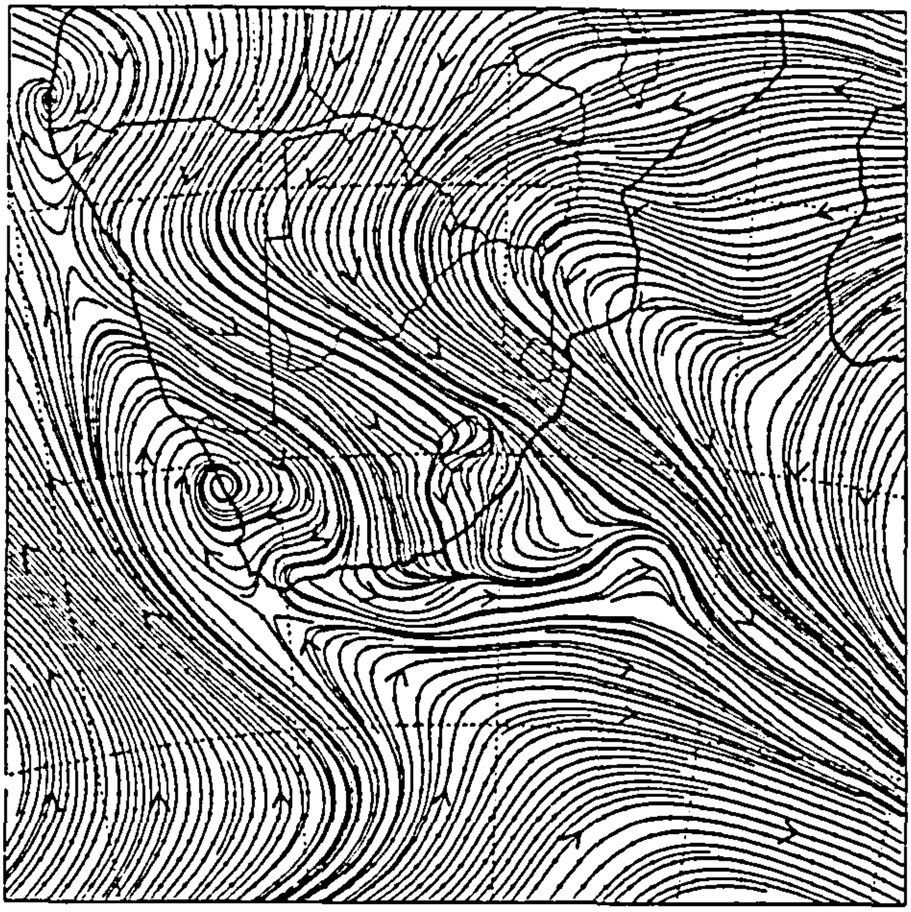

Figure 6.2 cont: Streamlines at 3,13 km (~ 700 hPa) above sea level from the finer resolution sensitivity test at (e) 24 Jan 12:00 UT.

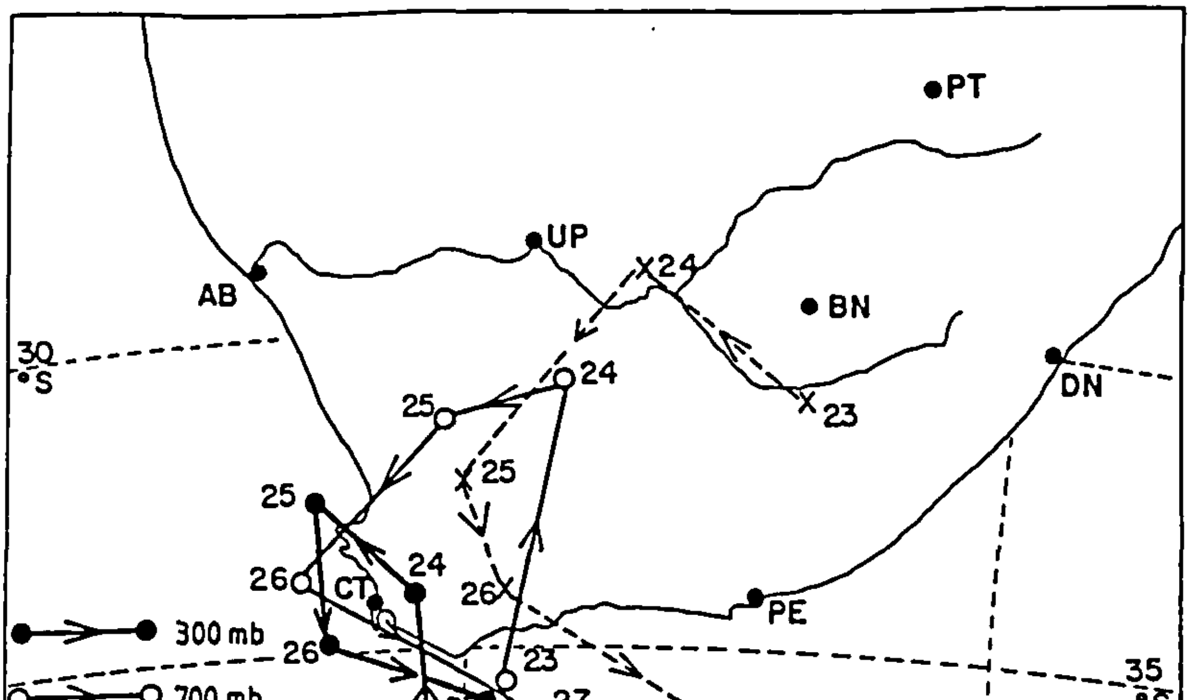

Figure 6.3: Tracks of the surface, 700 and 300 hPa lows on 23 to 27 January 1981 (after Taljaard, 1985).

a

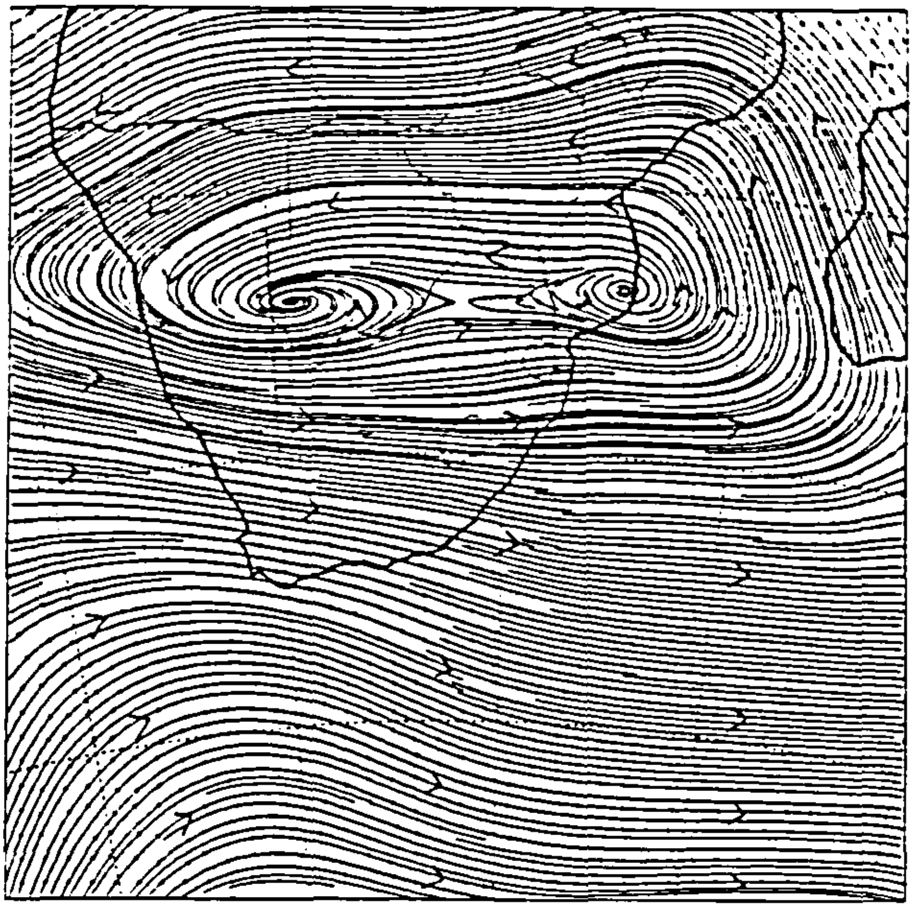

b

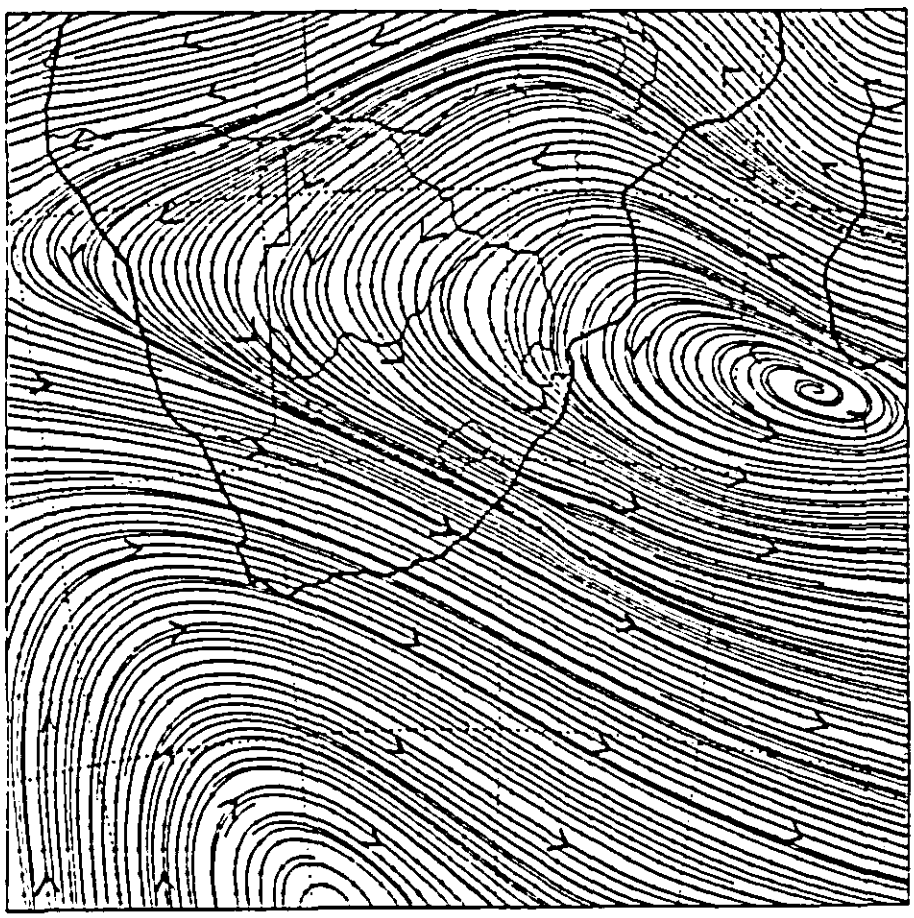

Figure 6.4: Streamlines at 9,66 km (~ 300 hPa) above sea level from the finer resolution sensitivity test at (a) 22 Jan 15:00 UT and (b) 23 Jan 9:00 UT.

c

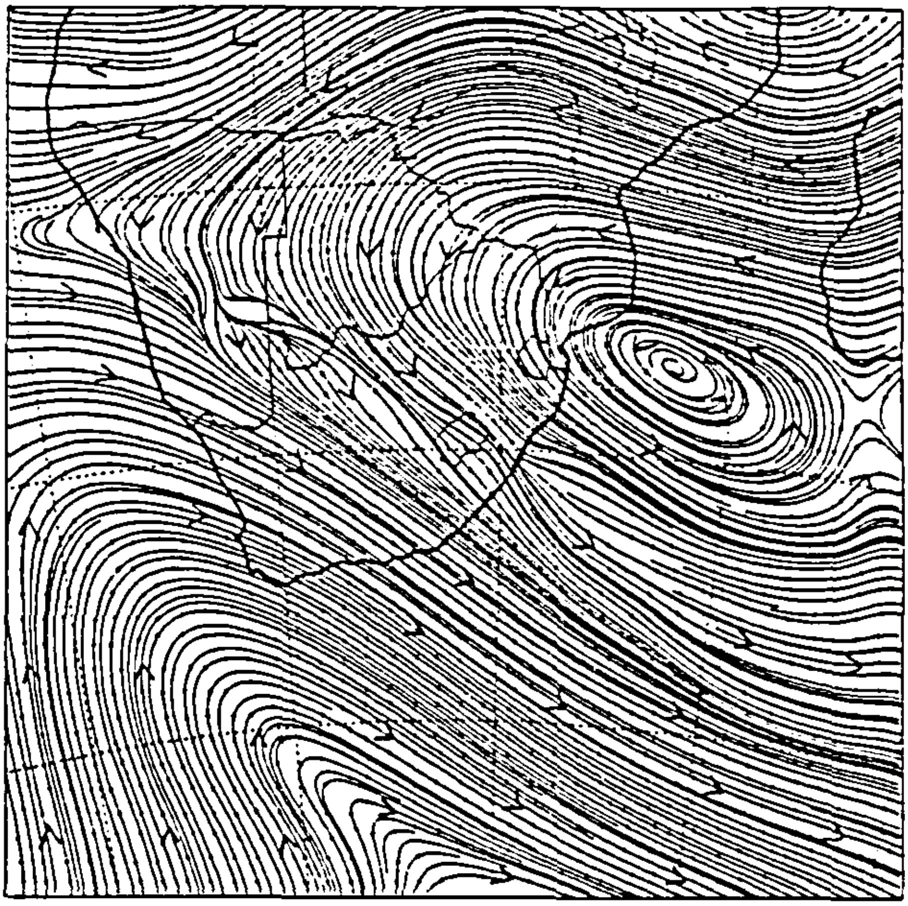

d

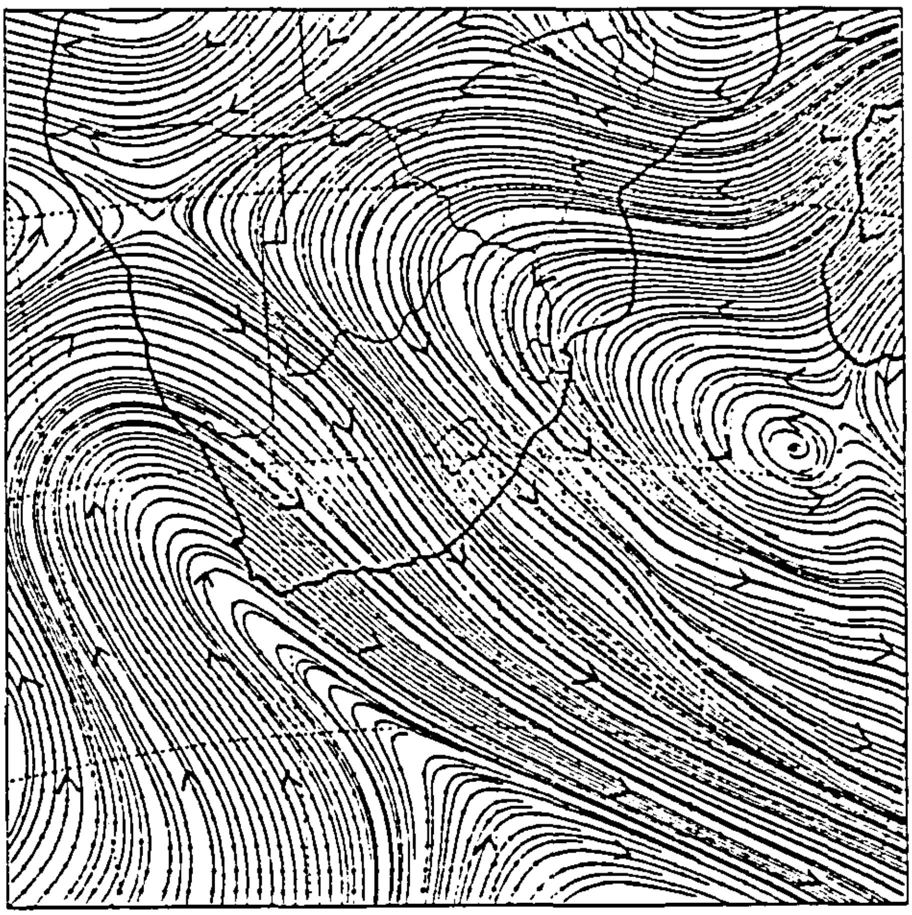

Figure 6.4 cont: Streamlines at 9,66 km (~ 300 hPa) above sea level from the finer resolution sensitivity test at (c) 23 Jan 21:00 UT and (d) 24 Jan 12:00 UT.

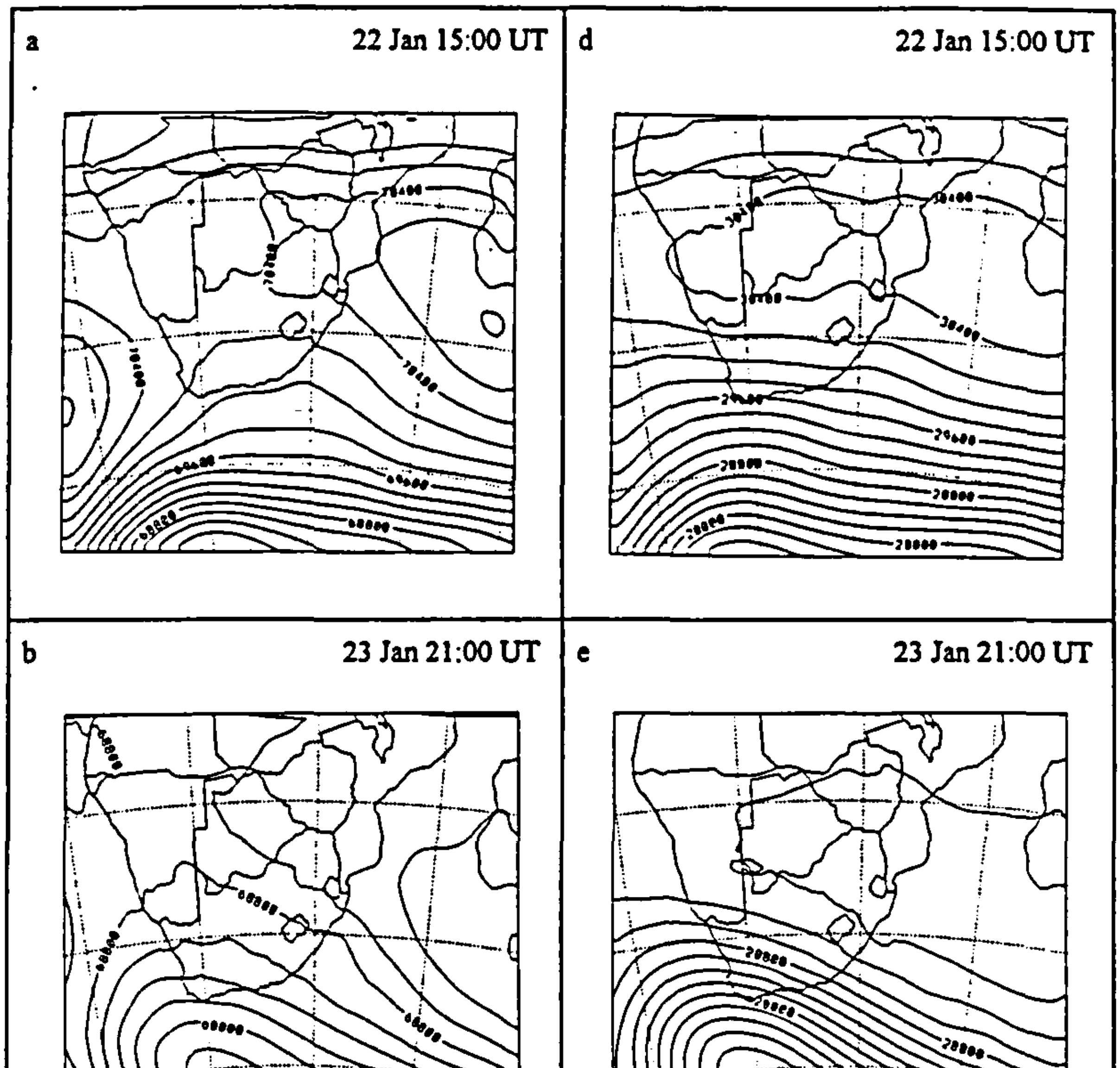

Figure 6.5: Pressure at 3,13 km (~ 700 hPa) above sea level from the finer resolution sensitivity test at (a) 22 Jan 15:00 UT, (b) 23 Jan 21:00 UT and (c) 24 Jan 12:00 UT, and at 9,66 km above sea level from the finer resolution sensitivity test at (d) 22 Jan 15:00 UT, (e) 23 Jan 21:00 UT and (f) 24 Jan 12:00 UT (Pa, contour interval of 200 Pa).

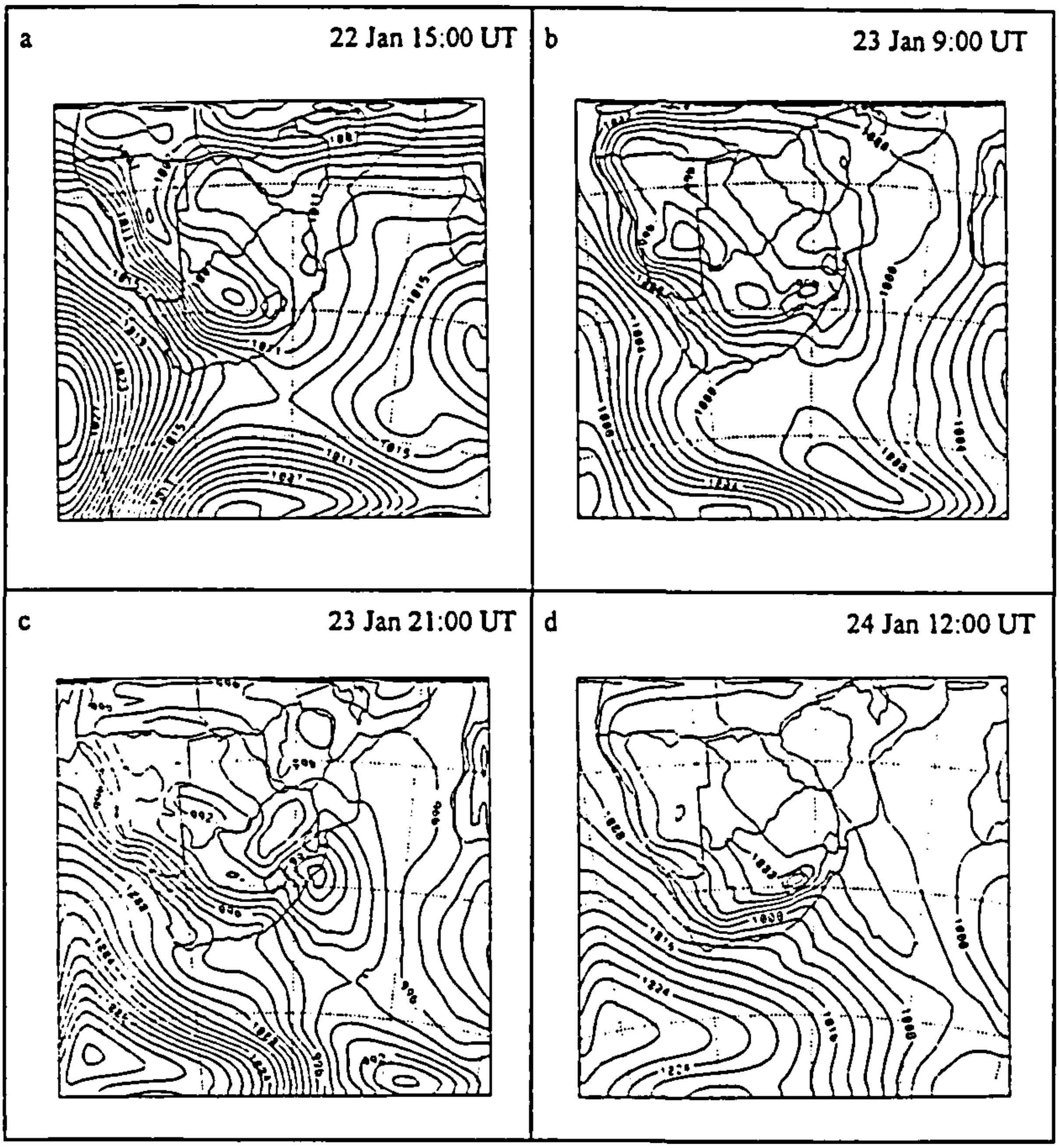

Figure 6.6: Reduced mean sea level pressure field from the finer resolution sensitivity test at (a) 22 Jan 15:00 UTC, (b) 23 Jan 15:00 UTC, (c) 23 Jan 21:00 UTC and (d) 24 Jan 12:00 UTC (hPa, contour interval of 1 hPa for a-c, 2 hPa for d).

During the dissipative stages (Day 3), the finer resolution pressures are still slightly lower than those of the control run.

Vertical Velocity

The modelled vertical velocity fields at 700 hPa of the finer resolution sensitivity test (Fig. 6.7a-f) are similar to those of the coarse control run in a qualitative sense (Fig. 4.7a-f), with the exception of the vertical uplift associated with the cut-off low over the southwestern Cape and the uplift of the onshore flow around the ridging anticyclone along the southern Cape coastal belt, which are simulated better in the finer resolution run. However, significant differences exist throughout the troposphere (Figs 6.7a-f, 6.8a-f) when considering the magnitude of the vertical uplift. The largest differences occur during the dissipative stages of the tropical-temperate trough (Figs 4.7d-f, 6.7d-f). These are associated with the vertical uplift in the Natal Drakensberg region, with the cut-off low and with the cold front following the break of the temperate link (Fig. 6.7f). Vertical uplift along the actual tropical-temperate trough is only moderately larger in the finer resolution output. The greater vertical velocities in the finer resolution sensitivity tests can be attributed to the improved resolution of the vertical uplift by the finer grid. The differences would be further enhanced by the convective nature of these systems. The more accurate resolution of the topography along the Drakensberg in the finer resolution run may also explain the discrepancies in the region of the mountain range. As no vertical velocity data are available, it is difficult to determine how closely the model output corresponds with the actual event in a qualitative sense.

The vertical velocity fields at 700 hPa from the finer resolution dry case sensitivity test (Fig. 6.9a-d) and those from the dry case control run (Fig. 4.19a-d) reveal a greater degree of correspondence than those of the wet case study. The intensification of the tropical low, evident toward the end of the simulation in the control run (Fig. 4.19c,d), is not apparent in the finer resolution sensitivity test (Fig. 6.9c,d). This is probably due to the close proximity of the lateral border to the system in this region. The magnitudes of the finer resolution vertical uplift are only slightly greater than those of the control run in the dry case.

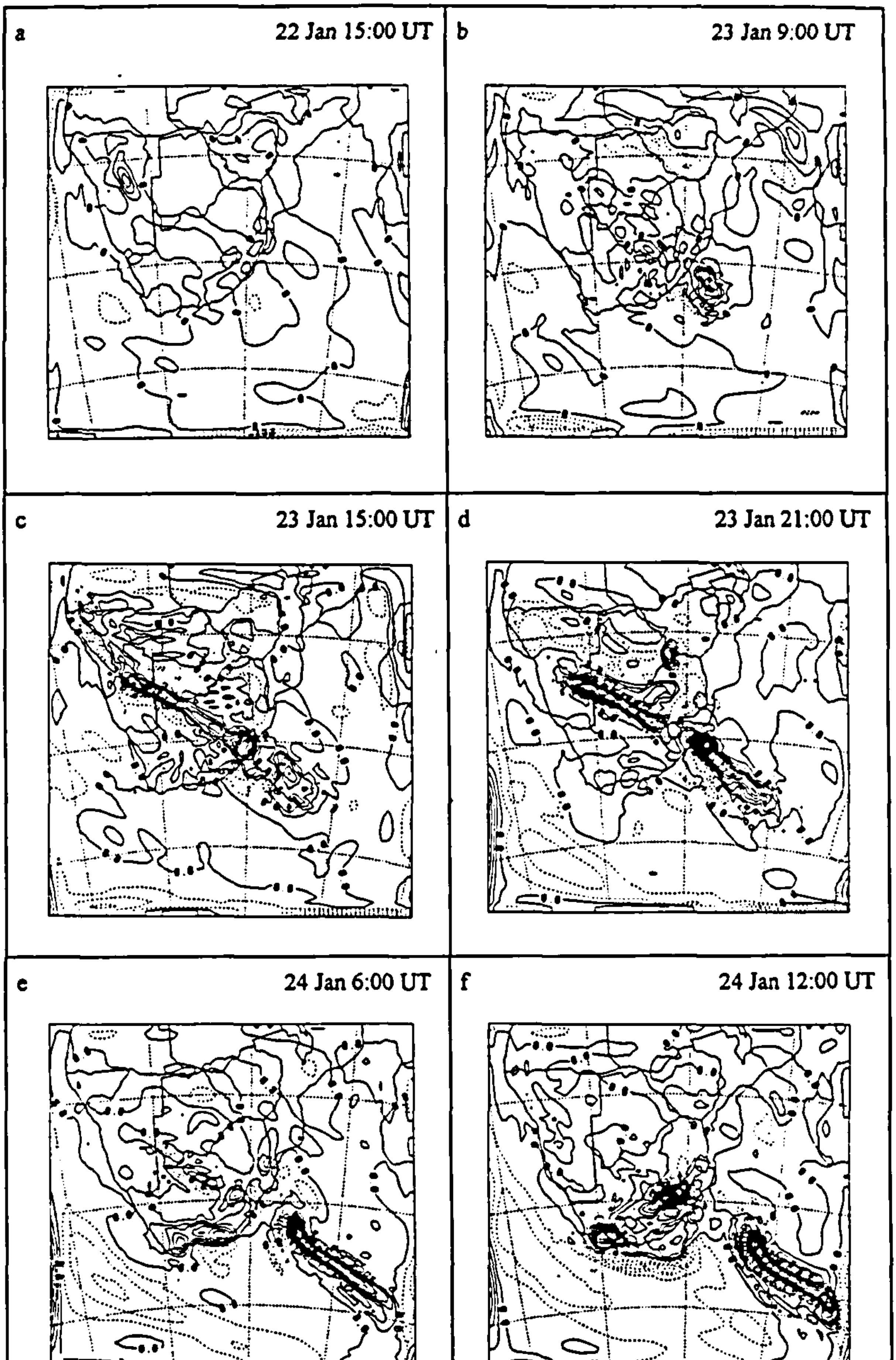

Figure 6.7: Vertical velocity at 3,13 km (~ 700 hPa) above sea level from the finer resolution sensitivity test at (a) 22 Jan 15:00 UT, (b) 23 Jan 9:00 UT, (c) 23 Jan 15:00 UT, (d) 23 Jan 21:00 UT, (e) 24 Jan 6:00 UT and (f) 24 Jan 12:00 UT ($cm.s^{-1}$; contour interval of 2 $cm.s^{-1}$; labels multiplied by 10^{-2}; solid lines indicate uplift and dashed lines indicate subsidence).

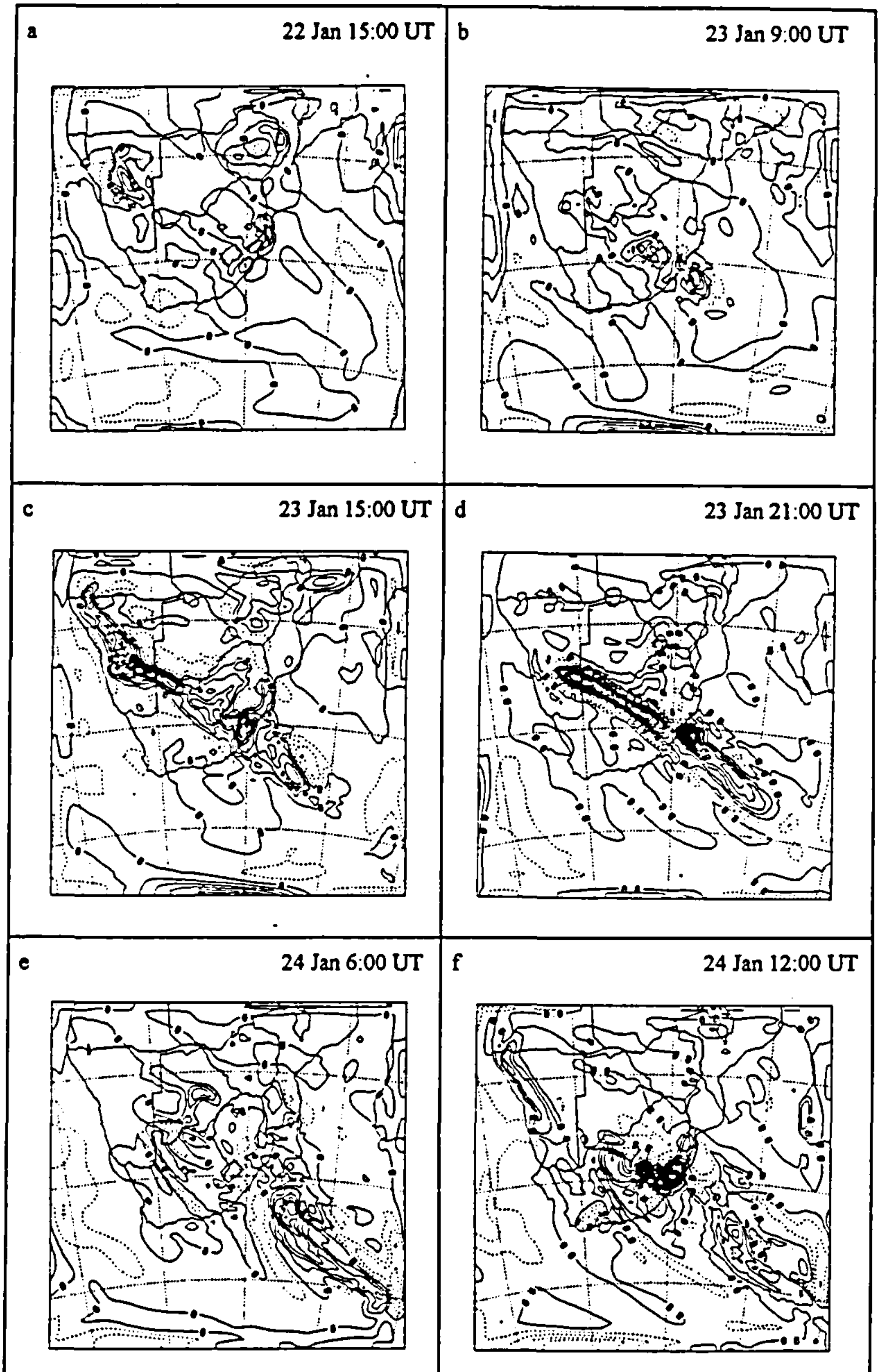

Figure 6.8: Vertical velocity at 9,66 km (~ 300 hPa) above sea level from the finer resolution sensitivity test at (a) 22 Jan 15:00 UT, (b) 23 Jan 9:00 UT, (c) 23 Jan 15:00 UT, (d) 23 Jan 21:00 UT, (e) 24 Jan 6:00 UT and (f) 24 Jan 12:00 UT (cm.s^{-1}; contour interval of 3 cm.s^{-1}; labels multiplied by 10; solid lines indicate uplift and dashed lines indicate subsidence).

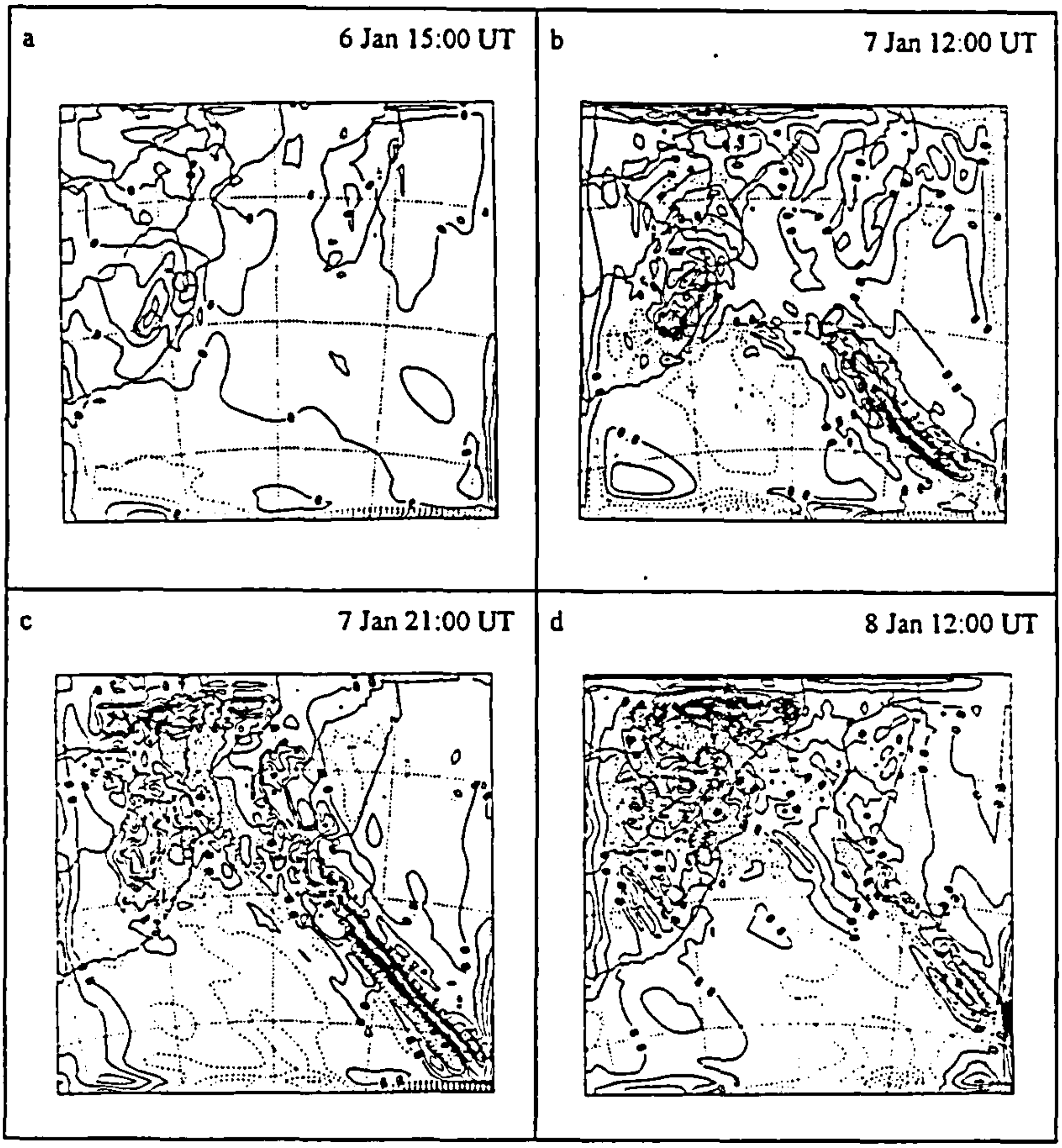

Figure 6.9: Vertical velocity at 3.13 km (~ 700 hPa) above sea level from the finer resolution sensitivity test for the dry case study at (a) 6 Jan 15:00 UTC, (b) 7 Jan 12:00 UTC, (c) 7 Jan 21:00 UTC, and (d) 8 Jan 12:00 UTC (cm.s^{-1}; contour interval of 2 cm.s^{-1}; labels multiplied by 10^{-2}; solid lines indicate uplift and dashed lines indicate subsidence).

Convective Precipitation Rate

Differences between the convective precipitation rates of the coarse control run (Fig. 4.10) and the finer resolution sensitivity test (Fig. 6.10) include the presence of convective precipitation over the southwestern Cape in association with the cut-off low toward the end of the simulation; the greater southward extension of the convective precipitation in the coarse control run, the reason for which is not immediately obvious; and the higher convective precipitation rate in the finer resolution output, which is not surprising given the larger vertical velocities generated using a finer grid resolution. The accumulative convective precipitation from the finer resolution sensitivity test is indicative of the presence of the cloud band (Fig. 6.11), but does not extend as far south as the coarse control run (Fig. 4.11). The maximum accumulated convective precipitation for the finer resolution run is slightly greater (4 mm) than that of the control run as a result of the greater convective precipitation rates. However, the fact that the finer resolution convective precipitation total is not significantly larger than that of the coarse control run adds credibility to the numerical model.

The convective precipitation rates from the dry case finer resolution sensitivity test (Fig. 6.12a-d) are generally greater than those of the dry case control run (Fig. 4.21a-d). However, the regions of convective precipitation match closely. The maximum accumulated convective precipitation from the dry case sensitivity test (Fig. 6.13) is also greater (4 mm) than that of the dry case control run (Fig. 4.22) from the dry case sensitivity test (Fig. 6.13) is also greater (4 mm) than that of the dry case control run (Fig. 4.22) and again can be attributed to the greater vertical velocities. The accumulated convective precipitation for both the wet and dry case finer-resolution sensitivity tests still grossly underestimates the observed accumulated rainfall.

Mixing Ratios

During the mature and dissipative stages of the finer-resolution simulation, the region covered by total mixing ratios greater than 8,4 $g.kg^{-1}$ does not extend beyond northern Botswana and Namibia (Fig. 6.14c-f) as in the coarse control run (Fig. 5.21c-f), although mixing ratios

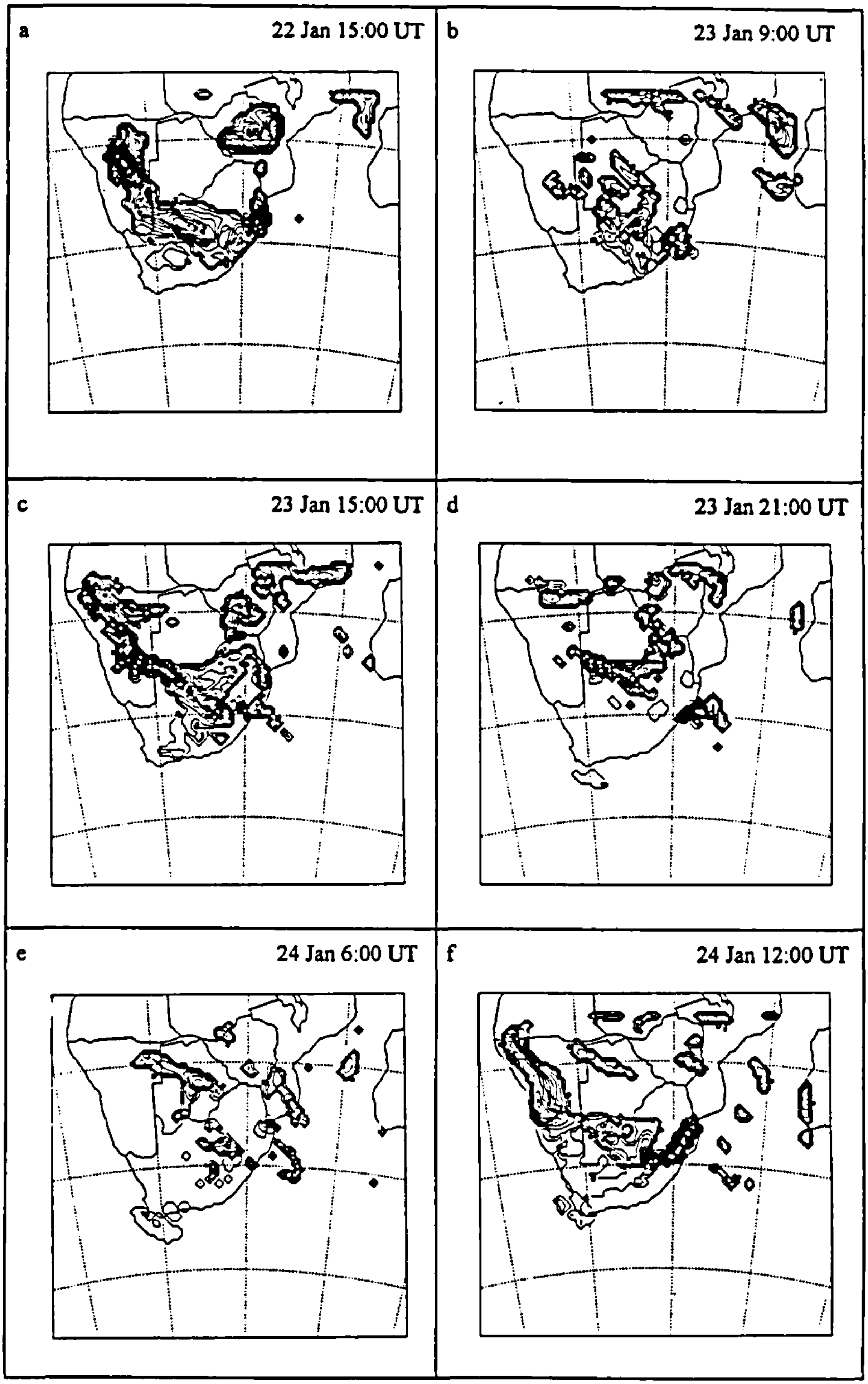

Figure 6.10: Convective parameterisation precipitation rate from the finer resolution sensitivity test at (a) 22 Jan 15:00 UT, (b) 23 Jan 9:00 UT, (c) 23 Jan 15:00 UT, (d) 23 Jan 21:00 UT, (e) 24 Jan 6:00 UT and (f) 24 Jan 12:00 UT ($mm.s^{-1}$; contour interval of 0,000035 $mm.s^{-1}$; labels multiplied by 10^7 for a-e, and by 10^6 for f).

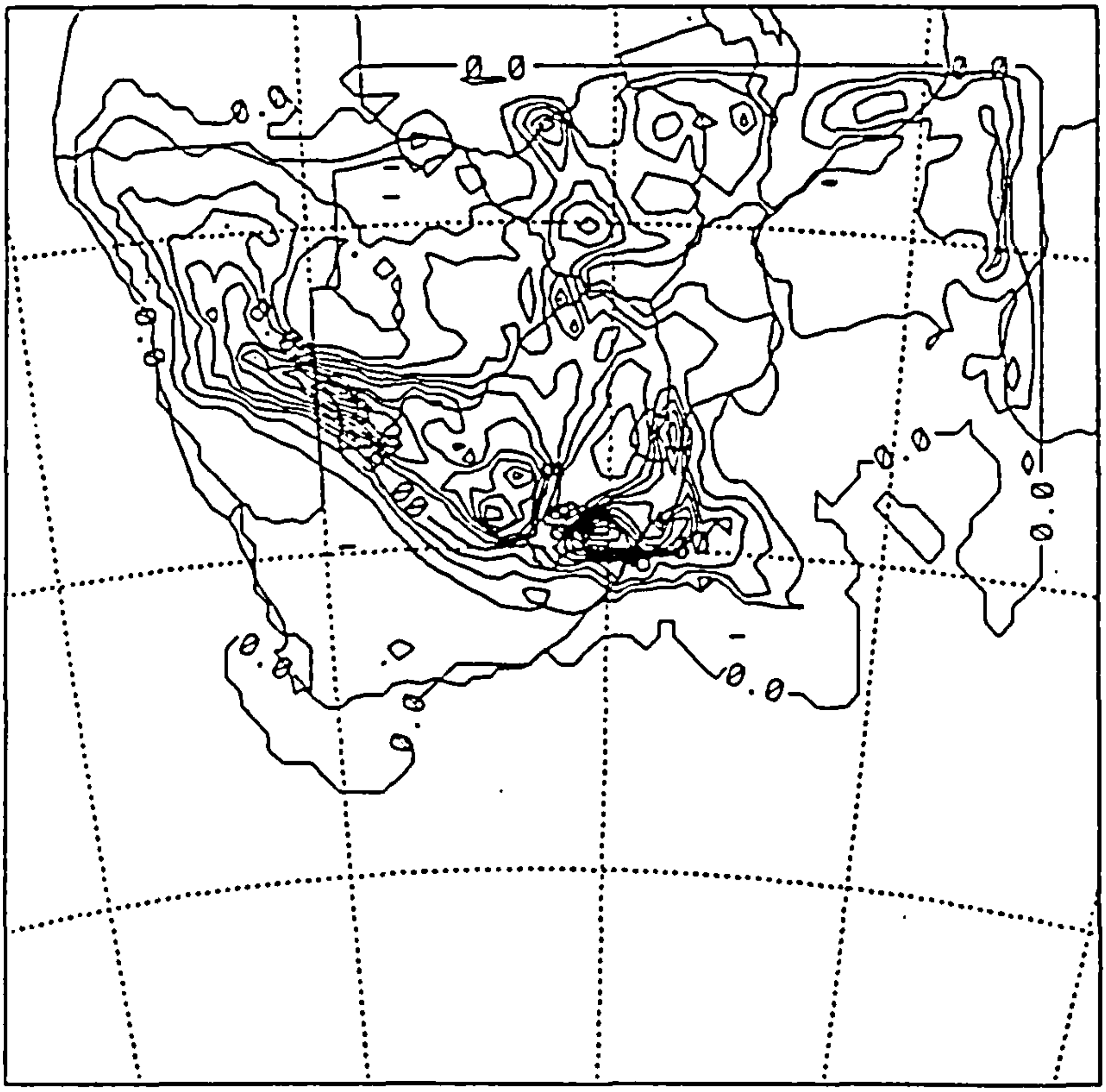

Figure 6.11: Precipitation produced by the cumulus parameterisation scheme between 22 Jan 12:00 UTC and 24 Jan 12:00 UTC from the finer resolution sensitivity test (mm; contour interval of 2 mm; maximum value of 22 mm).

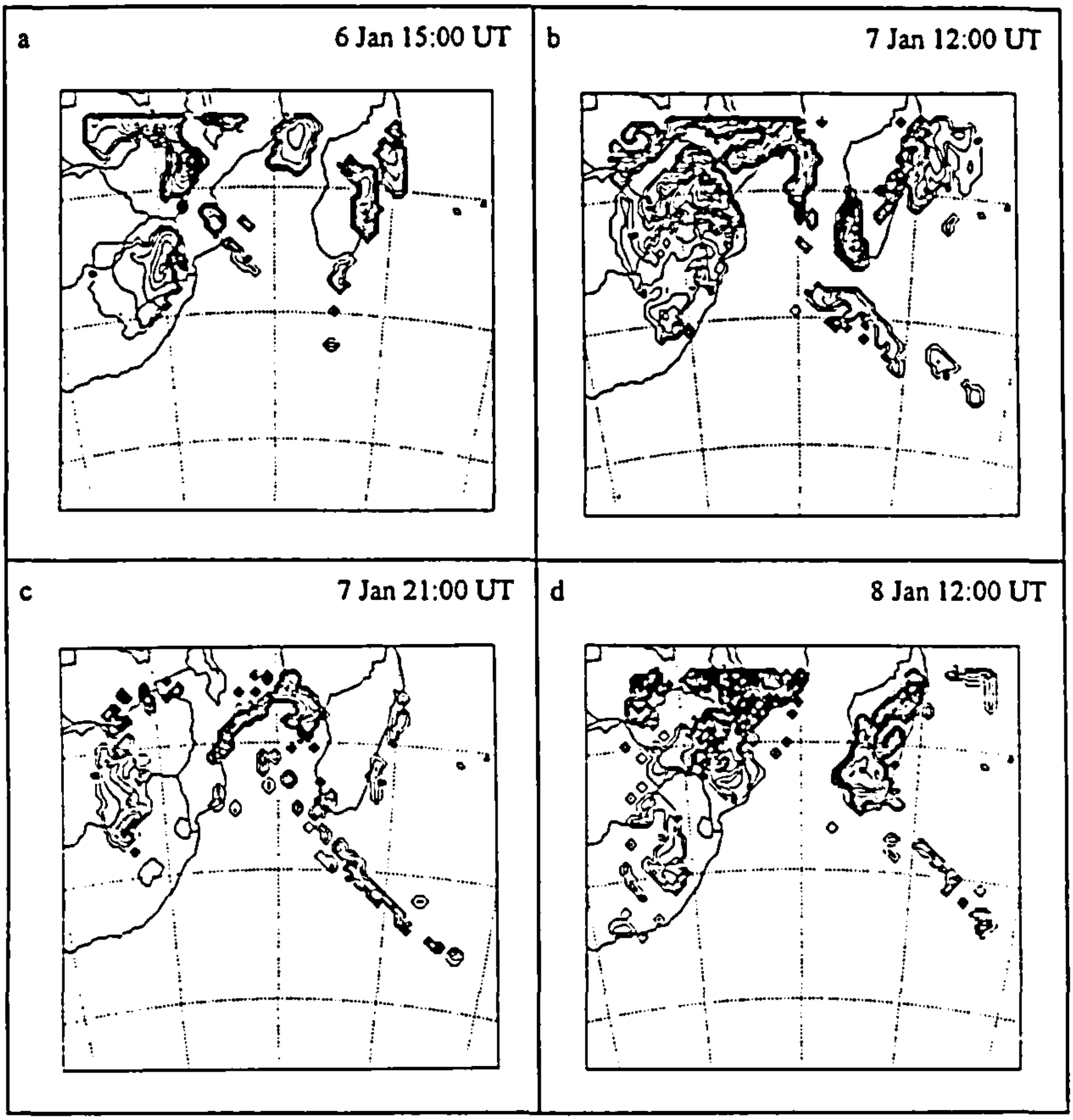

Figure 6.12: Convective parameterisation precipitation rate from the finer resolution sensitivity test for the dry case study at (a) 6 Jan 15:00 UTC, (b) 7 Jan 12:00 UTC, (c) 7 Jan 21:00 UTC, and (d) 8 Jan 12:00 UTC ($mm.s^{-1}$; contour interval of 0,000035 $mm.s^{-1}$; labels multiplied by 10^{*}).

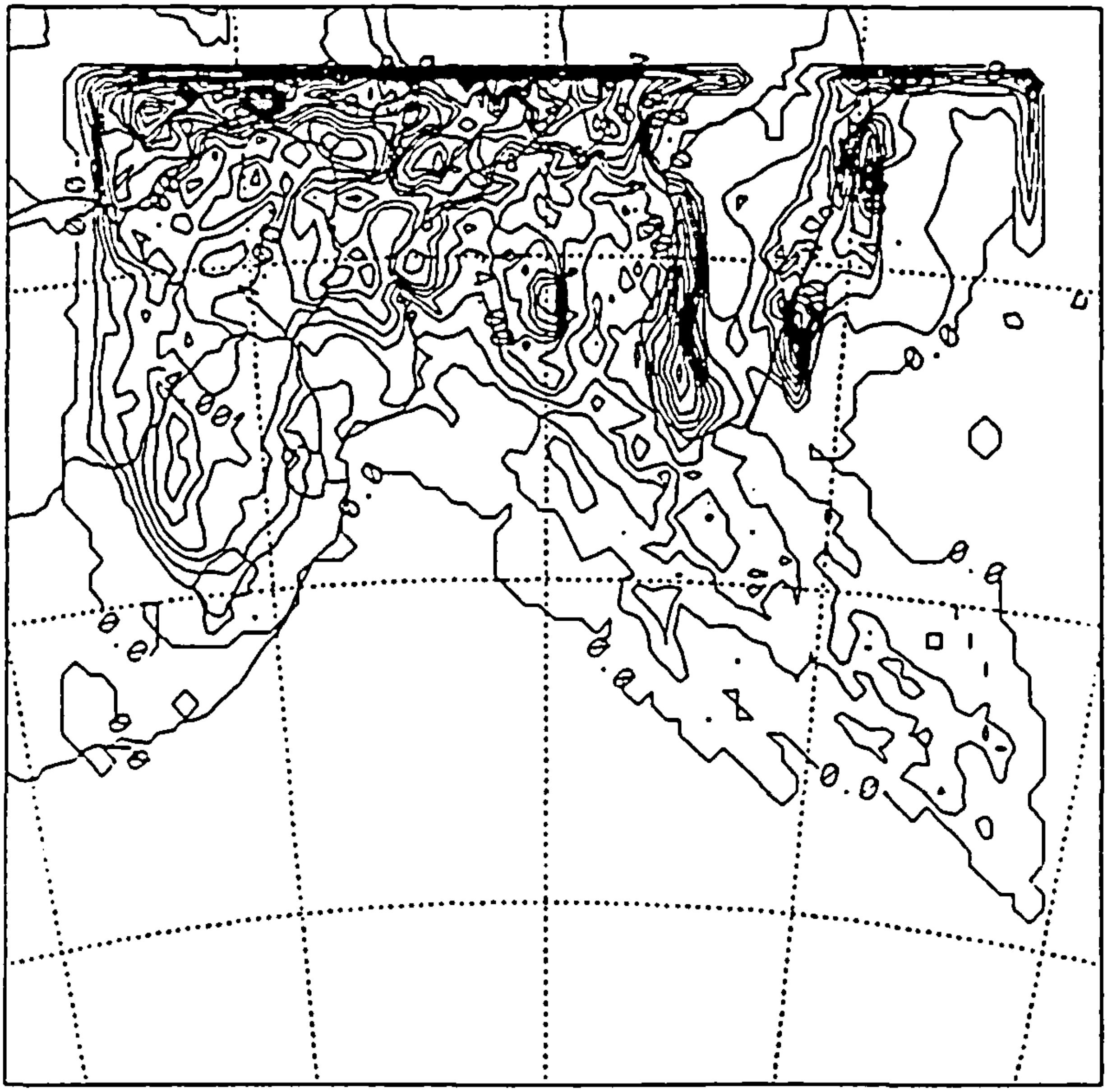

Figure 6.13: Precipitation produced by the cumulus parameterisation scheme between 6 Jan 12:00 UTC and 8 Jan 12:00 UTC from the finer resolution sensitivity test for the dry case study (mm: contour interval of 1 mm; maximum value of 17 mm).

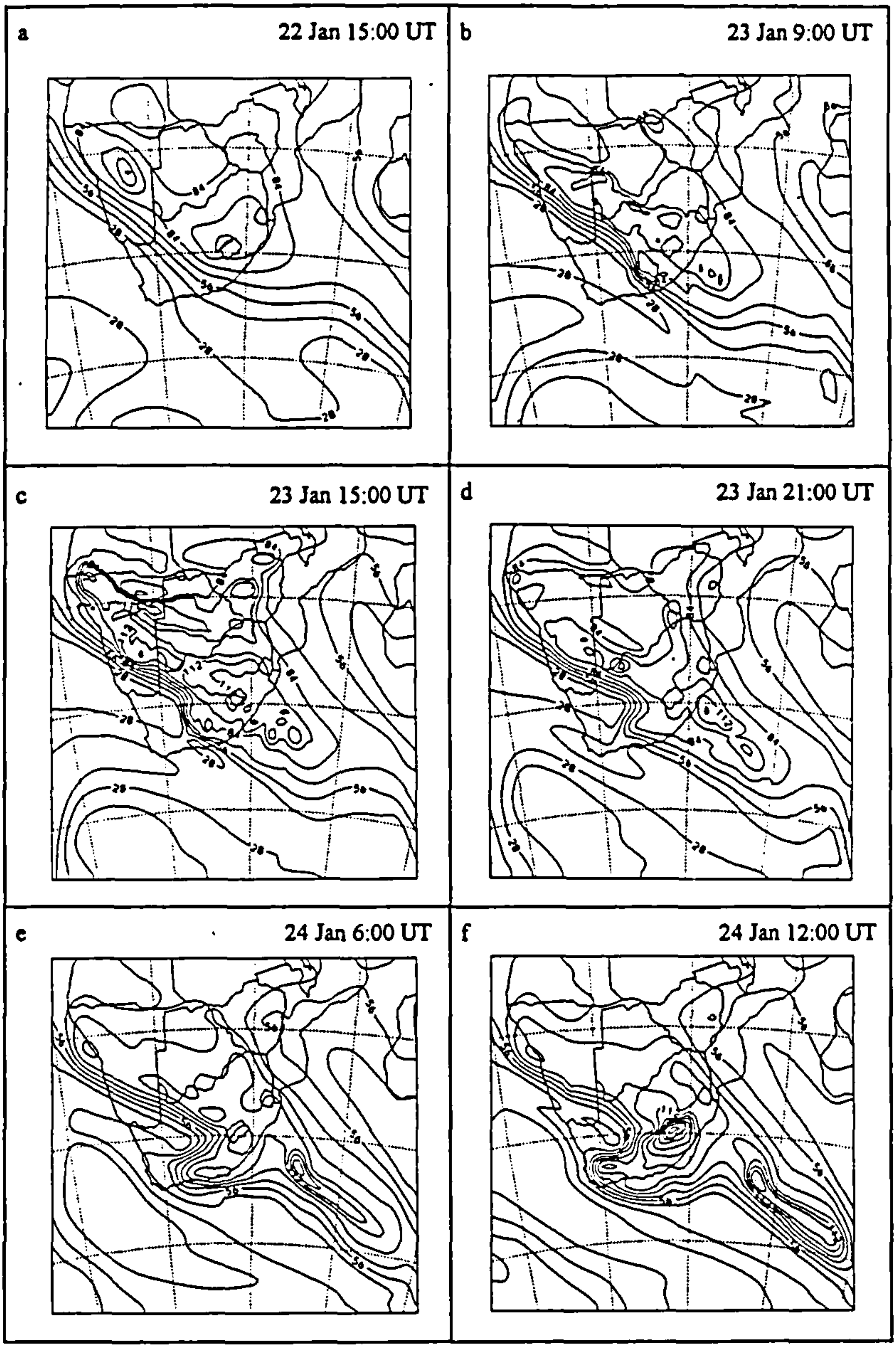

Figure 6.14: Total water mixing ratio at 3.13 km (~ 700 hPa) above sea level from the finer resolution sensitivity test at (a) 22 Jan 15:00 UT, (b) 23 Jan 9:00 UT, (c) 23 Jan 15:00 UT, (d) 23 Jan 21:00 UT, (e) 24 Jan 6:00 UT and (f) 24 Jan 12:00 UT ($g.kg^{-1}$; contour interval of 1.4 $g.kg^{-1}$; labels multiplied by 10).

greater than 7 $g.kg^{-1}$ do extend to the northern border of the domain. This may be due to the lateral boundary conditions. Also, as the oceanic region to the northwest of Madagascar is not situated within the model domain, the transport of water vapour over the interior is likely to be reduced. The zone of mixing ratios greater than 11,2 $g.kg^{-1}$ in the finer-resolution dissipative stages are situated over the Lesotho highlands and along the cold front (Fig. 6.14e,f) in response to the vertical uplift in these regions (Fig. 6.7e,f), whereas they occur over the central interior and along the cloud band in the dissipative stages of the coarse control run (Fig. 5.21e,f). At the 300 hPa level, the increase in cloud height with latitude along the cloud band in the control run (Fig. 5.23a-f), is also evident in the finer resolution sensitivity test (Fig. 6.15a-f). Total mixing ratios tend to be higher in the finer resolution output in response to the greater vertical velocities transporting moisture into this atmospheric level.

Discussion

Smaller-scale systems and vertical velocity were most affected by the finer grid resolution. The cut-off low that developed toward the end of the wet case study was not evident in the control run, but was adequately resolved in the finer resolution sensitivity test. The stronger vertical velocities of the finer-resolution sensitivity tests can be attributed to the improved resolution of the updrafts and downdrafts. The vertical velocity differences between the coarse and finer resolution runs were far greater during the wet than the dry case study. This may be due to the improved resolution of the topography. As tropical-temperate troughs form predominantly over the ocean during dry conditions, the topographical effects are small.

Greater vertical velocities during the finer resolution sensitivity tests result in higher convective precipitation rates and greater accumulated convective precipitation totals. However, the accumulated convective precipitation was still only about 50% of the observed rainfall in both case studies. The pressure differences can also be attributed to the increased vertical velocities. The lower total mixing ratios over the northern regions of the model domain suggest a possible problem with the lateral boundary conditions. Moisture from the oceanic region to the northwest of Madagascar which could not be included in the model

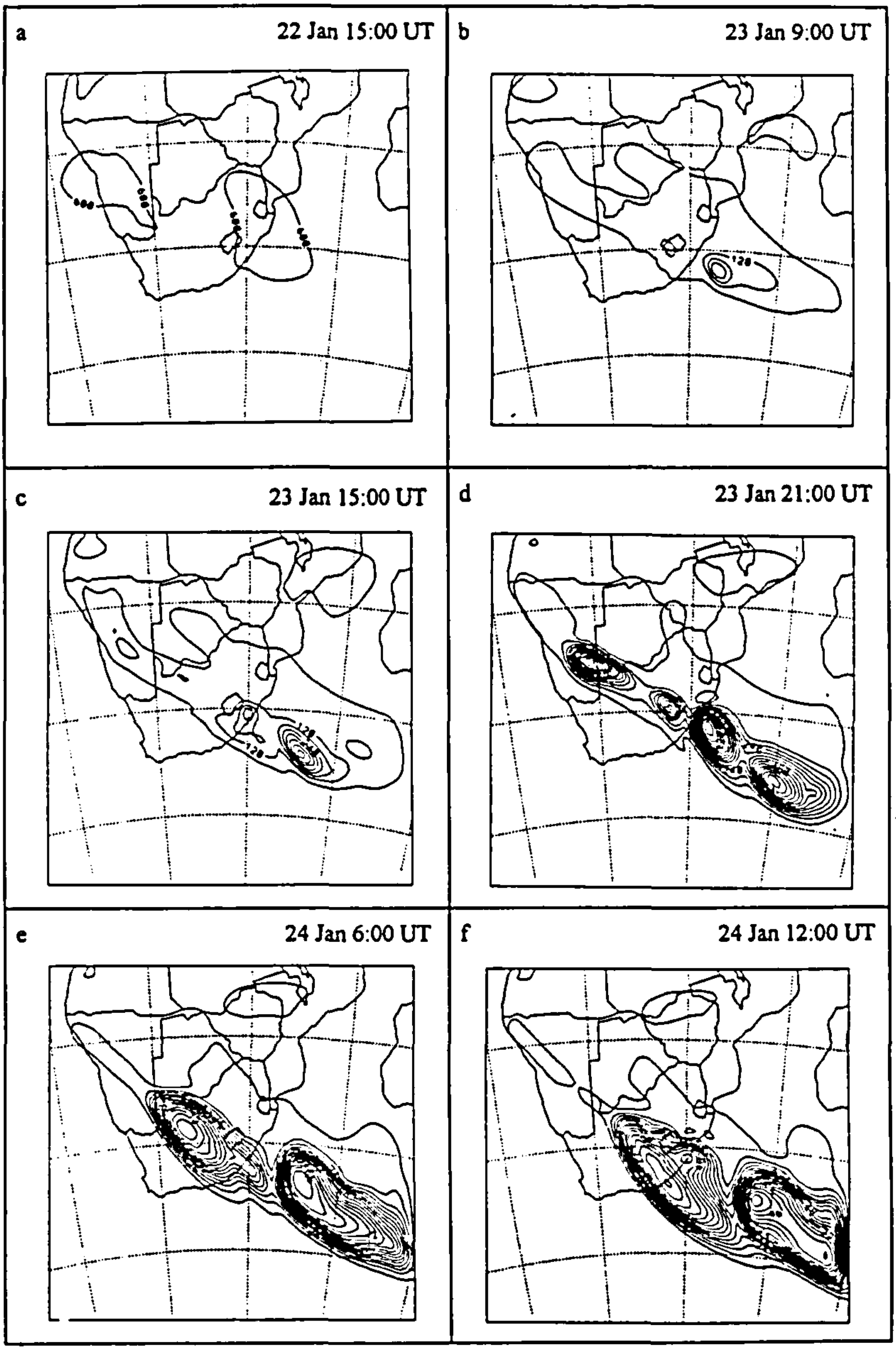

Figure 6.15: Total water mixing ratio at 9,66 km (~ 300 hPa) above sea level from the finer resolution sensitivity test at (a) 22 Jan 15:00 UT, (b) 23 Jan 9:00 UT, (c) 23 Jan 15:00 UT, (d) 23 Jan 21:00 UT, (e) 24 Jan 6:00 UT and (f) 24 Jan 12:00 UT ($g.kg^{-1}$; contour interval of 0,6 $g.kg^{-1}$; labels multiplied by 10^3 in a, 10^2 in b-d, 10 in e-f).

domain as a result of computer limitations, was not effectively introduced to southern Africa at the boundaries. Despite the differences, the modelled development of the tropical-temperate troughs using the 80 kilometre and 50 kilometre grids showed a high degree of correspondence, which adds credibility to the numerical model.

Microphysics Sensitivity

Resolvable microphysics have not been included in any of the simulations previously discussed. Condensation of supersaturation and the production of cloud water was allowed to occur and the resultant latent heat was released, but precipitation of the condensate did not occur. By including the microphysics module, the microphysics processes are resolved on the grid scale and precipitation occurs. The selected water species were rain water, aggregates and pristine crystals and the model default options specifying the mean diameter of these species were applied (Flateau *et al.*, 1989). Graupel, which is mainly formed in active convective updrafts, was not used as the updrafts are parameterised with the 50 kilometre grid resolution used (Tremback, 1990).

Convective Precipitation

The convective precipitation rate in the microphysics sensitivity test (Fig. 6.16a-c) becomes increasingly larger than that of its finer resolution counterpart (Fig. 6.10a-c). By 21:00 UTC on 23 January (Day 2) (Fig. 6.16d), convective precipitation is still evident along the northern sections of the tropical-temperate trough in the microphysics output, unlike that in the finer resolution output (Fig. 6.10d). The microphysics output corresponds more closely with that of the coarse control run at this stage (Fig. 4.10d). By 24 January (Day 3), the convective precipitation rate from the fine (Fig. 6.10e,f) and microphysics (Fig. 6.16e,f) sensitivity tests correspond closely, the rate being only slightly greater in the microphysics output. The accumulated convective precipitation from the microphysics (Fig. 6.17) and finer resolution (Fig. 6.11) sensitivity tests compare well in distribution and magnitude, the maximum values both being 22 mm for the 48 hour period.

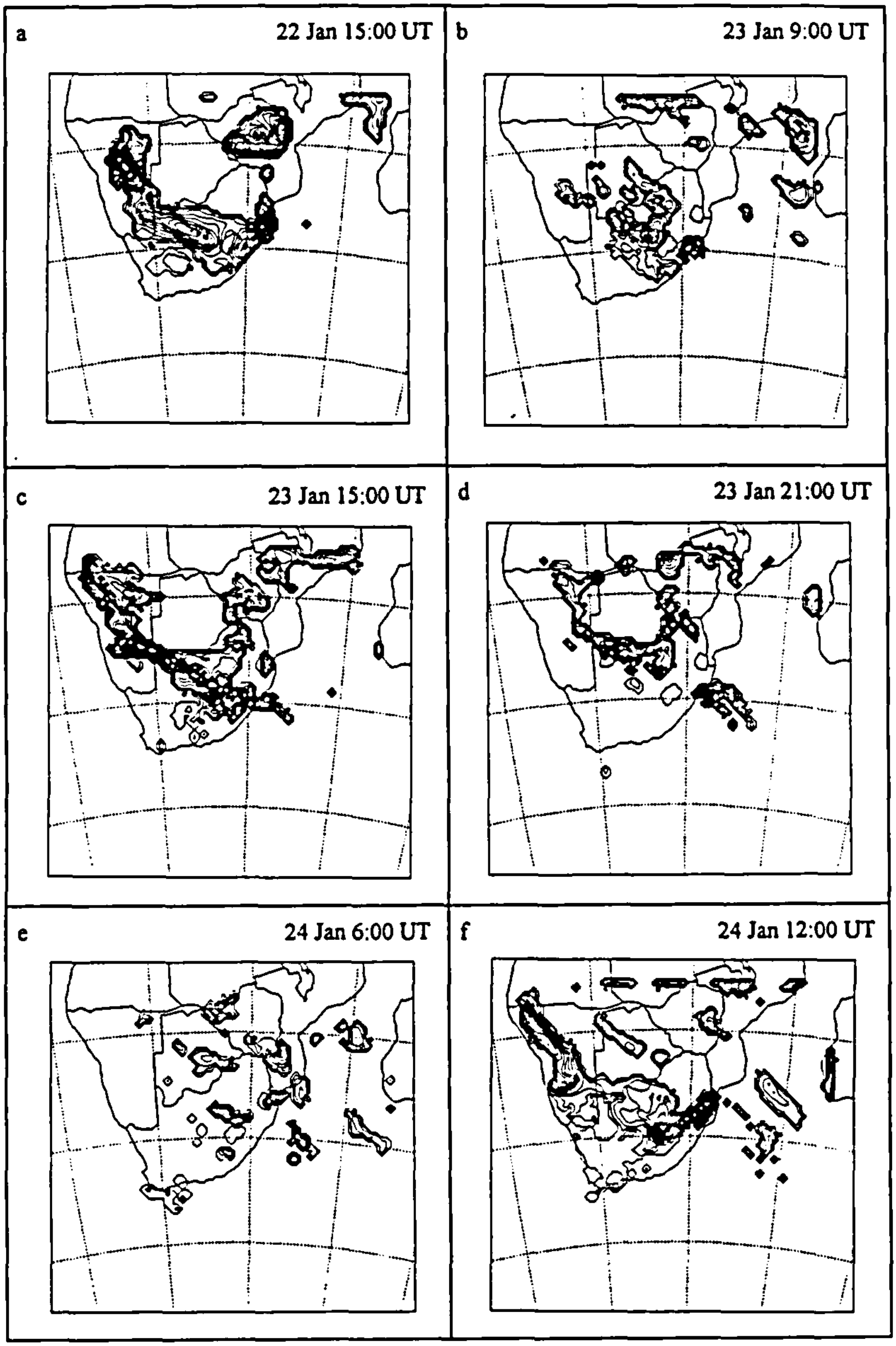

Figure 6.16: Convective parameterisation precipitation rate from the microphysics sensitivity test at (a) 22 Jan 15:00 UT, (b) 23 Jan 9:00 UT, (c) 23 Jan 15:00 UT, (d) 23 Jan 21:00 UT, (e) 24 Jan 6:00 UT and (f) 24 Jan 12:00 UT ($mm.s^{-1}$; contour interval of 0,000035 $mm.s^{-1}$; labels multiplied by 10^7).

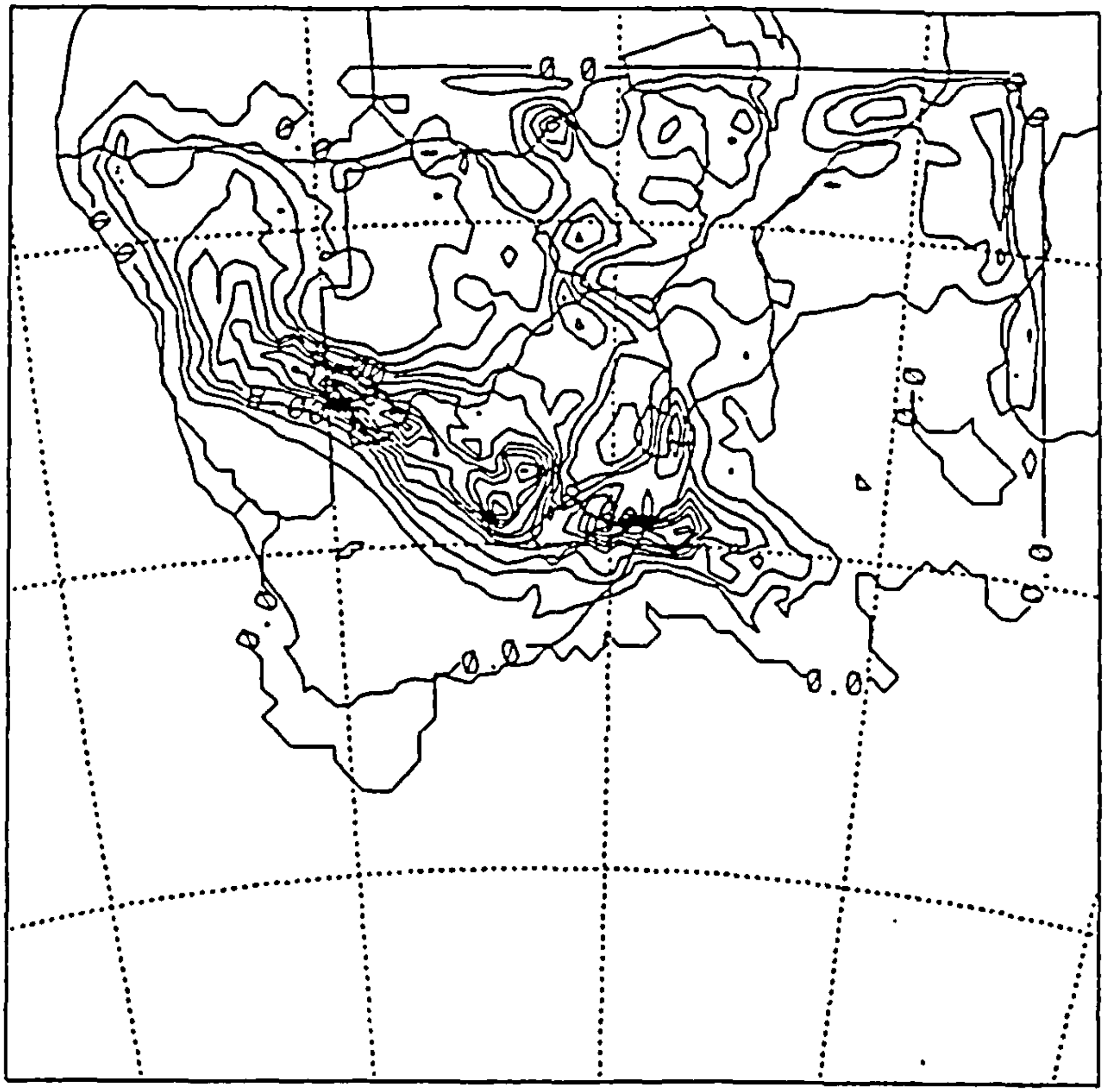

Figure 6.17: Precipitation produced by the cumulus parameterisation scheme between 22 Jan 12:00 UTC and 24 Jan 12:00 UTC from the microphysics sensitivity test (mm; contour interval of 2 mm; maximum value of 22 mm).

Mixing Ratios

The stages of development of the wet case tropical-temperate trough are clearly evident in the 700 hPa condensate mixing ratios of the microphysics sensitivity test (Fig. 6.18a-f). Very little condensate is obvious during the initial stages of development (Fig. 6.18a), but by 9:00 UTC on 23 January (Day 2), the condensate mixing ratios have increased significantly along most of the developing tropical-temperate trough (Fig. 6.18b). By 15:00 UTC, condensate occurs along the developing cloud band and over northern Namibia, Botswana, the Transvaal and southern Zimbabwe (Fig. 6.18c) and closely corresponds with the cloud cover in the satellite imagery (Plate 2.1c). The condensate is found predominantly along the tropical-temperate trough by the evening of 23 January (Fig. 6.18d). Dissipation of the tropical-temperate trough is evident in the lower-level condensate mixing ratio fields on 24 January (Day 3) (Fig. 6.18e,f). In the upper tropospheric levels, the condensate mixing ratios from the microphysics sensitivity test (Fig. 6.19a-f) are situated predominantly along the tropical-temperate trough. They extend further southward than those in the lower levels (Fig. 6.18a-f), reaching the southeastern border of the model domain during the mature stages of development (Day 2) (Fig. 6.19d-f).

The total mixing ratios at 700 hPa from the microphysics sensitivity test (Fig. 6.20a-f) compare well with those of the finer resolution sensitivity test (Fig. 6.14a-f) in distribution and magnitude although the total mixing ratios of the finer resolution test are slightly greater than those of the microphysics test toward the end of the simulation. At 300 hPa, the total mixing ratios from the microphysics sensitivity test (Fig. 6.21a-f) are significantly different than those from the finer resolution test (Fig. 6.15a-f) in magnitude, the finer resolution mixing ratios being a factor of ten greater than those of the microphysics sensitivity test throughout most of the simulation.

Rainfall

The resolved accumulated rainfall from the microphysics sensitivity test (Fig. 6.22b) is significantly greater than the precipitation produced by the cumulus parameterisation scheme

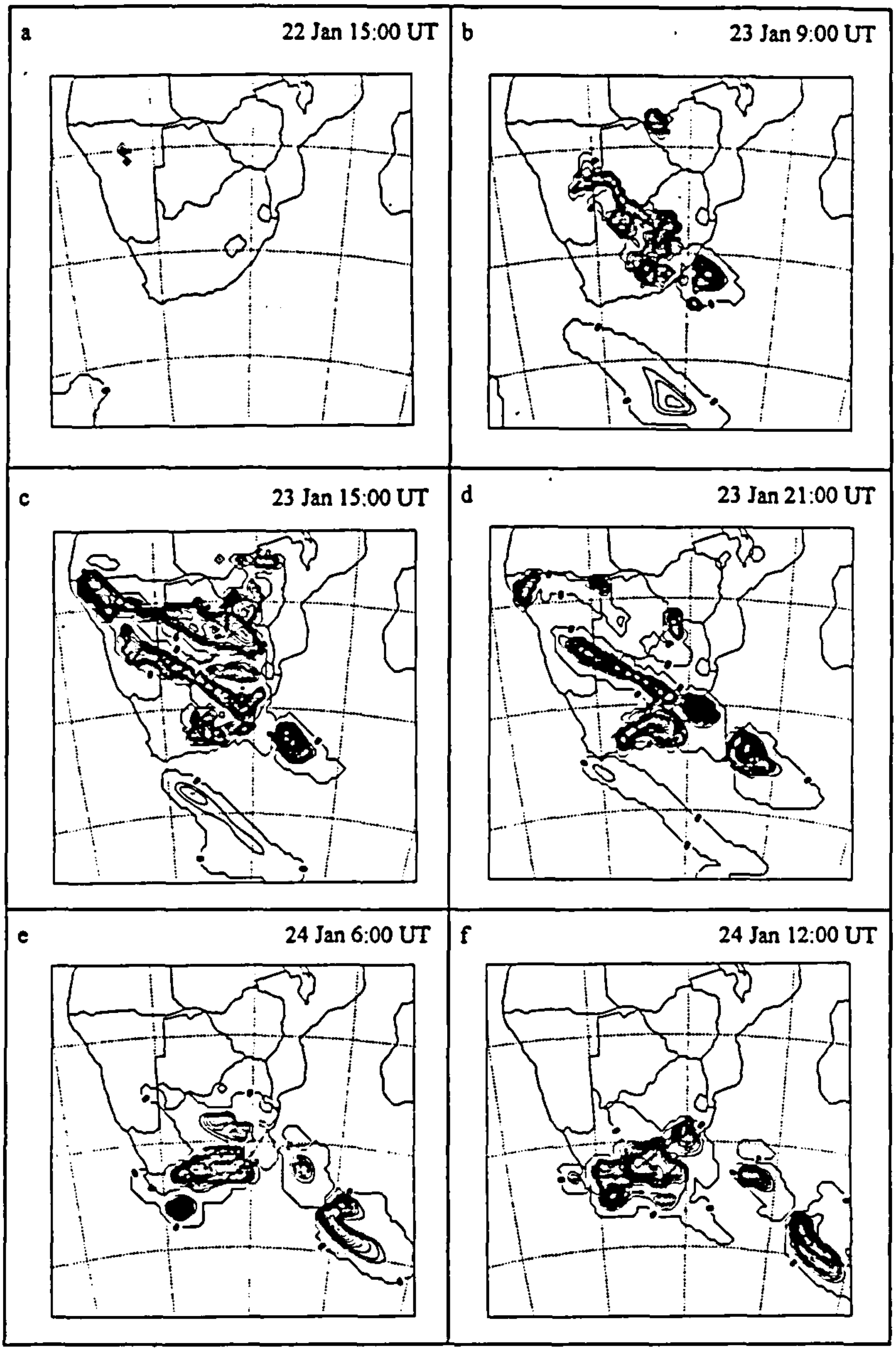

Figure 6.18: Condensate water mixing ratio at 3,13 km (~ 700 hPa) above sea level from the microphysics sensitivity test at (a) 22 Jan 15:00 UT, (b) 23 Jan 9:00 UT, (c) 23 Jan 15:00 UT, (d) 23 Jan 21:00 UT, (e) 24 Jan 6:00 UT and (f) 24 Jan 12:00 UT ($g.kg^{-1}$; contour interval of 0,1 $g.kg^{-1}$ for a-d, 0,07 $g.kg^{-1}$ for e-f; labels multiplied by 10^2).

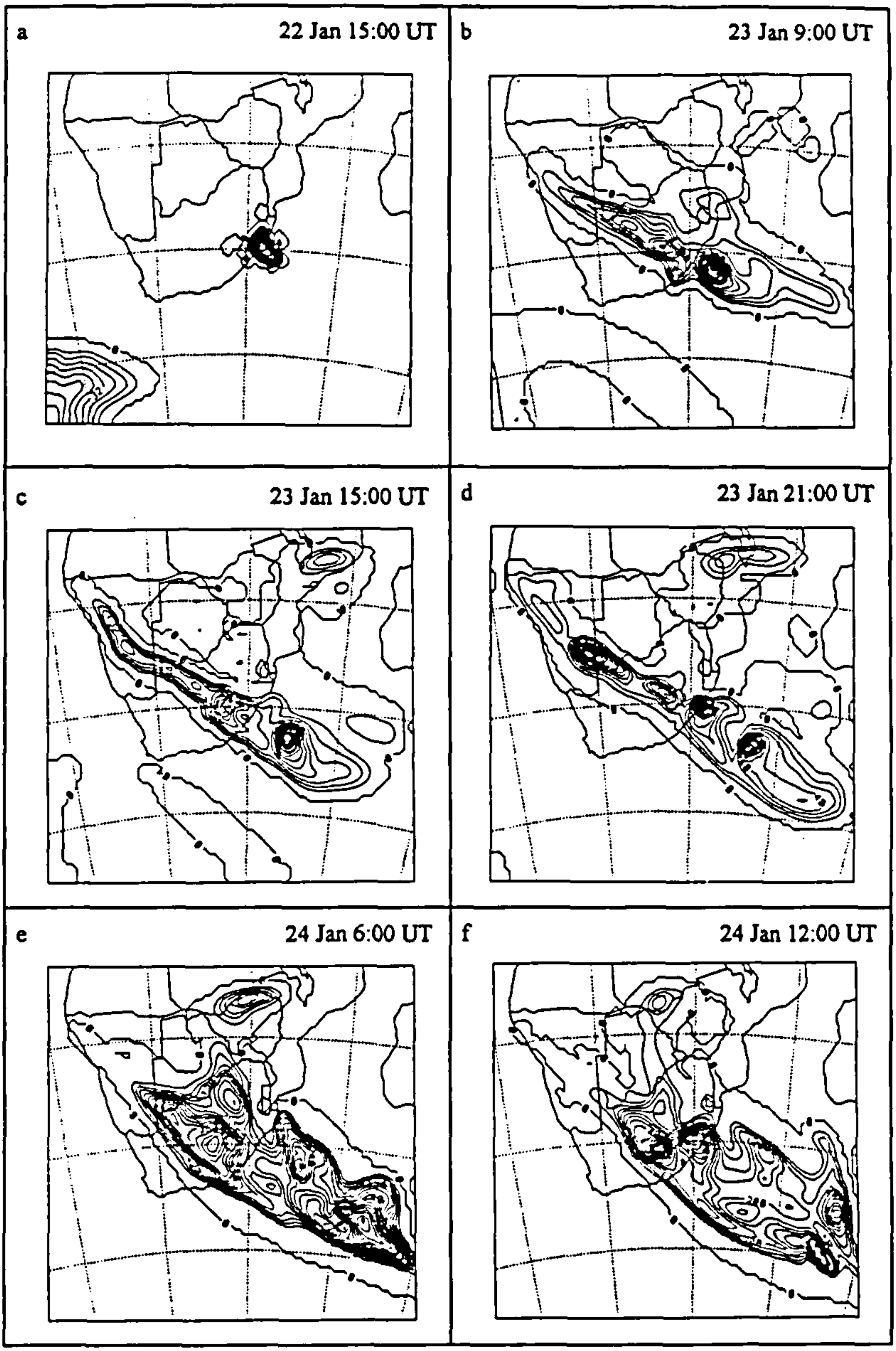

Figure 6.19: Condensate mixing ratio at 9,66 km (~ 300 hPa) above sea level from the microphysics sensitivity test at (a) 22 Jan 15:00 UT, (b) 23 Jan 9:00 UT, (c) 23 Jan 15:00 UT, (d) 23 Jan 21:00 UT, (e) 24 Jan 6:00 UT and (f) 24 Jan 12:00 UT ($g.kg^{-1}$; contour interval of 0,008 $g.kg^{-1}$ for a, 0,05 $g.kg^{-1}$ for b,f, 0,08 for c, 0,1 $g.kg^{-1}$ for d, 0,03 $g.kg^{-1}$ for e; labels multiplied by 10^3 in a-b, e-f, and by 10^2 in c-d).

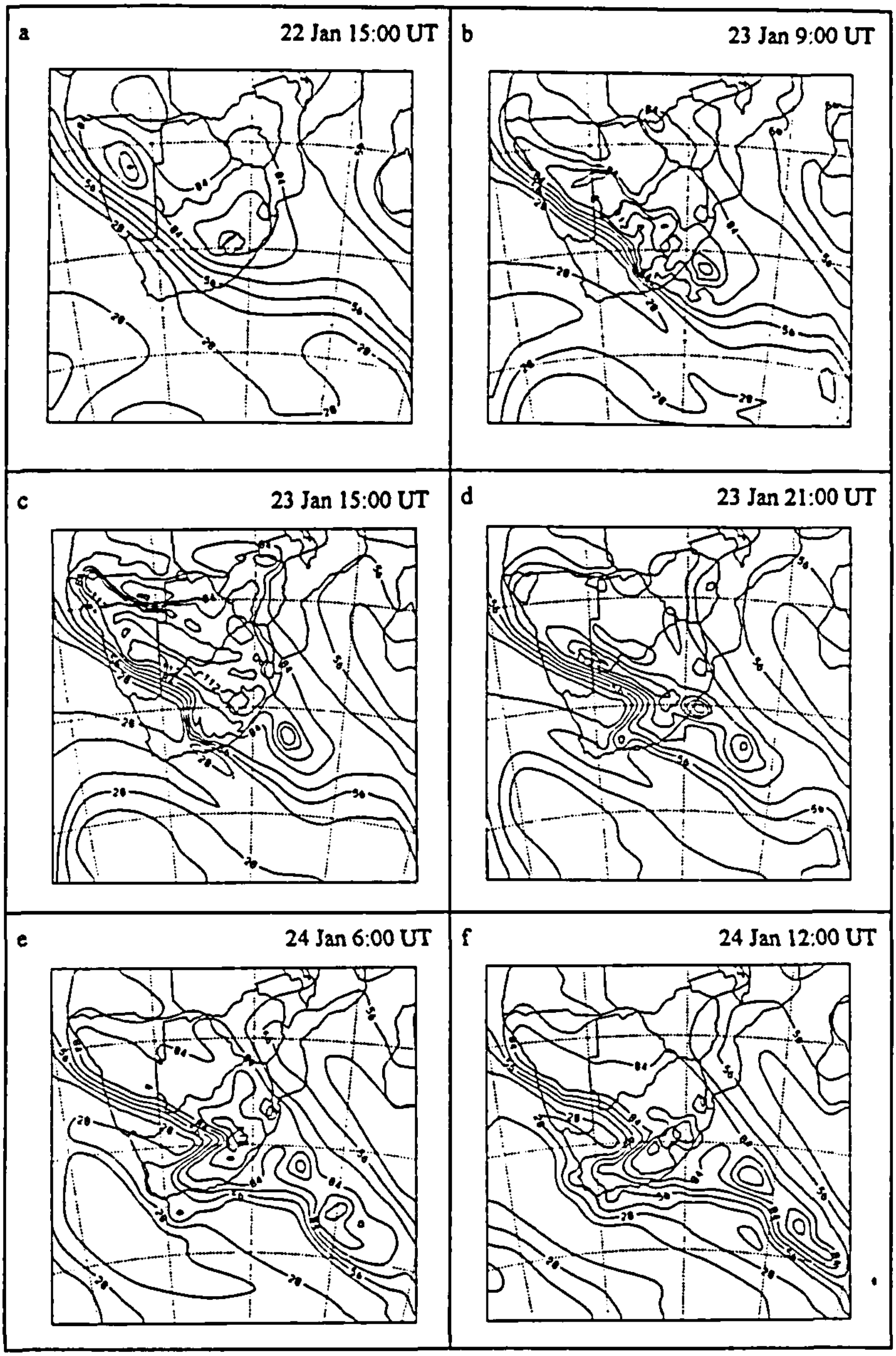

Figure 6.20: Total water mixing ratio at 3,13 km (~ 700 hPa) above sea level from the microphysics sensitivity test at (a) 22 Jan 15:00 UT, (b) 23 Jan 9:00 UT, (c) 23 Jan 15:00 UT, (d) 23 Jan 21:00 UT, (e) 24 Jan 6:00 UT and (f) 24 Jan 12:00 UT (g.kg^{-1}; contour interval of 1,4 g.kg^{-1}; labels multiplied by 10).

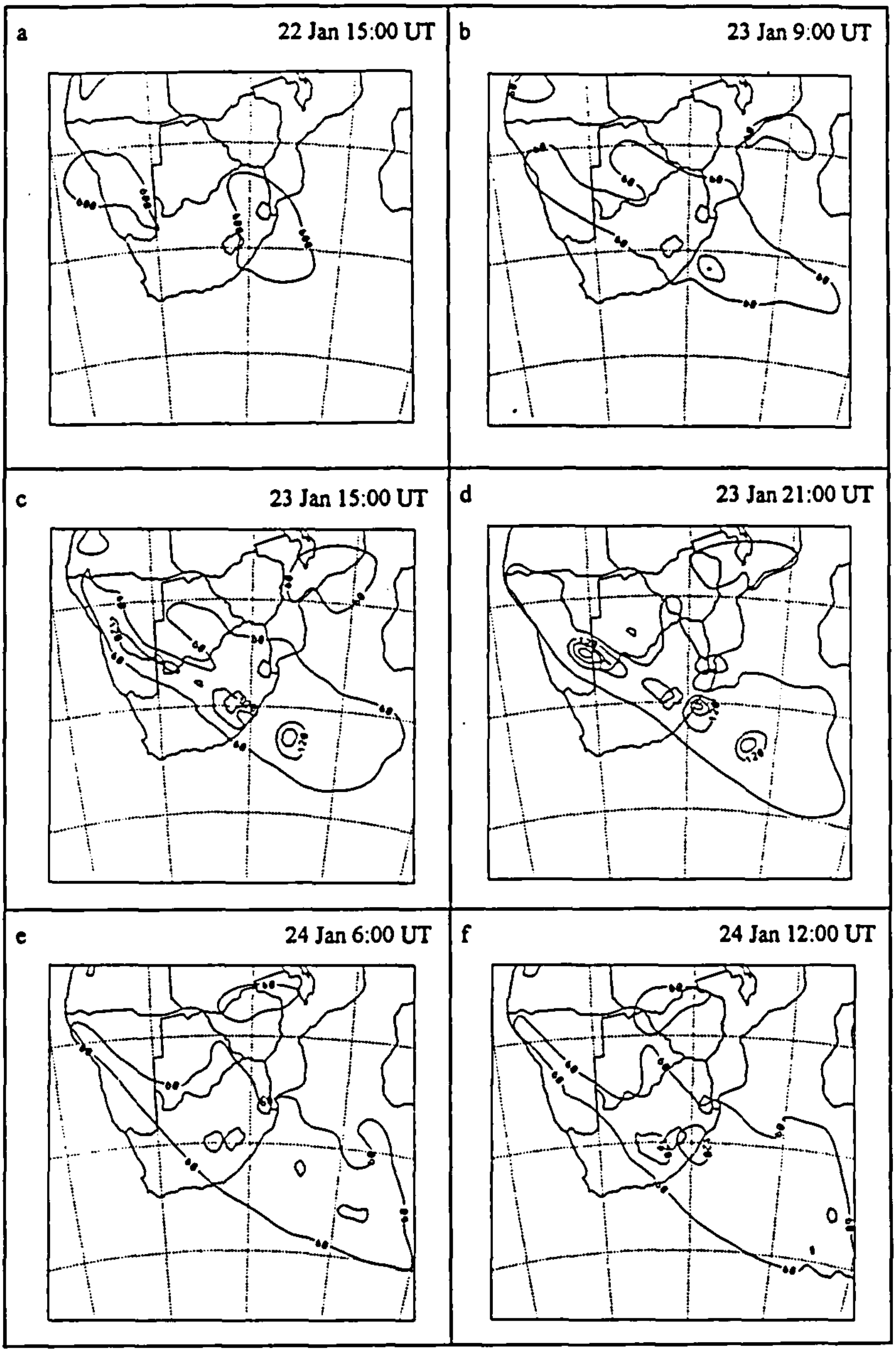

Figure 6.21: Total water mixing ratio at 9,66 km (~ 300 hPa) above sea level from the microphysics sensitivity test at (a) 22 Jan 15:00 UT, (b) 23 Jan 9:00 UT, (c) 23 Jan 15:00 UT, (d) 23 Jan 21:00 UT, (e) 24 Jan 6:00 UT and (f) 24 Jan 12:00 UT ($g.kg^{-1}$; contour interval of 0,6 $g.kg^{-1}$; labels multiplied by 10^3 in a, 10^2 in b-f).

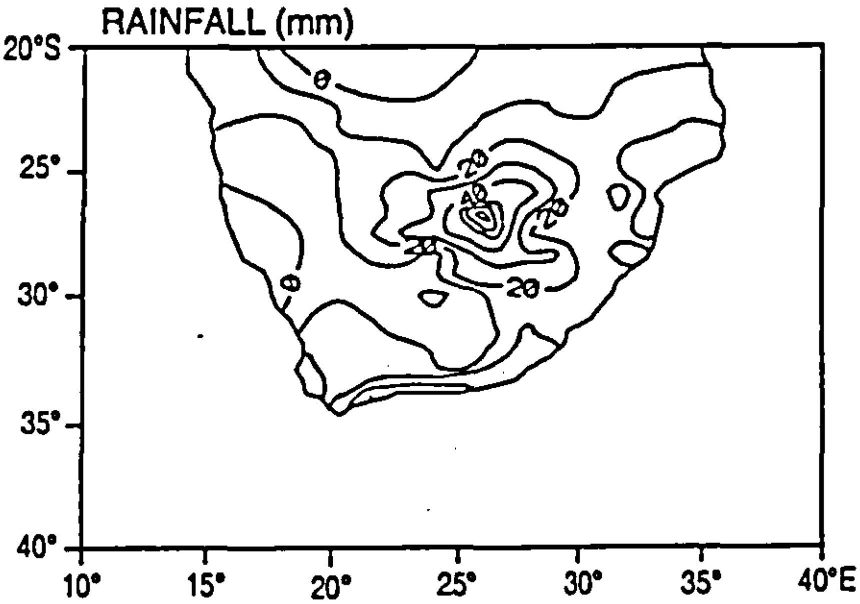

b

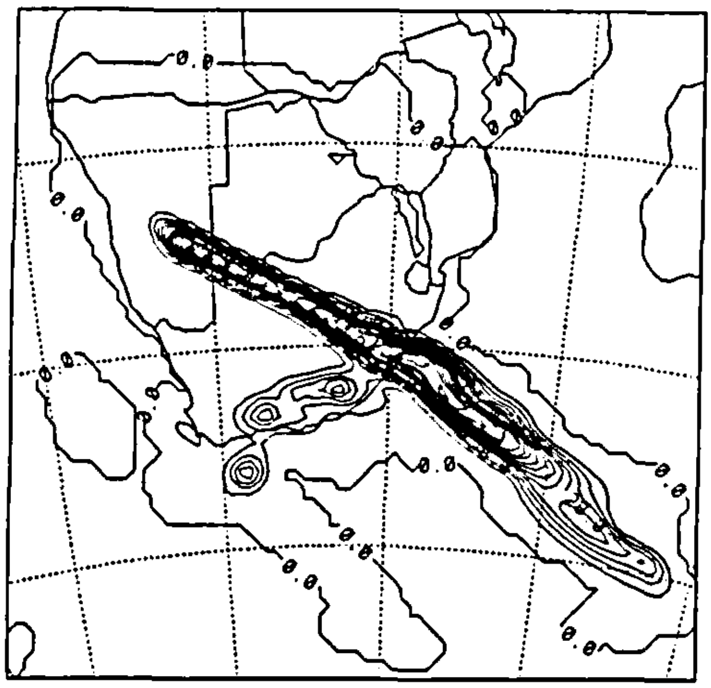

Figure 6.22: (a) The accumulated rainfall as recorded by the SAWB for the wet case study during the period 22 Jan 6:00 UT to 24 Jan 6:00 UT (mm, contour interval 10 mm), and (b) the wet case study microphysically produced rainfall for the period 22 Jan 12:00 UT to 24 Jan 12:00 UT (mm, contour interval 7 mm).

(Fig. 6.11). The maximum precipitation produced by the cumulus parameterisation scheme is 22 mm whereas the maximum microphysically-produced rainfall is 112 mm. The resolved accumulated rainfall (Fig. 6.22b) compares well with the observed accumulated rainfall (Fig. 6.22a). The observed rainfall along the southern Cape coastal belt ranges from 10 mm to 30 mm, while the simulated rainfall is between 7 mm to 35 mm in this region. Rainfall figures along the cloud band compare just as well and the rainfall extends along the entire tropical-temperate trough to the southeastern border of the model domain. The only apparent weakness of the resolved accumulated precipitation is that the rainfall is confined to a narrower band than that of the observed rainfall field.

It is difficult to determine how accurately the accumulated resolved rainfall produced by the dry case cloud band corresponds with the observed rainfall, as the rainfall occurs over data-sparse oceanic regions. However, the observed (Fig. 6.23a) and simulated rainfall (Fig. 6.23b) over the eastern regions of southern Africa compare well and it is assumed that those over the oceanic regions also compare favourably. The accumulated precipitation produced by the convective parameterisation scheme (Fig. 6.13) is much less than the accumulated resolved rainfall, the maximum values being 17 mm and 153 mm respectively.

Discussion

While the low-level total mixing ratios of the microphysics and finer resolution sensitivity tests compare well, the upper-level total mixing ratio fields of the microphysics test are significantly lower than those of the finer resolution and control simulations. To determine which fields are a better representative of reality is difficult as no such data is available for the case studies and no previous research has been conducted into this aspect of tropical-temperate troughs at upper tropospheric levels. It would appear however, that the mixing ratios of the finer resolution and coarse control runs are more in keeping with the actual structure of the tropical-temperate trough, although they may be higher than the observed values. Lower than normal condensate levels in upper tropospheric levels have previously been attributed to the fact that the cumulus parameterisation scheme only transports moisture upwards. No form of

a

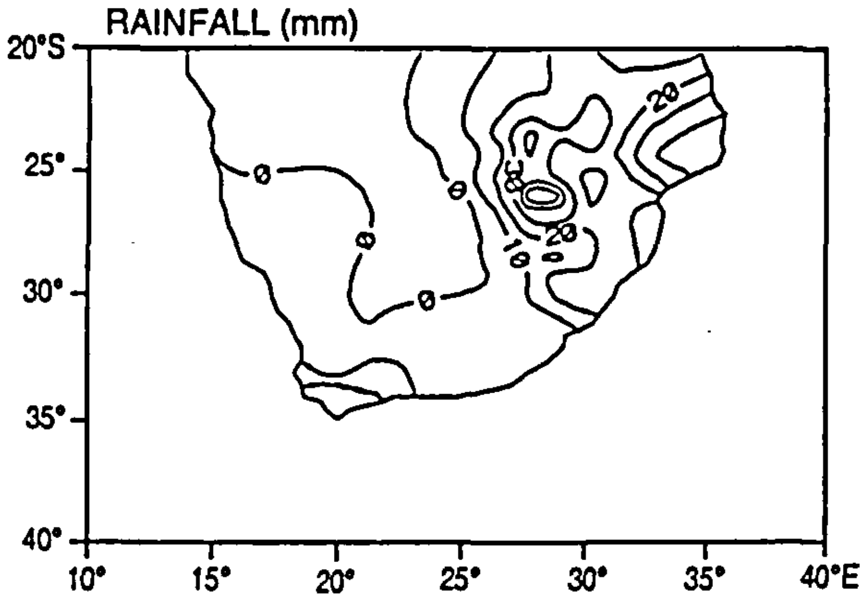

b

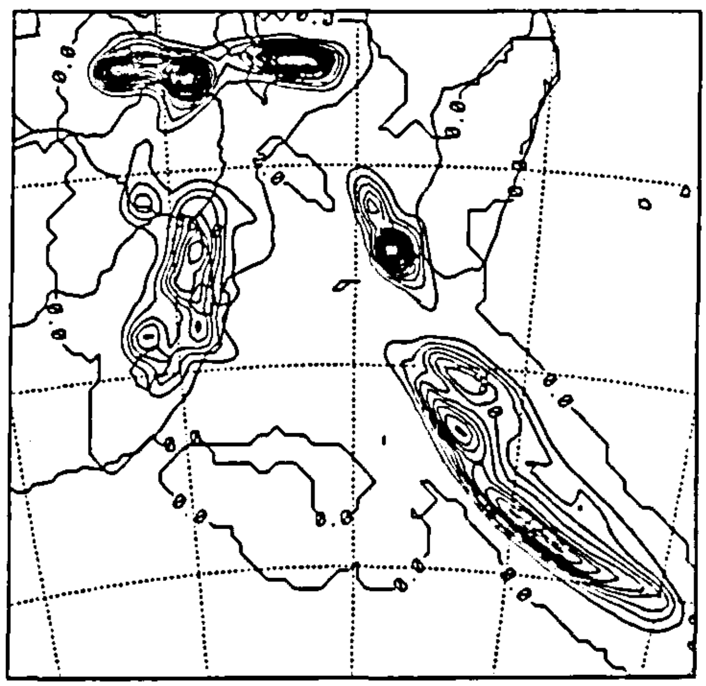

Figure 6.23: (a) The accumulated rainfall as recorded by the SAWB for the dry case study during the period 6 Jan 6:00 UT to 8 Jan 6:00 UT (mm, contour interval 10 mm), and (b) the dry case study microphysically produced rainfall for the period 6 Jan 12:00 UT to 8 Jan 12:00 UT (mm, contour interval 9 mm).

condensate is transported by the scheme, whereas regions of convection in nature explicitly produce and transport liquid and frozen condensate upward (Cram, 1990). Activating the microphysics module results in the explicit conversion of water vapour to condensate. As the condensate is not transported by the cumulus parameterisation scheme, the upper tropospheric condensate level in the microphysics test is very low. Hence the total water mixing ratios in the microphysics test are lower than those of the finer resolution sensitivity test in which the "unconverted" water vapour is transported to the upper troposphere by the cumulus parameterisation scheme. Precipitation of the condensate in the microphysics sensitivity test also results in lower total mixing ratios than those of the finer resolution sensitivity test in which the condensate remains suspended.

The accumulated convective precipitation for both the finer resolution and microphysics sensitivity tests indicates that the convective precipitation associated with the cloud band development does not extend much further south of 30°S. However, the accumulated rainfall produced in the microphysics sensitivity test extends beyond 40°S to the southeastern extremes of the model domain. This implies that south of about 30°S, processes such as those associated with stratiform precipitation rather than deep convection, are responsible for the rainfall along the cloud band in these regions which points to the large-scale slope convection associated with the westerly wave and cold front that constitute the temperate section of the tropical-temperate trough. As the rainfall totals from the microphysics sensitivity test are substantially greater than the convective precipitation totals in both the microphysics and finer resolution sensitivity tests, it would appear that stratiform processes may also be important north of 30°S. This suggests that large-scale uplift along the tropical-temperate trough in a poleward direction is also important in producing cloud band rainfall.

The microphysically-produced rainfall is therefore a better representation of the observed tropical-temperate trough rainfall than the accumulated convective precipitation produced by the parameterisation scheme. This implies that stratiform processes as well as convection are important in the rainfall production of tropical-temperate troughs. The inclusion of the microphysics module also resulted in low upper-tropospheric mixing ratios which suggests a weakness in the cumulus parameterisation scheme, in that it does not transport condensate vertically.

Soil Moisture Sensitivity

The importance of soil moisture in boundary forcing has started to receive an increasing amount of attention in general circulation models (Atlas *et al.*, 1993; Bounoua and Krishnamurti, 1993) and in mesoscale models (Bossert, 1990; Tremback, 1990). It has been found to have a significant effect on precipitation (Atlas *et al.*, 1993; Bounoua and Krishnamurti, 1993), surface temperatures (Atlas *et al.*, 1993; Bounoua and Krishnamurti, 1993), wind flow (Bossert, 1990) and the development of convective systems (Tremback, 1990). The susceptibility of southern Africa to drought and encroaching desertification (Tyson, 1986) raises the question as to how changes in soil moisture will effect the weather systems over the southern African continent. In all the previous simulations, the surface soil moisture was limited to between 40% and 80% of the saturation value at the surface (see Chapter 3). Two sensitivity tests were conducted to investigate the effects of soil moisture on cloud bands. The surface soil moisture was limited to between 75% and 90% and to between 10% and 20% of the saturation value at the surface, resulting in wetter and drier soil conditions than normal. The tests were performed with the 80 kilometre grid resolution.

Wet Soil

The vertical velocity fields at 700 hPa (Fig. 6.24a-f) and 300 hpa (not shown) from the wet soil sensitivity test and those from the control run (Fig. 4.7a-f) correspond closely both in distribution and magnitude. The wet-soil convective precipitation fields (Fig. 6.25a-f), enhanced by the vertical velocity, are also similar to those of the control run (Fig. 4.10a-f). The maximum accumulative convective precipitation from the wet soil sensitivity test (Fig. 6.26) is only 1 mm less than that of the control run (Fig. 4.11). Total water mixing ratios from the wet soil sensitivity test at the surface (not shown), 700 hPa (Fig. 6.27a-f) and 300 hPa

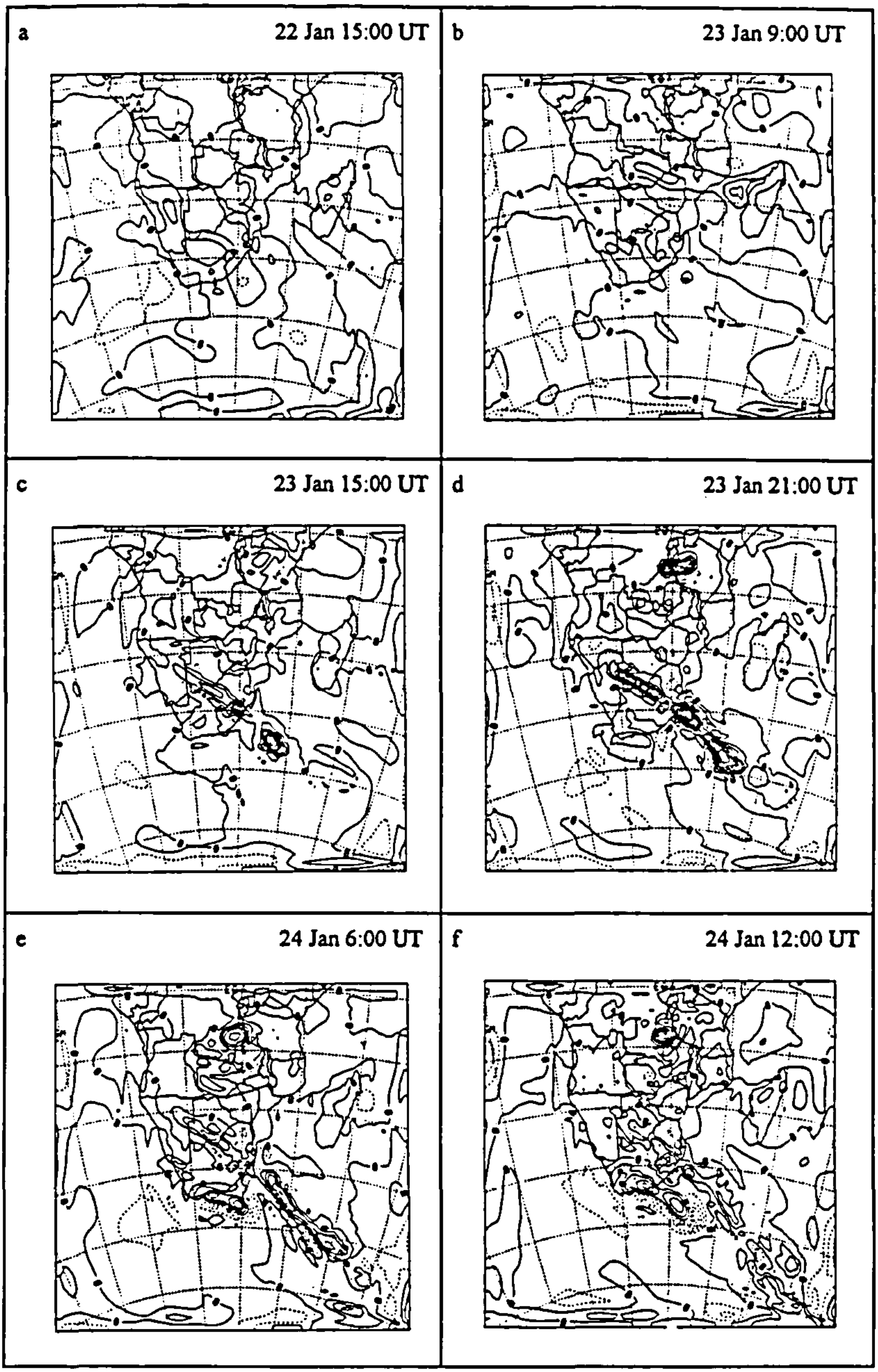

Figure 6.24: Vertical velocity at 3,13 km (~ 700 hPa) above sea level from the wet soil sensitivity test at (a) 22 Jan 15:00 UT, (b) 23 Jan 9:00 UT, (c) 23 Jan 15:00 UT, (d) 23 Jan 21:00 UT, (e) 24 Jan 6:00 UT and (f) 24 Jan 12:00 UT ($cm.s^{-1}$; contour interval of 2 $cm.s^{-1}$; labels multiplied by 10 in a-d,f and by 100 in e; solid lines indicate uplift and dashed lines indicate subsidence).

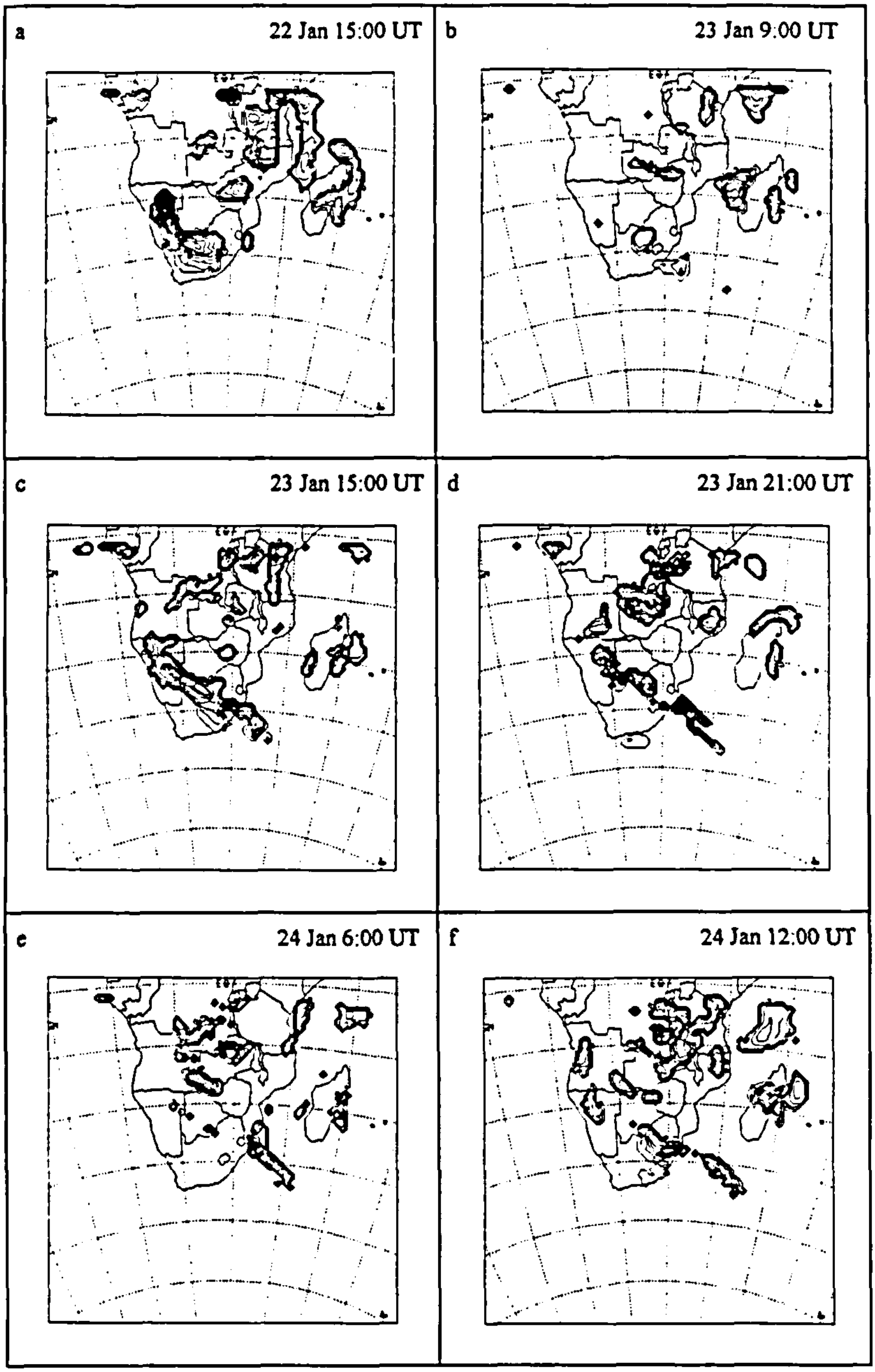

Figure 6.25: Convective parameterisation precipitation rate from the wet soil sensitivity test at (a) 22 Jan 15:00 UT, (b) 23 Jan 9:00 UT, (c) 23 Jan 15:00 UT, (d) 23 Jan 21:00 UT, (e) 24 Jan 6:00 UT and (f) 24 Jan 12:00 UT ($mm.s^{-1}$; contour interval of 0,000035 $mm.s^{-1}$; labels multiplied by 10^7).

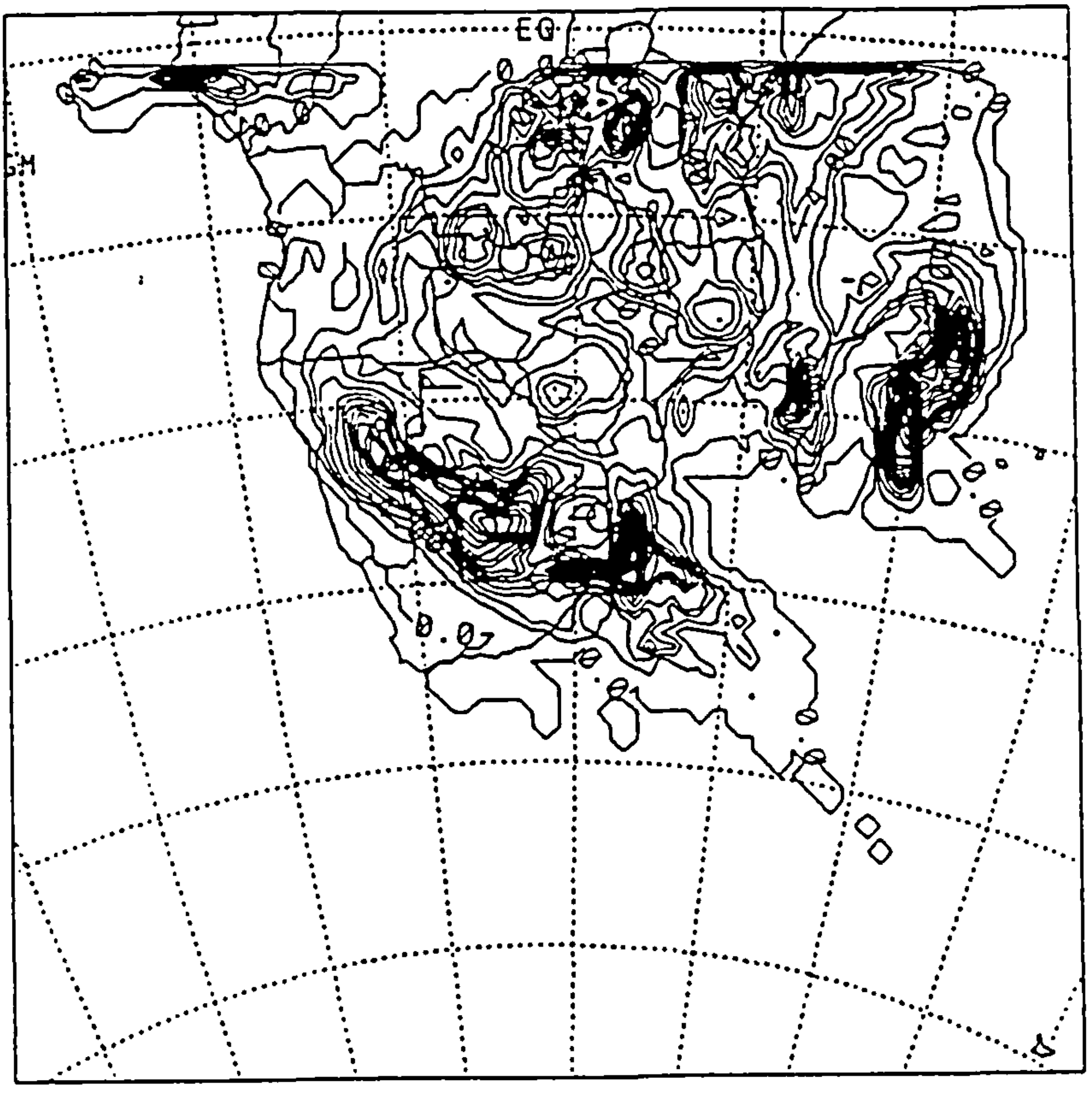

Figure 6.26: Precipitation produced by the cumulus parameterisation scheme between 22 Jan 12:00 UTC and 24 Jan 12:00 UTC from the wet soil sensitivity test (mm; contour interval of 1 mm; maximum value of 17 mm).

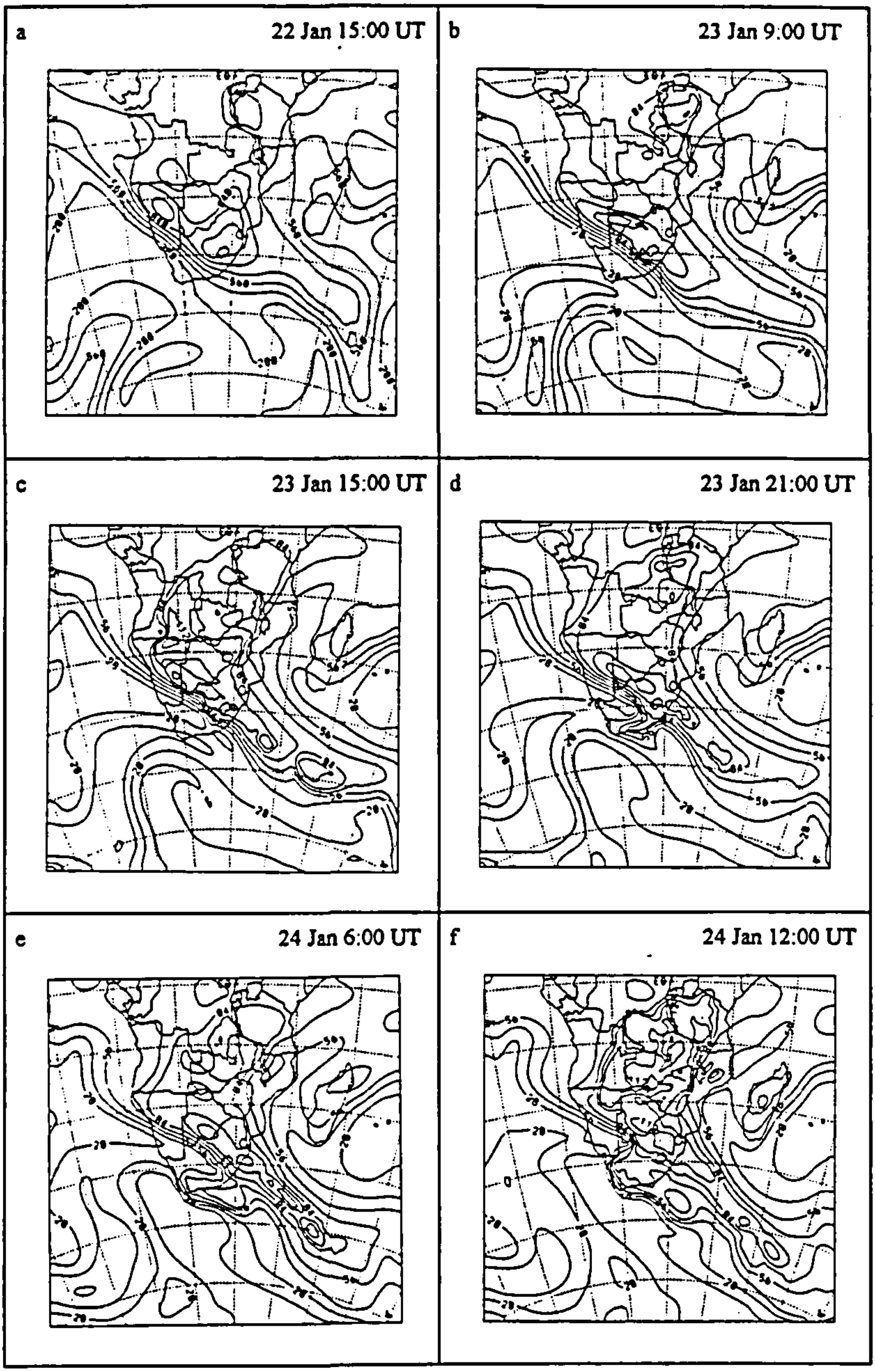

Figure 6.27: Total water mixing ratio at 3,13 km (~ 700 hPa) above sea level from the wet soil sensitivity test at (a) 22 Jan 15:00 UT, (b) 23 Jan 9:00 UT, (c) 23 Jan 15:00 UT, (d) 23 Jan 21:00 UT, (e) 24 Jan 6:00 UT and (f) 24 Jan 12:00 UT ($g.kg^{-1}$; contour interval of 1,4 $g.kg^{-1}$; labels multiplied by 100 in a, 10 in b-f).

(Fig. 6.28a-f) levels, all show a close degree of correspondence with those of the control run (Figs 5.20; 5.22).

Dry Soil

The vertical velocities of the dry soil sensitivity test differ quite significantly from those of the control run. By 15:00 UT on 23 January (Day 2), the interior trough at 700 hPa does not extend from northern Namibia to the Natal coast (Fig. 6.29c) as it does in the control run (Fig. 4.7c). The region of vertical uplift over the Natal Drakensberg extends along the southern coast and is of a greater extent in the dry soil sensitivity test (Fig. 6.29c) than that of the control run (Fig. 4.7c). Regions of greater vertical uplift are also evident over tropical Africa and Madagascar in the dry soil sensitivity test, which were not apparent in the control run. By 21:00 UT on 23 January (Day 2), the dry-soil vertical velocities at 700 hPa along the cloud band are limited to distinct zones (Fig. 6.29d) unlike that of the control run in which the vertical velocity extends along the entire tropical-temperate trough (Fig. 4.7d). The interior trough, evident in the control run at 300 hPa (Fig. 4.9d), is no longer apparent in the dry soil output (Fig. 6.30d). By the following day (Day 3), vertical uplift occurs along the southern Natal coast (Figs 6.29f, 6.30f) in the dry soil sensitivity test, whereas in the control run the remnants of the interior trough are evident (Fig. 4.7e,f).

The convective precipitation fields from the dry soil sensitivity test (Fig. 6.31a-d) correspond fairly closely with those of the control run (Fig. 4.10a-d) until late in the evening on 23 January 1981 (Day 2). By 21:00 UTC, the tropical-temperate trough structure which is still evident in the control run (Fig. 4.10d) is not apparent in the dry soil sensitivity test (Fig. 6.31d). This is in keeping with the absence of the interior trough in the vertical velocity fields (Figs 6.29d; 6.30d). Examining the convective precipitation at 18:00 UTC on 23 January (Day 2) reveals that the dry soil sensitivity test (Fig. 6.32a) and the control run (Fig. 6.32b) output compare well, except that the precipitation extends further north over northern Namibia in the control run. This implies that the most significant differences began to occur between 18:00 UTC and 21:00 UTC on 23 January (Day 2). In the dry soil sensitivity test, very little convective rainfall is evident by 6:00 UTC the following day (Day 3) (Fig. 6.31e) whereas in

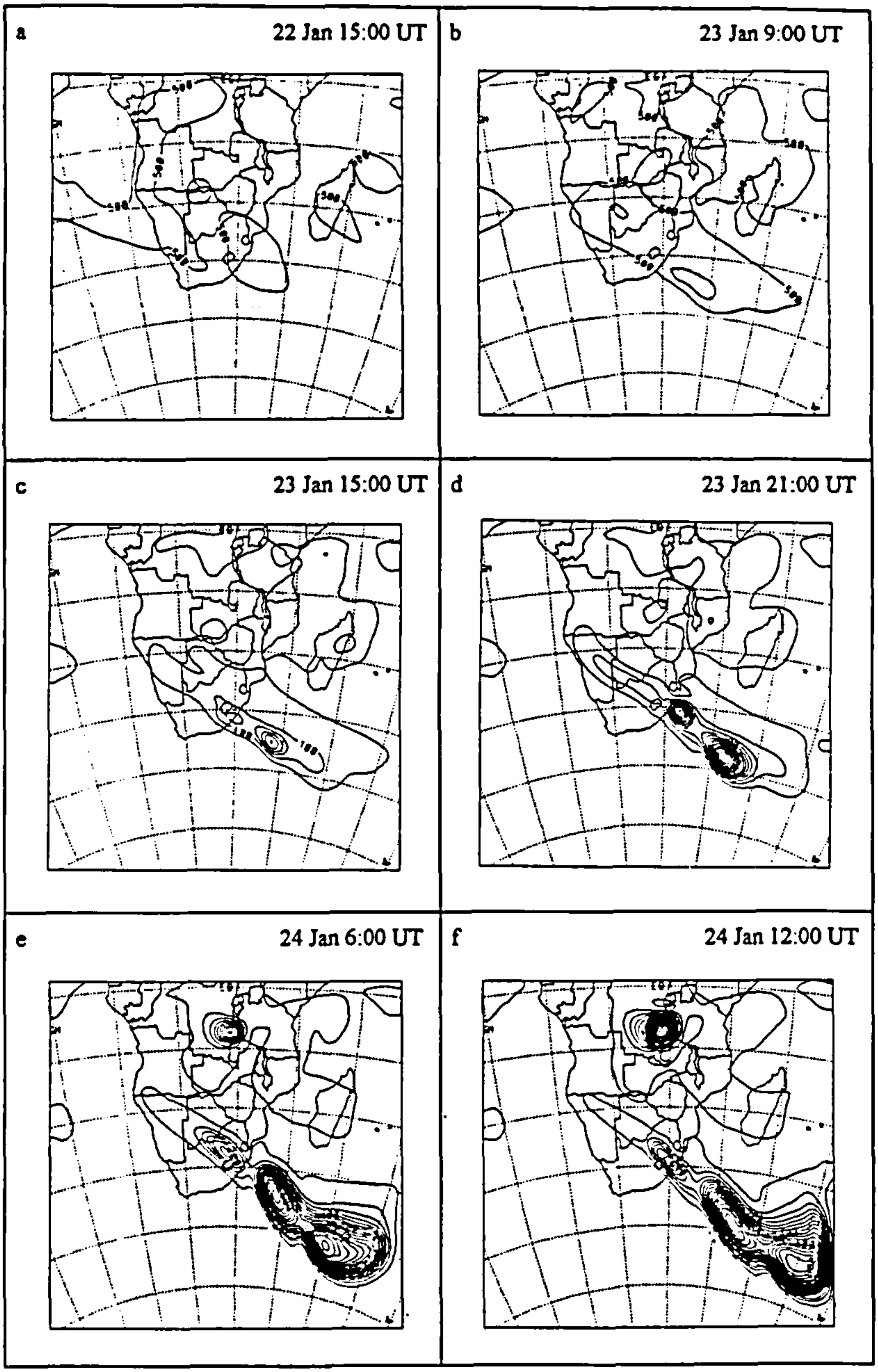

Figure 6.28: Total water mixing ratio at 9,66 km (~ 300 hPa) above sea level from the wet soil sensitivity test at (a) 22 Jan 15:00 UT, (b) 23 Jan 9:00 UT, (c) 23 Jan 15:00 UT, (d) 23 Jan 21:00 UT, (e) 24 Jan 6:00 UT and (f) 24 Jan 12:00 UT ($g.kg^{-1}$; contour interval of 0,5 $g.kg^{-1}$; labels multiplied by 10^3 in a-b, 10^2 in c-f).

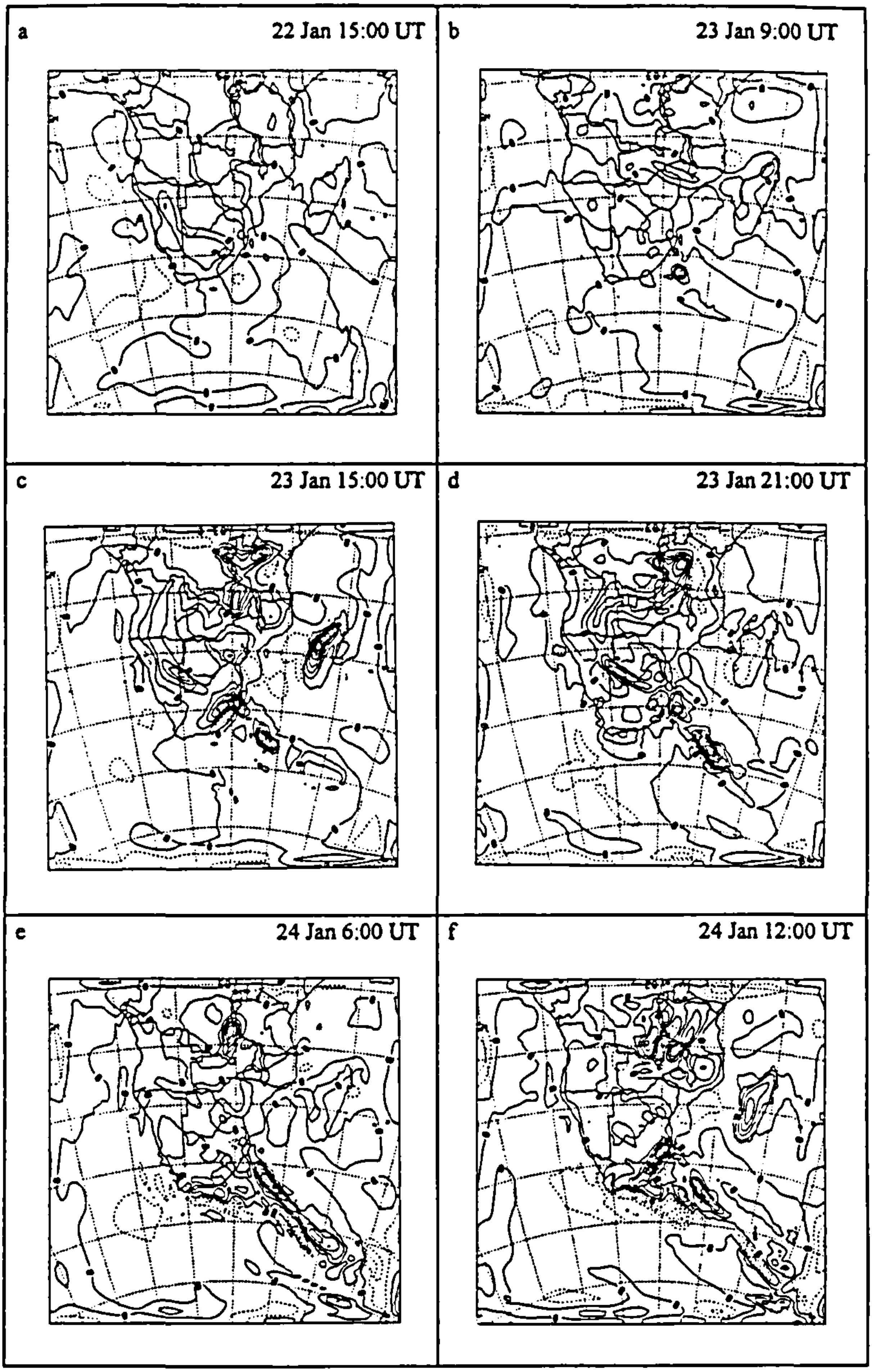

Figure 6.29: Vertical velocity at 3,13 km (~ 700 hPa) above sea level from the dry soil sensitivity test at (a) 22 Jan 15:00 UT, (b) 23 Jan 9:00 UT, (c) 23 Jan 15:00 UT, (d) 23 Jan 21:00 UT, (e) 24 Jan 6:00 UT and (f) 24 Jan 12:00 UT ($cm.s^{-1}$; contour interval of 2 $cm.s^{-1}$; labels multiplied by 10; solid lines indicate uplift and dashed lines indicate subsidence).

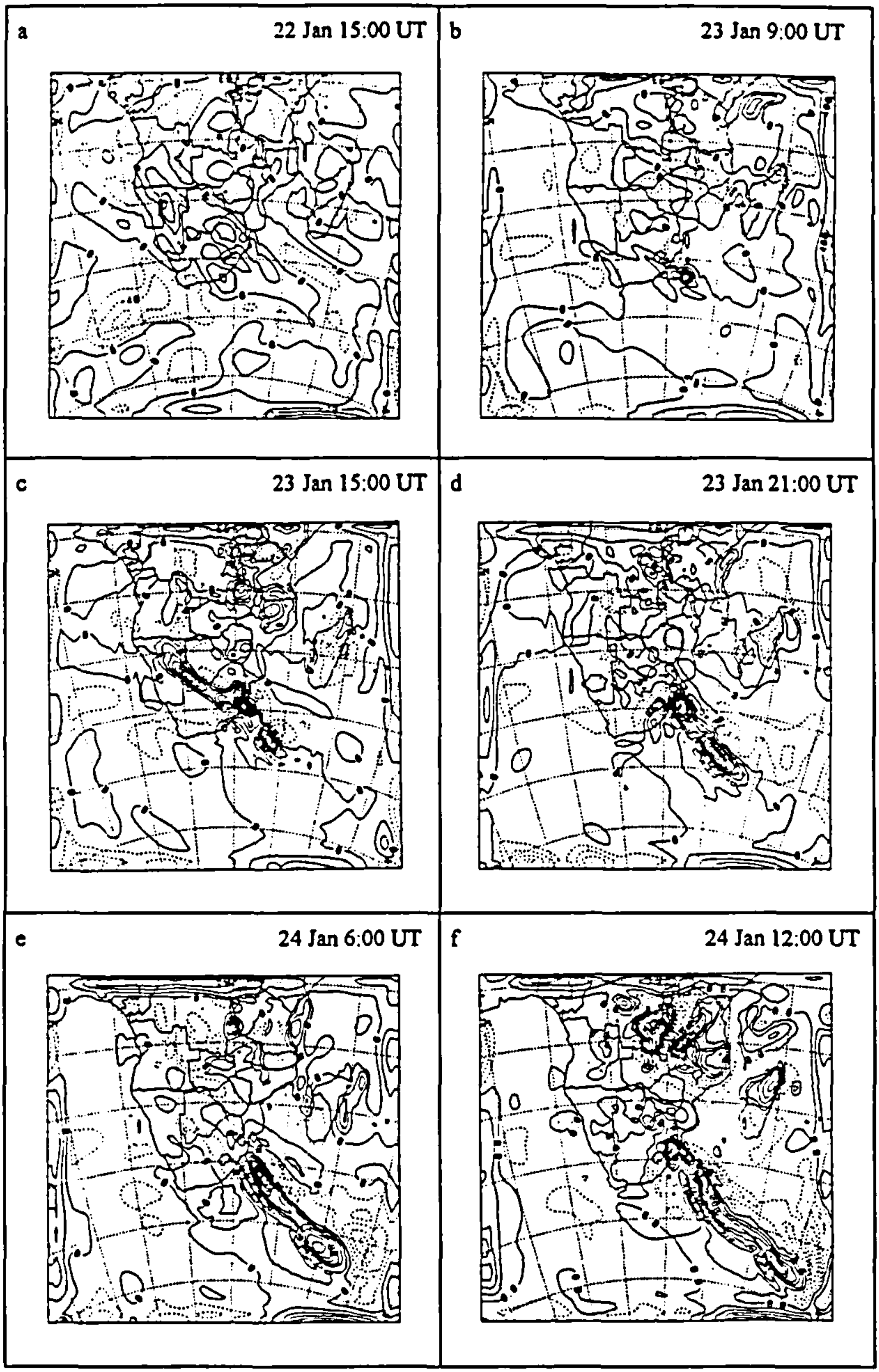

Figure 6.30: Vertical velocity at 9,66 km (~ 300 hPa) above sea level from the dry soil sensitivity test at (a) 22 Jan 15:00 UT, (b) 23 Jan 9:00 UT, (c) 23 Jan 15:00 UT, (d) 23 Jan 21:00 UT, (e) 24 Jan 6:00 UT and (f) 24 Jan 12:00 UT ($cm.s^{-1}$; contour interval of 3 $cm.s^{-1}$; labels multiplied by 10; solid lines indicate uplift and dashed lines indicate subsidence).

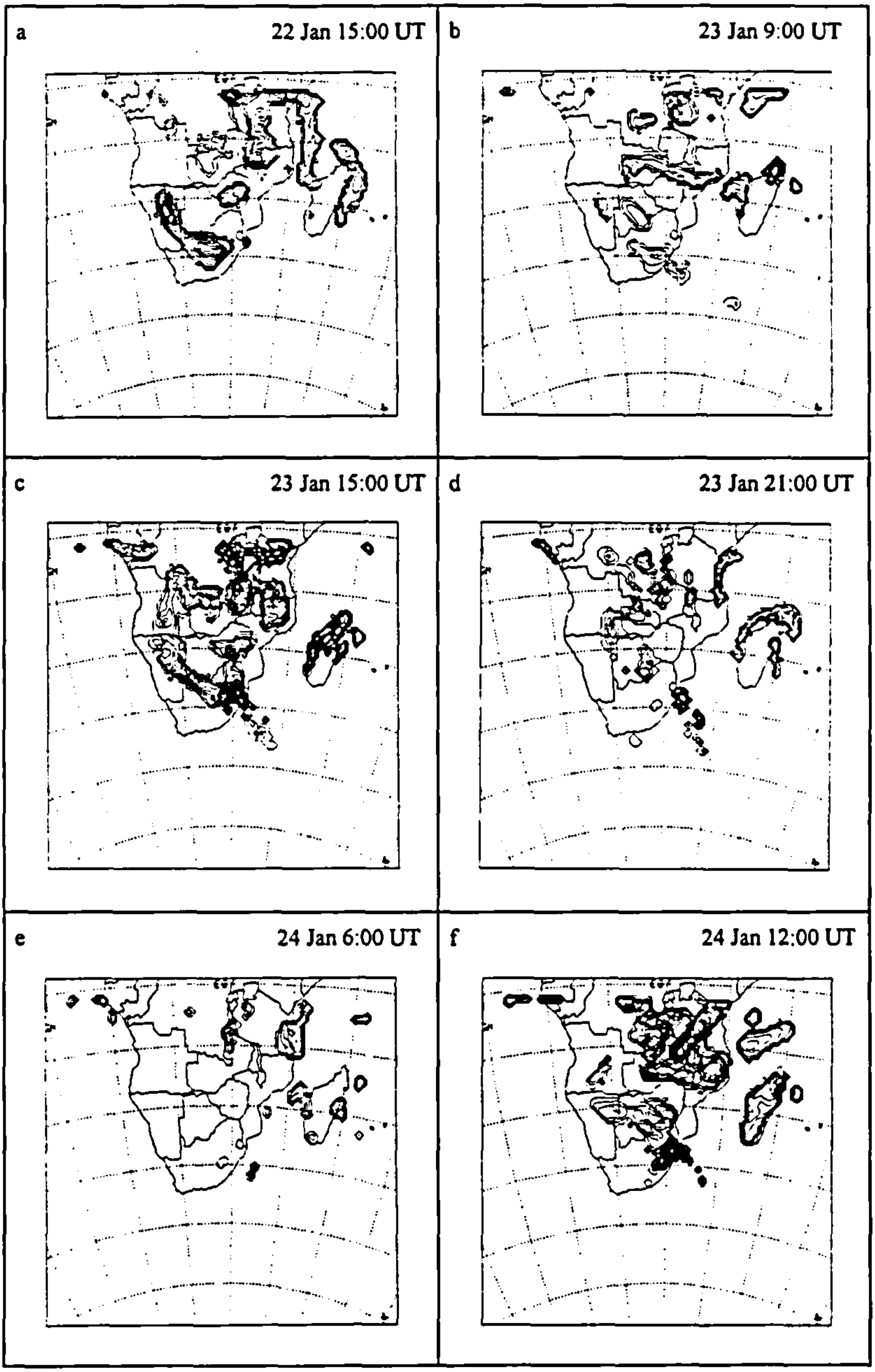

Figure 6.31: Convective parameterisation precipitation rate from the dry soil sensitivity test at (a) 22 Jan 15:00 UT, (b) 23 Jan 9:00 UT, (c) 23 Jan 15:00 UT, (d) 23 Jan 21:00 UT, (e) 24 Jan 6:00 UT and (f) 24 Jan 12:00 UT ($mm.s^{-1}$; contour interval of 0,000035 $mm.s^{-1}$; labels multiplied by 10^7).

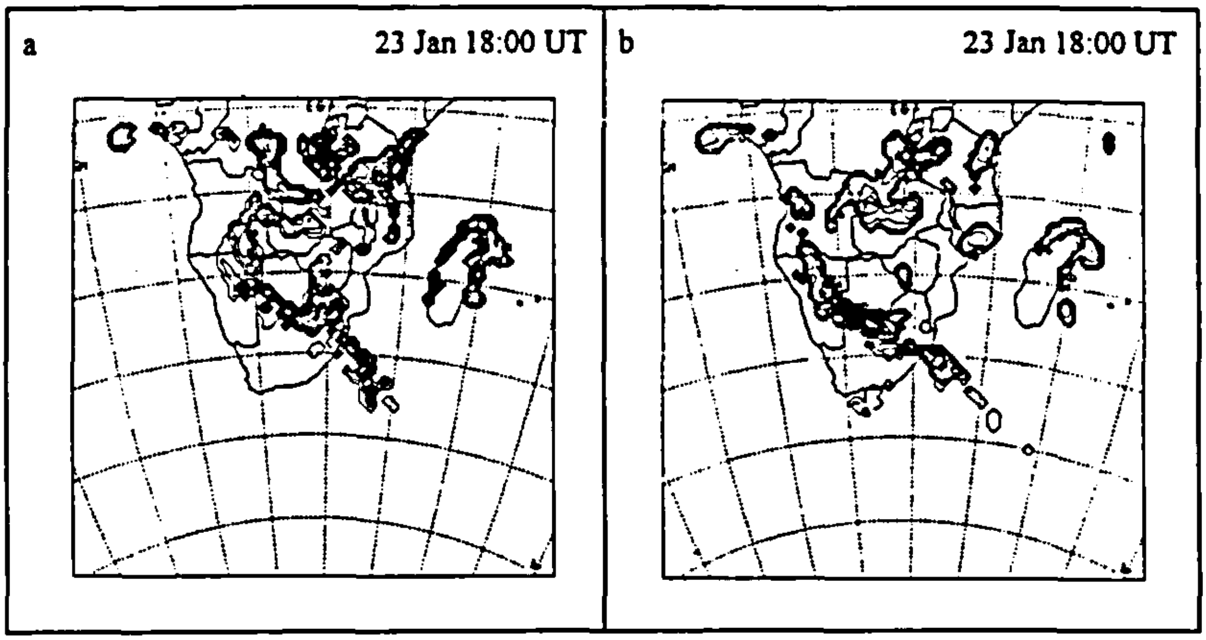

Figure 6.32: Convective parameterisation precipitation rate at 23 Jan 18:00 UT from (a) the dry soil sensitivity test, and (b) wet case study control run ($mm.s^{-1}$; contour interval of 0,000035 $mm.s^{-1}$; labels multiplied by 10^7).

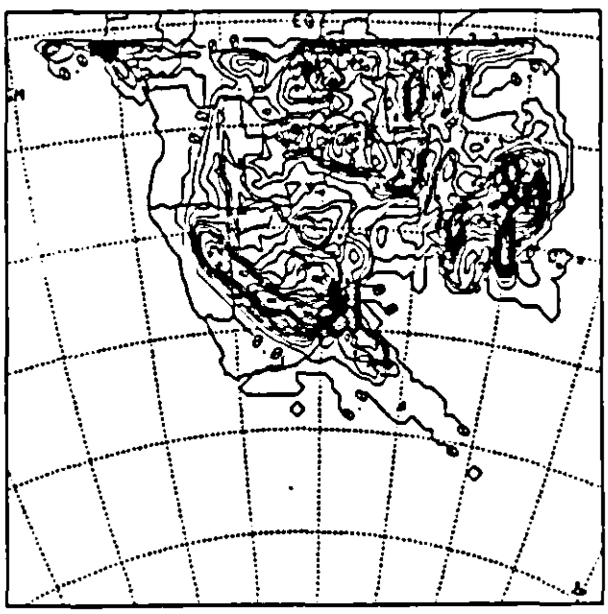

Figure 6.33: Precipitation produced by the cumulus parameterisation scheme between 22 Jan 12:00 UT and 24 Jan 12:00 UT from the dry soil sensitivity test (mm; contour interval of 0,9 mm; maximum value of 14 mm).

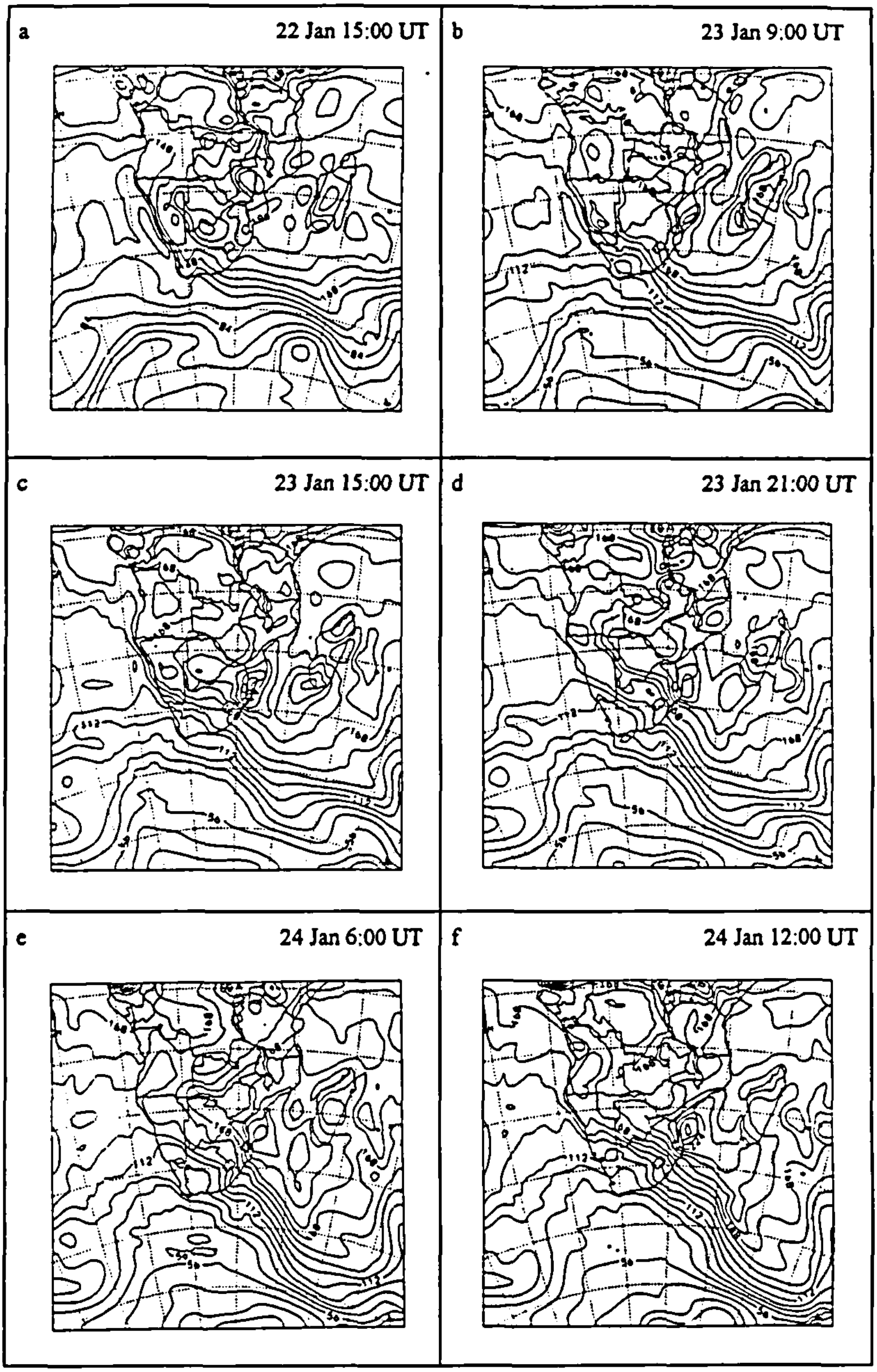

Figure 6.34: Total water mixing ratio at the surface (on the terrain-following coordinate surface 146,4 m above the ground) from the wet case study control run at (a) 22 Jan 15:00 UT, (b) 23 Jan 9:00 UT, (c) 23 Jan 15:00 UT, (d) 23 Jan 21:00 UT, (e) 24 Jan 6:00 UT and (f) 24 Jan 12:00 UT ($g.kg^{-1}$; contour interval of 1,4 $g.kg^{-1}$; labels multiplied by 10).

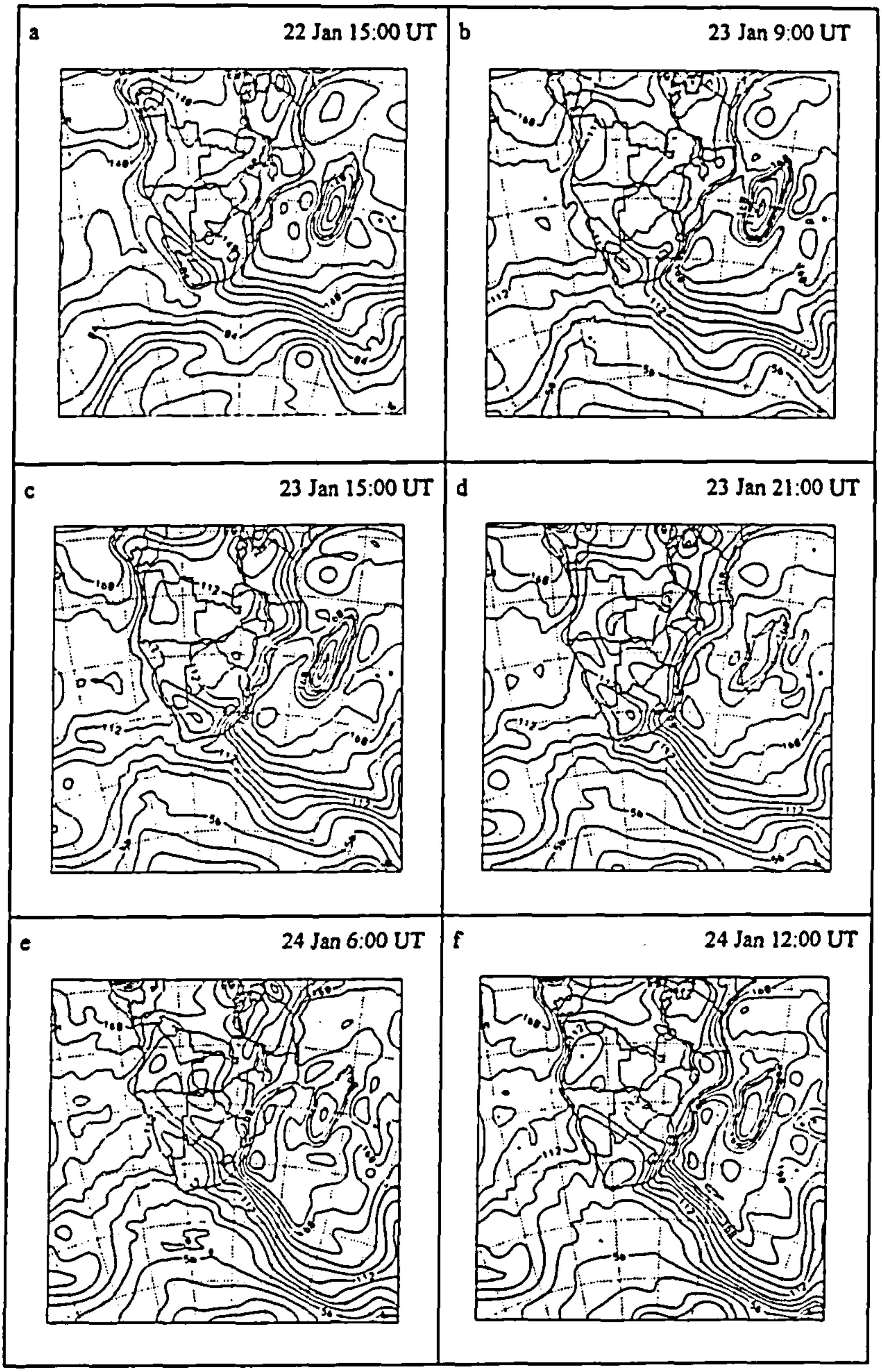

Figure 6.35: Total water mixing ratio at the surface (on the terrain-following coordinate surface 146,4 m above the ground) from the dry soil sensitivity test at (a) 22 Jan 15:00 UT, (b) 23 Jan 9:00 UT, (c) 23 Jan 15:00 UT, (d) 23 Jan 21:00 UT, (e) 24 Jan 6:00 UT and (f) 24 Jan 12:00 UT ($g.kg^{-1}$; contour interval of 1,4 $g.kg^{-1}$; labels multiplied by 10).

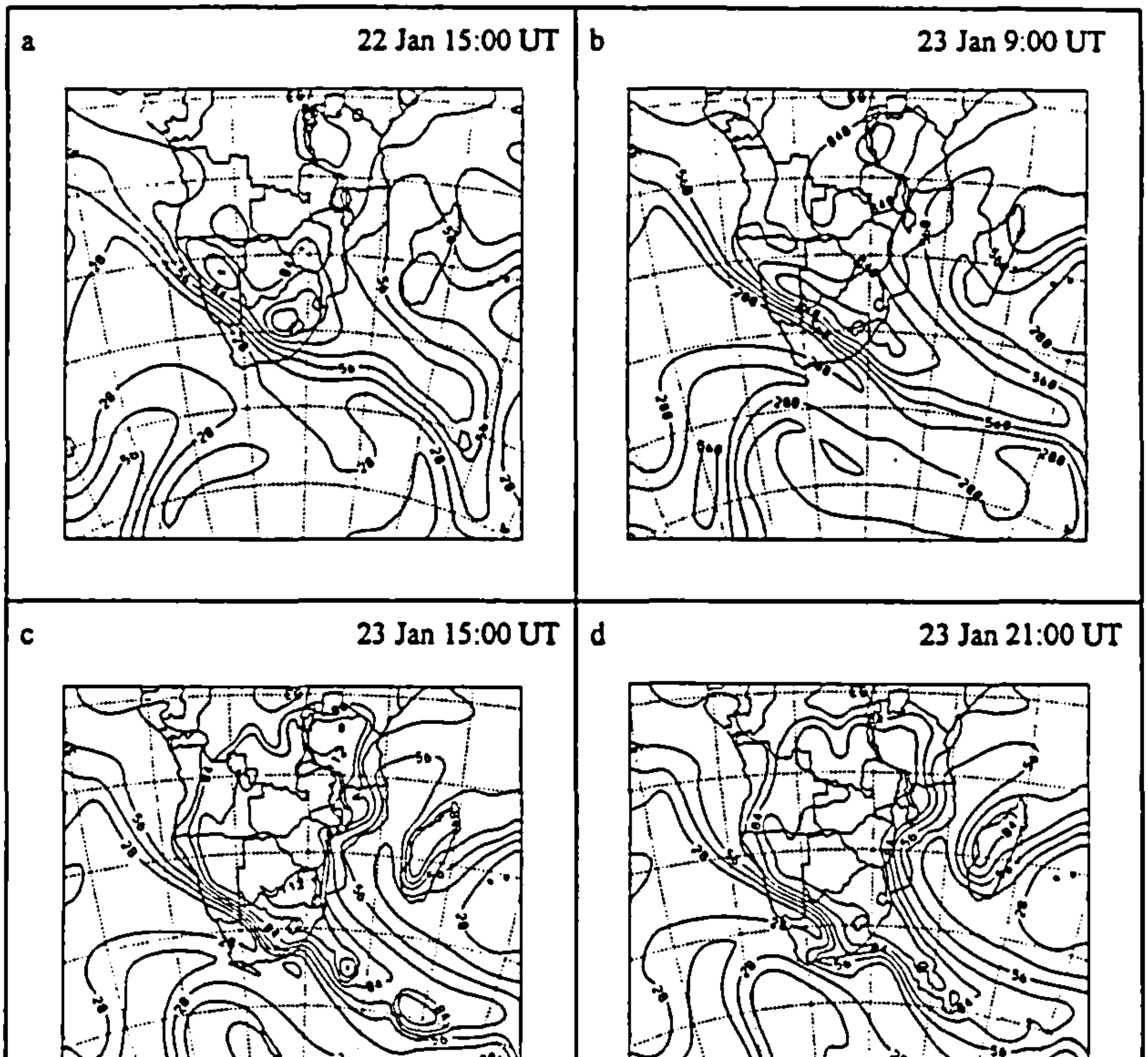

Figure 6.36: Total water mixing ratio at 3,13 km (~ 700 hPa) above sea level from the dry soil sensitivity test at (a) 22 Jan 15:00 UT, (b) 23 Jan 9:00 UT, (c) 23 Jan 15:00 UT, (d) 23 Jan 21:00 UT, (e) 24 Jan 6:00 UT and (f) 24 Jan 12:00 UT ($g.kg^{-1}$; contour interval of 1,4 $g.kg^{-1}$; labels multiplied by 100 in b, and by 10 in a,c-f).

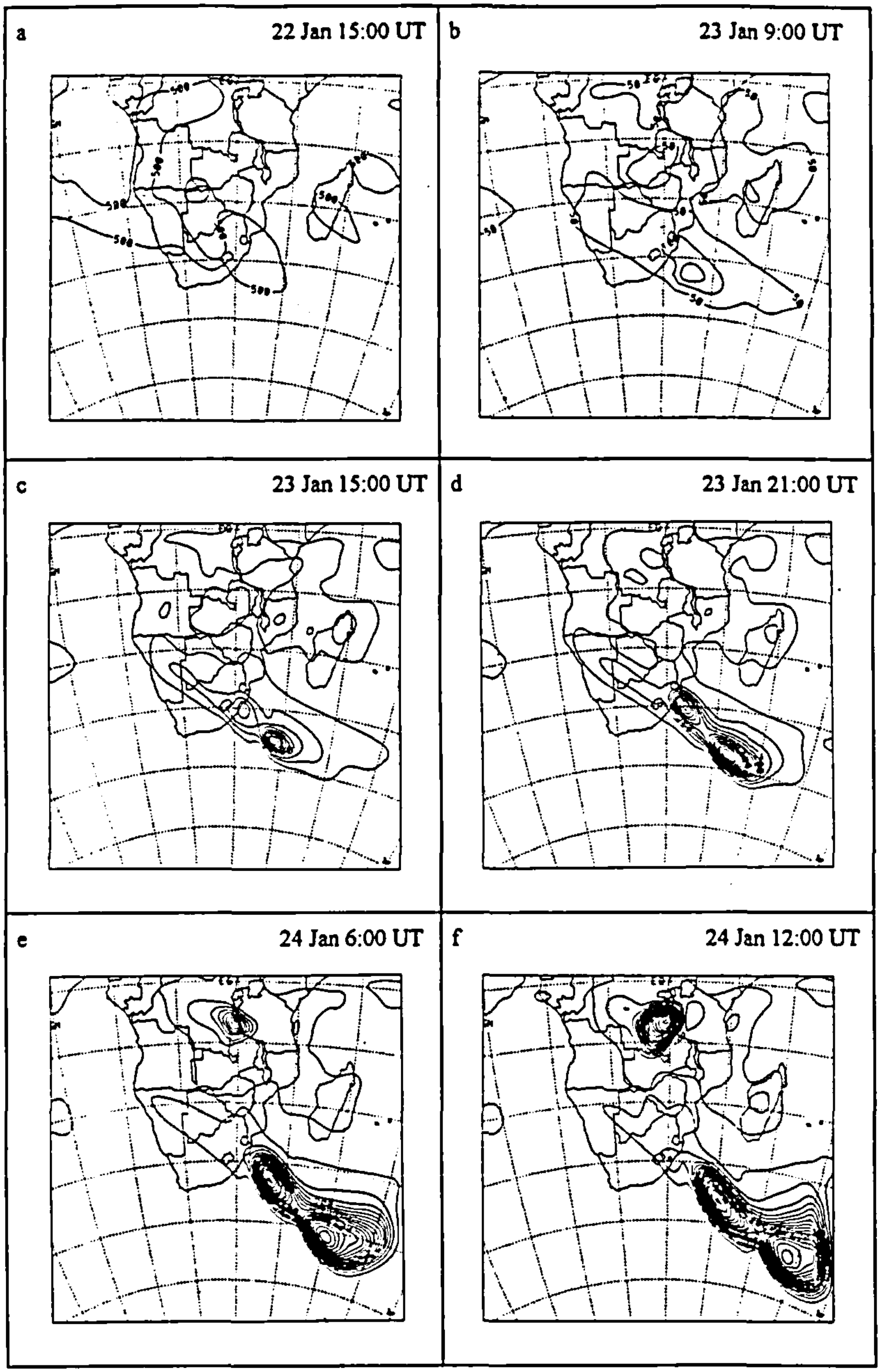

Figure 6.37: Total water mixing ratio at 9,66 km (~ 300 hPa) above sea level from the dry soil sensitivity test at (a) 22 Jan 15:00 UT, (b) 23 Jan 9:00 UT, (c) 23 Jan 15:00 UT, (d) 23 Jan 21:00 UT, (e) 24 Jan 6:00 UT and (f) 24 Jan 12:00 UT ($g.kg^{-1}$; contour interval of 0,5 $g.kg^{-1}$; labels multiplied by 10^3 in a, 10^2 in b-f).

the control run, convective rainfall still occurs along the temperate remnants of the tropical-temperate trough (Fig. 4.10e). Relatively heavy convective precipitation rates are situated along the southern Natal coastal regions in the dry soil sensitivity test (Fig. 6.31f) in response to the vertical forcing in this region (Figs 6.29f; 6.30f), but the convective precipitation along the interior trough remnants is not obvious.

The accumulated convective precipitation from the dry soil sensitivity test (Fig. 6.33) reveals the general cloud band structure, as well as the convective rainfall over the eastern and central region of tropical Africa and is similar to the total convective precipitation from the control run (Fig. 4.11). The maximum total convective precipitation is less (4 mm) in the dry soil sensitivity test than in the control run.

Total mixing ratios at the surface in the control run (Fig. 6.34) range between 11,2 $g.kg^{-1}$ over the western coast of southern Africa to greater than 16,8 $g.kg^{-1}$ over central and eastern southern Africa, and the regions of greatest total mixing ratios move eastward in accordance with the tropical-temperate trough movement. In the dry soil sensitivity test (Fig. 6.35a-f), the total mixing ratios at the surface are less than those of the control run, ranging from approximately 9,8 $g.kg^{-1}$ over the western interior, to about 11,2 $g.kg^{-1}$ over the central regions and to 16,8 $g.kg^{-1}$ along the extreme eastern regions of the subcontinent. However, at the 700 (Fig. 6.36a-f) and 300 (Fig. 6.37a-f) hPa levels, the total mixing ratio fields from the dry soil sensitivity test and from the control run (Figs 5.21a-f; 5.23a-f) compare well, although the upper tropospheric total mixing ratios over the interior are lower in the dry soil sensitivity test (Fig. 6.37c,e,f).

Discussion

Limiting the soil moisture to between 75% and 90% of saturation at the surface had little effect on the development, dissipation and convective precipitation of the wet case tropical-temperate trough. Even the surface level moisture fields underwent little change. However, by limiting the soil moisture to between 10% and 20% of saturation at the surface, the breakdown of the tropical-temperate trough structure was evident in the reduced vertical velocities and the lack of convective precipitation by 21:00 UT on 23 January (Day 2). By 24 January (Day 3), not even remnants of the interior trough were evident. In the dry soil moisture sensitivity test, the tropical-temperate trough was not as strongly developed as in the control run and the dissipation of the tropical-temperate trough occurred earlier and more rapidly than that of the control run.

As the mixing ratios at the 700 and 300 hpa levels revealed little difference between the control run and the wet and dry soil moisture sensitivity tests, a water vapour source other than the surface is implied. This points to the oceans as a moisture source for the atmospheric systems over southern Africa which corroborates previous hypotheses to this effect (Taljaard, 1986, 1987, 1990; Tyson, 1986), in particular, that the oceanic region to the northwest of Madagascar is an important source of water vapour for tropical-temperate troughs during wet and dry late summers (D'Abreton, 1992; D'Abreton and Tyson, 1994). The changes in the surface level moisture fields during the dry soil sensitivity test indicate that the surface does contribute moisture to the lowest atmospheric levels, but this does not appear to significantly affect the moisture transportation within tropical-temperate troughs. The lower moisture content of the surface atmospheric levels does, however, appear to affect the vertical uplift associated with the interior trough which forms the connection between the tropical and temperate systems. The lower water vapour content reduces the atmospheric buoyancy and enhances atmospheric stability. The reduced vertical uplift resulted in an earlier demise of the tropical-temperate trough and the lower accumulated convective precipitation totals. Lower soil moisture therefore seems to affect the strength and duration of the wet case cloud band, but not the tropical-temperate trough development and structure, nor the moisture transport along the cloud band which is of oceanic origin.

The sensitivity tests have revealed that a finer grid resolution does not significantly affect the development, dissipation and rainfall of tropical-temperate troughs, although the cut-off low in the wet case was better simulated with the finer resolution. The inclusion of resolved microphysics results in a more accurate representation of the observed rainfall, but in a reduction in the upper level condensate and total mixing ratios which appears to be due to a weakness in the convective parameterisation scheme. Wetter than normal soil has little effect on the development and precipitation of tropical-temperate troughs. Drier than normal soil caused lower total mixing ratios near the surface and an earlier dissipation of the tropical-temperate trough, but had little effect on the moisture transport at the 700 hPa level and above which implies that the oceans are a more important moisture source than the surface for the development of tropical-temperate troughs.

Synopsis

The effects of a finer grid resolution, the inclusion of explicit microphysics and changes in soil moisture on the development, dissipation and rainfall of tropical-temperate troughs have been investigated. The smaller scale cut-off low that developed during the wet case was not evident in the control run, but was well simulated in the finer resolution simulation. Vertical velocities and the resultant convective precipitation rates were greater in the finer resolution sensitivity test. The finer grid resolution did not, however, have a significant effect on the development of the tropical-temperate troughs which enhances the credibility of the numerical model. The inclusion of resolved microphysics resulted in an improved simulation of the observed rainfall during both the wet and dry case studies. The upper level mixing ratios were, however, much lower than the control runs and appears to be due to a weakness in the convection parameterisation scheme. Greater soil moisture had little effect on the wet case tropical-temperate trough. Lower soil moisture resulted in a lower moisture content of the atmosphere near the surface, weaker vertical velocities and the earlier dissipation of the dry case tropical-temperate trough. However, the mixing ratios at the 700 and 300 hpa level were not affected which points to the importance of the oceans in supplying water vapour for tropical-temperate trough development.

CHAPTER 7

THE TROPICAL INDIAN OCEAN SEA SURFACE TEMPERATURE ANOMALY

Sea surface temperatures have a direct effect on the atmospheric boundary layer, through a complex balance of energy fluxes and momentum transfer. Over intra-annual and inter-annual time scales the variability of sea surface temperatures surrounding the subcontinent has demonstrated a causative link with variations in rainfall (Walker, 1989; Mason, 1992). The tropical Indian Ocean in particular exhibits strong control over late summer precipitation, as it forms an important water vapour source to the subcontinent by means of easterly transport (D'Abreton, 1992). Anomalously warm sea surface temperatures result in reduced divergence of water vapour from the Indian Ocean to the African subcontinent as moisture is redirected to regions of heightend instability by the development of cyclonic vorticity. This causes a reduction in precipitation over the country due to lower moisture availability. Although these investigations have helped to develop some understanding of the importance of the tropical Indian Ocean as both a late summer moisture source and as a control on the longitudinal position of the African convective centre (Jury and Pathack, 1991; Lindsay and Jury, 1991; Mason, 1992; Jury, 1993), limited research efforts have investigated the influence this oceanic region has on a shorter time scale. Most research has been confined to statistical analyses, through correlation and cross-spectral techniques, and to investigations of inter-annual fluctuations of the ocean-atmosphere system, through the investigation of the Southern Oscillation and its global teleconnections (Bjerknes, 1969; Harrison, 1984b; Cane, 1986; Nicholson and Entekhabi, 1987; Lindesay, 1988a, 1988b; Harangozo, 1989; Walker, 1989; Jury and Pathack, 1991; Lindsay and Jury, 1991; Mason, 1991, 1995; Jury, 1993). With this in mind an attempt is made to investigate the effect the tropical Indian Ocean has on precipitation over a much smaller time frame (4 days) by testing the sensitivity of RAMS to imposed sea temperature anomalies. In this and the following oceanic sensitivity tests the simulation period was extended by a day to include 21 January 1981. The original 48 hour wet period control simulation was thus increased to 72 hours, along with the sensitivity experiments in order to allow a longer residence time for the sea surface temperature anomalies.

In the tropical Indian Ocean, north east of Madagascar, the observed mean sea surface temperature data set from the United Kingdom Meteorological Office (Parker, 1987; Parker and Folland, 1988), was modified to include a positive 2^{0}C increase in existing sea surface temperatures. Ocean temperatures on the boundary of the perturbed sea surface temperature field were increased by 1^{0}C in order to minimise any unwarranted effects of a strong temperature gradient (Fig 7.1).

Results

The sensitivity of the RAMS simulation of the tropical-temperate trough, to a tropical Indian Ocean positive sea surface temperature anomaly event is ascertained by the comparison of control and sensitivity wind components (u,v), streamlines, temperature, vertical velocity (w), vapour and cloud mixing ratios, and accumulated convective precipitation, at the surface (146,4 m) and the (807,2 m) near surface levels. These levels were chosen for comparison as it would be unrealistic to expect any significant changes in the upper-level dynamics over a 4-day period. The control and sensitivity simulations were initialised using the same parameterisation and data except for the sea surface temperature anomaly imposed in the sensitivity sea surface temperature data set. Differences in simulation are thus the product of different sea surface temperatures only.

Day one

At the start time of the simulation (1200 UTC, 21 January 1981), all the atmospheric components simulated in the sensitivity test were compared to the control at the 146,4 m sigma level, but no differences were identified (Fig 7.2 a,b). This is however not surprising as the initialisation of both the control and sensitivity simulations takes place from the same ECMWF atmospheric data sets. This data set provides the model with the 3-D atmospheric

Sensitivity Test 5 (Tropical Indian Ocean)

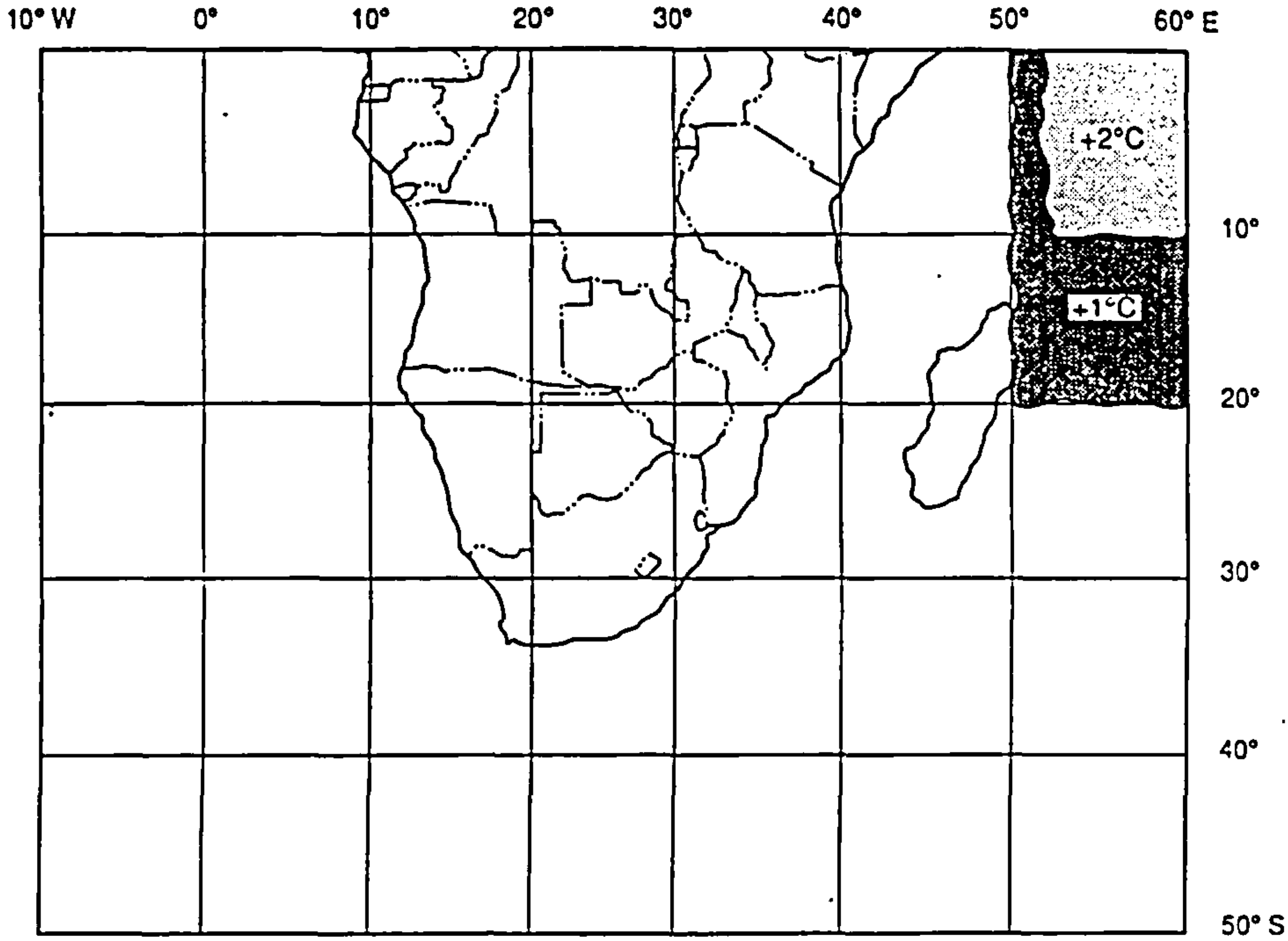

Figure 7.1: Representation of the fifth sensitivity test with anomalies placed between 0° and 20°S,extending east of 50°E.

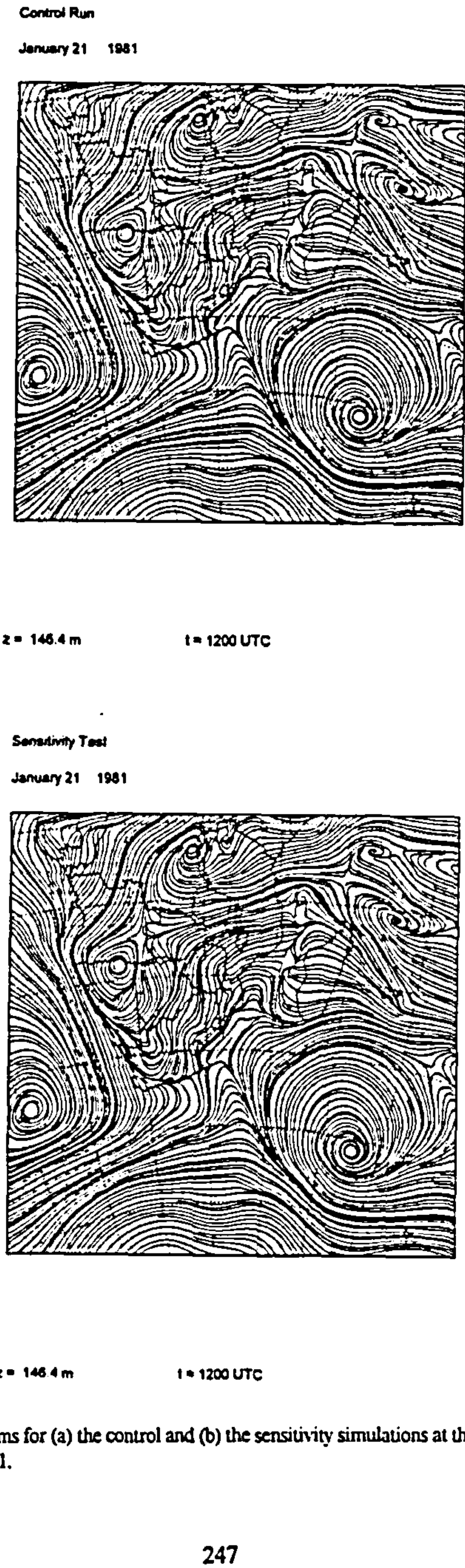

Figure 7.2: Streamline diagrams for (a) the control and (b) the sensitivity simulations at the 146.4m sigma level for 1200 UTC on 21 January 1981.

fields needed at the initial time-step. After the first time-step has been completed the ECMWF data sets are used only to maintain the lateral boundary conditions through the application of a nudging technique, and thus allowing simulation differences to develop. Both simulations model the moist air in circulation over Namibia, and around the tropical low, as well as the approximate positions of the quasi-stationary high pressures and westerly wave perturbations (Fig 7.3 a,b).

After nine hours of simulated time have elapsed (2100 UTC) the sensitivity output at the 146,4 m level begins to diverge from the control. The imposition of the sea surface temperature anomaly produced an initial strengthening of easterly flow to the east of Madagascar from between 4 to 5 ms^{-1} in the control simulation to between 5 to 6 ms^{-1} in the sensitivity test (Fig 7.4 a,b). Concomitant to the marginal strengthening of the easterly flow is an increase in simulated instability from a control value of 0,018 cms^{-1} to a sensitivity value of 0,021 cms^{-1} in the same area, and an increase in vapour and cloud mixing ratios south of 10^0S. Isolated areas to the east of Madagascar recorded higher convective precipitation values of 3,6 mm in the sensitivity test compared to 2,8 mm in the control simulation (Fig 7.5 a,b).

At the same time, at the 807,2 m level, easterly flow over the central regions of Madagascar and the Mozambique Channel strengthened (Fig 7.6 a,b). Vertical velocity, vapour and cloud mixing ratios, and accumulated convective precipitation simulated increases of the same magnitude as near the surface (Fig 7.7 a,b).

Day two

On 22 January (0600 UTC) at the 146,4 m level the easterly wind component anomaly to the east of Madagascar continued to strengthen. North of 10^0S the easterly component reduced, making way for the intrusion of northwesterly flow into the region north of Madagascar (Fig 7.8 a,b). At 0600 UTC cyclogenesis appears for the first time over the area of modified sea surface temperatures. Vertical velocity strengthened along the east coast of Madagascar with a maximum value of 0,028 cms^{-1} as opposed to the control value of 0,021 cms^{-1}. The maximum subcontinent precipitation values recorded decreased from 13,6 mm in the control simulation to 12,8 mm in the sensitivity experiment. Accumulated convective precipitation

Control Run

January 21 1981

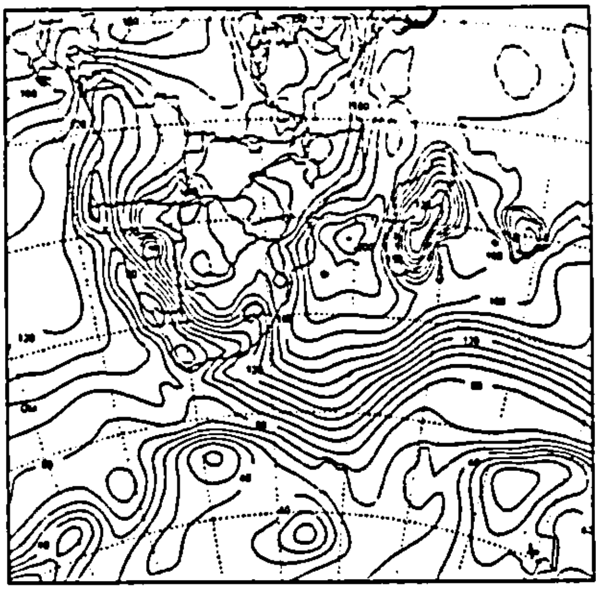

VAPOR AND CLOUDS

z = 146.4 m t = 1200 UTC

Sensitivity Test

January 21 1981

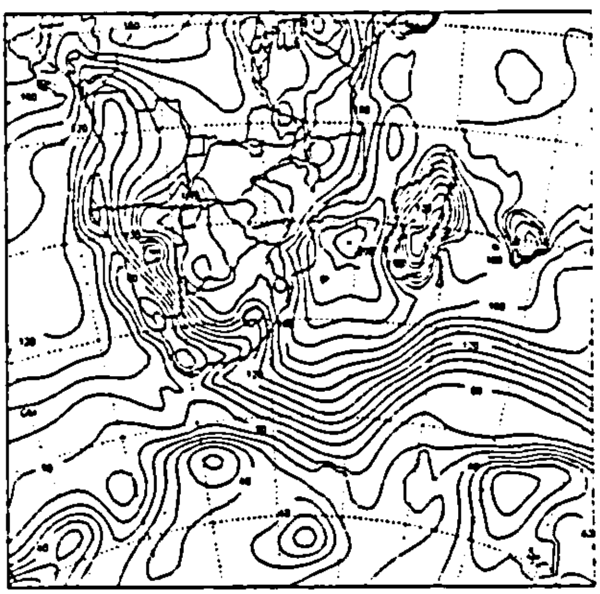

VAPOR AND CLOUDS

z = 146.4 m t = 1200 UTC

Figure 7.3: Vapour and cloud mixing ratios (g.kg^{-1} x 10^{-4}) for (a) the control and (b) the sensitivity simulations at the 146.4m sigma level for 1200 UTC on 21 January 1981.

Control Run

January 21 1981

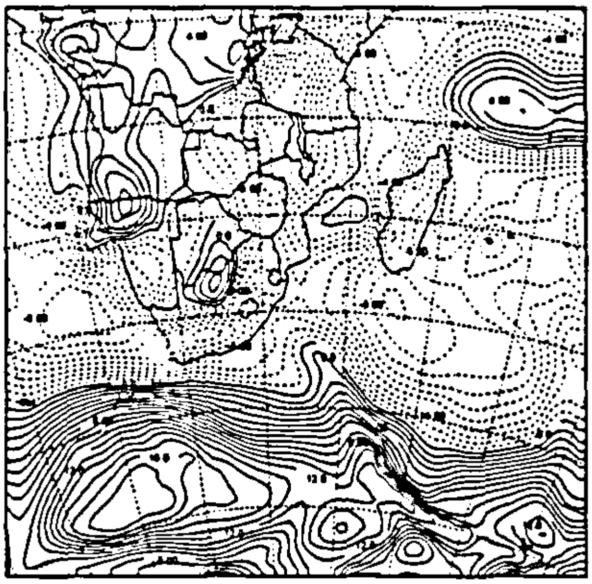

u

z = 146.4 m t = 2100 UTC

Sensitivity Test

January 21 1981

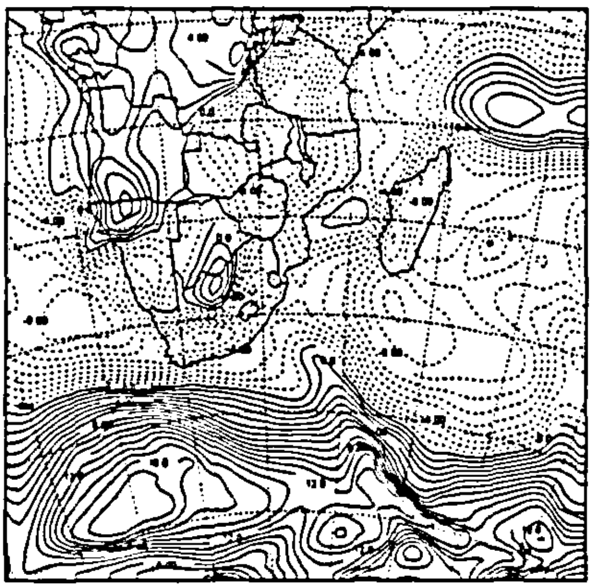

u

z = 146.4 m t = 2100 UTC

Figure 7.4: U Components (m.s^{-1}) for (a) the control and (b) the sensitivity simulations at the 146.4m sigma level for 2100 UTC on 21 January 1981.

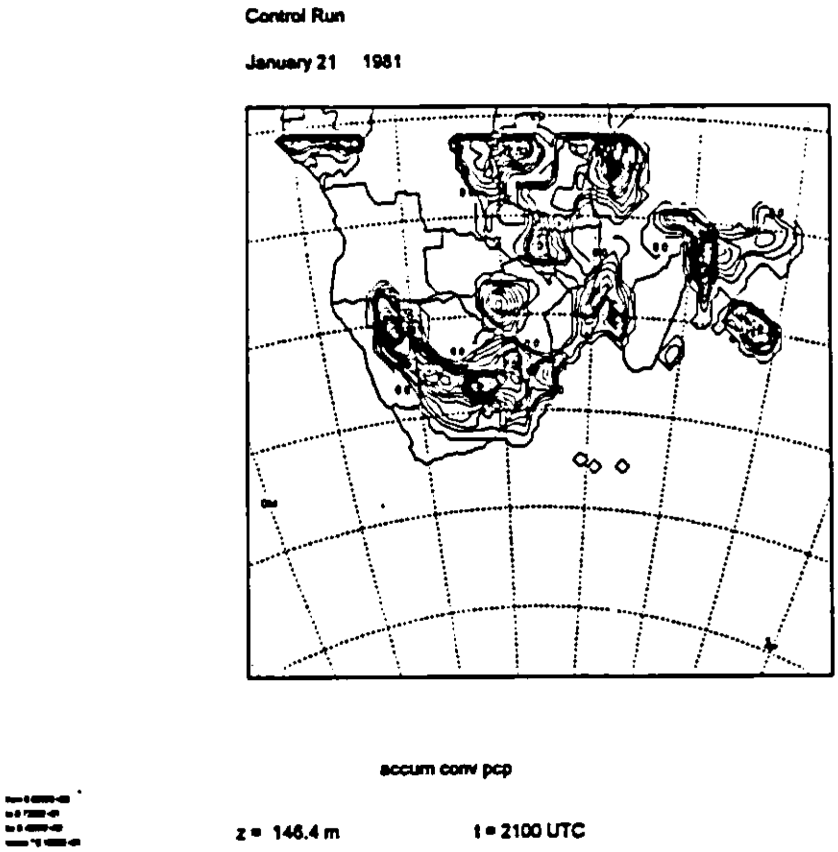

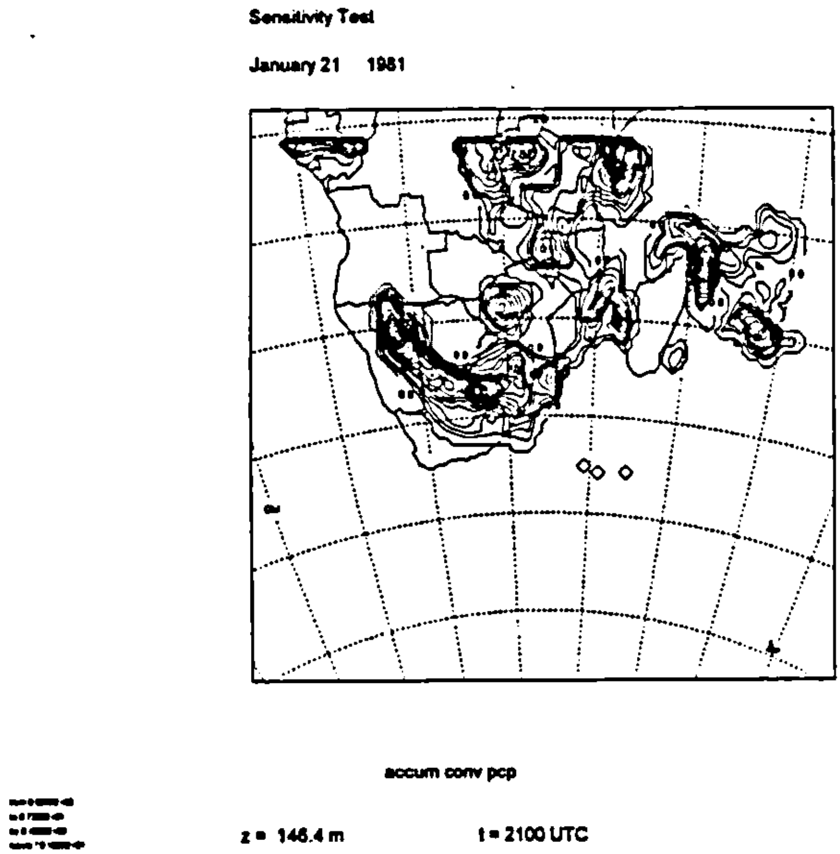

Figure 7.5: Accumulated convective precipitation (in mm)for (a) the control and (b) the sensitivity simulations at the 146,4m sigma level for 2100 UTC on 21 January 1981.

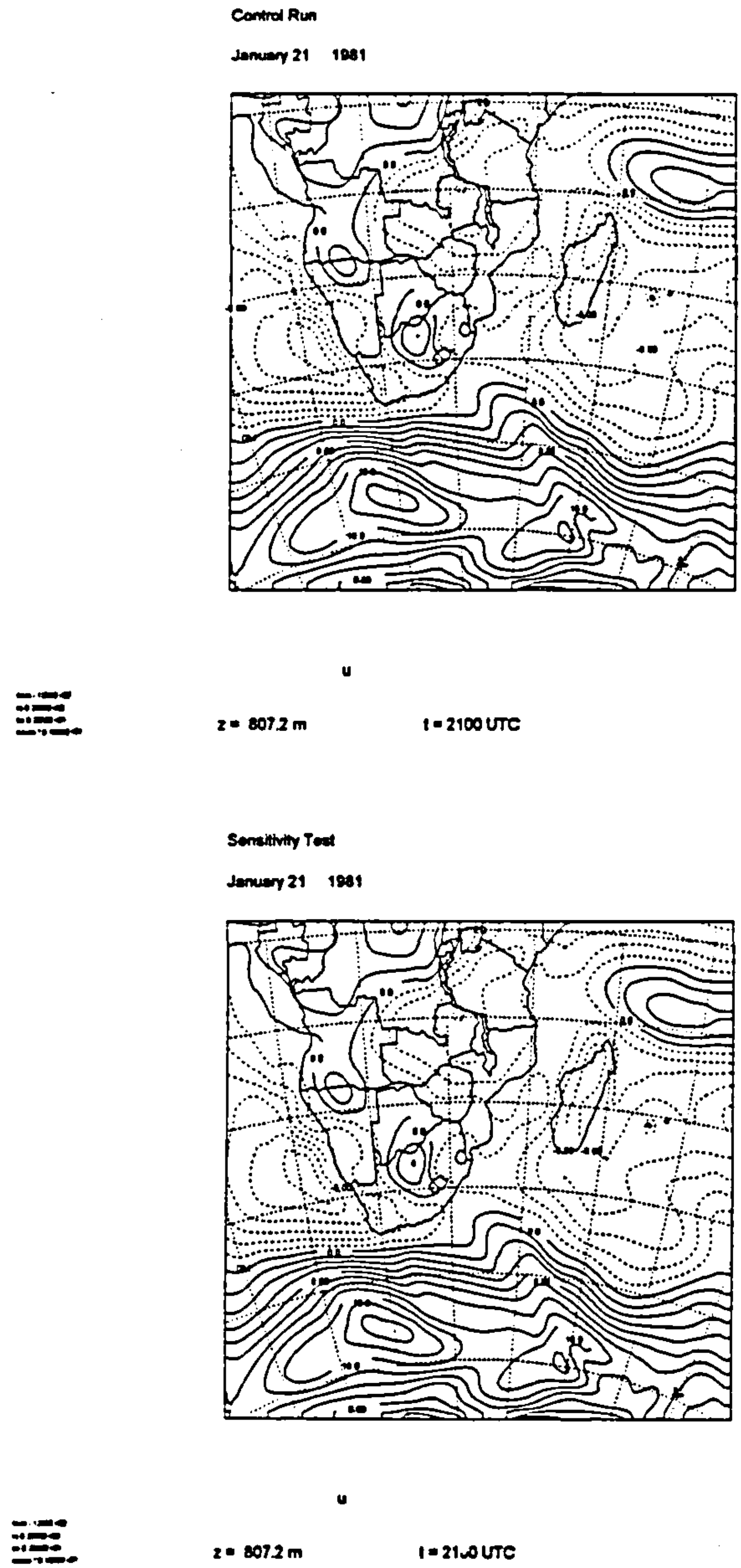

Figure 7.6: U components (in m.s^{-1}) for (a) the control and (b) the sensitivity simulations at the 807,2m sigma level for 2100 UTC on 21 January 1981.

Control Run

January 21 1981

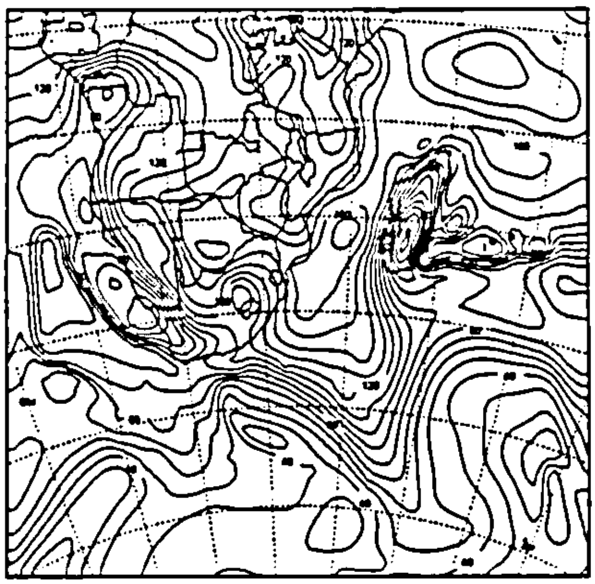

VAPOUR AND CLOUDS

z = 807.2 m t = 2100 UTC

Sensitivity Test

January 21 1981

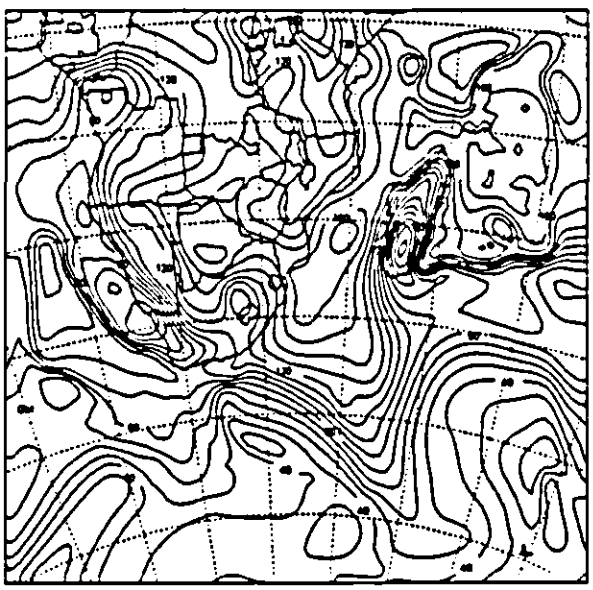

VAPOUR AND CLOUDS

z = 807.2 m t = 2100 UTC

Figure 7.7: Vapour and cloud mixing ratios (in g.kg^{-1} x10^{-4}) for (a) the control and (b) the sensitivity simulations at the 807.2m sigma level for 2100 UTC on 21 January 1981.

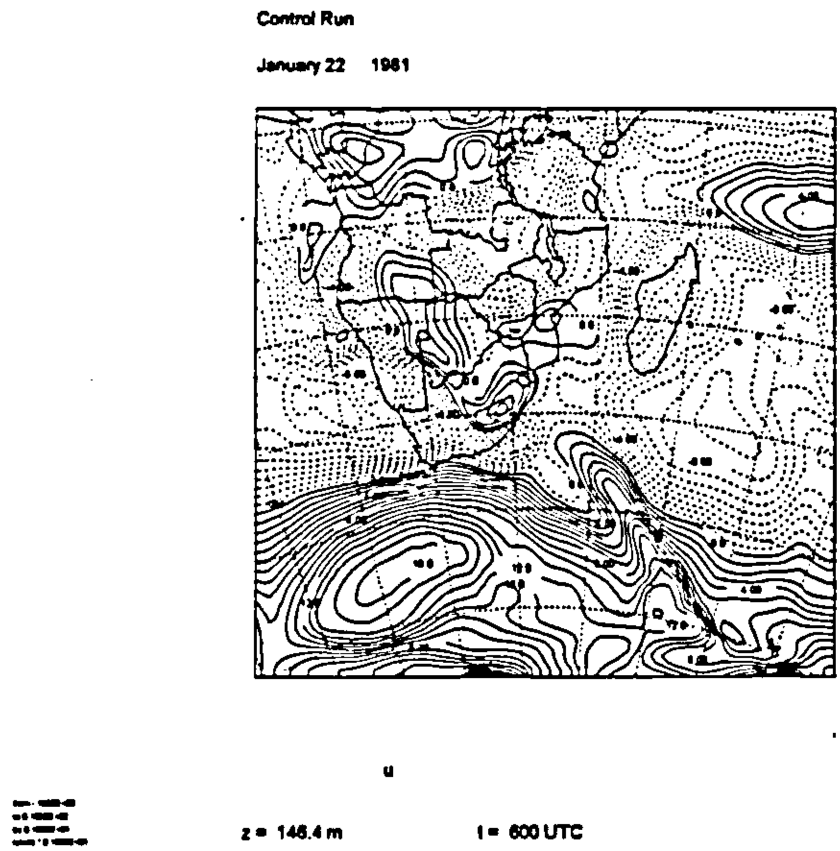

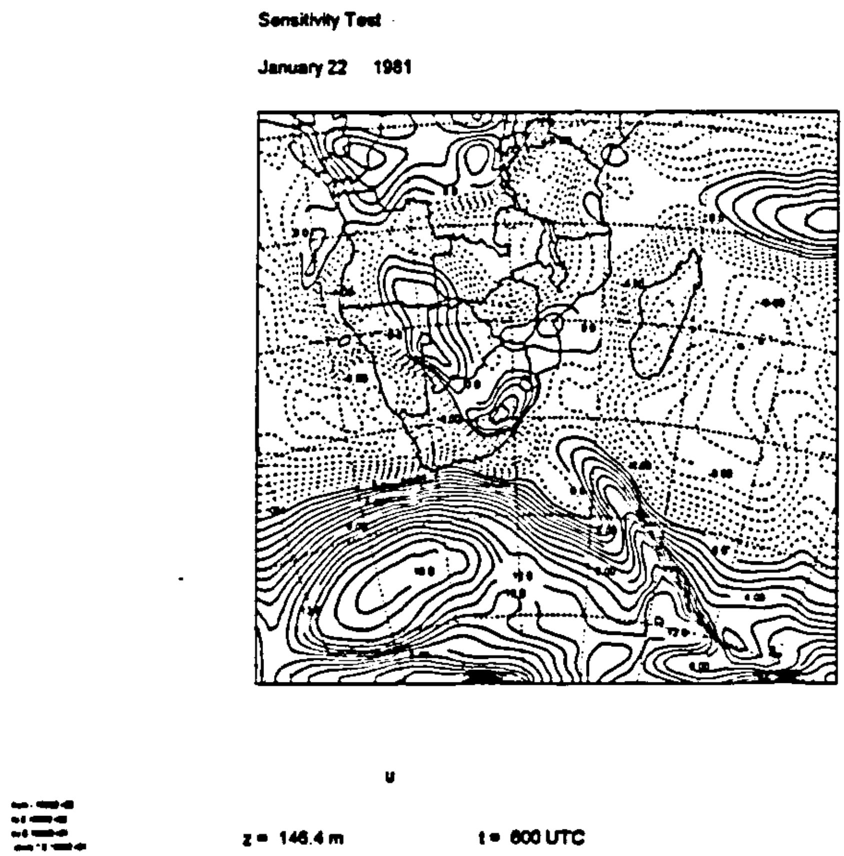

Figure 7.8: U components (in m.s^{-1}) for (a) the control and (b) the sensitivity simulations at the 146.4m sigma level for 0600 UTC on 22 January 1981.

increased to the east and northeast of Madagascar from between 1,6 mm and 2,4 mm in the control simulation to between 2,4 mm and 3,2 mm in the sensitivity test (Fig 7.9 a,b).

At 2100 UTC on 22 January a comparison of the control and sensitivity simulations at 146,4 m revealed that the recurved northwesterly flow further increased its westward extent along 10^0S (Fig 3.8 a,b). An intensification of the developing cyclogenesis is found over the area of modified sea surface temperatures, with a low pressure cell developing at the mouth of the Mozambique Channel. Surface divergence appeared for the first time along the 40^0E line of longitude deflecting moist tropical air away from the subcontinent and towards the developing low pressure. Vapour and cloud mixing ratios indicate a greater moisture availability north of Madagascar i.e. a greater southerly extent of the 0,017 $g.kg^{-1}$ contour line (Fig 7.11 a,b). Lower continental precipitation values were recorded due to the reduction of moist tropical flow from the east with sensitivity values over Durban approximately 9 mm as opposed to 11 mm in the control experiment. Increased convergence and orographic impetus along the east coast of Madagascar produced higher convective precipitation in the area, as well as along the north coast with values of 5 mm in the control compared to 8 mm in the sensitivity test (Fig 7.12 a,b).

Trends at the 807 m level, for the same period, indicate a continued westerly expansion of the recurved northwesterly flow. The upper-level easterly flow at approximately 5^0S strengthened and produced a concomitant intensification of the low pressure system found at 10^0S (Fig 7.13 a,b). Vertical instability is higher along the north and northeast coasts of Madagascar due to the proximity of the low pressure system with highest recorded values of 0,028 cms^{-1} for the control simulation and 0,042 cms^{-1} for the sensitivity experiment, along with heightened easterly winds (Fig 7.14 a,b).

Vertical velocities for the sensitivity simulation are lower along the east coast of South Africa with values of 0,077 cms^{-1} compared to 0,084 cms^{-1}, possibly due to stronger northwesterly winds in the area. Vapour and cloud mixing ratio values remained higher over the modified sea surface temperature field, as a result of the modification of the saturated mixing ratios by the warmer sea surface temperature anomalies. At 2100 UTC on 22 January the higher

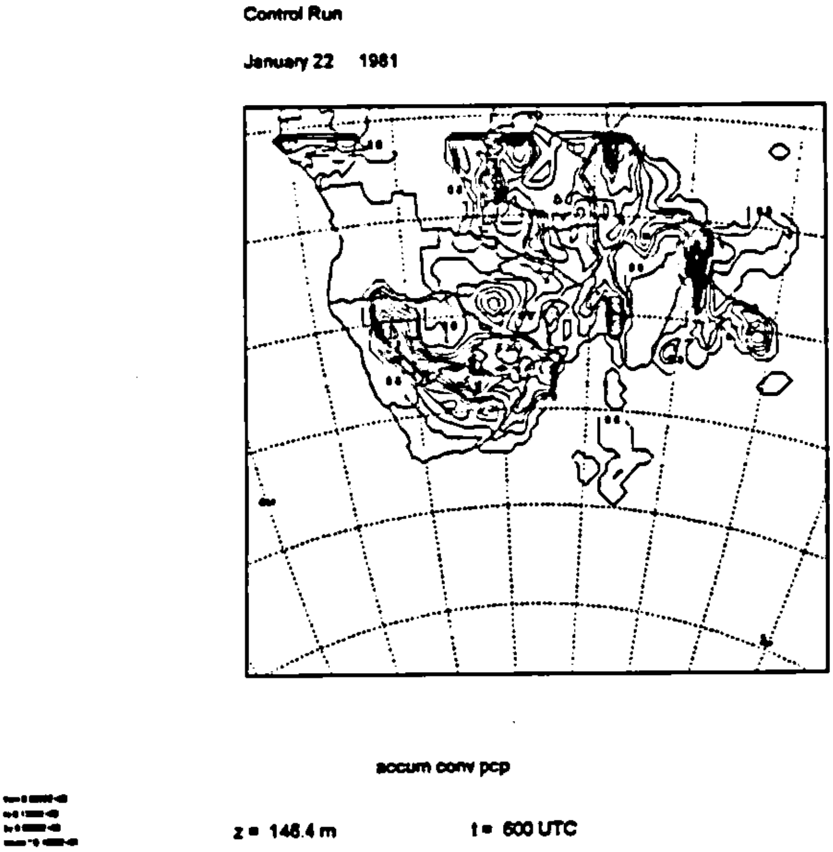

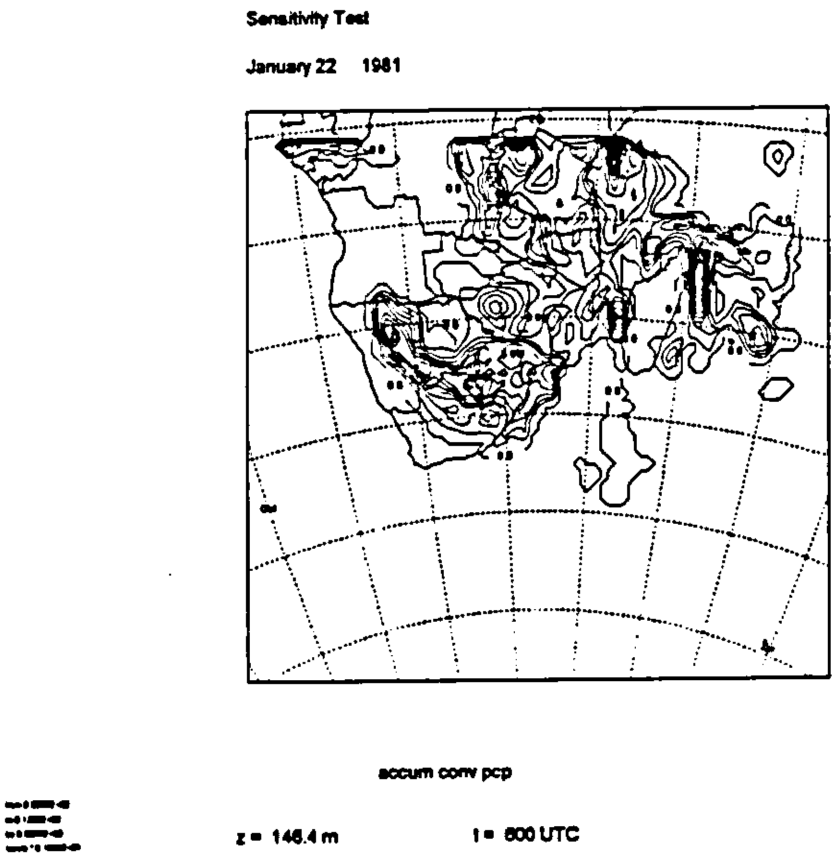

Figure 7.9: Accumulated convective precipitation (in mm) for (a) the control and (b) the sensitivity simulations at the 146,4m sigma level for 0600 UTC on 22 January 1981.

Control Run

January 22 1981

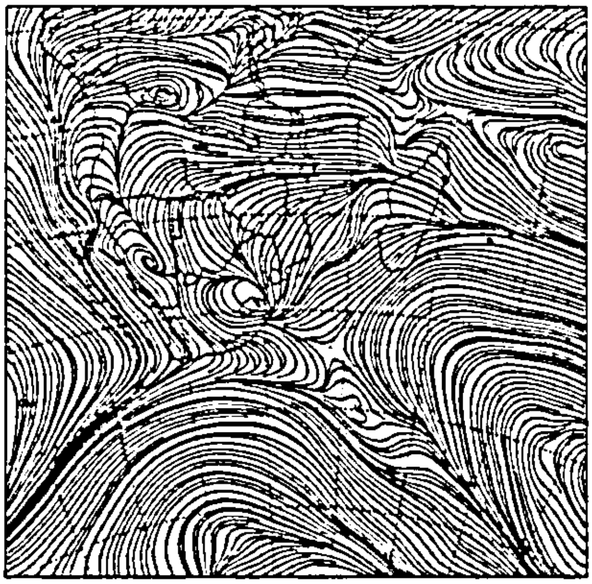

z = 146.4 m t = 2100 UTC

Sensitivity Test

January 22 1981

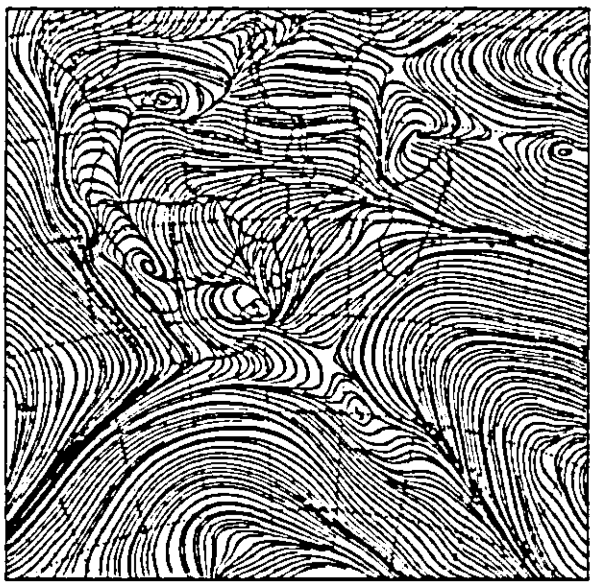

z = 146.4 m t = 2100 UTC

Figure 7.10: Streamlines diagrams for (a) the control and (b) the sensitivity simulations at the 146.4m sigma level for 2100 UTC on 22 January 1981.

Control Run

January 22 1981

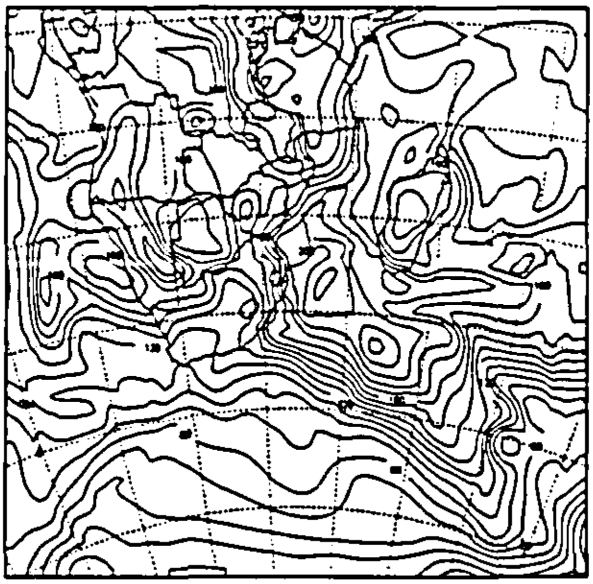

VAPOUR AND CLOUDS

z = 146.4 m t = 2100 UTC

Sensitivity Test

January 22 1981

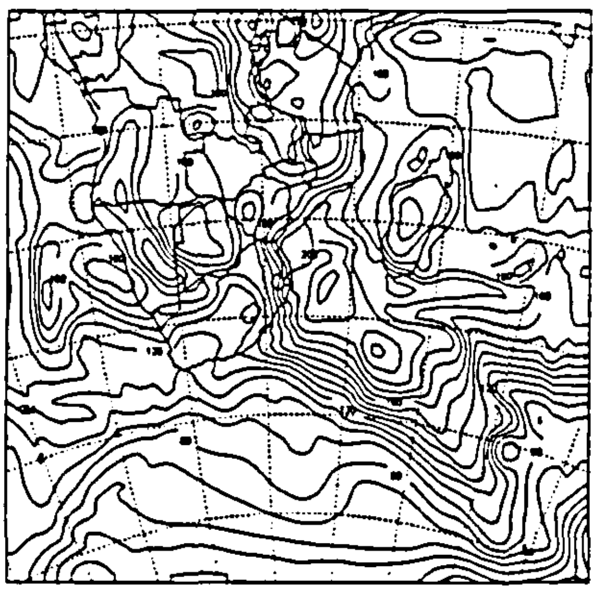

VAPOUR AND CLOUDS

z = 146.4 m t = 2100 UTC

Figure 7.11: Vapour and cloud mixing ratios (in g.kg^{-1} x10^{-4}) for (a) the control and (b) the sensitivity simulations at the 146.4m sigma level for 2100 UTC on 22 January 1981.

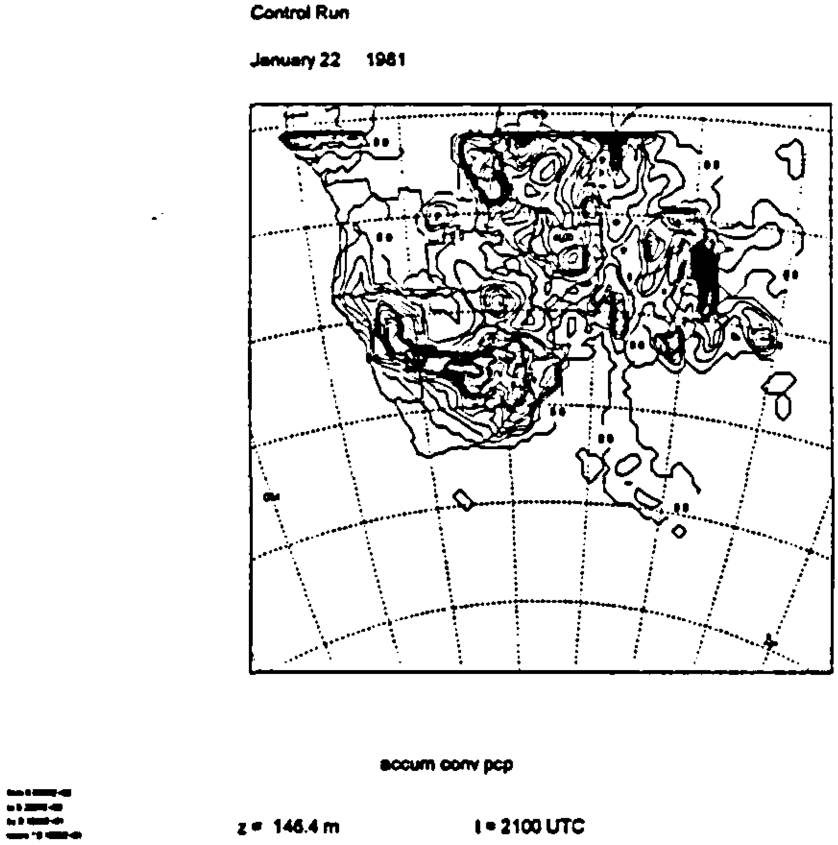

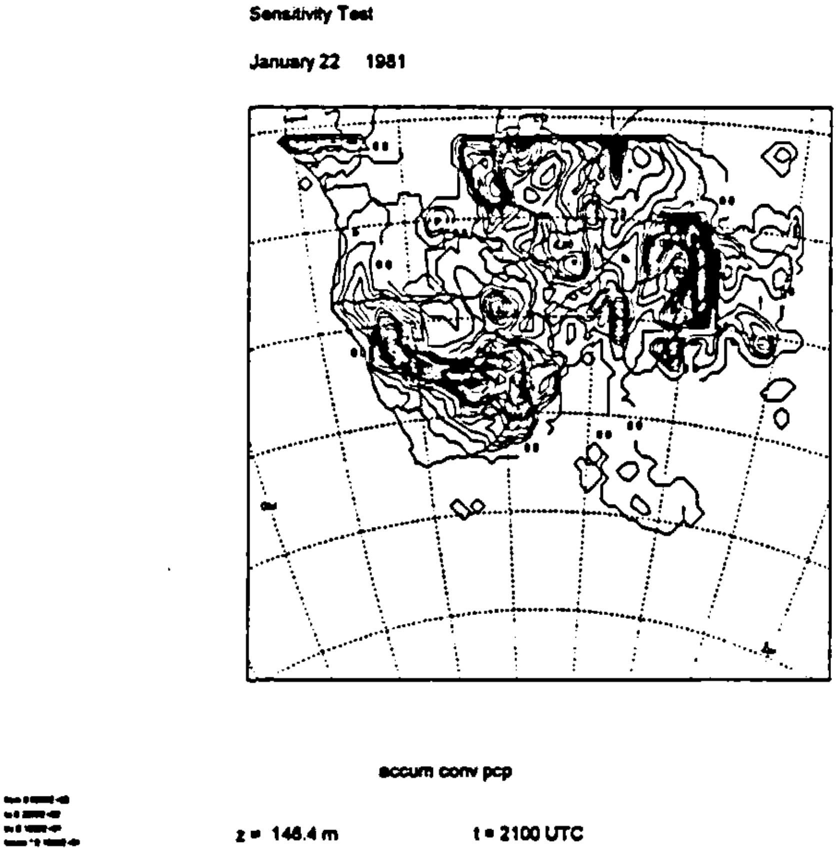

Figure 7.12: Accumulated convective precipitation (in mm) for (a) the control and (b) the sensitivity simulations at the 146,4m sigma level for 2100 UTC on 22 January 1981.

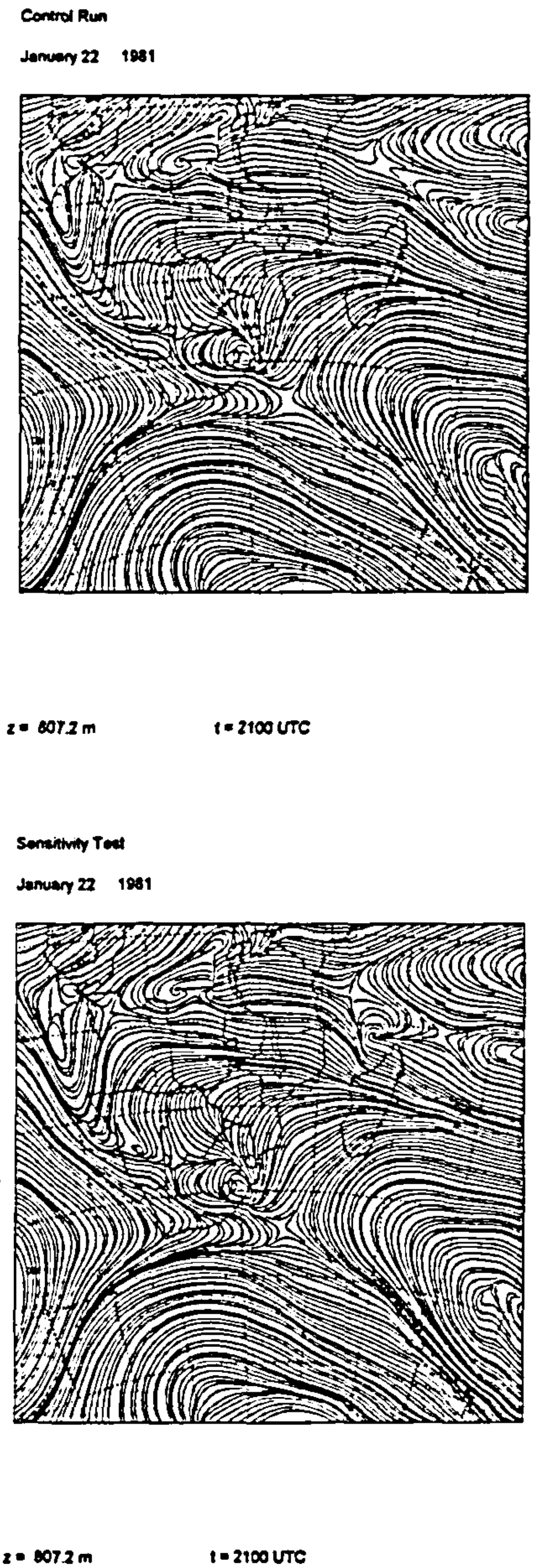

Figure 7.13: Streamline diagrams for (a) the control and (b) the sensitivity simulations at the 807.2m sigma level for 2100 UTC on 22 January 1981.

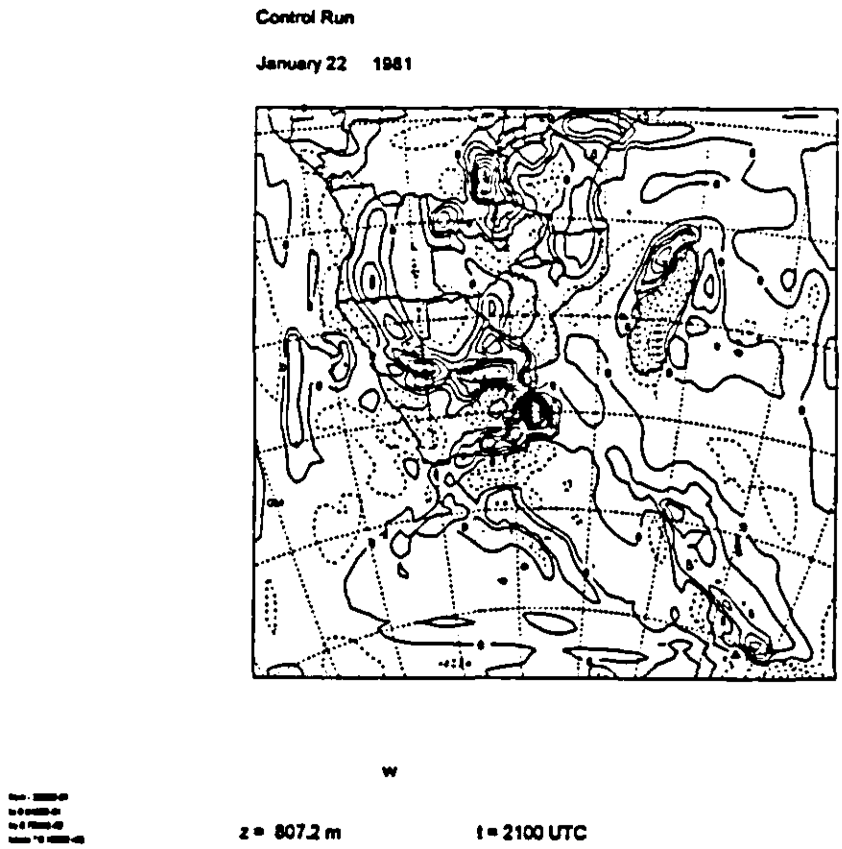

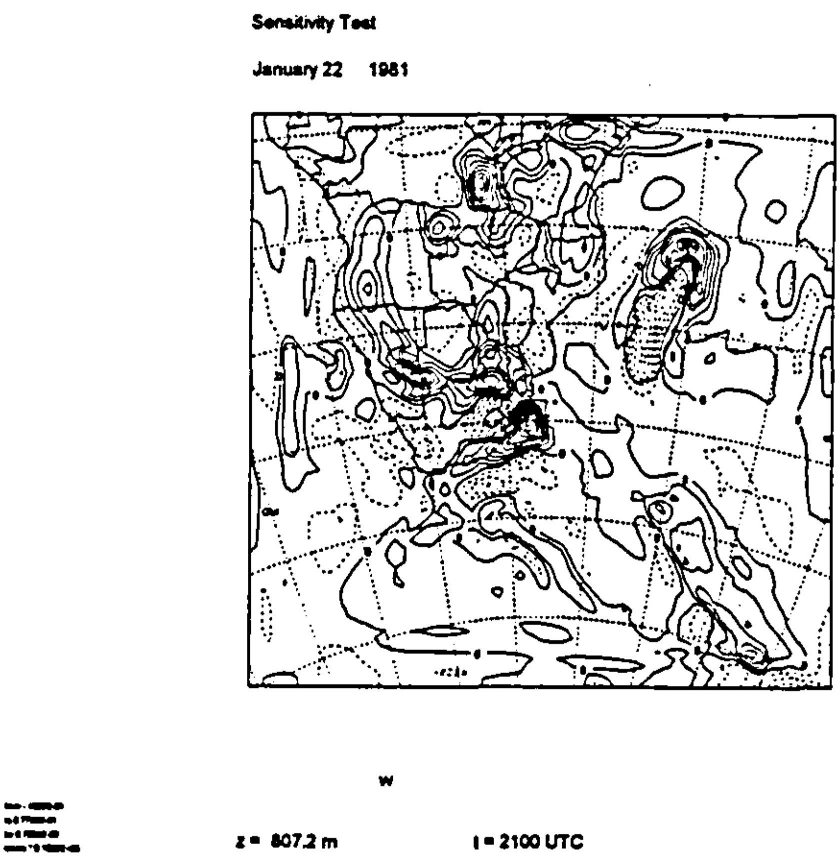

Figure 7.14: Vertical velocities (in $cm.s^{-1}$ $x10^{-4}$) for (a) the control and (b) the sensitivity simulations at the 807,2m sigma level for 2100 UTC on 22 January 1981.

atmospheric comparison level of the sensitivity experiment exhibits departures from the control simulation in the subtropical areas, and to a lesser extent in temperate areas.

Day three

By the third day (0900 UTC) of the sensitivity test, the simulated low pressure, to the north of Madagascar had intensified. The recurved northwesterly winds continued their expansion westward reaching the east coast of Africa (Fig 7.15 a,b). The easterly winds remained stronger than the simulated winds of the control experiment along the east coast of Madagascar and within the Mozambique Channel. Surface divergence (146,4 m) along 40^0E became more prominent, further reducing moisture input to the continental tropical low centered over the Namibia/Botswana border. The presence of strong divergence at the 146,4 m level aided in reducing precipitation over the subcontinent but also enhanced the vertical instability of the developing low, by diverting more water vapour into the area of convection. Later that day (2100 UTC) the tropical-temperate trough became fully developed. The westerly wind component at the 146,4 m level extended down the Mozambique Channel with continued characteristically strong easterly flow along the east coast of Madagascar i.e. 7 ms^{-1} simulated in the sensitivity simulation compared to 6 ms^{-1} simulated in the control simulation (Fig 7.16 a,b). Simulated control and sensitivity instability values remained the same on the west and east coasts, but over the central parts of southern Africa sensitivity values were lowered due to the reduction of moisture from over the tropical Indian Ocean. Moisture availability continued its higher trend over Madagascar and the modified sea surface temperature field with precipitation values showing a marked increase of maximum values of *46 mm for the sensitivity simulation compared with 36 mm in the control simulation* (Fig 7.17 a,b).

Day four

By the final day, the sensitivity simulation modelled the dissipation of the tropical-temperate trough through the easterly migration of the westerly wave perturbation. The low pressure circulation simulated from the second day of the sensitivity test weakened and moved southwards along the Mozambique Channel (Fig 7.18 a,b). A consistently stronger easterly

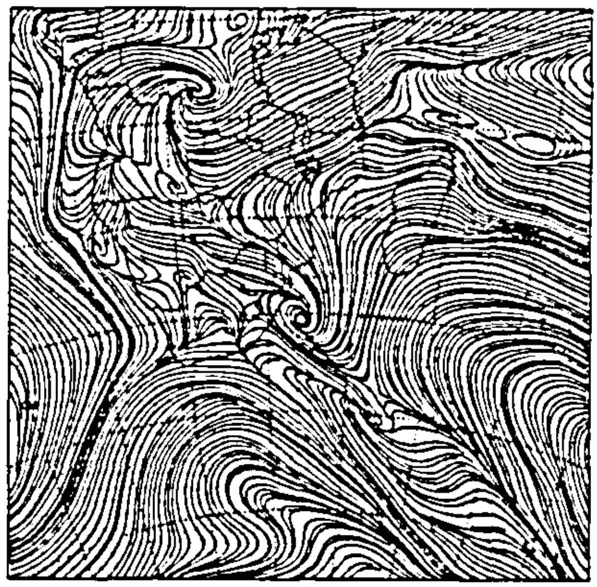

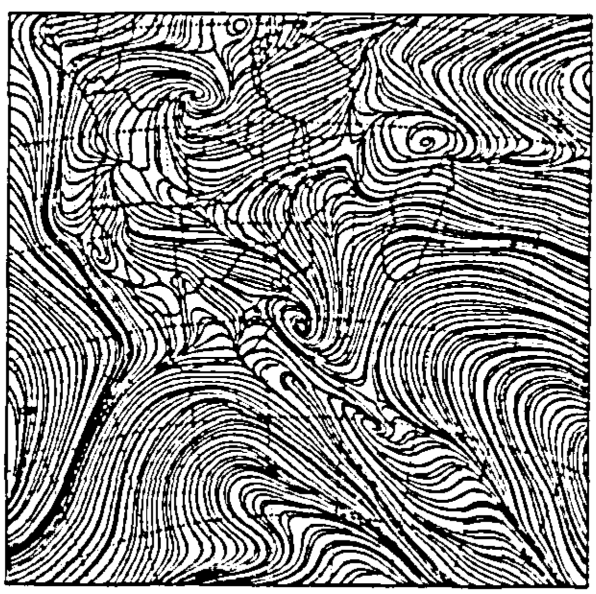

Figure 7.15: Streamline diagrams for (a) the control and (b) the sensitivity simulations at the 146,4m sigma level for 0900 UTC on 23 January 1981.

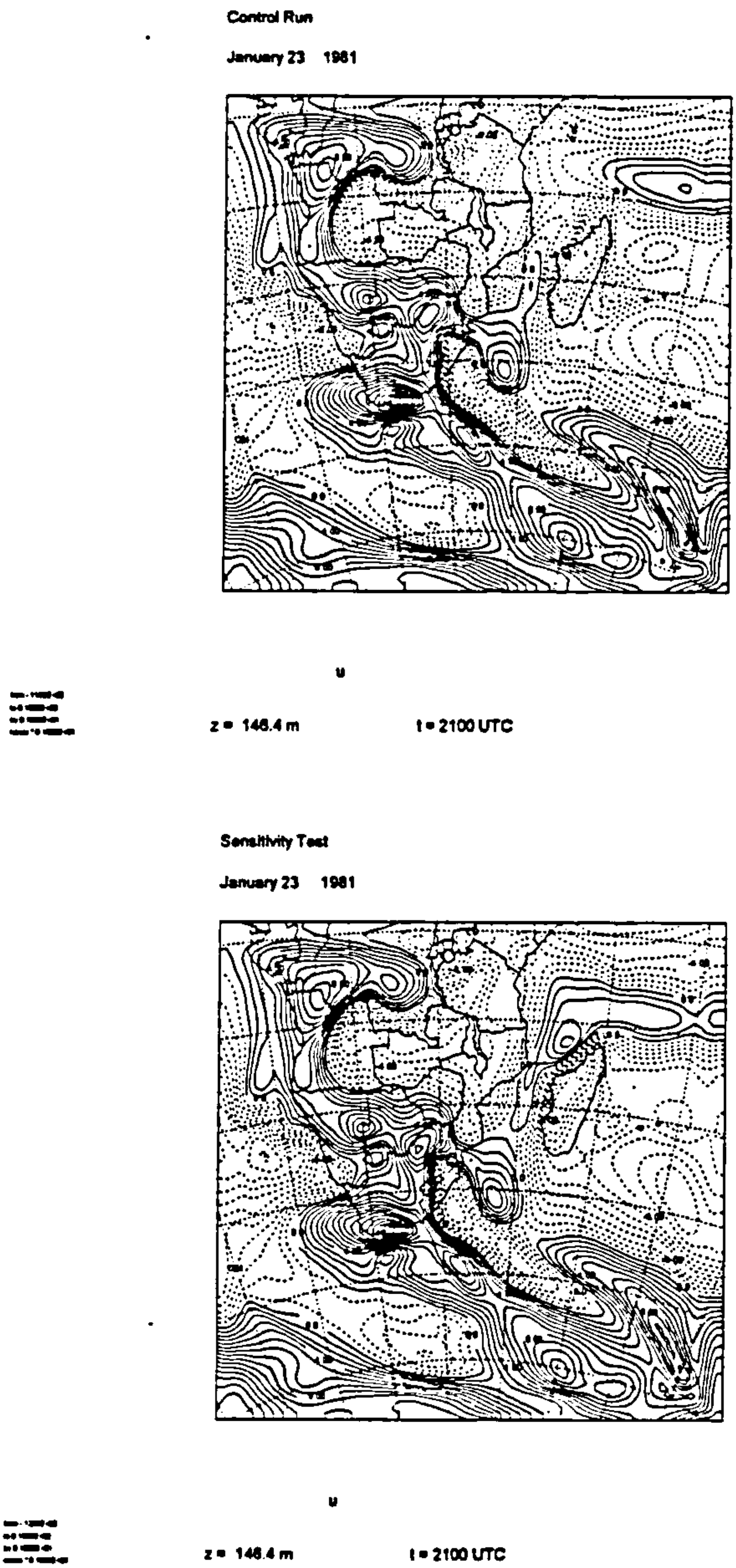

Figure 7.16: U components (in m.s^{-1}) for (a) the control and (b) the sensitivity simulations at the 146.4m sigma level for 2100 UTC on 23 January 1981.

Control Run

January 23 1981

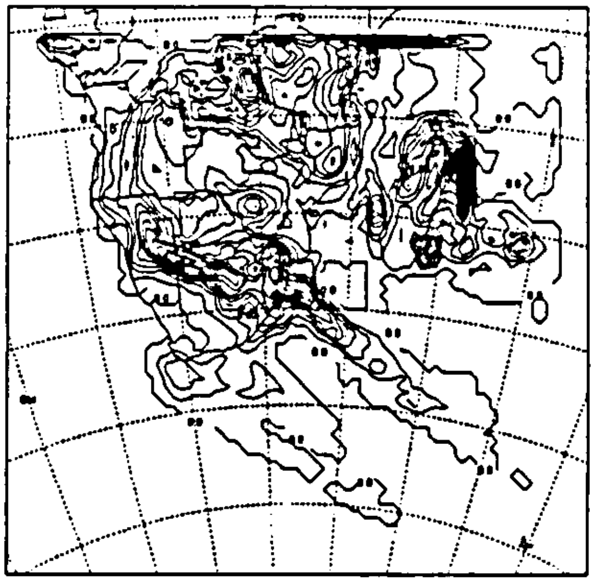

accum conv pcp

z = 146.4 m t = 2100 UTC

Sensitivity Test

January 23 1981

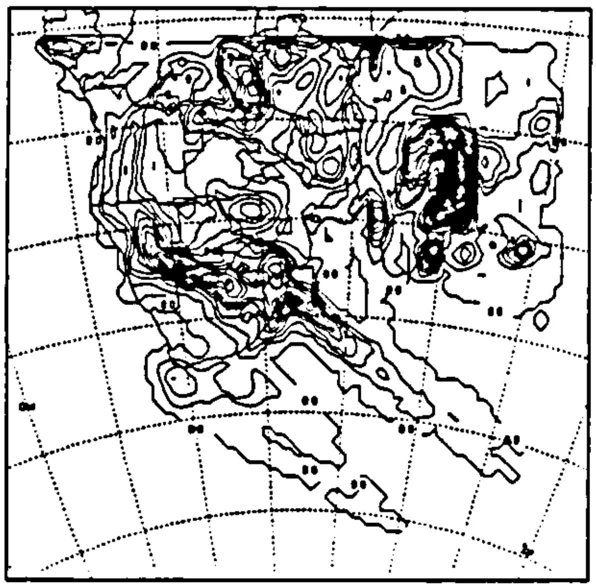

accum conv pcp

z = 146.4 m t = 2100 UTC

Figure 7.17: Accumulated convective precipitation (in mm) for (a) the control and (b) the sensitivity simulations at the 146.4m sigma level for 2100 UTC on 23 January 1981.

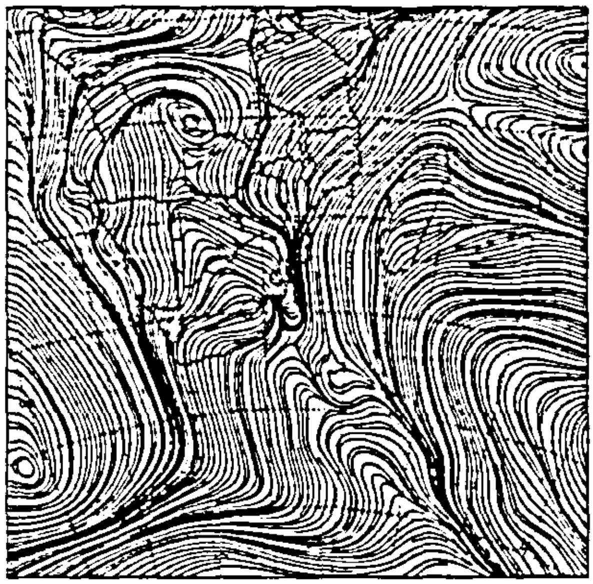

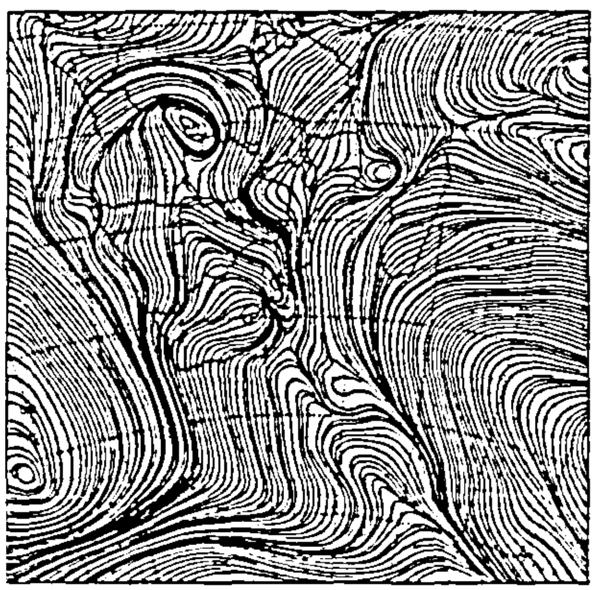

Figure 7.18: Streamline diagrams for (a) the control and (b) the sensitivity simulations at the 146,4m sigma level for 1200 UTC on 24 January 1981.

flow to the east of Madagascar was maintained with continually higher vapour and cloud mixing ratios indicative of greater moisture availability over Madagascar and the tropical Indian Ocean. Lower vapour and cloud mixing ratios along the east coast of southern Africa indicate the reduction of moisture availability in this area. This can be seen by the reduction in extent of the 0,023 $g.kg^{-1}$ contoured area over Durban (Fig 7.19 a,b). On 24 January at 1200 UTC higher accumulated convective precipitation values for the sensitivity experiment were recorded over the tip of Madagascar and tropical Indian Ocean (51 mm versus 42 mm), along with a decrease in precipitation on the southern African subcontinent from 18 mm in the sensitivity to 24 mm in the control simulation over Durban (Fig 7.20 a,b).

Higher-level (807,2 m) simulated circulation at 1200 UTC possessed similar trends to surface patterns. The moisture availability did, however, differ quite significantly from the control simulation with higher values to the east of Madagascar and within the Mozambique Channel (Fig 7.21 a,b).

Discussion

The modification of sea surface temperatures in the tropical Indian Ocean, by the addition of a positive 2^0C anomaly core bounded by a positive 1^0C anomaly, had little effect on the overall formation and dissipation of the simulated tropical-temperate trough. Localised differences were, however significant with sea surface temperature modification producing zones of heightened instability and cyclogenesis. The westerly wind component situated on the 5^0S latitude increased its westerly extent and on reaching the African east coast preceded to move down the Mozambique Channel. The presence of increased moisture availability due to the development of surface divergence along 40^0E and instability due to the increased temperature anomalies heightened the development of cyclogenesis over the tropical Indian Ocean. The development of both divergence at 40^0E and the tropical low at approximately 10^0S reduced atmospheric moisture input from the tropical Indian Ocean to the subcontinent, as the pathway of moisture transport was redirected to the Mozambique Channel. Easterly winds, to the east of Madagascar remained stronger throughout the simulation due to the development of the quasi-stationary low pressure.

Control Run

January 24 1981

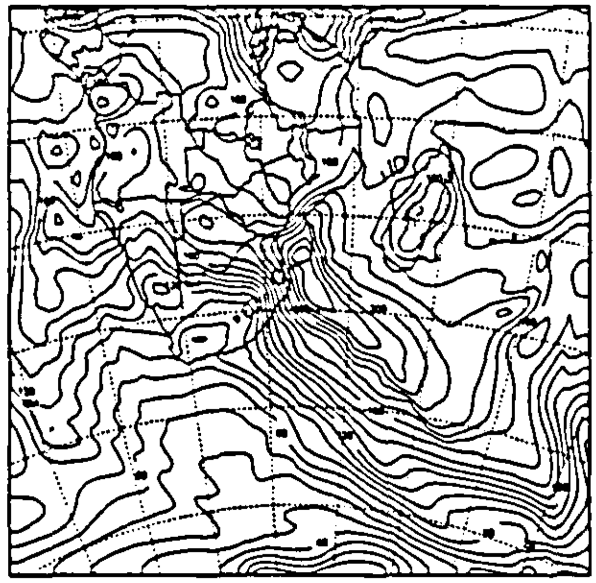

VAPOUR AND CLOUDS

z = 146.4 m t = 1200 UTC

Sensitivity Test

January 24 1981

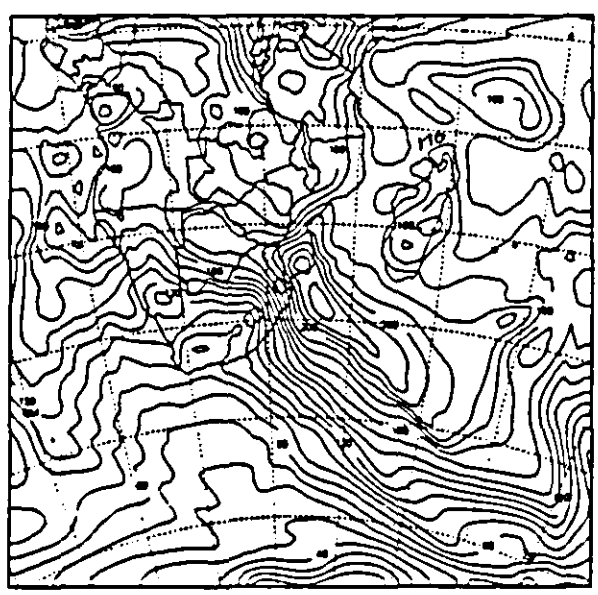

VAPOUR AND CLOUDS

z = 146.4 m t = 1200 UTC

Figure 7.19: Vapour and cloud mixing ratios (in $g.kg^{-1}$ $x10^{-4}$) for (a) the control and (b) the sensitivity simulations at the 146.4m sigma level for 1200 UTC on 24 January 1981.

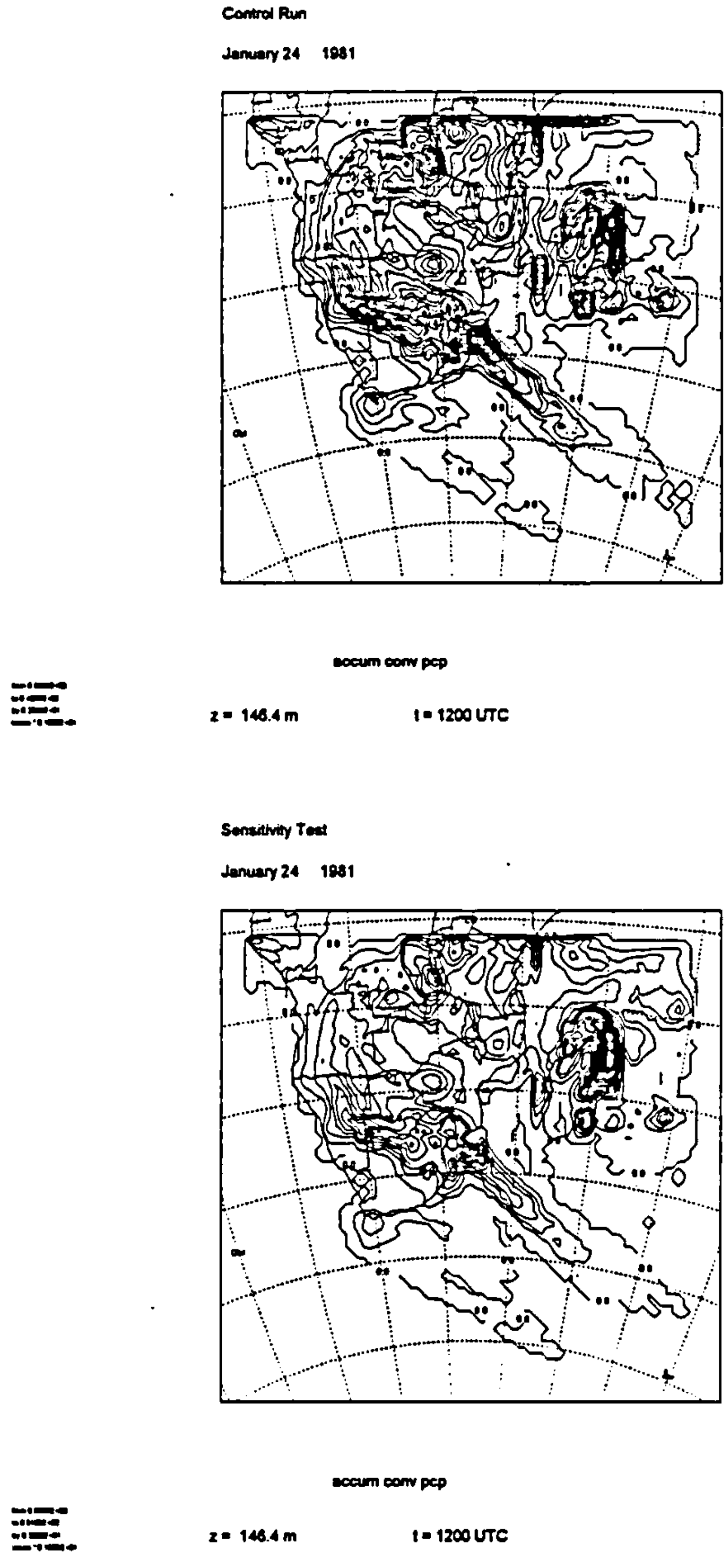

Figure 7.20: Accumulated convective precipitation (in mm) for (a) the control and (b) the sensitivity simulations at the 146,4m sigma level for 1200 UTC on 24 January 1981.

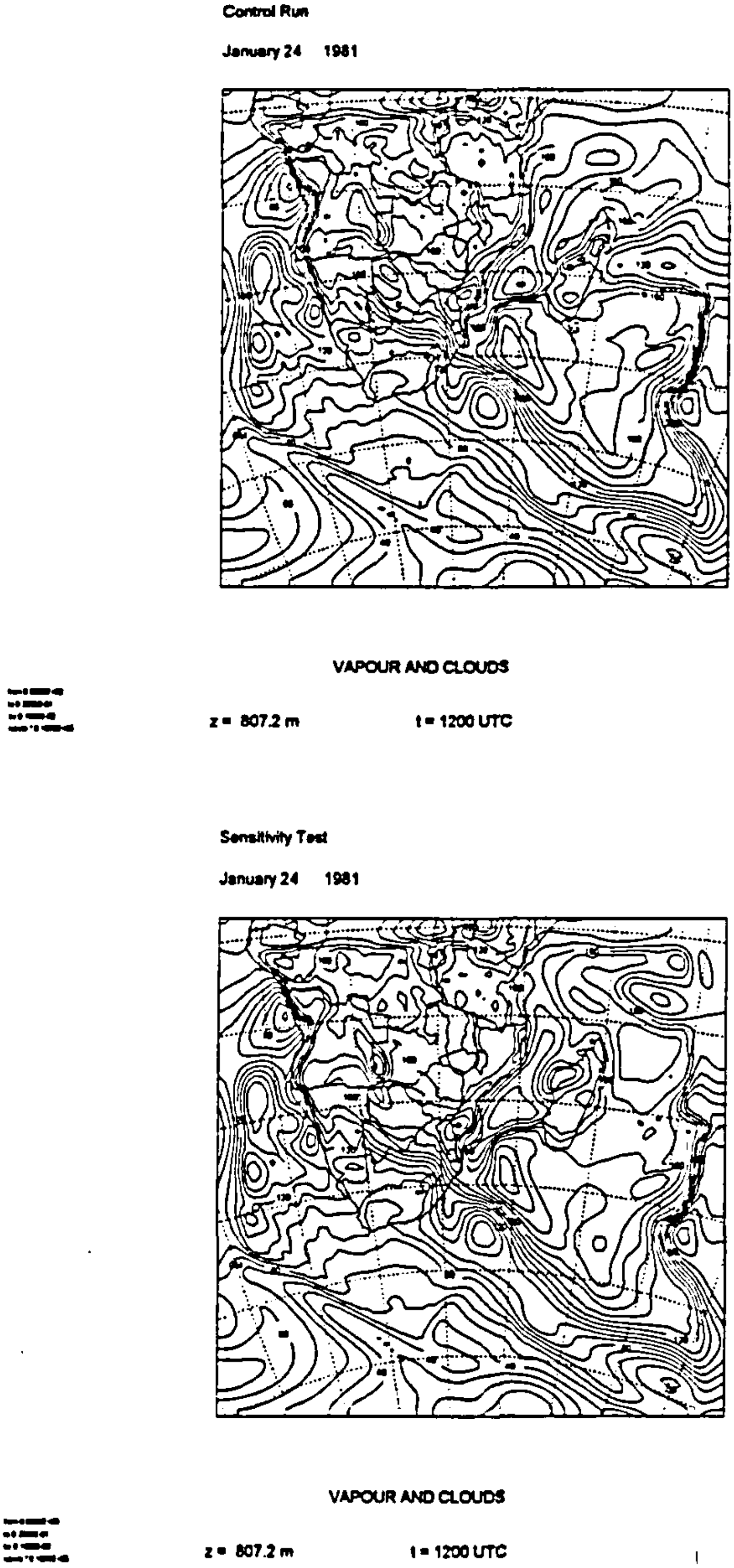

Figure 7.21: Vapour and cloud mixing ratios (in g.kg^{-1} x10^{-4}) for (a) the control and (b) the sensitivity simulations at the 807.2m sigma level for 1200 UTC on 24 January 1981.

Very few differences were found in the 807,2 m level, those that were simulated in the sensitivity simulation were consistent with the larger sensitivity simulation differences found near the surface (146,4 m). Departures from the model control iteration took much longer to translate to the continental regions and temperate zone, particularly in the higher-level sensitivity test. The simulated changes produced in the sensitivity experiment were consistent with inter-annual atmospheric circulation changes found in dry years around the subcontinent.(D'Abreton, 1992; Mason, 1992, 1993 ,1994; Jury *et al.*, 1991a,b; Barclay *et al.*, 1993; Jury, 1996).

Synopsis

The effects of the addition of anomalous sea surface temperatures to an area north of Madagascar have been investigated. The modification of oceanic temperatures in the tropical Indian Ocean, had little effect on the formation and dissipation of the tropical-temperate trough, but did have some influence on the structure of the synoptic feature. The sensitivity experiment simulated stronger surface easterly winds to the east of Madagascar for the entire time period. Surface divergence , convergence and westerly wind encroachment (along 5^{o}S) were also a product of the simulation. The development of divergence at 40^{o}E and a tropical low at approximately 10^{o}S served to reduce atmospheric moisture circulation over the southern African subcontinent. Accumulated convective precipitation values directly over the anomalous sea surface temperatures increased whereas values over South Africa were marginally lower.

CHAPTER 8

THE AGULHAS CURRENT RETROFLECTION ANOMALY

The oceanic region to the south of the subcontinent is thought to play a decisive role in weather modification on relatively short time scales (Walker, 1989). Research has indicated that the development of positive anomalies to the south of the subcontinent serve to strengthen the sea surface temperature gradient in this area (Walker, 1989). Positive sea surface temperature increases in the Agulhas retroflection region also produce heightened surface fluxes, particularly sensible heating (Walker, 1989; Jury, 1993). Thus the combination of both an increased sea surface temperature gradient and enhanced heat fluxes, facilitate the reduction of low-level stability, which in turn increases surface convergence, convection and finally precipitation within the westerly wave disturbance (Walker, 1989; Mey *et al*, 1990)

The second sensitivity test represents a modification of the long term mean sea surface temperatures within the zone of the Agulhas Current retroflection (Fig 8.1), in order to test whether circulation changes in the sensitivity experiment coincide with the conceptualised changes proposed by previous research (Walker, 1989). The second sensitivity simulation was run for the same period as the first, from 21 to 24 January 1981. The sensitivity simulation was then compared with the control simulation by the analysis of wind components (u,v), streamlines, temperatures, vertical velocity (w), vapour and cloud mixing ratios, and accumulated convective precipitation at the 146,4 m and 807,2 m sigma levels.

Sensitivity Test 6 (Agulhas Current Retroflection Anomaly)

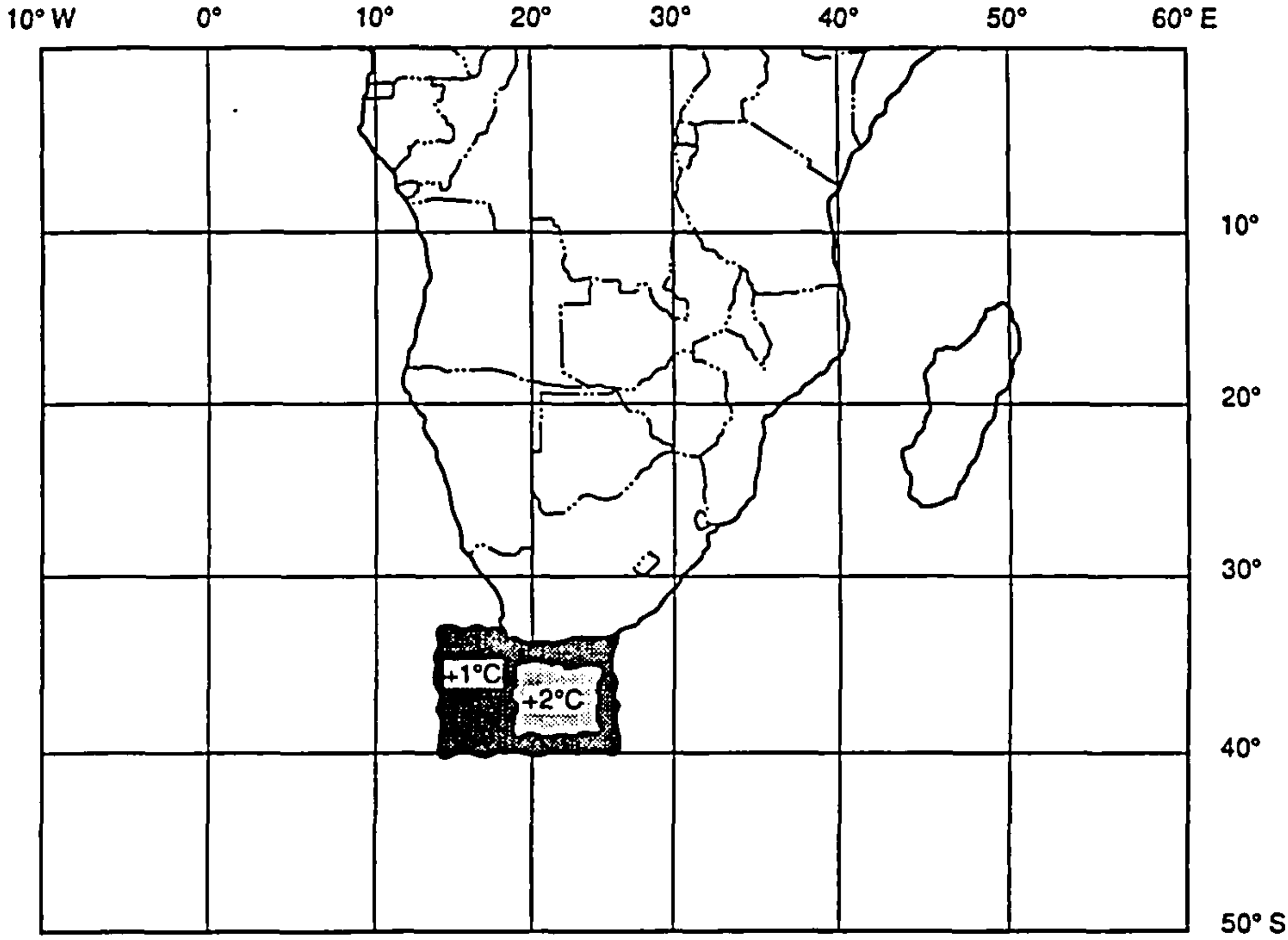

Figure 8.1: Representation of the sixth sensitivity test, whereby a positive 2^{0}C anomaly and positive 1^{0}C anomaly were added to the Agulhas Current region of Retroflection.

Results

Day one

When the Agulhas Current retroflection anomaly experiment was compared to the control simulation, the initial time-step (1200 UTC), exhibited no circulation or atmospheric parameter differences. As for the control and first sensitivity experiment, the South Atlantic and South Indian Highs were positioned relatively far south at 35^0S and 42^0S respectively. Two prominent tropical lows were simulated over the continent, with significant moisture availability in these areas. High vapour and cloud mixing ratio values were also simulated over Madagascar and over the tropical Indian Ocean to the east. Easterly winds were predominant to the east of Madagascar along with westerly winds in the temperate latitudes. At 2100 UTC on the first day of the simulation small disparities between the control and sensitivity test become apparent at the 146,4 m sigma level. A marginal decrease in onshore flow along the south coast became evident along with a slight increase in the availability of moisture found along the west coast of South Africa. When comparing the magnitude of change with the tropical Indian Ocean anomaly simulation, the Agulhas retroflection anomaly experiment exhibits a much smaller response over the same time period. This may be the result of the mid-latitude atmospheric circulation requiring a longer reaction time to the development of sea surface temperature anomalies.

Day two

On the second day of the simulation (0600 UTC) the weaker onshore flow continued (Fig 8.2 a,b), allowing the southeasterly extension of the 294 K contour line along the west coast of South Africa, bringing an increase in air temperature to the area. Over the region of sea surface temperature modification vertical velocities exhibited a slight increase, by the southwest displacement of the 0,003 cms^{-1} vertical velocity contour line (Fig 8.3 a,b), indicating that instability was beginning to under-cut the low-level stability in the area. The combination of weaker onshore flow and air temperature increase served to perpetuate the growth of instability over the anomalous sea surface temperature field. Instability also exhibited a slight increase over the modified sea surface temperatures. Accumulated

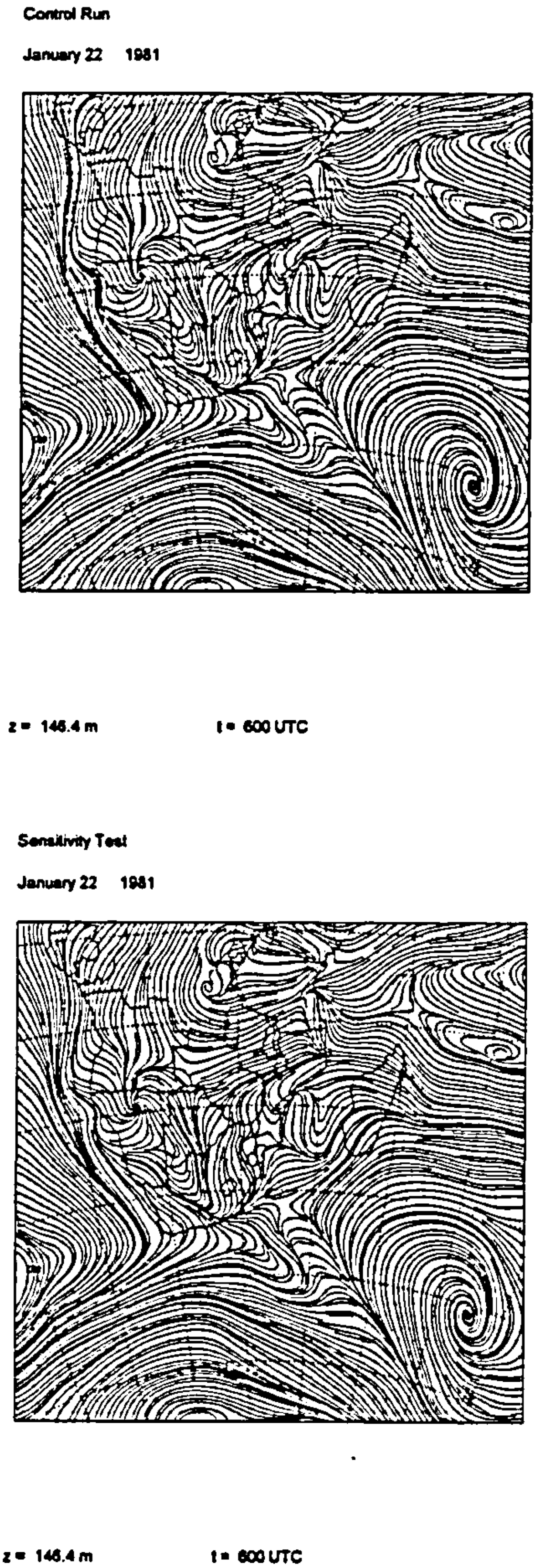

Figure 8.2: Streamline diagrams for (a) the control and (b) the sensitivity simulations at the 146,4m sigma level for 0600 UTC on 22 January 1981.

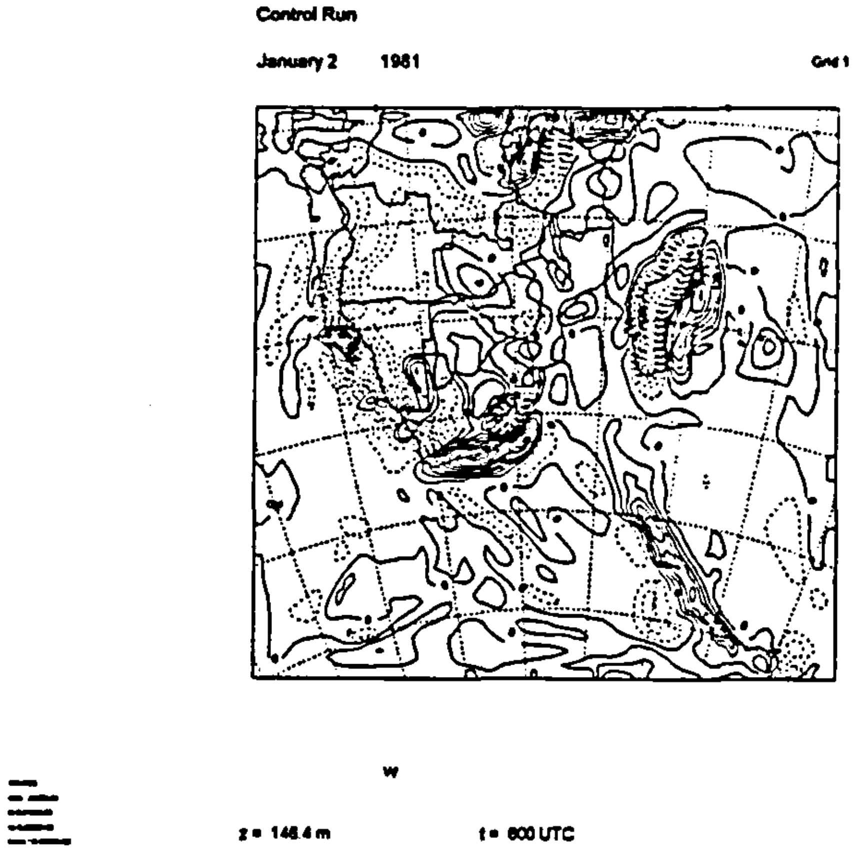

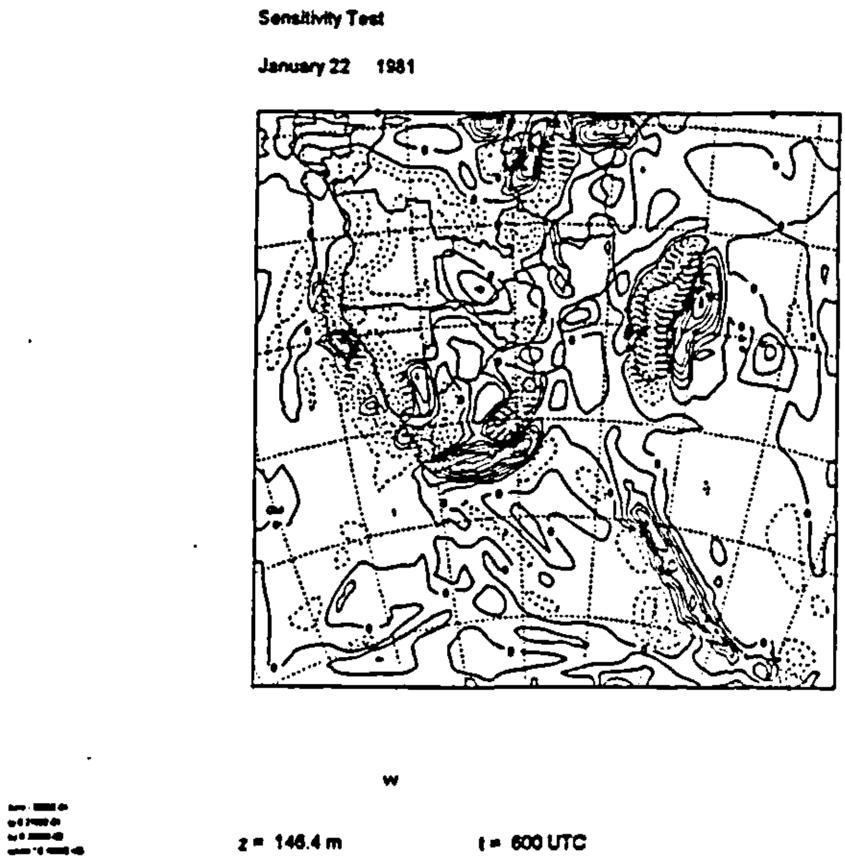

Figure 8.3: Vertical velocities (in $cm.s^{-1}$ $x10^{-4}$) for (a) the control and (b) the sensitivity simulations at the 146,4m sigma level for 0600 UTC on 22 January 1981.

convective precipitation recorded higher simulated values over the South Africa/Botswana border for this sensitivity simulation period with control values of 5,6 mm versus values of 6,4 mm. The increase had no effect on precipitation up to the period 0600 UTC (Fig 8.4 a,b).

By 1500 UTC southeasterly winds along the west coast strengthened, producing a marginal increase in convergence over Angola and Namibia, as well as a stronger cyclonic circulation over central Namibia (Fig 8.5 a,b). The subtropical trough situated over the northern half of South Africa indicated the same pattern of change as the streamlines, with higher positive vertical velocities at the eastern limits, the west coast of southern Angola, and northern Namibia. Localised increases in instability are found over the area of modified sea surface temperatures (Fig 8.6 a,b). Moisture availability increased over the eastern boundary of the modified sea surface temperature field with the southerly displacement of the 0,011 gkg^{-1} contour line (Fig 8.7 a,b).

By 2100 UTC on 22 January the stronger south easterly winds along the west coast of South Africa expanded to cover the subcontinent. This increase in south easterly wind flow served to heighten the circulation both around the tropical low over Namibia, and the subtropical trough over the northeast of the country (Fig 8.8 a,b). Simulated instability followed the same pattern as indicated by the streamlines, with vertical velocities having a greater magnitude on the eastern limits of the subtropical trough, as well as over the area of modified sea surface temperatures. Greater precipitation values continued over the central plateau and south eastern Namibia as a result of the stronger surface convergence and hence low level instability over these areas.

The sensitivity simulation at 807 m showed only marginal circulation differences to the control experiment, which would suggest a longer period for the translation of circulation differences through the atmospheric levels than for the tropical Indian Ocean experiment. Southeasterly flow over the continent does however appear to strengthen as well as circulation around the subtropical trough. Vertical velocities over the south eastern portion of Namibia, the central plateau of South Africa, and along the south east coast are higher, with the simulated developing front exhibiting higher instability values aligned in a northwest to south east direction, with values on the eastern limit of the subtropical trough showing a weakening trend

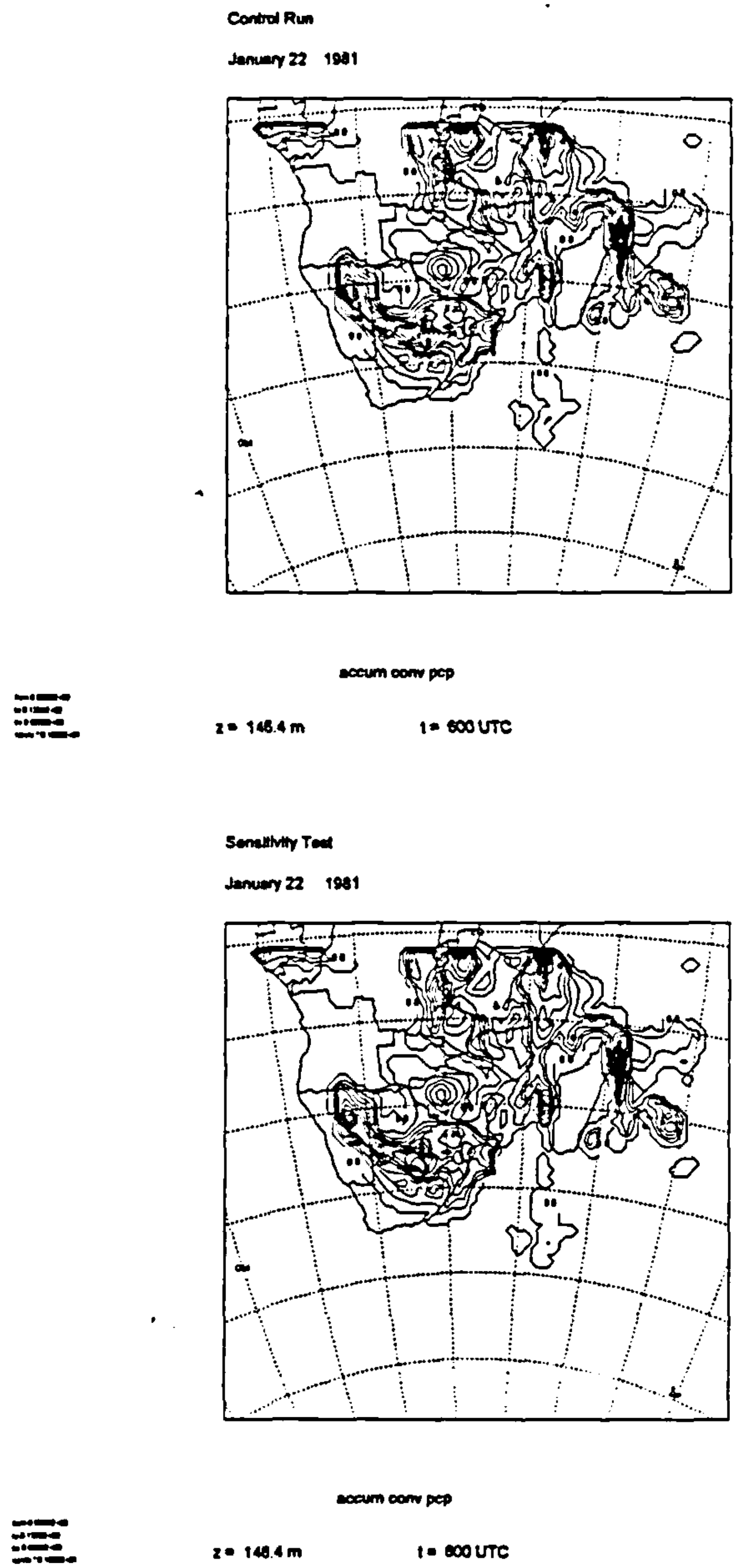

Figure 8.4: Accumulated convective precipitation (in mm) for (a) the control and (b) the sensitivity simulations at the 146.4m sigma level for 0600 UTC on 22 January 1981.

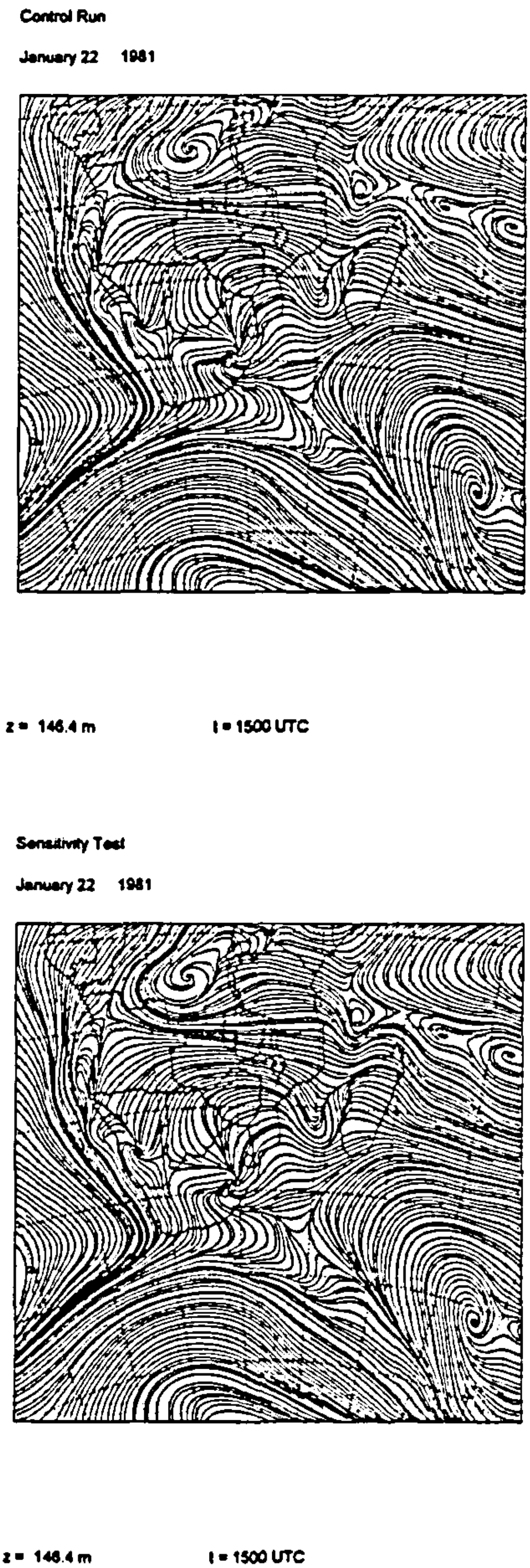

Figure 8.5: Streamline diagrams for (a) the control and (b) the sensitivity simulations at the 146.4m sigma level for 1500 UTC on 22 January 1981.

Control Run

January 22 1981

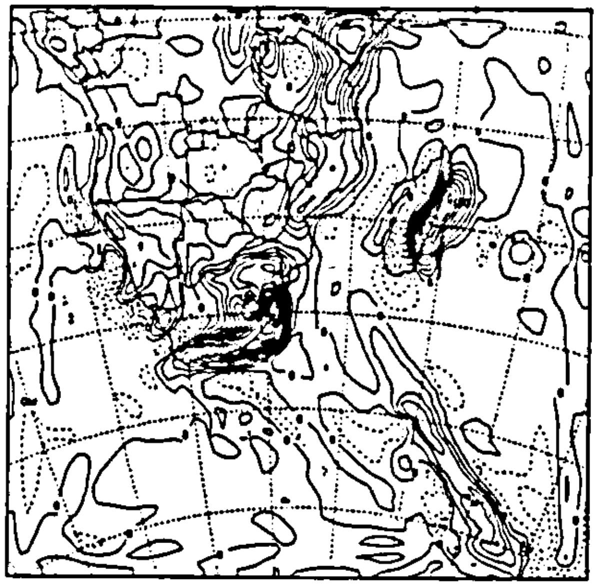

w

z = 146.4 m t = 1500 UTC

Sensitivity Test

January 22 1981

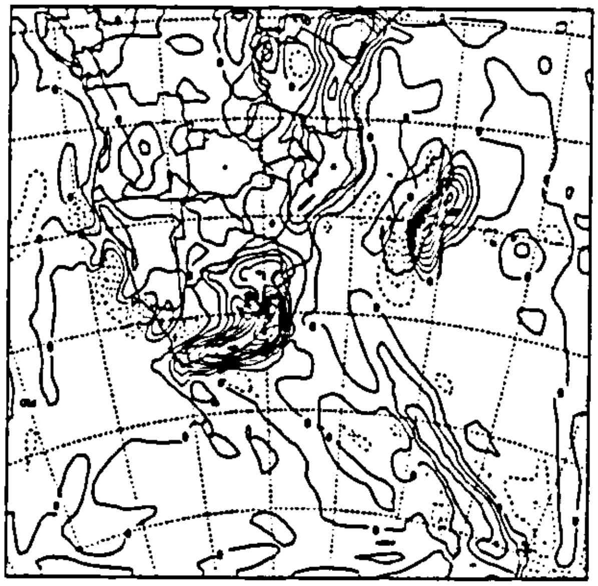

w

z = 146.4 m t = 1500 UTC

Figure 8.6: Vertical velocities (in cm.s^{-1} x10^{-4}) for (a) the control and (b) the sensitivity simulations at the 146,4m sigma level for 1500 UTC on 22 January 1981.

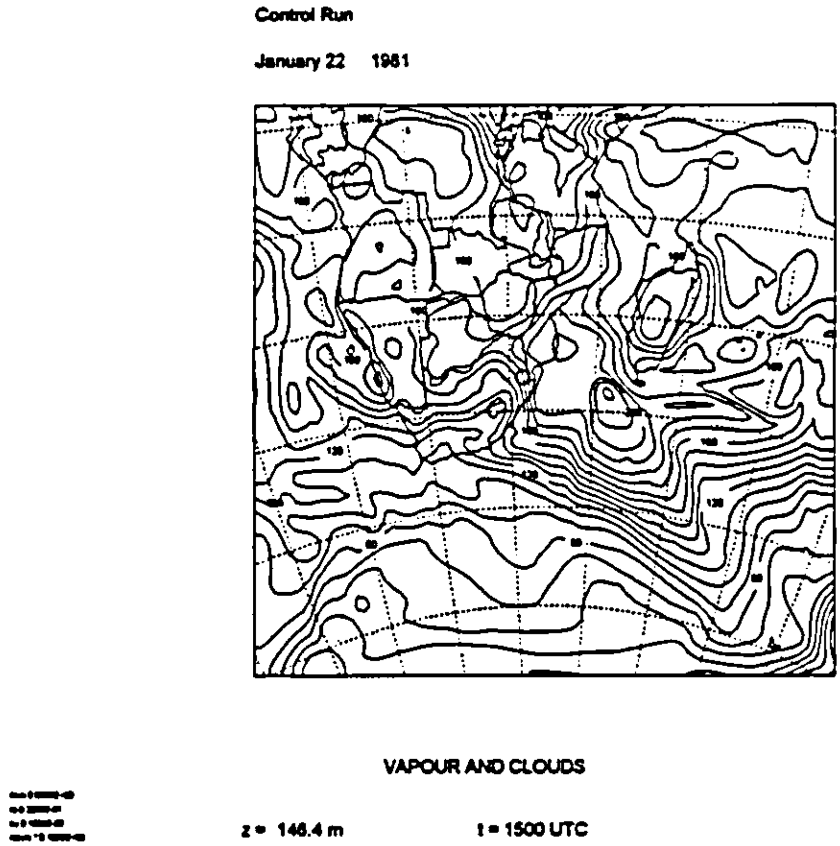

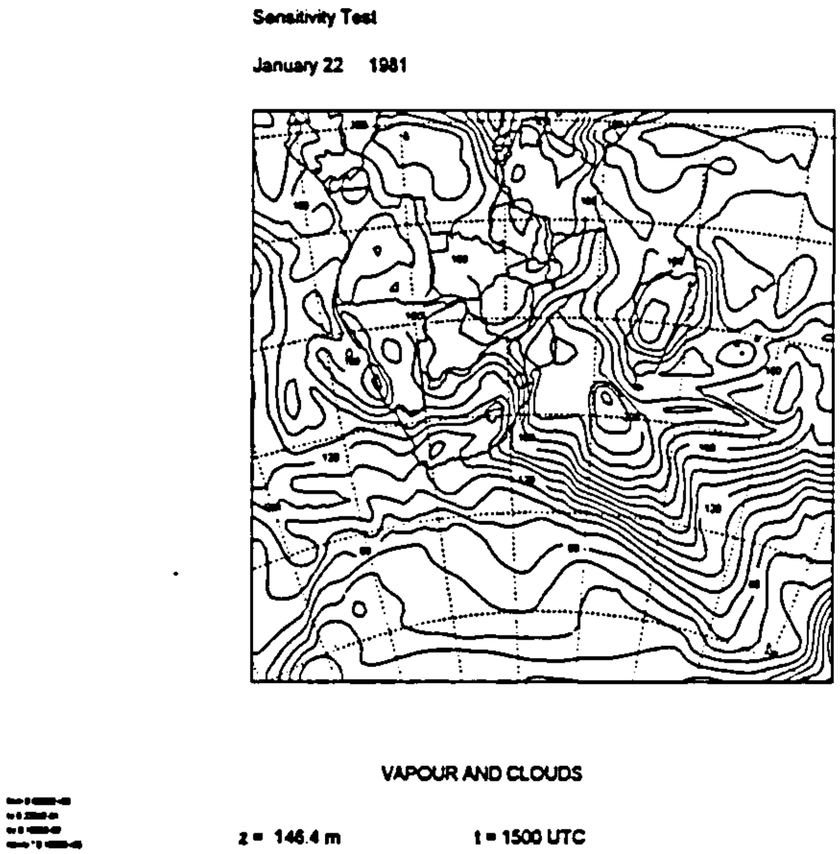

Figure 8.7: Vapour and cloud mixing ratios (in $g.kg^{-1} \times 10^{-4}$) for (a) the control and (b) the sensitivity simulations at the 146.4m sigma level for 1500 UTC on 22 January 1981.

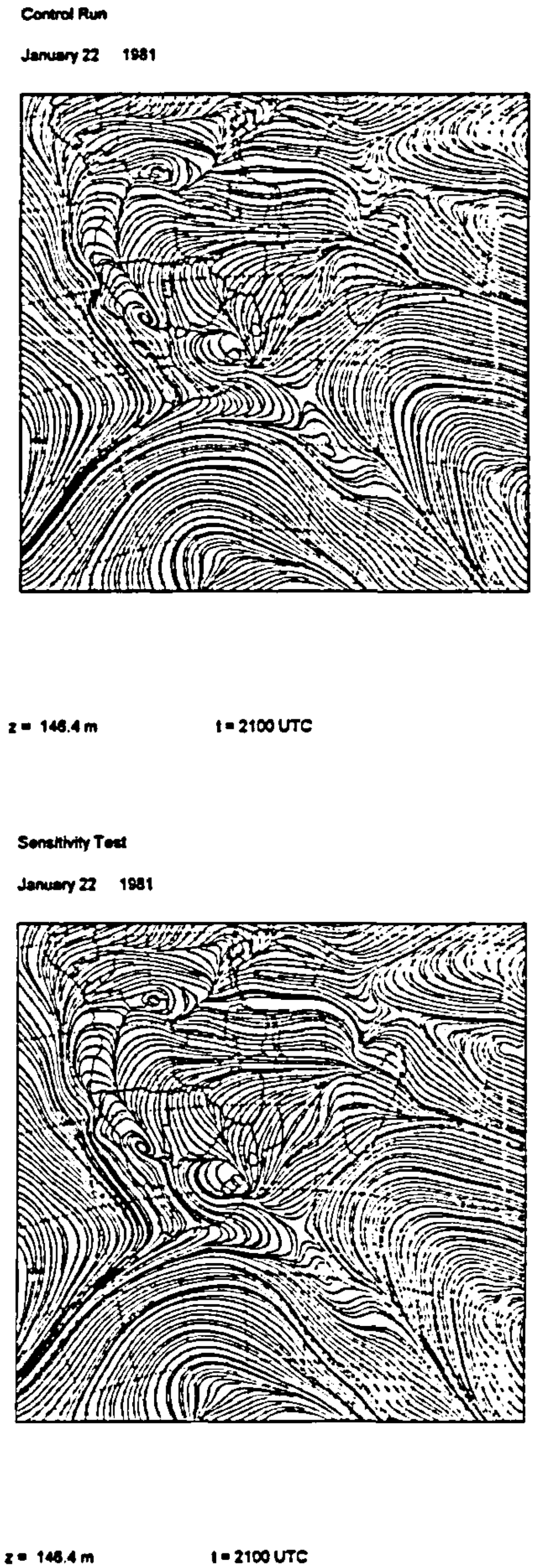

Figure 8.8: Streamline diagrams for (a) the control and (b) the sensitivity simulations at the 146.4m sigma level for 2100 UTC on 22 January 1981.

Control Run

January 22 1981

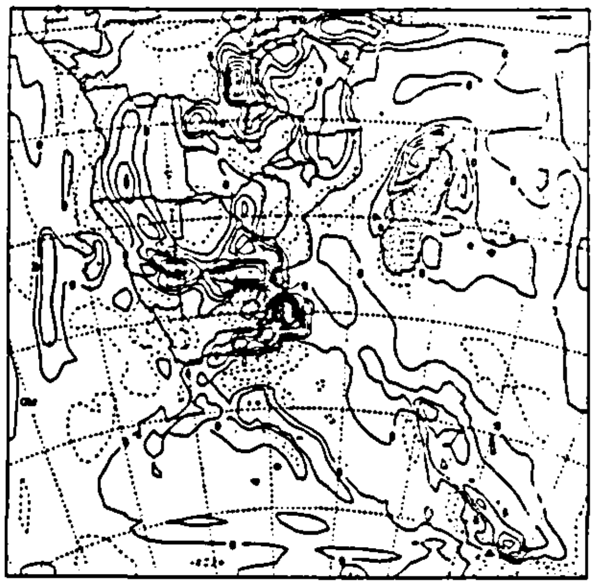

w

z = 807.2 m t = 2100 UTC

Sensitivity Test

January 22 1981

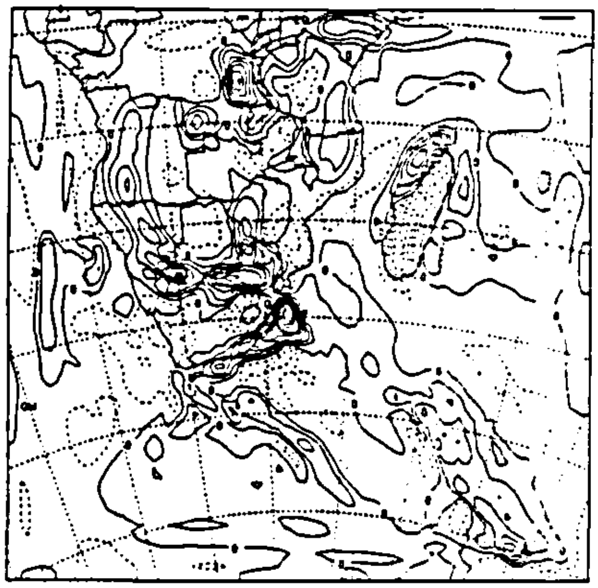

w

z = 807.2 m t = 2100 UTC

Figure 8.9: Vertical velocities (in $cm.s^{-1} \times 10^{-4}$) for (a) the control and (b) the sensitivity simulations at the 146,4m sigma level for 2100 UTC on 22 January 1981.

for the same time period (Fig 8.9 a,b). At the 807,2 m level, cloud and vapour mixing ratios show the same trend as the 146,4 m level with marginal increases evident over the Western Cape and Cape south coast of 0,0011 gkg^{-1} to 0,0010 gkg^{-1} over the northern limit of the modified sea surface temperature field (Fig 8.10 a,b).

Day three

By the third day (0900 UTC) the Agulhas retroflection anomaly experiment at the 146,4 m level, began to exhibit a zonal strengthening over the area of modified sea surface temperatures, with westerly wind components increasing from 15 ms^{-1} in the control experiment to 16 ms^{-1} in the sensitivity simulation. Westerly wind components over the initial westerly wave perturbation indicated a marginal decrease in strength at approximately 48°S, 70°E (Fig 8.9 a,b), but exhibited heightened instability in this area with values of 0,020 cms^{-1} in the sensitivity simulation compared to control simulation values of 0,016 cms^{-1} (Fig 8.12 a,b).

Areas also experiencing heightened instability are found over the developing front and along the east coast. The origin of instability is found over the modified sea surface temperature field and translated poleward by the predominant circulation (Fig 8.12 a,b). Vapour and cloud mixing ratios decreased over the southern Free State and northeastern Cape Province, but increased over southern Namibia and southwestern Botswana. Moisture availability remained high over the southeastern coast of South Africa and adjacent Indian Ocean. Precipitation increases in the simulation experiment coincide with the areas of heightened instability over the east coast of South Africa at 30°S, over the sea surface temperature anomaly with a marginal increase from 2 mm in the sensitivity simulation compared to 1 mm in the control simulation, over eastern Namibia (18 mm versus 16 mm), and over southern Botswana (Fig 8.13 a,b).

Later on during the day (1500 UTC) the stronger convergence zone over the south coast of South Africa, indicated at the 146,4 m sigma level, moved eastwards to find a position along the eastern half of the country. The westerly winds over the northern parts of South Africa, and the southwesterly flow along the west coast of the continent appeared stronger than the control simulation, with stronger cyclonic circulation around the low pressure east of Durban over the Indian Ocean.

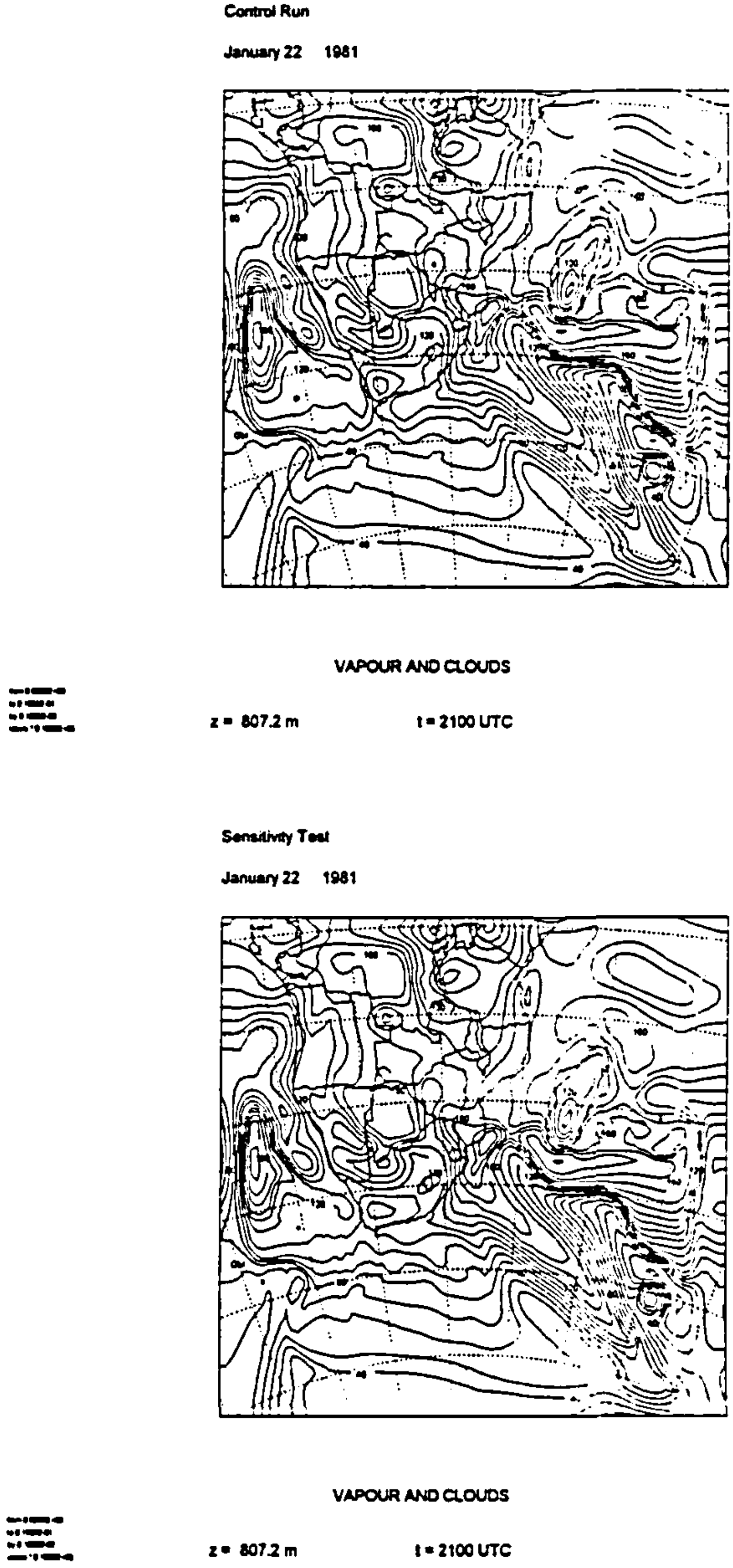

Figure 8.10: Vapour and cloud mixing ratios (in $g.kg^{-1} \times 10^{-4}$) for (a) the control and (b) the sensitivity simulations at the 807,2m sigma level for 2100 UTC on 22 January 1981.

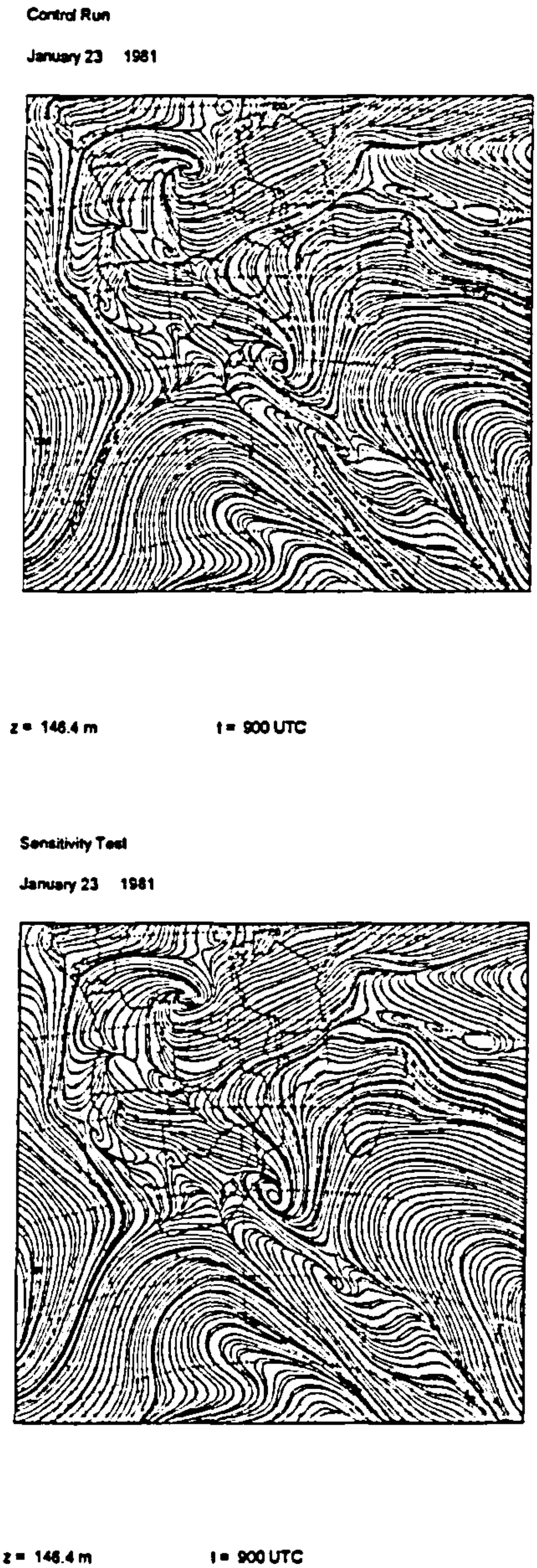

Figure 8.11: Streamline diagrams for (a) the control and (b) the sensitivity simulations at the 146,4m sigma level for 0900 UTC on 23 January 1981.

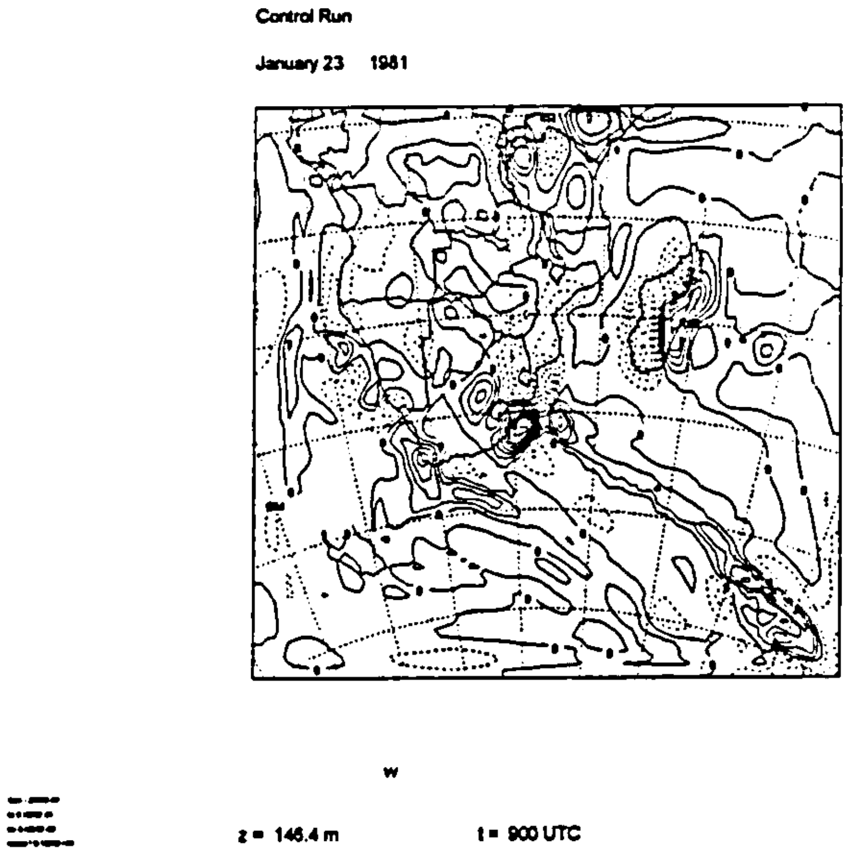

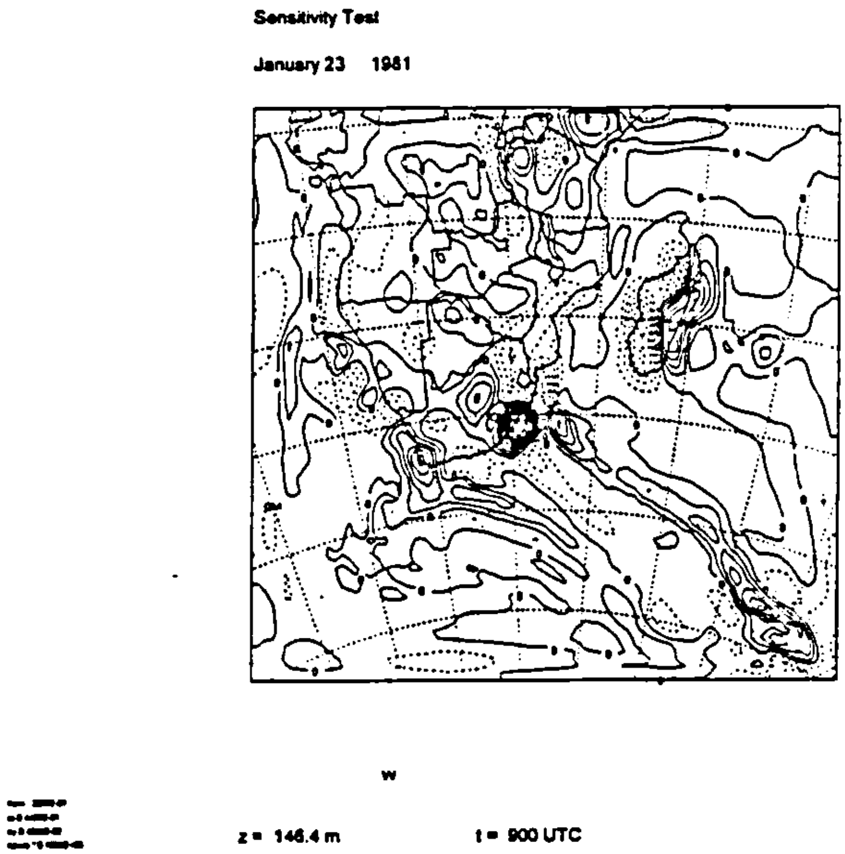

Figure 8.12: Vertical velocities (in $cm.s^{-1} \times 10^{-4}$) for (a) the control and (b) the sensitivity simulations at the 146,4m sigma level for 0900 UTC on 23 January 1981.

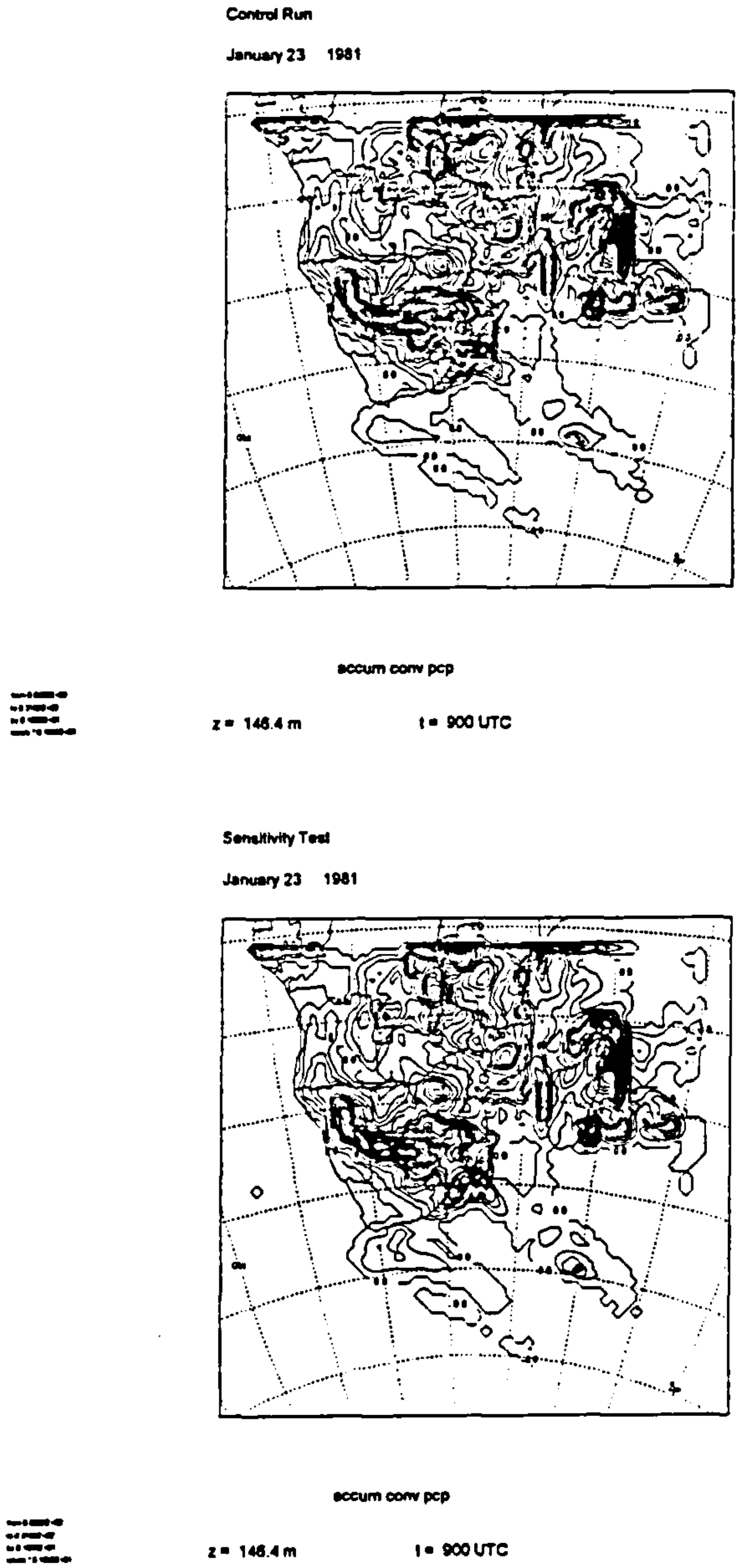

Figure 8.13: Accumulated convective precipitation (in mm) for (a) the control and (b) the sensitivity simulations at the 146.4m sigma level for 0900 UTC on 23 January 1981.

By the evening of 23 January 1981 (2100 UTC) the connection between the tropical and temperate regions was made possible by the coupling of the tropical low, the subtropical trough and the westerly wave perturbation. The magnitude of the westerly wind component was greater over the Cape south coast with values of 16 ms^{-1} compared to values of 15 ms^{-1}, poleward along the front, over the Northern Province, and over the Indian Ocean east of Durban (Fig 8.14 a,b). A secondary low pressure was simulated to the north of the subtropical trough in the sensitivity experiment (Fig 8.15 a,b). This feature is thought to be the product of reduced anticyclonic circulation over the northern parts of Namibia enabling greater north westerly wind flow towards the low. Vertical velocity showed higher instability over the Western Cape and along the cold front until the 40^0S line of latitude. Accumulated convective precipitation values remained higher over the sea surface temperature anomaly with sensitivity values of 6 mm compared to 4 mm in the control, eastern Namibia, southern Botswana (24 mm compared to 22 mm), and along the east coast of South Africa (Fig 8.16 a,b).

Day four

In the early morning (0600 UTC) of the last simulation day, the westerly winds continued to posses greater magnitude along the cold front down to approximately 37^0S. The simulated lows over the eastern half of south Africa and over the Indian Ocean dissipated although instability remained higher over the south coast (0,45 cms^{-1} compared to 0,40 cms^{-1}) and along the receding cold front (15 cms^{-1} compared to 10 cms^{-1}) (Fig 8.17 a,b). At the end of the simulation period a strong westerly component moved along the south coast in the same direction as the receding cold front, with localised stronger flow remaining in situ over the Northern Province and along the dissipating cold front (Fig 8.18 a,b). Once again streamlines indicate stronger south easterly winds along the west coast of South Africa, with a concomitant increase in northwesterly winds over the Northern Province and Zimbabwe. Northerly winds along the east coast of South Africa also remained stronger, weakening the zone of convergence along the east coast (Fig 8.19 a,b). Instability remained higher along the west and south coasts, and northern parts of the east coast, coinciding with zones of heightened westerly flow. Precipitation maintained the same pattern as from early on 23 January. Accumulated values were markedly higher over the area of modified sea surface temperatures with sensitivity values of 16 mm compared to control values of 8 mm. Similar

Control Run

January 23 1981

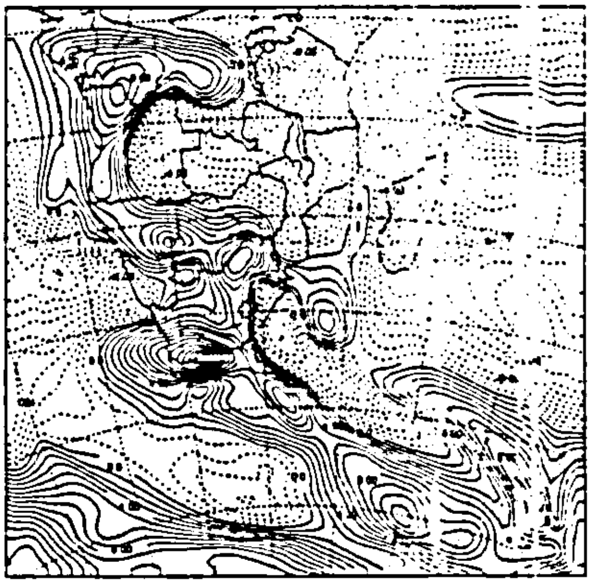

u

z = 146.4 m t = 2100 UTC

Sensitivity Test

January 23 1981

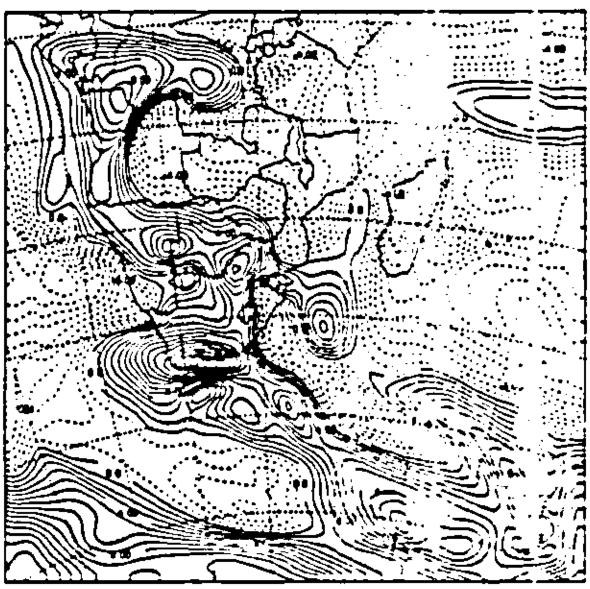

u

z = 146.4 m t = 2100 UTC

Figure 8.14: U components (in $m.s^{-1}$) for (a) the control and (b) the sensitivity simulations at the 146.4m sigma level for 2100 UTC on 23 January 1981.

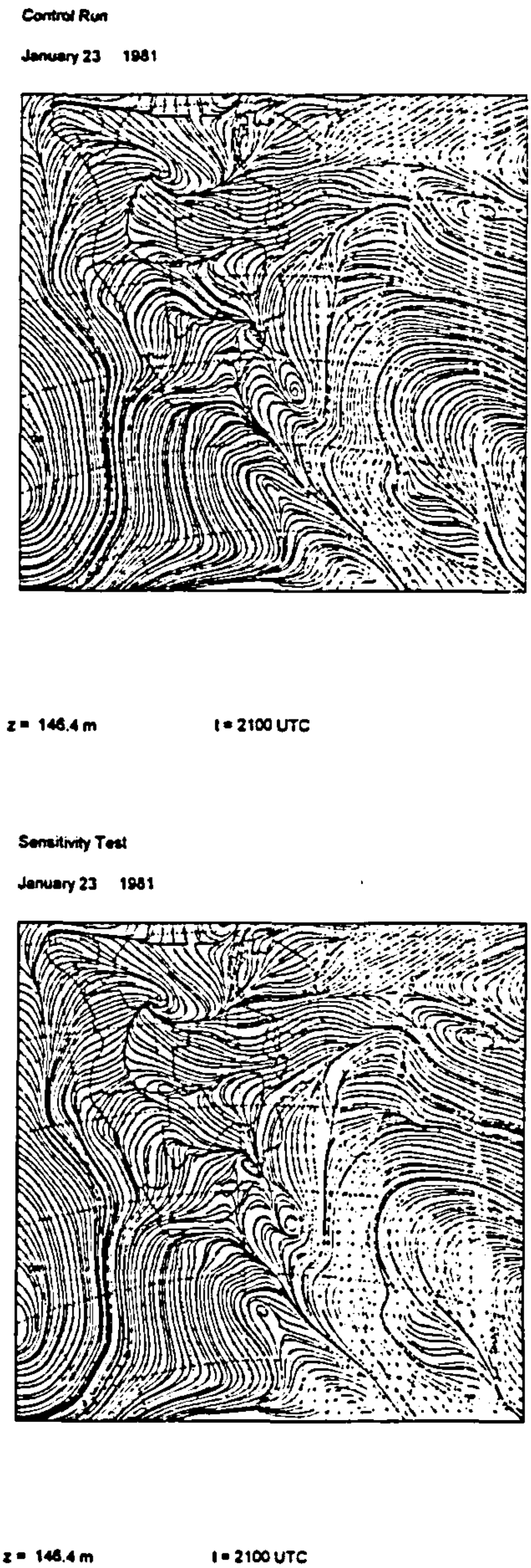

Figure 8.15: Streamline diagrams for (a) the control and (b) the sensitivity simulations at the 146,4m sigma level for 2100 UTC on 23 January 1981.

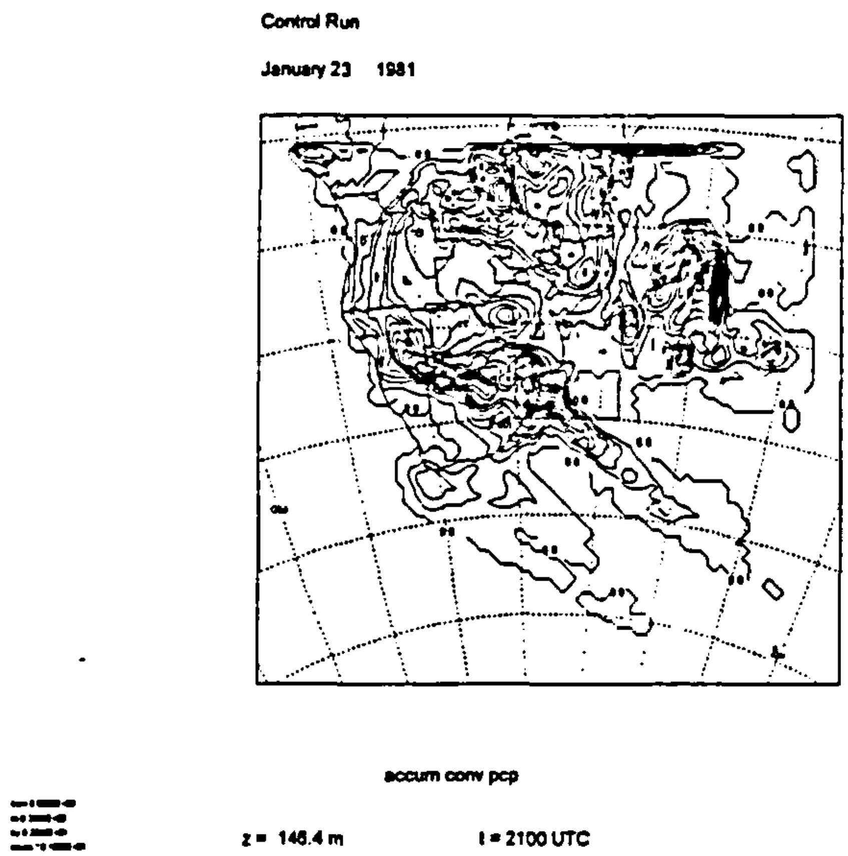

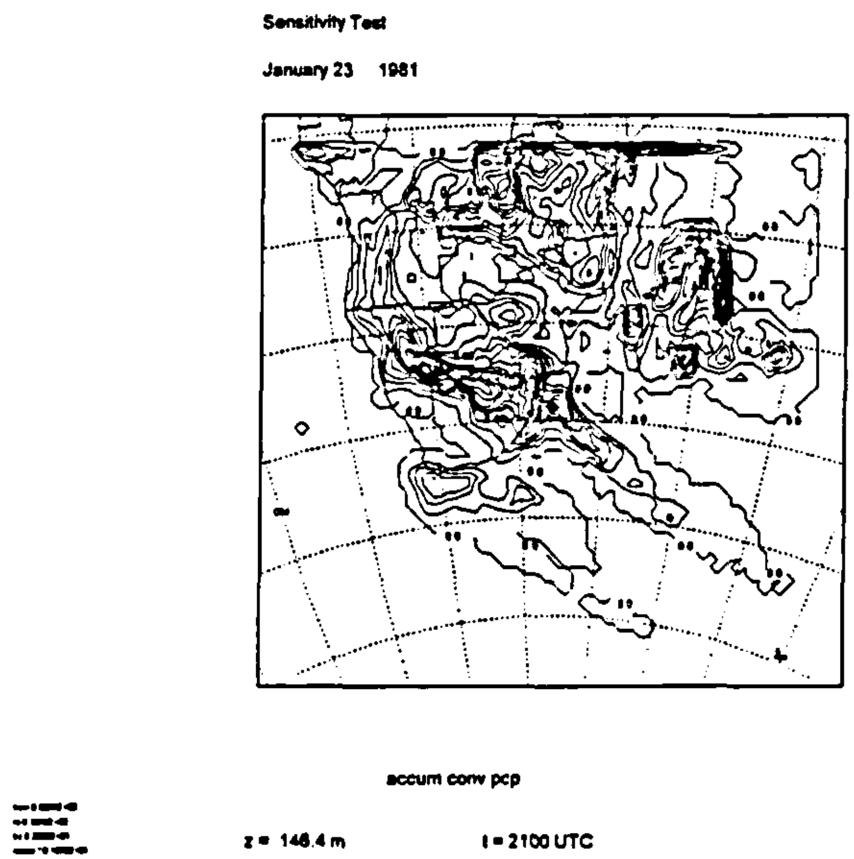

Figure 8.16: Accumulated convective precipitation (in mm) for (a) the control and (b) the sensitivity simulations at the 146.4m sigma level for 2100 UTC on 23 January 1981.

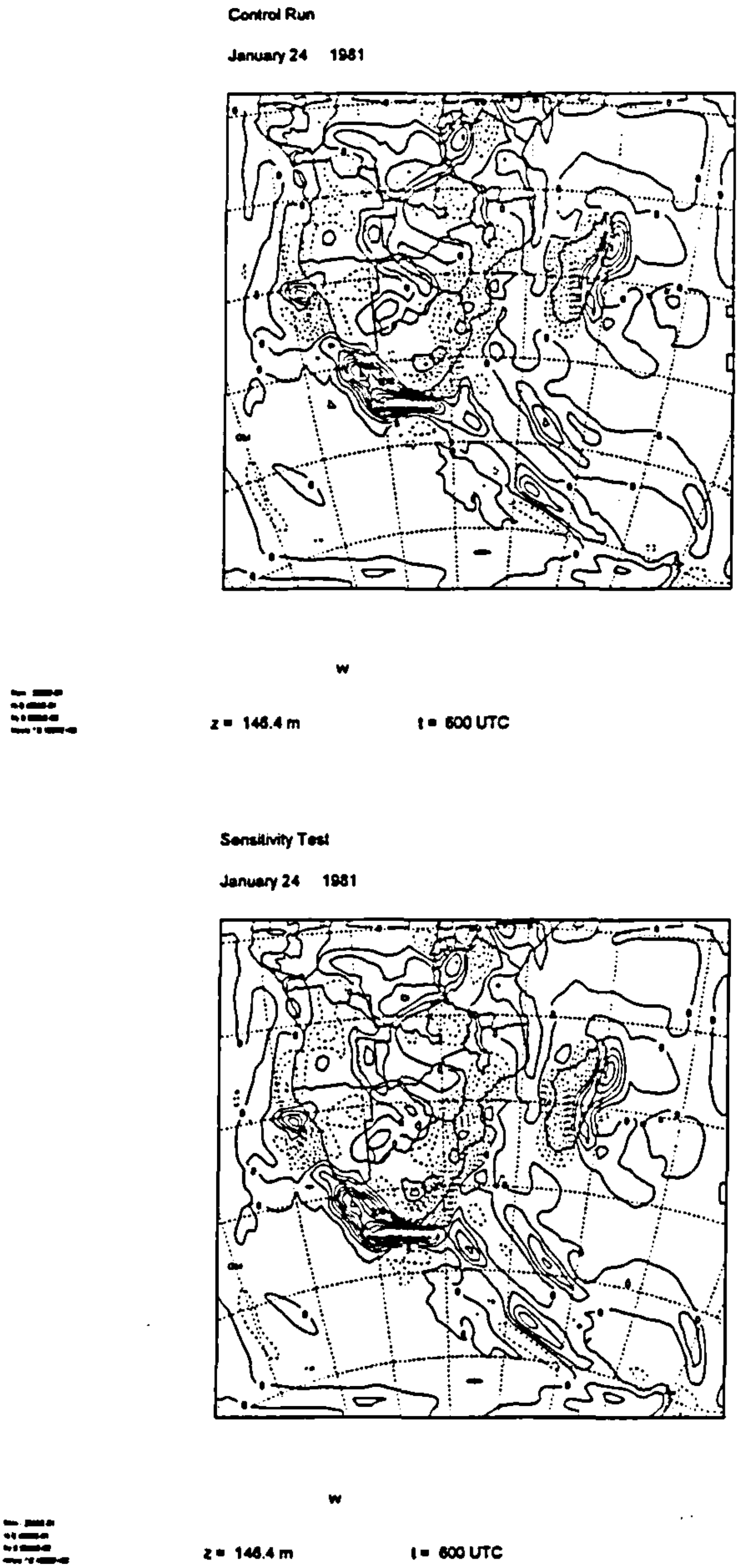

Figure 8.17: Vertical velocities (in $cm.s^{-1}$ $x10^{-4}$) for (a) the control and (b) the sensitivity simulations at the 146,4m sigma level for 0600 UTC on 24 January 1981.

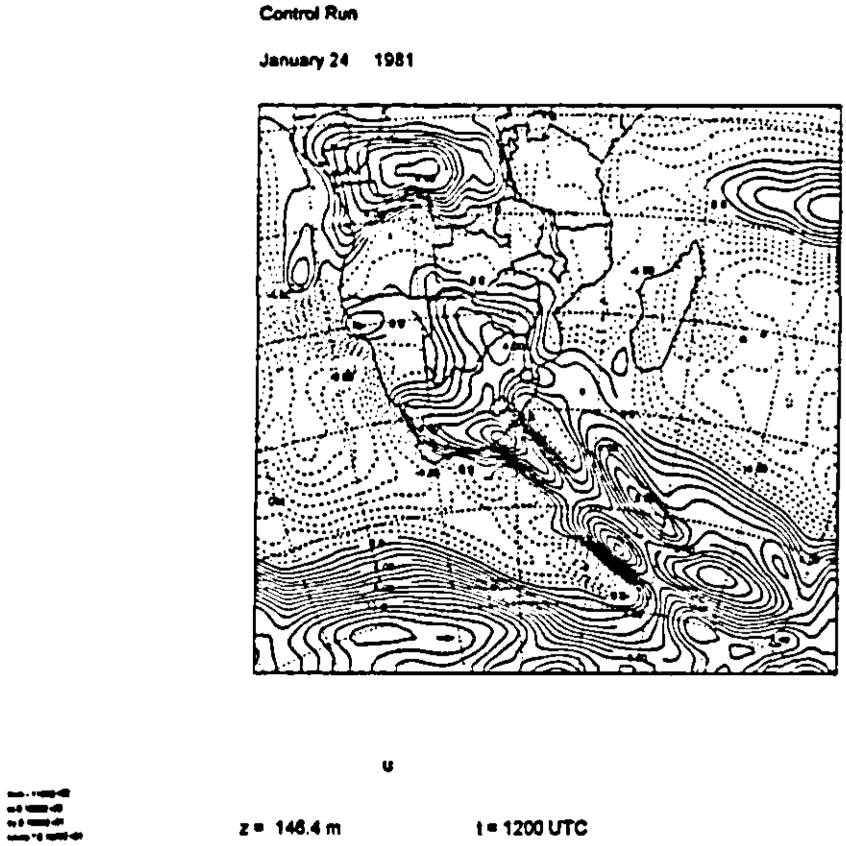

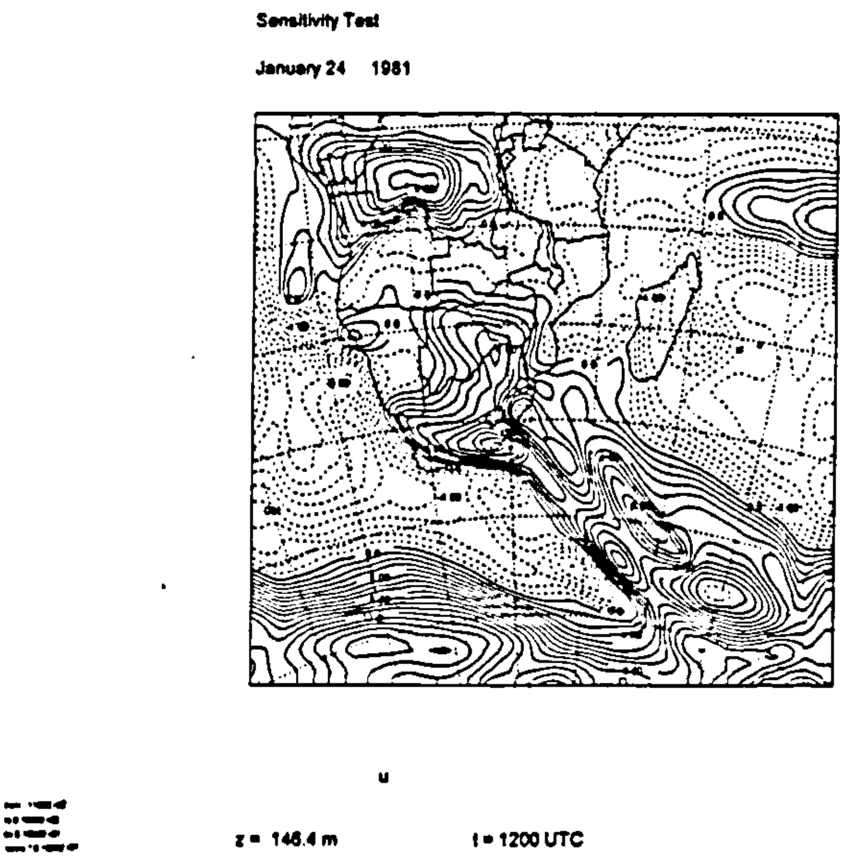

Figure 8.18: U components (in m.s^{-1}) for (a) the control and (b) the sensitivity simulations at the 146,4m sigma level for 1200 UTC on 24 January 1981.

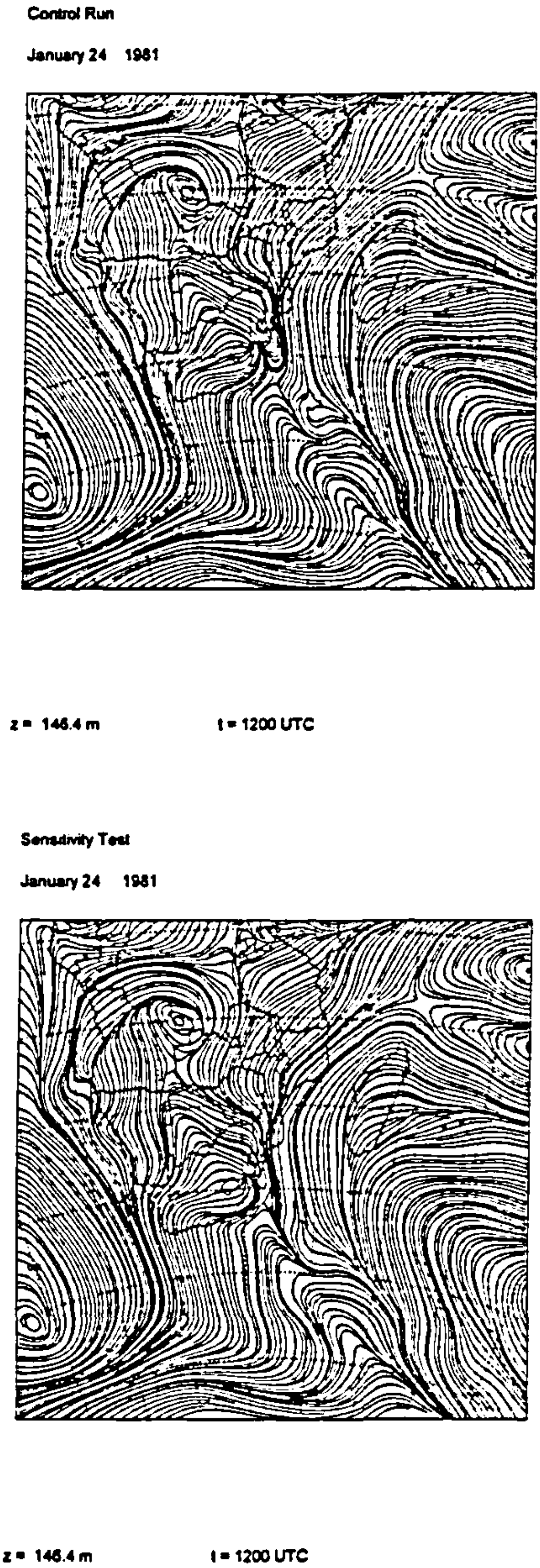

Figure 8.19: Streamline diagrams for (a) the control and (b) the sensitivity simulations at the 146,4m sigma level for 1200 UTC on 24 January 1981.

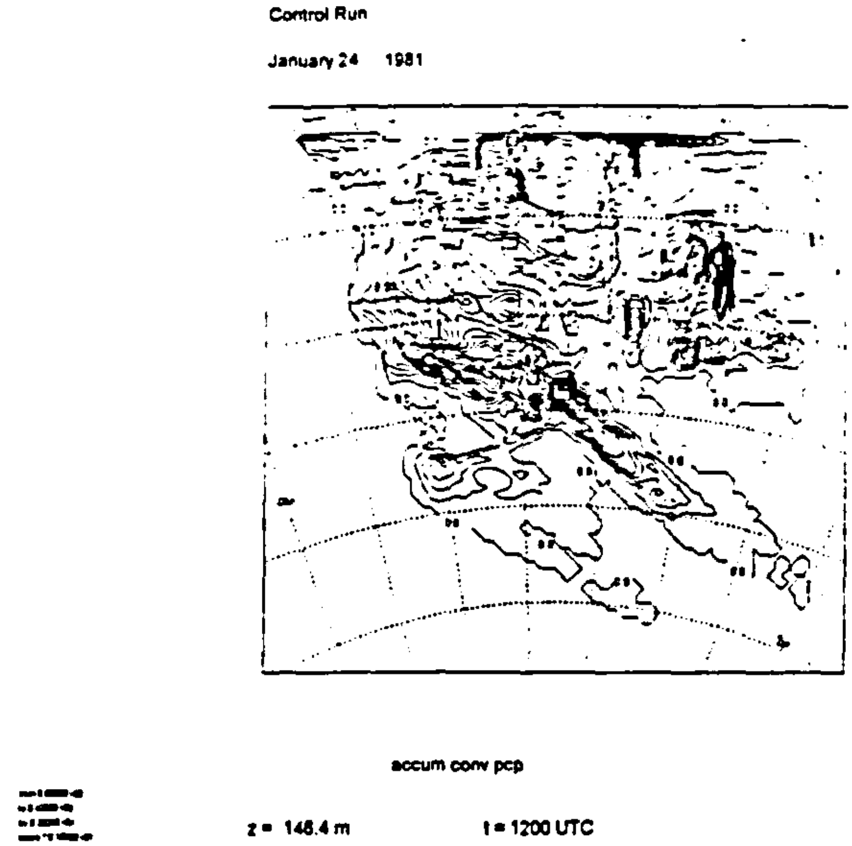

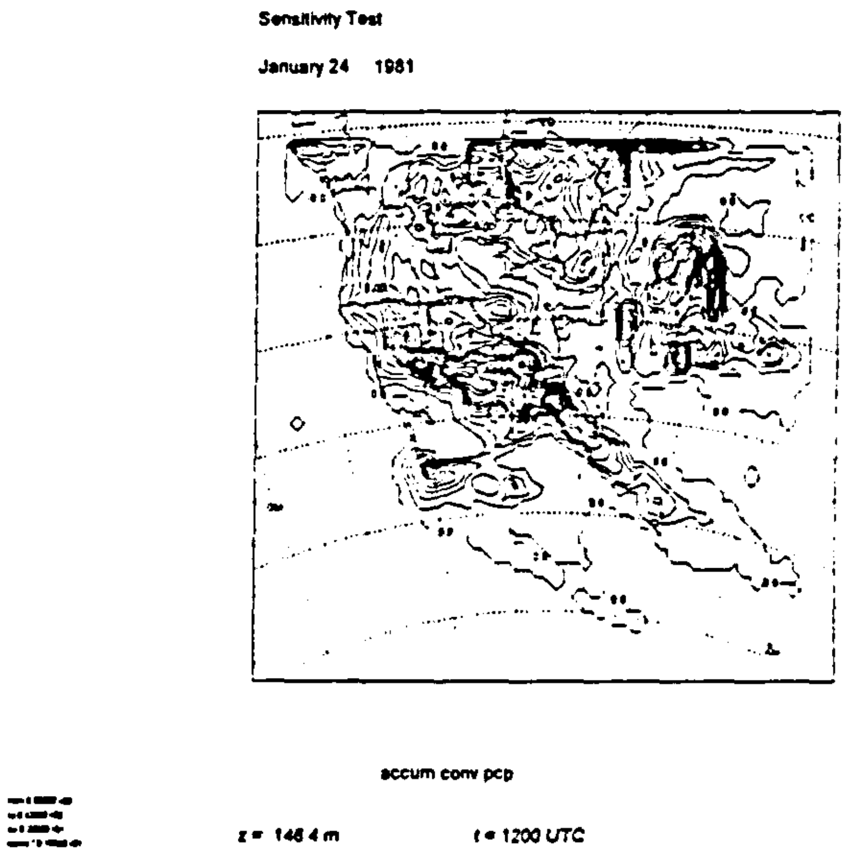

Figure 8.20: Accumulated convective precipitation (in mm) for (a) the control and (b) the sensitivity simulations at the 146.4m sigma level for 1200 UTC on 24 January 1981.

differences are found over the eastern half of the country and adjacent Indian Ocean, as well as eastern Namibia and southern Botswana (Fig 8.20 a, b).

As at the near surface, the 807,2 m atmospheric level exhibits the same general trend of strengthening in the westerly component, from 23 January onwards (Fig 8.21 a,b). The streamlines at this level suggest a stronger shallow low pressure development over the Indian Ocean (Fig 8.22 a,b). Instability, as in the lower surface level remained higher over the west (0,049 cms^{-1} compared to 0,048 cms^{-1}) and south coast of South Africa (0,077 cms^{-1} versus 0,072 cms^{-1}) with, however, lower magnitudes along the dissipating front (Fig 8.23 a,b). Vapour and cloud mixing ratios, again indicated marginally higher moisture availability along the southeast coast and also east of Durban over the adjacent Indian Ocean, with control values of 0,020 gkg^{-1} and sensitivity values of 0,021 gkg^{-1} (Fig 8.24 a,b).

Discussion

The atmospheric circulation changes brought about by the modification of sea surface temperatures took longer to translate into the atmosphere than did the tropical Indian Ocean anomaly experiment. The explanation for this greater delay, lies in a comparison of the background sea surface temperatures and moisture values over the two oceanic regions. In the tropical Indian Ocean background sea surface temperatures are higher, with stronger boundary layer heat fluxes and thus greater atmospheric heating. The enhanced atmospheric temperatures over the anomaly region, and neighbouring ocean, allow for a greater moisture carrying capacity of the localised atmosphere. In the Agulhas Current retroflection region the lower background temperatures less readily effect moisture availability, instability and hence general circulation.

The circulation changes found for the anomaly experiment over the Agulhas current retroflection closely resemble the ocean-atmosphere feedback mechanisms proposed by Walker (1989) for the southern Agulhas Current. As theorised (Walker, 1989), the development of sea temperature anomalies served to intensify the sea surface temperature front, leading to a poleward shift in the surface westerlies. The strengthened heat fluxes enhanced low-level instability and produced a marginal amplification of the westerly troughs.

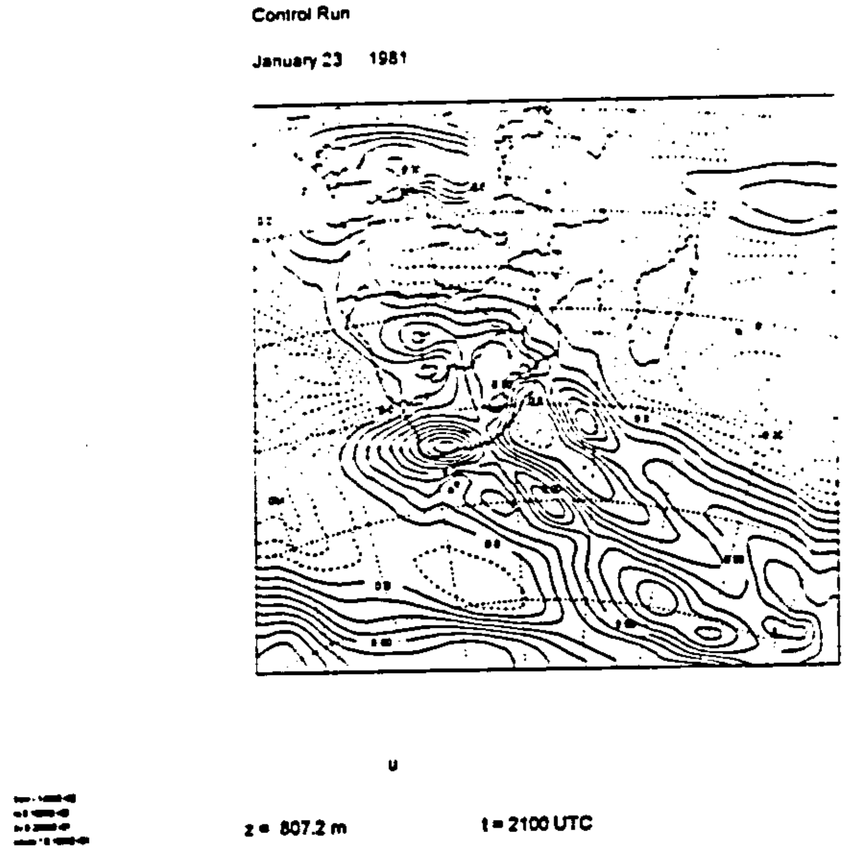

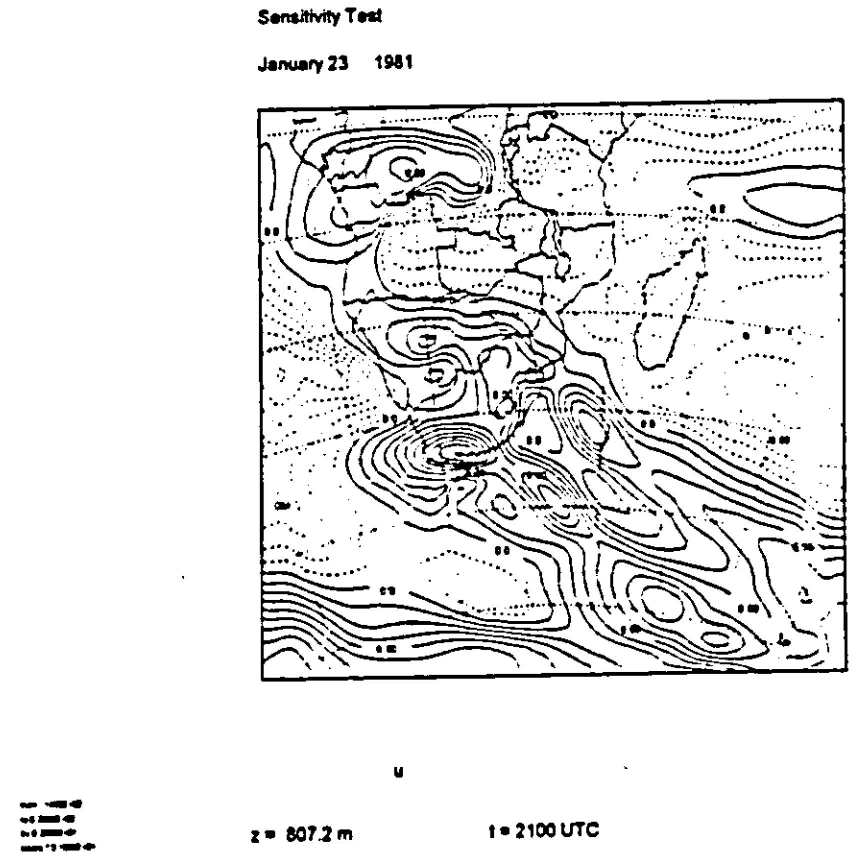

Figure 8.21: U components (in m.s^{-1}) for (a) the control and (b) the sensitivity simulations at the 807,2m sigma level for 2100 UTC on 23 January 1981.

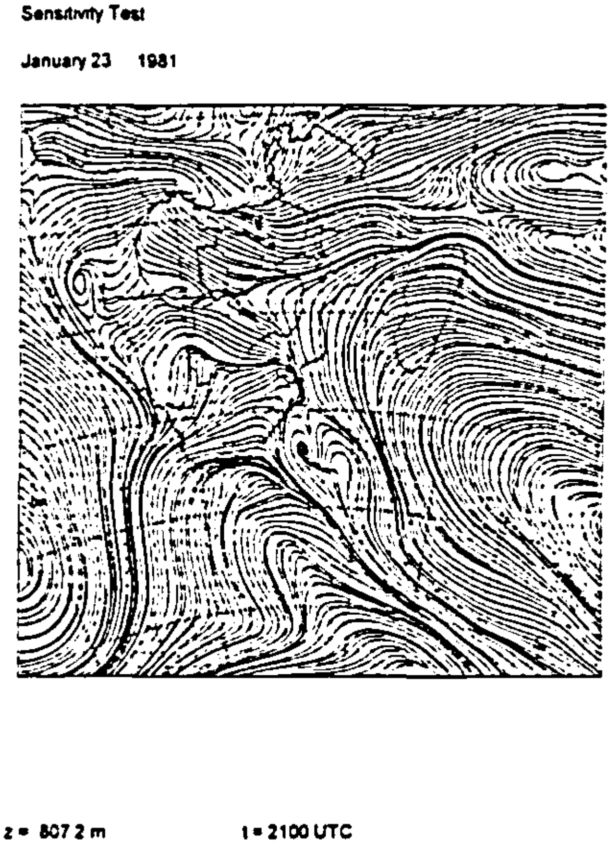

Figure 8.22: Streamline diagrams for (a) the control and (b) the sensitivity simulations at the 807.2m sigma level for 2100 UTC on 23 January 1981.

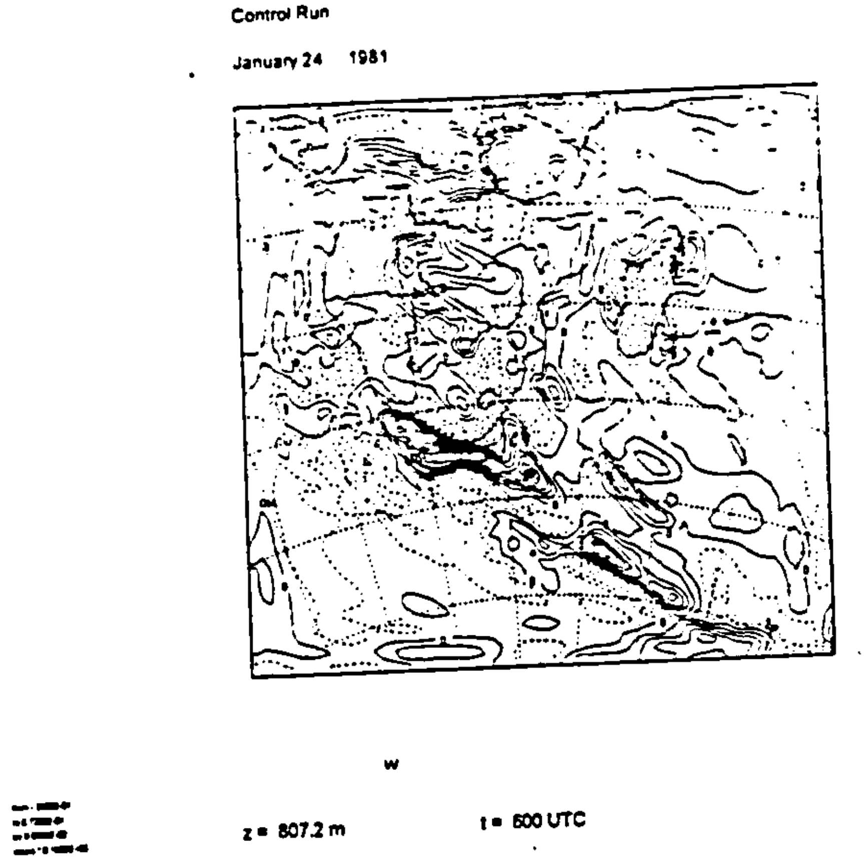

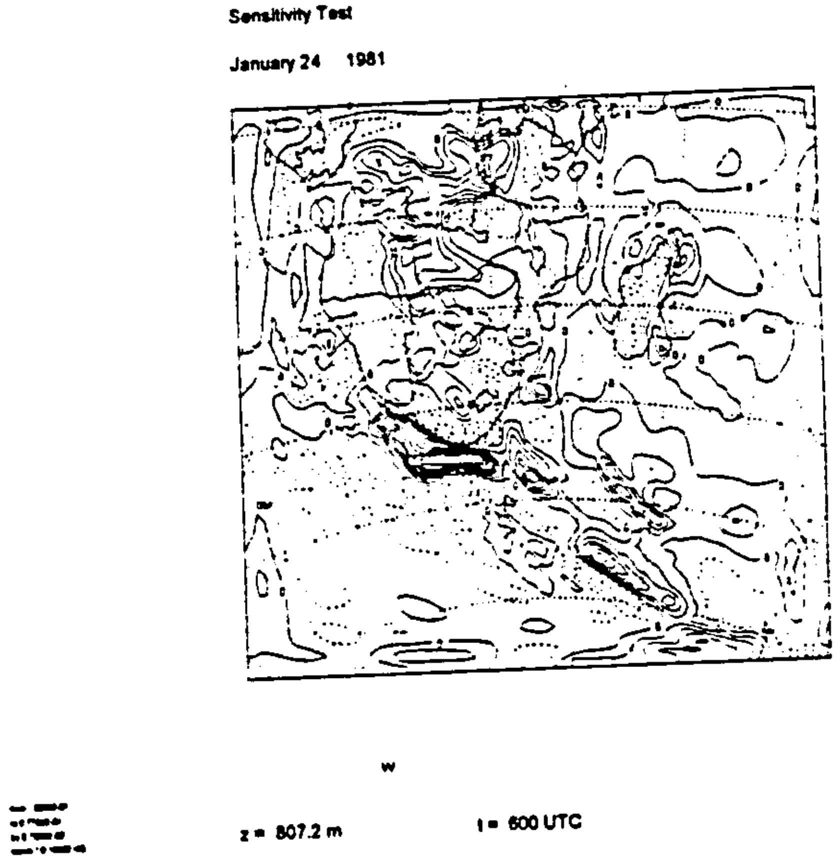

Figure 8.23: Vertical velocities (in $cm.s^{-1}$ $x10^{-4}$) for (a) the control and (b) the sensitivity simulations at the 807.2m sigma level for 0600 UTC on 24 January 1981.

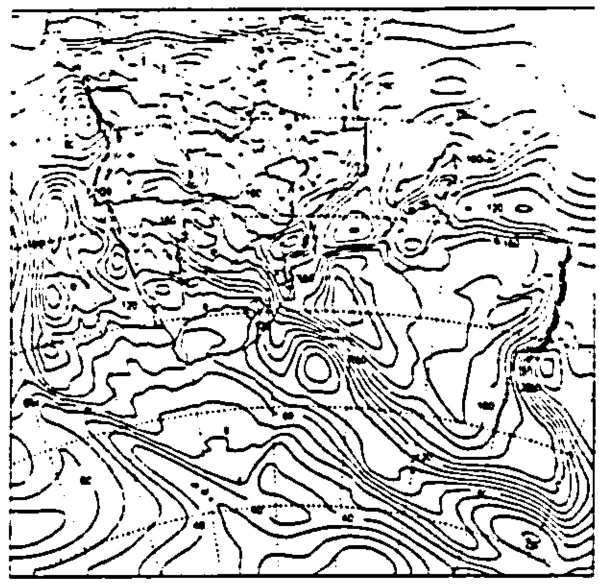

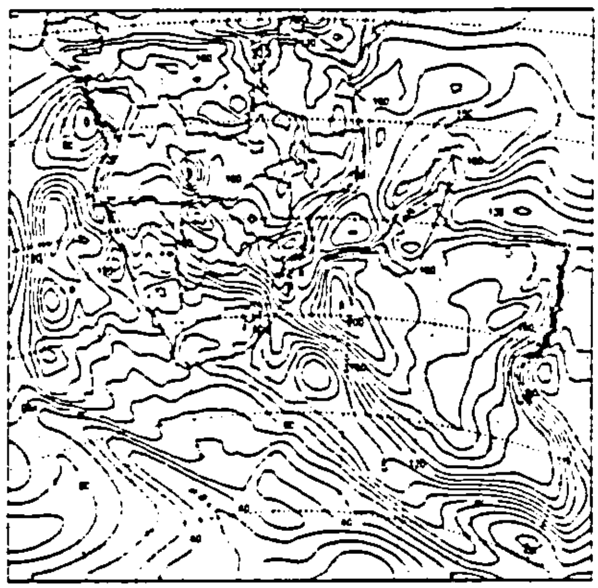

Figure 8.24: Vapour and cloud mixing ratios (in $g.kg^{-1} x10^{-4}$) for (a) the control and (b) the sensitivity simulations at the 807,2m sigma level for 1200 UTC on 24 January 1981.

The atmospheric differences that were found indicate that the origin of change lies over the modified sea surface temperature field, and that the atmospheric circulation anomalies were translated both along the coast, from southwest to northeast by the passage of the westerly troughs, and also by the enhanced recurved westerly flow over eastern Namibia, southern Botswana and the Northern Province of South Africa. Higher instability values began over the modified sea surface temperature field and migrated eastward along the coast, and poleward along the cold front. The greatest precipitation differences are found over the summer rainfall areas of South Africa, eastern Namibia and southern Botswana, with highest magnitude differences over the area of positive sea surface temperature increase.

Synopsis

The atmospheric response of RAMS to an positive Agulhas Current retroflection anomaly is investigated. Warm anomalous sea surface temperatures, defined by a positive 2°C and 1°C boundary, are added to an area south of South Africa centered on 20°E. A historical case study is chosen that spanned the development and dissipation of a tropical-temperate trough, for the period 21 to 24 January 1981. This feature is analysed for both the control simulation and sensitivity test in order to identify any circulation differences resulting from the warm sea surface temperature anomaly addition. The overall response is small due to model limitations and time constraints. The small perturbations in the simulated meteorological response are consistent with the expected climate response to anomalously warm sea surface temperatures in the region of the Agulhas Current retofelection. As theorised by Walker 1989 the model simulated greater instability values over the region of modification that in turn migrated eastwards along the coast , and poleward along the cold front.

CHAPTER 9

THE TROPICAL EASTERN ATLANTIC SEA SURFACE TEMPERATURE ANOMALY

The tropical western Atlantic Ocean is a major source of moisture for the west African countries of Angola, Zaire, Gabon, Congo, and to a lesser extent South Africa in early summer. A combination of varying onshore flow and fluctuating sea surface temperatures are, to a large extent, responsible for rainfall variability over this area (Hirst and Hastenrath, 1983; Hastenrath, 1984). Positive sea surface temperature anomalies, in conjunction with stronger than normal westerly onshore flow, result in increased moisture transport into tropical west Africa and are thus linked with heavier rainfall events during the duration of the oceanic and atmospheric anomalies (Hirst and Hastenrath, 1983). The association between the tropical western Atlantic sea surface temperature variability and rainfall over South Africa is poorly understood. The results of the third sensitivity experiment should illustrate some of the mechanisms involved in the association between the tropical western Atlantic Ocean and rainfall over South Africa. As for the previous two sensitivity experiments the model simulation was initialised using a modified long-term mean United Kingdom Meteorological Office sea surface temperature data set, with positive anomalies of 2^0C and 1^0C respectively added to the background temperature field between 4^0N and 20^0S, with a longitudinal extent between 6^0W and 14^0E (Fig 9.1).

Results

Day one

The initial time-step of the tropical eastern Atlantic Ocean simulation once again confirmed the precise circulation patterns of the control simulation experiment. At the 146,4 m sigma level

Sensitivity Test 7 (African West Coast Atlantic Anomaly)

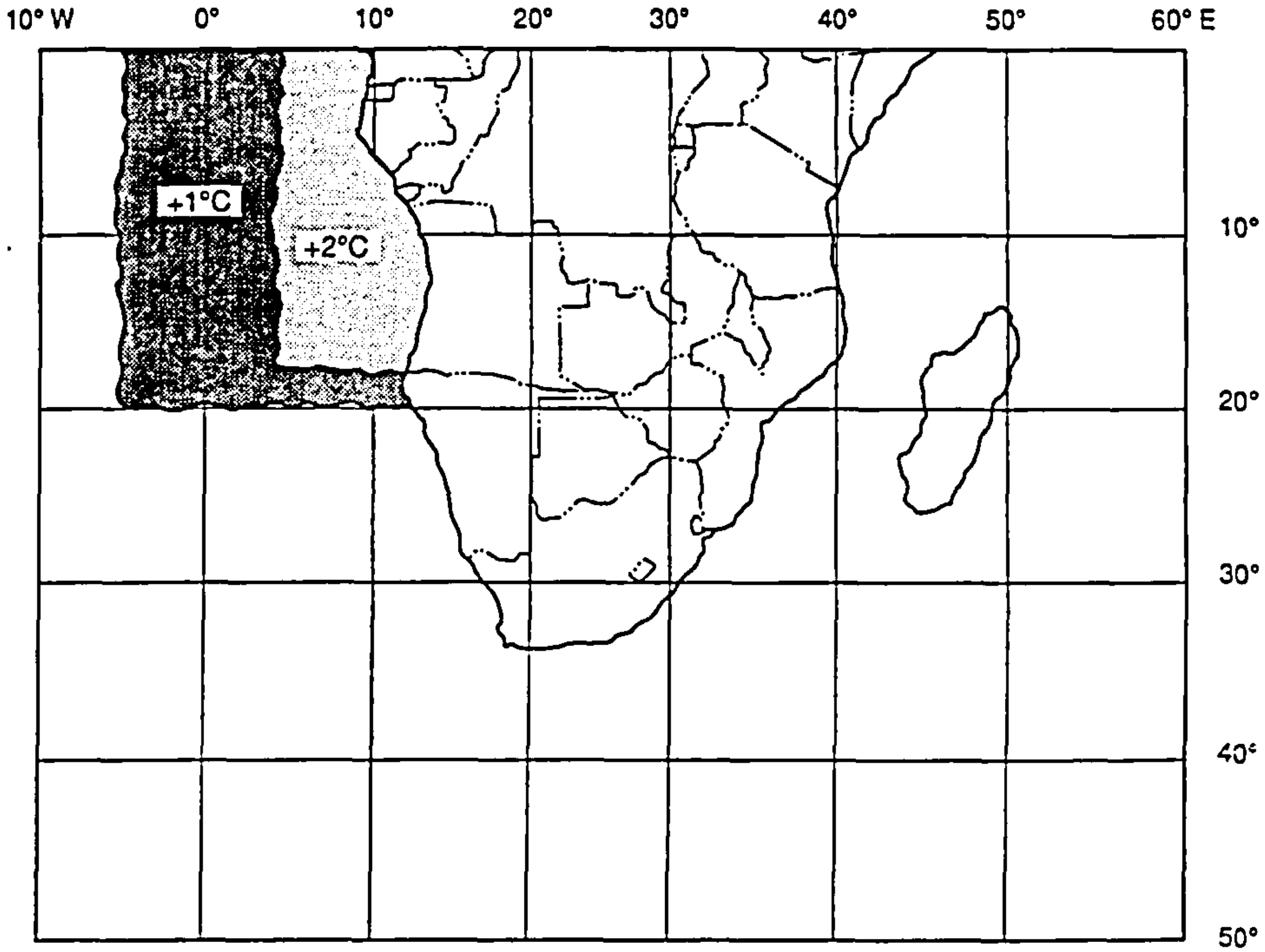

Figure 9.1: Representation of the seventh sensitivity test with anomalies placed between 4°N and 20°S, and from 6°W to the African West Coast.

the position of the general synoptic features, as well as high vapour and cloud mixing ratios in the tropical Indian Ocean (0,022 gkg^{-1}) and lower mixing ratios of between 0,0070 gkg^{-1} and 0,016 gkg^{-1} along the west coast were mirrored in the sensitivity simulation. By 2100 UTC of 21 January the anomalous sea surface temperatures in the tropical western Atlantic Ocean had been resident long enough to produce marginal circulation changes at the 146,4 m level. The increase in sea surface temperatures in this region produced a concomitant increase in air temperature through heightened sensible heating. This increase in air temperatures took place north of 10^0S along the west coast, with the southerly extension of the 297 K isotherm. Over the Atlantic Ocean, adjacent to Angola, the westerly wind component strengthened, increasing onshore flow in the area (Fig 9.2 a,b). These differences are confirmed by the streamlines, where it is evident that over the northern half of Angola circulation became slightly more onshore, whereas over southern Congo flow became more southerly. The combination of strengthened onshore flow and warmer air temperatures produced vertical velocity increases along the Angolan coast from 0,003 cms^{-1} in the control simulation to 0,006 cms^{-1} in the sensitivity experiment (Fig 9.3 a,b). Precipitation values for 2100 UTC indicated a marginal increase over Gabon and Congo coast (Fig 9.4 a,b). The presence of heightened instability over Angola had not produced rainfall in this area as moisture levels were still relatively low.

Day two

On the morning of the second day (0600 UTC), the stronger westerly component simulated in the sensitivity experiment continued. The significance of this atmospheric circulation anomaly at the 146,4 m level was that the coastal regions of Gabon and Congo, along with parts of the Zaire basin, began to experience the greater availability of moisture, and thus the potential for precipitation increased. Later in the afternoon (1500 UTC) the westerly wind component or onshore flow remained stronger over Gabon and Congo with an intensification of convergence along the Angolan coast. Circulation around the tropical low strengthened, due to the behaviour of the westerly wind component, as well as the development of higher atmospheric temperatures (297 K) extending from the north (Fig 9.5 a,b), heightened moisture availability over Gabon and the Congo (control values are less than 0,016 cms^{-1} and sensitivity values are greater than 0.016 cms^{-1}) (Fig 9.6 a,b). Higher precipitation values of 6 mm in the sensitivity experiment compared to 4 mm in the control simulation were found adjacent to the sea surface

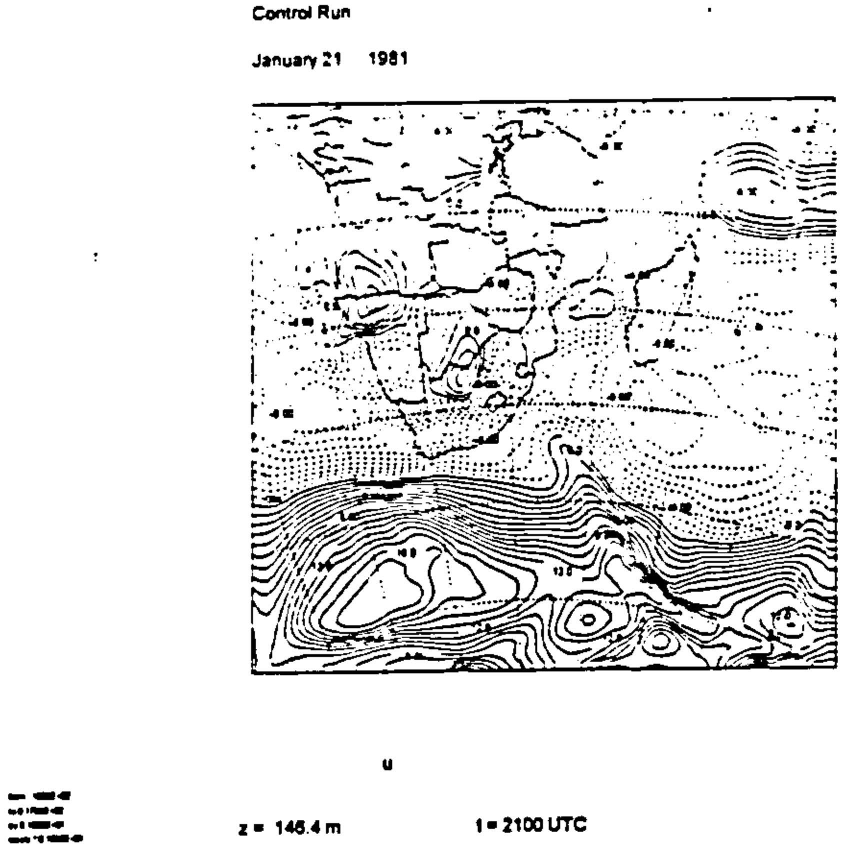

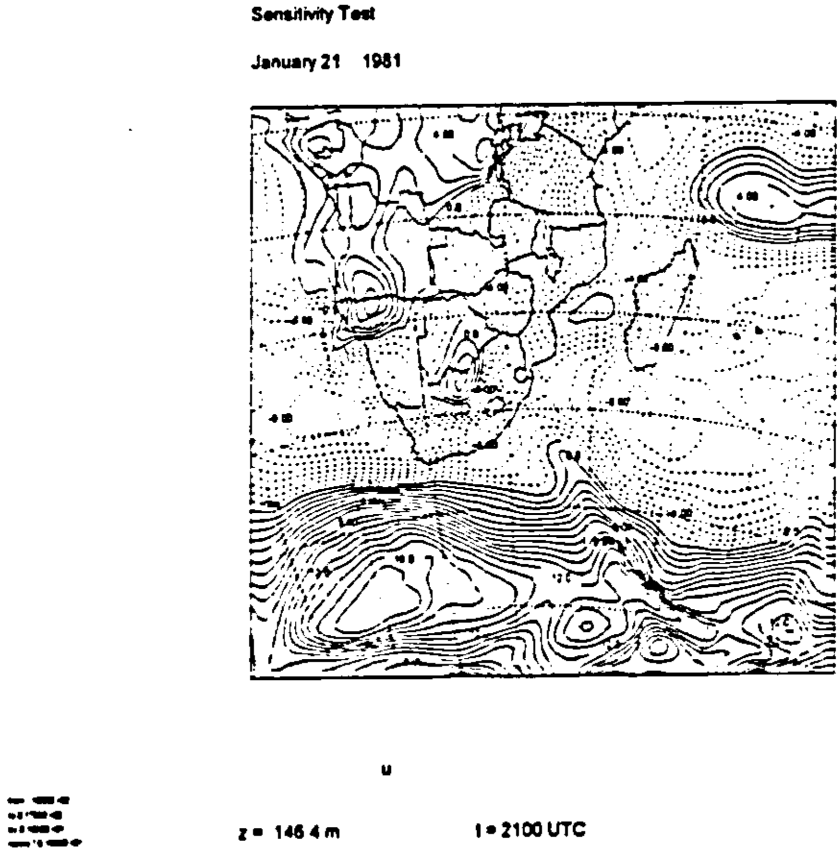

Figure 9.2: U components (in $m.s^{-1}$) for (a) the control and (b) the sensitivity simulations at the 146.4m sigma level for 2100 UTC on 21 January 1981.

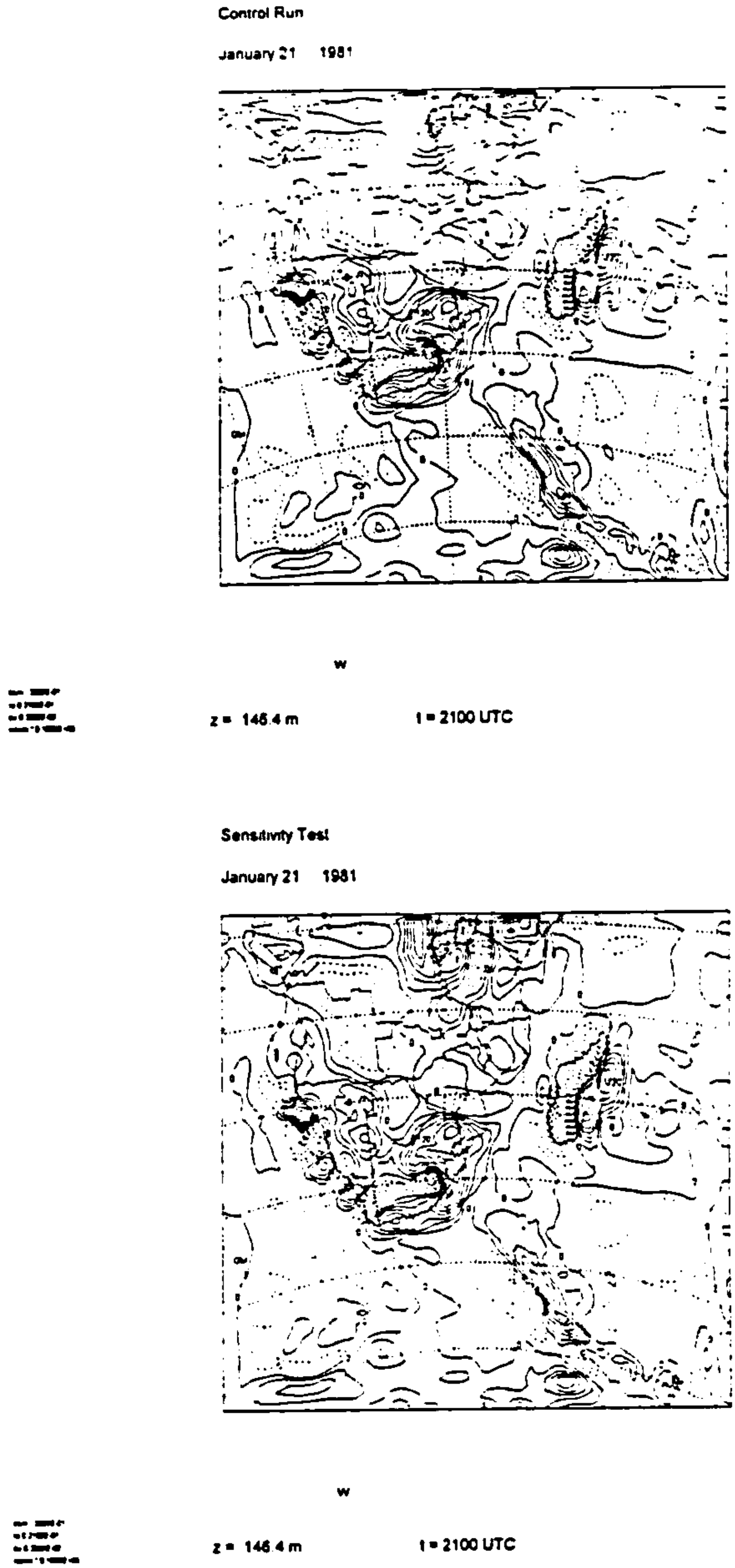

Figure 9.3: Vertical velocities (in $cm.s^{-1} \times 10^{-4}$) for (a) the control and (b) the sensitivity simulations at the 146.4m sigma level for 2100 UTC on 21 January 1981.

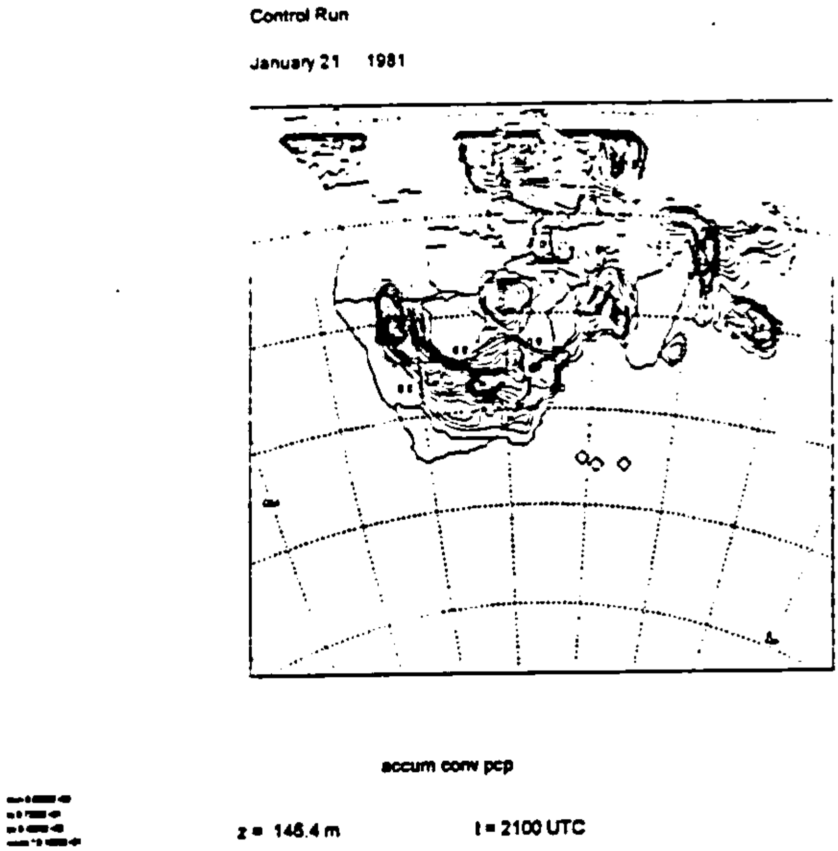

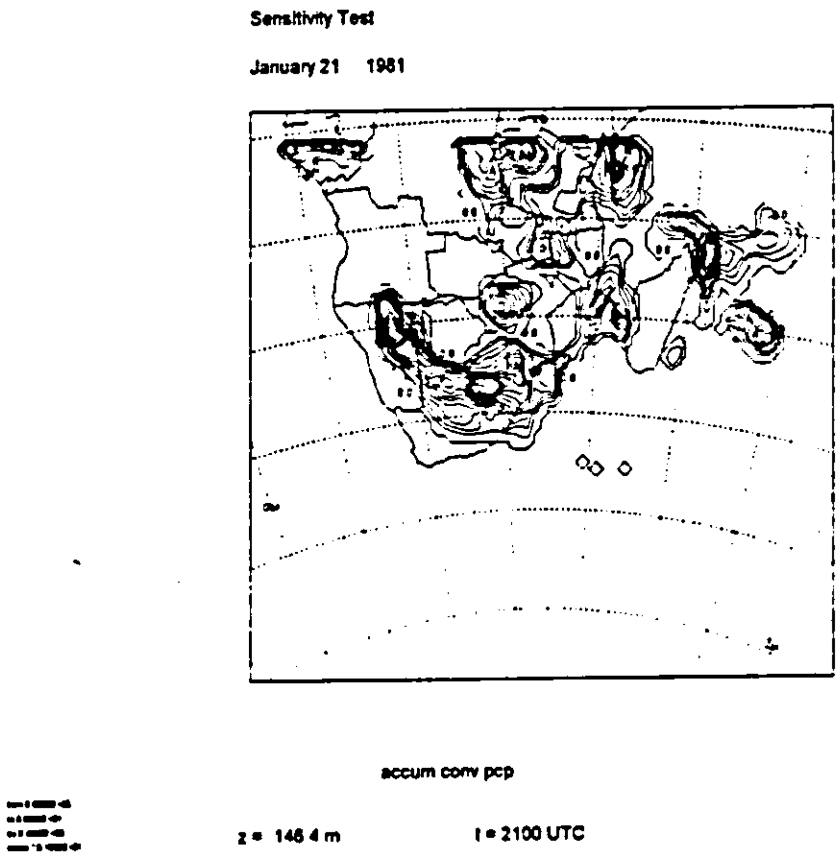

Figure 9.4: Accumulated convective precipitation (in mm) for (a) the control and (b) the sensitivity simulations at the 146,4m sigma level for 2100 UTC on 21 January 1981.

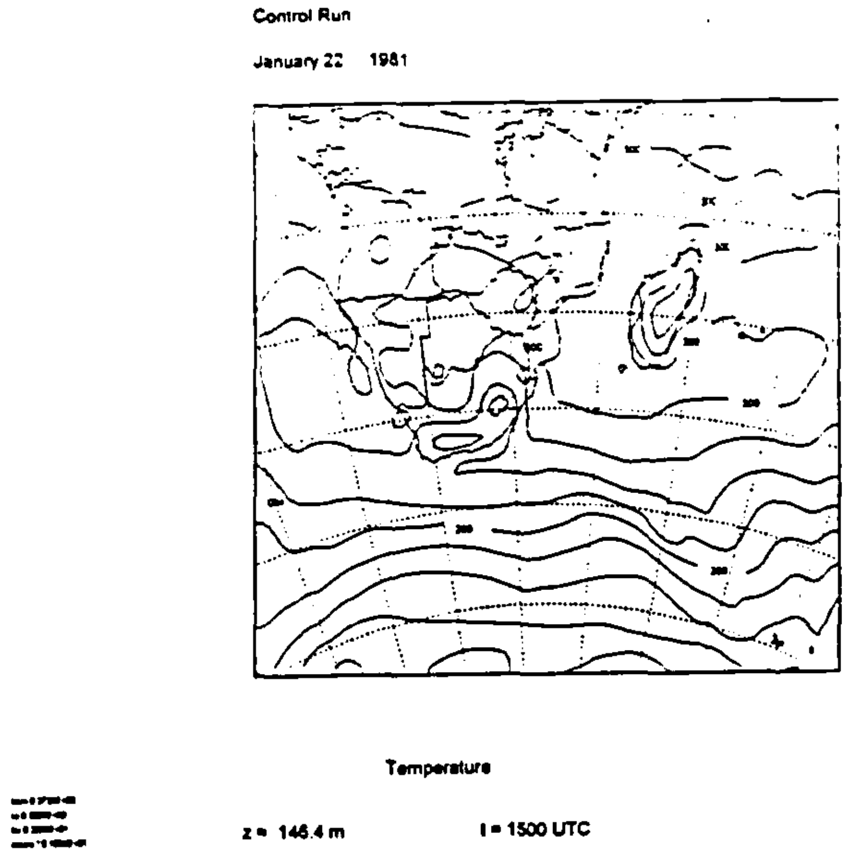

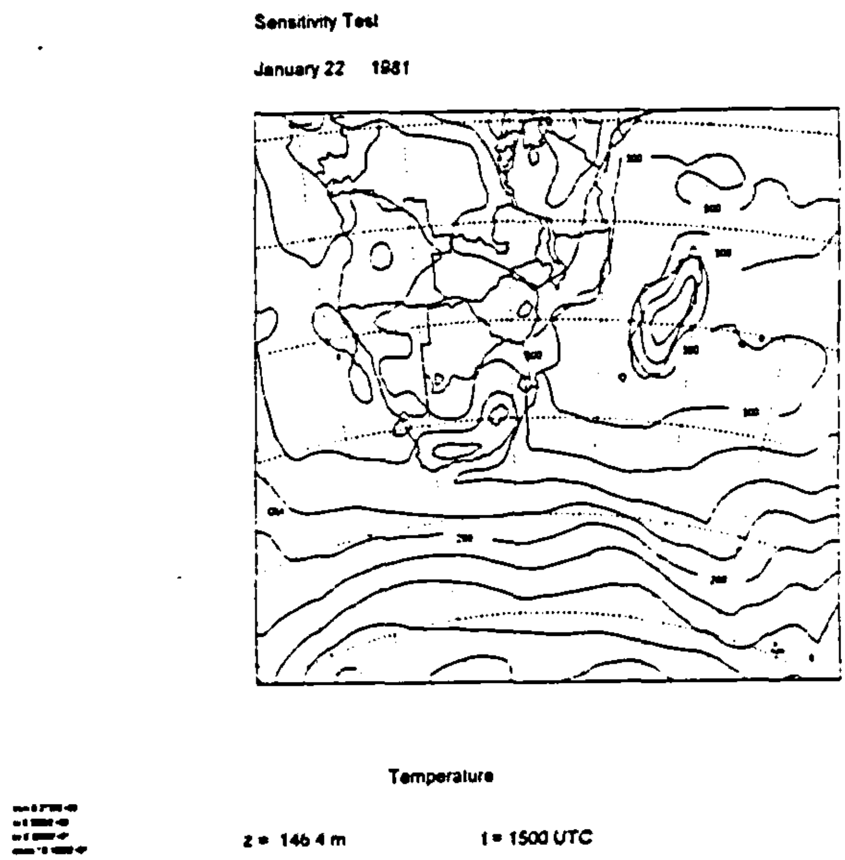

Figure 9.5: Temperature contours (in K) for (a) the control and (b) the sensitivity simulations at the 146.4m sigma level for 1500 UTC on 22 January 1981.

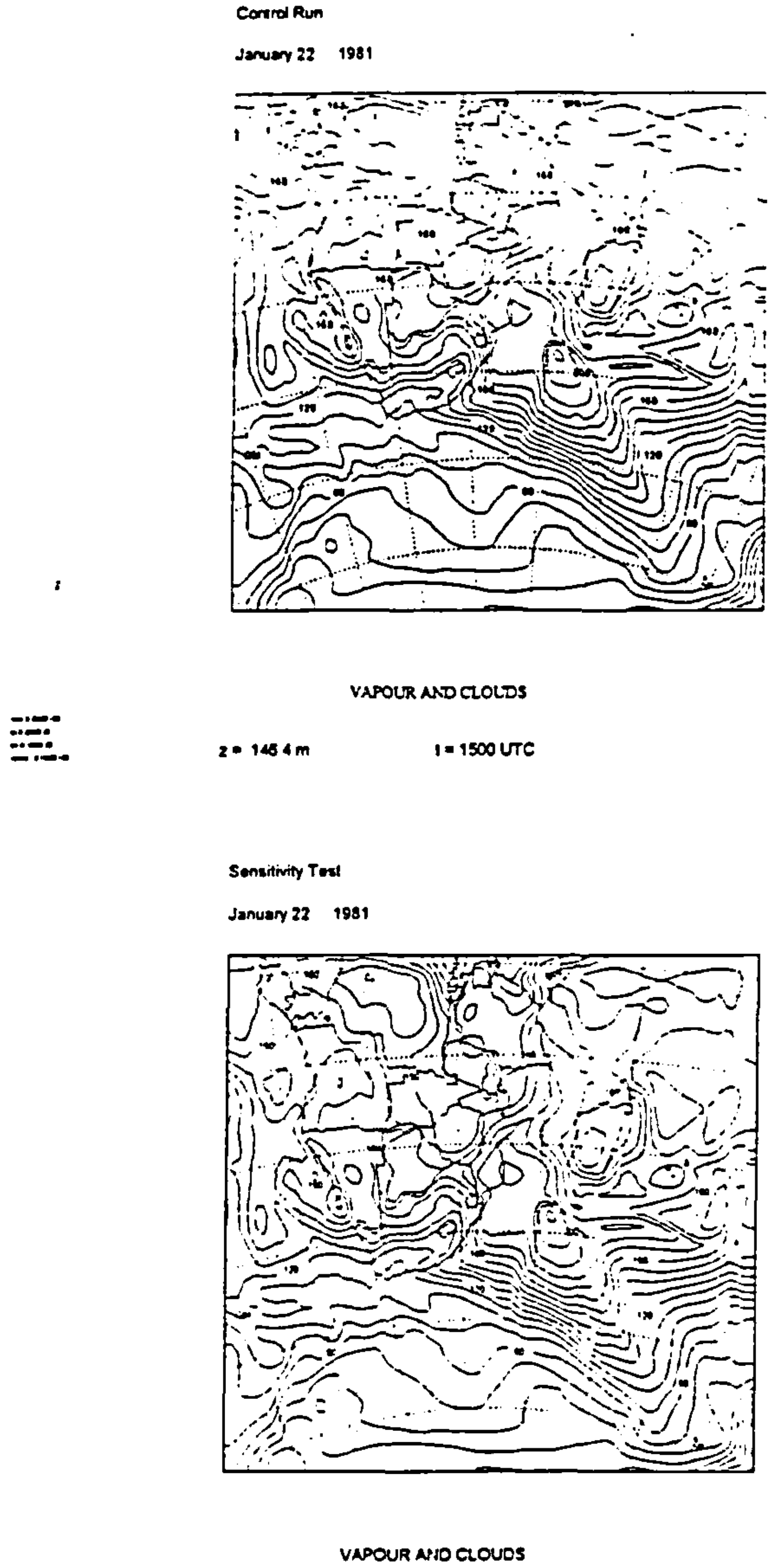

Figure 9.6: Vapour and cloud mixing ratios (in g.kg^{-1} x10^{-4}) for (a) the control and (b) the sensitivity simulations at the 146,4m sigma level for 1500 UTC on 22 January 1981.

temperature anomaly (Fig 9.7 a,b). Rainfall over the Gauteng region, however, showed a decrease from between 5 mm to 6 mm in the control simulation to less than 4 mm in the sensitivity experiment (Fig 9.7 a,b).

By the evening of 22 January the westerly wind component at the 146,6 m sigma level showed a slight increase over the Mpumalanga region, with the sensitivity experiment simulating values of 6 ms^{-1} over the southern Congo and northern Angola regions as opposed to values of 5 ms^{-1} for the control simulation (Fig 9.8 a,b). Circulation differences appeared to become prominent over South Africa with both stronger circulation and heightened instability present around the subtropical trough. Vertical velocities over the Indian Ocean east of Durban exhibit sensitivity values of 0,040 cms^{-1} compared to control values of 0,036 cms^{-1} (Fig 9.9 a,b). Circulation around the subtropical trough strengthened with higher vertical velocities present over the Indian Ocean east of Durban of 0,040 cms^{-1} compared to 0,036 cms^{-1} (Fig 9.9 a,b). In spite of the periodic reduction of the onshore component over Gabon and Congo simulated precipitation values for the sensitivity test remained higher with 7 mm in the sensitivity experiment compared 5 mm in the control simulation (Fig 9.10 a,b). Over the Guateng region and eastern Namibia precipitation values showed a decrease from 16 mm in the control simulation to 13 mm in the sensitivity experiment (Fig 9.10 a,b).

Until 1500 UTC on 22 January very few of the atmospheric circulation changes brought about by the inclusion of the positive sea surface temperature field had translated to the higher 807,2 m level. The only differences that are evident were vapour and cloud mixing ratios, which exhibited the same trend of increase as at the lower sigma level.

By 1500 UTC on 22 January sufficient simulation time had passed to allow for the vertical translation of the atmospheric circulation anomalies to take place. Again, the differences at the 807,2 m level were consistent with the 146,6 m level, with stronger westerly component north of 10^{0}S (Fig 9.11 a,b), which served to increase moisture availability over Gabon, Congo and the Zaire basin (Fig 5.12 a,b), as well as to encourage stronger cyclonic circulation around the tropical low to the west of Angola (Fig 9.13 a,b). Later in the day (2100 UTC) the simulated cyclonic circulation around the tropical low continued to be stronger (Fig 10 .14 a,b).

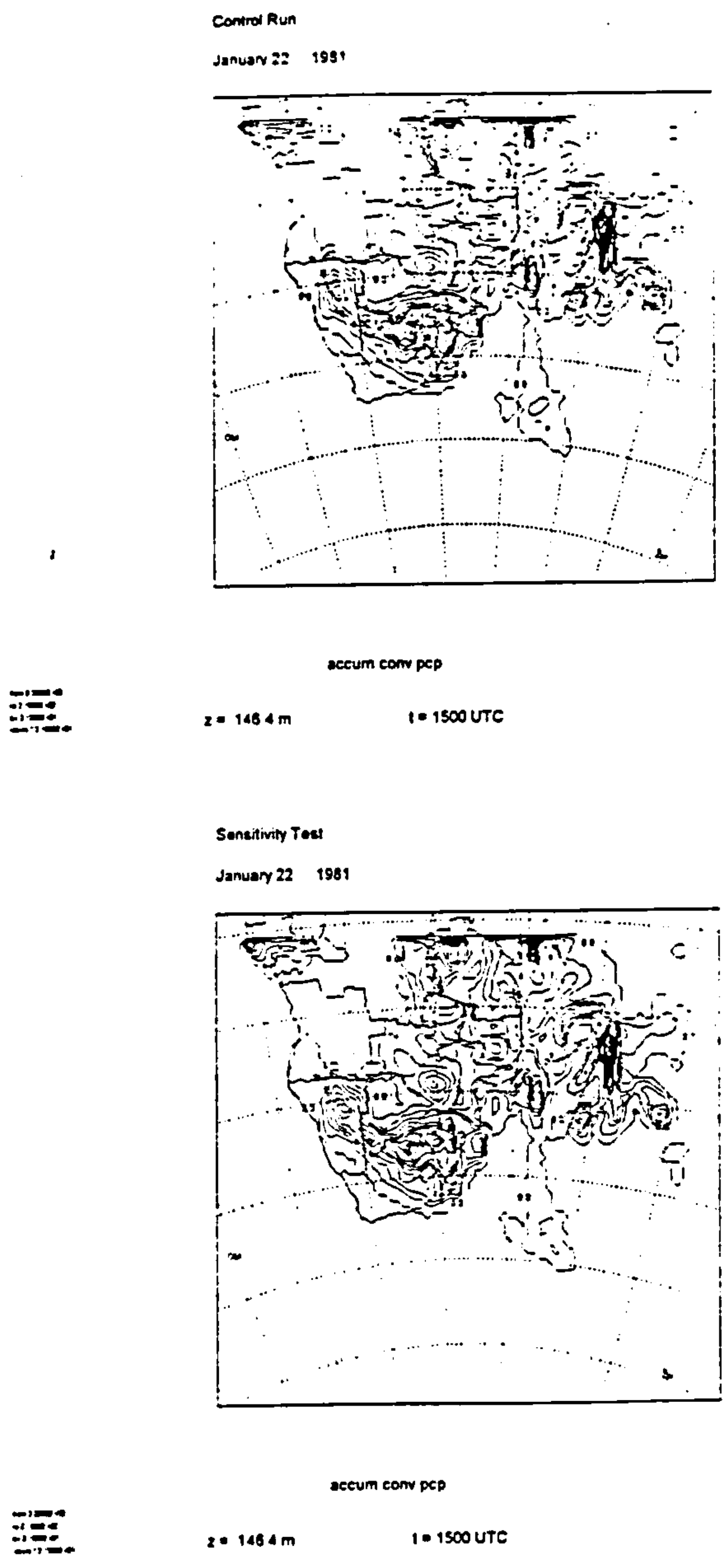

Figure 9.7: Accumulated convective precipitation (in mm) for (a) the control and (b) the sensitivity simulations at the 146,4m sigma level for 1500 UTC on 22 January 1981.

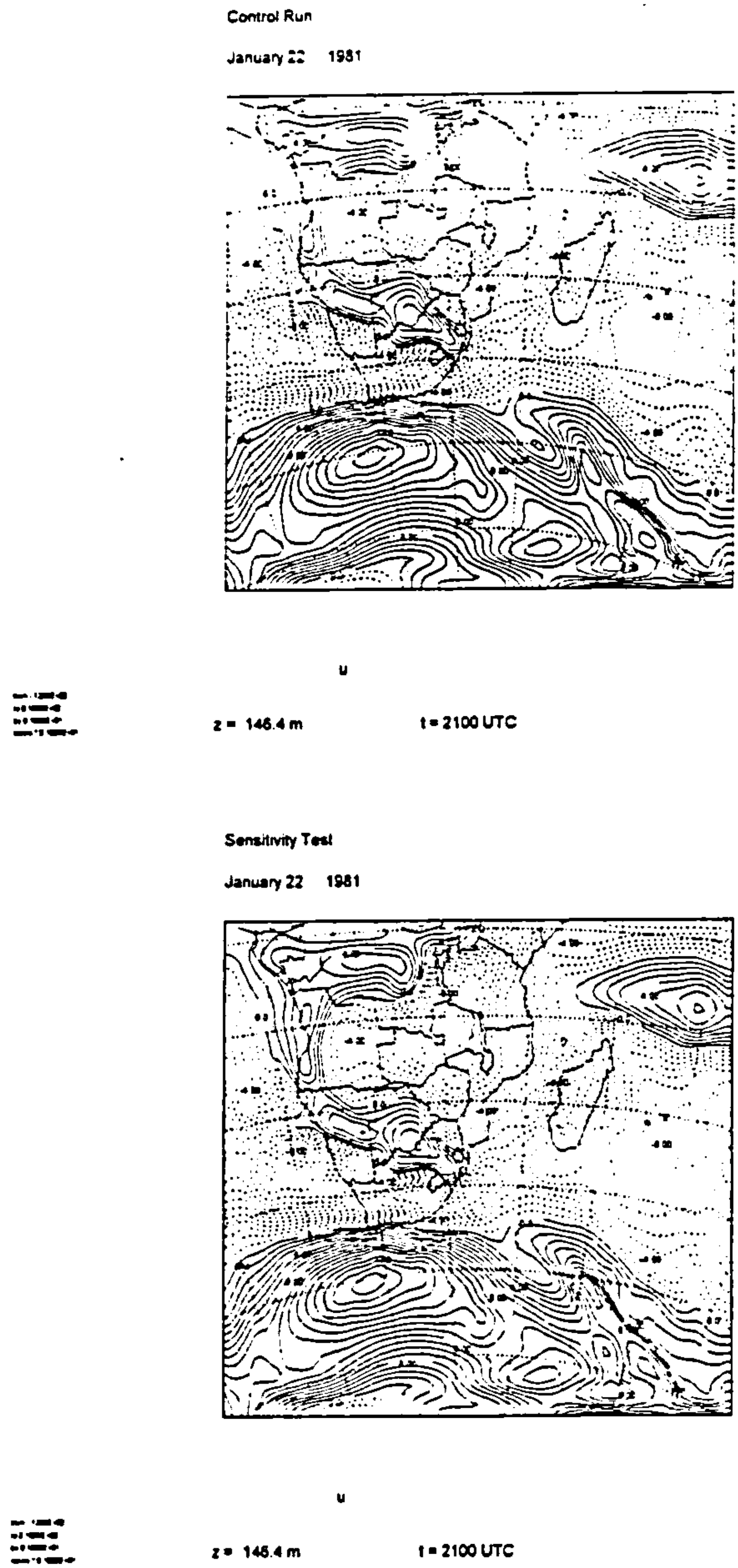

Figure 9.8: U components (in $m.s^{-1}$) for (a) the control and (b) the sensitivity simulations at the 146,4m sigma level for 2100 UTC on 22 January 1981.

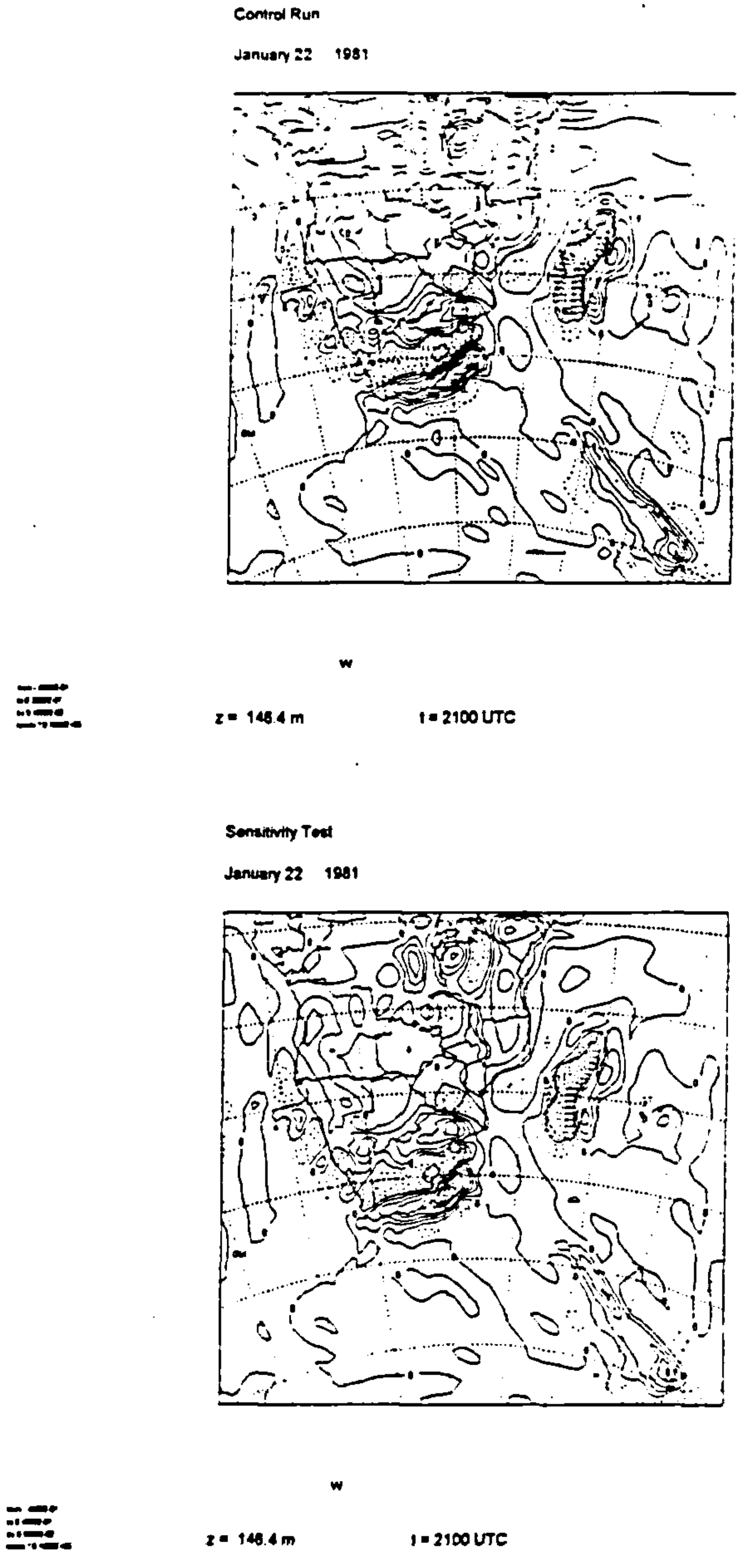

Figure 9.9: Vertical velocities (in $cm.s^{-1}$ $x10^{-4}$) for (a) the control and (b) the sensitivity simulations at the 146,4m sigma level for 2100 UTC on 22 January 1981.

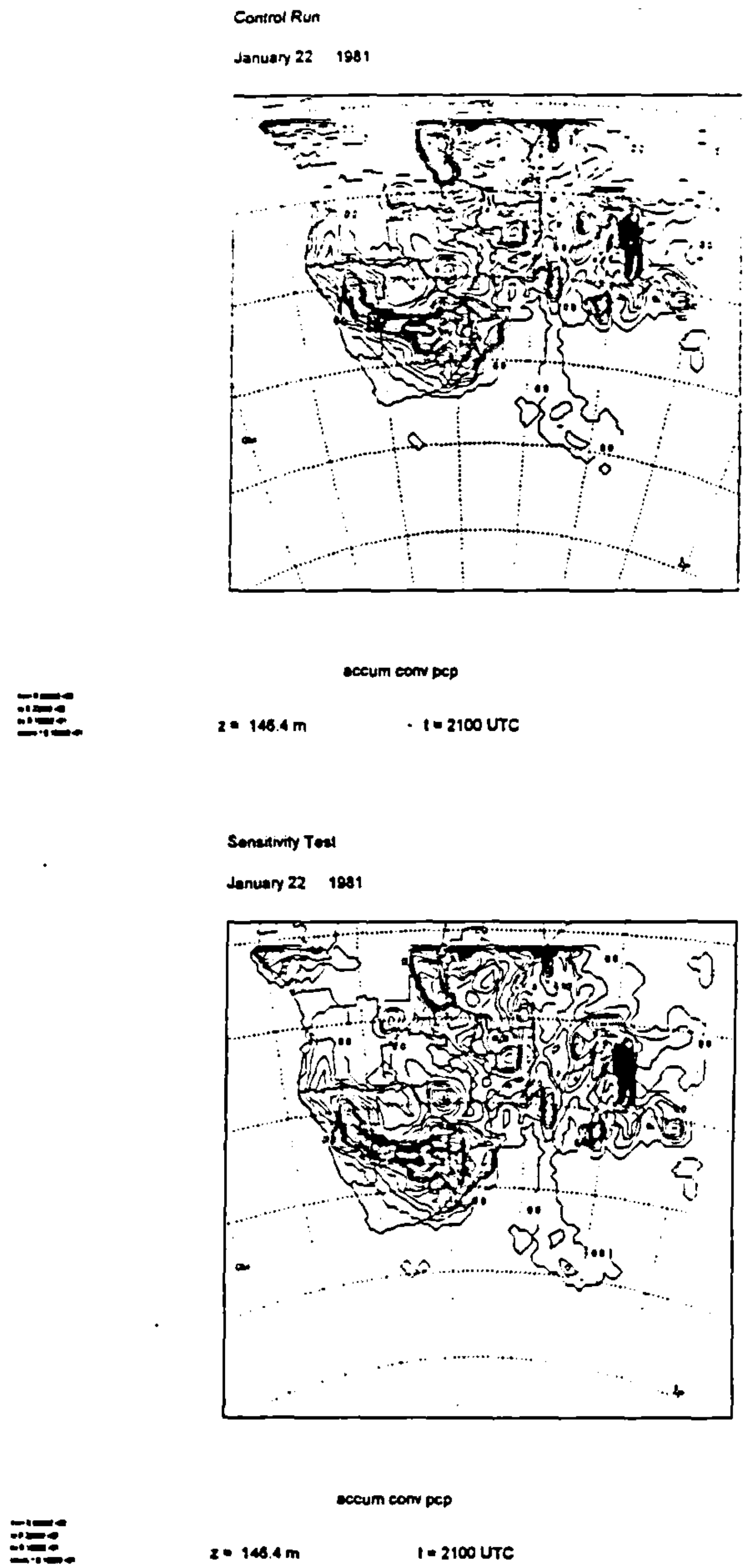

Figure 9.10: Accumulated convective precipitation (in mm) for (a) the control and (b) the sensitivity simulations at the 146,4m sigma level for 2100 UTC on 22 January 1981.

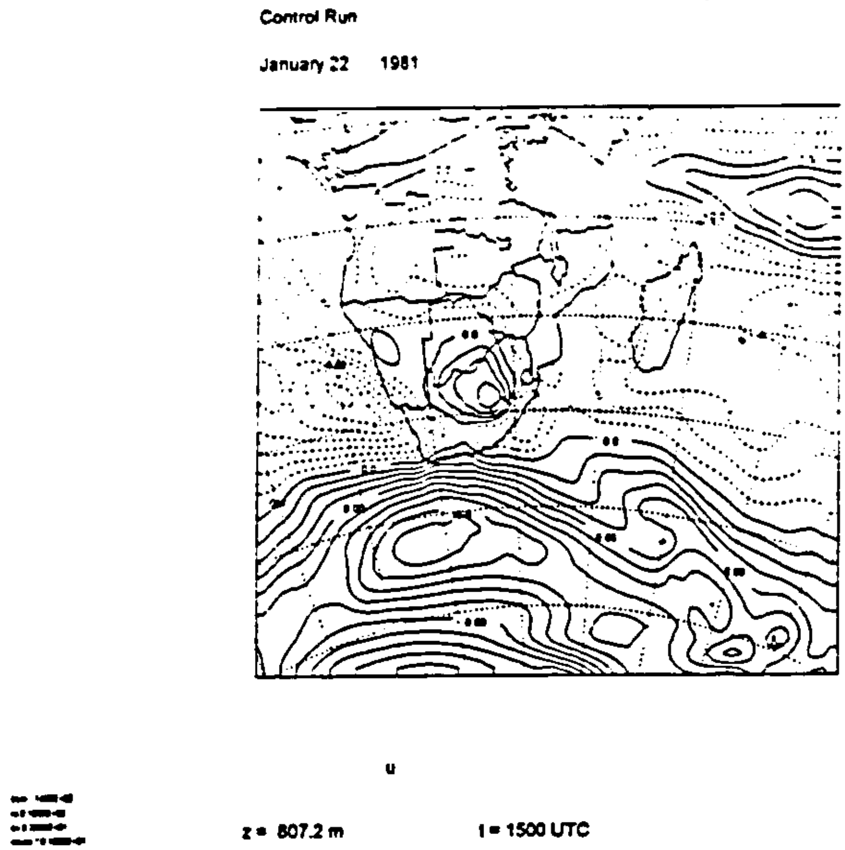

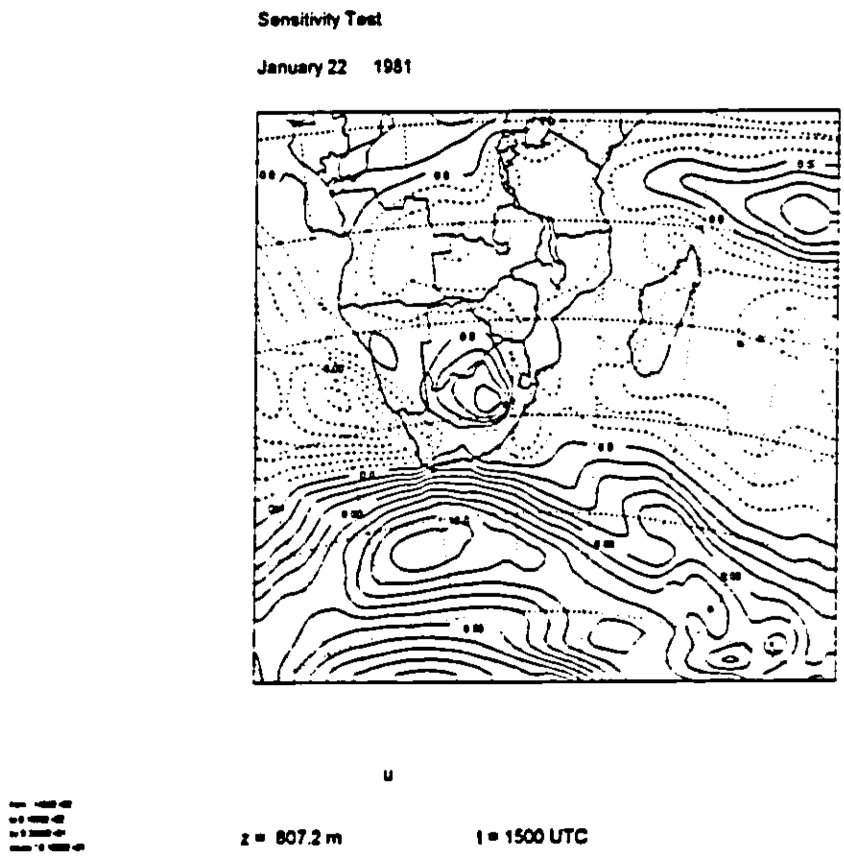

Figure 9.11: U components (in $m.s^{-1}$) for (a) the control and (b) the sensitivity simulations at the 807.2m sigma level for 1500 UTC on 22 January 1981.

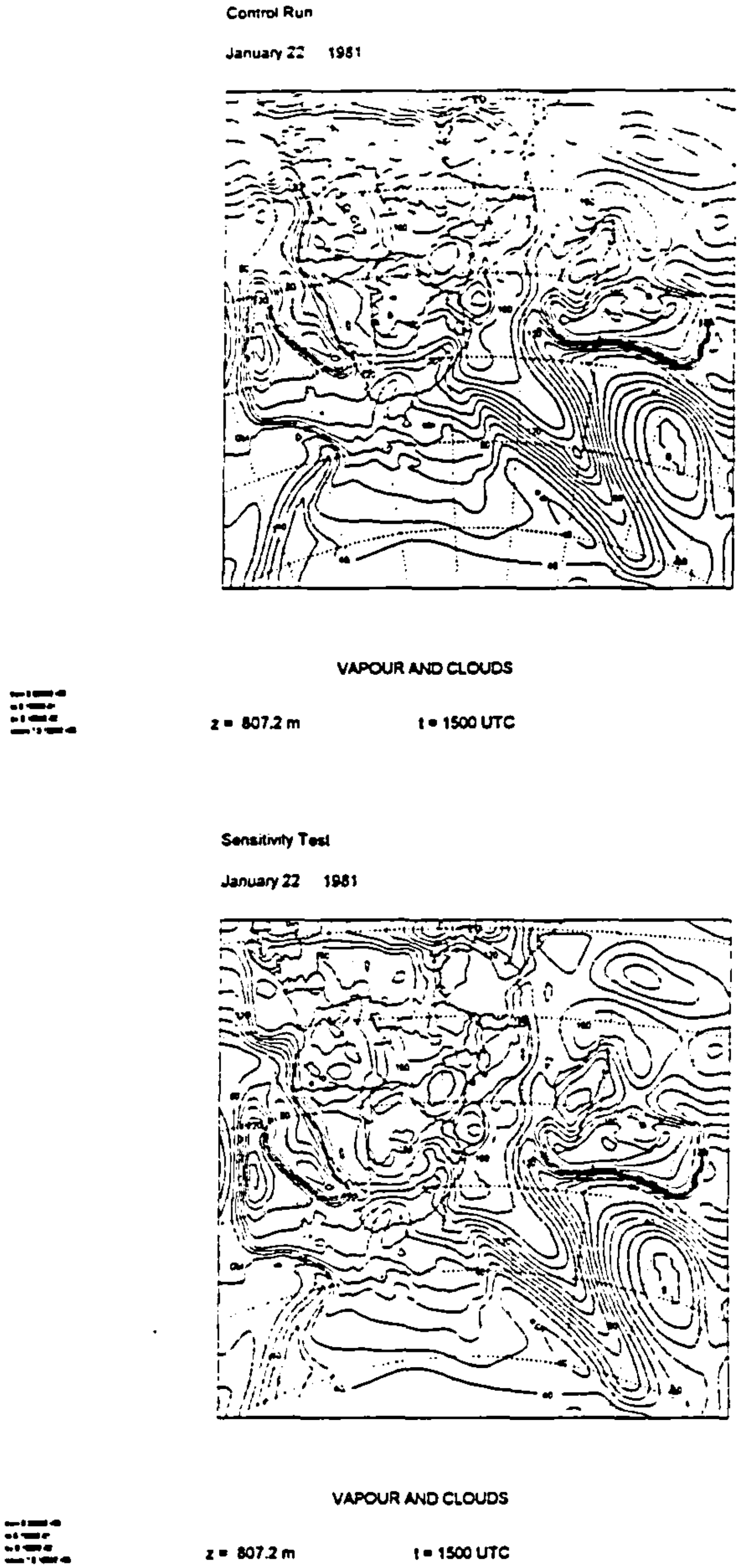

Figure 9.12: Vapour and cloud mixing ratios (in $g.kg^{-1}$ $x10^{-4}$) for (a) the control and (b) the sensitivity simulations at the 807.2m sigma level for 1500 UTC on 22 January 1981.

Control Run

January 22 1981

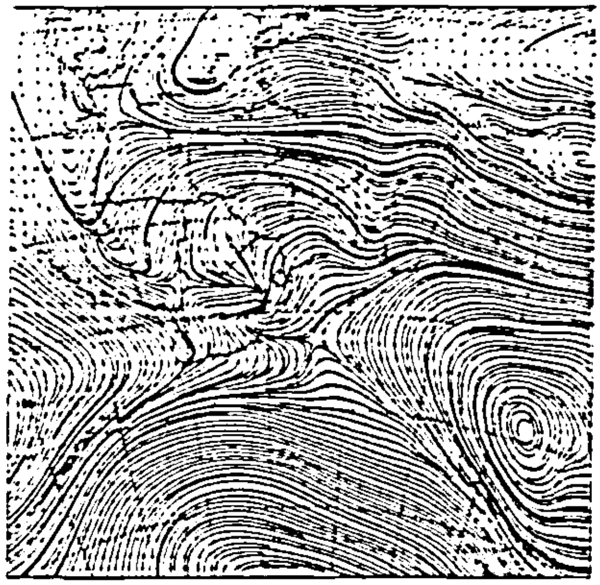

z = 807.2 m t = 1500 UTC

Sensitivity Test

January 22 1981

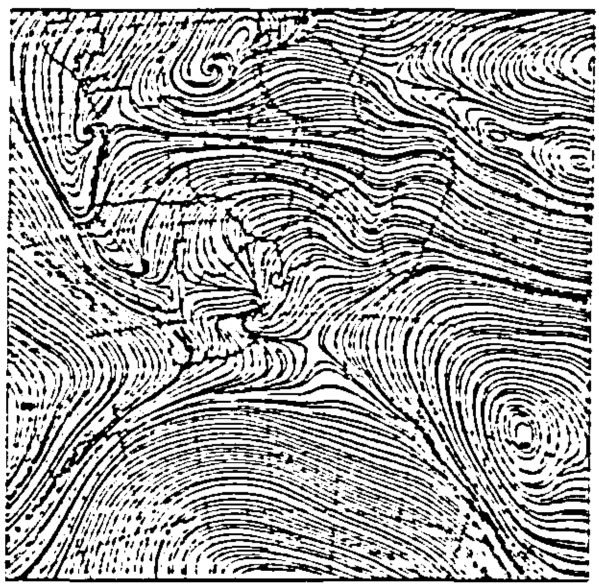

z = 807.2 m t = 1500 UTC

Figure 9.13: Streamlines for (a) the control and (b) the sensitivity simulations at the 807.2m sigma level for 1500 UTC on 22 January 1981.

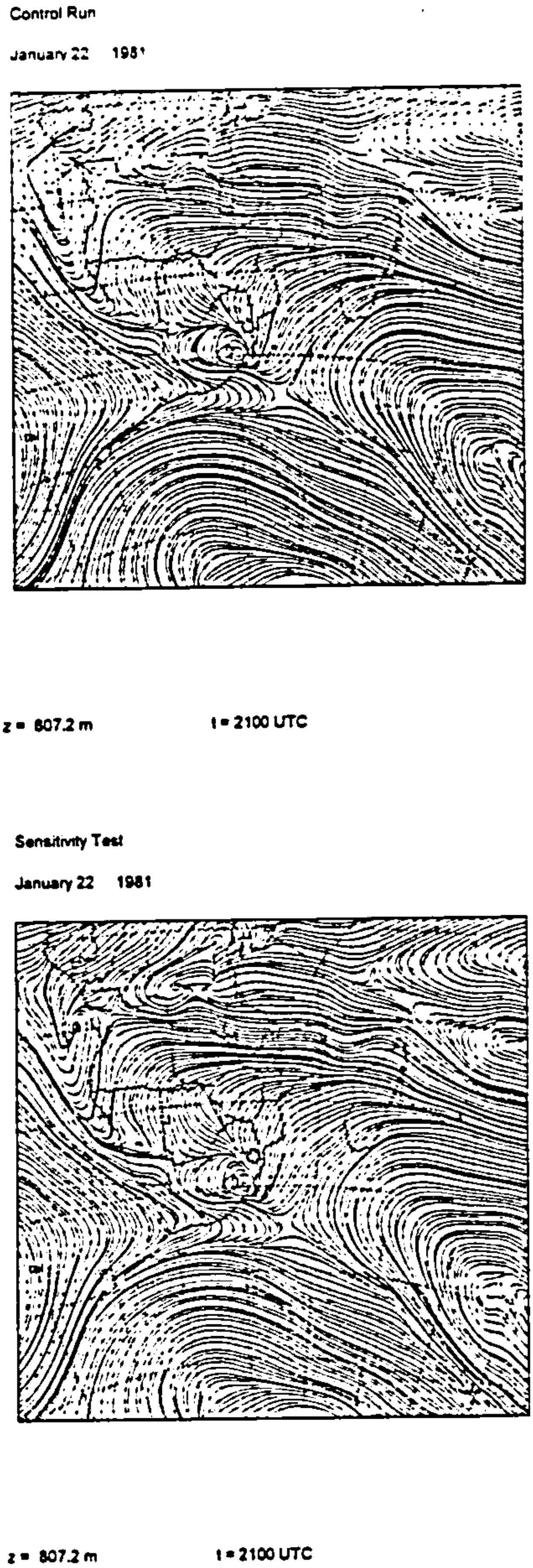

Figure 9.14: Streamline diagrams for (a) the control and (b) the sensitivity simulations at the 807.2m sigma level for 2100 UTC on 22 January 1981.

Day three

On the third day of the simulation (23 January 0900 UTC), the 146,4 m sigma level showed strong westerly components north of 10^{0}S (Fig 9.15 a,b). The heightened onshore flow began to not only influence circulation in coastal, or near-coastal regions, but also further inland. The influence of the circulation on the interior can be seen in the intensification of cyclonic circulation over southern Zaire (Fig 9.16 a,b). Moisture availability was also greater over the western coastline north of 15^{0}S (with the greater extent of the 0,017 gkg^{-1}), and over north western Botswana (with greater extent of the 0,020 gkg^{-1}) (Fig 9.17 a,b). The greater availability of moisture and hence heightened latent instability continued to produce higher accumulated precipitation values over Gabon, Congo, southern Zaire, Zimbabwe and in the vicinity of the Namibia/Botswana border (Fig 9.18 a,b).

By 2100 UTC the strong westerly wind component became prevalent over the Northern Province of South Africa with a simulated increase from 7 ms^{-1} in the control to 8 ms^{-1} in the sensitivity experiment (Fig 9.19 a,b). The strong simulated onshore flow that has been evident since 22 January has served to enhance convergence over Angola, and also east-west aligned convergence over the west coast of the continent and the immediate interior north of 12^{0}S (Fig 9.20 a,b).

The comparison of accumulated convective precipitation with the control simulation shows the influence of the modified sea surface temperature field limited predominantly to the western half of the continent and having little or no effect on the westerly wave perturbation. Simulated precipitation continued to be lower over the Mpumalanga, but remained higher over Gabon, Congo and in the vicinity of the Namibia/Botswana border. Precipitation increases are also noted for the first time over the southern portion of Zaire (Fig 9.21 a,b).

Day four

By the mid-day on 24 January the 146,4 m sigma level simulated the dissipation of the tropical-temperate trough through the eastward propagation of the westerly wave. Onshore winds remained strong north of 12^{0}S with the extent of the 9 ms^{-1} westerly wind component greater in the sensitivity simulation (Fig 9.22 a,b). The effects of the sea surface temperature

January 23 1981

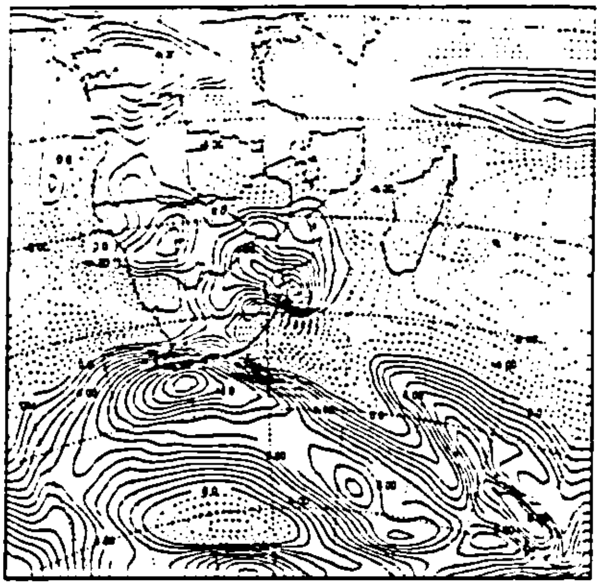

u

z = 146.4 m t = 900 UTC

Sensitivity Test

January 23 1981

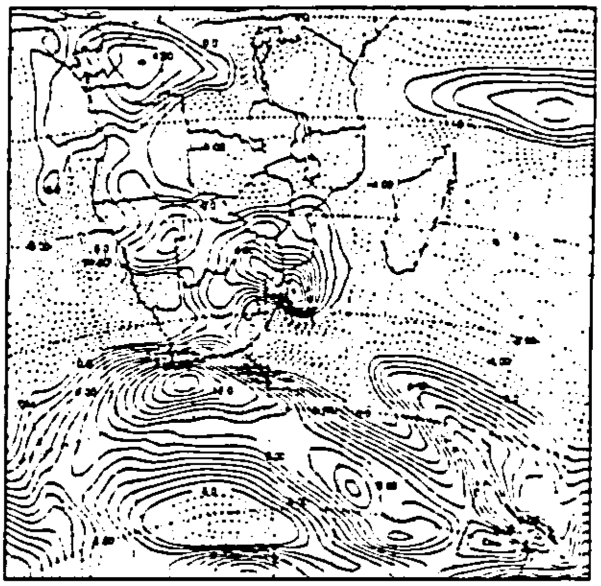

u

z = 146.4 m t = 900 UTC

Figure 9.15: U components (in $m.s^{-1}$) for (a) the control and (b) the sensitivity simulations at the 146.4m sigma level for 0900 UTC on 23 January 1981.

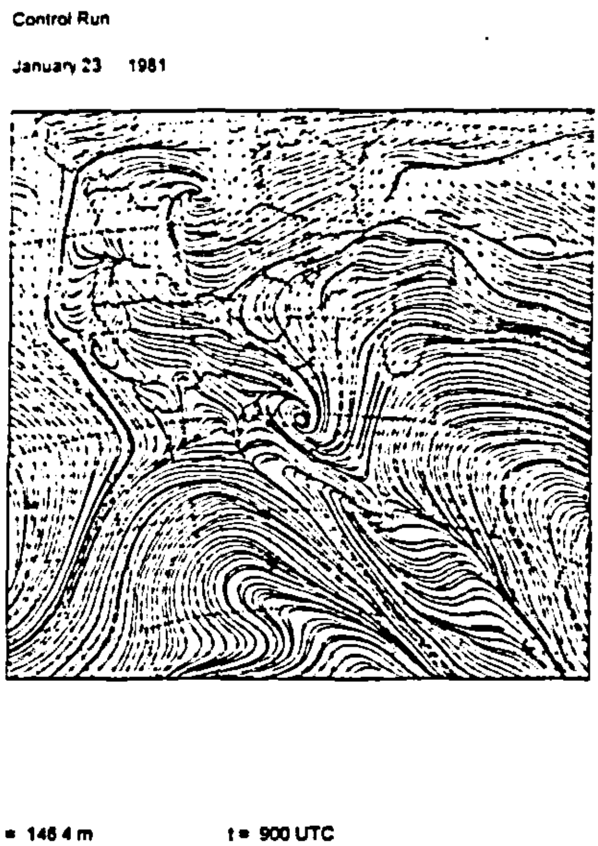

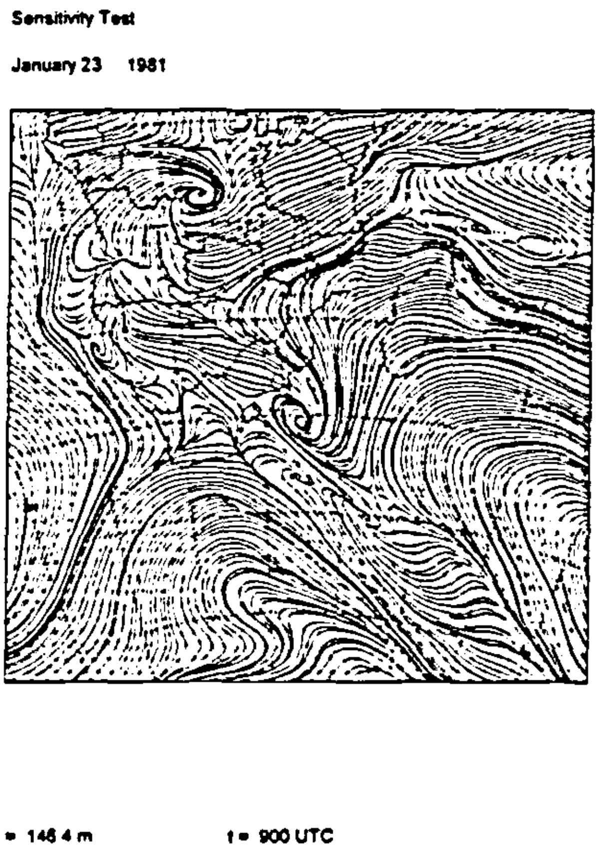

Figure 9.16: Streamlines for (a) the control and (b) the sensitivity simulations at the 146.4m sigma level for 0900 UTC on 23 January 1981.

Control Run

January 23 1981

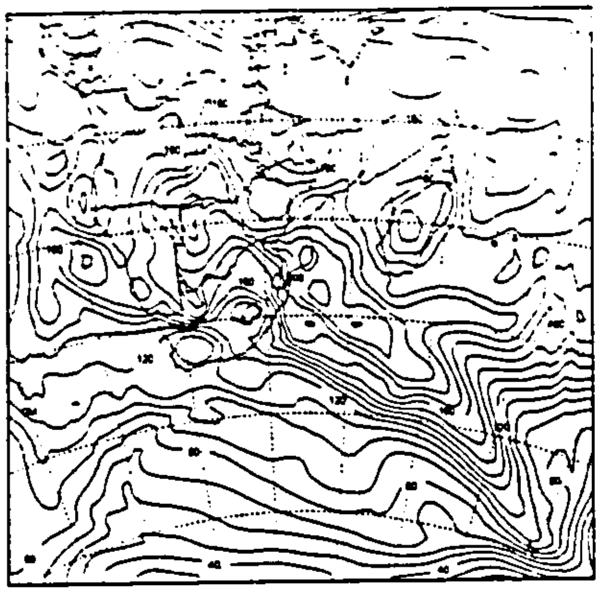

VAPOUR AND CLOUDS

z = 146.4 m t = 900 UTC

Sensitivity Test

January 23 1981

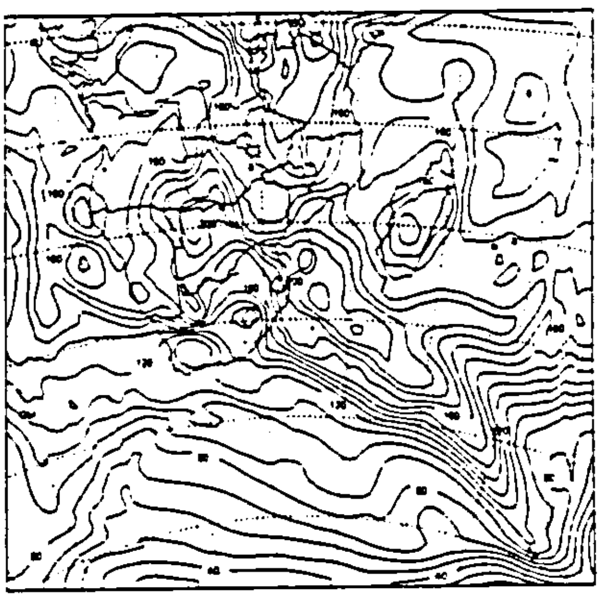

VAPOUR AND CLOUDS

z = 146.4 m t = 900 UTC

Figure 9.17: Vapour and cloud mixing ratios (in $g.kg^{-1}$ $x10^{-4}$) for (a) the control and (b) the sensitivity simulations at the 146.4m sigma level for 0900 UTC on 23 January 1981.

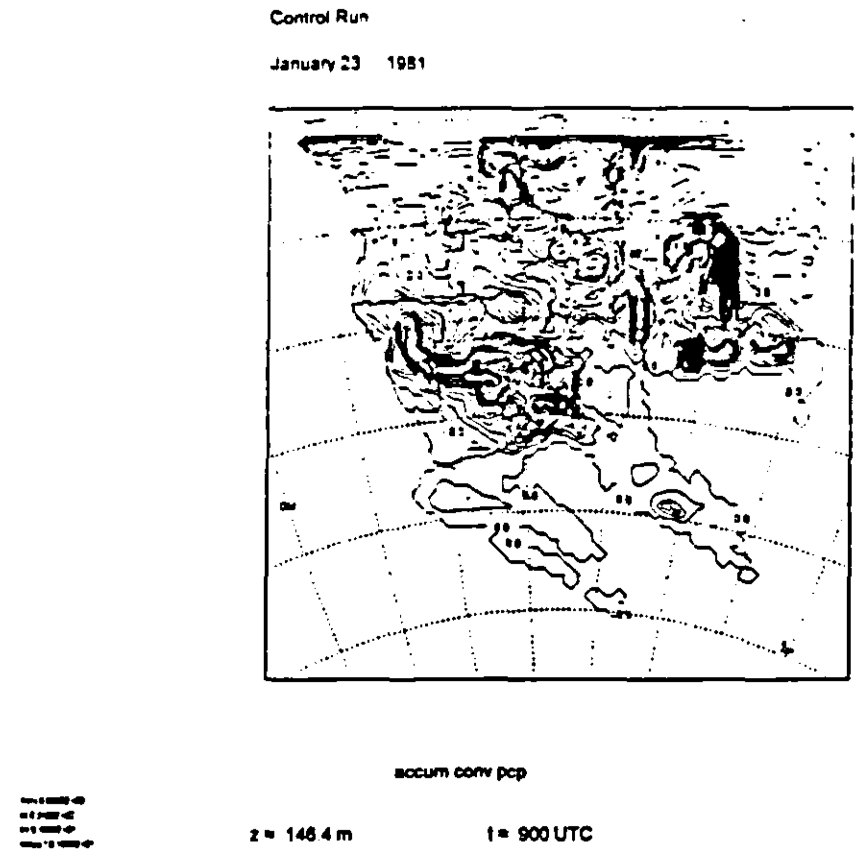

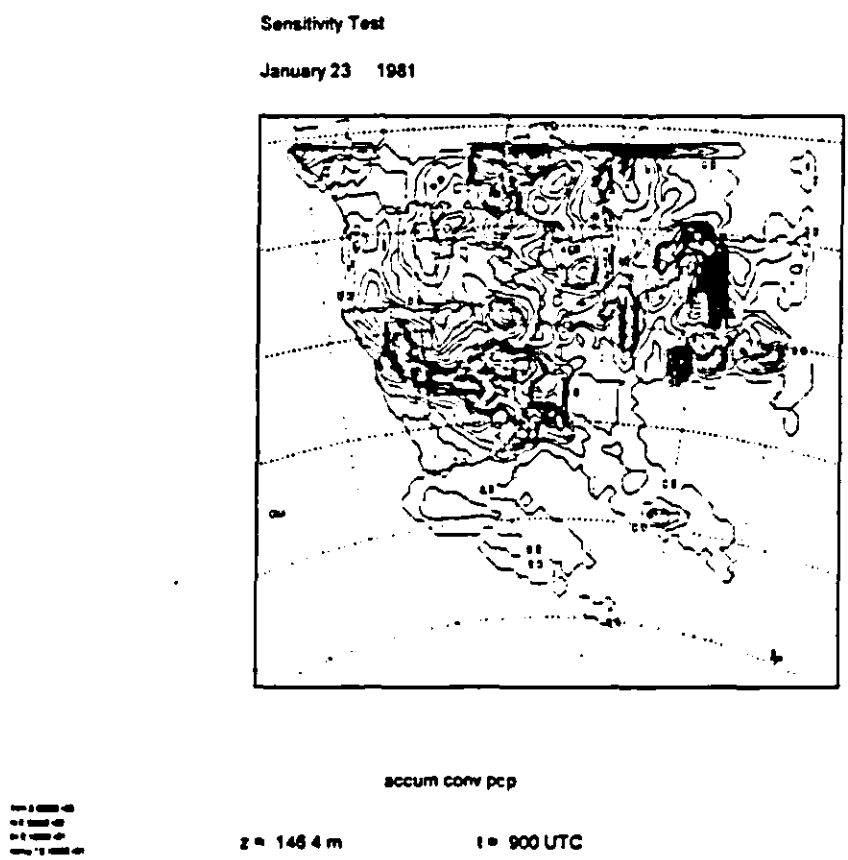

Figure 9.18: Accumulated convective precipitation (in mm) for (a) the control and (b) the sensitivity simulations at the 146.4m sigma level for 0900 UTC on 23 January 1981.

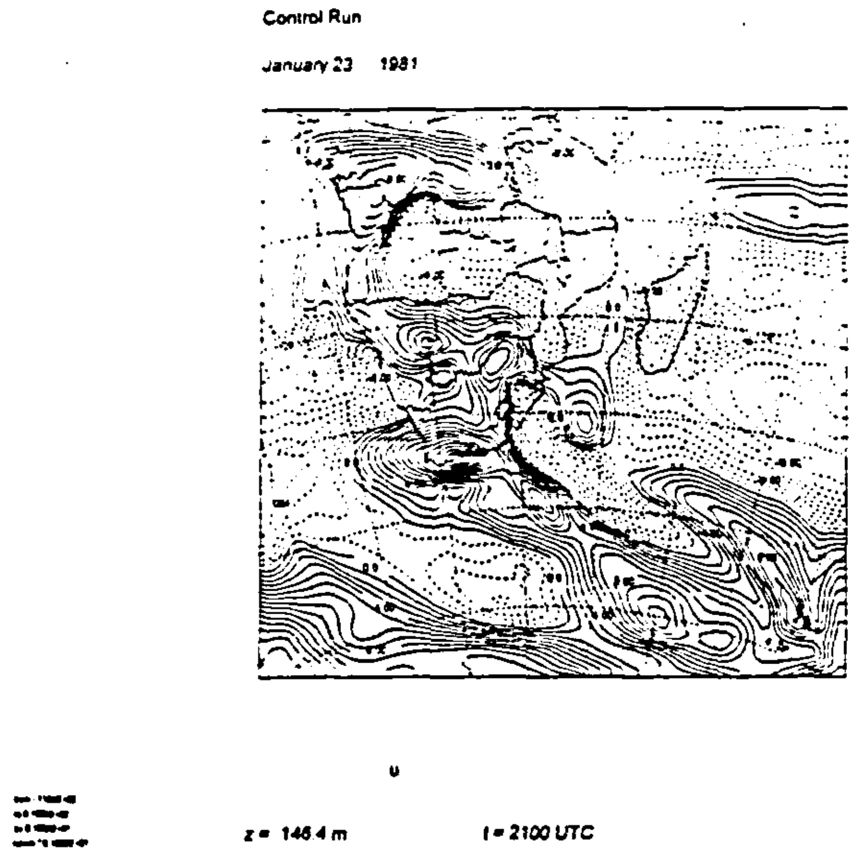

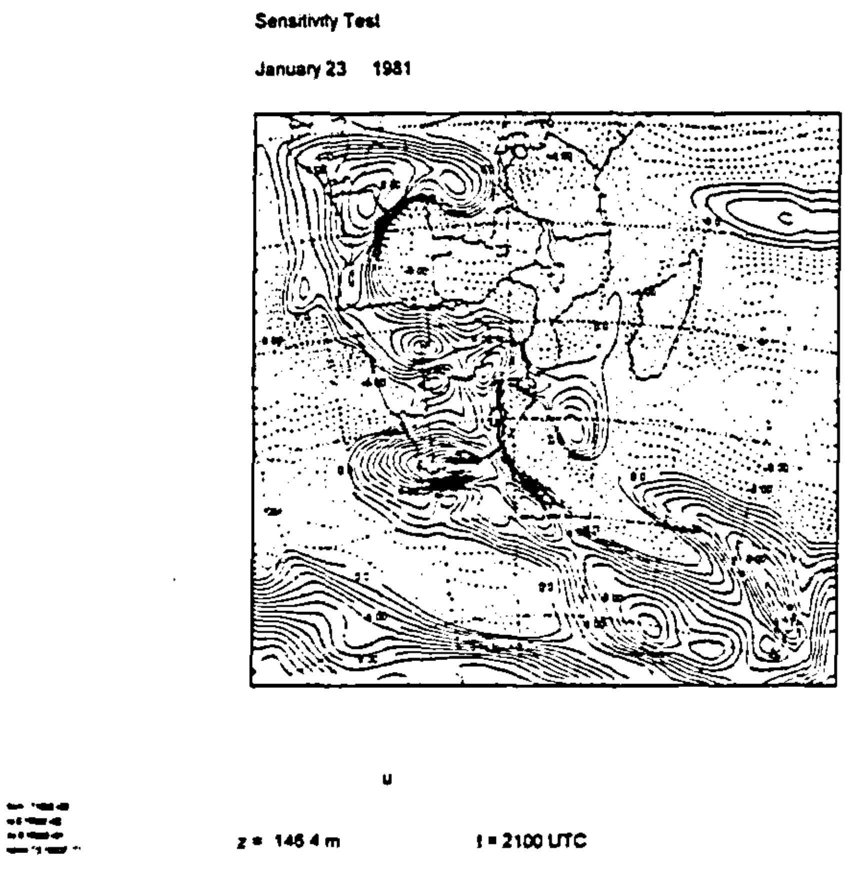

Figure 9.19: U components (in $m.s^{-1}$) for (a) the control and (b) the sensitivity simulations at the 146.4m sigma level for 2100 UTC on 23 January 1981.

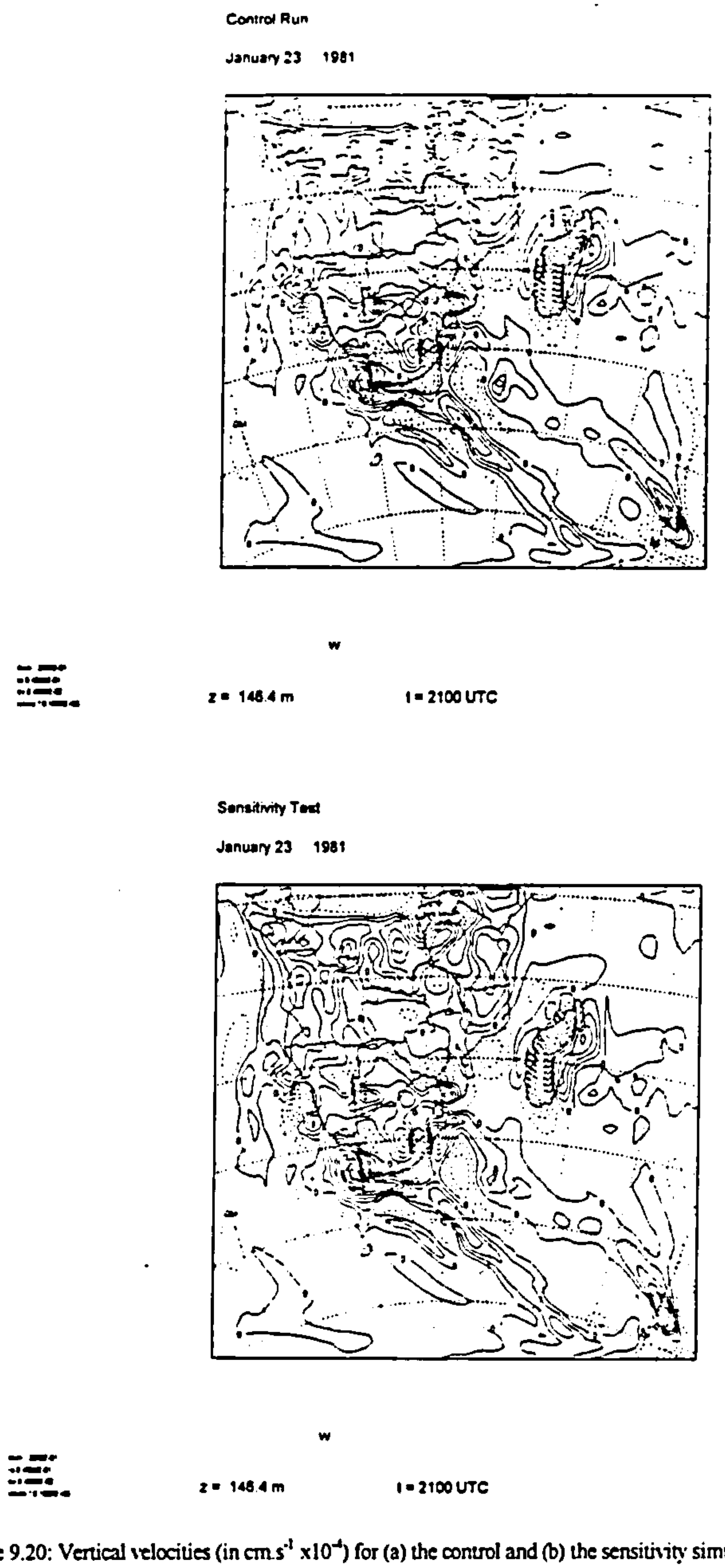

Figure 9.20: Vertical velocities (in $cm.s^{-1}$ $x10^{-4}$) for (a) the control and (b) the sensitivity simulations at the 146.4m sigma level for 2100 UTC on 23 January 1981.

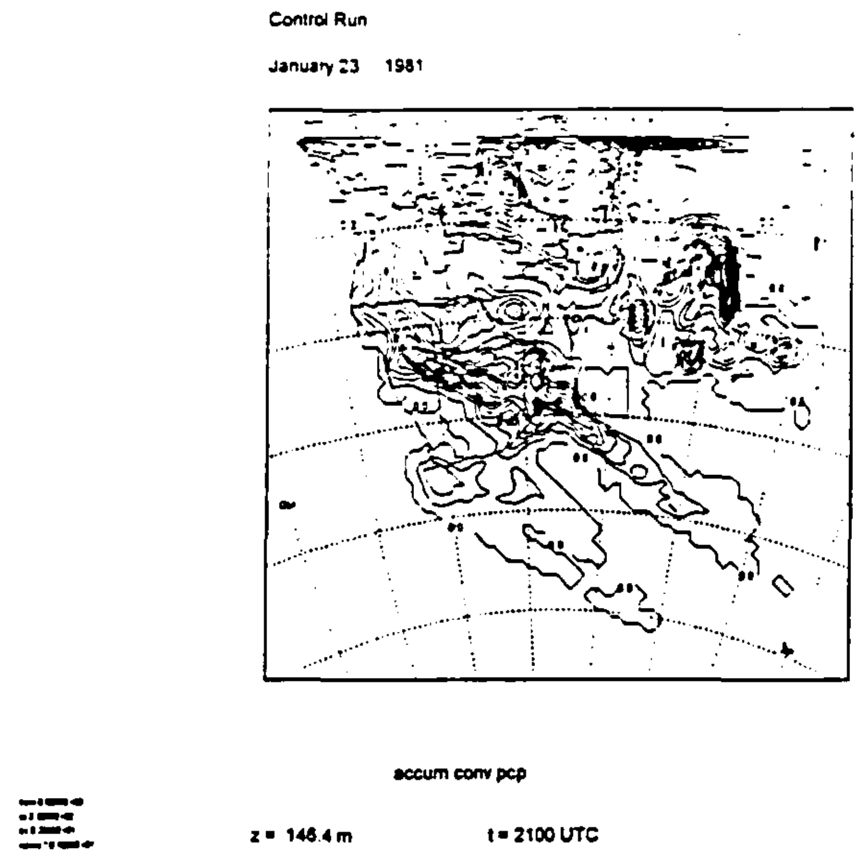

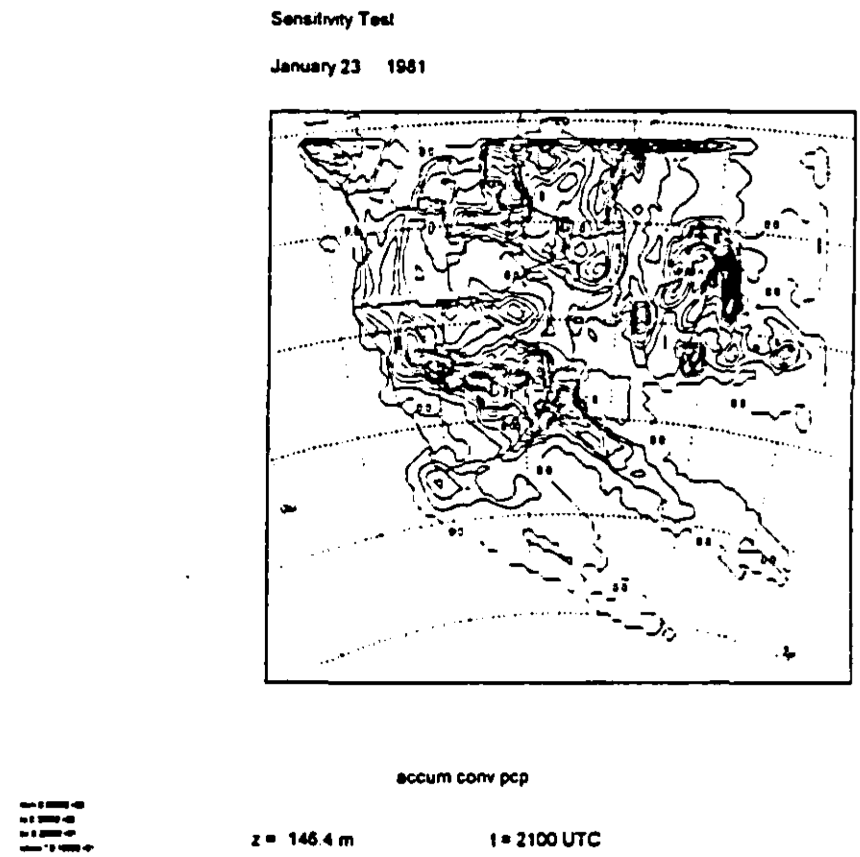

Figure 9.21: Accumulated convective precipitation (in mm) for (a) the control and (b) the sensitivity simulations at the 146,4m sigma level for 2100 UTC on 23 January 1981.

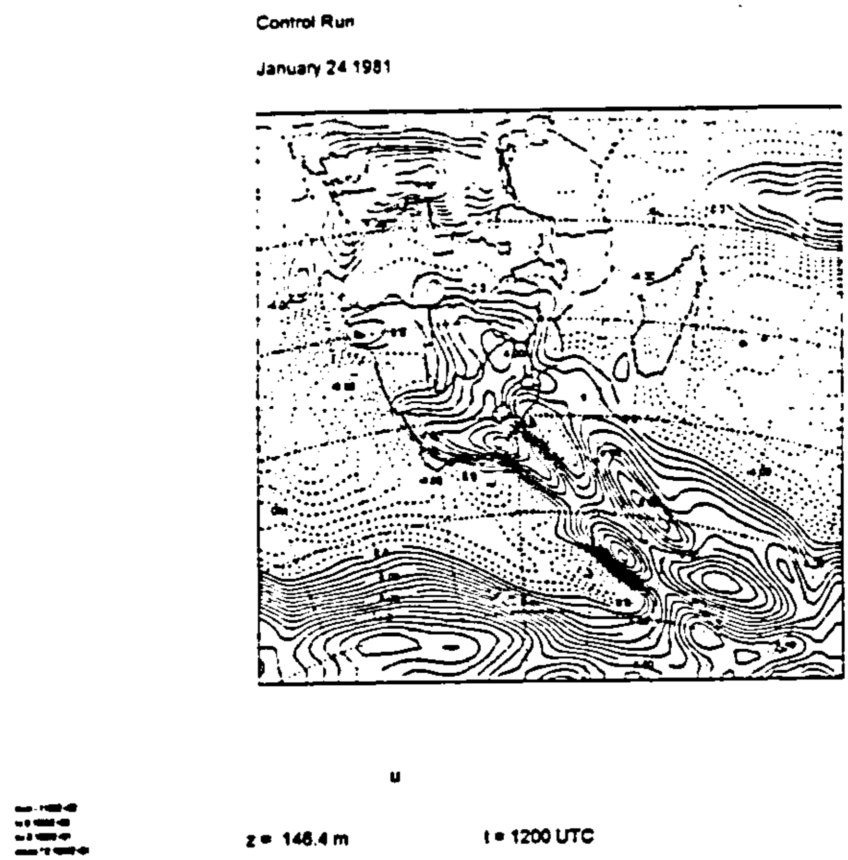

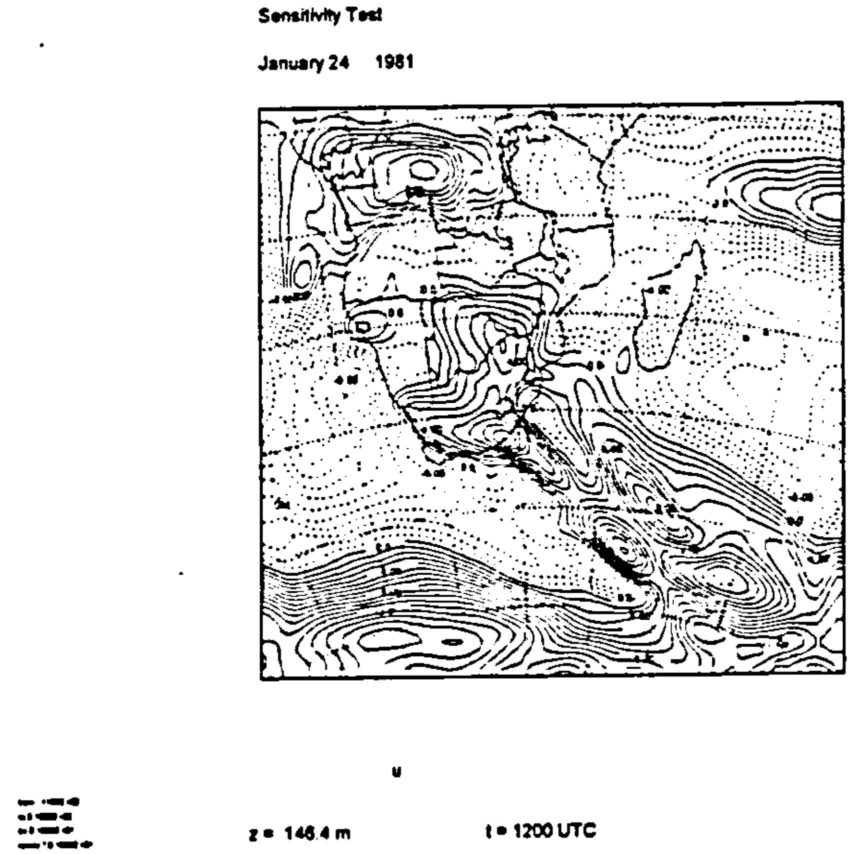

Figure 9.22: U components (in $m.s^{-1}$) for (a) the control and (b) the sensitivity simulations at the 146.4m sigma level for 1200 UTC on 24 January 1981.

anomaly became visible in the westerly wave perturbation only on the fourth day of the sensitivity simulation, with stronger westerly component values evident at 40^0S to 50^0S with 10 ms^{-1} compared to 9 ms^{-1} (Fig 9.22 a,b). The greater onshore flow north of 12^0S ensured the amplification of the tropical low over southern Zaire for the past 15 hours (Fig 9.23 a,b).

Total accumulated precipitation values showed continually higher precipitation over Gabon, Congo and the Namibia/Botswana border, along with marginally lower values over the Mpumalanga region. Precipitation over the southern portion of Zaire indicated increased falls for the past 15 hours (Fig 9.24 a,b). This is linked with the intensification of the tropical low and southerly return flow from this synoptic feature.

An overview of the upper level circulation changes from 2100 UTC on 23 January to the end of the simulation (1200 UTC on 24 January), continued to exhibit, a progression of circulation differences brought about by the presence of the sea surface temperature anomaly within the tropical west Atlantic ocean. By 2100 UTC on 23 January the 807,2 m sigma level continued to show stronger onshore flow north of 10^0S (Fig 9.25 a,b). The stronger onshore flow in turn enhanced cyclonic circulation around the tropical low centered over southern Zaire and caused the pattern of moisture availability to vary along the African west north of 10^0S. Maximum control values over Congo exhibited moisture ratios of 0,014 gkg^{-1} compared to maximum sensitivity values of 0,016 gkg^{-1} (Fig 9.26 a,b). These patterns continued well into the fourth day of the simulation and to the conclusion of the sensitivity experiment (Fig 9.27 a,b).

Discussion

Previous investigations of inter-annual variation in large-scale circulation over the tropical western Atlantic ocean, using water level values of the Zaire river, showed that these values were positively related to sea surface temperatures in the above mentioned area (Hirst and Hastenrath, 1983; Hastenrath, 1984). Positive anomalous sea surface temperatures were found to strengthen zonal westerly circulation over Zaire, Gabon, and Congo regions, and in this way modulate the moisture content of the flow (Hirst and Hastenrath, 1983; Hastenrath, 1984). A comparison of hypotheses and observations of the effect of positive sea surface temperature development on southern African atmospheric circulation with the

Control Run

January 24 1981

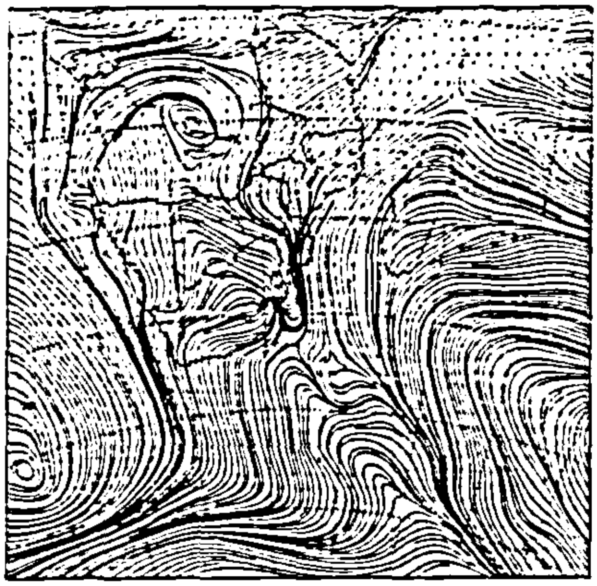

z = 146.4 m t = 1200 UTC

Sensitivity Test

January 24 1981

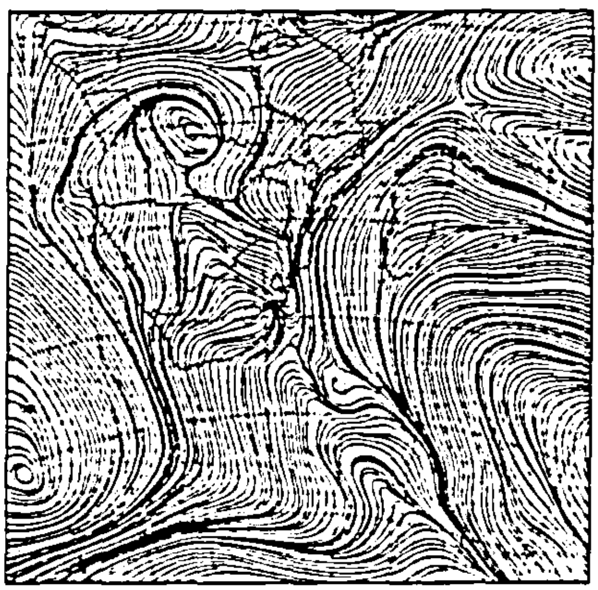

z = 146.4 m t = 1200 UTC

Figure 9.23: Streamline diagrams for (a) the control and (b) the sensitivity simulations at the 146.4m sigma level for 1200 UTC on 24 January 1981.

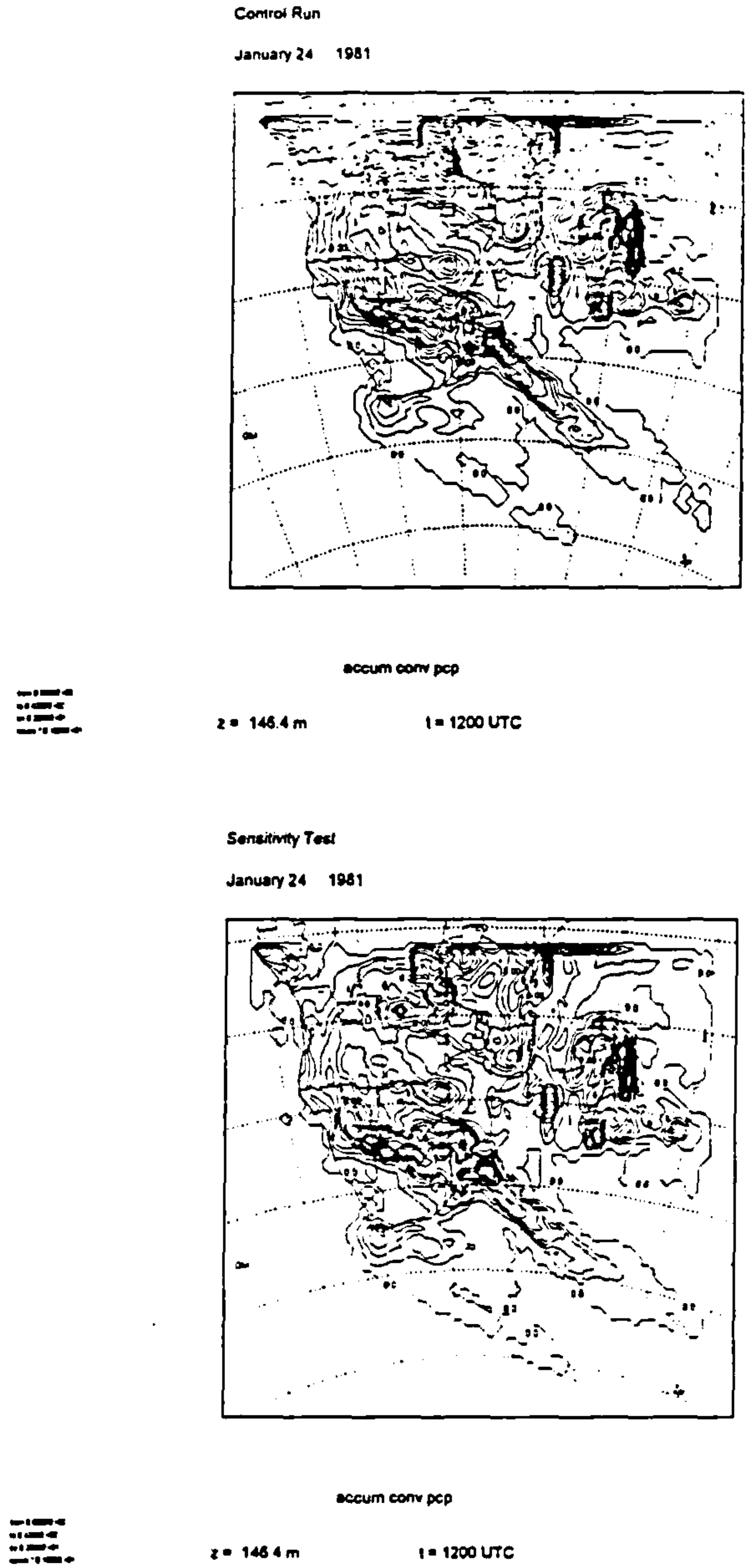

Figure 9.24: Accumulated convective precipitation (in mm) for (a) the control and (b) the sensitivity simulations at the 146.4m sigma level for 1200 UTC on 24 January 1981.

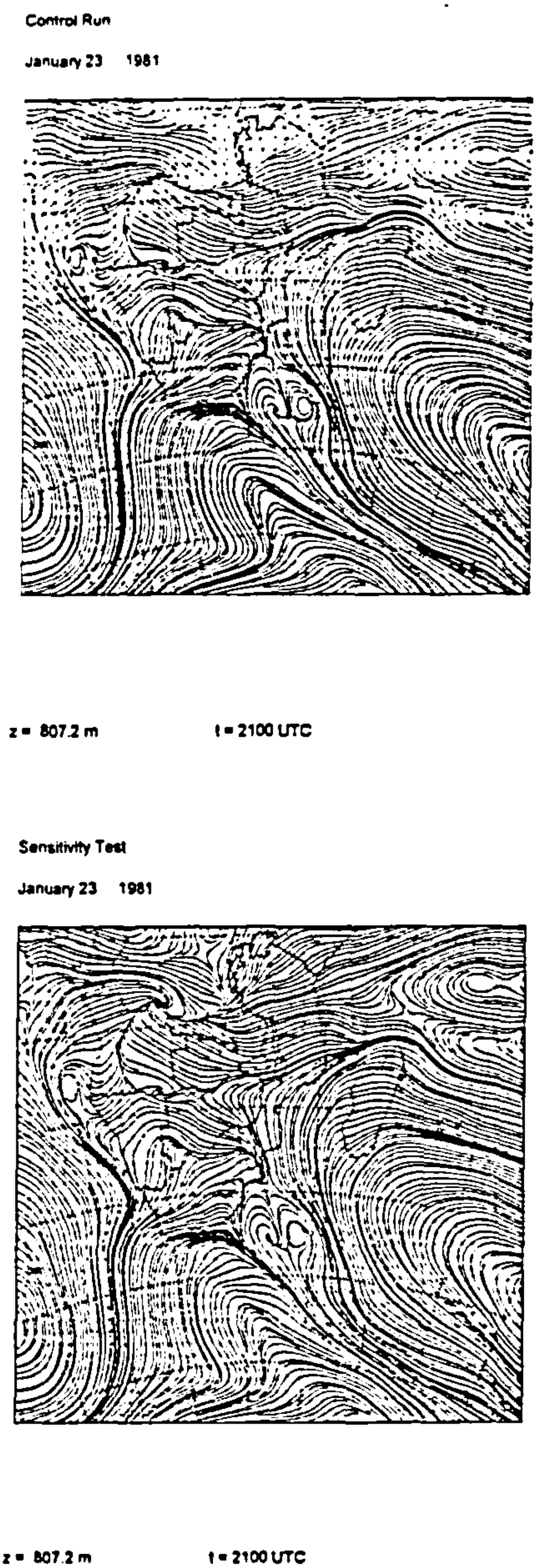

Figure 9.25: Streamline diagrams for (a) the control and (b) the sensitivity simulations at the 807.2m sigma level for 2100 UTC on 23 January 1981.

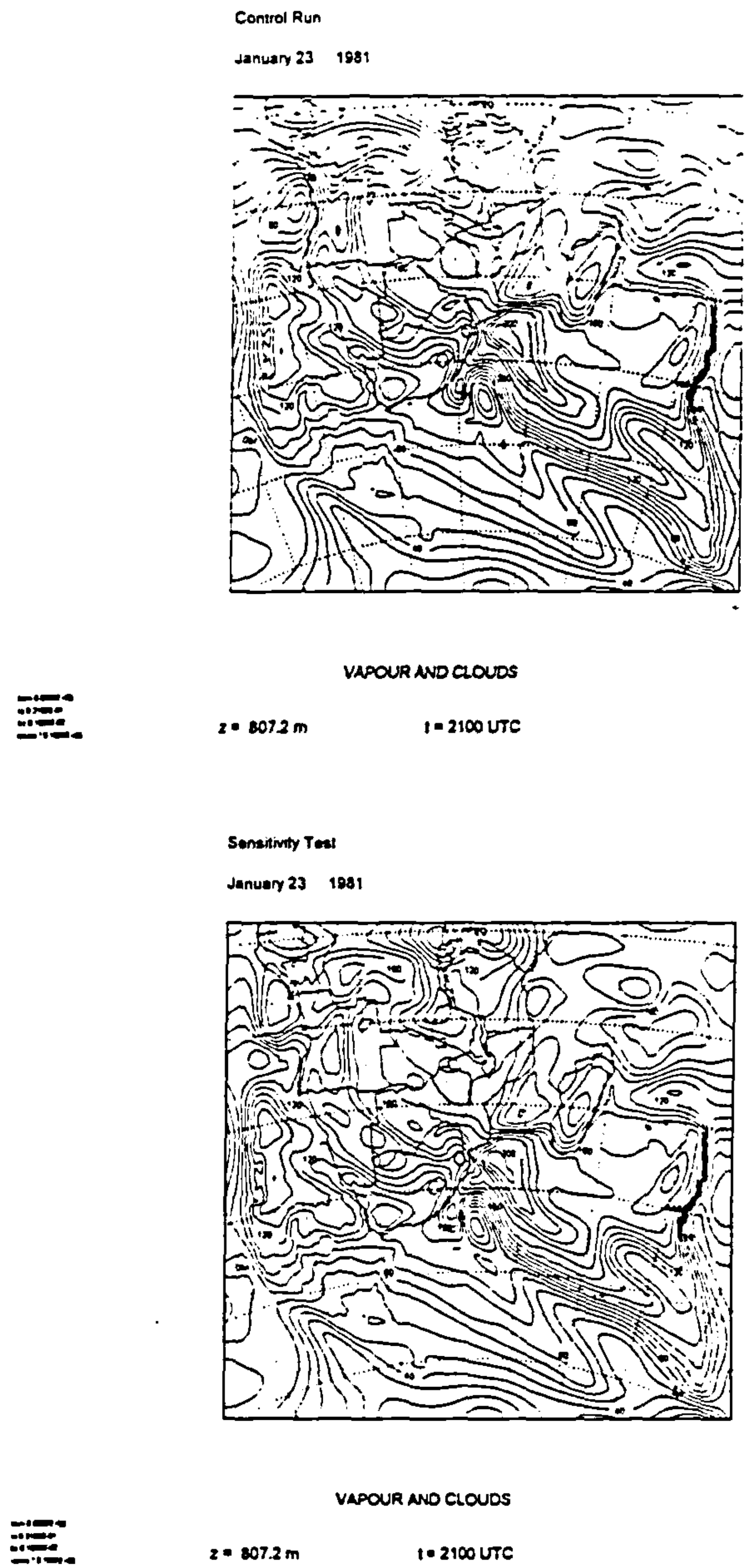

Figure 9.26: Vapour and cloud mixing ratios ($g.kg^{-1}$ $x10^{-4}$) for (a) the control and (b) the sensitivity simulations at the 807.2m sigma level for 2100 UTC on 23 January 1981.

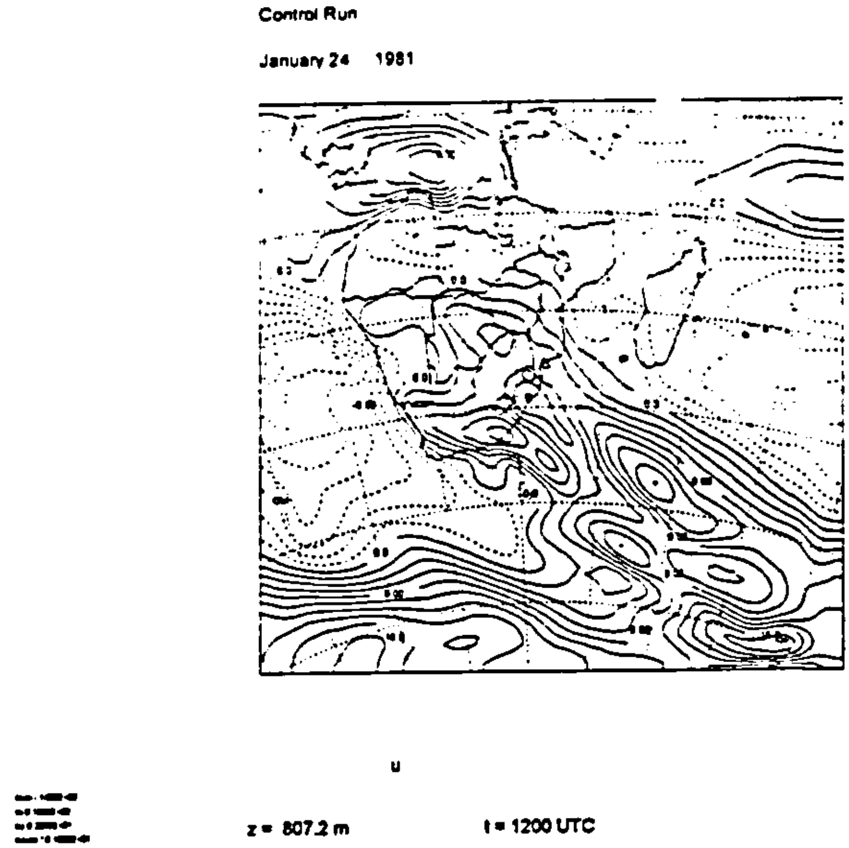

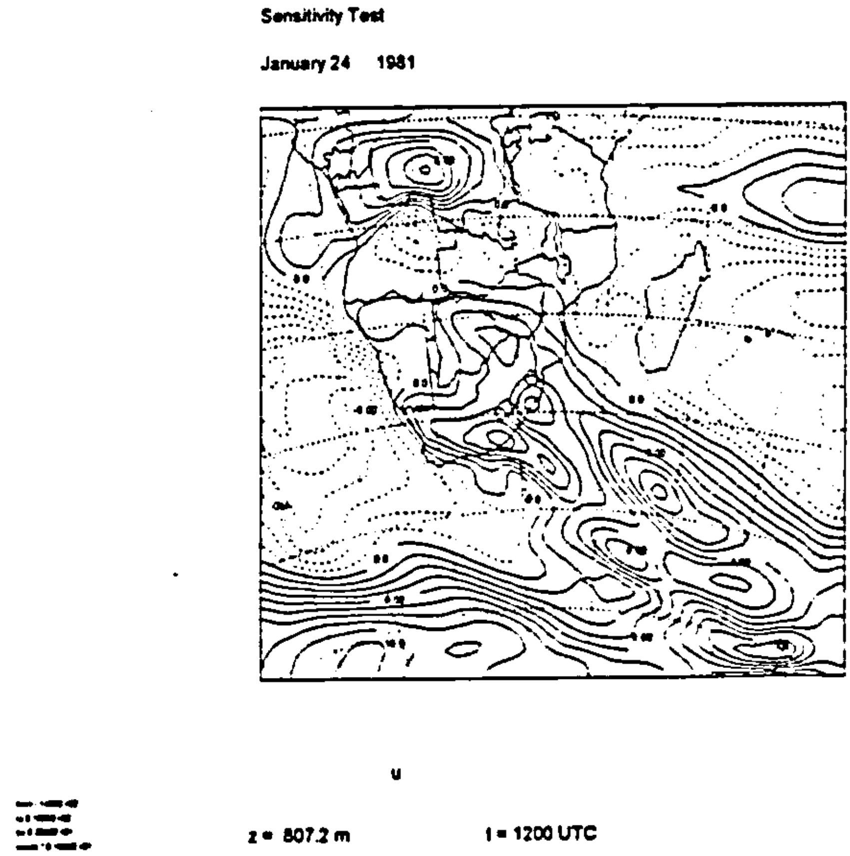

Figure 9.27: U components (in $m.s^{-1}$) for (a) the control and (b) the sensitivity simulations at the 807.2m sigma level for 1200 UTC on 24 January 1981.

numerical model simulation, a number of similarities occur.

Onshore westerly flows over the west coast are observed during periods of positive sea surface temperature anomalies, and are consistent with the numerical model simulation. By 2100 UTC on 21 January stronger onshore flow was simulated north of 10^0S. As this strengthened westerly zonal flow persisted, simulated moisture availability increased due to the influx of air over the warmer ocean. The simulation of heightened moisture availability and stronger onshore flow had a two-fold effect on the simulated circulation over the African west coast. Firstly the greater moisture availability served to increase instability north of 10^0S. Secondly the increased westerly component produced stronger convergence east of Angola. The combination of all these factors positively influenced rainfall, particularly over Gabon, Congo and southern Zaire. These circulation changes simulated in the sensitivity experiment where slowly translated southward along the west coast of Africa by the strengthened return flow from the tropical low and surface convergence east of Angola. It is still unclear as to the direct link of the tropical western Atlantic sea surface temperature anomalies and circulation differences over South Africa.

Synposis

The effects of a positive 2^0C core and 1^0C sea surface temperature anomaly boundary added to the tropical eastern Atlantic Ocean is investigated. Research in this area shows that positive sea surface temperature anomalies, in conjuction with stronger westerly onshore flow, cause an increase in moisture availability and thus heavier rainfall events for the duration of the anomaly. The results of this RAMS sensitivity simulation indicate similar findings. The model simulation produced stronger onshore westerly flow, as well as greater moisture availability resulting from a influx of moist oceanic air. This combined with heightened instability north of 10^0S served to increase localised precipitation values along the west coast and limited interior.

CHAPTER 10

TRAJECTORY ANALYSIS OF WATER VAPOUR TRANSPORT OVER THE SUBCONTINENT

Moisture content of the air plays an important role in determining the thermal stability of the atmosphere and is a crucial factor in the precipitation process. By virtue of its position within the subtropical belt of high pressure, South Africa is characterised by a semi-arid to arid climate. Among important factors affecting the moisture over the region, is the low levels of moisture available from the generally sparsely vegetated continental surface (Henning, 1989; Lindesay, 1992). Consequently, most of the moisture that contributes to precipitation over southern Africa must be imported over the subcontinent from source regions elsewhere.

Despite the importance of water vapour transport for the production of rainfall over southern Africa, few transport analyses have been undertaken for the region. Whereas studies of atmospheric moisture have been undertaken for West Africa (Adedokun, 1978; Anyadike, 1979), South America (Rathor *et al.*, 1989), North America (Hastenrath, 1966) and Australasia (Hutchings, 1961), similar studies only recently have been conducted for southern Africa (D'Abreton and Lindesay, 1993; D'Abreton and Tyson, 1995). During the often wet mid-summer month of January conditions are characterised by enhanced northerly meridional flow, in contrast to dry conditions when westerly zonal flow is the predominant circulation characteristic (D'Abreton and Lindesay, 1993). Analysis of divergent water vapour transport reveals that transport to the southwest from the tropical Indian Ocean is the most important source for water vapour in wet Januaries over South Africa (D'Abreton and Tyson, 1995). During dry Januaries, the vapour source regions appear to be located preferentially over the southwestern Indian Ocean (D'Abreton and Tyson, 1995).

In this chapter, water vapour transport over southern Africa will be examined further using Lagrangian kinematic trajectory modelling. A trajectory climatology of January water vapour transport for rain days and no rain days over the central interior of South Africa will be developed.

In addition, vapour transport for various individual rain-producing systems will be examined Finally, changes in air parcel water vapour content will be used to indicate in general major water vapour source and sink regions for South Africa.

Trajectory Fields

An indication of moisture transport into a region, or into a specific synoptic weather system, may be gained from superimposed specific humidity and atmospheric flow fields. Such is the case for transport into a tropical-temperate trough occurring on 24 January 1981 (Fig. 10.1a). Transport over a given region over a number of days may be assessed from Hovmöller diagrams. A case in point is the mid January 1981 propagation of vertically-integrated 850-300 hPa precipitable moisture from northeast to southwest through 20^0 of longitude over the northern parts of Southern Africa (from A to B in Figure 10.1b). Use of individual trajectories and integrated trajectory fields offers an even better way of assessing moisture transport.

Back trajectories from a point of origin over the Pretoria-Witwatersrand-Vereeniging (PWV) region in the Gauteng Province of South Africa have been selected for analysis on days in January 1980, 1981 and 1991 in which rainfall greater than 5 mm fell (classified here as rain days), and for days with no rainfall (classified as no-rain days) over the area. Previously it had been shown that the 700 hPa level is the level of greatest importance for moisture transport during rain events over the summer rainfall region of the south African plateau (D'Abreton and Tyson, 1995). Consequently, moisture transport at the 700 hPa level provides the major focus for investigation in this study.

Back trajectories reveal that on rain days the 700 hPa moisture transport field is characterised by easterly-component flow from the tropical Indian Ocean north of Madagascar (Fig. 10.2a). The mean frequency transport pathway indicates an easterly onshore flow over tropical Africa at approximately 10^0S. About 37 per cent of the trajectories involved in transporting moisture into precipitating systems over the PWV area cross the meridian at 40°E six days prior to reaching the point at which rainfall occurs. Four days before precipitation, the moisture being transported has reached, on average, a position at about 27^0E, 17^0S over Zambia en route to central South Africa. Average specific humidities increase from 9,5 $g.kg^{-1}$ over the tropical Indian Ocean at 50^0E to 10,5 $g.kg^{-1}$ over the northern Mozambique and southern Tanzanian coast and increase further to

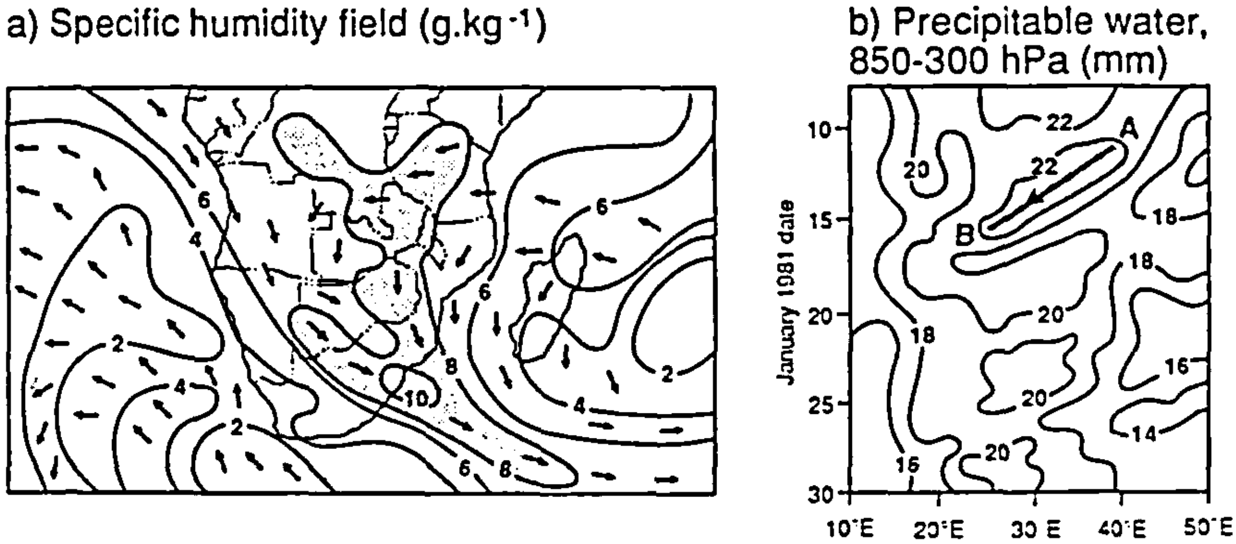

Figure 10.1: (a) Superimposed specific humidity ($g.kg^{-1}$) and 700 hPa flow fields for 24 January 1981, (b) Daily march of precipitable water (mm) integrated between 850 and 300 hPa over the period 10-30 January 1981. Shading indicates specific humidities > 8 $g.kg^{-1}$ in (a) and precipitable water > 22 mm in (b).

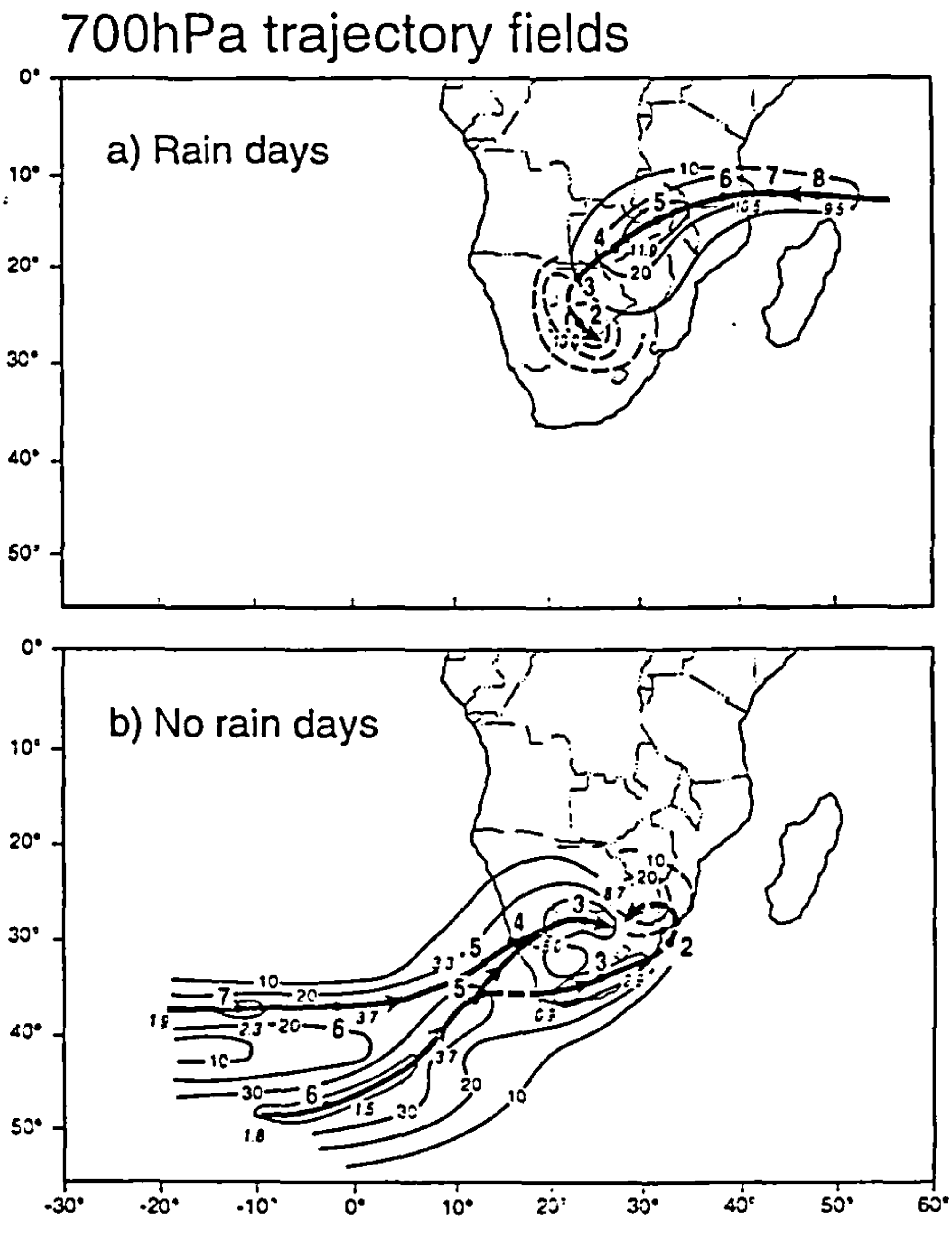

Figure 10.2: Mean trajectory fields for (a) rain-days and (b) no-rain days in January over the PWV region. Contours give percentage occurrence of trajectories and heavy lines the maximum frequency pathway of trajectories. Large, bold numbers denote average times of travel (days) from the PWV region. Italicised values give meridionally-averaged specific humidities ($g.kg^{-1}$) of mean air parcels at specific longitudes.

11,9 g.kg^{-1} over Zambia (Fig. 10.2a). Back trajectory modelling indicates that 75 per cent of the total moisture transport into January rainfall events over the PWV area has passed over Zimbabwe and Zambia.

The Indian Ocean region north of Madagascar coincides with a relatively high (>120 W.m^{-2}) vertical oceanic latent heat flux (Hastenrath and Lamb, 1979). This is the primary moisture source area where the air acquires its mean specific humidity of 9,5 g.kg^{-1} on average eight days before reaching central South Africa. The increase in specific humidity as the air is transported in a northeasterly stream over the continent south of the equator and over greater Southern Africa is the result of moisture convergence in air streams themselves converging (D'Abreton and Tyson, 1995).

Anticyclonic curvature of the moisture stream occurs over northern Botswana so that for the last two days of its transport the moisture stream approaches the PWV from the northwest, at which time, either by moisture divergence or precipitation, the mean specific humidity is 10,0 g.kg^{-1}. Of moisture-bearing trajectories traced back from the PWV during January rain events, 37 percent approach the area from the northwest. The remainder approach directly from the north or from the northeast.

Backward trajectories for no-rain days during January are markedly different to those of rain days (Fig. 10.2b). Rainless days are characterised by a southwesterly moisture transport from the South Atlantic Ocean to the south-west of Cape Town. Under such conditions, approximately 40 per cent of the moisture transport in the field shown in Figure 10.2b passes through the Greenwich meridian. Of the moisture transport reaching the PWV with a westerly component on rainless days, almost all crosses 20^{0}E about 3.5 days before reaching its destination over Gauteng in two streams, one over the southern coastal regions, the other via the Northern Cape. By comparison to specific humidities in the northerly component air streams on rain days, those on the no-rain days in the southerly component air streams are low. Thus just under six days before reaching the PWV the average specific humidity in the transport field on the Greenwich Meridian at 25^{0}S is 3,7 g.kg^{-1} and at about 45^{0}S is 1,5 g.kg^{-1}. The average moisture contents at 25^{0}E for the two main moisture streams are 5,0 g.kg^{-1} and 0,9 g.kg^{-1} for the northern and southern paths respectively (Fig. 10.1b).

In excess of 40 per cent of the moisture trajectories approach the PWV from the west along the maximum frequency pathway in the northerly airstream during rainless days; 30 per cent of the moisture trajectories approach from the east along the maximum frequency pathway of the southerly stream after having recurved anticyclonically from the southwest in their passage across the east coast of South Africa (Fig. 10.2b). In recurving over the coastal waters of the Indian Ocean, the average moisture content increases from Witwatersrand (Fig. 10.1b). This increase may be explained by the passage of the air over the warm approximately 3,0 to 4,0 $g.kg^{-1}$ along the southeast coast to more than 8 $g.kg^{-1}$ over the waters of the Agulhas Current, where latent heat flux from the sea surface is greater than 120 $W.m^{-2}$ (Hastenrath and Lamb, 1979). This mechanism is in agreement with earlier observations of a water vapour source over the region during dry Januaries (D'Abreton and Tyson, 1995). For rain-day conditions, air parcels originating from the tropical Indian Ocean north of Madagascar undergo almost no vertical displacement as they move toward South Africa (Fig. 10.3a). For the case studies examined, the maximum frequency pathway along which most moisture was transported maintained an almost constant height between 800 and 750 hPa over a period of eight eight days and over an approximate distance of 4500 km from source region to the PWV. By contrast, in the case of no-rain days, the mean trajectory pathway along which most moisture is transported indicates slope-wise descent of air parcels from the 550 hPa level over the central Atlantic Ocean to the 750 hPa level over the subcontinent (Fig. 10.3b). In excess of 150 hPa of subsidence occurs in approximately seven days.

The Tropical-Temperate Trough Case Study

A well-documented case study of a tropical-temperate trough and associated cloud bands occurring between 21 and 24 January 1981 has been selected for further investigation. Research using the Regional Atmospheric Modelling System (RAMS), generated specific humidity fields at 700 hPa for the case study. An example of a moisture maximum coinciding with the position of the cloud band over South Africa is given in Fig. 10.1a. In order to determine the major moisture source for the cloud band, backward trajectories emanating from regions of highest specific humidity over central South Africa and Namibia have been modelled. These have then been coupled to forward trajectories from the same points of origin to allow the combined history of the airstream 10 days before reaching the points of origin and for 10 days after leaving them to be determined. Specific humidities greater than 10 $g.kg^{-1}$ at 700 hPa were observed over central regions of South Africa on 22 January 1981. Backward trajectories for the day conform to the mean rain-day fields discussed

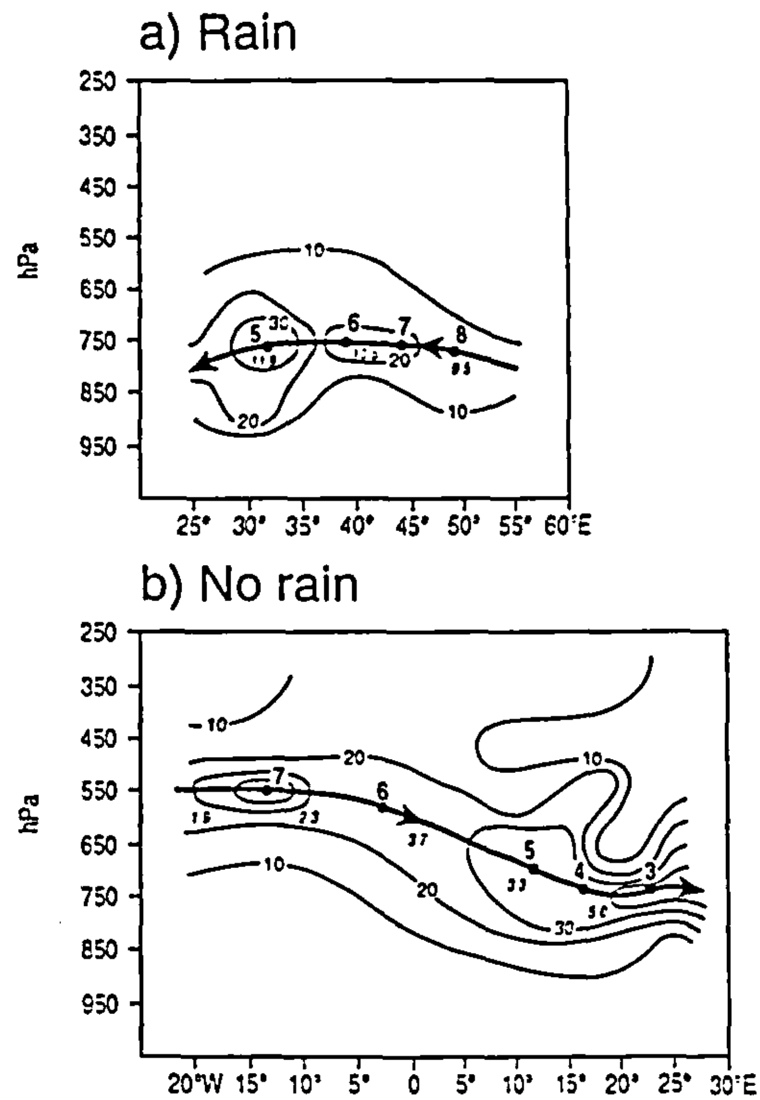

Figure 10.3: Trajectory fields in the vertical for (a) rain and (b) no-rain days during January over the PWV region. Labelling is as in Fig. 10.2.

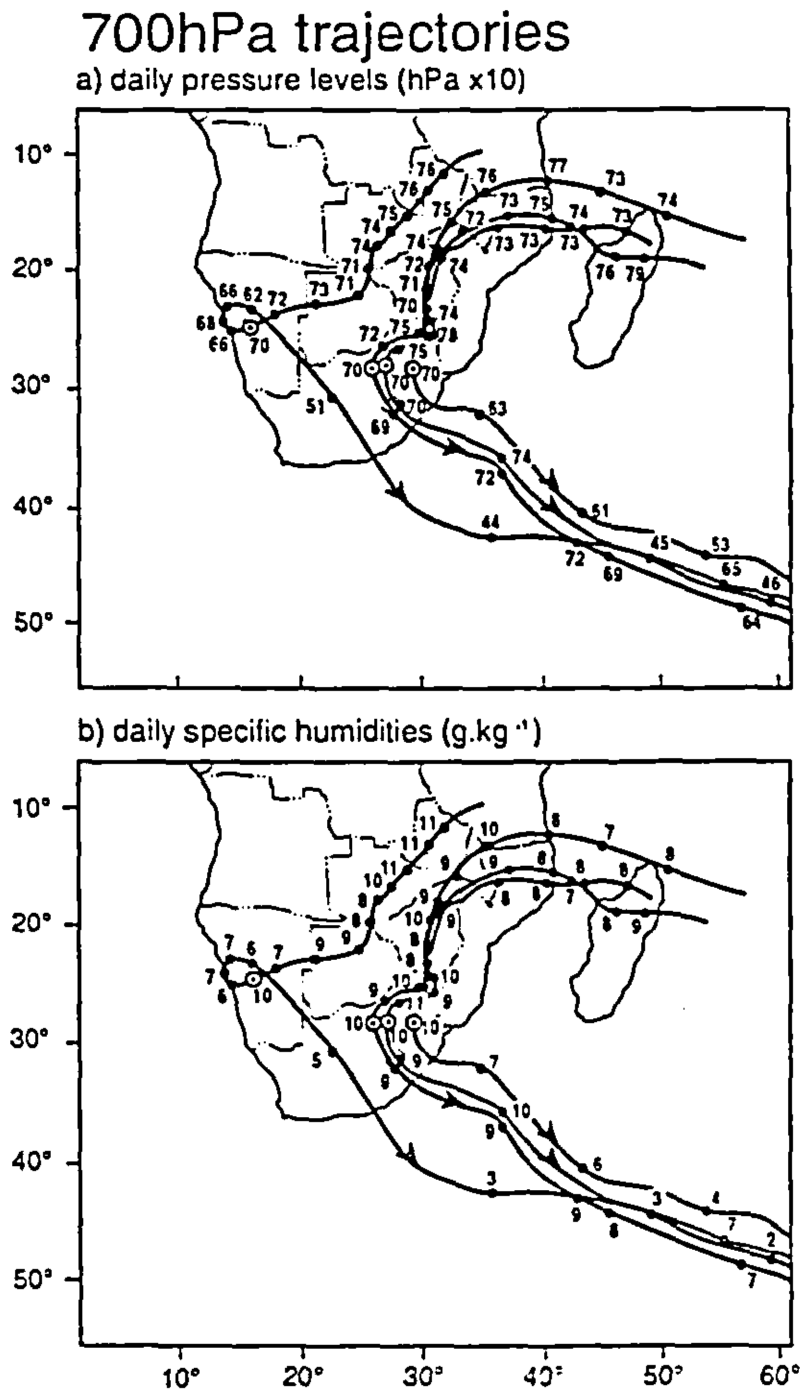

Figure 10.4: Backward and forward 700 hPa trajectories starting from selected points over South Africa (designated by heavy dots) starting on 22 January 1981 to show daily (a) pressure levels (hPa x 10) and (b) specific humidities (g.kg^{-1}).

earlier and trace back from central southern Africa, over the northern parts of subtropical southern Africa to an area over the tropical western Indian Ocean off the coast of East Africa (Fig. 10.4a). All trajectory pathways are confined to levels between 700 and 800 hPa. Specific humidities of 8 $g.kg^{-1}$ are uniform over the ocean source region, increasing to 9-10 $g.kg^{-1}$ over southern Zimbabwe, whereafter they increase by moisture convergence to about 10-11 $g.kg^{-1}$ over central South Africa (Fig. 10.4b). From this region gradual slantwise ascent is accompanied by desication as the airstream ascends out of the cloud band to an average height of about 550 hPa with an average specific humidity of about 5 $g.kg^{-1}$ over the middle of the Indian Ocean at 70^0E , 40^0S (Figs. 10.3a,b).

The trajectory fields and moisture pathways on the following day, 23 January 1981, are similar to those of the previous day. The transport of moisture from the tropical Indian Ocean is again at a nearly constant height of 750 to 700 hPa and slantwise ascent again occurs in the cloud band over the southeast coast of South Africa and the adjacent Indian Ocean to a level of about 550 hPa at 35^0S to the south of Madagascar (Fig. 10.5). The major difference on the second day of rain over much of South Africa is that once ascended to a position south of Madagascar, the 700 hPa cloud-band airstream recurved anticyclonically back towards Africa, tending towards subsidence as it did so. Nearly two weeks after having passed over Botswana it was back over the northern Mozambique Channel in the tropical Indian Ocean. Initiation of the recirculation appears to mark the onset of cloud band dissipation and supports earlier suggestions that such dissipation occurs with an eastward movement of the westerly wave trough and the weakening of the poleward flow (D'Abreton, 1993).

The question of how the vapour content of the airstream increases as it moves from the ocean north of Madagascar over the east coast of Africa is best answered by examining surface circulation and standing eddy vertical water vapour transport fields at 1000 hPa, i.e. at levels below the Great Escarpment of the interior plateau of southern Africa (Fig. 10.6). Circulation transport is that effected by the mean motion; standing eddy transport describes transport associated with the semi-permanent features of the atmosphere. Such fields have been determined for the day the air was crossing the east African coast (15 January) *en route* to precipitating over central South Africa on 22 January. Both circulation and standing eddy upward vertical water vapour transport is evident over southern Tanzania and northern Mozambique to provide for the increase in observed specific humidities along the moisture trajectories. This transport may be associated with disturbances along

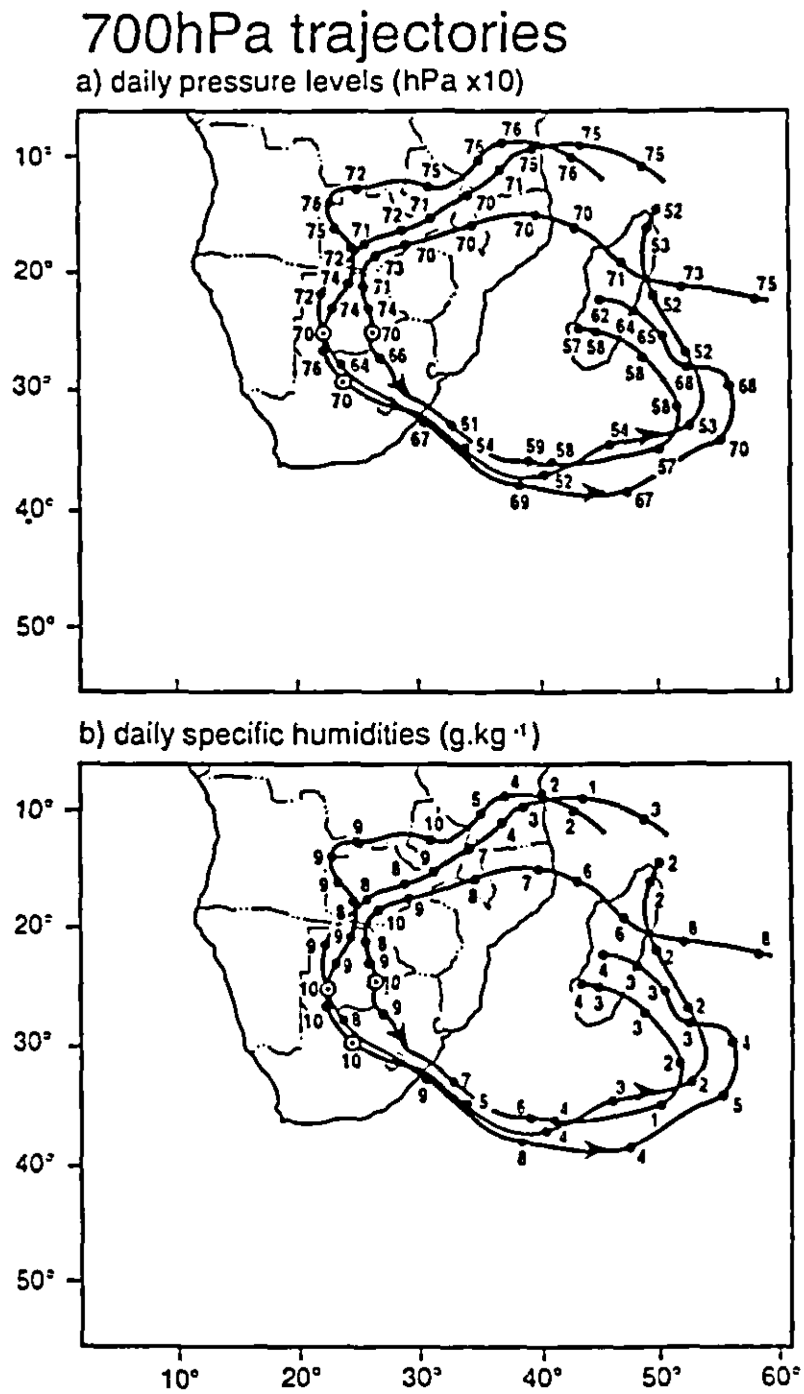

Figure 10.5: Backward and forward 700 hPa trajectories starting from selected points over South Africa (designated by heavy dots) starting on 23 January 1981 to show daily (a) pressure levels (hPa x 10) and (b) specific humidities ($g.kg^{-1}$).

a) Circulation vertical transport b) Eddy vertical transport

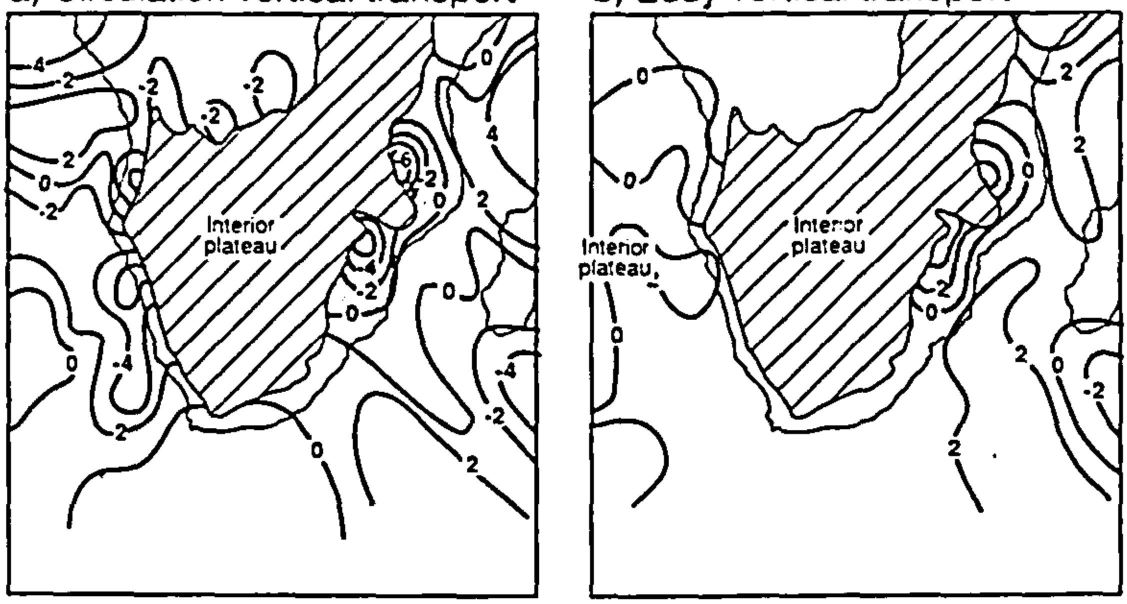

Figure 10.6: Circulation (a) and standing eddy (b) vertical transport of moisture from the 1000 hPa level for 15 January 1981. Units are x 100 $g.kg^{-1}.pa^{-1}.s^{-1}$ in (a) and x 10 $g.kg^{-1}.pa^{-1}.s^{-1}$ in (b).

the Inter-Tropical Convergence prevalent over the northern parts of southern Africa during summer. That the confluence of the northeast monsoon over the east African coastal area is a source of water vapour in mid-summer is supported by earlier work on vertically-integrated 850-700 hPa moisture divergence over southern Africa (D'Abreton, 1993; D'Abreton and Lindesay, 1993; D'Abreton and Tyson, 1995).

The Case study of a cut-off low pressure system

Cut-off low pressure systems are cold-cored baroclinic depressions associated with strong convergence and vertical motion. They are responsible for many of the flood-producing episodes over South Africa (Taljaard, 1985). On 25 January 1981, a cut-off low pressure system over the southwestern interior of South Africa resulted in excess of 180 mm being recorded in the so-called Laingsburg storm over a normally semi-arid region during a 24-hour period (Estie, 1981). Trajectory modelling of the moisture supply into the storm at the 700 hPa level has been undertaken. Aspects of the dynamics of the system are thereby illustrated as well.

The 700 hPa backward trajectories determined for several points around the core of the cut-off low reveal two diametrically-opposed conveyors feeding the low (Fig. 10.7). The warm conveyor of tropical origin has two sources of moisture. The first stream originates over Tanzania and the equatorial Indian Ocean off Kenya (Fig. 10.7a) and has a potential temperature of 32-37^{0}C and specific humidities of 10-12 g.kg^{-1} (Fig. 10.7b). A second tropical stream originates over Angola with specific humidities of 13-14 g.kg^{-1} and a potential temperature of about 37^{0}C. The confluence of the streams occurs over southern Zambia and both ascend by slow slantwise convection from northern Botswana into the low over South Africa.

The cold conveyor originates to the southwest of Cape Town around latitude 45^{0}S at about the 550-600 hPa level (Fig. 10.7a) with a potential temperature of about 22^0-26^{0}C and specific humidities of about 4,0 g.kg^{-1} (Fig. 10.7b). Over a distance of about 3000 km, dry air descends along the cold conveyor from the middle troposphere to the 700 hPa level over the Laingsburg area, where the heaviest rainfalls were recorded. The increase in water vapour content of the cold conveyor as it crosses the west coast is the result of moisture convergence with tropical air of

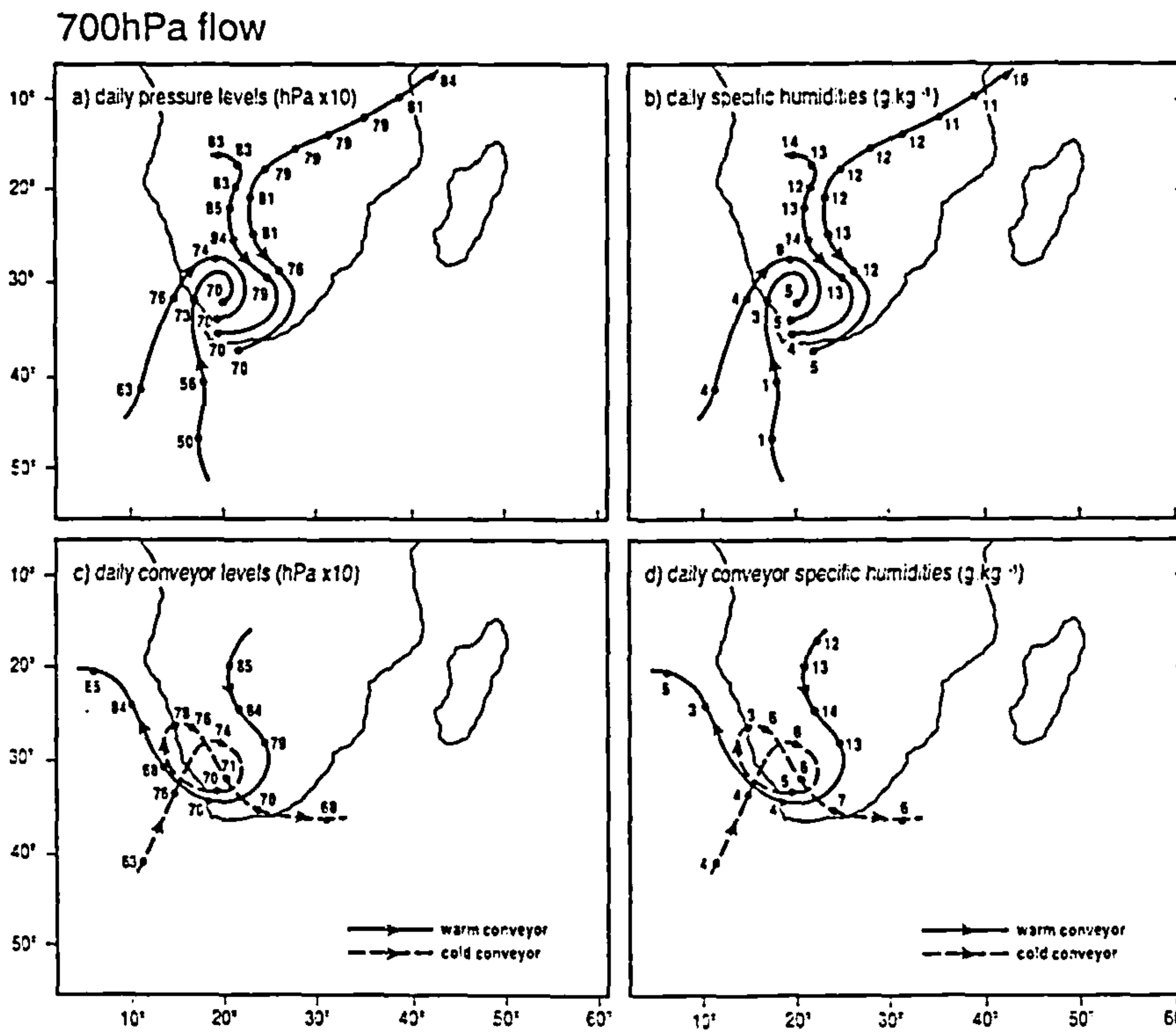

Figure 10.7: 700 hPa back trajectories from selected points in the Western Cape for the cut-off low on 25 January 1981 to show daily (a) pressure levels (hPa x 10) and (b) specific humidities ($g.kg^{-1}$). Coupled back and forward trajectories in (c) and (d) give levels and specific humidities on warm, tropical and cold, temperate conveyors into and through the cut-off low.

higher specific humidity. The most important source of moisture for the mid-latitude cut-off low pressure system is the tropical warm conveyor. The amount coming from elsewhere is negligible.

As the warm conveyor spirals towards the centre of the cut-off low, it ascends over the cold air descending in the cold conveyor (Fig. 10.7a,b). The average rate of ascent in the conveyor as the moist air moves south is the order of 55 hPa per day over about 4 days. A maximum height of about 680 hPa is reached northwest of Cape Town as the warm conveyor ascends through the centre of the storm before subsiding abruptly as it passes into the region of the Atlantic high pressure cell off the west coast. The pathway of the cold conveyor is more complicated than that of its tropical warm counterpart. The air in the cold conveyor descends from mid-tropospheric levels into the cyclonic vortex from the southwest. Thereafter, it begins to ascend as it spirals cyclonically upwards on the eastern side of the system. It then subsides again on the western side with further cyclonic rotation before ascending with continued cyclonic motion for a second time as it again passes through the eastern side of the cell. Finally, the conveyor rises by slantwise ascent toward the east before becoming entrained in the westerlies over the Indian Ocean.

The Laingsburg storm has been modelled using RAMS. Model streamlines at 700hPa show the cyclonic vortex to be located to the northwest of Cape Town (Fig. 10.8a). More importantly, the model is able to replicate the asymmetry in the vertical velocity field to the east and west of the system (Fig. 10.8b). The meso-scale atmospheric circulation model and the trajectory model both show ascent to the east of the cut-off low and descent to the west in the lower troposphere. At the 500hPa level, while the vortex of the low is still clearly evident, the trajectory model shows that the twin conveyor system is absent (Fig. 10.9). Instead, cold dry is entrained into the system from the west and exits to the east in just over a day.

Discussion

Water vapour transport over southern Africa has been examined using a Lagrangian trajectory model applied to ECMWF data stratified into two samples, one characterising rain days, the other non-rain days in the mid-summer month of January. The model is successful in the identification of major moisture streams feeding tropical-temperate troughs, despite the limitation inherent in the

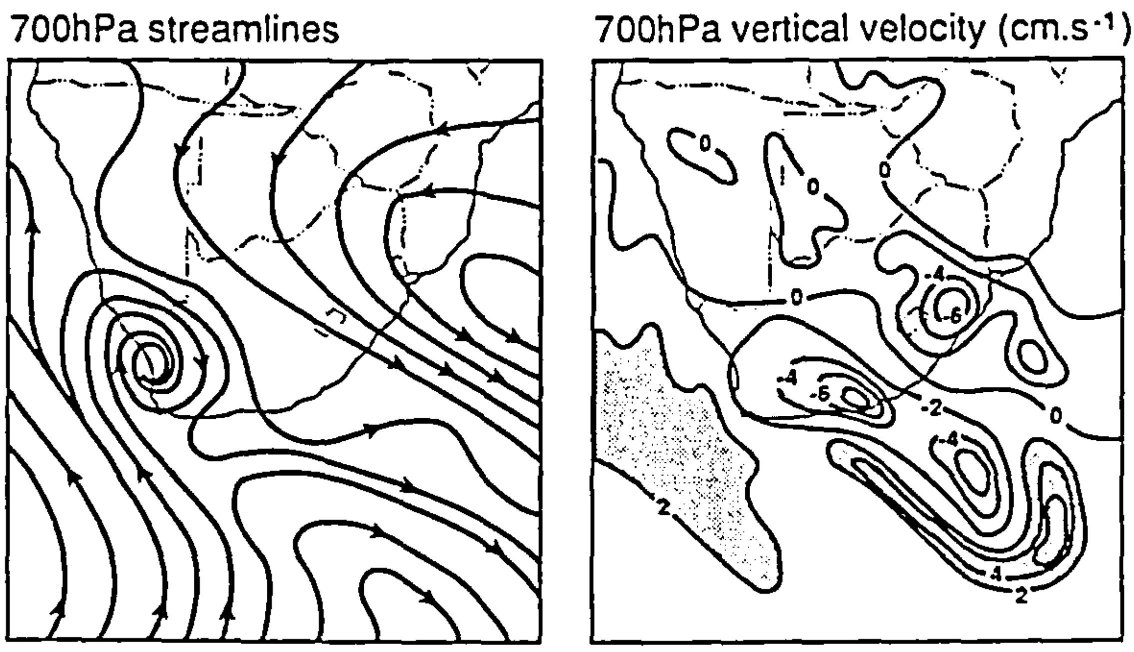

Figure 10.8: RAMS simulation (a) streamlines and (b) vertical velocities (cm.s^{-1}) for 1200 UT on 24 January 1981. Light shading indicates ascending motion and dark shading, descent.

500hPa flow

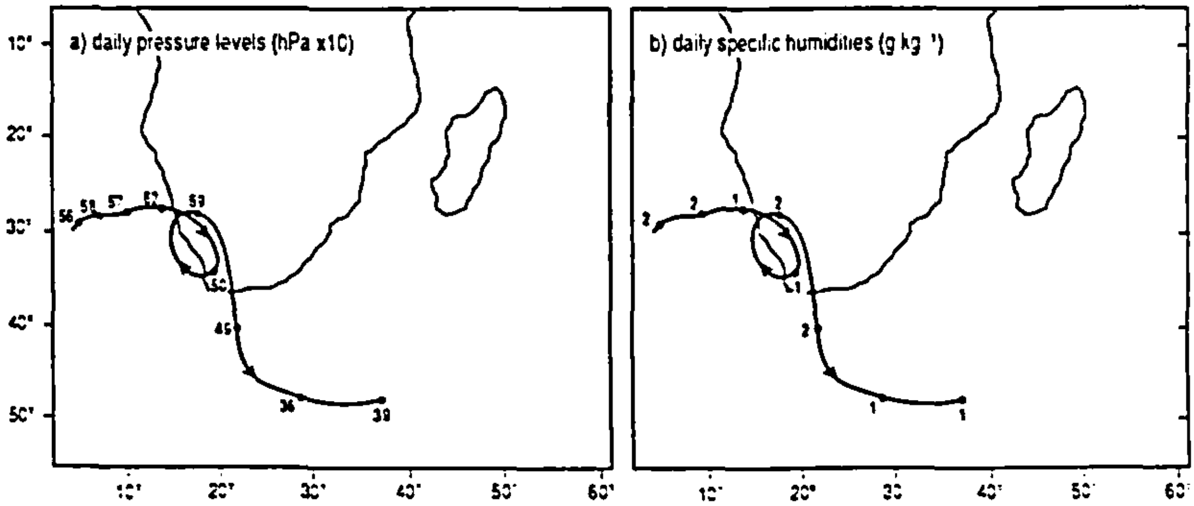

Figure 10.9: 500 hPa back trajectories into and forward trajectories out of the centre of the cut-off low (designated by a heavy dot) on 25 January 1981 to show daily (a) pressure levels (hPa x 10) and (b) specific humidities (g.kg^{-1}).

model imposed by the assumption that water vapour is a passive tracer. Large-scale convergence and divergence along trajectory pathways is modelled successfully.

In general, mid-summer, January rain-day conditions over the PWV and Gauteng are characterised by northerly transport in the lower troposphere, at about the 700 hPa level, of moist air from tropical east Africa and adjacent Indian Ocean south of the equator. By contrast, no-rain days over the PWV are characterised by southwesterly transport of dry subsiding air from the direction of Gough Island in the South Atlantic Ocean.

In the cases of rainfall events occurring with tropical-temperate troughs and associated cloud bands, a northerly flux of moist, tropical air takes place in a well-defined warm conveyor that recurves anticyclonically across Southern Africa. Water vapour source regions appear to be the western tropical Indian Ocean and adjacent continental regions. The model shows the warm conveyor transporting moist air to the southwest before undergoing southeasterly slantwise ascent over South Africa and the southwest Indian Ocean within the cloud band during the mature stage of the system (Fig. 10.10a). In later stages, as the cloud band begins to dissipate, the conveyor recurves anticyclonically as it begins to recirculate back towards Africa (Fig. 10.10b). Such recirculation commonly characterises fine-weather conditions and is a major feature of aerosol and trace gas transport patterns over southern Africa (Tyson *et al.*, 1996a; Garstang *et al.*, 1996; Tyson *et al.*, 1996b).

In contrast to the relatively simple structure of the conveyor system associated with tropical-temperate cloud bands, that of cut-off lows appears to be more complicated (Fig10.10c). In such cases the warm, moist conveyor appears to originate in the tropics over central Africa and adjacent Indian Ocean south of the equator. Over a period of several days the moisture is conveyed south towards South Africa in a stream in which the moisture content increases slightly due to flux convergence. Slantwise ascent occurs as the conveyor enters the region of cyclonic vorticity and begins to rotate clockwise into the vortex of the cut-off low. The structure of the warm conveyor, unlike its cold counterpart, is relatively uncomplicated. It ascends to about the 675 hPa level losing moisture through precipitation before subsiding rapidly as it moves over the Atlantic Ocean off the west coast.

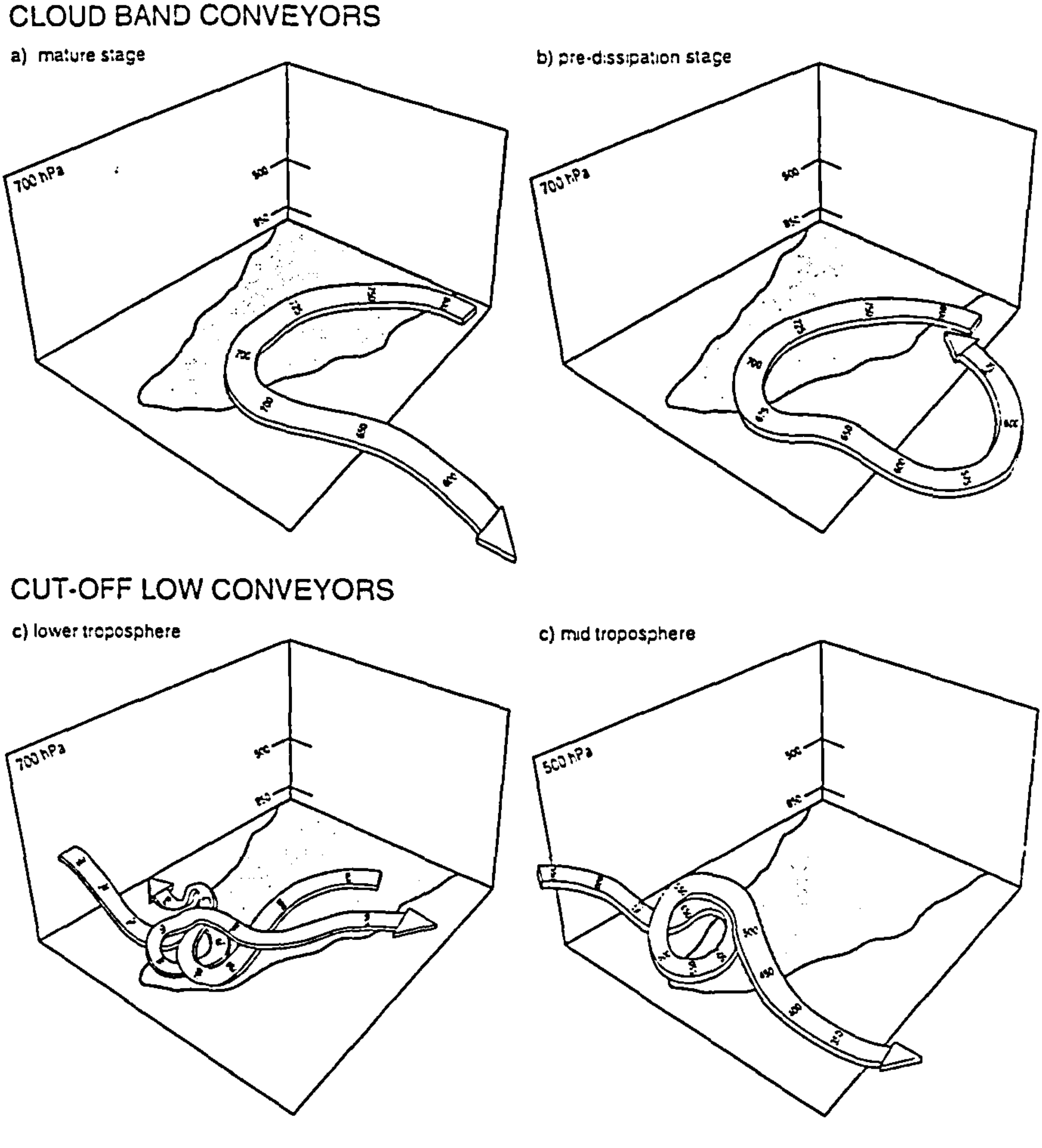

Figure 10.10: Schematic models to show the warm, moist 700 hPa conveyor feeding (a) mature and (b) immediately pre-dissipation stage tropical temperate troughs and cloud bands and to show (a) the interaction of the tropical warm, moist and temperate cool, dry 700 hPa conveyors in cut-off lows over Southern Africa and (b) the absence of such conveyors at the 500 hPa level. Approximate pressure levels are indicated along the conveyors.

The cold conveyor originates at mid-tropospheric levels to the southwest of Cape Town and cold dry air descends over several days before beginning the cyclonic spiral into the cut-off low. In descending into the vortex, the cold air forms the wedge over which the warm conveyor rises with slantwise convection, realises its thermal instability and precipitates. The cold conveyor then rises in an upward spiral to ascend over the warm conveyor before becoming entrained into the mid-level westerlies above the 650 hPa level.

It needs to be emphasised that a model of a cut-off low, such as the one proposed here, is not a statement of the structure at a given instant in time. Instead, it is one which portrays the history of the circulation into the system over a period of up to nearly a week. The structure of the interacting warm and cold conveyors is not dissimilar to that advanced by Browning (1985) for northern hemisphere cyclonic storms and transposed for southern hemisphere conditions by Preston-Whyte and Tyson (1989), but is more complicated in respect of the history of the downward spiralling cold conveyor, which contributes most to the total vorticity of the system.

Previously, Lagrangian modelling has been used for determining mass transports of aerosols and trace gases over southern Africa. Similar modelling of water vapour transport has been shown to be useful in the determination of the structure of rain-bearing systems over southern Africa. The modelling allows significant differences between rain and no-rain situations to be determined and offers a powerful means of further investigating the changing nature of atmospheric circulation systems during wet and dry spells over the region.

Synopsis

Back and forward kinematic trajectory modelling has been undertaken for rain and no-rain days over the central interior of South Africa in mid-summer. No rain-days (rain days) are shown to be characterised by dry (moist) southwesterly (northerly to northeasterly) flow originating over the South Atlantic (tropical Indian) Ocean. Air parcels for tropical-temperate troughs originate over the tropical Indian Ocean and trace south and southeastwards corresponding closely to the position of the trough-associated cloud band. Trajectory modelling of a cut-off low pressure system reveals the presence and interaction of a cold, dry, descending conveyor from the south and a warm, moist, ascending conveyor from the north.

CHAPTER 11

SUMMARY AND CONCLUSIONS

Mesoscale modelling offers a powerful means of investigating atmospheric systems at a much higher space and time resolution than is supplied by current station networks and provides an enhanced understanding of the processes and factors affecting the systems. This is particularly pertinent in the simulation of tropical-temperate troughs over southern Africa and the adjacent oceans where data is sparse or non-existent. The first step in simulating the occurrence of tropical-temperate troughs in wet and dry conditions was to establish that the model provides an accurate representation of observed events. This was accomplished successfully. Thereafter, the degree of influence that certain factors and processes have on circulation systems were determined using sensitivity tests. These proved illuminating. The Regional Atmospheric Modelling System has proved to be accurate and its use appropriate. New insights into the circulation adjustments and processes associated with tropical-temperate troughs have been obtained. Previous hypotheses and empirical analytical models have been verified.

Findings of the investigation may be summarised as follows:

Circulation Components

1. The model confirms earlier suggestions that three components of the circulation are necessary for the formation of tropical-temperate troughs during both wet and dry conditions. These are a tropical low, a westerly wave and a trough linking the two.

2. During wet conditions over southern Africa, the linking trough occurs over the western interior of southern Africa; during dry conditions a weaker trough over Mozambique performs the same function.

3. Tropical-temperate troughs form only once all three systems are in conjunction.

4. Divergence in the upper easterly wave, combined with surface convergence in the lower westerly wave, produce the vertical uplift that causes rainfall. Since the surface convergence occurs only to the east of the surface trough, rainfall occurs most frequently and copiously over the eastern regions of southern Africa during wet conditions and over the Mozambique Channel and Madagascar during dry conditions.

5. The dry summer tropical lows are situated further north than those during wet summers. The westerly wave stretches further north to connect with the tropical low during dry summers.

Structure

6. Simulated upper tropospheric mixing ratios reveal a poleward increase in the cloud top heights along the tropical-temperate trough. This is in keeping with the link between the lower-level tropical low and the middle to upper level westerly wave, and implies that moisture is being lifted upwards along the tropical-temperate trough through both convective and advective processes. An increase in cloud top height towards the poles has also been observed in the Northwest Australian Cloud Bands.

Dissipation

7. The model shows that the dissipation of tropical-temperate troughs during wet and dry summers occurs with the eastward movement of the westerly wave which results in the break of the temperate link.

Air Flow

8. The model reveals that northeasterly flow from the tropics and oceanic region to the northwest of Madagascar transported warm, moist air into the region of the tropical low during wet conditions, thereby substantiating previous hypotheses describing the importance of this flow during wet summer tropical-temperate troughs. Northeasterly flow is also important in dry summer tropical-temperate trough formation, but is greater during wet conditions.

9. Westerly flow from over the tropical South Atlantic Ocean contributes to the tropical low during dry conditions.

10. Following the establishment of the temperate link between the westerly wave and the interior trough, the faster flow within the westerly wave enhances air flow along the linking trough by kinematic divergence. This in turn encourages the northeasterly flow into the region of the tropical low.

11. The northeasterly flow into the tropical low breaks down with the dissipation of the tropical-temperate trough and is replaced by westerlies during wet conditions and easterlies to southeasterlies during dry conditions.

12. The westerlies are displaced substantially further northward during the dry than the wet conditions and the wet and dry summer upper-air westerlies extend further equatorward than those at the lower levels.

13. The model reveals that wet summer easterlies in the upper troposphere are better developed and extend substantially further southward than those during dry conditions. Southward displacement of the ITC occurs during wet conditions. During both wet and dry conditions, the dissipation of the tropical-temperate trough is associated with a weakening of the easterlies.

Transport

14. The simulations reveal that tropical-temperate trough development during both wet and dry conditions resulted in the organisation and enhancement of poleward transport throughout the troposphere along the cloud band situated over southern Africa and the Mozambique Channel, respectively.

15. The modelled poleward progression of the regions of greatest total mixing ratios with the development of the tropical-temperate trough shows how the systems facilitate transport of tropical moisture poleward.

16. The model shows that during both wet and dry conditions, higher temperatures occur along the cloud band compared with the surrounding air. This increase can be attributed to both the poleward transport of warm tropical air and to the release of latent heat within the cloud band.

17. An increase in the strength of the subtropical jetstream to the east of the mature tropical-temperate trough during both the wet and dry conditions is obvious in simulated meridional and zonal wind components and confirms the importance of tropical-temperate troughs in transporting westerly angular momentum poleward.

Water Vapour Sources

18. The simulated streamlines and poleward progression of the total water mixing ratios show that the oceanic region to the northwest of Madagascar is an important source of water vapour for wet and dry summer tropical-temperate troughs. The tropical South Atlantic Ocean also appears to contribute to the moisture flow along the tropical-temperate trough during dry conditions. The mid-latitude regions of the South Indian Ocean do contribute to the flow of moisture along the cloud band during both wet and dry conditions, but to a lesser extent than the oceanic region to the northwest of Madagascar.

19. The South Indian Anticyclone is situated closer to the subcontinent during the wet summers and enhances the easterly to northeasterly transport of maritime moisture over the interior. During dry summers, the South Indian Anticyclone is situated further east of the subcontinent thereby reducing its effect on the interior. However, it enhances the poleward flow along the temperate sections of the tropical-temperate trough. The effect of the South Indian Anticyclone on tropical-temperate troughs is greater during dry summers.

Zonal and Meridional Circulations

20. The westerly and easterly flow in the lower levels, the low-level convergence between 5° and 15°S, the eastward propagation of this zone of convergence from 20°E to 30°E and the predominant easterly flow in the upper troposphere are indicative of a more complex Walker circulation during wet late summers. During dry conditions, the zone of convergence between the low level easterlies and westerlies between 10°and 20°S, remains at approximately 20°E throughout the development of the cloud band.

21. The dry-summer Walker cell situated over the eastern regions of tropical Africa is positioned to the northeast over the South Indian Ocean in the simulated zonal flow. This allows for the presence of an easterly wave over the eastern regions of tropical Africa in which the tropical low developed.

22. The simulated eastward shift of the wet-summer cloud band in association with the eastward movement of the zone of convergence between 5° and 15° S, substantiates the hypothesis that cloud bands coincide with the convergence of easterly and westerly vapour transport along 10°S.

23. The model shows that a Hadley circulation occurs over the western regions of Africa during wet late summers between 10° and 35°S. South of about 35°S, the flow is predominantly equatorward due to the transportation of cold polar air northward along the westerly wave. Deep poleward flow occurs over the eastern and central regions of southern Africa, from the equator to beyond 50°S, during the initial and mature stages of tropical-temperate trough development. This substantiates previous descriptions of tropical-temperate troughs as being representative of Hadley cell intensifications.

24. A weak Hadley cell is apparent in the simulated output over the western regions of Africa during the initial and dissipative stages of the dry summer tropical-temperate trough. However, equatorward flow as a result of the flow in the trailing arm of the westerly wave is predominant during the mature stage.

25. Over the eastern regions of southern Africa, throughout the mature and dissipative cloud band stages, circulation of the Hadley-type is apparent. The Ferrel-type circulation described previously is only apparent along 30°E between the Equator and approximately 20°S during the initial dry-summer cloud band stages.

26. During dry conditions, a modelled Ferrel-type circulation occurs along 40°E initially between the Equator and 30°S and then between the Equator and 20°S. To the south of the Ferrel cell, the presence of the tropical-temperate trough results in a Hadley-type circulation. The simulated Hadley-type circulation, like that of wet summers, supports the hypothesis that cloud bands are representative of Hadley cell intensifications.

27. The dry-summer simulated meridional flow along 40°E reveals that the low-level poleward flow from the Equator to approximately 15°S, associated with the Ferrel-type circulation, is vertically lifted and incorporated into the middle to upper level flow by the Hadley-type circulation beyond 15°S. The lower-level poleward flow feeds the tropical low, after which it is uplifted and transported along the temperate sections of

the tropical-temperate trough. During the cloud band dissipation this link between the low- and upper-level poleward flow weakens.

28. The predominant poleward flow over tropical and southern Africa (extreme eastern regions of southern Africa and the western regions of the South Indian Ocean) and the predominant equatorward flow to the west and southwest of the subcontinent (central and western regions of southern Africa) during wet (dry) summers occur as a result of the position of the westerly wave over the subcontinent (to the east of the subcontinent), which in turn is influenced by the Walker circulation. Subsidence in the trailing arm of the westerly wave causes the stable and exceptionally dry conditions over the western (western and central) interior during wet (dry) conditions.

Model Strengths and Weaknesses

29. The Regional Atmospheric Modelling System is a particularly suitable tool with which to investigate the characteristics and rainfall of tropical-temperate troughs over southern Africa and the adjacent oceans. Most of the simulated variables compare closely with the observed variables. As the control runs provided accurate representations of the observed events, it is possible to investigate numerous hypotheses and characteristics of tropical-temperate troughs during wet and dry periods.

30. The convective parameterisation scheme is a model weakness. In both the wet and dry case studies, the convective parameterisation scheme underestimated the observed rainfall by approximately 65%. This points either to a weakness in the convective parameterisation scheme *perse*, or to a greater influence of stratiform-type processes in the development of tropical-temperate troughs. A combination of both factors may apply.

Model Sensitivities

31. When the microphysics module was activated, the microphysically-produced rainfall corresponded closely with the observed rainfall, both in magnitude and distribution. The precipitation totals from the convective parameterisation scheme were, however, less than half of the observed totals in both case studies. Inclusion of the microphysics module resulted in significantly lower upper tropospheric condensate mixing ratios than those obtained without resolvable microphysics. The problem appears to be caused by the inability of the convective parameterisation scheme to transport condensate vertically.The lower condensate levels may also be due to the precipitation process, which is activated by including the microphysics module, and which will deposit some of the condensate that was suspended in the simulations without the microphysics module.

32. Despite an increase in the vertical velocities and associated convective precipitation, the use of a finer grid resolution had little effect on the development, dissipation and rainfall of the tropical-temperate troughs during both case studies. The finer resolution did, however, result in a marked improvement in the simulation of the cut-off low that developed toward the end of the wet case study, and which was not clearly evident in the coarser control simulation. This result is not surprising given the smaller scale of the cut-off low. As the differences between the finer resolution and coarse control runs in both case studies were not substantial, the credibility of the Regional Atmospheric Modelling System is enhanced.

33. Increasing soil moisture has very little effect on the development and dissipation of cloud bands. A reduction in soil moisture results in a lower moisture content in the tropospheric levels close to the ground, but has little effect on the 700 and 300 hPa levels. Clearly the major cloud band moisture source is other than the soil surface over southern Africa. The oceanic region to the northwest of Madagascar is the most important source of water vapour for tropical-temperate trough development during both wet and dry late summers.

34. Lower soil moisture causes the dissipation of the tropical-temperate troughs to occur earlier than would otherwise be the case, probably due to reduced instability as a result of the lower moisture content in the lowest atmospheric levels.

35. When the individual oceanic sensitivity experiments are compared to the control simulation each initial simulation time-step for the three oceanic simulations shows no differences from the control. This indicates that the numerical model requires a certain time-period in which to allow for circulation differences to be produced. The response magnitude of the individual experiments differs, with most pronounced results found in the tropical Indian Ocean anomaly experiment. The degree of response is found to be related to the average temperature of the particular ocean in which the anomaly developed.

36. Comparing the average temperatures of the tropical Indian Ocean with those of the Agulhas Current retroflection and the tropical western Atlantic Ocean, it was found that the values were on average higher in the tropical Indian ocean. The addition of positive sea-surface temperature anomalies to a region of already high temperature values affects the flux equations of the numerical model, to a far greater degree than positive anomalies added to a region of colder background temperatures.

37. Although the atmospheric circulation changes produced by the Agulhas Current anomaly inclusions were less dramatic than the tropical Indian Ocean anomaly experiment, the results are by no means insignificant.

38. For the Indian Ocean Anomaly sensitivity test, the initial circulation differences become detectable after nine hours with changes in near-surface windfields, and accumulated convective precipitation. The general pattern of circulation change indicates the development of stronger easterly winds to the east of Madagascar, with precipitation increases in the same area, and to the north. The continued simulation of strong easterly flow to the east of Madagascar, for the remainder of the experiment, served to maintain higher vertical instability over the island.

39. Less than twelve hours into the Indian Ocean Anomaly simulation (0600 UTC, 22 January 1981), cyclogenesis began to occur over the modified sea-surface temperatures. The combination of higher sea-surface temperatures, moisture availability, and vertical instability initiates the development of cyclogenesis to the north of Madagascar. Other features such as the westward expansion of anticyclonic flow north of 10^0S and the development of surface divergence along 40^0E reduces the moisture inflow into the subcontinent by deflecting moisture to the region of developing cyclogenesis.

40. The tropical Indian Ocean anomaly experiment simulated the reduction of moisture availability over the subcontinent thus producing lower widespread precipitation values over the country by the time the tropical-temperate trough fully developed.Although the positive modification of sea-surface temperatures to the north and east of Madagascar had little effect on the formation and dissipation of the tropical-temperate trough, the simulated promotion of cyclogenesis over the area of sea-surface temperature modification served to reduce precipitation within the tropical-temperate trough.

41. The modification of the sea-surface temperature field within the region of the Agulhas current retroflection produces simulated weakened onshore flow over the southern coast of South Africa, with heightened zonal or westerly flow to the south of the Agulhas Current retroflection anomaly. This type of atmospheric circulation change is proposed by Walker (1989) who states that the development of sea-surface temperature anomalies in this region intensifies the sea-surface temperature front towards the poles and thus shifting the surface westerlies in a poleward direction.

42. In the Agulhas Current retroflection sensitivity simulation the positive sea-surface temperature anomalies aid in the enhancement of surface and near-surface convergence along the Angolan and Namibian coast, by increasing moisture inflow to the area. The anticyclonic circulation around the semi-permanent South Atlantic High pressure passes over the anomaly and flows equatorward along the west coast of the

subcontinent. The positive sea-surface temperatures will slowly allow moisture transfer from the anomaly source to the convergence zone along the west coast.

43. As the westerly waves passes over the sea-surface temperature anomaly, greater instability is imparted to the disturbance. The same was true for the second westerly wave disturbance.

44. The initial enhancement of convergence along the southern African west coast produces higher convective precipitation values over the Namibia/Botswana border, with the westerly wave disturbances increasing precipitation values along the South African east coast. Thus, the sea-surface temperature anomalies served as a source of instability for the tropical low and the westerly wave disturbances.

45. The addition of the anomalous sea-surface temperatures in the Agulhas current retroflection region has no effect on the general formation and dissipation of the tropical-temperate trough. The results of the Agulhas Current anomaly simulation closely resembles the circulation changes proposed by Walker (1989). The development of the anomaly produces higher sea-surface temperatures in the southern Agulhas region. This in turn intensifies the sea-surface temperature gradient thus enhancing westerly flow further southwards. The warmer sea temperature anomaly strengthens ocean-atmosphere heat fluxes increasing baroclinicity within the boundary layer and reducing static stability over the anomaly. The reduction of stability influences both the structure of the westerly troughs and meridional flow along the west coast, that in turn enhanced precipitation.

46. The origin of circulation differences for the tropical eastern Atlantic Ocean sensitivity experiment is found directly over the area in which the sea-surface temperature anomalies are placed. The variation in atmospheric circulation and atmospheric parameters begins with the modification of local surface wind-fields and surface air temperatures. The surface wind fields show a strengthening of westerly zonal circulation along with air temperatures increasing from the north.

47. The positive modification of air temperatures in the tropical eastern Atlantic Ocean experiment enhances the moisture carrying capacity of the onshore flow, which in turn encourages vertical instability and local precipitation. These changes in atmospheric circulation are translated over time to the Zaire air boundary and southwards through return flow to Namibia and Botswana. The effect of the sea-surface temperature anomaly on South Africa is much less clearly defined although stronger westerly flow and instability is present over the Northern Province.

48. In the tropical eastern Atlantic Ocean sensitivity experiment the modification of atmospheric circulation is limited, for the most part, to the localised coastal regions and immediate interior of the African west coast. As with the previous two sensitivity experiments, the tropical western Atlantic Ocean anomalies has no direct impact on the formation and dissipation of the tropical-temperate trough. The effect of the anomaly is very localised with enhanced precipitation found over the regions of Gabon, Congo and southern Zaire. Strengthened onshore flow over the coast, adjacent to the sea-surface temperature anomaly, serves to enhance convergence within the Zaire Air Boundary (ZAB).

Lagragian Trajectory Analysis

49. The Lagrangian trajectory model is successful in the identification of major moisture streams feeding tropical-temperate troughs. Large-scale convergence and divergence along trajectory pathways is also modelled successfully.

50. In general, mid-summer, January rain-day conditions over the PWV and Gauteng are characterised by northerly transport in the lower troposphere, at about the 700 hPa level, of moist air from tropical east Africa and adjacent Indian Ocean south of the equator. By contrast, no-rain days over the PWV are characterised by south-westerly transport of dry subsiding air from the direction of Gough Island in the South Atlantic Ocean.

51. In the cases of tropical-temperate trough and precipitation, a northerly flux of moist, tropical air takes place in a well-defined warm conveyor that recurves anticyclonically across Southern Africa. Water vapour source regions are found over the western tropical Indian Ocean and adjacent continental regions. The model shows the warm conveyor transporting moist air to the south-west before undergoing south-easterly slantwise ascent over South Africa. As the cloud band begins to dissipate, the conveyor recurves anticyclonically as it begins to recirculate back towards Africa.

52. The structure of the conveyor system of cut-off lows appears to be more complicated. The warm, moist conveyor appears to originate in the tropics over central Africa and adjacent Indian Ocean south of the equator. Over a period of several days the moisture is conveyed south towards South Africa in a stream in which the moisture content increases slightly due to flux convergence. Slantwise ascent occurs as the conveyor enters the region of cyclonic vorticity and begins to rotate clockwise into the vortex of the cut-off low.

53. The cold conveyor originates at mid-tropospheric levels to the south-west of Cape Town and cold dry air descends over several days before beginning the cyclonic spiral into the cut-off low. In descending into the vortex, the cold air forms the wedge over which the warm conveyor rises with slantwise convection, realises its thermal instability and precipitates. The cold conveyor then rises in an upward spiral to ascend over the warm conveyor before becoming entrained into the mid-level westerlies above the 650 hPa level.

Synopsis

RAMS and trajectory modelling has proved to be a most suitable tool with which to investigate the development and characteristics of southern African tropical-temperate troughs during wet and dry years. The successful simulation of observed events has resulted in the corroboration of numerous previous hypotheses which required substantiation using more spatially comprehensive data sets. No previous hypotheses have been shown to be untenable. More importantly, the modelling has allowed new insights to be developed and hypotheses to be refined and extended. These would have been difficult to achieve without the spatial resolution of a mesoscale model.

REFERENCES

Acharya, U.R. and Bhaskara Rao, N.S., 1981. Meteorology of Zambia: Parts I and II, Government Printers, Lusaka.

Adedokun, J.A., 1983. Intra-layer (low level/mid-tropospheric) precipitable water vapour relations and precipitations in West Africa, *Archiv für Meteorologie, Geophysik und Bioklimatologie, Ser B,* **33** 117-130.

Anderson, R.K. and Oliver, V.J., 1970. Some examples of the use of synchronous satellite pictures for studying changes in tropical cloudiness, *Proceedings of Symposium on Tropical Meteorology*, American Meteorological Society, E XII 1-6.

Anyadike, R.N.C., 1979. The content of water vapour in the atmosphere over West Africa, *Archiv für Meteorologie, Geophysik und Bioklimatologie, Ser A,* **28**, 245-254.

Atlas, R., Wolfson, N. and Terry, J., 1993. The effect of SST and soil moisture anomalies on GLA model simulations of the 1988 U.S. summer drought, *Journal of Climate*, 6, 2034-2048.

Bannon, P.R., 1981. Synoptic-scale forcing of coastal lows: forced double Kelvin waves in the atmosphere, *Quarterly Journal of the Royal Meteorological Society*, 107, 313-327.

Barclay, J.J., Jury, M.R. and Landman, W., 1993. Climatological and structural differences between wet and dry troughs over southern Africa in the early summer, *Meteorology and Atmospheric Physics*, **51**, 41-51.

Barnes, S.L., 1973. Mesoscale objective map analysis using weighted time-series observations, *NOAA Technical Memo, ERL NSSL-62*, United States Department of Commerce, 60pp.

Bell, I.D., 1986. The northwest Australian cloud band, *Preprints of the 2nd International Conference on Southern Hemisphere Meteorology*, American Meteorological Society, 42-45.

Bergeron, T., 1930. Richtlinien einer dynamischen Klimatologie, *Meteorologische Zeitschift*, 47, 246-262.

Bhalotra, Y.P.R., 1973. Disturbances of the summer season affecting Zambia, *Technical Memorandum 3*, Zambia Meteorological Department, Lusaka, 7pp.

Browning, K.A., 1985. Conceptual models of precipitation systems, *Meterological Magazine*, **114**, 293-319.

Brundit, G.B. and Shannon, L.V., 1989. Cape Storms and the Agulhas current: a glimpse of the future?, *South African Journal of Science*, 85, 619-620.

Bjerknes, J., 1969. Atmospheric teleconnections from the equatorial Pacific, *Monthly Weather Review*, 97, 163-172.

Bossert, J.E., 1990. Regional-scale flows in complex terrain: an observational and numerical investigation, Atmospheric Science Paper No. 472, Department of Atmospheric Science, Colorado State University, Fort Collins, 254pp.

Bounoua, L. and Krishnamurti, T.N., 1993. Influence of soil moisture on the Sahelian climate prediction II, *Meteorology and Atmospheric Physics*, 52, 205-224.

Chen, C. and Cotton, W.R., 1983. A one-dimensional simulation of the stratocumulus-capped mixed layer, *Boundary-Layer Meteorology*, 25, 289-321.

Chen, C. and Cotton, W.R., 1987. The physics of the marine stratocumulus-capped mixed layer, *Journal of the Atmospheric Sciences*, 44, 2951-2977.

Cione, J.J. and Raman, S., 1995. A numerical investigation of surface-induced mesocyclogenesis near the Gulf Stream, *Tellus*, 47A, 815-833.

Clark, T.L., 1977. A small-scale dynamic model using a terrain-following co-ordinate transformation, *Journal of Computational Physics*, 24, 186-215.

Clark, T.L. and Farley, R.D., 1984. Severe downslope windstorm calculations in two and three spatial dimensions using anelastic interactive grid nesting: A possible mechanism for gustiness, *Journal of the Atmospheric Sciences*, 41, 329-350.

Cotton, W.R., Stephens, M.A., Nehrkorn, T. and Tripoli, G.J., 1982. The Colorado State University three-dimensional cloud/mesoscale model - 1982. Part II: An ice phase parameterization, *Journal de Recherches Atmosphériques*, 16, 295-320.

Cotton, W.R., Tripoli, G.J., Rauber, R.M. and Mulvihill, E.A., 1986. Numerical simulation of the effects of varying ice crystal nucleation rates and aggregation processes on orographic snowfall, *Journal of Climate and Applied Meteorology*, 25, 1658-1680.

Cotton, W.R., Tremback, C.J. and Walko, R.L., 1988. CSU RAMS - A cloud model goes regional, *Procedures of the NCAR Workshop on Limited-Area Modeling Intercomparison*, November 15-18, NCAR, Boulder, Colorado, 202-211.

Cotton, W.R., Thompson, G., and Mielke, P.W., 1994. Real-time mesoscale prediction on workstations, *Bulletin of the American Meteorological Society*, 75, 349-362.

Cram, J.M., 1990. Numerical simulation and analysis of the propagation of a prefrontal squall line, Unpublished Ph.D Thesis, Colorado State University, 330pp.

Cram, J.M., Pielke, R.A. and Cotton, W.R., 1992a. Numerical simulation and analysis of a prefrontal squall line. Part I: Observations and basic simulation results, *Journal of the Atmospheric Sciences*, 49, 189-208.

Cram, J.M., Pielke, R.A. and Cotton, W.R., 1992b. Numerical simulation and analysis of a prefrontal squall line. Part II: Propagation of the squall line as an internal gravity wave, *Journal of the Atmospheric Sciences*, 49, 209-225.

D'Abreton, P.C., 1993. The dynamics and energetics of tropical-temperate troughs over southern Africa, Unpublished Ph.D Thesis, University of the Witwatersrand, 231pp.

D'Abreton, P.C. and Lindesay, J.A., 1993. Water vapour transport over southern Africa during wet and dry early and late summer months, *International Journal of Climatology*, 13, 151-170.

D'Abreton, P.C. and Tyson, P.D., 1995. Divergent and non-divergent water vapour transport over southern Africa during wet and dry conditions, *Meteorology and Atmospheric Physics*, 55, 47-59.

D'Abreton, P.C., 1996. Lagrangian kinematic and isentropic trajectory models for aerosol and trace gas transport studies in Southern Africa. *South African Journal of Science*, 92, 157-160.

Davies, H.C., 1983. Limitations of some common lateral boundary schemes used in the regional NWP models, *Monthly Weather Review*, 111, 1002-1012.

De Wet, L.W., 1979. Die invloed van die Suid-Afrikaanse hoogland op die ontwikkeling en voortplanting van atmosferiese druk en sirkulasiestelsels, Unpublished M.Sc. Thesis, University of Pretoria, 79pp.

De Felice, P. and Viltard, A., 1976. Aerojet subtropical d'hiver et nuages associes. *La Meteorologie, Vie Serie*, 6, 223-225.

Diab, R.D., Preston-Whyte, R.A. and Washington, R., 1991. Distribution of rainfall by synoptic type over Natal, South Africa, *International Journal of Climatology*, **11**, 877-888.

Doyle, J.D., 1995. Coupled ocean wave/atmosphere mesoscale model simulations of cyclogenesis, *Tellus*, 47A, 766-778.

Downey, W.K., Tsuchiya, T. and Schreiner, A.J., 1981. Some aspects of a Northwestern Australian cloudband, *Australian Meteorological Magazine*, 29, 99-113.

Druyan, L.M. and Hastenrath, S., 1991. Modelling the differential impact of 1984 and 1950 sea-surface temperatures on Sahell rainfall, *International Journal of Climatology*, **11**, 367-380.

Dubief, J. and Queney, P., 1935. Les grands traits du climat du Sahara Algerien, *La Meteorologie*, 119, 80-91.

Dyer, T.G.J., 1979. Rainfall anomaly patterns over southern Africa, *Water SA*, 5, 39-43.

Dyer, T.G.J., 1982. On the intra-annual variation in rainfall over the sub-continent of southern Africa, *Journal of Climatology*, 2, 47-64.

Dyer, T.G.J. and Tyson, P.D., 1978. Inter-hemispheric associations in the year-to-year variations of the general circulation of the atmosphere: 1910-1963, *South African Journal of Science*, 74, 325-328.

Eliassen, A., 1978. The OECD study of long-range transport of air pollutants: Long-range transport modelling. *Atmospheric Environment*, 17, 479-487.

Eliassen, A., 1980. A review of longe-range transport modeling, *Journal of Applied Meteorology*, 19, 231-240.

Eliassen, A. and Palm. E., 1960. On the transfer of energy in stationary mountain waves, *Geofysiske Publikasjoner*, 22, 1-23.

Eliassen, A. and Saltbones, J., 1975. Decay and transformation rates for SO2,as estimated from emission data, trajectories and measured air concentrations. *Atmospheric Environment*, 9, 425-429.

Erasmus, D.A., 1980. The formulation of a classification procedure for specific use on cumulus cloud weather modification experiments, Unpublished M.Sc. Thesis, University of Cape Town, 143pp.

Erickson, C.O. and Winston, J.S., 1972. Tropical storms, mid-latitude cloudband connections and the autumnal buildup of the planetary circulation, *Journal of Applied Meteorology*, 11, 23-46.

Estié, K.E., 1981. The Lainsburg flood disaster of 25 January 1981, *South African Weather Bureau Newsletter*, 383, 19-32.

Flatau, P.J., Tripoli, G.J., Verlinde, J., and Cotton, W.R., 1989. The CSU-RAMS cloud microphysics module: general theory and code documentation, Atmospheric Science Paper No. 451, Colorado State University, 88pp.

Fourie, M., 1981. Weer van die Maand, *South African Weather Bureau News Letter*, No. 382, 76-79.

Fox-Rabinovitz, M.S., 1991. Computational dispersion properties of horizontal staggered grids for atmospheric and ocean models, *Monthly Weather Review*, 119, 1624-1639.

Gal-Chen, T. and Somerville, R.C.J., 1975a. On the use of a coordinate transformation for the solution of the Navier-Stokes Equations, *Journal of Computational Physics*, 17, 209-228.

Gal-Chen, T. and Somerville, R.C.J., 1975b. Numerical solution of the Navier-Stokes equations with topography, *Journal of Computational Physics*, 17, 267-310.

Garstang, M., Kelbe, B.E., Emmitt, G.D., London, W.B., 1987. Generation of convective storms over the escarpment of northeastern South Africa, *Monthly Weather Review*, 115, 429-443.

Garstang, M., Tyson, P.D., Swap, R., Edwards, M., Kållberg, P. and Lindesay, J.A. 1996. Horizontal and vertical transport of air over Southern Africa. *Journal of Geophysical Research, SAFARI Special Issue*.

Gates, D.M., 1980. *Biophysical Ecology*. Springer-Verlag, New York, 611pp.

Gillooly, J.F. and Walker, N.D., 1984. Spatial and temporal behaviour of sea-surface temperatures in the South Atlantic, *South African Journal of Science*, 80, 97-100.

Grasso, L.D., 1992. Tornado genesis, Unpublished M.Sc. Thesis, Colorado State University, 102pp.

Gray, T.I. and Clapp, P.F., 1978. An interaction between low- and high-latitude cloud bands recorded on GOES-I imagery, *Bulletin of the American Meteorological Society*, 59, 808-809.

Gründlingh, M.L., 1987. On the seasonal temperature variation in the southwestern Indian Ocean, *South African Geographical Journal*, 69, 129-138.

Gordon, H.B. and Hunt, B.G., 1991. Droughts, floods, and sea-surface temperature anomalies: a modelling approach, *International Journal of Climatology*, **11**, 347-365.

Hamilton, K. and Garcia, R.R., 1986. El Niño/Southern Oscillation events and their associated midlatitude teleconnections, *Bulletin of the American Meteorological Society*, 67, 1354-1361.

Harangozo, S. and Harrison, M.S.J., 1983. On the use of synoptic data in indicating the presence of cloud bands over southern Africa, *South African Journal of Science*, 79, 413-414.

Harangozo, S., 1989. Circulation characteristics of some South African rainfall systems, Unpublished Msc Dissertation, University of the Witwatersrand, 123pp.

Harrison, M.S.J., 1983a. Rain day frequency and mean daily rainfall intensity as determinants of total rainfall over the eastern Orange Free State, *Journal of Climatology*, 3, 35-45.

Harrison, M.S.J., 1983b. The Southern Oscillation, zonal equatorial circulation cells and South African rainfall, *Preprints of the 1st International Conference on Southern Hemisphere Meteorology*, American Meteorological Society, 302-305.

Harrison, M.S.J., 1984a. A generalised classification of South African summer rain-bearing synoptic systems, *Journal of Climatology*, 4, 547-560.

Harrison, M.S.J., 1984b. The annual rainfall cycle over the central interior of South Africa, *South African Geographical Journal*, 66, 47-74.

Harrison, M.S.J., 1984c. Note on the origins of the dry zone of the Limpopo valley. *South African Journal of Science*, 80, 333-334.

Harrison, M.S.J., 1986a. A synoptic climatology of South African rainfall variations, Unpublished PhD Thesis, University of the Witwatersrand, 341pp.

Harrison, M.S.J., 1986b. Verification of the Eliassen-Palm relationship over southern Africa, *Preprints of the 2nd International Conference on Southern Hemisphere Meteorology*, American Meteorological Society, 283-286.

Harrison, M.S.J., 1993. Elevated inversions over southern Africa: climatological properties and relationships with rainfall, *South African Geographic Journal*, 75, 1-8.

Harrison, M.S.J. and Theron, G.F., 1991. Kinematic properties of the mean circulation over southern Africa, *Theoretical and Applied Climatology*, 43, 75-89.

Hastenrath, S.L., 1966. The flux of atmospheric water vapor over the Caribbean Sea and the Gulf of Mexico, *Journal of Applied Meteorology*, 5, 778-788.

Hastenrath, S.L. and Lamb, P.J., 1979. *Climatic Atlas of the Indian Ocean. Part I: Surface Climate and Atmospheric Circulation*. University of Wiscosin Press. 117pp.

Hastenrath, S., 1984. Inter-annual variability and annual cycle: mechanisms of circulation and climate in the tropical Atlantic sector, *Monthly Weather Review*, **112**, 1097-1107.

Hastenrath, S., 1985. *Climate and Circulation of the Tropics*, D. Reidel, Dordrecht, 455pp.

Hastenrath, S., Greischar, L. and van Heerden, J., 1995. Prediction of the summer rainfall over South Africa, *Journal of Climate*, 8, 1511-1518.

Henning, D., 1989. *Atlas of the Surface Heat Balance of the Continents.* Gebruder Borntraeger, Berlin. 402pp.

Hirst, A.C. and Hastenrath, S., 1983a. Atmosphere-ocean mechanisms of climate anomalies in the Angola-tropical Atlantic sector, *Journal of Physical Oceanography*, 13, 1146-1157.

Hirst, A.C. and Hastenrath, S., 1983b. Diagnostics of hydrometerological anomalies in the Zaïre (Congo) Basin, *Quarterly Journal of the Royal Meteorological Society*, 109, 881-892.

Hofmeyr, W.L. and Gouws, V., 1964. A statistical and synoptic analysis of wet and dry conditions in the northwestern Transvaal, *Notos*, 13, 37-48.

Horel, J.D. and Wallace, J.M., 1981. Planetary-scale atmospheric phenomena associated with the Southern Oscillation, *Monthly Weather Review*, 109, 813-829.

Hutchings, J.W., 1961. Water vapour transfer over the Australian continent, *Journal of Meteorology*, 18, 615-624.

Hunt, H.A., Taylor, G. and Qualye, E.T., 1913. The climate and weather of Australia, *Bureau of Meterology*, Melbourne.

Jackson, S.P., 1961. *Climatological Atlas of Africa*, CCTA/CSA, Nairobi, 55 plates.

James, I.N. and Anderson, D.L.T., 1984. The seasonal mean flow and distribution of large scale weather systems in the Southern Hemisphere: the effects of moisture transports, *Quarterly Journal of the Royal Meteorological Society*, 110, 943-966.

Janjic, T.Z. and Janjic, Z.I., 1993. Spectral distributions of the pressure gradient force errors in σ-coordinate spectral and grid-point models in an idealized case, *Meteorology and Atmospheric Physics*, 52, 129-135.

Johnson, D.R., Townsend, R.D. and Wei, M-Y., 1985. The thermally coupled response of the planetary scale circulation to the global distribution of heat sources and sinks, *Tellus*, 37A, 106-125.

Jury, M.R. and Reason, C.J.C., 1989. Extreme subsidence in the Agulhus-Benguela air mass transition, *Boundary-Layer Meteorology*, 46, 35-51.

Jury, M.R. and Lindesay, J.A., 1991. Atmospheric circulation controls and characteristics of a flood event in central South Africa, *Journal of Climatology*, 11, 609-627.

Jury, M.R. and Pathack, B., 1991. A study of climate and weather variability over the tropical southwest Indian Ocean, *Meteorology and Atmospheric Physics*, 47, 37-48.

Jury, M.R., Pathack, B., Campbell, G., Wang, B. and Landman, W., 1991. Transient convective waves in the tropical southwest Indian Ocean, *Meteorology and Atmospheric Physics*, 47, 27- 36.

Jury, M.R., Pathack, B. and Sohn, B.J., 1992. Spatial structure and interannual variability of summer convection over southern Africa and the SW Indian Ocean, *South African Journal of Science*, 88, 275-280.

Jury, M.R., 1993. A thermal front within the marine atmospheric boundary layer over the Agulhus Current south of Africa: Composite aircraft observations, *Journal of Geophysical Research*, 99 C2, 3297-3304.

Jury, M.R. and Pathack, B., 1993. Composite climatic patterns associated with extreme modes of summer rainfall over southern Africa: 1975-1984, *Theoretical and Applied Climatology*, 47, 137-145.

Jury, M.R., Lindesay, J.A. and Wittmeyer, I., 1993. Flood episodes in central South Africa from satellite and ECMWF data, *South African Journal of Science*, 89, 263-269.

Jury, M.R. and Lyons, S.W., 1994. Contrasting synoptic weather events over southern Africa in the dry summer of 1983, *South African Geographical Journal*, 76, 6-10

Jury, M.R., 1996. Regional teleconnection patterns associated with summer rainfall over South Africa, Namibia and Zimbabwe, *International Journal of Climatology*, 16, 135-153.

Kalnay, E. and Paegle, J., 1983. Large amplitude stationary Rossby waves in the Southern Hemisphere: observations and theory, *Preprints of the 1st International Conference on Southern Hemisphere Meteorology*, American Meteorological Society, 89-92.

Kershaw, R., 1988. The effect of a sea surface temperature anomaly on a prediction of the onset of the south-west monsoon over India, *Quarterly Journal of the Royal Meteorological Society*, 114, 325-345.

Kelbe,B., 1988. Features of westerly waves propagating over southern Africa during summer, *Monthly Weather Review*, 116, 60-70.

Kiladis, G.N. and Diaz, H.F., 1986. An analysis of the 1977-78 ENSO episode and comparison with 1982-83, *Monthly Weather Review*, 114, 1035-1047.

Klemp, J.B. and Wilhelmson, R.B., 1978a. The simulation of three-dimensional convective storm dynamics, *Journal of the Atmospheric Sciences*, 35, 1070-1096.

Klemp, J.B. and Wilhelmson, R.B., 1978b. Simulations of right- and left-moving storms produced through storm-splitting, *Journal of the Atmospheric Sciences*, 35, 1097-1110.

Kousky, V.E., 1979. Frontal influences on northeast Brazil, *Monthly Weather Review*, 107, 1140-1153.

Kousky, V.E., Gan, M.A. and Virji, H., 1983. Low latitude upper troposphere cyclonic vortices in the South Atlantic: Their origin, characteristics and effects on tropical convection over eastern Brazil, *Preprints of the 1st International Conference on Southern Hemisphere Meteorology*, American Meteorological Society, 221-223.

Kriel, J.P., 1983. Atmosferiese waterdamptransport oor Suid-Afrika in verhouding tot die reënval en die benutbare waterbronne: ñ voorlopige raming, Unpublished Water Research Commission Report, Pretoria, 55pp.

Krishnamurti, T.N., Fuelberg, H.E., Sinha, M.C., Oosterhof, D., Bensman, E.L., and Kumar, V.B., 1993. The meteorological environment of the tropospheric ozone maximum over the tropical South Atlantic Ocean, *Journal of Geophysical Research*,98, 10621-10641.

Kuhnel, I., 1989. Tropical-extratropical cloudband climatology based on satellite data, *International Journal of Climatology*, 9, 441-463.

Kuhnel, I., 1990. Tropical-extratropical cloudbands in the Australian region, *International Journal of Climatology*, 10, 341-364.

Kumar, S., 1978. Interaction of Upper Westerly Waves with the Intertropical Convergence Zone and their effect on the Weather over Zambia During the Rainy Season, Government Printer, Lusaka, 36pp.

Kuo, H.L., 1965. On the formation and intensification of tropical cyclones through latent heat release by cumulus convection, *Journal of the Atmospheric Sciences*, 22, 40-63.

Kuo, H.L., 1974. Further studies of the parameterization of the influence of cumulus convection on the large-scale flow, *Journal of the Atmospheric Sciences*, 31, 1232-1240.

Lindesay, J.A., Harrison, M.S.J. and Haffner, M.P., 1986. The Southern Oscillation and South African rainfall, *South African Journal of Science*, **82**, 196-198.

Lindesay, J.A. and Harrison, M.S.J., 1986. The Southern Oscillation and flow fields over southern Africa, *Preprints of the 2nd International Conference on Southern Hemisphere Meteorology*, American Meteorological Society, 457-460.

Lindesay, J.A., 1988a. The Southern Oscillation and atmospheric circulation changes over southern Africa, Unpublished PhD Thesis, University of the Witwatersrand, 284pp.

Lindesay, J.A., 1988b. South African rainfall, the Southern Oscillation and a Southern Hemisphere semi-annual cycle, *Journal of Climatology*, **8**, 17-30.

Lindesay, J.A. and Vogel, C.H., 1990. Historical evidence for Southern Oscillation-southern African rainfall relationships, *International Journal of Climatology*, **10**, 679-689.

Lindesay, J.A. and Jury, M.R., 1991. Atmospheric circulation controls and characteristics of a flood event in central South Africa, *International Journal of Climatology*, **11**, 609-627.

Lindesay, J.A., 1993. Present climates of southern Africa, in *Southern Hemisphere Climates: Present, Past and Future*, Ed. Hobbs, J.E., Belhaven Press, London, in press.

Longley, R.W., 1976. Weather and weather maps of South Africa, *South African Weather Bureau Technical Paper*, No. 3, 76pp.

Lyons, S.W., 1991. Origins of convective variability over equatorial southern Africa during summer, *Journal of Climate*, 4, 23-39.

Mahrer, Y. and Pielke, R.A., 1977. A numerical study of the airflow over irregular terrain, *Beiträge zur Physik der Atmosphäre*, 50, 98-113.

Manton, M.J. and Cotton, W.R., 1977. Parameterization of the atmospheric surface layer, *Journal of Atmospheric Sciences*, 34, 331-334.

Mason, S.J., 1990. Temporal variability of sea surface temperatures around southern Africa: a possible forcing mechanism for the 18-year rainfall oscillation?, *South African Journal of Science*, 86, 243-252.

Mason, S.J., 1992. Sea surface temperatures and South African rainfall variability. Unpublished Ph.D. Thesis, University of the Witwatersrand. 235pp.

Mason, S.J., 1995. Sea-surface temperature - South African rainfall associations, 1910-1989, *International Journal of Climatology*, 15, 119-135.

Mason, S.J. and Tyson, P.D., 1992. The modulation of sea surface temperature and rainfall associations over southern Africa with solar activity and the Quasi-Biennial Oscillation, *Journal of Geophysical Research*, 97 D5, 5847-5856.

Mason, S.J. and Lindesay, J.A., 1993. A note on the modulation of Southern Oscillation-southern African associations with the Quasi-Biennial Oscillation, *Journal of Geophysical Research*, 98 D5, 8847-8850.

Mason, S.J., Lindesay, J.A. and Tyson, P.D., 1994. Simulating drought in southern Africa using sea surface temperature variations, *Water SA*, 20, 15-22.

Mason, S.J. and Jury, M.R., 1996. Climatic varaibility and change over southern Africa: a reflection on underlying processes, *Progress in Physical Geography*, (in press).

Matarira, C.H. and Jury, M.R., 1992. Contrasting meteorological structure of intra-seasonal wet and dry spells in Zimbabwe, *International Journal of Climatology*, 12, 165-176.

McCumber, M.C. and Pielke, R.A., 1981. Simulation of the effects of surface fluxes of heat and moisture in a mesoscale numerical model, *Journal of Geophysical Research*, 86 C10, 9929-9938.

McGee, O.S., 1970. Wind and humidity conditions over Durban during 1967, *South African Geographical Journal*, 52, 44-57.

McGuirk, J.P., Thompson, A.H. and Smith, N.R., 1987. Moisture bursts over the tropical Pacific Ocean, *Monthly Weather Review*, 115, 787-798.

Mechoso, C.R., 1981. Topographical influences on the general circulation of the southern hemisphere: a numerical experiment, *Monthly Weather Review*, 109, 2131-2139.

Mechoso, C.R., Kitoh, A., Moorthi, S. and Arakawa, A., 1987. Numerical simulations of the atmospheric response to a sea surface temperature anomaly over the equatorial eastern Pacific Ocean, *Monthly Weather Review*, 115, 2936-2956.

Meehl, G.A., 1988. Tropical-midlatitude interactions in the Indian and Pacific sectors of the Southern Hemisphere, *Monthly Weather Review*, 116, 472-484.

Mesinger, F. and Arakawa, A., 1976. Numerical methods used in atmospheric models, GARP Publication Series No. 17, WMO/ICSU Joint Organising Committee, 64pp.

Mesinger, J., Janjic, Z.I., Nickovic, S., Gavrilov, D. and Deaven, D.G., 1988. The step-mountain co-ordinate: model description and performance for cases of Alpine lee cyclogenesis and for a case of an Appalachian redevelopment, *Monthly Weather Review*, **116**, 1493-1518.

Mey, R.D., Walker, N.D. and Jury, M.R., 1990. Surface heat fluxes and marine boundary layer modification in the Agulhus retroflection region, *Journal of Geophysical Research*, **95 C9**, 15 997-16 015.

Meyers, M.P., 1989. An evaluation of the factors affecting wintertime quantitative precipitation forecasts in an explicit cloud model over mountainous terrain, Unpublished M.Sc. Thesis, Colorado State University, 120pp.

Meyers, M.P. and Cotton, W.R., 1992. Evaluation of the potential for wintertime quantitative precipitation forecasting over mountainous terrain with an explicit cloud model. Part I: Two-dimensional sensitivity experiments, *Journal of Applied Meteorology*, 31, 26-50.

Miron, O. and Lindesay, J.A., 1983. A note on changes in airflow patterns between wet and dry spells over South Africa, 1963 to 1979, *South African Geographical Journal*, 65, 141-147.

Miron, O. and Tyson, P.D., 1984. Wet and dry conditions and pressure anomaly fields over South Africa and the adjacent oceans, 1963-79, *Monthly Weather Review*, **112**, 2127-2132.

Mo, K.C. and Kalnay, E., 1991. Impact of sea surface temperature anomalies on the skill of monthly forecasts, *Monthly Weather Review*, 119, 2771-2793.

Mo, K.C., Wang, X.L., and Tracton, M.S., 1994. Tropical and extratropical interaction and its impact on extended-range forecasting. Part I: the impact of sea surface temperature anomalies, *Monthly Weather Review*, **122**, 274-290.

Newell, R.E., 1979. Climate and the ocean, *American Scientist*, 67, 405–416.

Nicholson, S.E., 1986. The spatial coherence of African rainfall anomalies: interhemispheric teleconnections, *Journal of Climate and Applied Meteorology*, 25, 1365-1381.

Nicholson, S.E. and Entekhabi, D., 1986. The quasi-periodic behaviour of rainfall variability in Africa and its relationship to the Southern Oscillation, *Archiv fur Meteorologie, Geophysik und Bioklimatologie, Ser. A.*, 34, 311-348.

Nicholson, S.E. and Entekhabi, D., 1987. Rainfall variability in equatorial and southern Africa: relationships with sea surface temperatures along the southwestern coast of Africa, *Journal of Climate and Applied Meteorology*, 26, 561-578.

Nicholson, S.E., Kim, J. and Hoopingarner, J., 1988. *Atlas of African Rainfall and its Interannual Variability*, Department of Meteorology, The Florida State University, Tallahassee, 237pp.

Paegle, J.N., Lewis, F.P. and Paegle, J., 1983. Observed and modelled long wave patterns of the Southern Hemisphere, *Preprints of the 1st International Conference on Southern Hemisphere Meteorology*, American Meteorology Society, 37-40.

Paegle, J.N and Kalnay, E., 1983. Large amplitude stationary Rossby waves in the Southern Hemisphere: observations and theory, *Reprints of the 1st International Conference on Southern Hemisphere Meteorology*, American Meteorological Society, 89-92.

Palmén, E. and Newton, C.W., 1969. *Atmospheric Circulation Systems: their Structure and Physical Interpretation*, Academic Press, London, 603pp.

Parker, D.E., 1987. The Meteorological Office historical sea-surface temperature data set, *Meteorological Magazine*, 116, 250-254.

Parker, D.E. and Folland, C.K., 1988. The Meteorological Office historical sea surface temperature data set, in *Recent Climatic Change*, Ed. Gregory, S., Belhaven Press, London, 41-50.

Parsons, D.B. and Hobbs, P.V., 1983. The mesoscale and microscale structure and organisation of clouds and precipitation in midlatitude cyclones, IX: Some effects of orography on rainbands, *Journal of Atmospheric Science*, 40, 1930-1949.

Perkey, D.J. and Kreitzberg, C.W., 1976. A time-dependent lateral boundary scheme for limited-area primitive equation models, *Monthly Weather Review*, 104, 744-755.

Physick, W.L., Abbs, D.J., and Pielke, R.A., 1989. Formulation of the thermal internal boundary layer in a mesoscale model, *Boundary-Layer Meteorology*, 49, 99-111.

Pielke, R.A., 1974. A three-dimensional numerical model of the sea breezes over south Florida, *Monthly Weather Review*, 102, 115-139.

Pielke, R.A., Cotton, W.R., Walko, R.L., Tremback, C.J., Lyons, W.A., Grasso, L.D., Nicholls, M.E., Moran, M.D., Wesely, D.A., Lee, T.J. and Copeland, J.H., 1992. A comprehensive meteorological modelling system - RAMS, *Meteorology and Atmospheric Physics*, 49, 69-91.

Preston-Whyte, R.A. and Tyson, P.D., 1988. *The Atmosphere and Weather of Southern Africa*, Oxford University Press, Cape Town, 374pp.

Preston-Whyte, R.A., Diab, R.D. and Washington, R., 1991. Diurnal variation of rainfall events by synoptic type in Natal, *South African Geographical Journal*, 73, 22-28.

Raschke, E. and Bandeen, W.R., 1967. A quasi-global analysis of tropospheric water vapour content from TIROS IV radiation data, *Journal of Applied Meteorology*, 6, 468-481.

Rathor, H.S., De Araujo, M.A. and De Mello, C.C., 1989. The divergence of water vapor flux during a typical rainy month over north-east Brazil, *Preprints of the 3rd International Conference on Southern hemisphere Meteorology and Oceanography*. American Meterological Society, 134-142

Riehl, H., 1979. *Climate and Weather in the Tropics*, Academic Press, London, 611pp.

Rind, D. and Rossow, W.B., 1984. The effects of physical processes on the Hadley circulation, *Journal of the Atmospheric Sciences*, 41, 479-507.

Rouault, M. and Lutjeharms, J.R.E., 1994. Air-sea interaction in the marine atmospheric boundary layer: a new South African research venture, *South African Journal of Science*, 90, 11-12.

Sadler, J.C., 1968. Average cloudiness in the tropics from satellite observations, *International Indian Ocean Expedition Meteorological Monographs No. 2*, East-West Center Press, University of Hawaii, 5-7.

Schulze, B.R., 1972. Climate of South Africa: Part 8: General Survey. WB28. *South African Weather Bureau*, 330pp.

Sellers, W.D., 1965. *Physical Climatology*, The University of Chicago Press, Chicago & London, 272pp.

Shannon, L.V., 1985. The Benguela ecosystem. Part 1. Evolution of the Benguela, physical features and processes, *Annual Review of Oceanography and Marine Biology*, 23, 105-182.

Smagorinsky, J., 1963. General circulation experiments with the primitive equations. I. The basic experiment, *Monthly Weather Review*, 91, 99-164.

Soden, B.J. and Bretherton, F.P., 1994. Evaluation of water vapour distribution in general circulation models using satellite observations, *Journal of Geophysical Research*, 99 **D1**, 1187-1210.

Sonka, S.T., Lamb, P.J., Hollinger, S.E. and Mjelde, J.W., 1986. Economic use of weather and climate information: concepts and an agricultural example, *Journal of Climatology*, 6, 447-457.

Snook, J.S., Cram, J.M. and Schmidt, J.M., 1995. LAPS/RAMS. A nonhydrostatic mesoscale numerical modeling system cinfigured for operational use, *Tellus*, 47A, 864-875.

Stoeckenius, T., 1981. Interannual variations of tropical precipitation patterns, *Monthly Weather Review*, 109, 1233-1247.

Streten, N.A., 1968. A note on multiple image photo-mosaics for the Southern Hemisphere, *Australian Meteorological Magazine*, 18, 31-37.

Streten, N.A., 1973. Some characteristics of satellite-observed bands of persistent cloudiness over the Southern Hemisphere, *Monthly Weather Review*, **101**, 486-495.

Streten, N.A., 1980. Some synoptic indices of the southern hemisphere mean sea level circulation 1972-77, *Monthly Weather Review*, 108, 18-36.

Taljaard, J.J., 1953. The mean circulation in the lower troposphere over southern Africa, *South African Geographic Journal*, 35, 33-45.

Taljaard, J.J., 1959. South African air-masses: their properties, movement and associated weather, Unpublished Ph.D Theses, University of the Witwatersrand, 221pp.

Taljaard, J.J., 1972. Synoptic meteorology of the Southern Hemisphere, in *Meteorology of the Southern Hemisphere*, Ed. Newton, C.W., Meteorological Monographs 35, American Meteorological Society, Boston, 139-213.

Taljaard, J.J., 1981. The anomalous climate and weather systems of January to March 1974, *South African Weather Bureau Technical Paper*, No. 10, 94pp.

Taljaard, J.J., 1982. The March maximum of the rainfall over the western plateau of southern Africa, *South African Weather Bureau Newsletter*, 397, 51-53.

Taljaard, J.J., 1985. Cut-off lows in the South African region, *South African Weather Bureau Technical Paper*, No. 14, 153pp.

Taljaard, J.J., 1986a. Change of rainfall distribution and circulation patterns over southern Africa in summer, *Journal of Climatology*, 6, 579-592.

Taljaard, J.J., 1986b. Contrasting atmospheric circulation during dry and wet summers in South Africa, *South African Weather Bureau News Letter*. No. 445, 1-5.

Taljaard, J.J., 1989. Climate and circulation anomalies in the South African region during the dry summer of 1982/83, *South African Weather Bureau Technical Paper*, No. 21, 45pp.

Taljaard, J.J., 1990. The cloud bands of southern Africa, *South African Weather Bureau Newsletter*, 493, 6-8.

Tapp, R.G. and Barrell, S.L., 1984. The north-west Australian cloud band: climatology, characteristics and factors associated with development, *Journal of Climatology*, 4, 411-424.

Thepenier, R.M., 1981. Etude climatologique des bandes nuageuses pour l'ensemble de l' Hemisphere Nord, *La Meteorologie*, *Vie Serie*, 25, 61-68.

Theron, G.F. and Harrison, M.S.J., 1990. Thermodynamic properties of the mean circulation over southern Africa, *Theoretical and Applied Climatology*, 43, 75-89.

Thompson, G., 1993. Prototype real-time mesoscale prediction during the 1991-92 winter season and statistical verification of model data, Unpublished Msc Dissertation, Colorado State University, 105pp.

Torrance, J.D., 1972. Malawi, Rhodesia and Zambia, in *Climates of Africa*, Ed. Griffiths, J.F., World Survey of Climatology, Vol. 10, Elsevier, Amsterdam, 409-460.

Torrance, J.D., 1979. Upper windflow patterns in relation to rainfall in south-east central Africa, *Weather*, 34, 106-115.

Tremback, C.J., Tripoli, G.J. and Cotton, W.R., 1985. A Regional Atmospheric Modelling System, in *Proceedings of the International Conference on the Development and Application of Computer Techniques to Environmental Studies*, Ed. Zannetti, P., Computational Mechanics Publications, Boston, 601-607.

Tremback, C.J. and Kessler, R., 1985. A surface temperature and moisture parameterisation for use in mesoscale numerical models, Reprints of the 7th Conference of the American Meteorlogical Society, Boston, 355-358.

Tremback, C.J., Tripoli, G.J., Arritt, R., Cotton, W.R. and Pielke, R.A., 1986. The Regional Atmospheric Modelling System, in *Proceedings of the International Conference on the Development and Application of Computer Techniques to Environmental Studies*, Ed. Zannetti, P., Computational Mechanics Publications, Boston, 601-607.

Tremback, C.J., 1990. Numerical simulation of a mesoscale convective complex: model development and numerical results, Unpublished Ph.D Thesis, Colorado State University, 247pp.

Trenberth, K.E., 1980. Planetary waves at 500-mb in the Southern Hemisphere. *Monthly Weather Review*, 108, 1378-1389.

Triegaardt, D.O. and Kits, A., 1963. Die drukveld by verskillende vlakke oor suidelike Afrika en aangrensende oseane tydens vyfdaagse reën en droë periodes in suid-Transvaal en noord-Vrystaat gedurende die 1960-1961 somer, *South African Weather Bureau Newsletter*, 168, 37-43.

Triegaardt, D.O., 1989. Hemispheric long wave patterns during the periods 26 October to 5 November and 18 to 31 December 1989, *South African Weather Bureau Newsletter*, 489, 2-4.

Triegaardt, D.O., Van Heerden, J. and Steyn, P.C.L., 1991. Anomalous precipitation and floods during February 1988, *South African Weather Bureau Technical Paper*, No. 23, 53pp.

Triploi, G.J. and Cotton, W.R., 1980. A numerical investigation of several factors leading to the observed variable intensity of deep convection over South Florida, *Journal of Applied Meteorology*, 19, 1037-1063.

Tripoli, G.J. and Cotton, W.R., 1982. The Colorado State University three-dimensional cloud/mesoscale model - 1982. Part I: general theoretical framework and sensitivity experiments, *Journal de Atmosphériques*, 16, 185-219.

Tyson, P.D., 1964. Berg winds of South Africa, *Weather*, 19, 7-11.

Tyson, P.D., Dyer, T.G.J. and Mametse, M.N., 1975. Secular changes in South African rainfall: 1880 to 1972, *Quarterly Journal of the Royal Meteorological Society*, 101, 817-833.

Tyson, P.D. and Dyer, T.G.J., 1978. The predicted above-normal rainfall of the seventies and the likelihood of droughts in the eighties in South Africa. *South African Journal of Science*, 74, 372-377.

Tyson, P.D. and Dyer, T.G.J., 1980. The likelihood of droughts in the eighties in South Africa, *South African Journal of Science*, 76, 340-341.

Tyson, P.D., 1981. Atmospheric circulation variations and the occurrence of extended wet and dry spells over southern Africa, *Journal of Climatology*, **1**, 115-131.

Tyson, P.D., 1984. The atmospheric modulation of extended wet and dry spells over South Africa, 1958-1978, *Journal of Climatology*, 4, 621-635.

Tyson, P.D, 1986. *Climatic Change and Variability in Southern Africa*, Oxford University Press, Cape Town, 220pp.

Tyson, P.D., Garstang, M., Swap, R., Kållberg, P. and Edwards, M., 1996a. An air transport climatology for subtropical Southern Africa. *International Journal of Climatology*, In press.

Tyson, P.D., Garstang, M. and Swap, R., 1996b. Large-scale recirculation of air over Southern Africa, *Journal of Applied Meteorology*, Submitted.

United States Department of Commerce, Key to Meteorological Records Documentation No. 5.4, *Environmental Satellite Imagery*, 1980 and 1981.

van Loon, H., 1972. Pressure in the Southern Hemisphere, in *Meteorology of the Southern Hemisphere*, Ed. Newton, C.W., Meteorological Monographs 35, American Meteorological Society, Boston, 59-86.

Vianello, R.L., 1985. Vertical velocity forced by topography in the Southern Hemisphere. *Journal of Climatology*, 5, 213-219.

Vincent, D.G., 1982. Circulation features over the South Pacific during 10-18 January 1979; *Monthly Weather Review*, 110, 981-993.

Virji, H. and Kousky, V.E., 1983. Regional and global aspects of a low latitude frontal penetration in Amazonas and associated tropical activity, *Preprints of the 1st International Conference on Southern Hemisphere Meteorology*, American Meteorology Society, 215-220.

Vonder Haar, T.H., 1968. Variations of the Earth's radiation budget in Meteorological satellite instrumentation and data processing, *Final Report, Contract NASW-65, 1958-68, Department of Meteorology*, University of Wisconsin, 179pp.

Vowinckel, E., 1955. Southern Hemisphere weather map analysis: five year mean pressures, *Notos*, 4, 17-50.

Vowinckel, E., 1956. Ein Beitrag zur Witteringsklimatologie des suedlichen Mozambiquekanals. Miscelanea Geofisica Publicada Pelo Servico Meteorologico de Angola em Comemoracao do X Aniversario do Servico Meteorologico Nacional, Luanda, 63-86.

Walker, N.D., 1989. Sea surface temperature-rainfall relationships and associated ocean-atmosphere coupling mechanisms in the southern African region, Unpublished Ph.D Thesis, University of Cape Town, 171pp.

Walker, N.D. and Lindesay, J.A., 1989. Preliminary observations of oceanic influences of the February-March 1988 floods in central South Africa, *South African Journal of Science*, 85, 164-169.

Walker, N.D., 1990. Links between South African summer rainfall and temperature variability of the Agulhas and Benguela Current Systems, *Journal of Geophysical Research*, 95 C3, 3297-3319.

Walko, R.L. and Tremback, C.J., 1991. RAMS. The Regional Atmospheric Atmospheric Modelling System Version 2C, User's Guide , ASTeR Inc., Fort Collins, 89pp.

Webster, P.J., 1972. Response of the tropical atmosphere to local, steady forcing, *Monthly Weather Review*, 100, 518-541.

Webster, P.J., 1983. The large-scale structure of the tropical atmosphere, in *Large-Scale Dynamical Processes in the Atmosphere*, Eds Hoskins, B.J. and Pearce, R.P., Academic Press, London, 235-275.

Webster, P.J. and Curtin, D.G., 1975. Interpretations of the EOLE experiment II. Spatial variation of transient and stationary modes, *Journal of the Atmospheric Sciences*, 32, 1848-1863.

Webster, P.J. and Holton, J.R., 1982. Cross-equatorial response to middle-latitude forcing in a zonally-varying basic state, *Journal of the Atmospheric Sciences*, 39, 722-733.

Whitaker, R.N., 1981. Sea surface temperatures around Australia 1978, Meteorological Note 117, Bureau of Meteorology, Melbourne, 13pp. .

Wright, W.J., 1988. The low latitude influence on winter rainfall in Victoria, south-eastern Australia - I. Climatological aspects, *Journal of Climatology*, 8, 437-462.

Yasunari, T., 1977. Stationary waves in the Southern Hemisphere mid-latitude zone revealed from average brightness charts, *Journal of the Meteorological Society of Japan*, 55, 274-285.

Zhang, D.-L., 1985. Meso-β scale structure and evolution of the Johnstone Flood of July 1977 using a two-way nested grid. Unpublished Ph.D Thesis. The Pennsylvania State University.

Zillman, J.W. and Johnson, D.R., 1985. Thermally-forced mean mass circulations in the Southern Hemisphere, *Tellus*, 37A, 56-76.

Zwatz-Meise, W. and Hailzl, G., 1980. Interpretation of so-called shear bands in satellite images, *Archiv fur Meteorologie, Geophysik und Bioklimatologie, Ser. B*, 28, 299-315.